

Qualitative and quantitative spectral characterisation of iron- and steelworks by-products - Combining information from the visible light to the longwave infrared

Dissertation

zur Erlangung des
Doktorgrades der Naturwissenschaften (Dr. rer. nat.)

der

Naturwissenschaftlichen Fakultät III
Agrar- und Ernährungswissenschaften,
Geowissenschaften und Informatik

der Martin-Luther-Universität Halle-Wittenberg

vorgelegt von

Dipl.-Geogr. Denk, Michael

geb. am 14.08.1983 in Halle (Saale)

Gutachter:

1. Prof. Dr. C. Gläßer
2. Assist. Prof. Dr. C.A. Hecker

Tag der Verteidigung: Halle (Saale), 02. Juli 2018

Acknowledgement

This thesis developed at the Department of Remote Sensing and Cartography at the Institute of Geosciences and Geography at the Martin Luther University Halle-Wittenberg. I would like to express my gratitude to Prof. Dr. C. Gläßer for encouraging me to work on this topic, for supervising this thesis and for reducing the workload in the last months. Furthermore, she enabled me to participate in various national and international conferences to present the results of my work in several oral and poster presentations. Additionally, she supported me to partake in a bilateral exchange project funded by the German Academic Exchange Service and the Research Council of Norway through a DAAD PPP programme (project 225192).

Parts of the works leading to the results presented in this thesis were embedded within the project REStrateGIS. This project was funded by the German Federal Ministry of Education and Research (BMBF, funding code 033R103B) and embedded within the r³-initiative (<http://www.r3-innovation.de>) and the BMBF framework programme “Research for Sustainable Development – FONa”. The members of the REStrateGIS consortium cooperatively conducted the major sampling campaigns. I profited from the profound work of the Fraunhofer Institute for Environmental, Safety, and Energy Technology (UMSICHT) in Oberhausen on the history of the test site. Here, I want to particularly thank A. Mrotzek-Blöß, M. Jandewerth and J. Nühlen. Sample preparation and the chemical and mineralogical analyses were carried out by FEhS - Building Materials Institute (Institut für Baustoff-Forschung e. V., Duisburg). The enlightening discussions with Dr. P. Drissen, Dr. D. Mudersbach and D. Algermissen as well as their helpful feedback on the manuscript are greatly acknowledged.

Special thanks go to the Stahlwerk Thüringen GmbH for providing access to the dump site, archive materials and for logistical support during the field campaigns. In particular, U. Tinz and M. Michele-Naussed are thanked for common test site visits, numerous discussions, and profound explanations of the history of iron- and steelmaking in Unterwellenborn.

The spectral analyses in this thesis were partly conducted utilising the software DISPEC, which was developed by Dr. H.M.A. van der Werff and kindly provided by Dr. C.A. Hecker from the Faculty of Geo-Information Science and Earth Observation (ITC) of the University of Twente.

Further thanks go to the staff members of the geographical and geological laboratories of the Institute of Geosciences and Geography for enabling me to use the equipment required for sample preparation. Parts of the utilised R script for calculating the PLSR models are based on a code written by F. Beyer. SphereOptics GmbH provided the handheld FTIR spectrometer and H.-J. Fischer and Dr. A. Eisele are thanked for helpful information on the instrument.

G. Meißner, H. Kollai, B. Gaberle as well as Dr. T.H. Kurz and Dr. S.J. Buckley, and particularly D. Schwefel, immensely supported the sample collection and other field work. The fruitful discussions with Dr. T. Jarmer helped to improve the thesis.

Vera, Heike, Frank, Mike, Henning, Patrick, Karl, Danilo and D. Kley supported me technically as well as morally through all the ups and downs during the last months. Particularly, I am thankful to Vera for checking the references, to Mike for feedback on several chapters, to both for taking over some of my tasks and to Frank for his R support and many professional as well as joyful discussions. My family provided steady support, encouragement, understanding of my absence. Anette's help is greatly appreciated. My greatest thank goes to Ally for her enormous patience, encouraging and supporting me, the private R sessions and for proof-reading.

Wholehearted thanks to all of you and everybody whom I forgot to mention in these few lines!

Table of Contents

List of Figures	vii
List of Tables	xi
List of Appendices	xiii
Glossary.....	xvi
Abstract (English).....	xix
Abstract (German)	xxi
1. Introduction.....	1
1.1 Background and Motivation - Exploration of Anthropogenic Deposits	1
1.2 Objectives, Scope and Research Questions	4
1.3 Structure of this Work	5
2. Background Information and State of Research	6
2.1 Iron- and Steelmaking Processes, By-Products and their Properties	6
2.1.1 Major Iron- and Steelmaking Processes and By-Products	6
2.1.2 Types, Chemical Composition and Utilisation of Iron- and Steelworks By-Products...	12
2.1.3 Mineralogical Composition of Iron- and Steelworks By-Products	17
2.2 Reflectance Spectroscopy of Minerals	19
2.2.1 Basic Principles and Terminology.....	19
2.2.2 Causes of Mineral Spectral Features.....	22
2.2.2.1 Electronic Processes	22
2.2.2.2 Vibrational Processes.....	24
2.2.3 Physicochemical Impact Factors on Reflectance Spectra	28
2.2.4 Spectroscopy of High-Temperature Formations (Meteorites, Glasses and Melts)	30
2.3 Reflectance Spectroscopy and Geological Remote Sensing – A Review	34
3. Test Site.....	36
3.1 Geographical Overview	36
3.2 Geology and Mining History.....	38
3.3 Local History of Iron and Steel Production	40
3.4 Dump Site Characterisation	44
3.4.1 “Hochhalde”	45
3.4.2 “Plateau 312”	46
3.4.3 “Plateau 274”	47
4. Data and Methods.....	48
4.1 Sampling Approach, Analytical Strategy and Workflow	48
4.2 Sample Collection and Generation of a Heterogeneous Sample Dataset	50
4.3 Sample Preparation.....	52
4.4 Mineralogical and Chemical Analyses.....	52
4.5 Statistical Analysis of the Chemical Data	53

4.6 Spectral Measurements and Spectral Preprocessing.....	54
4.6.1 Spectroscopic Measurements.....	54
4.6.1.1 Acquisition of Spectra in the Visible Light, Near and Shortwave Infrared.....	54
4.6.1.2 Acquisition of Spectra in the Mid- and Longwave Infrared.....	55
4.6.2 Spectroscopic Preprocessing.....	56
4.6.2.1 Basic Spectral Preprocessing.....	56
4.6.2.2 Spectral Smoothing.....	56
4.6.2.3 Spectral Normalisations and Transformations.....	57
4.7 Spectral Analysis.....	58
4.7.1 Separability Analyses and Classification.....	58
4.7.2 Qualitative Spectral Analyses.....	58
4.7.3 Quantitative Spectral Analyses.....	60
5. Results and Discussion.....	62
5.1 Types of Iron- and Steelworks By-Products Analysed in this Study.....	62
5.2 Mineralogical Composition of the Samples.....	63
5.3 Chemical Composition of the Samples.....	67
5.3.1 Descriptive Statistics of the Chemical Composition of the Samples.....	67
5.3.2 Inter-Correlations of the Chemical Constituents.....	71
5.3.3 Principal Component and Cluster Analysis of the Chemical Data.....	72
5.4 Spectral Separability Analysis of Iron- and Steelworks By-Products.....	75
5.4.1 Spectral Separability based on PCA of VNIR/SWIR Spectra.....	75
5.4.2 Spectral Separability based on PCA of MWIR/LWIR Spectra.....	77
5.4.3 Spectral Separability based on PCA of VNIR-LWIR Spectra.....	79
5.4.4 PCA Results and Major Chemical Constituents.....	80
5.4.5 Spectral Separability Analysis based on Hierarchical Cluster Analysis.....	81
5.4.6 Spectral Separability Analysis based on Support Vector Machine Classification.....	82
5.4.7 Conclusions on the Spectral Separability Analyses.....	84
5.5 Spectral Characteristics of Iron- and Steelworks By-products.....	86
5.5.1 Spectral Library (VNIR-LWIR) of Major By-Product Types.....	86
5.5.1.1 Blast Furnace Slag (historic material, most likely not “pure”).....	87
5.5.1.2 Granulated Blast Furnace Slag (“Slag Sand”, historic by-product).....	88
5.5.1.3 Thomas Slag.....	89
5.5.1.4 Electric Arc Furnace Slag (carbon steel production).....	90
5.5.1.5 Electric Arc Furnace Slag (medium-alloy steelmaking).....	91
5.5.1.6 Electric Arc Furnace Slag (high-alloy steelmaking).....	92
5.5.1.7 Foamed Electric Arc Furnace Slag (high-alloy steelmaking).....	93
5.5.1.8 Ladle Furnace Slag.....	94
5.5.1.9 Stainless Steel Slag.....	95
5.5.1.10 AOD (Desulphurisation) Slag.....	96
5.5.1.11 Blast Furnace Flue Dust (mixture, not “pure”).....	97
5.5.1.12 Converter (Dedusting) Sludge.....	98
5.5.1.13 Mill Scale.....	99

5.5.2 Interpretation and Discussion of the Spectral Characteristics of the By-Products	100
5.5.2.1 Reflectance Intensities	100
5.5.2.2 Spectral Features	102
5.5.2.3 Relationships between Major Absorption Features and Chemical constituents ...	109
5.5.3 Spectral Variations within By-Product Classes	111
5.5.3.1 Blast Furnace Slag	111
5.5.3.2 Granulated Blast Furnace Slag	112
5.5.3.3 Thomas Slag.....	113
5.5.3.4 Stainless Steel Slag.....	114
5.5.3.5 Converter Dedusting Sludge.....	115
5.5.4 Impacts of Moisture and Sample Preparation.....	117
5.6 Spectral Quantification of Iron- and Steelworks By-Product Constituents.....	121
5.6.1 Modelling Results Based on VNIR/SWIR Spectra.....	121
5.6.2 Modelling Results Based on MWIR/LWIR Spectra	122
5.6.3 Modelling Results Based on VNIR-LWIR Spectra	124
5.6.4 Important Variables for the Prediction	126
5.6.5 Summarised Model Assessment and Discussion.....	128
5.6.6 Modelling Results Based on Spectra of Unprepared Samples	130
6. Synthesis.....	132
6.1 Summary and Discussion of the Research Questions.....	132
6.2 Conclusions, Assessment of the Results and Possible Applications.....	138
6.3 Outlook	143
7. References	145
Books, Journal Articles, Reports, etc.....	145
R and R Packages	172
DIN, EN and other Norms.....	173
8. Appendix	175
Appendices Chapter 3	175
Appendices Chapter 4	179
Appendices Chapter 5	181
Curriculum vitae Michael Denk	251
Declaration Under Oath / Eidesstattliche Erklärung.....	256

List of Figures

Fig. 1.1: General structure of this thesis	5
Fig. 2.1: Production of crude steel in the year 2000 and 2016.....	6
Fig. 2.2: Iron production in a blast furnace and ongoing chemical reactions	8
Fig. 2.3: Development of the different steelmaking procedures	9
Fig. 2.4: Historical steelmaking furnaces.....	10
Fig. 2.5: Major iron- and steelmaking and refinement procedures and associated by-products	11
Fig. 2.6: Slag samples	12
Fig. 2.7: Comparison of the chemistry of iron- and steelworks slags and natural rocks	13
Fig. 2.8: Produced amounts and utilisation of blast furnace slag and steelworks slag in Germany in 2016.....	14
Fig. 2.9: Left: Fresh AOD converter reduction slag with metal granules.....	18
Fig. 2.10: Reflection mechanisms.....	19
Fig. 2.11: Bidirectional reflectance measurement set-up as typically used in spectrometry and occurring scattering processes	20
Fig. 2.12: Overview of absorption features due to electronic and vibrational processes in the VNIR/SWIR for selected minerals and corresponding functional groups	23
Fig. 2.13: VNIR/SWIR and MWIR/LWIR reflectance spectra of the iron oxides goethite, hematite and magnetite.....	24
Fig. 2.14: VNIR/SWIR and MWIR/LWIR reflectance spectra of calcite	25
Fig. 2.15: Overview of the locations and causes of features found in mid- and longwave infrared spectra of silicates.....	26
Fig. 2.16: Structural units and features likely to be present in silicate glasses	27
Fig. 2.17: Surface and volume scattering at particulate surfaces.....	28
Fig. 3.1: Large-scale overview map of Unterwellenborn in southern Thuringia (see Appendix 3.1 for a larger version)	37
Fig. 3.2: Scheme of the geological setting at Unterwellenborn	38
Fig. 3.3: Structure of the dump site of the Stahlwerk Thüringen GmbH.....	44
Fig. 3.4: Field impressions of the “Hochhalde”	46
Fig. 3.5: Field impressions of the “Plateau 312”.....	47
Fig. 3.6: Field impression of the “Plateau 274”	47
Fig. 4.1: Overview map of the dump site of the Stahlwerk Thüringen GmbH with relevant structural areas and highlighted sampling locations	48
Fig. 4.2: Sampling and analytical approach and general workflow utilised in this thesis	49

Fig. 4.3: Excavator prospectings	51
Fig. 4.4: Hand surface sampling at the Unterwellenborn dump site	51
Fig. 4.5: Setup for the spectral laboratory measurements carried out with the ASD FieldSpec Pro FR.....	55
Fig. 4.6: Spectral measure-ments with the Agilent 4300 Handheld FTIR	55
Fig. 4.7: Parameterisation of absorption features based on continuum removed spectra.....	59
Fig. 5.1: Boxplots of the ten major chemical constituents of the sample ensemble	67
Fig. 5.2: Boxplots of ten minor chemical constituents of the sample ensemble.....	68
Fig. 5.3: Ternary plot of the chemical composition of the samples.....	69
Fig. 5.4: Inter-correlations between 23 major and minor components.....	71
Fig. 5.5a: Results of the principal component analysis of 15 chemical constituents after square root adjustment of the sample ensemble.....	73
Fig. 5.5b: Explained variance of the first 10 components of the principal component analysis of 15 chemical constituents of the sample ensemble and contributions of each variable to the first four PCs.....	73
Fig. 5.6: Results of the hierarchical cluster analysis of 15 chemical constituents.....	74
Fig. 5.7: Results of the PCA analysis of VNIR/SWIR spectra.....	76
Fig. 5.8: Results of the PCA analysis of MWIR/LWIR spectra.....	78
Fig. 5.9: Results of the PCA analysis MWIR/LWIR spectra.....	79
Fig. 5.10: Results of the PCA analysis of VNIR/SWIR absorbance spectra (PC1 and PC2) colour-coded based on the CaO, SiO ₂ , Al ₂ O ₃ and Fe _{total} contents of the samples	81
Fig. 5.11: Dendrogram obtained from hierarchical cluster analysis of VNIR/SWIR continuum removed spectra	82
Fig. 5.12: Tanglegram of results from hierarchical cluster analysis of VNIR-LWIR continuum removed spectra and chemical constituents after square root adjustment.....	85
Fig. 5.13: Reflectance and continuum removed spectra of a historic blast furnace slag sample in the VNIR/SWIR and MWIR/LWIR.....	87
Fig. 5.14: Reflectance and continuum removed spectra of a historic granulated blast furnace slag sample in the VNIR/SWIR and MWIR/LWIR.....	88
Fig. 5.15: Reflectance and continuum removed spectra of a Thomas slag sample in the VNIR/SWIR and MWIR/LWIR	89
Fig. 5.16: Reflectance and continuum removed spectra of an EAF slag sample from carbon steelmaking in the VNIR/SWIR and MWIR/LWIR	90
Fig. 5.17: Reflectance and continuum removed spectra of an EAF slag sample from medium-alloy steelmaking in the VNIR/SWIR and MWIR/LWIR	91
Fig. 5.18: Reflectance and continuum removed spectra of an EAF slag sample from high- alloy steelmaking in the VNIR/SWIR and MWIR/LWIR.....	92

Fig. 5.19: Reflectance and continuum removed spectra of a foam slag sample in the VNIR/SWIR and MWIR/LWIR	93
Fig. 5.20: Reflectance and continuum removed spectra of a ladle furnace slag sample in the VNIR/SWIR and MWIR/LWIR	94
Fig. 5.21: Reflectance and continuum removed spectra of a stainless steel slag sample in the VNIR/SWIR and MWIR/LWIR	95
Fig. 5.22: Reflectance and continuum removed spectra of an AOD slag sample in the VNIR/SWIR and MWIR/LWIR	96
Fig. 5.23: Reflectance and continuum removed spectra of a blast furnace flue dust sample in the VNIR/SWIR and MWIR/LWIR.	97
Fig. 5.24: Reflectance and continuum removed spectra of a converter dedusting sludge sample in the VNIR/SWIR and MWIR/LWIR.....	98
Fig. 5.25: Reflectance and continuum removed spectra of a mill scale sample in the VNIR/SWIR and MWIR/LWIR	99
Fig. 5.26: Correlations between the VNIR/SWIR and MWIR/LWIR reflectance spectra of all samples (N = 102) and the content of the constituents Al_2O_3 , CaO, Fe_{total} and SiO_2	100
Fig. 5.27: Relation between the Fe_{total} content and the reflectivity of the samples determined at 1600 and 4500 nm.....	101
Fig. 5.28: Overview of spectral features found in the VNIR/SWIR spectra of the by-product samples presented in Chapter 5.5.1	107
Fig. 5.29: Overview of spectral features found in the MWIR/LWIR spectra of the by-product samples presented in Chapter 5.5.1	108
Fig. 5.30: Characteristics of dominant features in the VNIR/SWIR spectra versus contents of chemical constituents	109
Fig. 5.31: Relative depths of features in the MWIR/LWIR versus contents of chemical constituents	110
Fig. 5.32a: Variations in reflectance and continuum removed spectra of selected blast furnace slag samples.....	112
Fig. 5.32b: Spectral feature variations of blast furnace slag samples versus contents of chemical constituents.....	112
Fig. 5.33a: Variations in the reflectance and continuum removed spectra of selected GBFS samples.....	113
Fig. 5.33b: Spectral feature variations of selected GBFS samples versus contents of chemical constituents.....	113
Fig. 5.34a: Variations in the reflectance and continuum removed spectra of Thomas slag samples.....	114
Fig. 5.34b: Spectral feature variations of Thomas slag samples versus contents of chemical constituents	114

Fig. 5.35a: Variations in the reflectance and continuum removed spectra of stainless steel slag samples	115
Fig. 5.35b: Spectral feature variations of stainless steel slag samples versus contents of chemical constituents.....	115
Fig. 5.36a: Variations in the reflectance and continuum removed spectra of converter sludge samples	116
Fig. 5.36b: Spectral feature variations of converter sludge samples versus contents of chemical constituents.....	116
Fig. 5.37: VNIR/SWIR and MWIR/LWIR reflectance and continuum removed spectra of a sample of stainless steel slag of different grain sizes.....	119
Fig. 5.38: VNIR/SWIR and MWIR/LWIR reflectance and continuum removed spectra of a sample of stainless steel slag of different grain sizes.....	119
Fig. 5.39: Reflectance and continuum removed spectra of unprepared samples near <i>in situ</i> moisture, air-dried samples and crushed samples < 10 mm and < 90 μm	119
Fig. 5.40: PLSR results based on VNIR/SWIR spectra for selected iron- and steelworks by-product constituents	122
Fig. 5.41: PLSR results based on MWIR/LWIR spectra for selected iron- and steelworks by-product constituents.....	123
Fig. 5.42: PLSR results based on VNIR-LWIR spectra for selected iron- and steelworks by-product constituents	125
Fig. 5.43: VIP scores for the best PLSR models obtained for Al_2O_3 , CaO , Fe_{total} , Fe_2O_3 , SiO_2 , TIC and $\sum(\text{Mo, Ni, V, Zn, Al, Cr, Fe, Mn})$ using VNIR/SWIR, MWIR/LWIR as well as VNIR-LWIR spectra.....	127
Fig. 5.44: PLSR results based on VNIR/SWIR spectra of air-dried samples for the constituents CaO and MgO	130
Fig. 5.45: PLSR results based on VNIR/SWIR spectra of unprepared samples for the constituents CaO and MgO	131
Fig. 6.1: Differences in visual material characterisation and application of spectral measurements.	140
Fig. 6.2: Diagram showing the major outcomes of this thesis and potential application fields	142

List of Tables

Tab. 2.1: By-products associated with iron- and steelmaking procedures	12
Tab. 2.2: Composition and utilisation of iron- and steelwork slags.....	15
Tab. 2.3: Composition and utilisation of dusts and sludges from iron- and steelmaking	16
Tab. 2.4: Minerals in iron- and steelworks slags	17
Tab. 2.5: Wavelength ranges and terminology used in this thesis.....	21
Tab. 2.6: Overview of spectral features in infrared spectra of natural and synthetic glasses and related functional groups	31
Tab. 3.1: Overview of major iron- and steelmaking procedures applied in the Unterwellenborn (iron- and) steel-works, associated by-products and their utilisation	43
Tab. 4.1: Selected technical characteristics of the ASD FieldSpec Pro spectroradiometer.....	54
Tab. 5.1: Typification of the 102 samples in four major by-product classes and several sub- classes	62
Tab. 5.2: Mineralogical composition of the by-product classes considered relatively “pure”	65
Tab. 5.3: Descriptive statistics of the major chemical constituents of the sample pool.....	67
Tab. 5.4: Descriptive statistics of minor chemical constituents of the sample pool.....	68
Tab. 5.5: Al ₂ O ₃ , CaO, Fe _{total} and SiO ₂ contents of the 18 material types	70
Tab. 5.6: SVM classification results for separability analysis of seven major by-product types.....	83
Tab. 5.7: Chemical constituents and photographs of a blast furnace slag sample.....	87
Tab. 5.8: Chemical constituents and photographs of a granulated blast furnace slag sample	88
Tab. 5.9: Chemical constituents and photographs of a Thomas slag sample.....	89
Tab. 5.10: Chemical constituents and photos of an EAFS sample (carbon steelmaking).....	90
Tab. 5.11: Chemical constituents and photos of an EAFS sample (med.-alloy steelmaking	91
Tab. 5.12: Chemical constituents and photos of an EAFS sample (high-alloy steelm.)	92
Tab. 5.13: Chemical constituents and photographs of an EAF foam slag sample.....	93
Tab. 5.14: Chemical constituents and photographs of a ladle furnace slag sample.....	94
Tab. 5.15: Chemical constituents and photographs of a stainless steel slag sample.....	95
Tab. 5.16: Chemical constituents and photographs of an AOD slag sample.....	96
Tab. 5.17: Chemical constituents and photographs of a blast furnace flue dust sample.....	97
Tab. 5.18: Chemical constituents and photographs of a converter dedusting sludge sample.....	98
Tab. 5.19: Chemical constituents and photographs of a mill scale sample.....	99
Tab. 5.20: PLSR results based on VNIR/SWIR spectra.....	121
Tab. 5.21: PLSR results based on MWIR/LWIR spectra	123

Tab. 5.22: PLSR results based on VNIR-LWIR spectra	124
Tab. 5.23: R^2_{val} and RMSE_{val} of the PLSR models using VNIR/SWIR, MWIR/LWIR or VNIR-LWIR spectra.....	128
Tab. 5.24: PLSR results based on spectra of air-dried samples for selected chemical parameters	130
Table 5.25: PLSR results based on spectra of samples with near <i>in situ</i> moisture	131

List of Appendices

A3.1: Large-scale overview map of Unterwellenborn in southern Thuringia	175
A3.2: Stratigraphy of the Saalfeld-Kamsdorf deposit	176
A3.3 Utilisation of the iron- and steelmaking by-products of the Maxhütte in the 1950s	176
A3.4: Overview map of the dump site of the Stahlwerk Thüringen GmbH with relevant structural areas and highlighted sampling locations	177
A3.5: Differences in altitude occurring at the dump site of the Stahlwerk Thüringen GmbH	178
A3.6: Differences in slope occurring at the dump site of the Stahlwerk Thüringen GmbH	178
A4.1: Instrumental parameters of the XRD measurements as conducted by FEhS	179
A4.2: DIN standards utilised for analysing the different chemical constituents by FEhS	179
A4.3: Comparison of MWIR/LWIR spectra recorded with the Agilent 4300 Handheld FTIR spectrometer of samples showing distinct diagnostic spectral features with corresponding reference spectra	180
A5.1: Mineralogical composition of the samples assigned to the specific by-product types	181
A5.1.1: Mineralogical composition of the “BFS+” samples	181
A5.1.2: Mineralogical composition of the “granulated blast furnace slag” samples	182
A5.1.3: Mineralogical composition of the “converter dedusting sludge” samples	182
A5.1.4: Mineralogical composition of the “stainless steel slag” samples	182
A5.1.5: Mineralogical composition of the “EAFS (carbon steel)” samples	183
A5.1.6: Mineralogical composition of the “ladle furnace slag” samples	183
A5.1.7: Mineralogical composition of the “EAFS (medium-alloy steel)” samples	183
A5.1.8: Mineralogical composition of the “EAFS (high-alloy steel)” samples	183
A5.1.9: Mineralogical composition of the “EAF foam slag” sample	184
A5.1.10: Mineralogical composition of the “AOD slag” sample	184
A5.1.11: Mineralogical composition of the “unspecified steelworks slag” samples	184
A5.1.12: Mineralogical composition of the “blast furnace flue dust” samples	184
A5.1.13: Mineralogical composition of the “Thomas slag”	185
A5.1.14: Mineralogical composition of the “mill scale” sample	185
A5.1.15: Mineralogical composition of the “mixtures with high amounts of sand” samples	186
A5.1.16: Mineralogical composition of the “unspecified dusts and sludges” samples	186
A5.1.17: Mineralogical composition of the “unspecified others” samples	187
A5.1.18: Mineralogical composition of the “limestone+natural sand” sample	187
A5.2: Statistics on the chemical composition (m%) of the major by-product classes	188
A5.3: Histograms, density and normal fits for the analysed chemical constituents	194

A5.4.1: Results of the PCA of VNIR/SWIR reflectance spectra	196
A5.4.2: Results of the PCA of VNIR/SWIR absorbance spectra.....	197
A5.4.3: Results of the PCA of VNIR/SWIR continuum removed spectra.....	198
A5.4.4: Results of the PCA of MWIR/LWIR reflectance spectra.....	199
A5.4.5: Results of the PCA of MWIR/LWIR absorbance spectra.....	200
A5.4.6: Results of the PCA of MWIR/LWIR continuum removed spectra.....	201
A5.4.7: Results of the PCA of VNIR-LWIR reflectance spectra.....	202
A5.4.8: Results of the PCA of VNIR-LWIR absorbance spectra.....	203
A5.4.9: Results of the PCA of VNIR-LWIR continuum removed spectra.....	204
A5.4.10: Axis loadings of the PCA based on VNIR/SWIR spectra.....	205
A5.4.11: Axis loadings of the PCA based on MWIR/LWIR spectra.....	206
A5.4.12: Axis loadings of the PCA based on VNIR-LWIR spectra.....	207
A5.5.1: Results of the HCA based on VNIR/SWIR spectra.....	208
A5.5.2: Results of the HCA based on MWIR/LWIR spectra.....	209
A5.5.3: Results of the HCA based on VNIR-LWIR spectra.....	210
A5.5.4.1: SFF and SAM scores of the converter dedusting sludge spectra (N = 7).....	211
A5.5.4.2: SFF and SAM scores of the stainless steel slag spectra (N = 5).....	211
A5.5.4.3: SFF and SAM scores of the EAFS from carbon steelmaking spectra (N = 3).....	212
A5.5.4.4: SFF and SAM -scores of the LFS spectra (N = 3).....	212
A5.5.4.5: SFF and SAM scores of the Thomas slag spectra (N = 14)	212
A5.6.1: VNIR/SWIR and MWIR/LWIR spectra of the blast furnace slag samples	213
A5.6.2: VNIR/SWIR and MWIR/LWIR spectra of the “GBFS” samples	219
A5.6.3: VNIR/SWIR and MWIR/LWIR spectra of the “Thomas slag” samples.	221
A5.6.4: VNIR/SWIR and MWIR/LWIR spectra of the “EAFS (carbon steelm.)” samples.	225
A5.6.5: VNIR/SWIR and MWIR/LWIR spectra of the “EAFS (med.-alloy steelm.)” samples.....	226
A5.6.6: VNIR/SWIR and MWIR/LWIR spectra of the “EAFS (high-alloy steelm.)” samples.....	226
A5.6.7: VNIR/SWIR and MWIR/LWIR spectra of the “EAF foam slag” sample	227
A5.6.8: VNIR/SWIR and MWIR/LWIR spectra of the “AOD slag” sample	227
A5.6.9: VNIR/SWIR and MWIR/LWIR spectra of the “stainless steel slag” sample.	227
A5.6.10: VNIR/SWIR and MWIR/LWIR spectra of the “ladle furnace slag” sample.....	229
A5.6.11: VNIR/SWIR and MWIR/LWIR spectra of the “Unspecified sSWS” samples	230
A5.6.12: VNIR/SWIR and MWIR/LWIR spectra of the “blast furnace flue dust” samples	231

A5.6.13: VNIR/SWIR and MWIR/LWIR spectra of the “unspecif. dusts/sludges” samples	232
A5.6.14: VNIR/SWIR and MWIR/LWIR spectra of the “converter ded. sludge” samples.....	235
A5.6.15: VNIR/SWIR and MWIR/LWIR spectra of the “mill scale” sample.....	237
A5.6.16: VNIR/SWIR and MWIR/LWIR spectra of the “mixtures with nat. sand” samples ...	237
A5.6.17: VNIR/SWIR and MWIR/LWIR spectra of the “limestone+sand” sample.....	239
A5.6.18: VNIR/SWIR and MWIR/LWIR spectra of the “unspecified other” samples.....	239
A5.7: List of the reflectance maxima observed in the LWIR spectra of the reference samples of the by-product classes considered relatively “pure”	243
A5.8a: Correlations between the contents of Cd, Cr ₂ O ₃ , Ni, Pb and Zn and the reflectance values of the samples	243
A5.8b: Correlations between the contents of H ₂ O, MgO, P ₂ O ₅ , TIC and $\sum(\text{Mo, Ni, V, Zn, Al, Cr, Fe, Mn})$ and the reflectance values of the samples	243
A5.9.1: Variations of major absorption features in the VNIR/SWIR spectra of blast furnace slag samples (N = 6)	244
A5.9.2: Variations of major absorption features in the VNIR/SWIR spectra of “slag sand” samples (N = 6)	244
A5.9.3: Variations of major absorption features in the VNIR/SWIR spectra of Thomas slag samples (N = 14)	245
A5.9.4 Variations of major absorption features in the VNIR/SWIR spectra of stainless steel slag samples (N = 5)	245
A5.9.5: Variations of major absorption features in the VNIR/SWIR spectra of converter sludge samples (N = 7).....	246
A5.10: PLSR results based on VNIR/SWIR spectra for selected iron- and steelworks by-product constituents.	247
A5.11: PLSR results based on MWIR/LWIR spectra for selected iron- and steelworks by-product constituents	248
A5.12: PLSR results based on VNIR-LWIR spectra for selected iron- and steelworks by-product constituents.	248
A5.13: VIP scores for the best PLSR models obtained for Fe _{total} , H ₂ O and MgO using VNIR/SWIR, MWIR/LWIR as well as VNIR-LWIR spectra.	249
A5.14: VIP scores for the best PLSR models obtained for Al ₂ O ₃ , CaO, Fe _{total} and MgO using VNIR/SWIR spectra of air-dried but not further prepared sample material.	249
A5.15: VIP scores for the best PLSR models obtained for Al ₂ O ₃ , CaO, Fe _{total} and MgO using VNIR/SWIR spectra of sample material with near in situ moisture.	250
Curriculum vitae Michael Denk	251
Declaration Under Oath/Eidesstattliche Erklärung	256

Glossary

a.s.l.	above sea level
AOD (S)	argon oxygen decarburisation (slag)
App.	Appendix
ASCII	American Standard Code for Information Interchange
ASD	Analytical spectral devices
ASTER	Advanced Spaceborne Thermal Emission and Reflection Radiometer
BF(S)	blast furnace (slag)
BFF(D)	blast furnace flue (dust)
BOF(S)	basic oxygen furnace (slag)
CDS	converter dedusting sludge
CF	Christiansen feature
Ch.	chapter
cm	centimetre
CR	continuum removed
CS	carbon steel
CSV	comma-separated values
EAF(S)	electric arc furnace (slag)
EnMap	Environmental Mapping and Analysis Program, German hyperspectral satellite mission (http://www.enmap.org/ , last accessed 2018-03-26)
FOV	field of view
FTIR	Fourier-transform infrared (spectroscopy)
g	gramme
GFBS	granulated blast furnace slag
GPS	Global Positioning System
HCA	hierarchical cluster analysis
HM	hot metal
IDL	Interactive Data Language
kg	kilogramme
km	kilometre
LD(S)	Linz-Donawitz converter (slag)
LF(S)	ladle furnace (slag)
LWIR	longwave infrared

µm	micrometre
m	metre
MD	median
mg	milligramme
mm	millimetre
MN	mean
m%	mass percentage
MIR	mid(wave) infrared
MSC	multiple scatter correction
MT	megaton
MW	megawatt
MWIR	mid-wave infrared
NIR	near infrared
nm	nanometre
PCA	principal component analysis
PC(s)	principal component(s)
RPD	Ratio of Performance to Deviation
RMSE	root-mean-square error
SAM	Spectral Angle Mapper
SD	standard deviation
SFF	Spectral Feature Fitting
SNV	standard normal variate
SSS	stainless steel slag
SVMC	support vector machine classification
SWIR	shortwave infrared
SWS	steelworks slag
TIC	total inorganic carbon
TIR	thermal infrared
t	tonne
TXT	text
USGS	United States Geological Survey
UV	ultraviolet
VEB	nationally-owned enterprise (“Volkseigener Betrieb”)

VIP	variable importance in projection
VIS	visible light
VNIR	visible light and near infrared
VNIR/SWIR	visible light, near infrared and shortwave infrared
W	Watt
XRD	X-ray diffraction
$\Sigma(\text{metals})$	$\Sigma(\text{Mo, Ni, V, Zn, Al, Cr, Fe, Mn})$

Abstract (English)

The exploration of anthropogenic deposits is of increasing relevance in times of fluctuating world market prices, limited resource availabilities and increasing demands for raw materials. Aside from landfills of mining residuals, secondary deposits encompass dump sites of industrial by-products. The iron- and steel industry is one of the most important basic industries and iron- and steelmaking is accompanied by a large variety of different by-products. Especially dump sites associated with iron and steel plants with long reaching history and manifold applied procedures may comprise a variety of secondary materials that have not been treated with present standards. Such materials are potentially rich in economically relevant materials that are valuable for extraction and reuse in today's world market situation (e.g. various metals, constituents that might be used as fertiliser, or materials suitable for the construction industry).

The exploration of historic iron- and steelworks dump sites is challenging due to the anthropotechnogenic material deposition, which is often not well-documented, and the heterogeneous chemical and mineralogical composition of different material types. Furthermore, such materials are hardly discriminable *in situ* due to similar visual appearance in many cases. Consequently, the exploration of such deposits requires comprehensive sampling campaigns, and extensive laboratory analyses for material typification and geochemical characterisation. These procedures are time consuming and cost-intensive. Thus, new and innovative approaches are required to aid the exploration of iron- and steelworks dump sites, to assist material typification and the assessment of relevant chemical properties within urban mining applications.

As non-contact method, reflectance spectroscopy has been widely applied within the exploration of natural deposits and for qualitative as well as quantitative spectral analyses of geological materials. In contrast to the profound knowledge of spectral properties of minerals and natural rocks, the number of studies on the specific spectral characteristics of the variety of iron- and steelworks by-products is limited within the remote sensing community. Most slags and other by-products show a differing mineralogy and chemistry compared to natural rocks. Thus, existing information on spectra of monomineralic samples or natural formations cannot be directly transferred to such "industrial rocks" in every case. However, profound knowledge about the spectral properties of potential target materials is the prerequisite for their successful spectral detection and analyses.

Thus, this thesis aims to extend the knowledge of reflectance properties of common iron- and steelworks by-products that might be found at historic dump sites related to this industrial branch. Focus is put on two relevant wavelength ranges for spectral measurements within remote sensing applications: the visible light, near and shortwave infrared (VNIR/SWIR, 350-2500 nm) as well as the mid- and longwave infrared (MWIR/LWIR, 2500-15000 nm). The work follows a deductive approach and the main objectives are: a) the analysis of the feasibility of using reflectance data for spectrally discriminating a large variety of iron- and steelworks by-product types; b) the comprehensive characterisation of the spectral properties of these materials and c) analysing the potential for spectrally assessing the quantities of relevant chemical constituents.

The data basis for this work is a pool comprising 102 samples, of which the majority was collected at the dump site of the Stahlwerk Thüringen GmbH at Unterwellenborn, Germany. The sample pool comprises various historic as well as recent slags from iron- and steelmaking, different dusts, sludges and mixed materials. The spectral separability analyses encompassed principal component analyses and hierarchical clustering. Furthermore, the general potential for

spectral classification and separation of the different by-products was analysed using Support Vector Machine Classification, Spectral Feature Fitting and Spectral Angle Mapper. The impact of moisture and sample preparation on the reflectance signatures was studied as this is of relevance for the transferability of obtained results at the laboratory scale to field applications. For the spectral quantification of relevant chemical constituents typically used to characterise iron- and steelworks by-products, Partial Least Square Regression (PLSR) was applied.

The outcome of this thesis reveals a high potential for the spectral discrimination of a large variety of recent and historic iron- and steelworks by-products that are potentially present at dump sites. These findings are of considerable relevance for improving the classification and typification of visually similar by-products. Utilising generalised separability approaches based on full spectral ranges, the VNIR/SWIR range provided a better separability of most by-product types compared to the more complex MWIR/LWIR. This thesis is further novel in providing detailed information on the spectral properties of various slags and other by-products for the VNIR/SWIR as well as for the MWIR/LWIR in a spectral-library-like manner. This contributes to a better understanding of the reflectance properties of such materials and may be used within spectral analyses and material detection applications. The results of PLSR modelling indicated a high potential for the spectral prediction of relevant chemical constituents commonly used to characterise iron- and steelworks by-products. Robust predictions ($R^2_{\text{val}} > 0.8$) were achieved for CaO, Fe_{total}, Fe₂O₃, TIC, SiO₂ and the sum of various metals. The errors for these predictions were moderate to low (2-4 m%), indicating that accurate predictions of these parameters can be obtained utilising spectral methods. For other constituents, comprising Al₂O₃ and MgO, less robust but still promising results were obtained. Solid predictions for CaO, Fe₂O₃ and Fe_{total} were obtained using the VNIR/SWIR data, while the robust prediction of SiO₂ and TIC required MWIR/LWIR data due to the specific spectral properties of these constituents not found in the VNIR/SWIR. The combination of both spectral ranges improved the predictive performance of the PLSR models but was in some cases achieved at the cost of higher model complexity. Especially for CaO, reliable estimations can be accomplished based on spectra of prepared and homogenised sample material and based on spectra of material near *in situ* conditions as well.

In summary, non-invasive reflectance measurements and spectral analyses related to remote sensing applications were found to be suitable tools for discriminating and qualitatively as well as quantitatively characterising iron- and steelworks by-products. Considering that such measurements can be conducted quickly and results derived rapidly, a strong capability for aiding the exploration of anthropogenic deposits related to the iron and steel industry was found. This offers a great potential for reducing the required number of samples as well as the extent of cost-intensive and time-consuming chemical and mineralogical analysis within urban mining applications. The obtained results further promote VNIR/SWIR and MWIR/LWIR reflectance spectroscopy - and subsequently remote sensing methods using these ranges - for analytical purposes of iron- and steelworks by-products in general, and for various screening applications within the exploration of secondary deposits related to this industry in particular. The results benefit material detection and analyses and a variety of possible applications arise. These comprise the sole laboratory usage for spectral-chemical material characterisation, *in situ* screenings using field-portable instruments or terrestrial or airborne imaging spectroscopy for discriminating and spatially mapping different material types of interest. Subsequently, the achieved results offer the potential to substantially benefit urban mining workflows aiming at finding and characterising materials of (economic) interest, their subsequent extraction and reuse.

Abstract (German)

Die Exploration anthropogener Lagerstätten gewinnt in Zeiten fluktuierender Weltmarktpreise, begrenzter Ressourcenverfügbarkeiten und steigender Rohstoffnachfrage zunehmend an Bedeutung. Neben Bergbauhalden umfassen sekundäre Lagerstätten Deponien industrieller Nebenerzeugnisse. Insbesondere Halden von Eisen- und Stahlwerken mit langer Historie und vielfältigen angewandten Verfahren können eine Fülle von Sekundärmaterialien beinhalten, die nicht nach derzeitigen Aufbereitungsstandards behandelt wurden. Solche Materialien sind potentiell reich an wirtschaftlich relevanten Stoffen, deren Extraktion und Wiederverwertung in der gegenwärtigen Weltmarktsituation von Interesse sind (z. B. verschiedene Metalle und Materialien, die als Dünger oder für die Baustoffindustrie verwendet werden können).

Infolge lückenhaft dokumentierter Ablagerungsvorgänge sowie der heterogenen chemischen und mineralogischen Zusammensetzung verschiedener Materialtypen stellt die Erkundung historischer Eisen- und Stahlwerkshalden eine Herausforderung dar. Darüber hinaus sind viele Materialien aufgrund ähnlichen Erscheinungsbildes in vielen Fällen selbst für Experten kaum im Gelände zu unterscheiden. Die Exploration solcher Lagerstätten erfordert daher umfangreiche Probenahmekampagnen sowie zeit- und kostenintensive Laboranalysen zur Charakterisierung der abgelagerten Stoffe. Daher sind neue und innovative Ansätze erforderlich, um die Untersuchung von Halden der Eisen- und Stahlindustrie im Rahmen des Urban Mining zu unterstützen sowie die Typisierung verschiedener Materialien und die quantitative Einschätzung relevanter chemischer Eigenschaften zu erleichtern.

Reflexionsspektrometrie ist ein etabliertes, nicht-invasives Verfahren zur Exploration natürlicher Lagerstätten sowie für quali- und quantitative geochemische Analysen. Im Gegensatz zu bestehenden umfangreichen Kenntnissen der spektralen Eigenschaften von Mineralen und natürlichen Gesteinen, ist die Anzahl der Studien über die spezifischen spektralen Charakteristika verschiedener Eisen- und Stahlwerksnebenprodukte im Kontext fernerkundungsrelevanter Anwendungen begrenzt. Die meisten Schlacken und andere Nebenprodukte weisen im Vergleich zu natürlichen Gesteinen unterschiedliche mineralogische und chemische Eigenschaften auf. Somit können bestehende spektrale Informationen zu monomineralischen Proben oder natürlichen Gesteinen aus Referenzdatenbanken nicht direkt auf diese "industriellen Gesteine" übertragen werden. Die Kenntnis der spektralen Eigenschaften potentieller Zielmaterialien ist jedoch zwingende Voraussetzung für deren erfolgreiche spektrale Detektion und Analyse.

Diese Arbeit zielt daher darauf ab, die Wissensbasis zu Reflexionseigenschaften von Eisen- und Stahlwerksnebenprodukten zu erweitern. Der Schwerpunkt liegt auf zwei in der geologischen Fernerkundung relevanten Wellenlängenbereichen: dem sichtbaren Licht, nahen und kurzwelligen Infrarot (VNIR/SWIR, 350-2500 nm) sowie dem mittel- und langwelligen Infrarot (MWIR/LWIR, 2500-15000 nm). Die Arbeit folgt einem deduktiven Ansatz und die Hauptziele sind: a) die Analyse der generellen spektralen Differenzierbarkeit einer Vielzahl verschiedener Typen von Eisen- und Stahlwerks-Nebenprodukten; b) die umfassende Charakterisierung der spektralen Eigenschaften dieser Materialien und c) die Analyse des Potentials reflexionsspektrometrischer Methoden zur quantitativen Abschätzung der Mengen relevanter chemischer Bestandteile.

Die Datengrundlage für diese Arbeit bilden 102 Proben, die zum Großteil auf der Halde der Stahlwerk Thüringen GmbH in Unterwellenborn (Deutschland), erhoben wurden. Diese

umfassen verschiedene historische Schlacken, Staube und Schlamme sowie Materialien aus der aktuellen Stahlerzeugung. Die spektrale Trennbarkeit wurde mittels Hauptkomponenten- und hierarchischen Clusteranalysen untersucht. Daruber hinaus wurde das Potential zur spektralen Klassifizierung und Trennung verschiedener Nebenprodukte mittels Support Vector Machine Klassifikation, Spectral Feature Fitting und Spectral Angle Mapper analysiert. Spektrale Merkmale verschiedener Materialtypen wurden umfassend im VNIR/SWIR und MWIR/LWIR erfasst und interpretiert. Der Einfluss von Feuchtigkeit und Probenaufbereitung auf die spektralen Signaturen wurde untersucht, da dies fur die Ubertragbarkeit der auf Laborebene generierten Ergebnisse auf Feldanwendungen von Bedeutung ist. Zur spektralen Quantifizierung relevanter chemischer Bestandteile, die zur Charakterisierung von Eisen- und Stahlwerksnebenprodukten verwendet werden, wurde das Partial-Least-Square-Regressions-Verfahren (PLSR) angewendet.

Im Ergebnis dieser Arbeit konnten verschiedene Haldenmaterialien uber ihre spektralen Signaturen differenziert und detektiert werden. Dabei zeigte sich im Rahmen der generalisierten Trennbarkeitsanalysen eine bessere Differenzierbarkeit der Materialien unter Verwendung des vollstandigen VNIR/SWIR-Bereichs im Vergleich zum komplexeren MWIR/LWIR. Ein weiterer wesentlicher Beitrag dieser Arbeit ist die detaillierte Beschreibung der spektralen Eigenschaften verschiedener Nebenprodukte. Diese Informationen wurden erstmals in Form einer Spektralbibliothek und von Ubersichtsschemata prasentiert. Diese tragen zu einem besseren Verstandnis der Reflexionseigenschaften solcher Materialien bei und konnen als Basis fur fortfuhrende Spektralanalysen und fur die Materialdetektion verwendet werden. Basierend auf PLSR-Modellen wurden robuste Vorhersagen ($R^2_{\text{val}} > 0.8$) mit niedrigem Schatzfehler fur CaO, Fe_{gesamt}, Fe₂O₃, TIC, SiO₂ und die Summe verschiedener Metalle erzielt. Auch fur Al₂O₃ und MgO wurden vielversprechende Ergebnisse generiert. Solide Vorhersagen fur CaO, Fe₂O₃ und Fe_{gesamt} konnten unter Verwendung des VNIR/SWIR erzielt werden. Fur die robuste Schatzung von SiO₂ und TIC wurden MWIR/LWIR-Daten benotigt. Die Kombination beider Spektralbereiche verbesserte die Gute der modellgestutzten Vorhersagen, wurde in einigen Fallen aber auf Kosten einer hoheren Modellkomplexitat erreicht. Insbesondere fur CaO wurden zuverlassige Schatzungen auf der Basis von Spektren homogenisierten als auch unaufbereiteten Probenmaterials erzielt.

In dieser Arbeit wurden reflexionsspektrometrische Messungen im Bereich des VNIR/SWIR und MWIR/LWIR und anschließende Spektralanalysen als geeignete Werkzeuge zur Differenzierung, Detektion und quantitativen Analyse von Eisen- und Stahlwerksnebenprodukten aufgezeigt. Da entsprechende Messungen rasch durchgefuhrt und Ergebnisse mit geringem Zeitaufwand abgeleitet werden konnen, hat dieser Ansatz erhebliches Potential zur Unterstutzung explorativer Screenings von Halden der Eisen- und Stahlindustrie, zur Optimierung von Probenahmestrategien und zur Reduzierung des Umfangs von kosten- und zeitintensiven Laboranalysen. Die Ergebnisse der Arbeiten tragen damit auch zur weiteren Etablierung bildgebender fernerkundlicher Methoden zur Analyse von Materialien der Eisen- und Stahlindustrie sowie zur Untersuchung entsprechender Halden bei. Dadurch ergibt sich eine Vielzahl von Anschlussoptionen. Diese umfassen den Einsatz reflexionsspektrometrischer Verfahren im Rahmen rein laborbasierter Analysen von Eisen- und Stahlwerks-Nebenprodukten, *in-situ*-Screenings mittels tragbarer Feldinstrumente sowie die terrestrische oder flugzeuggestutzte Fernerkundung zur Erfassung der raumlichen Verteilung von Materialien und deren Eigenschaften auf Halden. Damit haben die erzielten Ergebnisse das Potential, Urban-Mining-Workflows zu optimieren, die auf die Detektion und anschließende Ruckgewinnung von Materialien von (wirtschaftlichem) Interesse abzielen.

1. Introduction

1.1 Background and Motivation - Exploration of Anthropogenic Deposits

Today's world market situation is characterised by an increasing demand for energy and resources, increasing difficulty to acquire raw materials, fluctuating prices and variable resource availabilities. This affects various primary materials and causes an increasing demand for securing a sustainable raw material supply (e.g. BMWi 2010, Drobe and Killiches 2014, Arndt et al. 2015, BMUB 2015, BMUB 2016, BGR 2017). As a consequence, the exploitation of new resource deposits is crucial to assure raw material supply for basic but also high-tech industries, which has been broadly debated within economy and society. The exploitation of new deposits is not restricted to natural resources and therefore exploration of anthropogenic deposits and subsequent reuse of secondary resources is gaining increasing relevance (e.g. Wittmer 2006, Graedel 2009, BMWi 2010, Klinglmair and Fellner 2010, Krook and Baas 2013, BMUB 2016). As the conventional mining of natural deposits is often accompanied with high landscape and energy consumption (e.g. Priester and Dolega 2015), the exploitation of anthropogenic secondary deposits and the subsequent reuse of raw materials in existing anthropogenic metal stocks is of increasing importance considering the sustainable use of georesources (e.g. Wittmer 2006, Graedel 2009). Mining residuals represent one type of anthropogenic deposits. In 2012, the total amount of residuals of quarrying and mining activities in the EU was estimated to be > 700 million tonnes (European Union 2016). Also, industrial dump sites or landfills play an important role in the context of urban mining (see e.g. Dürkoop et al. 2016). The iron and steel industry is an essential industry and steel can be considered the most significant metallic base material (IPCC 2007, Remus et al. 2013), with a crude steel production of 1630 million tonnes in the year 2016 (World Steel Association 2017). The production of iron and steel is accompanied by the generation of various by-products. As such, more than 400 million tonnes of iron and steel slags as well as dusts, sludges and other secondary products are generated per year (World Steel Association 2016). Such materials have been widely used for different purposes (Geiseler 1996), e.g. the fabrication of bricks and ceramics (e.g. Das et al. 2007), for cement manufacturing or as construction material (e.g. Heußen and Markus 2013, Merkel 2014), as landfill liners (e.g. Diener et al. 2007, Herrmann et al. 2010) and fertiliser (e.g. Motz and Geiseler 2001, Dohlen and Steinweg 2009). In Europe, North America and Japan, current recycling and reuse rates of recent iron and steel slags reach nearly 100% to reduce landfill waste, CO₂ emissions and preserving natural resources (Chiang and Pan 2017, World Steel Association 2016). In contrast, the reuse rates in other countries are much lower (e.g. 22% reuse of steel slag in China 2012, Yi et al. 2012). However, historical iron- and steelworks dump sites encompass materials not treated with present standards that can be rich in materials of economic interest. These materials comprise residuals from metallurgical smelting processes like slags, but also sludges, dusts or ashes that might be reusable in the cement industry, as construction material, fertiliser or contain relevant quantities of metals. For Germany, the total number of larger dumps has been estimated as greater than 1000, comprising a maximum theoretical potential of 45 million tonnes of iron in dump sites (Mrotzek-Blöß et al. 2016).

Not only the origin of iron- and steelworks by-products is technogenic, but also their deposition is realised on an industrial scale and thus not comparable to natural depositional environments. The deposition of recent secondary products is usually conducted in a well-documented systematic way. However, with changes in production and deposition technology throughout the

existence of iron- and steelworks and due to material movements, the complexity of disposed materials and the structure of dump sites can substantially increase. The composition of the materials found at historic iron- and steelworks dump sites encompasses a multitude of slags from primary and secondary processes accompanied by sludges and dusts, e.g. from cleaning procedures of flue gases. Deposited materials might further comprise refractories, demolition material, soil, sand and others. The above-mentioned issues explain the arising difficulties for the exploration of dump sites associated with the iron and steel industry. Typically, the *in situ* assessment or mapping of historic by-products at dump sites is difficult, as different by-products or other materials tend to be similar in their visual appearance but show contrasting geochemical properties. In other cases, visually different materials might be assigned to different material classes but show nearly identical mineralogical or chemical properties. Thus, the detection of materials of interest requires comprehensive sampling campaigns with subsequent geochemical analyses in order to assess material types and their corresponding chemical composition. Such efforts are time consuming, cost-intensive and cannot provide spatially comprehensive information on the overall material distribution at dump sites (Jandewerth et al. 2013; Mrotzek-Blöß et al. 2016; Nühlen et al. 2016a, 2016b, 2016c). Further information might be provided by drill-core analyses, but such approaches are known to be difficult to conduct on iron- and steelworks dump sites and provide only point-based information (e.g. Ullrich 2005, Tinz 2006). Analyses of historical maps, archived documents and aerial photographs as well as local experts' knowledge provide valuable information on the historical material. However, it was found that even after elaborating detailed mass flows based on archive data and analyses of historical aerial photographs, the specific material composition at dump sites could not be fully reconstructed and remains unclear in many cases (Jandewerth et al. 2013, Mrotzek-Blöß et al. 2016). Here, one must also consider that such detailed information is not available in all cases, resulting in a less documented historic treatment and tipping of iron- and steelworks by-products and an unknown material composition.

For the successful exploration of anthropogenic deposits in general and for iron- and steelworks dumps in particular, the origin and composition of the disposed secondary materials must be precisely determined, and their content of relevant constituents estimated. Therefore, innovative approaches are required for explorative screenings of historical disposal sites, aiming at improving material typification and detection, as well as for quantitatively assessing properties of such materials. This is supposed to consequently aid raw material recovery, to reduce costs for sample collection and analyses and benefit the overall workflow of reusing or recycling industrial by-products (e.g. Jandewerth et al. 2013, Krook and Baas 2013, Mrotzek-Blöß et al. 2016).

As non-invasive methods, reflectance spectroscopy and hyperspectral remote sensing are well established tools for the remote exploration of natural deposits (e.g. Goetz and Rowan 1981, van der Meer et al. 2012). Such methods are applied in a plurality of mining related fields, e.g. for analyses of acid mine drainage phenomena (e.g. Swayze et al. 2000, Montero et al. 2005), mining accidents (e.g. Kemper and Sommer 2002, Fernandes et al. 2016), for monitoring post-mining landscapes (e.g. Schmidt and Glaesser 1998, Gläßer et al. 2011) and tailing sites as well as for mine waste analyses (e.g. Gannouni et al. 2012, Buzzi et al. 2014, Mielke et al. 2014). Despite the growing variety of application fields, which encompass also urban materials (e.g. Rashed and Jürgens 2010, Yang 2011) or industrial applications (e.g. Tatzner et al. 2005), only few studies focussed on the utilisation of hyperspectral methods for analysing nonferrous materials or within

the steel foundry process (e.g. Picón et al. 2009, 2012, 2017; Gutiérrez et al. 2010). Even less research was conducted with focus on the remote spectral exploration of iron- and steelworks dump sites and the characterisation of heterogeneous historical materials based on reflectance spectroscopy using field portable instruments (Denk et al. 2015).

The knowledge of the spectral characteristics of the target materials is a prerequisite for the qualitative and quantitative analysis of spectroscopic measurements and subsequently remote sensing data. Thus, profound studies on the spectral properties of minerals and rocks have been established for several decades (e.g. Estep-Barnes 1977, Hunt 1977, Clark 1999). Today, various digital spectral libraries for minerals and also partially for rocks are available (Clark et al. 2007, Baldrige et al. 2009, Kokaly et al. 2017). With the technological advancement and increasing number of instruments to acquire high-resolution information in the thermal infrared (e.g. Hecker et al. 2011), this wavelength range gains further relevance in remote sensing applications, due to better discrimination and analytical capabilities for several mineralogical and chemical constituents, e.g. silicates (e.g. Hunt 1980). Iron- and steelworks by-products, particularly slags, represent industrial high-temperature formations that show a differing chemical as well as mineralogical composition compared to naturally occurring rocks and can thus be considered as “industrial” or “anthropogenic rocks” (Drissen 2004). As such, their spectral properties are different from natural rocks. However, several spectral properties of high temperature minerals and silicates might also occur in slags were studied by various authors (e.g. spinels and chromites by Cloutis et al. 2004; silicates by Launer 1952, Moenke 1962, Ghosh and Chatterjee 1974). A multitude of works exists on the spectral properties of natural and technogenic silicate glasses (see King et al. 2004b and references therein), which show similarities to glass-like solidified slags. For analyses of slags and melts, especially transmittance measurements in the mid- and longwave infrared on the laboratory scale are established analytical tools (see e.g. Waseda and Toguri 1998; Park et al. 2002, 2012).

In contrast to the aforementioned plurality of studies on the spectral properties of various geological and technogenic materials, the reflectance properties of the large variety of chemically and mineralogically different by-products potentially occurring at historic iron- and steelworks dump sites have - to the best of the author’s knowledge - not yet been comprehensively described combining information from the visible light to the longwave infrared. Furthermore, the capabilities for spectrally discriminating these materials as well as for quantifying chemical constituents of such heterogeneous material compositions with potential application for the remote exploration of iron- and steelworks dump sites have not been shown previously. This underlines the necessity for building a more detailed knowledge base of the reflectance properties of common historical as well as recent iron- and steelworks by-products for the visible light, near and shortwave infrared as well as for the mid- and longwave infrared, as these ranges are commonly utilised in laboratory as well as in *in situ* spectroscopy with portable instruments as well as within the field of geological remote sensing (e.g. Hecker et al. 2011, van der Meer et al. 2012). Furthermore, the feasibility for spectrally differentiating various by-product types and for spectral quantification of relevant chemical constituents in order to assist material discrimination and characterisation within urban mining applications still needs to be assessed.

1.2 Objectives, Scope and Research Questions

Against the described background, this thesis aims to provide extensive information on the reflectance characteristics of a variety of typical iron- and steelworks by-products, analyse the spectral separability of such materials and assess the potential for spectrally quantifying their chemical constituents. The work incorporates the common wavelength range utilised in optical geological remote sensing (350-2500 nm) as well as the mid-and longwave infrared range (2500-15000 nm), as this wavelength region is known to provide more detailed information on several constituents (e.g. silicates; cf. Schodlok et al. 2016). Apart from the different wavelength ranges, different spectra types (i.e. spectral preprocessings), are utilised in order to address that the reflectance intensity as well as specific spectral features (reflectance maxima and minima) might be relevant for discriminating and analysing the secondary materials. Although this work is conducted based on laboratory data, it will also analyse the possibilities to support field exploration of iron- and steelworks dump sites using spectral methods. Thus, the analyses incorporate the impacts of moisture and grain size on the qualitative and quantitative information that can be derived from the spectral measurements, as these are two of the major factors known to affect reflectance signatures.

Because of the little available information on the specific spectral characteristics of iron- and steelworks by-products in reflectance data covering the analysed wavelength ranges, this work follows a deductive approach to investigate the following objectives and arising research questions:

I. Analysis of the spectral differentiability of typical iron- and steelworks by-products

- Ia Which potential does reflectance spectroscopy offer for discriminating iron- and steelworks by-products?*
- Ib Which spectral range and spectral preprocessings are preferable?*

II. Building a spectral library for major iron- and steelworks by-products and characterising reflectance properties as well as major spectral features occurring in the spectra

- IIa What are the spectral properties of common iron- and steelworks by-products?*
- IIb Which relationships between spectral features and chemical constituents can be observed?*
- IIc What is the impact of moisture and sample preparation on spectra of iron- and steelworks by-products?*

III. Spectral quantification of chemical constituents of iron- and steelworks by-products

- IIIa Which chemical constituents of iron- and steelworks by-products can be spectrally predicted?*
- IIIb Which spectral range provides the best results for which constituent?*
- IIIc Which impacts do different preprocessings have on the model performance?*
- IIId Which variables are important for the spectral prediction of chemical constituents?*
- IIIe Which prediction results can be obtained based on spectra of materials near in situ conditions?*

1.3 Structure of this Work

The structure of this thesis is schematically visualised in Fig. 1.1. Chapter 2 comprises two major parts: the first will provide background information on iron- and steelmaking procedures, associated by-products and their chemical and mineralogical composition. The second addresses basic principles of reflectance spectroscopy of rocks and minerals, causes of features occurring in mineral spectra and physicochemical factors influencing spectral signatures. An introduction to spectral properties of high-temperature formations with relevance for this work and a brief review on geological remote sensing of rocks and minerals will close this chapter. Most of the samples used in this work were collected at the dump site of the Stahlwerk Thüringen GmbH in Unterwellenborn (Thuringia, Germany). As the structure and composition of this dump is strongly linked to the local history of iron- and steelmaking in Unterwellenborn, Chapter 3 will introduce the geographical and geological setting of this area, describe former mining activities, introduce the dump site and the history of iron and steel production at this location.

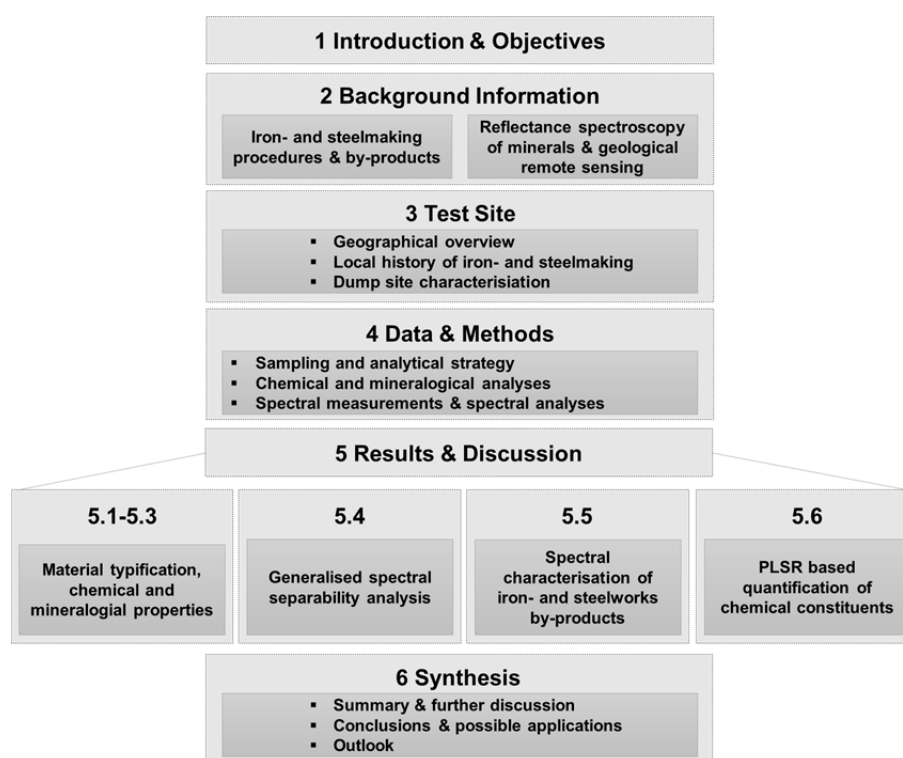


Fig. 1.1: General structure of this thesis.

Chapter 4 will focus on the utilised data and methods, encompassing sample collection and preparation, chemical and mineralogical analyses, reflectance measurements as well as qualitative and quantitative spectral analyses. Results are presented and discussed in Chapter 5, wherein Chapter 5.1-5.3 focus on the chemical and mineralogical properties of the samples. Results of the spectral separability analyses are reported in Chapter 5.4. In Chapter 5.5, reflectance spectra of common iron- and steelworks by-products are presented and discussed, encompassing analyses of spectral variations within by-product classes and impacts of moisture and sample preparation on the spectra. Chapter 5.6 provides results of the quantification of chemical constituents, comprising results achieved using spectra of homogenised samples as well as results based on spectra of samples with near *in situ* conditions. A summary of the results, general discussions and an outlook on subsequent research and possible applications are presented in Chapter 6.

2. Background Information and State of Research

2.1 Iron- and Steelmaking Processes, By-Products and their Properties

2.1.1 Major Iron- and Steelmaking Processes and By-Products

In 2016, world crude steel production was 1630 million tonnes, which is nearly twice the amount produced in the year 2000 (850 million tonnes). In the year 2000, Europe was the world's most relevant steel producer (25%) followed by North America (16%) and China (15%). In contrast, China (50%) is by far the most important steel producer today, followed by Europe (12%), North America (7%), Japan (6%), and India (6%) (World Steel Association 2017, Figure 2.1).

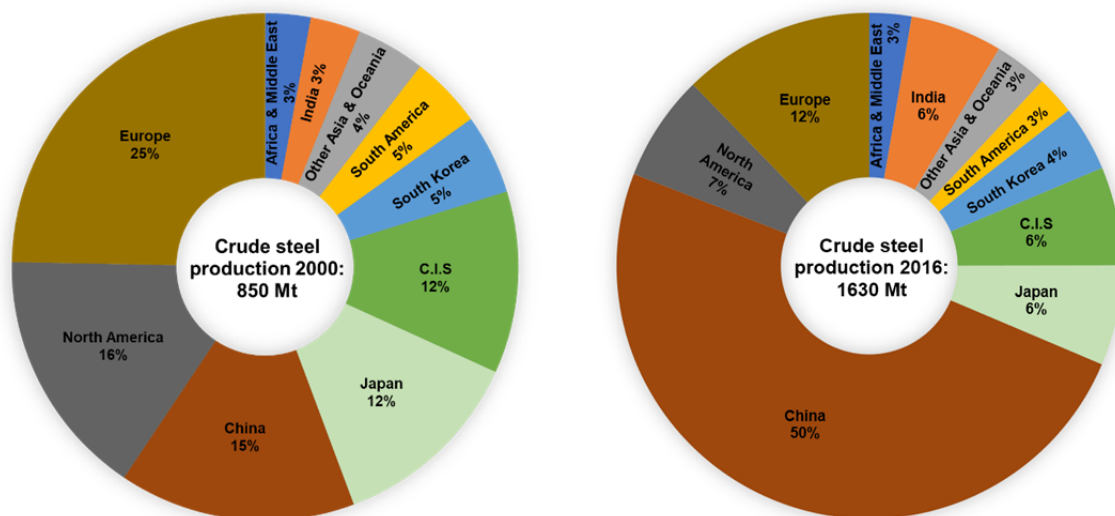


Fig. 2.1: Production of crude steel in the year 2000 (left) and 2016 (right) (after World Steel Association 2017).

The earliest steel discoveries reach back to 2000 B.C. and to the present, various iron- and steelmaking procedures have been utilised (World Steel Association 2012). Today, the two most important procedures are the primary or blast furnace basic oxygen furnace route (BF-BOF) and steelmaking via the electric arc furnace (EAF) route. The BF-BOF route encompasses the reduction of iron ore to iron in blast furnaces (BF) utilising mainly the raw materials iron ore, coal (coke) and limestone. The so produced iron is subsequently processed into crude steel via basic oxygen furnaces (BOF). This route is applied in ca. 50 countries and more than 2/3 of the world's steel production is based on this procedure. The second route comprises the melting of scrap metal in electric arc furnaces (EAF) via electricity and graphite electrodes (IPCC 2007, World Steel Association 2012, Remus et al. 2013). The energy consumption of the secondary route is 30-40% lower compared to the primary route (Beer et al. 1998). Variations of both routes might be applied as well (e.g. World Steel Association 2018).

As it is out of scope of this work to provide a complete overview of all iron- and steelmaking procedures, only major recent procedures and the associated by-products and historical processes and secondary materials of relevance for this work are introduced in the following paragraphs. For further and more comprehensive information on iron and steel production, by-products and their utilisation see e.g. Ghosh and Chatterjee (2008) and VDEh (2015).

Ore preparation – Pelletising, sintering, Krupp-Renn procedure

For the BF-BOF route, iron ore can be used in form of lumpy iron ore, sinter or pellets. While lumpy ore can directly be used for iron making in the blast furnace, fine ore requires preparation via pelletising or sintering (e.g. World Steel Association 2018). Pelletising means the compacting of fine ore by adding binder materials (typically limestone or dolomite), imbuing and subsequent burning the mixture at temperatures $> 1000^{\circ}\text{C}$ in rotary or shaft furnaces to produce pellets with a purity of 63-65% iron (e.g. Ruge 1987, Remus et al. 2013, Singh et al. 2015). Sintering is realised in belt type sintering plants. Here, firstly a mixture of fine iron ore, coke dust and various additives, called sinter cake, is produced. Afterwards, the coke is burned, and air is blown through the sinter cake. The temperatures in this process are kept below the melting point of iron but lead to an aggregation of the fine particles to sinter. The sintering process generates dusts mainly composed of iron oxides and other components. Depending on the dedusting process and their composition, filtered dusts are reused within the sintering process or deposited (e.g. Ruge 1987, Geschichtsverein Maxhütte e.V. 2005, Fernández-González et al. 2017).

The Krupp-Renn process is a pre-treatment procedure invented in 1930 (Ruge 1987). The procedure was utilised to prepare acidic low-grad iron ore in large rotary furnaces, resulting in iron-rich blooms. The rotary furnaces were loaded with iron ore or iron-rich by-products and coke breeze for iron reduction. Accompanying elements in the ore served as slag former. The furnace temperature was between $500\text{-}1300^{\circ}\text{C}$. The resulting iron-slag mixture was quenched with water and subsequently air-cooled. After pestling the mixture, iron blooms could be separated via magnets and used for ironmaking in the blast furnace. The procedure lost importance in the 1960s (Geschichtsverein Maxhütte e.V. 2005).

Iron production in the blast furnace

The main function of a blast furnace is to reduce and liquidise iron. Blast furnaces are loaded from top to bottom in alternating layers of coke (used as reducing agent) and a mixture of sinter, pellets, iron ore and additives called burden (German: “Möller”). The additives are mainly composed of limestone and dolomite and are supposed to bind the non-metallic ore components, the so-called gangue. From the bottom of the blast furnace, air with temperatures of $> 1200^{\circ}\text{C}$ is blown through these layers, which must exhibit certain porosity in order to allow the hot air to pass through. This explains the necessity for preparing fine grained ores beforehand. The liquid iron, i.e. hot metal (HM), and slag are collected at the bottom of the blast furnace. After extraction through a taphole, the mixture runs through a slag runner and is separated in a skimmer by different densities (e.g. Ruge 1987). The hot metal is directly transferred to steel plants or cast into ingots. The product of the latter procedure is called pig iron, which typically shows high carbon contents, contains Mn, P and Si from the iron ore as well as sulphur from the coke. To increase the hot forming properties of the produced hot metal and to reduce the sulphur content, hot metal is typically further processed by adding additives, resulting in desulphurisation slag (see e.g. Ruge 1987, Chiang and Pan 2017). Current blast furnaces reach heights of 40 m, provide capacities of up to 5000 m^3 and a daily production of up to 10000 t iron (Ruge and Wohlfart 2013). About 900 kg of slag per ton of HM was an average figure in the 1940s, but decreased to about 300 kg/t HM in recent past, due to process optimisation (VDEh 2016). An illustration of a blast furnace and the ongoing chemical processes is given in Fig. 2.2.

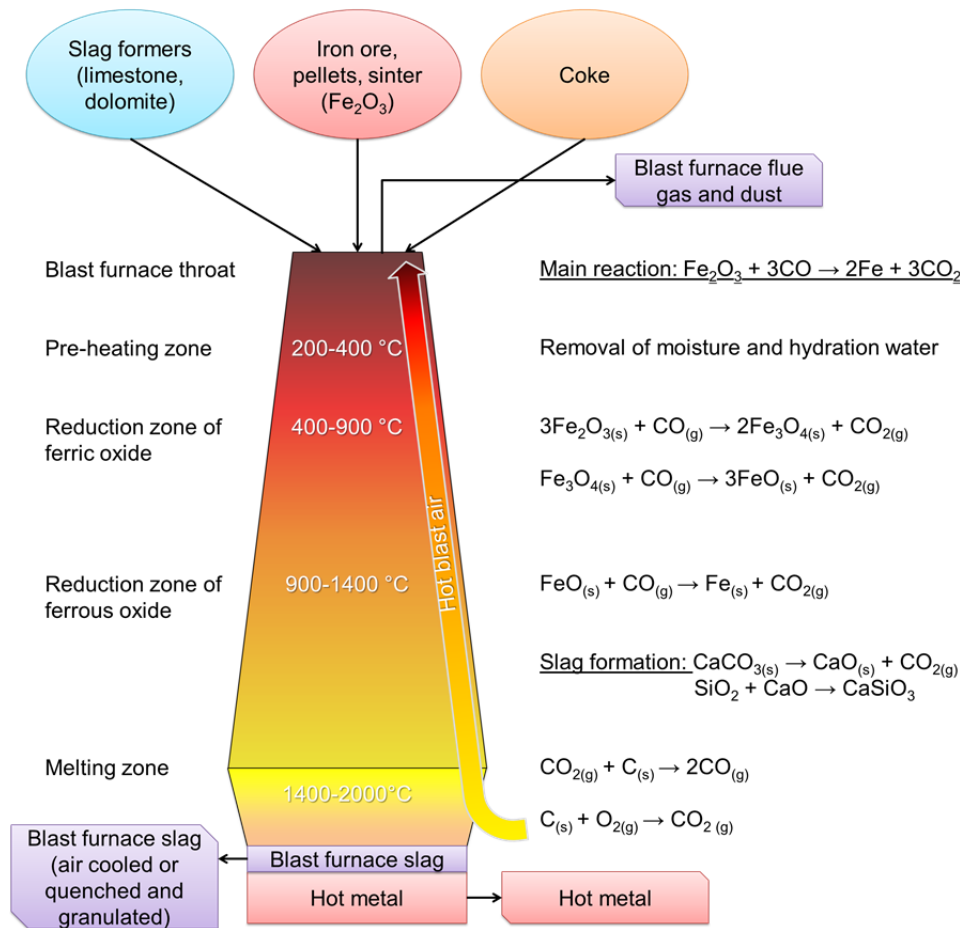


Fig. 2.2: Iron production in a blast furnace and ongoing chemical reactions (after Ruge 1987, VDEh 2015).

Relevant solid by-products of the blast furnace iron production are blast furnace slag (BFS) and blast furnace flue (BFF) dust and sludge (e.g. Das et al. 2002, Das et al. 2007). Blast furnace slags are calcium aluminium silicates, which are generated in the reaction of iron ore and additives. Iron ore rich in aluminium silicates is charged with CaO-rich additives and lime-rich ore is charged with additives rich in SiO_2 and Al_2O_3 (Ehrenberg 2006a). Depending on how the blast furnace slag is cooled, one differentiates into two major types of slag. Air cooled BFS results from slowly cooling the liquid blast furnace slag at slag yards and is mostly crystalline. This slag is mainly used for road and track construction (e.g. Merkel 2017). In contrast, granulated blast furnace slag (GBFS) is generated by quickly cooling blast furnace slag with water. GBFS is an important raw material for the cement industry (e.g. Ehrenberg 2006a, 2006b; Merkel 2017). Blast furnace flue dust is typically cleaned using mechanical and wet de-dusting techniques. Coarse fractions are reused in sinter plants, whereas most of the fine fractions are disposed (see e.g. Gara and Schrimpf 1998, Das et al. 2002, Drissen and Algermissen 2016).

Steel production

Steel production aims to minimise carbon and impurities contained in hot metal (e.g. manganese, silica and sulphur) by oxidative reactions. Starting from the 1860s, the Bessemer-Thomas procedure, and from the 1870s, the Siemens-Martin procedure were the dominant steelmaking procedures applied. Since the 1960s, the basic oxygen furnace (BOF) (Linz-Donawitz, LD) procedure became the dominating steelmaking process apart from steelmaking in the electric arc furnace (see Fig. 2.3; e.g. Ruge 1987, World Steel Association 2012).

The Bessemer procedure comprised the removal of unwanted impurities from hot metal in an egg-shaped converter encased with acidic linings (German: “Bessemer-Birne”) by injecting air through the molten iron (see Figure 2.4 for an illustration of a Bessemer converter). The Thomas procedure was a further development of the Bessemer approach. Thomas converters were encased with dolomite bricks instead of the clay linings in Bessemer converters, allowing the processing of alkaline phosphate-rich iron ore (Ruge 1987, World Steel Association 2012). Slag resulting from the Thomas process is rich in phosphate and has been used as fertiliser (e.g. Motz and Geiseler 2001). In 1976, the last Thomas converter in Germany was shut down (Ruge 1987).

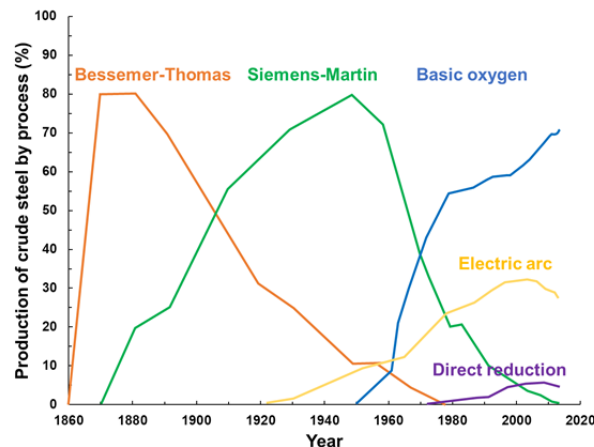


Fig. 2.3: Development of the different steelmaking procedures (modified from Borvan53, CC BY-SA 3.0, <https://commons.wikimedia.org/w/index.php?curid=13284004>).

The Siemens-Martin open hearth furnace procedure was developed by Carl Wilhelm Siemens and further advanced by Pierre-Émile Martin in the mid-1860s. The advantage of this procedure compared to the Bessemer process was an improved temperature control allowing the production of higher quality steel at the cost of a higher energy demand and longer process times (World Steel Association 2012). Figure 2.4 provides a scheme of a Siemens-Martin furnace.

Steelmaking via basic oxygen furnaces (BOF), also known as the Linz-Donawitz (LD) procedure (named after the Austrian cities Linz and Donawitz), was established starting in the 1950s (see Fig. 2.3). Within this procedure, a LD-converter is first loaded with scrap metal and subsequently filled with hot metal. Carbon in the hot metal is oxidised to CO and unwanted impurities like Si, Mn and P are captured by adding slag formers like limestone (CaCO_3) or dolomite $\text{CaMg}(\text{CO}_3)_2$. The resulting slag from this procedure is called basic-oxygen-furnace slag (BOF) (Yildirim and Prezzi 2011). Instead of air like in the Bessemer process, the BOF procedure uses oxygen injected via an “oxygen lance” to reduce carbon and other unwanted impurities in the hot metal to produce steel. The process is exothermal due to the oxidative reactions of C, Mn, P and Si. The presence of scrap metal in the BOF is relevant for adjusting the temperature. A modern BOF is able to melt 350 tonnes of iron into steel within 40 minutes, while up to 12 hours were required for a charge in an open-hearth furnace (World Steel Association 2012).

With increasing amounts of scrap metal in the 1960s, steelmaking via electric arc furnaces (EAF) gained importance as this procedure allowed to melt steel scrap. The required heat for this process is provided by electric energy via electrodes and the purification of the steel is managed by injecting oxygen. An advantage of EAF compared to BOF is that they do not require hot metal (World Steel Association 2012). Typically, one (DC) or three (AC) graphite electrodes are

in operation, and ca. 300 kWh are required to melt one tonne of scrap metal. The melting point of scrap metal is at 1520 °C and the EAF is lined with refractory bricks to protect the furnace shell against the temperatures that can reach 1800 °C in the melt (e.g. Chiang and Pan 2017). CaO, a result of the burning of carbonate-rich slag formers, reacts with oxidised impurities (e.g. Al, C, Mn, Si) and forms slag (Yildirim and Prezzi 2011). The resulting slag of the EAF procedure is called electric arc furnace slag (EAFS). The formation of CO during this process leads to a foaming of the slag (e.g. Juhart et al. 2001, Yildirim and Prezzi 2011, Liukkonen et al. 2012).

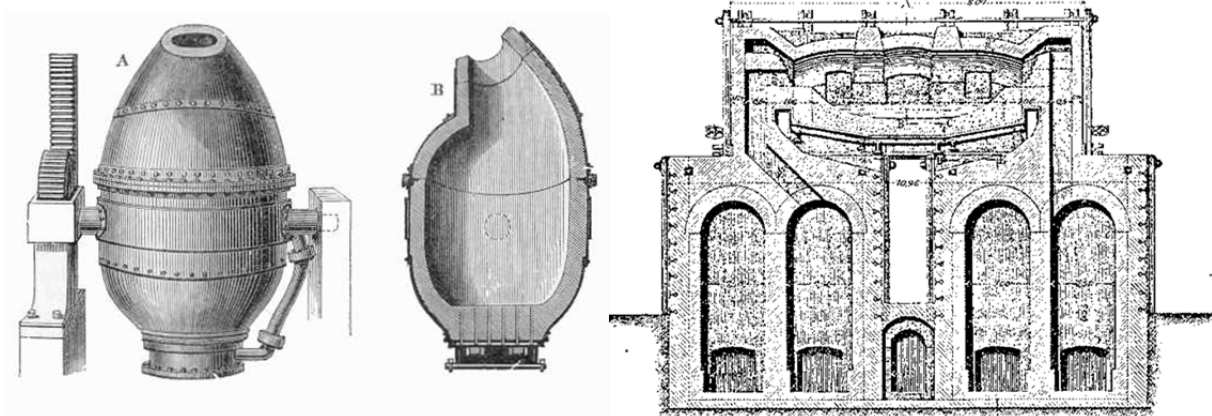


Fig. 2.4: Historical steelmaking furnaces. Left: Bessemer converter (Source: Public Domain, <https://commons.wikimedia.org/w/index.php?curid=91836>), right: Siemens furnace from 1895 (Public Domain, <https://commons.wikimedia.org/w/index.php?curid=508236>).

Steel refinement

After the BOF or EAF process - the primary steelmaking - (liquid) crude steel can be transferred to other vessels to apply refinement procedures, so-called secondary steelmaking operations. These procedures are especially relevant for the production of high-grade steels and primarily aim to increase the quality of the steel and modify its chemical properties. The most important processes are desulphurisation, degassing (H, N₂ and O₂), the removal of impurities and decarburisation and temperature adjustment prior to casting. The function of ladle furnaces is to reheat the crude steel utilising graphite electrodes and to control the temperature and chemical composition of the liquid steel. During the steel refinement processes in the ladle furnace, again limestone (CaCO₃) or dolomite CaMg(CO₃)₂ act as slag formers. Additionally, Ca, Mg, CaSi and CaC₂ might be added as desulphurising agents. Si and Al aid the deoxidisation by forming SiO₂ and Al₂O₃, which are absorbed by the slag (Yildirim and Prezzi 2011). Another important steel refinement procedure is stainless steelmaking, i.e. producing steel with high amounts of Cr as alloying element. After melting of high-alloy steel scrap, the crude steel is submitted to the so-called AOD- (argon oxygen decarburisation) or VOD-process (vacuum oxygen decarburisation). Both aim at decarburisation with oxygen by simultaneously preventing oxidation of Cr. By-products of these processes are AOD reduction and desulphurisation slags. These are utilised e.g. for reuse of chrome (see e.g. Krivsky 1973, Adamczyk et al. 2008, Yan et al. 2014, Chiang and Pan 2017). Slags generated in stainless steelmaking are summarised as stainless steel slag (SSS).

The current annual production of by-products associated with the iron and steel industry is more than 400 million tonnes, of which ca. 90% are iron and steel slags. Aside from slags, sludges and dusts are relevant solid by-products. Per tonne of produced crude steel via the BF/BF-BOF route, ca. 400 kg of by-products are generated and per tonne of crude steel produced via the EAF

route, ca. 200 kg (World Steel Association 2016). In previous studies, 500 kg by-products per tonne of crude steel were reported (375 kg slag, up to 65 kg dust and sludge, 4% deposited; Gara and Schrimpf 1998). Reuse rates of recent by-products in France, Germany, Japan and in the USA reach nearly 100% (Chiang and Pan 2017). However, in China, the current world leader in steel production, the slag reutilisation rate in 2012 was only 22% (Yi et al. 2012). A diagram of major iron- and steelmaking procedures and resulting by-products is given in Figure 2.5.

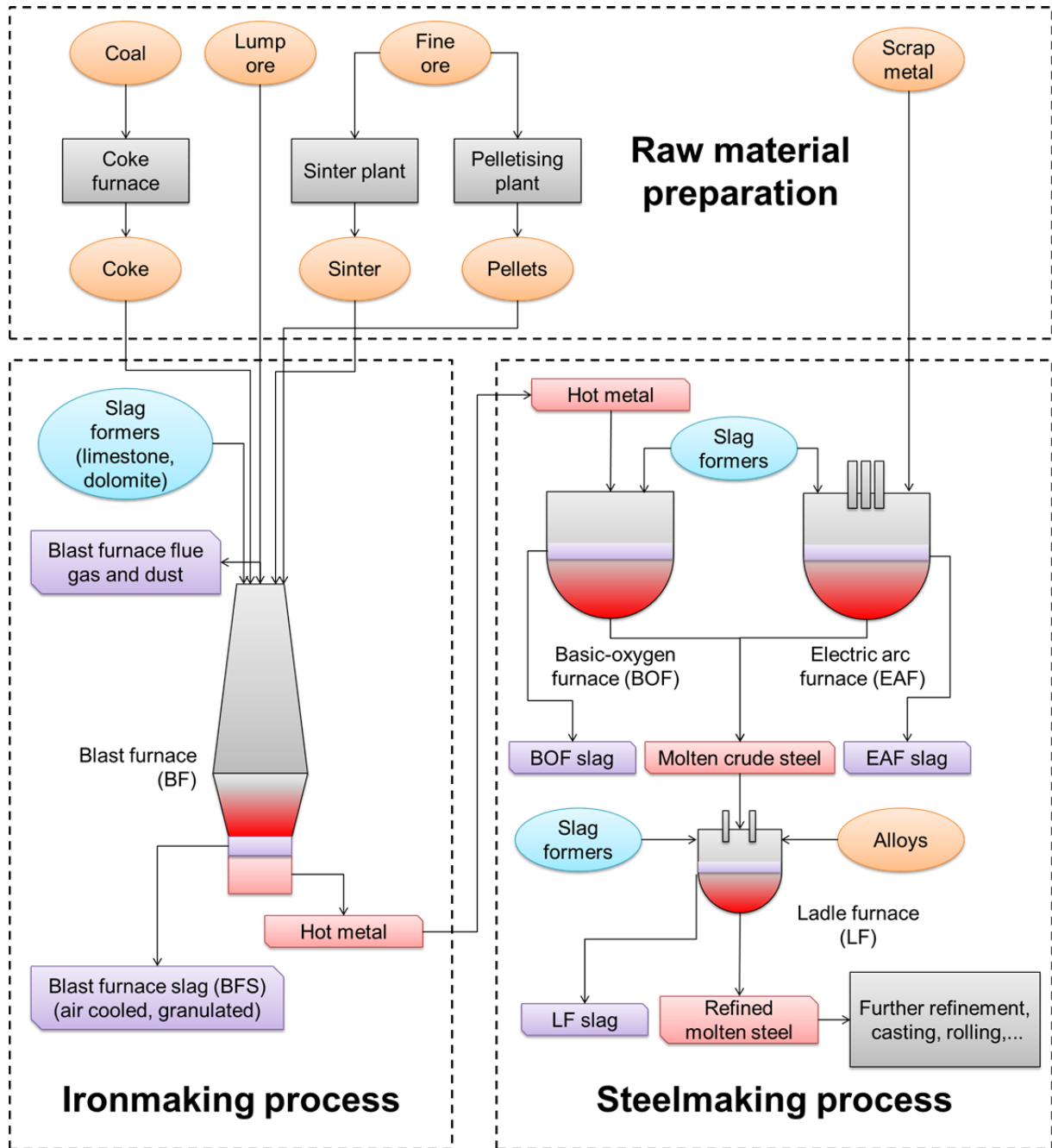


Fig. 2.5: Major iron- and steelmaking and refinement procedures and associated by-products (after Yildirim and Prezzi 2011 and World Steel Association 2018).

2.1.2 Types, Chemical Composition and Utilisation of Iron- and Steelworks By-Products

As described in the previous chapter, the manifold iron- and steelmaking as well as steel refinement procedures generate different by-products (Tab. 2.1). The main by-products are slags. Blast furnace slags (BFS) are differentiated in air-cooled BFS and granulated blast furnace slag (GBFS) (e.g. Drissen 2004). Steelworks slags (SWS) summarise slags from electric arc furnaces (EAFS), LD converter slags (LDS, i.e. BOS), stainless steel slags (SSS) and various slag qualities from secondary steelmaking (e.g. ladle furnace (LF) slags) (see e.g. Schüler et al. 2016).

Tab. 2.1: By-products associated with iron- and steelmaking procedures (modified after Chiang and Pan 2017).

Blast furnace (BF)	Basic oxygen furnace	Steelmaking shop	Electric arc furnace (EAF)	Rolling mills
Air cooled BFS	Basic oxygen furnace slag (BOFS, also LD-slag)	Secondary metallurgical slags (SECS, including LFS)	EAF slag (EAFS)	Mill sludge
Granulated BFS		Ladle furnace sludge	EAF dust	Mill scale
BF (flue) dust		Refractory bricks		
BF (flue) sludge		Fly ash		

Aside from slags, further solid by-products are generated during processes associated with iron- and steelmaking. These are dusts and sludges generated in the different production steps and mill scale generated in casting and rolling of steel. Table 2.2 summarises information on the chemical composition and utilisation of iron- and steelworks slags and for corresponding information on dusts and sludges associated with the iron and steel industry see Table 2.3.

Chemical composition and utilisation of iron- and steelworks slags

Iron- and steelworks slags are by-products of smelting and refinement processes in the iron and steel industry and thus anthropogenic materials by nature. Except for the granulated blast furnace slag (“slag sand”), which is rapidly cooled by quenching with water, most slags are tipped from the furnaces and transferred into slag beds for cooling. Liquid slags solidify in these beds over several days and form crystalline, relatively homogeneous bodies, in which escaping gases can produce prominent cavities (Fig. 2.6). Compared to natural rocks, the technogenic formation of slags occurs in a relatively short period of time, but the formation conditions and structure of slags show a certain similarity to magmatic, particularly volcanic rocks (Drissen 2004).

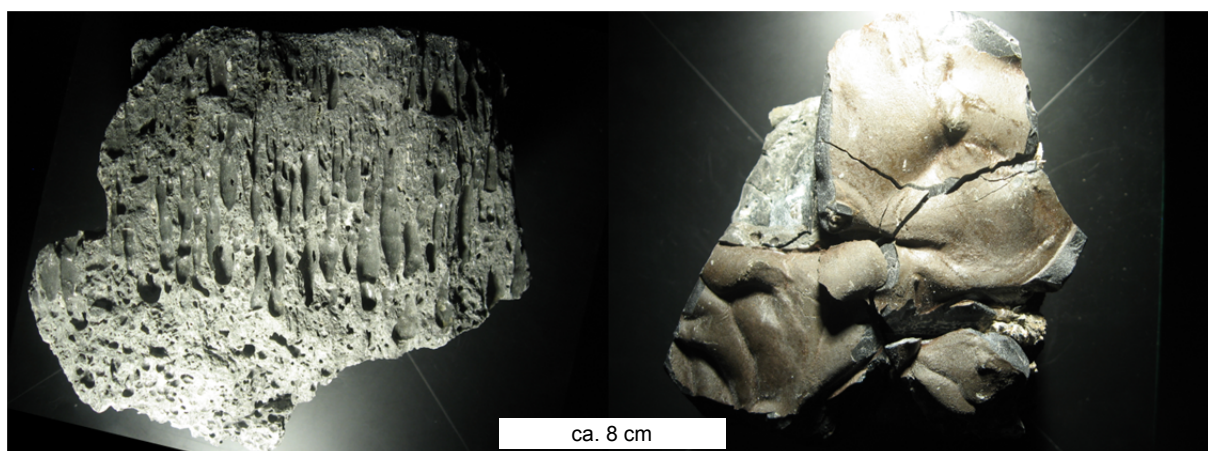


Fig. 2.6: Slag samples. Left: Electric arc furnace slag from high-alloy steelmaking with distinct degassing marks as a result of slow cooling in the slag bed. Right: Top view of a cooling crust of an AOD converter slag sample.

The chemical composition of slags is largely variable and related to the specific iron- and steelmaking process applied (see Tab. 2.1). In general, the chemistry of slags is characterised by lower SiO_2 but higher CaO contents compared to natural rocks. In contrast, except for the blast furnace slag, slags typically show higher Fe and Mn contents. Stainless steel slags also exhibit higher Cr contents due to the addition of alloying elements. While Al_2O_3 is in most cases on a comparable level to natural rocks, alkaline materials are of less relevance in iron and steel slags. Figure 2.7 presents the differences in the chemical composition of various iron- and steelworks slags compared to the chemistry of natural rocks in a $\text{CaO}+\text{MgO}-\text{SiO}_2-\text{Al}_2\text{O}_3+\text{Fe}_2\text{O}_3+\text{Cr}_2\text{O}_3$ pseudo-ternary plot (Drissen 2004, a similar diagram is provided e.g. in Chiang and Pan 2017).

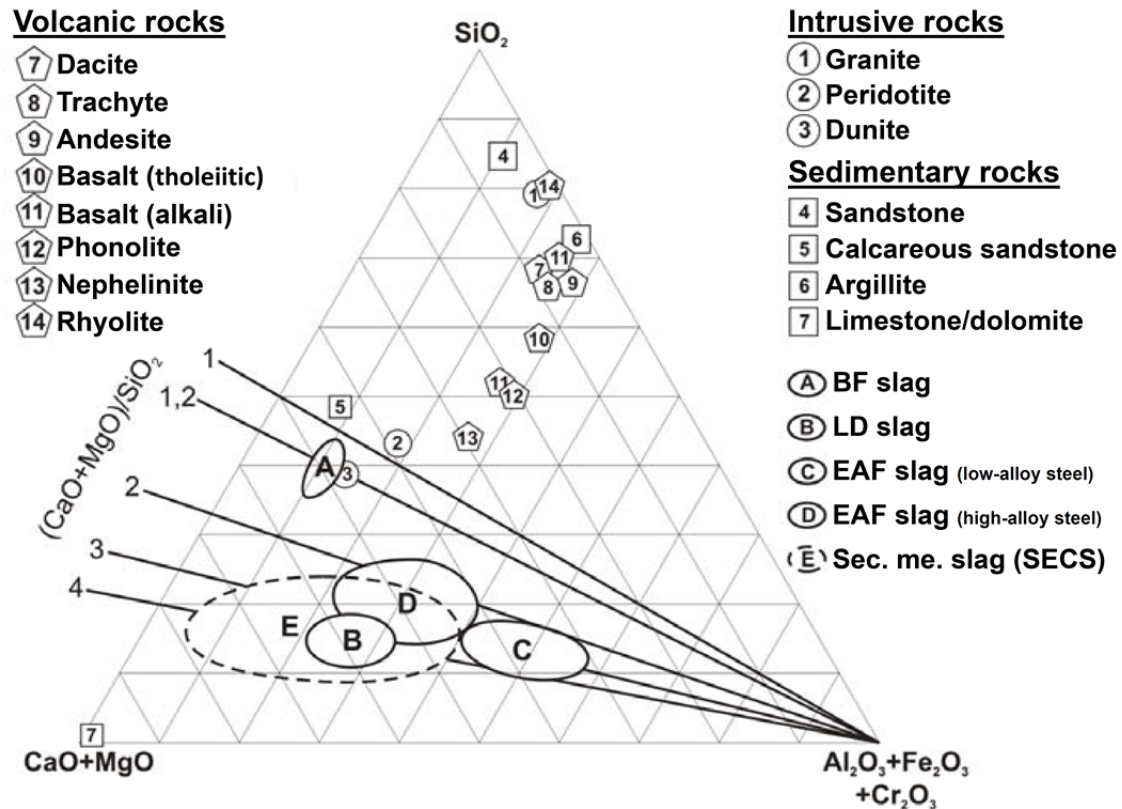


Fig. 2.7: Comparison of the chemistry of iron- and steelworks slags and natural rocks (after Drissen 2004).

By-products of the BF are mainly BF slag, BF off-gas as well as dusts from cleaning the blast furnace's flue. Blast furnace flue gas is mainly used for heating and power generation (Ramírez-Santos et al. 2017). Air-cooled and granulated BFS are mainly composed of CaO and SiO_2 (each ca. 30-40%), up to ca. 10% Al_2O_3 and 10% MgO (Gara and Schimpf 1998, Drissen 2004, Das et al. 2007). In contrast to the comparably slowly air-cooled BFS, the granulated BFS shows a glassy structure due to its quick cooling (Drissen 2004). In 2016, ca. 8.1 million tonnes of BFS were produced in Germany, of which granulated blast furnace slag represented the vast majority (92%) and was almost completely used as raw material for the cement industry. Air-cooled BFS was mainly used as aggregate in road construction (see Fig. 2.8, Merkel 2017).

The composition of steelworks slags is strongly variable depending on the specific process, the raw materials used and the quality of the produced steel. Due to the nature of the main slag formers (limestone and dolomite), the composition of steelworks slags is dominated by CaO , followed by SiO_2 , MgO and Al_2O_3 , and a varying content of Fe and various heavy metals as trace elements. Stainless steel slags are characterised by higher amounts of Cr and other trace elements

compared to other slags, as these metals are used as alloying elements (e.g. Gara and Schrimpf 1998, Drissen 2004, Rekersdrees et al. 2014; Tab. 2.2). By-products from stainless steelmaking are typically rich in valuable metals (e.g. Huaiwei and Xin 2011), which are mainly retrieved and reused within steelmaking processes (Guldan 2013). Secondary metallurgical slags are partially reused within steelmaking processes as substitute for lime due to their high CaO content or as construction material (e.g. Das et al. 2007, Setién et al. 2009). In 2016, 5.1 million tonnes of steel slag were produced in Germany, of which 53% were utilised as construction material, 7% as fertiliser, 11% were recycled and reused, 9% were intermediately deposited and 15% of the steelworks slags were deposited in landfills (Fig. 2.8, Merkel 2017).

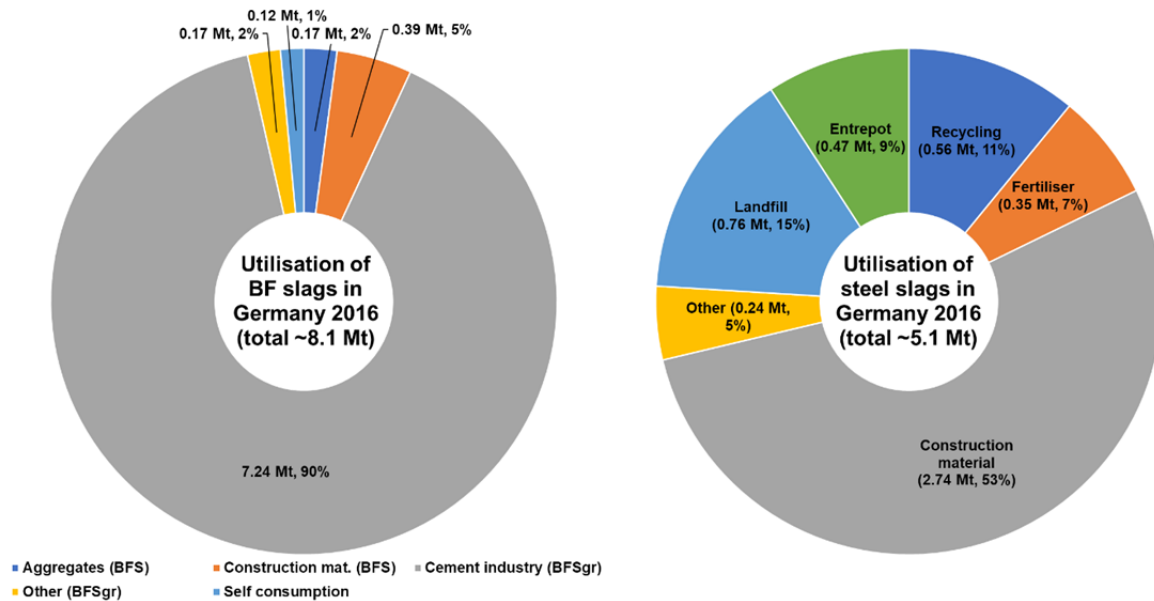


Fig. 2.8: Produced amounts and utilisation of blast furnace slag (BFS, BFSgr = granulated blast furnace slag) and steelworks slag in Germany in 2016 (data from Merkel 2017).

Thomas slag is the major by-product of the Bessemer-Thomas procedure and characterised by its high P_2O_5 content. It was mainly used as fertiliser. Today, Thomas slag is not available anymore (Motz and Geiseler 2001, Dohlen and Steinweg 2009, Drissen 2012). Further details on the composition of slags and their utilisation are aggregated in Tab. 2.2. More detailed information on the chemistry of slags is given in VDEh (1995).

Chemical composition and utilisation of dusts, sludges and other by-products

Aside from slags, various dusts and sludges are of relevance for material reuse (Tab 2.3). Typical by-products of sinter facilities are sludges and dusts, of which especially the dusts are potentially rich in iron (up to $> 50\%$ Fe_{total}). However, they might also contain heavy metals and alkaline elements that are unwanted components in the blast furnace. Thus, sinter dusts are mainly reused within the sinter process (Gara and Schrimpf 1998). LD converter sludges as well as blast furnace flue dusts are potentially rich in iron and might thus be used in sinter facilities as well (Gara and Schrimpf 1998, Das et al. 2007). Mill scale represents a material formed at hot rolled steel. It mainly consists of iron oxides (Fe_{total} 65-70%, FeO 40-70%, Fe_3O_4 20-30%) (Gara and Schrimpf 1998) and its reuse rate in Germany is 100% (Drissen 2011). For further information on other by-products, which may include also dusts from production halls, filter facilities and others, see e.g. Gara and Schrimpf 1998, Das et al. 2002, Dippenaar 2004, Das et al. 2007, Yi et al. 2012 and Chiang and Pan 2017 and Table 2.3.

2.1 Iron- and Steelmaking Processes, By-Products and their Properties

Tab. 2.2: Composition and utilisation of iron- and steelwork slags (modified after Mrotzek-Blöß et al. 2016).*

Iron- and steel-making procedure	By-product	Chemical constituents (>2 m%)		Utilisation	
Blast furnace	Air cooled BFS	SiO ₂	34-37	Cement industry, fabrication of bricks (Das et al. 2007)	
		CaO	39-41		
		Al ₂ O ₃	10-12		
		MgO	7-12		
	Granulated BFS (“slag sand”)	(Drissen 2004)		Mainly cement industry (Merkel 2017)	
Electric arc furnace	EAF slag (no/low-alloy steel)	Fe	24-40	Construction material (Heußen and Markus 2013)	
		CaO	26-38		
		SiO ₂	11-16		
		Al ₂ O ₃	3-6		
		MgO	3-10		
		(Drissen 2004)			
	EAF slag (high-alloy steel)	CaO	37-40		
		SiO ₂	14-28		
		MgO	7-13		
		Mn _{total}	2.6-4.1		
Fe _{total}		6-7			
	(Drissen 2004)				
LD converter (BOF)	LD-converter slag (BOFS)	CaO	18-24	Construction material, fertiliser (Bartusch et al. 2013) Potential substitute for limestone in blast furnaces (Das et al. 2007)	
		CaO	36-50		
		SiO ₂	10-15		
		Al ₂ O ₃	1.0-3.5		
		MgO	4-8		
		MnO	5		
	(Gara and Schrimpf 1998)				
Thomas converter	Thomas slag	CaO	45	Fertiliser (Dohlen and Steinweg 2009, Motz and Geiseler 2001)	
		SiO ₂	5		
		Fe	14		
		P ₂ O ₅	12 - 17		
		MnO	2 - 4		
	(results within this study)				
Ladle furnace	Ladle furnace slag (LF slag)	CaO	50.5–57.5	Construction material (Setién et al. 2009)	
		SiO ₂	12.6–19.8		
		Al ₂ O ₃	4.3–18.6		
		MgO	7.5–11.9		
		Fe ₂ O ₃	1.6–3.3		
	CaO _{free} 3.5–19				
	(Setién et al. 2009)				
Other secondary metallurgy	Secondary metallurgical slag (SECS)	FeO	< 3	Potential substitute for limestone, re-use of scrap metal for EAF (Rekersdrees et al 2014)	
		CaO	30-60		
		SiO ₂	5-18		
		Al ₂ O ₃	20-40		
		MgO	4-14		
	(Rekersdrees et al. 2014)				
Stainless steel production	Stainless steel slag	Fe _{total}	0.7-10.4	Recovery of alloy metals (e.g. Cr, Ni, Mo), Construction material (Guldan 2013)	
		CaO	25-56		
		SiO ₂	14-33		
		Al ₂ O ₃	1.5-9.6		
		MgO	4.6-12.3		
		MnO	0.4-6.8		
		F	0.8-5.1		
Cr ₂ O ₃	0.5-20.4				
	(Drissen 2004)				

*It must be strongly considered that especially by-products found at historic dump sites may vary in their composition and differ from the data given above. For example, blast furnace slags from the beginning 20th century often showed higher CaO and F contents compared to recent by-products (Interview with P. Drissen, FEhS, 2018).

Tab. 2.3: Composition and utilisation of dusts and sludges from iron- and steelmaking (modified after Heite 2015).

Procedure	By-product	Chemical constituents (>2 m%)	Typical Utilisation	
Sinter plant	Sinter dust	CaO	1.2 – 14	Reuse in the sinter plant (Gara and Schrimpf 1998)
		C	1.5 – 10	
		Fe _{total}	35 – 56	
		MgO	0.1 – 11	
		Pb	0.04 – 10	
		SiO ₂	0.6 – 8	
		S _{total}	0.2 – 4 (Gara and Schrimpf 1998)	
Blast furnace	Blast furnace flue dust	Al ₂ O ₃	3 – 5	Reuse in the sinter plant (Gara and Schrimpf 1998)
		C	29-34	
		CaO	2.5 – 5	
		Fe _{total}	~51	
		SiO ₂	6 - 8 (Das et al. 2002)	
	Blast furnace flue sludge	Al ₂ O ₃	2 – 4	Disposal (Gara and Schrimpf 1998)
		C	25 – 40	
		CaO	4 – 6	
		Fe _{total}	25 – 35	
		Pb	0.5 – 3	
	SiO ₂	5 – 8		
	Zn	1 – 8 (Gara and Schrimpf 1998)		
LD converter	LD converter sludge	Fe _{total}	61-64	Reuse in the sinter plant (Das et al. 2007)
		CaO	9-11 (Das et al. 2007)	
Electric arc furnace	Electric arc furnace dust	C	1-5	Waelz-procedure (Pichler et al. 2013) Re-use in EAF (Gara and Schrimpf 1998)
		CaO	3-10	
		Cl	1-5	
		FeO	20-45	
		Pb	2-8	
		SiO ₂	3-6	
		Zn	14-35 (Rütten 2006)	
Bloom	Mill scale	Fe _{total}	65-70	100% re-use within the plant internal material cycle (Drissen 2011)
		FeO	40-70	
		Fe ₃ O ₄	20-30 (Gara and Schrimpf 1998)	

2.1.3 Mineralogical Composition of Iron- and Steelworks By-Products

As a result of the specific chemical composition, the mineralogy of slags is also different from the mineralogical composition of natural rocks. However, most of the minerals found in slags are known from natural rocks and minerals (Drissen 2004). The mineralogy of slags is not only determined by their chemical composition, but also by their cooling rate and slags tend to show non-crystalline properties, especially when rapidly cooled (Yildirim and Prezzi 2011). Non-crystalline means the lack of long range positional order. Here, one differentiates amorphous solids and glasses (Gupta 1996). The structure of glassy materials can be understood as “frozen liquid”, which is the result of rapid solidification of a liquid melt due to quenching (e.g. King et al. 2004b). As such, rapidly cooled slag might solidify in a glass-like amorphous structure, like for example the granulated blast furnace slag (Drissen 2004, Tossavainen et al. 2007, Shimoda et al. 2008). Quantitative analysis of blast furnace slags indicated that the quantity of amorphous constituents can reach > 90 % (Westphal 2007). LF slag was found to show a high amount of glass when rapidly cooled, while BOF and EAF slags are of a high crystallinity when either slowly air-cooled or rapidly quenched (Tossavainen et al. 2007). According to the literature, slags require extreme high cooling rates for a glassy state (Liu et al. 2017).

Due to the nature of the used raw materials (ore, scrap) and slag formers (calcium or magnesium carbonates) the resulting crystalline slags from iron and steel production are mainly composed of calcium or aluminium silicates (e.g. Drissen 2004). The typical mineralogical composition of iron- and steelworks slags is presented in Table 2.4.

Typical minerals in air-cooled BFS are akermanite ($\text{Ca}_2\text{Mg}(\text{Si}_2\text{O}_7)$) and gehlenite ($\text{Ca}_2\text{Al}(\text{AlSi})\text{O}_7$), which are assigned to the melilite group, as well as merwinite ($\text{Ca}_3\text{Mg}(\text{SiO}_4)_2$). These phases can also occur in EAF slags (Drissen 2004). Monticellite (CaMgSiO_4) is a further mineral commonly found in BFS (Ghosh and Chatterjee 2008), but also in EAFS (Diener 2006).

Tab. 2.4: Minerals in iron- and steelworks slags (after Drissen 2004, Diener 2006, Drissen and Mudersbach 2012). BFS (air-c.) = air-cooled blast furnace slag, BOFS = basic oxygen furnace slag, EAFS = electric arc furnace slag (cs = carbon, i.e. low-alloy, steelmaking, ha = high-alloy steelmaking), SECS = slags from secondary steelmaking).

Mineral phase	Formula	BFS (air-c.)	BOFS	EAFS(cs)	EAFS (ha)	SECS
Akermanite	$\text{Ca}_2\text{Mg}(\text{Si}_2\text{O}_7)$	x		x	x	
Bredigite	$\text{Ca}_7\text{Mg}(\text{SiO}_4)_4$			x		
Brownmillerite	$\text{Ca}_2(\text{Al,Fe})_2\text{O}_5$			x		
Cuspidine	$\text{Ca}_4(\text{Si}_2\text{O}_7)(\text{F,OH})_2$					x
Dicalcium ferrite	$2\text{CaO}*\text{Fe}_2\text{O}_3$		x			
Fluorite, Oldhamite	CaF_2, CaS					x
Free lime	CaO		x			
Gehlenite	$\text{Ca}_2\text{Al}(\text{AlSi})\text{O}_7$	x		x	x	
Jasmondite	$\text{Ca}_{11}(\text{SiO}_4)_4\text{O}_2\text{S}$					x
Mayenite	$\text{Ca}_{12}\text{Al}_4\text{O}_{33}$			x		x
Merwinite	$\text{Ca}_3\text{Mg}(\text{SiO}_4)_2$	x			x	
Monticellite	CaMgSiO_4			x		
Periclase	MgO		x	x	x	
Spinel	MgAl_2O_4			x	x	
Wüstite	FeO_x		x	x		
β -dicalcium silicate	$\beta\text{-Ca}_2\text{SiO}_4$		x	x		x
γ -dicalcium silicate	$\gamma\text{-Ca}_2\text{SiO}_4$					x

Steelworks slags are characterised by different calcium aluminium silicates and iron oxides. Tricalcium silicate usually only occurs in rapidly cooled lime-rich BOF slags. In contrast, β -dicalcium silicate ($\beta\text{-Ca}_2\text{SiO}_4$, also referred as $\beta\text{-C}_2\text{S}$) is a major constituent of steel slags. In some cases, γ -

dicalcium silicate ($\gamma\text{-Ca}_2\text{SiO}_4$) is formed out of $\beta\text{-C}_2\text{S}$ during cooling of secondary metallurgical slags (SECS). Due to the relatively high amount of iron, calcium ferrites may occur, e.g. Brownmillerite ($\text{Ca}_2(\text{Al,Fe})_2\text{O}_5$) in Al_2O_3 -rich EAF slags and dicalcium ferrite ($2\text{CaO}\cdot\text{Fe}_2\text{O}_3$) in BOF slags. The high iron content further benefits the formation of wüstite (FeO_x) and spinels (MgAl_2O_4). Free lime and periclase (free MgO) may occur in steelworks slags related to the utilisation of limestone and dolomite as slag formers. Secondary metallurgical slags (SECS) are mainly used for desulphurisation and deoxidisation of steel. The high CaO and relatively high Al_2O_3 contents benefit the formation of tricalcium aluminate and mayenite ($\text{Ca}_{12}\text{Al}_{14}\text{O}_{33}$). Further major mineral components of SECS are $\beta\text{-Ca}_2\text{SiO}_4$ and $\gamma\text{-Ca}_2\text{SiO}_4$. Gehlenite-akermanite, merwinite, rankinite ($\text{Ca}_3\text{Si}_2\text{O}_7$), cuspidine ($\text{Ca}_4(\text{Si}_2\text{O}_7)(\text{F,OH})_2$), oldhamite (CaS) and jasmundite ($\text{Ca}_{11}(\text{SiO}_4)_4\text{O}_2\text{S}$) are other typical constituents of SECS (Drissen 2004). Fluorite (CaF_2) is used to improve the liquefaction of highly calcium-rich slags and might thus be present in SECS, too (Yildirim and Prezzi 2011). For further details on the mineralogy of iron- and steelworks slags see e.g. Drissen (2004), Diener (2006), Das et al. (2007), Ghosh and Chatterjee (2008).

Slags might contain unstable mineral phases, mainly free lime (CaO_{free}) and periclase (MgO_{free}). “Free” refers to the fact that CaO or MgO are not bound as silicate or ferrite in the solid slag. Free CaO in solidified, cold slags can react with water (or water vapour) and form portlandite ($\text{Ca}(\text{OH})_2$) within a few days, which is accompanied with a volume increase. In contrast, free MgO hydrates at much slower rates (e.g. Ramachandran et al. 1964, Yildirim and Prezzi 2011). Another type of “instability” is related to dicalcium silicate, a common mineral in slags from iron- and steelmaking and is called dicalcium silicate decomposition. This process is due to the transformation of $\beta\text{-Ca}_2\text{SiO}_4$ (larnite) to $\gamma\text{-Ca}_2\text{SiO}_4$ (calcio-olivine) at temperatures $< 500^\circ\text{C}$, resulting in a volume increase of 10-12%. Due to the homogeneous distribution of $\beta\text{-C}_2\text{S}$ within the slag, this process leads to a complete destruction of the slag-aggregate and results in a “self-dusting-effect”, that is known e.g. for LF slag (e.g. Drissen and Arlt 2000, Shi 2002, Yildirim and Prezzi 2011, Drissen et al. 2012). This process was also observed for an AODS sample, which disintegrated into powder after several days, revealing metal shots (Fig. 2.9). Such phase transformations can be blocked by rapid cooling or by inhibitors like phosphorous (Pontikes et al. 2010).



Fig. 2.9: Left: Fresh AOD converter reduction slag with metal granules. Right: Self-pulverisation of the sample due to dicalcium silicate decomposition leaving only the formerly embedded granulated metal shots.

2.2 Reflectance Spectroscopy of Minerals

2.2.1 Basic Principles and Terminology

The following chapter will summarise basic principles of reflectance spectroscopy and define the relevant terminology later used in this work. For more comprehensive descriptions of the fundamentals of geological remote sensing see e.g. Hunt 1980, Hunt 1982, Clark 1999, Hirschmugl 2004 and Gupta 2018. The basic interactions of electromagnetic radiation with objects are: absorption, transmission or scattering (Clark 1999, Gupta 2018). According to the Law of Conservation of Energy, the relation of incoming (E_{i_λ}), absorbed (E_{a_λ}), transmitted (E_{t_λ}) and reflected radiation (E_{r_λ}) as a function of wavelength can be described by the formula (1):

$$E_{i_\lambda} = E_{a_\lambda} + E_{t_\lambda} + E_{r_\lambda} \text{ (see e.g. Gupta 2018).} \quad (1)$$

Transmission, absorption and reflectance processes are strongly related to the material composition and wavelength-specific, which constitutes the basis for spectroscopic applications and subsequently remote sensing (Clark 1999, Gupta 2018). Consequently, Clark (1999) defined spectroscopy as the “[...] the study of light as a function of wavelength that has been emitted, reflected or scattered from a solid, liquid, or gas”. Minerals show a large variety of wavelength-related absorption processes caused by their mineralogical and structural composition. Thus, measuring reflected radiation allows drawing conclusions about the chemical and mineralogical composition of minerals and mineral mixtures. The emission of radiation in the thermal infrared is negligible under laboratory conditions when using a sufficient illumination source (Clark 1999).

Reflection on surfaces can occur as specular reflection at which the incident angle corresponds to the angle of the reflected radiation (Fig. 2.10a). This type of reflection is usually observed for mirror-like surfaces. Diffuse Lambertian reflection on rough surfaces describes the scattering of radiation equally in all directions independent of the incident angle (Fig. 2.10b). Typically, natural surfaces show neither only specular nor Lambertian reflectance but a mixture of both, the former constituting the major part of reflected light (Fig. 2.10c; Albertz 2009, Gupta 2018).

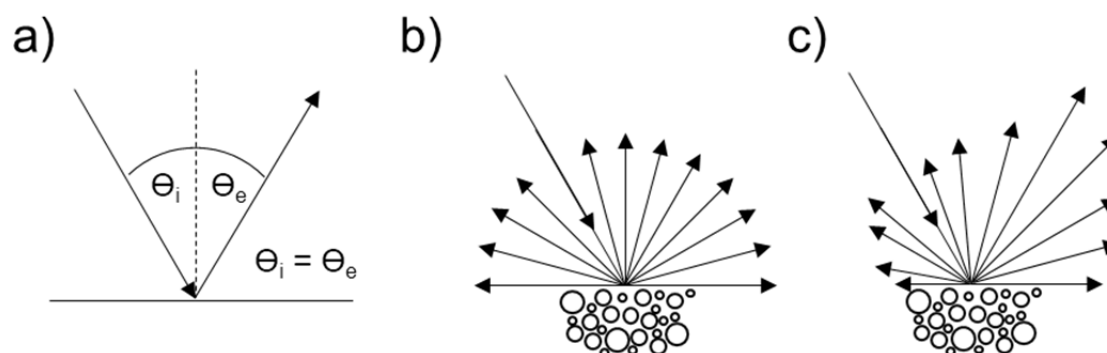


Fig. 2.10: Reflection mechanisms. a) specular reflection from a plane surface; b) Lambertian reflection from a rough surface (diffuse reflection); c) semi-diffuse reflection (natural bodies) (modified after Gupta 2018).

Reflectance measurements are usually conducted as bidirectional measurements, i.e. the incident illumination and the observation of reflected radiation occur at two different directions (Fig. 2.11, Gupta 2018). Usually, the reflectance measured at a sensor is influenced by various parameters: the spectral properties of the materials themselves caused by their specific composition (see Chapter 2.2.2), grain size (see Chapter 2.2.3) and mixtures of different minerals. An additional

important factor impacting spectral measurements is the viewing geometry of the utilised set-up, which comprises the angles of the incident and reflected radiation. Changes in the measurement geometry might result in variations of shadowing and the relation of single to multiple scattering (see Chapter 2.2.3, Fig. 2.11) (Clark 1999, Hapke 2012). Thus, measurements from different angles might provide different results for the same target surface (Gupta 2018). The complex interactions of different factors affecting reflectance properties of surfaces are described using the bidirectional reflectance distribution function (BRDF), for which first definitions and various theories reach back until the 1960s (e.g. Nicodemus 1965, Torrance and Sparrow 1967). Theories elaborated in the 1980s further improved the BRDF theories (Hapke 1981, Goguen 1981, Lumme and Bowell 1981) by considering also shadowing occurring between the grains of particulate surfaces. The approach provided by Hapke (1981), which also incorporated mixtures, can be considered the predominant theory utilised in the field of remote sensing (Clark 1999). Comprehensive details of this theory are provided in Hapke (2012).

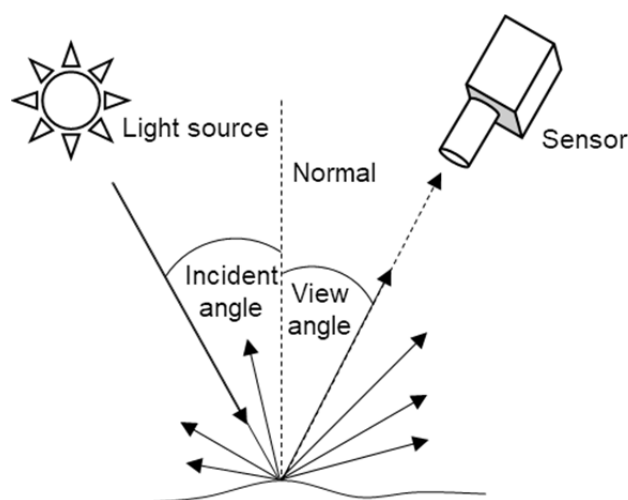


Fig. 2.11: Bidirectional reflectance measurement set-up as typically used in spectrometry and occurring scattering processes (modified from Gupta 2018).

Measured reflected radiation may be utilised for qualitative analyses of the composition of materials and for quantitative purposes, as the strength of absorptions is linked to the amount of the absorbing constituent. This can be described according to the Beer-Lambert's Law (2):

$$I = I_0 e^{-kx} \quad (2)$$

where I is the intensity of the measured radiation, I_0 is the original intensity, k is an absorption coefficient and x is the distance photons travel through the medium (see e.g. Clark 1999).

The characteristics of such absorption features (e.g. position, shape, etc.) can be linked to the crystal and chemical structure of minerals (e.g. Clark and Roush 1984, Clark 1999, van der Meer 2004) and thus used for qualitative and mineral identification analyses. Wold et al. (2001) mentioned that “[...] the spectrum of a sample is the sum of the spectra of the constituents multiplied by their concentrations in the sample”. Consequently, spectroscopy has been applied in various studies for quantifying constituents in soils (e.g. Vohland et al. 2009, Riedel et al. 2018) and rocks (e.g. Ruff et al. 1997, Schodlok 2004, Hecker et al. 2012).

As mentioned before, the basic interactions of radiation and matter are transmittance, emittance and scattering/reflection. Consequently, the spectroscopic acquisition of absorbance, reflectance, transmittance or emittance data provides different information of the spectral properties of a sample (e.g. Hecker et al. 2010, Ramsey 2004). However, attention has to be paid when transferring observations made in one spectrum type to another as the interdependencies between the different types are not yet completely understood (Gupta 2018). While the wavelength units nm or μm are typically utilised in the remote sensing community, wavenumbers (cm^{-1}) are commonly used in laboratory infrared spectroscopy, as this unit is proportional to the frequency (see e.g. Schodlok 2004). This thesis will solely focus on reflectance measurements and provide wavelength units in nm. Consequently, wavenumbers given in the literature were transformed in nanometres for better comparability according to the following equation (3):

$$\text{nm} = (1/\text{cm}^{-1}) * 10^7 \quad (3)$$

The “classical” wavelength region utilised in remote sensing-associated studies covers the range of 350-2500 nm. However, relevant rock-forming minerals, especially silicates, exhibit no distinctive spectral features in this wavelength region but show diagnostic characteristics in the thermal infrared (e.g. Salisbury et al. 1987, Schodlok et al. 2016, Gupta 2018; see the following Chapter 2.2.2). Thus, a large number of remote sensing studies focussed on this wavelength range and successfully demonstrated the capacities of such spectral data for the qualitative and quantitative determination of the mineral composition of rocks (e.g. Salisbury and D’Aria 1992a; Feely and Christensen 1999; Vaughan et al. 2003, 2005; Hecker et al. 2012).

The reflectance measurements in this thesis were conducted using two different spectrometers covering different parts of the electromagnetic spectrum: the wavelength range of 350-2500 nm as well as the range of ca. 2000-15000 nm (see Chapter 4.6.1). These wavelength ranges encompass parts of the ultraviolet, the visible light and infrared. The infrared is further differentiated into sub-regions that are known as near-infrared, shortwave infrared, mid-infrared, longwave infrared, far infrared and thermal infrared. Confusingly, these terms are not fixed and vary depending on the literature and the user group (see e.g. Clark 1999, Hirschmugl 2004, Hecker et al. 2010). For this thesis, considering the wavelength ranges covered by the two utilised spectrometers and following the subdivision of the electromagnetic spectrum and terminology used e.g. in Eisele et al. (2015), ranges and terms were defined as shown in Table 2.5.

Tab. 2.5: Wavelength ranges and terminology used in this thesis. The most frequently used terms are in bold letters.

Wavelength range (name)	Wavelength range (nm)	Abbreviation
Visible light	350-700	VIS
Near infrared	700-1300	NIR
Visible light and near infrared	350-1300	VNIR
Shortwave infrared	1300-2500	SWIR
Visible light, near and shortwave infrared	350-2500	VNIR/SWIR
Midwave infrared	2500-5000	MWIR
Longwave infrared	5000-15000	LWIR
Mid- and longwave infrared	~2500-15000	MWIR/LWIR
Visible light to longwave infrared	~350-15000	VNIR-LWIR

2.2.2 Causes of Mineral Spectral Features

2.2.2.1 Electronic Processes

The absorption features present in mineral spectra can be caused by electronic or vibrational processes. These processes have been comprehensively described in various works, of which the books by Farmer (1974) and Burns (2005) can be considered as two of the most fundamental works. Summarising descriptions of the causes of features in mineral spectra are for example provided e.g. in Hunt (1977, 1980, 1982), Clark (1999) and Gupta (2018).

Electronic processes summarise the effects that can occur when the energy state of isolated atoms or ions is changed due to the absorption and subsequent emission of photons. Features related to such processes mainly occur in the ultraviolet, visible light and near infrared (Clark 1999). These processes are further differentiated into four categories:

Crystal field effects are the most common electronic processes causing absorptions in mineral spectra (Clark 1999). In minerals, the energy levels of electrons in the outer shell of transition elements (e.g. Cr, Cu, Fe, Mn, Ni, Ti, V) are influenced by interactions with neighbouring ions and the energy level for one ion might vary in different crystal fields (Hunt 1980, Clark 1999, Gupta 2018). The transition of electrons between different energy levels is influenced mainly by the valence state of the ion, the coordination number and site symmetry (Clark 1999). Transitions of electrons cause absorption features occurring at wavelengths corresponding to the energy required for the electron transition (Schläfer and Gliemann 1980).

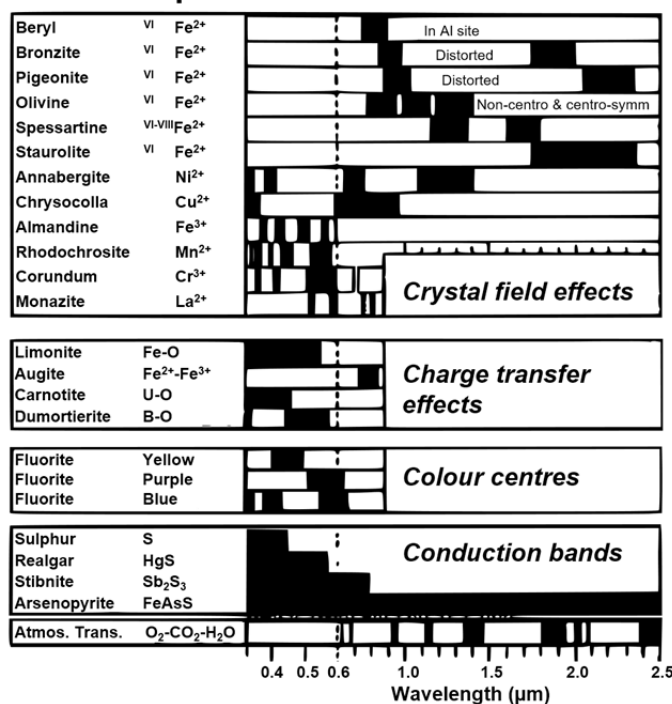
Charge transfer absorptions are caused when the energy provided by photons leads to the migration of electrons between neighbouring ions. This process is known to produce strong absorptions in the ultraviolet and visible light. The commonly observed falloff in reflectance of mineral spectra towards the “blue” is caused by the Fe-O charge transfer (Hunt 1980, Clark 1999). Gupta (2018) also provides the example of carnotite, for which the charge-transfer of the UO_2^{2+} ion causes absorptions $< 500 \mu\text{m}$ and the typical yellow colour of the mineral.

In some minerals showing periodic lattices, the energy levels at which electrons can exist are differentiated in a higher energy conduction band and a lower energy valence band. The difference between the two bands is called band gap and is different for metals, dielectrics and semiconductors. In some of the latter, absorption processes can occur, which are related to the specific interaction of the material’s band gap and VNIR radiation. Such features are called conduction bands. Examples for minerals affected by this process are sulphur and cinnabar, showing sharp absorption edge effects in their spectra (Hunt 1977, Hunt 1980, Clark 1999).

Natural crystals typically show defects or irregularities in their mineral lattice, for example due to impurities, which cause discrete energy levels. Irradiation on such “imperfect” crystals might induce the binding of electrons into these defects. The described phenomenon is called colour centre and produces absorptions and consequently colours of minerals which cannot be explained by their chemical composition. For example, the colours observed for fluorites are related to colour centre absorptions (Hunt 1980, Clark 1999).

Hunt (1977) presented an often-cited diagram illustrating the wavelength positions and widths of features due to electronic processes, which is presented in a slightly modified version in Fig. 2.12.

Electronic processes



Vibrational processes

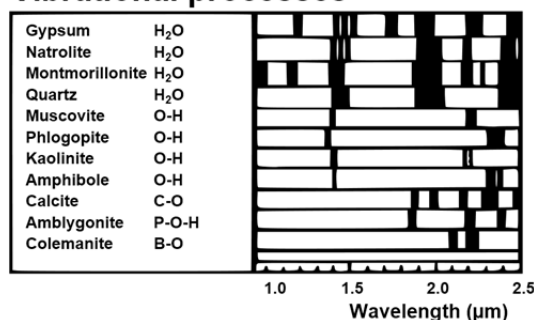


Fig. 2.12: Overview of absorption features due to electronic and vibrational processes in the VNIR/SWIR for selected minerals and corresponding functional groups. The black bars indicate the wavelength position and width of the absorption features (modified after Clark 2004 and Hunt 1977).

Absorption features due to electronic processes are described in a multitude of works reaching back to the 1950s-1970s (e.g. McClure 1957, Burns 1970). In the following, a brief summary of this subject is provided, focussing on metals to be expected in iron- and steelworks by-products. Absorptions caused by the ferrous iron can occur near 430, 450, 510, 550-570 nm and 1000 nm as well as in the range of 1800-2000 nm (Hunt et al. 1971a, Burns 2005, Gupta 2018). Features related to the ferric iron are typically present at 350, 500 and 870 nm (Gupta 2018). For soils, absorptions related to the presence of the Fe³⁺-ion were reported at 404, 430, 444, 480, 520, 650, 850 and 940 nm (Demattê et al. 2016). The presence of copper might produce features near 800 nm, while chromium might cause a feature at 550 nm with two sharp absorptions near 350 and 450 nm. Spectral characteristics associated with the presence of nickel are known to be found near 400, 740 and 1250 nm (Hunt 1977, Hunt 1980, Gupta 2018). Manganese (Mn²⁺) might show absorptions near 340, 370, 410, 450 and 550 nm (Gupta 2018). Hunt (1977) summarised several studies of the late 1960s and early 1970s concerning absorption features caused by the Ti³⁺ ion and listed features present at 450, 550, 600 and 640 nm. However, according to Rossman (2014) several of the features described for Ti³⁺ in the earlier studies are more likely to be caused by Fe²⁺-Ti⁴⁺ interactions. Due to the lack of valence d-electrons, Ti⁴⁺ does not produce absorption features itself (Hunt 1977, Rossman 2014). The absorption bands of trivalent vanadium are described as similar to the features caused by Cr³⁺ (Schmetzer 1982, Rossman 2014). Features at 445 and 680 nm were reported for V-bearing pyroxenes (Cloutis 2002). The manifold absorptions due to ferric and ferrous iron, chromium, titanium and vanadium occurring in minerals is comprehensively described using the example of garnets in Izawa et al. (2018). This indicates the challenges of interpreting and specifically assigning such features in samples containing high amounts of different metals and representing mineral mixtures.

Figure 2.13 provides reflectance spectra of the common iron oxides goethite, hematite and magnetite with distinctly visible absorption features due to electronic processes in the VNIR. For more comprehensive details on features due to electronic process (encompassing also cobalt, rare earth elements and uranium) see e.g. Farmer (1974), Burns (2005) and Rossman (2014).

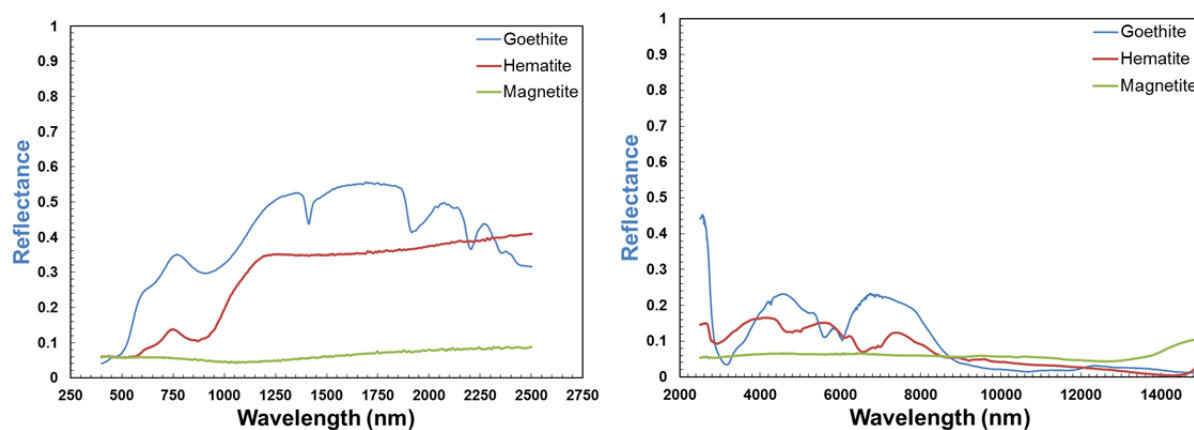


Fig. 2.13: VNIR/SWIR and MWIR/LWIR reflectance spectra of the iron oxides goethite, hematite and magnetite. Goethite shows distinct features near 480, 670 and 970 nm due to electronic processes, hematite near 570, 670 and 880 nm. Magnetite is basically featureless in both wavelength ranges (spectra from Kokaly et al. 2017).

2.2.2.2 Vibrational Processes

The absorption of energy by molecules causes vibrations of the molecular system, where the strength of the bonds and the masses of each molecular component determine the frequency of the vibration (Clark 1999). The number of atoms in a molecule defines the number of different vibrational modes of a molecule. Except for linear molecules, the possible motions of a molecule comprise three constitute translations and rotations each. Thus, in a molecule of n atoms, there are $3n-6$ possible vibrations, which are called fundamentals and typically labelled with ν_1 , ν_2 , ν_3 , etc. (Hunt 1980). Overtones (e.g. $2\nu_1$, $3\nu_1$, $2\nu_2$) of such fundamentals might occur at multiples of the frequency of the original vibration, while the concurrence of various vibrational modes can produce so-called combinations (e.g. $\nu_1+\nu_2$, $\nu_2+\nu_3$, $\nu_1+\nu_2+\nu_3$, Clark 1999). Features caused by fundamental vibrations are typically found in the mid- and longwave infrared and overtones and combinations in the shortwave infrared (Gupta 2018). These absorptions can be measured and utilised for diagnostic purposes (Clark 1999). For detailed information on vibrational features in minerals see the fundamental works provided by Famer (1974) and Estep-Barnes (1977).

Absorption features caused by vibrational processes at the atomic-molecular level occur in carbonates, hydroxyls, sulphates and other mineral components, of which most are present in the majority of rock-forming minerals. The following lines will briefly summarise the vibrational features caused by the major functional groups.

Carbonates

The CO_3^{2-} ion can exhibit four fundamental vibrational modes: the symmetric stretch (ν_1 : 9407 nm), the out-of-plane bend (ν_2 : 11376 nm), the asymmetric stretch (ν_3 : 7067 nm), and the in-plane bend (ν_4 : 14700 nm). The ν_1 vibration is not infrared active (Clark 1999). Combination and overtone bands of these fundamental vibrations occur in the shortwave infrared near 1850-1870, 1970-2000, 2120-2160, 2300-2350 nm and 2500-2550 nm (Clark 1999). As shown in several

studies, the wavelength position of the absorption maxima depends on the mineral composition, allowing for example the differentiation of the spectrally similar calcite and dolomite (e.g. Hunt and Salisbury 1971, Gaffey 1986). Calcite is a weathering product to be expected in iron- and steelworks by-products and VNIR/SWIR and MWIR/LWIR spectra are provided in Fig. 2.14.

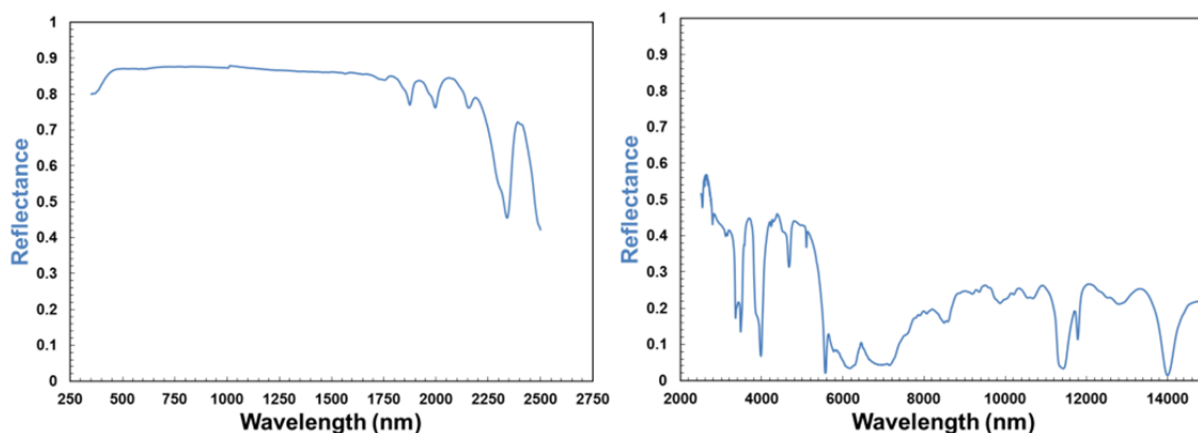


Fig. 2.14: VNIR/SWIR (left) and MWIR/LWIR (right) reflectance spectra of calcite (spectra from Kokaly et al. 2017). The SWIR range shows multiple diagnostic features with the most prominent one near 2330 nm. The MWIR/LWIR spectrum exhibits various distinct features.

Water and hydroxyl

The fundamental vibrations of the water molecule produce absorptions near 3106 nm (ν_1 , symmetric stretch), at 2903 nm (ν_2 , H-O-H bend) and close to 6080 nm (ν_3 , asymmetric stretch). Absorptions due to combinations and overtones of these fundamental vibrations might occur at 942, 1135, 1380, 1454 and 1875 nm (Hunt 1980). The only fundamental vibration of the hydroxyl ion can be found near 2770 nm and its first overtone appears near 1440 nm (Hunt 1980, Clark 1999). However, the exact wavelength position of the hydroxyl fundamental is related to the ion that is bound to the OH group and may vary between 2670-3450 nm while typically occurring near 2700-2800 nm in OH-bearing minerals (Clark et al. 1990b, Clark 1999, Anderson et al. 2005). Combination absorptions related to Al-OH typically appear near 2200 nm and related to Mg-OH near 2300 nm. This is particularly helpful as it allows to spectrally discriminate different clay minerals, e.g. kaolinite, muscovite and specimen of the illite group (Gupta 2018). According to Rossman (1996), also anhydrous silicates and oxides often contain hydroxide or water molecules. This has also been mentioned by Clark (1999), who pointed out that even though the presence of hydroxyl is not reflected in the chemical formula of a mineral, it might still be present in the crystal and produce spectral features, as for example known for quartz (Clark 1999).

Silicates

While many silicate minerals contain OH-groups producing absorptions in the shortwave infrared as described above (e.g. Hunt and Salisbury 1970), most silicate features are not visible in the VNIR/SWIR but occur in the mid- and longwave infrared. Especially the region of 8000-15000 nm shows several features indicative for silicates, of which the most prominent features were described to occur near 10000 nm (e.g. Launer 1952, Moenke 1962, Ghosh and Chatterjee 1974). Hunt (1980) differentiated the spectral ranges in which features in silicate spectra appear as follows:

7000-9000 nm: In transmission or emission spectra of silicates, a distinct peak is typically observed in the region of 7000-9000 nm. This transmission maximum corresponds to a reflectance minimum and is called Christiansen feature (CF). This feature is related to the strongest molecular vibrational feature and can be usually observed before the dominant Si-O stretching features in silicates (Fig.15; Hunt 1980; Salisbury et al. 1988, 1991). The position of the Christiansen feature is related to the refraction index (n) of a material and occurs at the wavelength where $N = 1$ (Christiansen frequency; Clark 1999). The position of the Christiansen feature is helpful for analysing rocks and minerals (Conel 1969, Cooper et al. 2002, Gupta 2018).

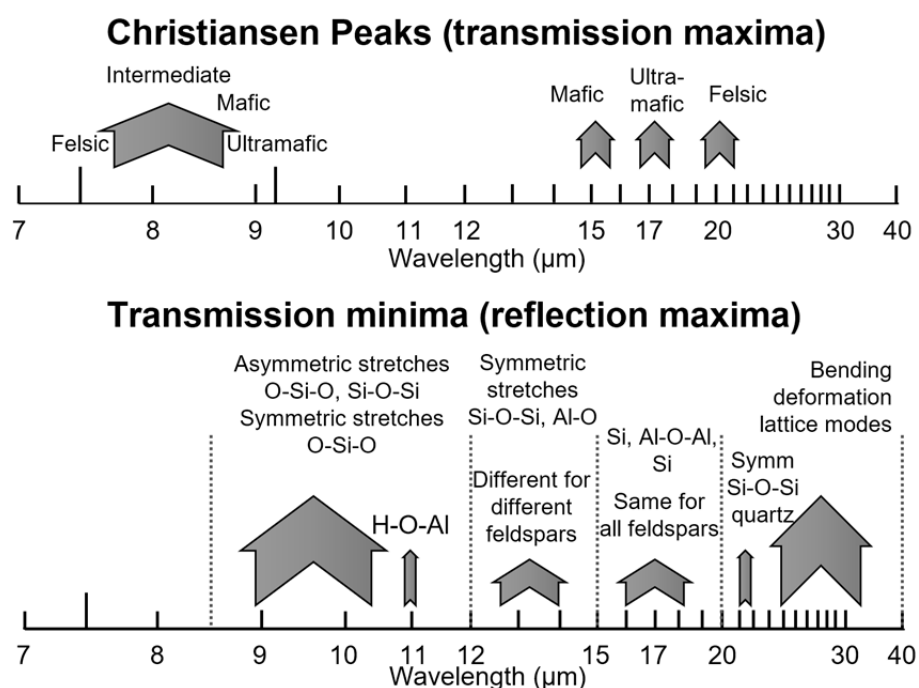
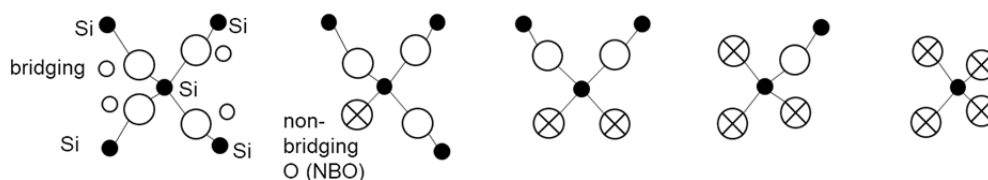


Fig. 2.15: Overview of the locations and causes of features found in mid- and longwave infrared spectra of silicates (modified after Clark 2004 and Hunt 1982).

8500-12000 nm: According to Hunt (1980), this region is commonly known as the “Si-O stretching region”, at which silicate spectra might show multiple features, which are mainly due to asymmetric O-Si-O, Si-O-Si or O⁻-Si-O⁻ stretching vibrations of SiO₄ tetrahedra. The specific wavelength position of these features depends on the mineral structure (tectosilicates, disilicates, etc.) and the molecular groups, which is schematically visualised in Figure 2.16. This region is also known as the reststrahlen region (see e.g. Salisbury and Wald 1992), where the strongest features typically occurs near 10000 nm due to Si-O vibrations. The position of the reststrahlen bands is close to 9000 nm for framework silicates and for felsic minerals near 11500 nm (Gupta 2018). Features near 11000 nm are typically related to H-O-Al vibrations (Hunt 1980, 1982). Reststrahlen features of silicates occur as reflectance peaks (Salisbury and Wald 1992). They are usually only weakly expressed in spectra of fine powders of minerals (e.g. Salisbury et al. 1991), yet still present and of potential diagnostic character (Salisbury 1993).

12000-15000 nm: Features present in this wavelength region are mainly due to symmetric stretches of Si-O-Si and Al-O-Si vibrations as they are occurring in tectosilicates (Hunt 1980, Gupta 2018, see Figures 2.15 and 2.16).



Structure type	Tectosilicate	Disilicate	Metasilicate	Pyrosilicate	Orthosilicate
Tetrahedral unit	TO ₂	T ₂ O ₅	TO ₃	T ₂ O ₇	TO ₄
Molecular group	=Si=	≡SiO	=SiO ₂	-SiO ₃	SiO ₄
Q-species	Q ⁴	Q ³	Q ²	Q ¹	Q ⁰
NBO/T	NBO/T = 0	NBO/T = 1	NBO/T = 2	NBO/T = 3	NBO/T = 4
IR band (nm, ca.)	$\nu = 6660-8330,$ 9100-10000	$\nu = 9100-10000$	$\nu = 10000-11100$	~11100-12500 ~12500(-14300)	

Fig. 2.16: Structural units and features likely to be present in silicate glasses (modified after King et al. 2004b).

Arsenates, borates, halides, phosphates, sulphates and vanadates

Spectral features found in the infrared spectra of arsenates, phosphates and vanadates, which are not related to the presence of H₂O or OH, are mainly caused by the fundamental vibrations of the XO₄³⁻ ion. In arsenates, spectral features might be present near 11400, 11900, 22200 and at 28600 nm. Phosphates show characteristics at 9250, 10300, 18200 and 27800 nm. In sulphates, the SO₄²⁻ ion is known to produce features in the mid- and longwave infrared wavelengths near 9060, 10190, 16310 and 22170 nm, but usually not in VNIR/SWIR (Hunt et al. 1972, Hunt 1980). Features present in the VNIR/SWIR spectrum of gypsum are for example caused by overtones and combinations of H₂O groups while the VNIR/SWIR spectrum of anhydrite is nearly featureless (see e.g. Kokaly et al. 2017). Further details on sulphates can be found among others in Adler and Kerr (1965) and Hunt et al. (1971b).

Organic compounds

Especially relevant for soil sciences is the analysis of organic compounds (amines, aromatic carbons, alkyls, carboxylic acids, etc.) which produce spectral characteristics due to for example C=O and C-H stretches in the VNIR (e.g. near 850 and 1100 nm) as well as throughout the SWIR and MWIR/LWIR ranges (see Demattê et al. (2016) for a comprehensive feature list). Considering the multitude of historical materials collected at the Unterwellenborn dump site, the presence of organic constituents in individual samples cannot be excluded.

2.2.3 Physicochemical Impact Factors on Reflectance Spectra

Rocks are typically assemblages of various minerals (which is also true for iron and steel slags). Subsequently, spectra of natural or “anthropogenic” rocks represent spectral mixtures of their individual components. Such signatures show more complex properties compared to spectra of monomineralic samples, making their interpretation challenging, and less well-defined features are to be expected compared to spectra of “pure” minerals (e.g. Hunt 1980, Gupta 2018). In addition, spectra acquired from samples near *in situ* conditions may show impacts of moisture, different grain sizes and surface roughness, sample aggregation or weathering (Geerken 1991, Schodlok 2004, Metternicht and Zinck 2009, Gupta 2018). Thus, such spectra might differ from spectra provided in spectral libraries, which are often recorded under controlled laboratory conditions of homogenised powders of mono-mineralic samples at specific grain size fractions. In the following, known impacts of particle size and moisture are briefly discussed as these are important factors to be considered in application-oriented experiments.

Particle size

The reflectance of minerals is affected by particle size and texture (Hapke 1981, Clark and Roush 1984, Arnold and Wagner 1988). The physical principals behind these effects are two major processes known as volume and surface scattering. Surface scattering occurs directly at the surface of grains and can be further differentiated into single- and multi-surface scattering. Volume scattering describes the processes of scattering of radiation that has penetrated grains and is refracted within them before leaving the grain again (Vincent and Hunt 1968, Clark 1999). These effects are illustrated in Figure 2.17.

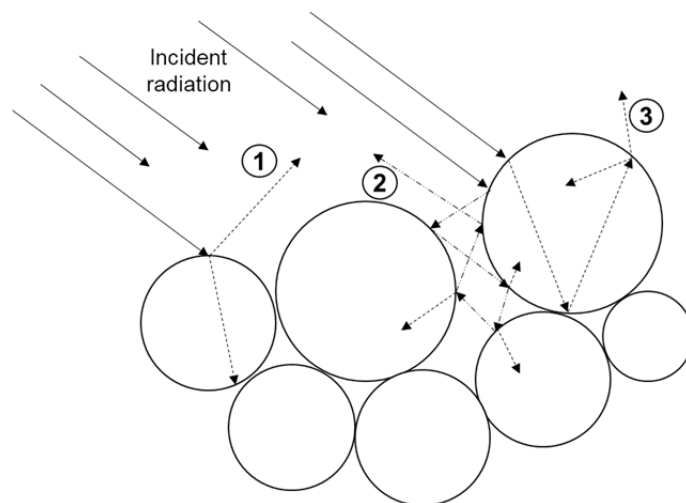


Fig. 2.17: Surface (1: single scattering, 2: multiple scattering) and volume scattering (3) at particulate surfaces (modified after Vincent and Hunt 1968).

Which of the two processes dominates is mainly dependent on the grain size and the absorption coefficient of the material. Also, the ratio of grain size to the wavelength of the incident radiation must be considered. At larger grain sizes, the ratio from surface to volume scattering is shifted towards the latter, as the scattering and refraction of photons in larger grains is more intense compared to grains of smaller diameters. In the visible light, near and shortwave infrared, the grain size is usually larger than the wavelength of the radiation and multiple scattering is predominant, causing an increase of reflectance with decreasing grain size of the mineral sample.

In contrast, as the absorption coefficients of materials are typically stronger in the mid- and longer infrared and the refraction index more variable at the Christiansen frequencies, the scattering processes of radiation at particulate materials in this wavelength region are more complex. Thus, in some cases, in the MWIR/LWIR, the opposite spectral behaviour of samples of certain grain sizes compared to VNIR/SWIR region can be observed (Clark 1999).

As described in Nash et al. (1993) and summarised in Eisele (2014), the processes of surface and volume scattering in the mid- and longwave infrared for silicates can be differentiated as follows: the 4000-7000 nm wavelength region is dominated by volume scattering, while between 7000-9500 nm surface scattering is predominant (except for the Christiansen feature); scattering processes in the 9500-12000 nm region are strongly depended on the grain size of the material and very fine powders might show a feature that is known as transparency feature (Salisbury et al. 1991). The intensity of the reststrahlen bands is affected by volume scattering and decreases with decreasing grain sizes (Salisbury and Wald 1992). According to Salisbury et al. (1988) “SiO bands are greatly diminished and distorted in reflectance spectra of powdered rocks” but remain identifiable for some minerals in spectra of fine powdered samples. Between 12000 and 25000 nm surface scattering is dominant.

Studies conducted on carbonates demonstrated that spectra of geological or mineralogical samples can be obtained from powders or hand rock samples likewise, but sample reflectivity and absolute depths of absorptions are a function of particle size. The overall “brightness” (i.e. reflectivity) tends to increase with increasing particle size, while the absolute depths of absorption features will decrease (Gaffey 1986, van der Meer 1995). In another study focussing on carbonates, it was found that calcite features might change from reflectance peaks to reflectance minima with very fine grain sizes in the longwave infrared (Zaini et al. 2012). Other studies on the impact of grain size and weathering crusts on mineral spectra revealed that weathering crusts might mask mineral features that are diagnostic in unweathered samples (Geerken 1991, Salisbury and D’Aria 1992a). Studies on the properties of fresh and weathered rocks pointed out that the geochemical as well as the spectral properties are variable depending on the rock type (Zhou and Wang 2017). In the MWIR/LWIR, it must be further considered that voids and pores between grains might act as black bodies and decrease the overall spectral contrast and the shape and intensity of reststrahlen bands (Salisbury and Wald 1992; “cavity effect”). The above listed effects highlight that grain size might have distinct impacts on mineral spectra, which must be considered in qualitative as well as quantitative spectral analyses.

Moisture

As described before, molecular water is known to produce strong absorption features near 1400, 1900, 2900 and 6100 nm and several minor features in the near infrared (e.g. Hunt 1980, see Chapter 2.2.2.2). Studies on the impact of moisture on soil spectra showed a decrease in the overall reflectance intensity concomitant with no major alteration of the general shape of the spectrum (e.g. Bowers and Hanks 1965, Baumgardner et al. 1986). However, other studies (e.g. Mulders 1987) found that moisture might mask for example the hydroxyl features of clay minerals near 2200 nm, hampering the identification of these constituents in spectra of samples with relatively high *in situ* moisture. For soils, it was reported that moisture will decrease the spectral contrast of quartz features in the LWIR range (Salisbury and D’Aria 1992b).

2.2.4 Spectroscopy of High-Temperature Formations (Meteorites, Glasses and Melts)

As discussed before, only few studies on the VNIR/SWIR as well as MWIR/LWIR reflectance properties of iron- and steelworks by-products or on the exploration of dump sites related to the iron and steel industry are available within the remote sensing community. However, as slags represent solidified silicate melts, studies on spectral properties of high-temperature minerals are relevant for this thesis. Furthermore, as slags might be of glass-like structure, studies on silicate glasses and similar materials are of particular interest for this thesis. Laboratory analyses of slags often comprise spectroscopic techniques. Thus, the next chapter will provide findings in such studies concerning spectral characteristics of potential relevance for this thesis as well.

Spectroscopic studies on high-temperature minerals, meteorites, impactites, silicate glasses and melts

Gehlenite is a high-temperature mineral often found in blast furnace slags (e.g. Drissen 2004). This mineral is known to show various vibrational features, encompassing absorption features due to H₂O near 2900 nm and 6200 nm. Si-O-Si features might occur near 9800 nm, Si-O-Al features near 9900 nm and various (Si, Al)₂O₇-vibrational modes were reported towards the longer wavelengths (Marincea et al. 2011). Cloutis et al. (2004) analysed VNIR/SWIR and MWIR/LWIR reflectance spectra of spinels and chromites and found that e.g. the wavelength position of spinel features near 460, 930, 2800 and 12300 nm correlated with the Fe²⁺ content. Al and Fe³⁺ showed strong correlations to the position of a feature near 930 nm and the depth of a feature near 550 nm was correlated with the Cr content. In spectra of chromites, the positions of features at ca. 490, 590 and 2000 nm show correlations with Cr, the position of the feature at 1300 nm varied with the Fe²⁺ and Mg content and the position of the feature at 2000 nm was correlated with the Al content (Cloutis et al. 2004). VNIR/SWIR spectra of melilite, another mineral found in blast furnace slag, exhibits features near 1400 nm and in the range 1600-2000 nm due to ferrous iron transitions. Garnet spectra have features related to Fe²⁺ and Fe³⁺ near 430, 600, 800 and 1000 nm (Cloutis and Gaffey 1993). Magnetite is known to show opaque spectral behaviour and thus a basically featureless spectrum of low reflectance (Hunt et al. 1971a). Studies focussing on the spectra of meteorites and other materials found that magnetite tends to appear dark and show low reflectance intensities as well (Miyamoto et al. 1982, Cloutis et al. 1990). Hunt et al. (1975) analysed meteorite spectra in the VNIR/SWIR range and showed that most absorptions were due to ferrous iron of which the most prominent one was located near 1000 nm while ferric iron produced features near 500 nm in other cases. Furthermore, large amounts of opaque material caused samples to exhibit nearly featureless spectra of low reflectance (Hunt et al. 1975). Other studies on meteorite spectra indicated that amorphous carbon caused overall low reflectance (Miyamoto et al. 1981). This is of relevance for this work as sludges from the iron and steel industry might contain amorphous carbon as well. The spectrum of artificial wüstite, another common slag mineral, was found to be spectrally similar to chondrite metal and is characterised by few absorption features and low reflectance (Cloutis et al. 1990).

Besides spectroscopic studies on meteorites and for extraplanetary applications, comprehensive research has been conducted on basaltic and rhyolitic lavas and glasses (see e.g. the numerous references in King et al. 2004b). For example, Ramsey and Fink (1999) studied silicic lava and reported an absorption band near 9250 nm present in emission spectra as diagnostic of glass to be caused by stretching vibrations of silica tetrahedra. Smith et al. 2017 studied VNIR/SWIR reflectance spectra of basaltic materials, whereas Si-O stretching and bending features were found

to occur in the longer infrared region. Morlok et al. (2016) analysed mid-longwave infrared spectra of impactites (suevites and glasses) from the Nördlinger Ries. These materials showed water bands near 2770 and 6100 nm, Christiansen features between ~ 7000 -8000 nm, Reststrahlen bands between ca. 8900 and 10300 nm as well as transparency features near 11000-1200 nm. Farrand et al. (2016) found features in basaltic glasses indicative for hydration near 1900 and 3000 nm and due to ferric oxide near 480 nm in VNIR/SWIR reflectance data. For MWIR/LWIR emission spectra, these authors reported a doublet with centres near 9500 and 11000 nm related to SiO_4 . Rice et al. (2013) conducted a comprehensive study on silica-rich materials with implications for the detection of similar materials on mars utilising VNIR/SWIR spectra. These authors reported features near 950, 1140, 1410, 1780 and 1910 nm due to OH and H_2O and a feature due to Si-OH near 2210-2260 nm. Faulques et al. (2001) described (amongst others) features near 2200 nm in natural silica-rich glasses, which are due to water trapped in the structure (as e.g. also described in Adams 1961). Features due to Si-OH and H_2O near 2200 nm as well as further characteristics related to water occurring at other wavelentghs in the mid- and longwave infrared are also discussed in Efimov et al. (2003). King et al. (2004b) provide a comprehensive work on infrared spectroscopy of natural and technogenic silicate glasses and elaborated a profound compilation of species and vibrations found in spectra of such materials based on reviews of the works of various authors (see Table 2.6). For further information on properties of glasses and melts see for example Wong and Angell (1970, 1971), Efimov (1995) and Stebbins et al. (1995).

Tab. 2.6: Overview of spectral features in infrared spectra of natural and synthetic glasses and related functional groups (modified from King et al. 2004b, see references therein; original cm^{-1} units translated to nm).

Species	Vibration	Wavelength range (nm)
Si-O	Overtone, comb. ν_{as} Si-O	~ 5260
	ν_{as} Si-O	9009-10000
	Asymmetric stretching	8000-8333
	ν_{as} Si-O stretching	11111
	ν_{as} Si-O	~ 11100 -12500
	ν_{as} O-Si or OAlO-Si	12500-14286
(Si)-Al-O	ν_{as} (Si, Al)-O stretching	~ 9090
	ν Al-OH or H-AlOSi	~ 11100
	ν_{as} Al-O	14706
H-O	2ν OH (in H_2O and OH)	~ 1410
	δ HOH + ν OH	1905-1984
	ν OH + ν_{as} (Si, Al)-O	2198- 2299
	ν OH + ν O-metal	~ 2500
	ν_{ss} HOH + 2δ HOH + ν_{ss} Si-OH	2632-3333
	δ HOH	6061-6211
	ν_{ss} (Si, Al)-OH	10309
CO_3^{2-}	δ C-O out of plane	11364-11628
	δ C-O in plane	13514-14706
	ν C-O	6623-7092

Spectroscopic studies on slags and cement minerals

Following Waseda and Toguri (1998), spectroscopic techniques, including infrared and Raman spectroscopy, can be considered as established methods to analyse silicate glasses and melts. As such, various studies on the structural and chemical analyses of slags comprised spectroscopic measurements. Features due to Si-O, Si-OH, Al-O-Al, Si-O-Si bending and stretching vibrations are typically observed in Raman and infrared spectra of silicate minerals in slags, whereas the identification of specific vibrational modes is complex and increasingly challenging with higher numbers of constituents and subsequent spectral contributions (Mohassab and Sohn 2015). The transmittance spectrum of blast furnace slag was found to exhibit distinct features near 11100 and 14300 nm due to Si-O stretching vibrations and near 22200 nm due to MO_4 in the study of Song et al. (2017). Titanium-bearing blast furnace slags with differing CaO/SiO_2 and Al_2O_3 contents showed features due to symmetric stretching vibrations of SiO_4^{4-} tetrahedra between 8300-13300 nm in FTIR transmittance spectra (Feng et al. 2016). Bláhová et al. (2015) reported various spectral features for blast furnace slag. Here, features between ca. 9100-11800 nm were due to vibrations of Si-O, Si-O-Si and Si-O-Al bonds. The carbonate ion was found to cause a feature near 7100 nm. Spectral characteristics related to structural OH-vibrations were determined near 2830 nm and due to the presence of water at 2920 nm. Bláhová et al. (2015) also spectrally characterised steelmaking slag. Although less rich in silicates compared to the BFS, silicates showed features in form of a broad band with several shoulders in the range 9100–12500 nm. Features near 5560, 7000 and 11440 nm indicated the presence of calcite. A feature near 3080 nm was supposed to be caused by OH-groups and again the presence of water was indicated by features at ca. 2900 and 6200 nm (Bláhová et al. 2015). A feature due to OH in $\text{Ca}(\text{OH})_2$ was reported to occur at 2745 nm in another study on the spectral characteristics of steel slag (Aimoto et al. 2015). FTIR transmittance spectra of CaO-SiO_2 as well as of $\text{CaO-SiO}_2\text{-CaF}_2$ slags were reported in several studies and showed features mainly due to stretches of SiO_4 -tetrahedra, asymmetric Si-O-Si bending and Si-O-Si rocking in the range of ca. 7000-25000 nm (Park et al. 2002, 2012). For LF slag, features near 11500 nm related to mayenite and for periclase near 2650, 4200, 4560, 4870 and 6800 nm were reported in a transmittance spectrum (Rađenović et al. 2013). Another study analysing transmittance spectra of LF slag reported features due to calcite-vaterite near 2820, 3970, 5560, 6830, 11430 and 14000 nm (Setién et al. 2009). In the study of Diener (2006) similar features related to calcite were reported for LF slag. In that study, the precise assignment of features related to calcium silicate and calcium aluminate phases was found difficult. However, features near 10300 nm were determined to be related to the presence of calcium silicates while iron, aluminium and magnesium oxides produced Al-O stretching vibrations between ca. 10500-12500 nm with maxima near 11550 nm for the studied LF slag and near 11600 for EAF slag (Diener 2006). Anhydrous calcium silicates are also known to show features near 10900 nm as well as in longer wavelength ranges (Gomes and Ferreira 2005). Aside from transmission spectra, several studies comprised infrared emission and UV/VIS reflectance spectroscopy for analysing the crystallisation processes and oxidation states of slags (e.g. Mausbach et al. 1997a, 1997b; Nowack et al. 2001, 2007).

Apart from studies on slags from iron- and steelmaking, several works provided information on the spectral properties of other slags. For example, spectra of slags produced from radioactive waste were found to exhibit features due to OH near 2900 and 3400 nm as well as vibrations related to silicates (Si-O-Si, Si-O) in the longwave infrared (Malinina and Stefanovsky 2014). A

study on the infrared spectra of coal slags described features near 1200, 1800 due to Fe^{2+} and at 2800 nm due to OH, as well as a broad reflectance peak due to Si-O vibrations at 9000 nm (Goodwin and Mitchner 1986).

Ghosh and Chatterjee (1974) studied features in the infrared transmission and reflectance spectra of a variety of cement minerals, including β - and γ - C_2S . These phases are common in steelwork slags as well. For C_2S , the most distinct absorption characteristics were reported near 10500, 11800 and 17700 nm. Launer (1952) reported similar features between 10000-12000 nm for β - Ca_2SiO_4 . Infrared spectra of anhydrous clinker phases are known to exhibit multiple features due to Si-O vibrations near 10000 nm, and Al-O might produce features near 11100 nm. Hydrated clinker phases might show additional features due to OH near 2750 nm, and due to H_2O at 2980 and 6040 nm (Horgnies et al. 2013).

The selected examples listed above demonstrated that the majority of research involving spectroscopic measurements of slags was conducted for the purpose of laboratory chemical analyses of solid slags or in terms of analytical applications for high-temperature liquid slags. These studies showed little relation to the spectral exploration of historic iron- and steelworks dump sites, aiming for discriminating a large variety of different by-products as well as for the quantification of relevant chemical constituents as aspired by this work. Furthermore, most of the studies were realised as transmittance or emission set-ups covering the LWIR range and fewer on the UV/VIS range. As mentioned earlier, attention must be paid when translating features in transmittance and emittance spectra into characteristics observable in reflectance spectra. However, the information on spectral features provided in the mentioned studies is a solid basis for the analysis of the reflectance signatures of iron- and steelworks by-products in this thesis. As the underlying fundamental mechanics of vibrational and electronic processes are associated to specific functional groups, the features described in the spectra of slags are in general agreement with the features reported for spectra of “naturally” occurring minerals and rocks, meteorites and planetary surfaces as well as silicate glasses (see Table 2.6). In summary, features of relevance are: various absorptions due to electronic processes in the VNIR range; absorptions due to H_2O and OH near 1400, 1900, 2200, 2900 and 6100 nm; characteristics caused by carbonates near 4000, 5600, 7000 and 11400 nm and a variety of features due to silicates in the region > 8000 nm.

2.3 Reflectance Spectroscopy and Geological Remote Sensing – A Review

Geological and mineralogical spectral libraries

As indicated in the previous chapter, the features observed in mineral spectra are caused by their specific chemical and structural composition. As a result, most minerals show specific patterns of shoulders, minima and maxima in their spectral signatures that are unique to a certain degree and can be understood as “spectral fingerprints”. These specific spectral characteristics allow the qualitative characterisation of samples and the identification of mineral phases (see. e.g. Clark and Roush 1984, Clark 1999, van der Meer 2004). The research of such spectral characteristics of minerals and rocks reaches back to the beginning of the 20th century (e.g. Schaefer et al. 1926) and major works were established in the 1950s and 1960s, (e.g. Launer 1952; Hunt and Turner 1953; Adler and Kerr 1962, 1963a, 1963b; Lyon and Burns 1963; Lyon 1965). Other comprehensive studies on the VNIR/SWIR spectra of major rock forming minerals and rocks have been published in the 1970s and 1980s (e.g. the works by Hunt 1977, 1980, 1982; Hunt and Salisbury 1970, 1971, 1976a, 1976b; as well as Hunt et al. between 1971-1975). Since the late 1980s, an increasing number of studies has been published on mineral reflectance spectra in the MWIR/LWIR (e.g. Salisbury et al. 1987, 1988; 1991; Salisbury 1992, 1993). Today, several compilations of hundreds of mineral spectra are available as digital libraries, e.g. by the United States Geological Survey (USGS, e.g. Clark et al. 2007, Kokaly et al. 2017) and the ASTER digital spectra library (Baldrige et al. 2009). Both the USGS and ASTER spectral libraries comprise VNIR/SWIR as well as MWIR/LWIR reflectance signatures of the majority of rock forming minerals and additionally provide spectra of other materials, including vegetation, ice, water and various anthropogenic materials (see Baldrige et al. 2009, Kokaly et al. 2017). Schodlok et al. (2016) recently presented a high-resolution library of thermal infrared reflectance mineral data. Spectral libraries establish an important knowledge base for the analysis and interpretation of samples with unknown mineralogy in laboratory applications as well as in geological remote sensing. Comparing unknown to reference spectra can be realised in many different ways, ranging from the empirical assessment of spectroscopic data to (semi or fully) automated approaches. Widely known mineral mapping approaches based on feature fitting techniques of unknown to reference spectra are the Tri- and Tetracorder algorithms by the USGS (Clark et al. 2003) and the recent development EnGeoMAP 2.0 by Mielke et al. (2016).

Despite the number of existing spectral libraries and compilations of reflectance spectra of minerals and rocks, no comprehensive compilations of the VNIR/SWIR and MWIR/LWIR reflectance characteristics of the variety of by-products typically found at iron- and steelworks dump sites have been reported so far in remote sensing-associated publications. This underlines the necessity for building a spectral database for such “anthropogenic rocks” for spectroscopic analyses as well as for potential remote sensing applications using imaging data.

Geological and mineralogical remote sensing

As a non-contact and non-invasive technique, reflectance spectroscopy found its way into the imaging domain and has been widely used for a diverse range of applications in the field of mineralogical and geological remote sensing starting decades ago (e.g. Abrams et al. 1977, Goetz and Rowan 1981, Goetz et al. 1983, Goetz 2009). Depending on the spectral resolution (the number and width of bands at which spectral information is recorded), one differentiates multi-spectral (low spectral resolution) and hyperspectral instruments (high spectral resolution, up to

several hundreds of spectral bands). Today, a large variety of multispectral spaceborne and hyperspectral airborne sensors is available, and a plurality of research fields are established. This comprises the exploration of natural deposits and geological mapping (e.g. Goetz et al. 1983, Sadeghi et al. 2008, Mshiu et al. 2015, Mielke et al. 2016), the analysis of phenomena related to acid mine drainage (e.g. Anderson and Robbins 1998, Swayze et al. 2000, Williams et al. 2002, Montero et al. 2005, Zabcic et al. 2014), monitoring of tailing sites and analysis of mine waste (e.g. Intera Kenting Ltd. 1992, Riaza et al. 2010, Gannouni et al. 2012, Buzzi et al. 2014, Mielke et al. 2014, Glanville and Chang 2015) and the study of mining accidents (e.g. Kemper and Sommer 2002, Fernandes et al. 2016). Further common applications for remote sensing methods are the observation of the whole mining cycle, including the monitoring of post-mining landscapes (e.g. Schmidt and Glaesser 1998, Gläßer 2004, Gläßer et al. 2011, Götze et al. 2016). Numerous studies were published in the field of planetary remote sensing (e.g. Sprague et al. 2000, Cloutis and Bell 2004, Cloutis et al. 2008, Cloutis et al. 2010, Horgan and Bell 2012, Horgan et al. 2014). A relatively recent development and research field is the terrestrial application of hyperspectral imaging at close-range in geology and mining (e.g. Kurz et al. 2012, 2013; Murphy and Monteiro 2013; Boesche et al. 2015) and the scanning of drill cores with hyperspectral instruments (e.g. Koerting et al. 2015). Much more profound information on geological remote sensing, sensors, methods and applications are for example provided in the reviews by Cloutis (1996) and van der Meer et al. (2012). For hyperthermal applications see Hecker et al. (2011), Kuenzer and Dech (2013) and Tang and Li (2014). A review of research topics in soil remote sensing is provided by Ben-Dor et al. (2009), and for vegetation remote sensing see Thenkabail et al. (2012). Besides the mentioned topics, various studies focussed on urban materials (e.g. Roberts and Herold 2004, Roessner et al. 2011, Kotthaus et al. 2014) and industrial applications (e.g. Tatzer et al. 2005), including the food industry (e.g. Sun 2010).

In contrast to the plurality of applications of reflectance spectroscopy and (hyperspectral) remote sensing described before, only very few studies are available focussing on the analysis of by-products and dumps sites related to the iron and steel industry using such methods. Picón et al. (2009, 2012) published studies on the application of hyperspectral techniques for the classification of non-ferrous materials. Rodriguez et al. (2010) presented a study on the automated slag characterisation using hyperspectral methods. Gutiérrez et al. (2010) proposed the application of hyperspectral methods during the steel foundry process and Picón et al. (2017) recently presented a study on the application of hyperspectral methods for the quantification of chemical constituents of LF slag for optimising metallurgical processes. However, these studies did not aim for the exploration of dump sites and the detailed spectral characterisation of the variety of iron- and steelworks by-products. Denk et al. (2015) conducted an *in situ* case study at an iron- and steelworks dump site and demonstrated the application of hyperspectral methods for the differentiation of a variety of recent and historic materials found at such sites and provided spectral characteristics of selected materials. As mentioned, no comprehensive compilations of the reflectance properties of common iron- and steelworks by-products covering both the VNIR/SWIR as well as the MWIR/LWIR have been reported so far. However, the understanding of the reflectance characteristics of the plurality of by-products commonly found at iron- and steelworks dump sites is important for their spectral detection and quantification purposes at the laboratory and field scale as well as for remote analyses of dump sites using hyper- or multispectral instruments.

3. Test Site

The test site of this research is the dump site of the Stahlwerk Thüringen GmbH, formerly known as Maxhütte, situated in Unterwellenborn in southern Thuringia, Germany (see Fig. 3.1). This site is a representative iron and steel site with a production history reaching back to the second half of the 19th century. Since then, a large variety of the major iron- and steelmaking and treatment technologies were applied, and the site changed from an ironworks to an integrated iron and steel plant to today's electric steel plant. The resulting by-products of these different procedures changed concomitant with the changes in iron and steel production and processing technologies. Thus, the dump site affiliated to the today's Stahlwerk Thüringen GmbH comprises a large variety of historical as well as recent iron- and steelworks by-products. Considering the basic research-oriented character of this thesis, the dump site of this iron and steel plant must be understood as a model site, which provided the basis for the generation of a large and heterogeneous sample pool that was supposed to cover an extensive range of typical iron- and steelworks by-products. Secondary products not present at this study site were added to the sample pool (see Chapters 4.1 and 4.2), aiming at extending the pool for the development of generalised models on a heterogeneous dataset.

Due to the model character of this dump site and based on the fact that the dump and studied by-products are anthropogenic by nature, the relevance of the natural conditions for the spectral analysis of the dumped materials is limited. Thus, only a brief geographical overview and description of the geological setting and mining history of the area around Unterwellenborn will be given. Instead, the following chapters will focus on the specific local mining history as local iron ore was used for iron production in former times. The descriptions will further provide details on the history of iron and steel production and the structure of the dump site.

3.1 Geographical Overview

The dump site of the Stahlwerk Thüringen GmbH is located close to the city Unterwellenborn (31.12.2016: 5928 inhabitants, TLS 2018) in Thuringia. Unterwellenborn is located approximately 7 km east of Saalfeld und around 12 km west of Pößneck and is situated on the federal highway 281. The average ground elevation in Unterwellenborn is ca. 270 m above sea level and the centre coordinates of the dump site are 50.652° N and 11.418° E. An overview map of Unterwellenborn and its surroundings is presented in Figure 3.1.

Unterwellenborn is located within the Orla depression landscape unit, a subunit of the "Zechstein belt at the mountain edges", which is located between the Saale-Sandstone plate (as part of the Buntsandstein rolling country) in the north and the upper Saale valley and the east Thuringian slate mountains/Vogtland (as part of the low mountain range unit) in the south (Grundmann 2001, Hiekel et al. 2004). The Orla depression was created by leaching processes of Zechstein sediments and reaches about 32 km from Saalfeld to Triptis and its north-south expansion varies between three and five kilometres. Overall, this landscape unit is nearly free of forests and characterised by agriculture. Along the federal highway 281, several industrial and commercial areas can be found (Hiekel et al. 2004).

Within the Orla depression, most of the Zechstein bedrock is karstified, resulting in the quick drainage of precipitation, the presence of only minor streams and springs with strongly varying discharges. In the Orla depression, the depth of discharge varies between 80-150 mm, the catchment yield factor between $2.6\text{-}4.2\text{ l}\cdot(\text{s}\cdot\text{km}^2)^{-1}$ and the drainage system density is $0.8\text{ km}\cdot\text{km}^{-2}$ (Hiekel et al. 2004). In Unterwellenborn, only one minor stream, the Weira, can be found. The closest major river is the Saale, which is dammed about 6 km to the south of Unterwellenborn in the Hohenwarte and the Eichlicht reservoirs, and afterwards passes Saalfeld in northern direction.

The dominant soil types in this region are brown calcareous soils (“Braunerde”) and rendzina soils (“Rendzina”), while mixed rendzina (“Pararendzina” and “Braunerde-Pseudogley”) represent less dominant soil types (Seidel 2003, BGR 2015). More detailed descriptions of the prevalent soil types in the Orla depression can be found in Hiekel et al. (2004), who further specify Silt-Vega (“Schluff-Vega”) and Loam-Vega (“Lehm-Vega”) as typical soil types for the loess-like floodplain sediments of the small streams like the Weira.

The Orla depression is located on the lee side of the Thuringian Slate Mountains and is thus characterised by relatively low amounts of precipitation (Hiekel et al. 2004). The long-term average annual precipitation is 568 mm, with average values of 60-70 mm in the months May to August and a maximum in July (1981-2010, values of the DWD station 4332 at Saalfeld, DWD 2015). The average annual air temperature is 8-8.5 °C (1971-2010, TLUGa). The test site can be assigned to the climate district “Thüringisch-Sächsisches Mittelgebirgsvorland” within the “Mitteldeutsches Berg- und Hügellandklima” climate area (Hiekel et al. 2004). Furthermore, the region belongs to the climate sectors “Erzgebirge, Thüringer und Bayerischer Wald” and “Südostdeutsche Becken und Hügel” (TLUGb). Further geographical details of the Orla depression, encompassing flora and fauna, are given in Hiekel et al. (2004) and Zündorf et al. (2006).

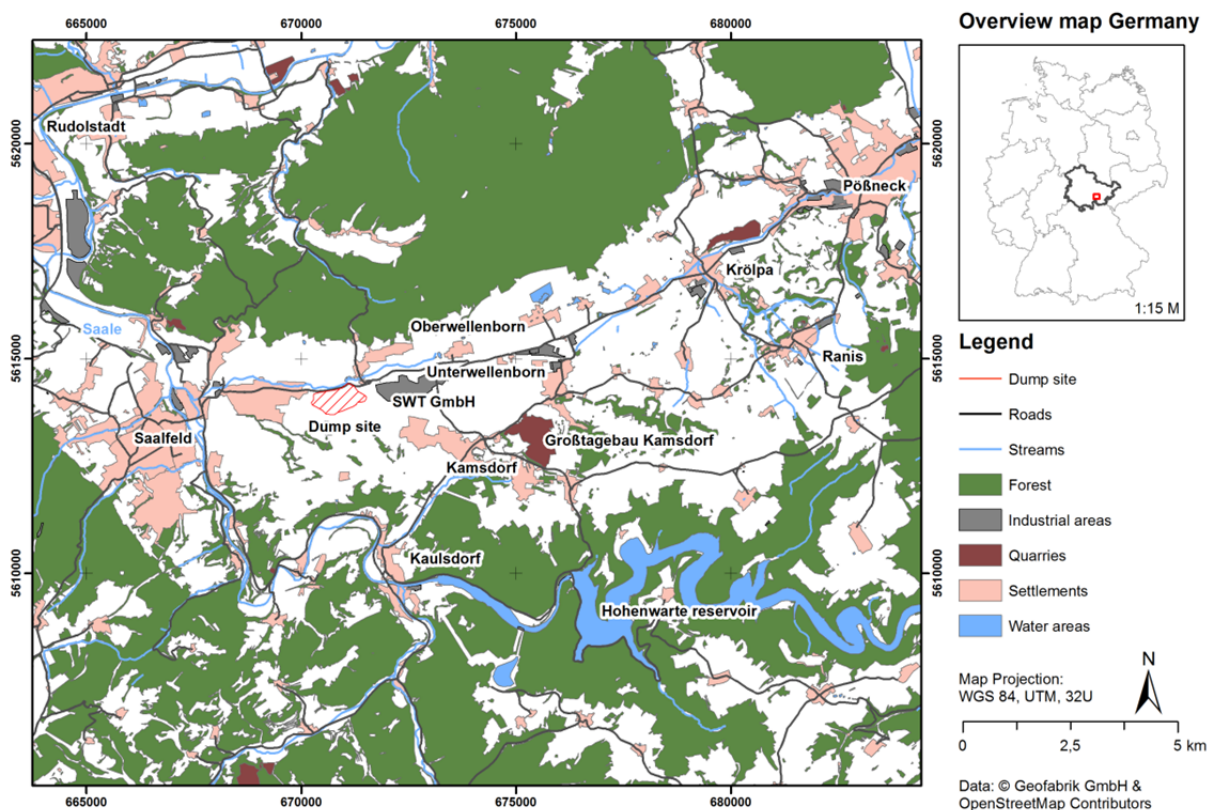


Fig. 3.1: Large-scale overview map of Unterwellenborn in southern Thuringia (see Appendix 3.1 for a larger version).

3.2 Geology and Mining History

The basis for the long reaching mining history in the Saalfeld-Kamsdorf area is a large ore field, reaching from Saalfeld (west) to Könnitz (east), which has its centre near Kamsdorf close to Unterwellenborn. This deposit is the most important historical ore mining area in Thuringia, both in terms of its spatial extent as well as of its economic relevance (Grundmann 2001). The ore field is located within the Zechstein outcrop along the northern edge of the Thuringian Slate Mountains and at the southern border of the Thuringian Basin (TLUG 2005). The ore-bearing layers belong to the Werra layers, which represent the oldest layers of the central European Zechstein sediments. The Zechstein layers are discordant to the basement rock, which consists of folded layers of argillaceous slate and greywacke from the Lower Carboniferous that were eroded and reddened within a longer lasting continental period. The Zechstein layers strike towards ENE-WSW and the inclination is 5-10° towards NNW (Decker and Rüger 1991, Rüger and Decker 1992).

A schematic representation of the geological setting of the area near Unterwellenborn is given in Fig. 3.2. The stratigraphy of the Saalfeld-Kamsdorf deposit is presented in App. 3.2. Today's bedrock in the surrounding of Unterwellenborn is composed of Zechstein strata of the Werra, Leine and Fulda formations (e.g. Werra dolomite, "Leinekarbonat", "Oberer Bröckelschiefer"), reworked loess and solifluidal deposits from the Pleistocene. Within the Weira Valley, Holocene flood plain sediments can be found. The range of hills to the north of Unterwellenborn mainly encompasses strata from the Bernburg and Calvörde formation of the Lower Buntsandstein and strata from several formations of the Middle Buntsandstein (TLUG 2001).

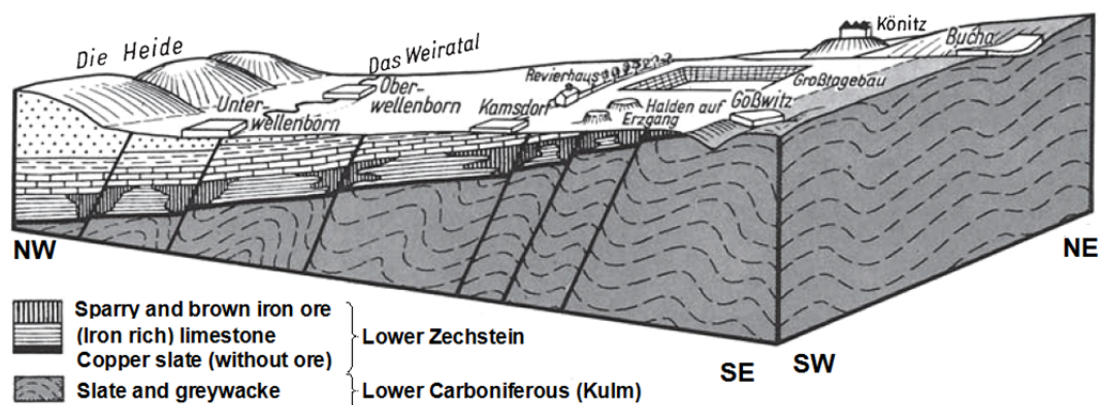


Fig. 3.2: Diagram of the geological setting at Unterwellenborn (modified after Wagenbreth and Steiner 2015).

A multitude of geological faults present in the Zechstein layers and in the underlying basement rock were the prerequisite for the formation of the Saalfeld-Kamsdorf ore deposits. These faults were caused by impacts of the Saxonian tectonic processes, which affected the underlying layers of the Thuringian Slate Mountains that had already been deformed by the Variscan orogeny (Rüger and Decker 1992). Hydrothermal solutions ascended along these faults and dykes and led to the formation of copper-, silver, nickel- and cobalt-bearing veins in the layers of the Lower Zechstein. These mineralisations occurred in the "Lower Slate", better known as Kupferschiefer (which is in this region poor in ore compared to the Mansfeld region) and the "Upper Slate", another bituminous layer. Along these veins, Zechstein limestone was altered to siderite and ankerite. In the Upper Werra Dolomite, the limestone was transformed to ferriferous dolomitic limestone by iron-manganese-magnesium metasomatism. After erosion of the covering

Buntsandstein layers in the Quaternary, the Zechstein sediments weathered and limonite with contents of up to 52% iron and 10% manganese was formed out of the ferriferous and mineralised limestone along with various minerals (Rüger and Decker 1992, Grundmann 2001, TLUG 2005). Despite the previous descriptions, Rüger and Decker (1992) pointed out, that there are several theories on the formation of the deposit and that the genesis of the Saalfeld-Kamsdorf ore field is not yet conclusively clarified.

Analyses of archaeological findings prove that the area at Unterwellenborn has been characterised by mining and metallurgical activities since the Bronze Age (Rüger and Decker 1992, Grundmann 2001). The origin of iron production reaches back to the La-Tène culture, approximately 450 B.C. until 0, when iron was mainly used for manufacturing weapons and tools (Rüger and Decker 1992). Coinages from the middle of the 11th century most likely indicate the first finding and usage of silver ore poor in copper in the area near Saalfeld. The invention of the Saiger procedure, which allowed separating copper and silver, intensified the copper and silver mining in the 15th and 16th century and various new ore deposits were tapped. The most profitable silver ore bodies were mined at the end of the 16th century. Within the 'Thirty Years' War, most of the ore pits and smelteries were demolished. In the 17th and 18th centuries, copper and cobalt mining gained economic importance (Rüger and Decker 1992, TLUG 2005). However, cobalt mining ended in 1848 and silver ore mining in 1867 (Rüger and Decker 1992, Grundmann 2001).

While the mining of iron ore in the Kamsdorf-Könitz mining area was of negligible relevance during the middle ages, it became increasingly important in the early modern period (Rüger and Decker 1992, Grundmann 2001). The local Kamsdorf iron ore played an important role for the production of iron in small ironworks along the upper Saale and various tributary rivers. The "Eisenstraße" is a relic of these times and received its name from the transport of iron ore along the Rennsteig (Grundmann 2001). With the beginning of the 18th century, the iron ore mining focused on brown iron ore, which was easily reducible and thus well suited for iron production. In the early 19th century also siderite was mined (Rüger and Decker 1992, TLUG 2005). Starting in the midst of the 19th century, the charcoal powered blast furnaces of the small ironworks in the Thuringian valley struggled heavily with the lack of wood, increasing wood prices and missing railroads for the transportation of coke. In addition, ironworks abroad (e.g. England, France) were already based on hard coal. As a consequence, most of the charcoal powered blast furnaces were shut down and the iron ore mining at Kamsdorf was closed in 1867. However, iron ore mining continued in the Könitz mining area (Rüger and Decker 1992, Grundmann 2001). The mining claims and mining shares of the "Vereinigte Reviere Kamsdorf" trade union, which was founded in the 19th century, were acquired by the Bavarian "Eisenwerk-Gesellschaft Maximilianshütte" in 1869, who re-established iron ore mining in Kamsdorf in the early 1870s and continued the mining of the ferriferous limestone. From 1869 until 1958, the mining was realised belowground and starting from 1949 in more efficient open-pit mines (Rüger and Decker 1992, Grundmann 2001, TLUG 2005). In 1963, mining of ferriferous limestone was started in an open pit approximately 4 km to the east of Unterwellenborn at Kamsdorf, aiming at providing aggregate material for the iron producing industry in the GDR (see Fig. 3.1). While the production of aggregate limestone became less important in late 1960s, the production of agricultural lime gained economic relevance (Rüger and Decker 1992, Grundmann 2001). Today, limestone and dolomite as well as greywacke and argillaceous shale are mined and used for the production of agricultural lime and building materials (Großtagebau Kamsdorf GmbH).

3.3 Local History of Iron and Steel Production

The history of iron and steel production in Unterwellenborn reaches back to the middle of the 19th century. Since then, the iron- and steelmaking technologies along with the used raw materials and resulting primary and secondary products have changed significantly. Profound descriptions of the history of the “Maxhütte” are given in the comprehensive book series published by the historical society of the Maximilianshütte/Maxhütte (Geschichtsverein Maxhütte e.V. 1997-2012). Furthermore, Grundmann (2001) as well as Rüger and Decker (1992) provide information on the local history. Based on the aforementioned references, interviews with local experts and extensive analyses of historical archive data of the Stahlwerk Thüringen GmbH, Mrotzek-Blöß et al. (2016) elaborated a detailed overview of the history of the former iron- and steelmaking in Unterwellenborn and the dump site, including material flow models for relevant periods. The Stahlwerk Thüringen GmbH offers a brief summary of the history (SWT 2017). This chapter will present the local historical developments summarising information given in the references mentioned above, as the structure of the dump site and the materials found there are closely linked to the history of iron- and steelmaking in Unterwellenborn and thus of paramount importance in this thesis.

Early stages of iron- and steelmaking in Unterwellenborn (1869 to the early 20th century)

The origin of iron- and steelmaking in Unterwellenborn is strongly connected with the metallurgical and metalworking industry in Haidhof, Bavaria. To secure the raw material supply for the iron- and steelworks in Haidhof, the Eisenwerk-Gesellschaft Maximilianshütte acquired mining claims for the ore deposits at Saalfeld-Kamsdorf and Schmiedefeld in 1869. In 1872, the Eisenwerk-Gesellschaft Maximilianshütte received the permission to build a metallurgical plant for iron production in Unterwellenborn. The first blast furnace was completed in 1873 and a second one went into operation in 1878. The resulting blast furnace slag was partially granulated or cut to blocks, which were used for construction purposes. In the same year, steel production began based on the Bessemer process and was realised using two converters of five tons capacity resulting in an average daily steel production of 50 t. The local deposits in Kamsdorf provided large amounts of manganiferous iron ore in form of sparry iron ore (siderite: Fe 39.4 m%, Mn 10 m%) and brown iron ore (limonite: Fe 48.9 m%, Mn 4.85 m%). These ores were almost free of phosphorous and thus important raw materials for ironmaking based on the Bessemer process (Rüger and Decker 1992, Geschichtsverein Maxhütte e.V. 1997, Grundmann 2001, SWT 2017).

At the end of the 19th century, the iron- and steelworks were modernised, and two blast furnaces were replaced with more efficient units (daily production of 150 t each instead of 100 t). The blast furnace slag was granulated and transported to the dump site using a cable way system. As the formerly used local iron ore, which only showed low contents of phosphate, declined, the Bessemer steelmaking procedure was closed down in 1898. Instead, the meanwhile established Thomas procedure was introduced. This procedure required iron ore rich in phosphate, which was still present in the local deposits at Kamsdorf. In order to remove the phosphorous, scrap metal and limestone were added during the steelmaking process. The slag from iron production in the blast furnaces was used as a basis for cement production in a cement plant in Unterwellenborn starting in 1907 (Geschichtsverein Maxhütte e.V. 1997, Grundmann 2001, Mrotzek-Blöß et al. 2016).

World War I until World War II

During World War I, iron and steel production was regressive. Between the years 1921 and 1928, the iron- and steelworks were modernised, encompassing the building of four new blast furnaces and rebuilding of the Thomas steelworks. At this time, the local phosphate rich iron from the mining pits in Schmiedefeld was utilised for iron and steel production. The slag from the Thomas steelmaking was broken and ground and the resulting Thomas ground basic slag was used as fertiliser due to its high phosphate content of up to 14%. The Eisenwerk-Gesellschaft Maximilianshütte and subsequently the iron- and steelworks at Unterwellenborn as well as the local mining were heavily affected by the world finance crisis of the late 1920s. As a result, the nearby mining sites at Kamsdorf and Schmiedefeld were closed at the end of 1931. Prior to this, the Thomas steelworks was closed, and iron was produced only in one blast furnace (Geschichtsverein Maxhütte e.V. 1998, Grundmann 2001, Mrotzek-Blöß et al. 2016, SWT 2017).

In the early 1930s, the steel mill in Unterwellenborn re-commenced production and in 1934, a second blast furnace went operational. In 1936 and 1938, two 17.5 t rotary current arc furnaces went into operation for high-grade steel production. In the following years, various production and processing facilities were modernised. As a consequence of the efforts to process German iron ore, ore was processed in a blast furnace to pre-smelted iron, which was rich in sulphur and silicate, and afterwards re-smelted to Thomas iron. The slag of these processes was used for cement production and road construction. During the last years of World War II, the supply chain of slag formers and other materials was hampered, obstructing the iron and steel production in Unterwellenborn. As a result, the production of Thomas iron decreased from ca. 250000 t in the year 1943 to less than 50000 t in 1945. In April 1945, the iron- and steelworks stopped production after bomb strikes and American troops entered the facilities peacefully (Geschichtsverein Maxhütte e.V. 1998, Grundmann 2001, Mrotzek-Blöß et al. 2016, SWT 2017).

Post-war period

At the end of 1945, the production of iron and steel was continued under supervision of the Red Army. However, a continuous production was not possible due to the lack of supplementary materials in the supply chain, especially coke. As the supply chain was unstable, a low shaft furnace was used for the processing of local ore with relatively low contents of iron (up to 24%) and high amounts of silica (up to 40%) starting in 1951. In 1950, the production numbers for iron reached 337300 t, 275600 t for the roll mill, 218400 t for the Thomas steel production and 43700 t of electric steel (Geschichtsverein Maxhütte e.V. 2004, Mrotzek-Blöß et al. 2016).

In 1948/49, the initiative *Max needs water* (“Max braucht Wasser”) was launched by the Free German Youth (FDJ). In this campaign, a water pipeline to secure cooling water supply for the iron works was constructed within 90 days by more than 2700 adolescents and students. In later years, further initiatives were launched under the slogans *Max needs scrap metal* (“Max braucht Schrott”) and *Max needs bones* (“Max braucht Knochen”) (Grundmann 2001). In August 1945, the slag brickworks started reusing materials from the slag dump site for stone production and the cement industry. Furthermore, a facility for the production of slag wool was erected (Geschichtsverein Maxhütte e.V. 2004). Slag wool is artificial wool of fine slag fibres, which is produced by blowing a high-pressure stream of air or steam through liquid slag, and mainly used for thermal insulation in the building industry or as electrical insulator (e.g. Zhao et al. 2014).

1950 to 1960

To overcome the lack of scrap metal and high-grade iron ore during the GDR period and to increase the usage of local resources, a sintering plant and two Renn furnaces were put into operation in 1951, 1953 and 1954, respectively. In Unterwellenborn, concentrated ore from the Renn facility, blast furnace dust, fine-grained ore from local mining and further materials were used within the sinter process. The Krupp-Renn procedure aimed for processing acidic ore poor in iron, which could not be utilised otherwise in the blast furnace, in a rotary furnace. In Unterwellenborn, five tonnes of input materials (iron ore from Eisenberg and Badeleben, pyrite cinder, converter dedusting sludge, lime stone from Kamsdorf and coke breeze) were required for the production of one tonne of loop. The daily production of sinter was 750 to 1000 t. The coarse fraction of the resulting slag was utilised for the construction industry while the fraction < 1 mm was deposited at the dump site. The steelmaking processes were optimised by utilising oxygen instead of air, resulting in higher quality steel and reduced smelting times as well as less amounts of needed alloying additions within the electric steel plant. Further improvements were applied to the blast furnace gas cleaning system and henceforth blast furnace gas was used as main source for heat-requiring processes in the iron- and steelworks (Geschichtsverein Maxhütte e.V. 2005, Mrotzek-Blöß et al. 2016). An overview of the utilisation of the slags from the different iron- and steelmaking processes in the 1950s is given in Appendix 3.3.

1961 until 1982

Despite the modernisation of the blast furnaces and other facilities in the early 1960s, the iron- and steelworks in Unterwellenborn struggled due to the suboptimal infrastructure connection - no nearby waterways and ports - and due to the unprofitable local ore reserves within this period. After the local ore grounds at Wittmannsgereuth and Schmiedefeld were closed in the late 1960s, the iron- and steelworks processed imported iron ore from abroad and coke from the former Czechoslovakia. The ore crunching facilities, the roasting and Renn furnaces as well as the low shaft furnaces were closed down. Subsequently, also the production of slag wool ended (Geschichtsverein Maxhütte e.V. 2005, 2011, Mrotzek-Blöß et al. 2016). In the early 1970s, the blooming mill as well as the Thomas steel plant were reconstructed and modernised. Furthermore, filtering facilities for cleaning the blast furnace top gases and dedusting systems in the electric and converter steel plants were installed. The resulting sludges of these cleaning processes were transported to the dump site for temporary storage and drying in various basins (see Chapter 3.4.2). Starting in 1975, a new roll line was initialised, which was modernised in the following years and which played an important role for the future of the steel plant. As the introduction of the LD steelmaking procedure was postponed in the GDR, the QEK procedure (“Qualitäts- und Edelstahl-Kombinat”) was introduced (Geschichtsverein Maxhütte e.V. 2011, Mrotzek-Blöß et al. 2016, SWT 2017).

1982 until today

In the 1980s, great efforts were undertaken to increase production efficiency. The rolling mill was extended and a combined section rolling mill (KFS – “Kombinierte Formstahlstraße”) was ready for production in the mid of 1985 (SWT 2017). Furthermore, several converters were adapted to more modern procedures (Geschichtsverein Maxhütte e.V. 2011, Mrotzek-Blöß et al. 2016).

In the course of increasing world market prices for raw and construction materials, the reuse of dump site materials gained economic relevance. Thus, great efforts existed for reclaiming and reusing the disposed materials from the Unterwellenborn dump site. Consequently, several measures have been taken. These encompassed the introduction of the magnet separation of scrap metal from slag, which allowed the extraction of up to 4000 t of scrap metal per year, and the production of fertiliser based on ground Thomas slag starting in 1983. In 1989, 230000 t of blast furnace slag and nearly the complete annual production of Thomas slag (in form of Thomas ground slag, 76000 t of 83000 t) were sold. To further increase material reuse, exploration investigations were conducted and provided promising results. However, further undertakings were cancelled due to the foreseeable political turn at the end of the GDR times (Geschichtsverein Maxhütte e.V. 2011, 2012; Mrotzek-Blöß et al. 2016). Until 1989, electricity and air blast for the Thomas converters were produced from seven generators in the Gas Engine Central (“Gasmaschinenzentrale”) based on blast furnace top gas. The Gas Engine Central is a further relic of the long history of iron and steel production in Unterwellenborn and can today be visited as a museum (Förderverein Schaudenkmal Gaszentrale Unterwellenborn e.V.).

Until 1987, a prison labour camp for convicts and political prisoners existed in Unterwellenborn (Sonntag 2011). In 1990, the formerly VEB Maxhütte became the Maxhütte Unterwellenborn GmbH. To improve the company’s competitiveness, the electric steel plant was closed in 1991 and various production facilities as well as several attendant facilities were partially privatised. In 1992, the blast furnaces, the basic oxygen steelmaking plant and the blooming train were shut down. On July 1st, 1992, the today’s Stahlwerk Thüringen GmbH was founded, and comprehensive modernisation works were conducted in the following years. In 1995, a new electric steel plant went into operation with an electric arc furnace of 120 t capacity. In 2006, after fusion of Arcelor and Mittal Steel, the Spanish group Alfonso Gallardo became new owner of the Stahlwerk Thüringen GmbH. Since 2012, the Stahlwerk Thüringen has belonged to the Brazilian company Companhia Siderúrgica Nacional (CSN) (Grundmann 2001, Geschichtsverein Maxhütte e.V. 2012, Mrotzek-Blöß et al. 2016, SWT 2017). Today, the Stahlwerk Thüringen GmbH has about 700 employees and the annual steel production exceeds 900000 t of carbon steel (i.e. low-alloyed steel). The steel production is based solely on scrap metal and the steel is exported to over 60 countries. The electric arc furnace allows the melting of 135 tonnes of scrap metal within one hour using 100 MW. After production in the electric arc furnace, the crude steel is transferred to ladle furnaces for further processing (SWT 2017). For the most part, the EAF slag is prepared and marketed by the RGA GmbH & Co. KG. A summary of the major iron- and steelmaking procedures, primary and secondary products and their utilisation is given in Tab. 3.1.

Tab. 3.1: Overview of major iron- and steelmaking procedures applied in the Unterwellenborn (iron- and) steel-works, associated by-products and their utilisation (after Grundmann 2001, Mrotzek-Blöß et al. 2016, SWT 2017)

Year	Process	Primary product	By-product	Usage
1878–1945 1946–1992	Blast furnace	Pig iron	BF slag (and dust)	Blast furnace cement Construction material Slag wool
1878–1898 1898–1945	Bessemer procedure Thomas procedure	Thomas steel	Thomas slag	Thomas phosphate (Fertiliser)
1995–today	Electric arc furnace Ladle Furnace	Crude steel Processed Steel	EAF slag LF slag	Construction material, interim storage Disposal

3.4 Dump Site Characterisation

The diversified past of the affiliated dump site, which has its origin in 1872, reflects the more than 100 years lasting history of iron and steel production in Unterwellenborn, starting from the ironworks to an integrated iron and steel plant to today's steel processing based on electric arc furnaces and converters. The basis of the dump site is the original ground surface and is formed of Zechstein sediments. The historic parts of the dump are mainly formed by blast furnace slag, linings and refractories, construction rubble and further materials (Tinz et al. 1996). Aside from the multitude of by-products of former iron- and steelmaking procedures, the dump comprises by-products of the recent steel production as well.

A comprehensive and detailed description of the historical development of the dump site is given in the report by Mrotzek-Blöß et al. (2016). Thus, the following chapters will provide an overview of the major structures of today's dump site and introduce areas that were of relevance within the sampling campaigns, encompassing sections, which were directly accessible from the dump surface as well as structures that were accessed using excavator prospectings.

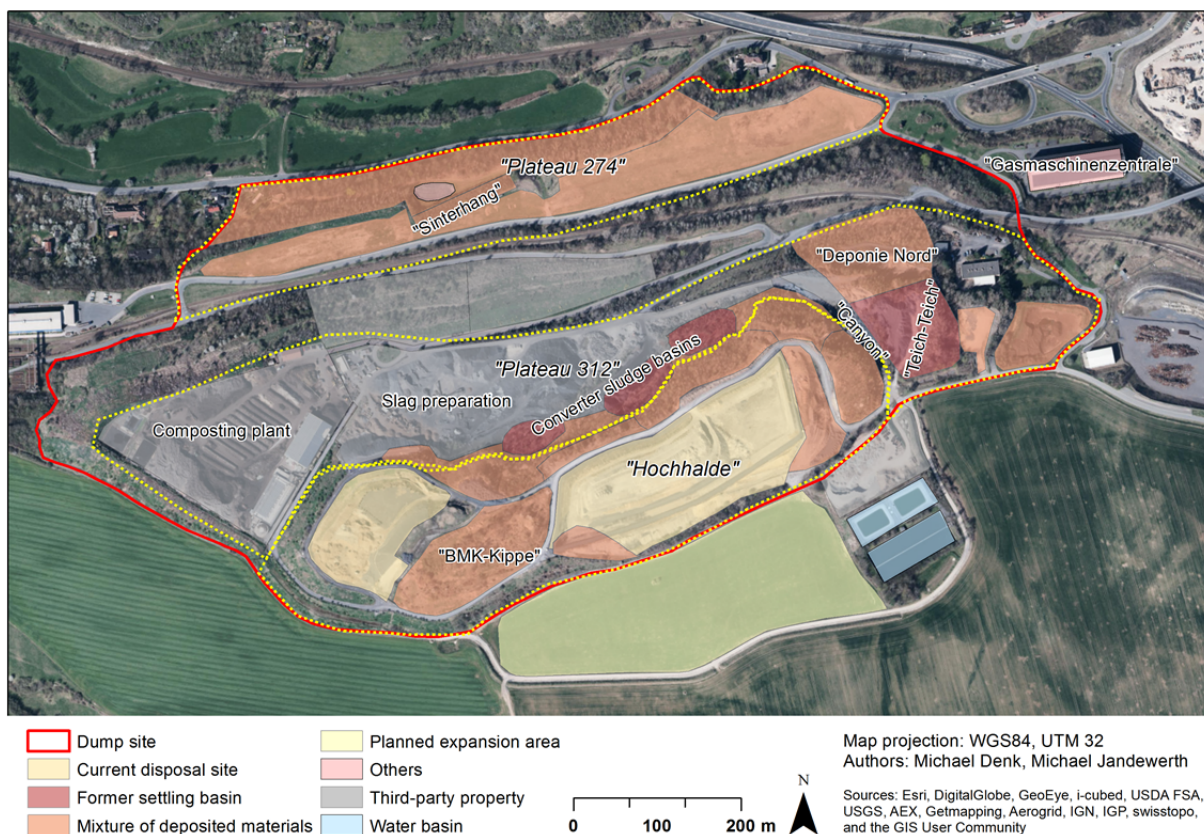


Fig. 3.3: Structure of the dump site of the Stahlwerk Thüringen GmbH (modified after Mrotzek-Blöß et al. 2016). See Appendix 3.4 for a larger and more detailed map.

The dimensions of the dump site are approximately 1.5 km from east to west and 0.5 km in north-south direction and it covers an area of about 0.62 km². In 1995, the total amount of disposed material at the dump site was estimated at 12 million tonnes of slag and further by-products (Tinz et al. 1996). According to Tinz and Stamm (1996) and Tinz et al. (1996), the dump site can be structured in three plateaus based on their average elevation level (Fig. 3.3). These plateaus are: "Plateau 274" which represents the northern part of the dump site, the "Plateau 312", representing the central area and the "Hochhalde" in the southern part of the

dump site. The dump site morphology is characterised by numerous slopes and further plateaus. The differences in altitude occurring between the different plateaus and especially the steep slopes present at the northern part of the dump site are visualised in Appendices 3.5 and 3.6.

At the western part of the dump site, the Arcelor Mittal steel cutting plant can be found. The factory premises are situated at the former train station of the Maxhütte. This area can already be assigned to Gorndorf, the largest district of Saalfeld. The areas north and south of the dump site are utilised as agricultural sites. The premises of the Stahlwerk Thüringen GmbH are located to the northeast of the dump site. Unterwellenborn, with its settlement Röblitz, is situated a little further to the north. In the south of the Stahlwerk Thüringen and to the east of the dump site, several commercial and industrial areas can be found. The area directly to the south of the dump is intended for the expansion of the current by-product disposal site. The basins in the south-west of the dump site represent water reservoirs and infiltration basins (Fig. 3.3).

3.4.1 “Hochhalde”

The “Hochhalde” has its origin at the beginning of the 20th century. Using a cableway system, especially blast furnace slag and blast furnace dusts as well as demolition materials from the Maxhütte were deposited. The disposal site reached heights of up to 345 m above sea level (Mrotzek-Blöß et al. 2016). Today, major parts of this area are used for the disposal of recent by-products, mainly ladle furnace slag and dusts from the steelmaking facilities as well as electric arc furnace slag of larger grain sizes (Fig. 3.4, left). Between the 1950s and 1970s, major parts of the recent slag disposal site were used for the deposition of slag from the Renn procedure. According to the analyses of historical records and aerial photographs conducted by Mrotzek-Blöß et al. (2016) and the report from EPC (1996), the Renn slag dump reached dimensions of at least 4.7 ha and an altitude of 377 m above sea level. After closing down the Renn facilities in 1968, the Renn slag was quarried for production of hollow blocks (Mrotzek-Blöß et al. 2016). Results of drillings indicate that remains of slag from the Krupp-Renn procedure are partly still present in the underground of the current by-product disposal site (Ullrich 2005).

A former monofill of fine sludge from cleaning procedures of the blast furnace top gas is still present in the western part of the today’s Hochhalde. This monofill was built in 1985 and covers an area of approximately 0.5 ha (Mrotzek-Blöß et al. 2016). The average thickness of the layers in the monofill is 3 to 6 m and the volume 11250 m³. The former monofill has been recultivated. Today, it is covered by layers of excavated soil, demolition waste, electric arc furnace and ladle furnace slag (Tinz and Stamm 1998a, Dyck 2004). Analyses of the deposited sludges indicated iron contents of 15-25%, up to 13.9% zinc and 3.3% lead (EPC 1996, Tinz and Stamm 1998a).

In the eastern part of the “Hochhalde”, a plateau mainly consisting of blast furnace slag, pervaded by individual layers of brick fragments from demolition works can be found (Tinz 2006, Mrotzek-Blöß et al. 2016). This plateau is separated from the by-product dumping site by an access ramp. As a result of the construction activities, multiple layers of several historic by-products have been laid open at both sides of the driveway, which were used for the collection of samples (Fig. 3.4, right). Originally, blast furnace slag, partially covered with Thomas slag and blast furnace flue dust, could be found in the eastern part of the “Hochhalde”, but these materials were reused for the stone and cement industry (Mrotzek-Blöß et al. 2016). In the

northern part of the “Hochhalde”, mixtures of blast furnace slag and blast furnace dusts are present (Tinz et al. 1996). An area of around 8000 m² at approximately 330 m a.s.l. is located in the western part of the “Hochhalde”, which has been used for the disposal of different metallurgical by-products, refractories and demolition waste (Mrotzek-Blöß et al. 2016). Today, parts of this area are recultivated and partially covered with asphalt. Thus, this area was assigned as “no-go area” and not available for sample collection.



Fig. 3.4: Field impressions of the “Hochhalde”: The current by-product disposal site (left) and an access road to the “Hochhalde”, revealing a variety of historic by-products and a distinct basin-like structure (right).

3.4.2 “Plateau 312”

The “Plateau 312” (see Fig. 3.3) is a result of multiple backfillings of various dips in the northern, eastern and western slope areas to the “Hochhalde” with slag, demolition materials, refractories and excavated soil (EPC-1996, Mrotzek-Blöß et al. 2016). Similar to the “Hochhalde”, the “Plateau 312” has a long history of deposition and dismantling. It was primarily used as temporary storage and transshipment point. In addition, deposited historical blast furnace slag was dismantled and partially re-used for block stone fabrication. After 1979, the “Plateau 312” was extended due to the recovery and reuse of blast furnace slag in the eastern part of the “Hochhalde”. To the east of the “Hochhalde”, a distinctive “valley” can be found that is known as the “Canyon” (Fig. 3.5, left). This structure was created in order to provide access to the southern parts of the dump site. In the northern parts of the “Canyon”, Thomas slag can still be found. After 1984, no further materials were disposed at the “Plateau 312” (Mrotzek-Blöß et al. 2016). Today, the western parts of the “Plateau 312” are used for slag preparation and a composting plant can be found further to the west. Three former settling basins are located directly at the northern steep slope of the “Hochhalde”. Until 1992, these basins were used for temporary storing and drying of sludge from wet cleaning procedures of the flues from the electric and the converter steelworks. The maximum thickness of the deposited material was 10 m. Until 1978, minor quantities of sludge from the fine gas cleaning of the blast furnaces tops were disposed in these basins (Tinz and Stamm 1996).



Fig. 3.5: Field impressions of the “Plateau 312”: View through the “Canyon” - a structure mainly formed of historic blast furnace slag - in northern direction (left), the eastern converter (dedusting) sludge basin (right).

The underground and the dams of the basins are made of different residues of metallurgical processes like linings, slag, refractory materials and building rubble. The basins were originally used for temporary storing and drying of the sludge before transporting the material to the close-by municipal landfill of Kamsdorf or other areas of the dump site (Tinz et al. 1996, Tinz and Stamm 1996, VTI 1997, Mrotzek-Blöß et al. 2016). Today, the eastern and the western basins are still intact. The area of the former middle basin is currently used as interim storage for mill scale.

A further settling basin, also known as “Teich-Teich”, with an approximate former area of 2400 m² can be found to the east of the “Hochhalde” (e.g. Tinz and Stamm 1998b). The basin was established in 1974, and analogous to the fillings of the formerly described three settling basins, the sludges deposited in the “Teich-Teich” are by-products of cleaning procedures of dusts and off-gases from the electric and converter steel production facilities (Tinz and Stamm 1996). Today, the basin is covered by construction rubble, excavated soil and slag and is used as temporary storage for electric arc furnace slag (Mrotzek-Blöß et al. 2016). The historic reddish converter sludges resulted from cleaning flue gases and dusts from the electric steelworks and the converter plant and should not be confused with the red sludges from aluminium processing.

3.4.3 “Plateau 274”

The metallurgical facilities were originally located in the northern part of the dump site, known as “Plateau 274” (Fig. 3.3). The original train station of the iron- and steelworks was situated in the western part of this area. The plateau was used as temporary storage and loading area for iron ore, aggregates, coke and other materials. The original slopes were backfilled with materials like slag, excavated soil and construction waste. Today, the “Plateau 274” is remediated and re-cultivated and not used for slag disposal anymore (Mrotzek-Blöß et al. 2016, Fig. 3.6). An excavator prospecting was conducted at the former “Sinterhang” in this area (Ch. 4.1).



Fig. 3.6: Impression of the “Plateau 274”.

4. Data and Methods

4.1 Sampling Approach, Analytical Strategy and Workflow

Despite the comprehensive research of the local history of the dump site and even though its major structures and units were known (see Chapter 3.4), the exact location of disposed historic by-products, the extension of individual layers, and the exact composition of these materials was unknown in many cases for various areas of the dump site. Furthermore, due to the anthropogenic material deposition, the spatial distribution of the dumped materials did not follow natural gradients as they occur in soils or as they are present in natural deposits. Thus, no established sampling strategies, such as raster or transect sampling as described, for example, in Soil Survey Staff (2009) and BGR (2005), could be applied. Instead, a knowledge-based approach was chosen to determine sampling locations. This approach encompassed the development of an up-to-date overview map of the dump site (Fig. 4.1), which was based on multiple site visits and interviews of local experts from the Stahlwerk Thüringen GmbH as well as on analyses of archive data and historical records. This map highlighted the current material distribution at the dump surface as well as known historic subsurface structures. It further allowed determining suitable sampling locations where by-products of interest of recent and historic processes were expected. The map was developed in cooperation with Fraunhofer UMSICHT (see Jandewerth et al. 2013, Mrotzek-Blöß et al. 2016, Nühlen et al. 2016a-c).

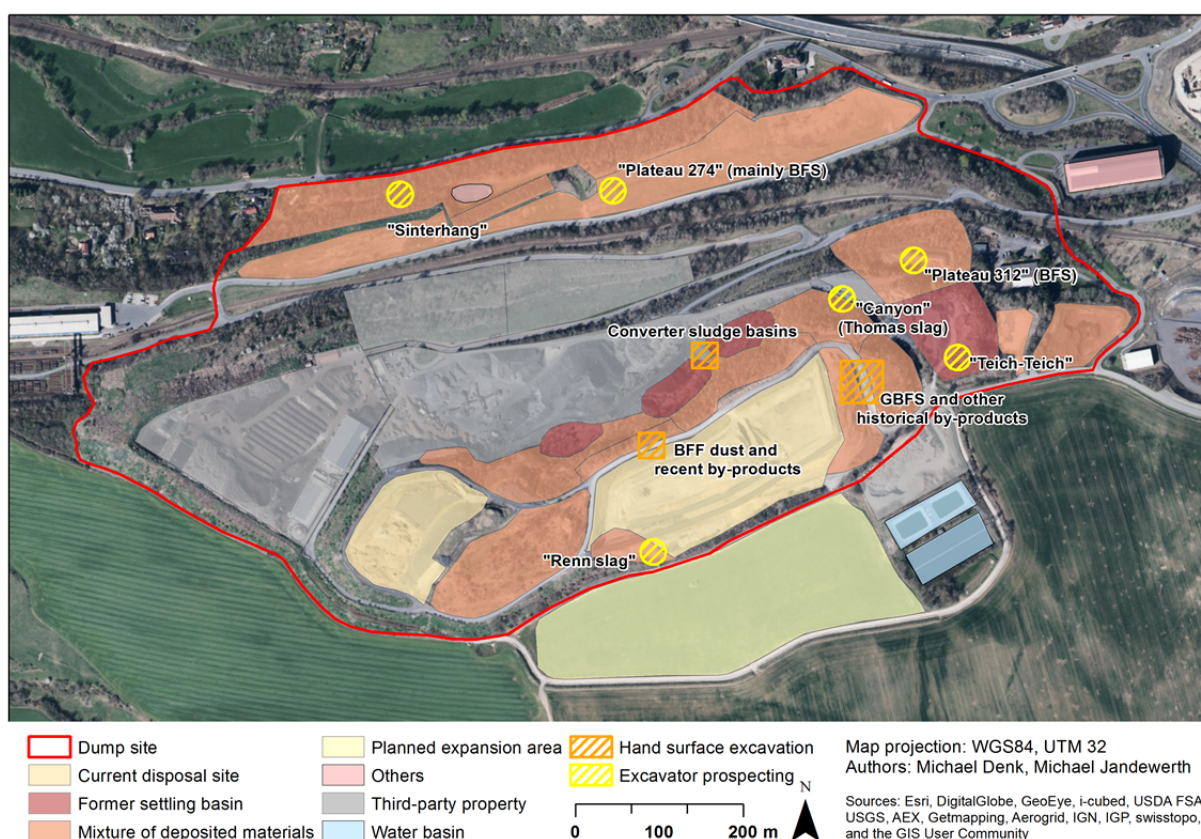


Fig. 4.1: Overview map of the dump site of the Stahlwerk Thüringen GmbH with relevant structural areas and highlighted sampling locations (modified after Mrotzek-Blöß et al. 2016). See Appendix A3.4 for more information.

Based on this map and the acquired expert information, sampling locations at the dump surface and along existing outcrops as well as locations for excavator prospectings were assigned. The aim was to collect representative samples of the majority of the different iron- and steelworks by-

products present at the dump site, including recent by-products but focussing mainly on the multitude of historical materials from the different former iron- and steelmaking phases applied in Unterwellenborn. Covered and rehabilitation areas were defined as not accessible areas and excluded from the sampling campaigns. More detailed descriptions of the sampling locations and sample collection are given in Chapter 4.2.

As the aim was the generation of a comprehensive spectral dataset of typical iron- and steelworks by-products, sampling focussed on the collection of a wide range of materials regardless of the content of potential valuable materials (e.g. iron, phosphate, etc.). In contrast, industrial-driven dump site exploration usually focusses on materials that are potentially rich in economically relevant components. Furthermore, the typical procedures for sampling and subsequent analysis of iron- and steelworks by-products within industrial applications differ from the typical sampling in the field of geological, mineralogical and soil remote sensing, both in terms of the type of sampling as well as the amount of collected material. Thus, a common analysis and sampling strategy was developed in cooperation with FEhS. This approach comprised the collection of larger amounts of material from mixed layers at the excavator prospectings and at other major sampling locations as well as the acquisition of minor amounts of material by hand surface excavation. Subsamples of the bulk samples were taken on-site for subsequent spectral laboratory measurements in order to assess potential impacts of moisture and sample aggregation on the spectra of these materials. Retained samples of prepared materials (crushed, sieved < 0.09 mm), which were utilised for the chemical and mineralogical analyses, were provided by FEhS.

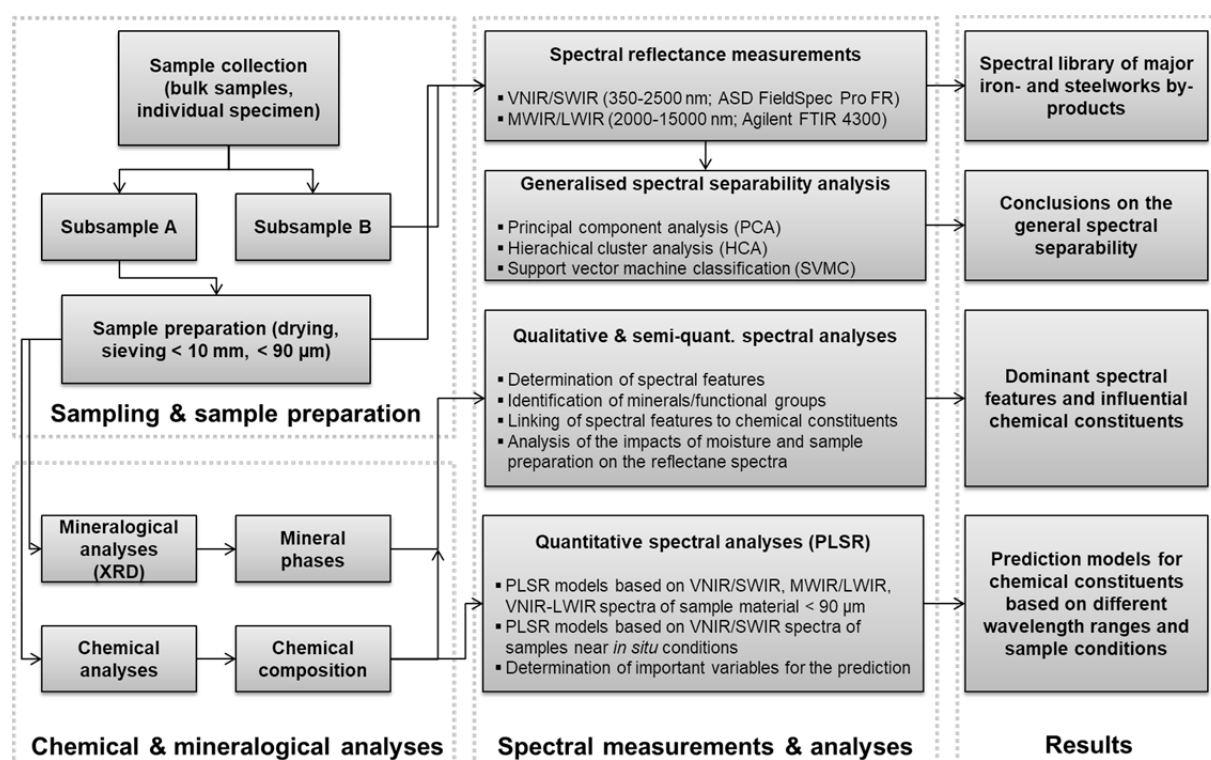


Fig. 4.2: Sampling and analytical approach and general workflow utilised in this thesis.

The spectra of the homogenised samples formed the basis for most of the quali- and quantitative spectral analyses, as they could be directly linked to the chemical and mineralogical composition of the prepared samples. Additionally, for selected samples, retained material of < 10 mm (that was used for eluate investigations), was provided for further analysis of grain size effects on the

spectral characteristics of the studied by-products. The results of the chemical and mineralogical analyses were essential for the qualitative as well as for the quantitative spectral analyses. Here, the mineral phases determined via XRD analysis (see Chapter 4.4) were utilised as reference for the spectral identification of minerals and the determination of functional groups potentially causing absorptions. The chemical composition of the samples was required for the multivariate spectral modelling. Figure 4.2 summarises the described workflow.

4.2 Sample Collection and Generation of a Heterogeneous Sample Dataset

The dataset for the analyses conducted in this thesis comprised 102 samples. Most of these samples were gathered at the slag disposal site of the Stahlwerk Thüringen GmbH within sampling campaigns at April 19th and June 18th-20th in 2013. These campaigns comprised the collection of samples directly at the dump surface as well as at artificially generated outcrops from excavator prospectings. The selection of sampling locations was based on the map described in Chapter 4.1 (see Fig. 4.1). The excavator prospectings were conducted at six locations for which the opening of relevant historical materials was promising:

- In the “Canyon”, where the phosphate-rich Thomas slag was supposed to be found (Fig. 4.3a)
- Close to the former “Sinterhang”, where several historical layers could be laid open (Fig. 4.3b)
- At the “Teich-Teich” (Fig. 4.3c) and at a slope in the NE part of the Plateau 312 (Fig. 4.3d)
- At the Plateau 274, where several layers of BFS could be accessed (Fig. 4.3e)
- At the western part of the today’s slag disposal site at the “Hochhalde”, aiming at assessing remains of the formerly deposited slag from the Renn procedure (Fig. 4.3f)

The sampling of the major layers accessed via the excavator prospectings was conducted by FEhS according to DIN EN 932-1, which comprised the collection of multiple kilogrammes of material for mineralogical and chemical analyses. Subsamples of these bulk samples were taken and stored in sealed polyethylene bags for subsequent spectral measurements of fresh and unprepared material for the systematic analysis of grain size and moisture effects on the by-product spectra.

In addition to the samples collected at the above mentioned artificial trenches, further samples were collected by hand sampling. At the northern edge of the “Hochhalde” (see Chapter 3.4.1), samples thought to comprise blast furnace flue dust were collected, while EAF and LF slag from recent steelmaking were sampled at the current slag disposal site (Fig. 4.4a). Further sampling was carried out to both sides of the access road to the current disposal site where a large variety of historical materials was laid open (Fig. 4.4b). These materials comprised granulated blast furnace slag (GBFS) but also several layers of materials that could not be identified *in situ*. The mentioned outcrop was selected for the case study conducted by Denk et al. (2015).



Fig. 4.3: Excavator prospectings: a) in the “Canyon”, b) close to the former “Sinterhang”, c) in the “Teich-Teich”, d) at the eastern part of the Plateau 312, e) at the Plateau 274 and f) at the western part of the “Hochhalde”.

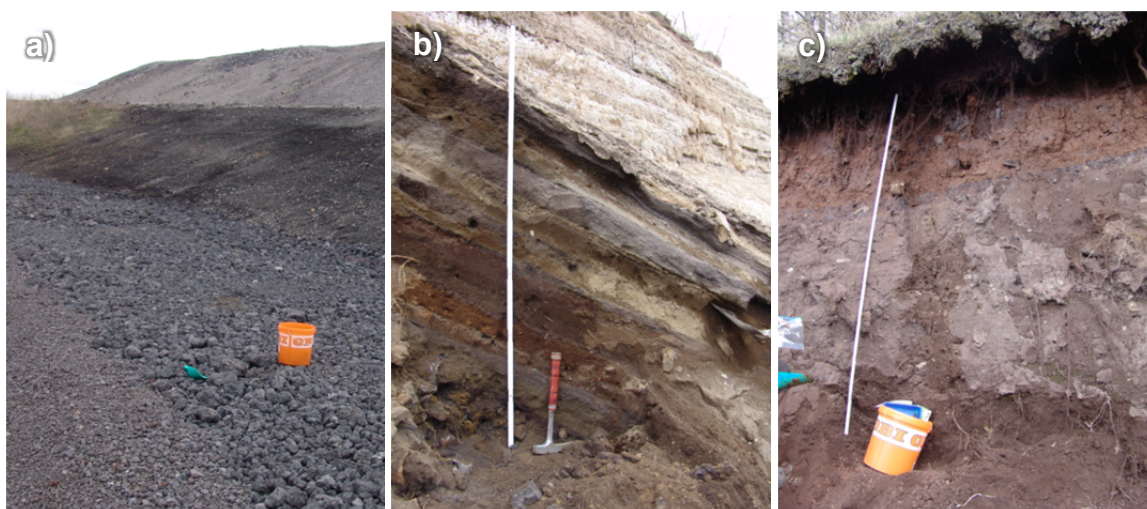


Fig. 4.4: Hand surface sampling at the Unterwellenborn dump site: a) Electric arc furnace slag (foreground) and (amongst others) ladle furnace slag (background) at the current slag disposal site of the Stahlwerk Thüringen GmbH, b) multiple layers of unspecified historical iron- and steelworks by-products present at the western slope of a small plateau at the east of the “Hochhalde”, c) red dedusting sludge in the former middle “converter sludge” basin.

Additional samples were collected in the eastern basin and at the remains of the former middle converter dedusting sludge settling basins, which are located at the northern steep slope of the “Hochhalde” and which contained sludge from cleaning procedures of the flues from the electric and the converter steel plants (Fig. 4.4c; see Chapter 3.4.2). In the area of the former middle converter sludge basin, temporarily stored mill scale was sampled.

In general, sampling took differences in colour, structure and texture of the materials as well as their magnetic properties into account. The sampling locations were captured with a Garmin GPSMAP 60CSx and photographically documented.

Besides the samples collected at the dump site of the Stahlwerk Thüringen GmbH, the sample pool was enriched with samples provided by FEhS from other iron and steel plants. These materials comprised different slags from high-alloy steel production (stainless steel slag, electric arc furnace slag, foamed electric arc furnace slag) and EAF slag from former production of medium-alloyed steel. These materials were not present at the Unterwellenborn test site.

4.3 Sample Preparation

Sample preparation for mineralogical and chemical analyses was realised by FEhS and followed internal protocols. After drying the samples, the physical separation of slag and metallic components was conducted utilising a vibratory disc mill and metallic mesh sieves with grid widths of 0.5 mm to 0.09 mm. Based on the different ductility of slag and metal, the fractions < 0.5 mm (metal-rich), 0.5–0.09 mm (poor in metal) and < 0.09 mm (free of metal) were extracted by grinding until weight constancy and continuous sieving. No further treatment of these metallic components was conducted, as only three samples showed fractions poor in metal with 1–2 m% (see also Mrotzek-Blöß et al. 2016). The < 0.09 mm fractions of the samples were used for chemical and mineralogical analyses. In addition, retained samples of air-dried and crushed material < 10 mm (which was prepared for eluate analyses following DIN EN 12457-4 as conducted in the project REStrateGIS) were provided for 36 samples.

4.4 Mineralogical and Chemical Analyses

As described in Chapters 2.1.2 and 2.1.3, the various iron- and steelworks by-products show a diverse chemical composition and mineralogy. Thus, assessing the chemical and the mineralogical properties was crucial for the typification of the samples, especially as the *in situ* identification of the disposed historic materials based on visual inspection was challenging even for experts. The entire chemical and mineralogical analyses were conducted by FEhS and provided for this thesis.

In order to assess the mineralogical composition of the sampled iron- and steelworks by-products, X-ray diffraction (XRD) analysis was conducted using a PANalytical X'Pert PRO powder diffractometer. Instrumental parameters are summarized in Appendix 4.1.

X-Ray powder diffraction is an established method for determining crystalline phases in organic and inorganic samples. Furthermore, quantitative phase analysis can be performed, too, applying different approaches like RIR (Hubbard and Synder 1988) - or the Rietveld method (Rietveld 1969). The advantages of the Rietveld method are the possibility to determine the quantitative phase assemblages based on the crystal structures of the present phases and to determine the amorphous contents using inner (Madsen et al. 2001) or outer standard (Jansen et al. 2011) procedures. Therefore, the analytical method is utilised in various scientific disciplines (e.g. Das et al. 2014, Bunaciu et al. 2015). It is based on the principle that crystalline materials produce specific diffraction patterns when irradiated with monochromatic X-rays depending on their atomic composition and crystalline structure, as described

by Bragg's law (Bragg and Bragg 1913). The determination of mineral phases was realised with the software X'Pert HighScore Plus from PANalytical (Version 2.2.5) utilising the PDF-1 database from the International Centre for Diffraction Data. For selected samples, the determined phases were roughly quantified based on Reference Intensity Ratios (see e.g. Snyder 1992) and categorised into major (> 20%), minor (5-20%) and trace (< 5%) constituents. This information only refers to the crystalline part of the samples. Amorphous constituents have not been quantified. The XRD data provided the basis for the qualitative spectral analysis of the collected samples (see Chapter 4.7.2). For more details on the theoretical background and XRD procedures see for example Allmann (2003), Spieß et al. (2009) and Waseda et al. (2011).

The determination of chemical main, minor and trace constituents of the sampled by-products was based on wet chemical procedures after microwave digestion (EN 13656). Oxidic and metallic components that could not be physically separated as described in Ch. 4.3, were analysed using the bromine-methanol process (Kraft and Fischer 1963). The elementary analysis of the samples was realised using inductively coupled-plasma optical emission spectrometry (ICP-OES, Spectro Ciros CCD instrument, analysis according to EN ISO 11885 (2009-09)), which is a well-established approach for analysing the chemical composition of samples (Brenner and Taylor 1992, Hall 1992, Ghosh et al. 2013). The SiO₂ content was analysed according to DIN EN 196-2 (2013-10). Free lime and the S_{total} were determined according to DIN EN 1744-1: 2009+A1:2012. See App. 4.2 for an overview of analysed constituents, used methods and DIN standards.

The results of the before mentioned analyses provided the basis for the chemical characterisation of the samples (see Chapter 5.3) as well as for the qualitative and quantitative spectral investigations (see Chapters 5.5 and 5.6). In total, 40 chemical parameters were analysed. Due to financial restrictions, not all samples could be analysed for all constituents.

4.5 Statistical Analysis of the Chemical Data

For assessing the amplitude of chemical constituents present in the collected samples, basic descriptive statistics were calculated. These parameters comprised the mean (MN), median (MD), standard deviation (SD), minimum (MIN) and maximum (MAX) values as well as the resulting ranges. In addition, the kurtosis and skew of the data distribution function were calculated to assess its form. Shapiro-Wilk tests were conducted to analyse the data for normal distribution as this method is robust for sets with relatively low numbers of samples.

In order to investigate potential intercorrelations among the chemical parameters and to assess the strength and direction of these correlations, principal component analysis (PCA, Pearson 1901, Hotelling 1933) was conducted. This widely used multivariate approach aims to structure and simplify complex data by transforming multiple highly correlated variables into uncorrelated variables, so-called principal components (PC). These PC are formed successively by linear combinations of the original data and each new component aims at describing the maximum variance still present in the data (e.g. Eckey et al. 2002, Jolliffe 2002, Dormann 2017).

Descriptive statistical parameters and intercorrelation matrices were calculated and visualised in R (version 3.4.2, R Core Team) and R Studio (version 1.1.383, RStudio Team 2017), utilising the packages "psych" by Revelle (2017), "MASS" by Venables and Ripley (2002) and "corrplot" by Wie and Simko (2017). The PCA was calculated using the "stats" package integrated in R. Additionally, ternary plots, as they are typically used for visualisation of the chemical composition of natural rocks as well as iron- and steelworks slags (e.g. Drissen 2004), were created using the R package "ggtern" by Hamilton (2017), an extension to "ggplot2" by Wickham (2009).

4.6 Spectral Measurements and Spectral Preprocessing

4.6.1 Spectroscopic Measurements

4.6.1.1 Acquisition of Spectra in the Visible Light, Near and Shortwave Infrared

Diffuse reflectance measurements were conducted using a FieldSpec Pro FR spectroradiometer from Analytical Spectral Devices Inc. (ASD, ASD 2002). The instrument covers a wavelength range of 350 to 2500 nm, which comprises parts of the ultraviolet (UV, 350-400 nm), the visible light (VIS, 400-700 nm), the near infrared (NIR, 700-1300 nm) and the shortwave infrared (SWIR, 1300-2500 nm). The instrument records reflectance values utilising three individual detectors with different spectral resolutions and sampling intervals (see Table 4.1).

Tab. 4.1: Selected technical characteristics of the ASD FieldSpec Pro spectroradiometer (ASD 2002).

Detector	Spectral range	Sensor type	Spectral sampling	Spectral resolution
1	350-1050 nm	512-channel silicon photodiode array overlaid with separation filter	1.4 nm	3 nm at 700 nm
2	900-1850 nm	InGaAs photodiode detector	2 nm	10-12 nm
3	1700-2500 nm	InGaAs photodiode detector	2 nm	10-12 nm

Figure 4.5 illustrates the measurement set-up. An ASD Pro Lamp, equipped with a 50 W bulb, served as illumination source (45° incident angle). The distance from the lamp to the measurement object was approximately 30 cm. For the measurements, the bare fibre optic with a Field of View (FOV) of 25° has been located approximately 15 cm above the measurement object, resulting in a measurement diameter of about 6.7 cm. On the one hand, this measurement field size ensured measuring a representative sample spot as the utilised petri dishes had a diameter of around 8.8 cm. On the other hand, it could be avoided to record the edges of the dish, potential shadowing or the underlying material outside of the sample dishes. The measurements were conducted in the spectroscopy laboratory of the Department of Remote Sensing and Cartography at the Institute of Geosciences and Geography of the MLU Halle. This chamber is equipped with black painted walls and curtains in order to minimise unwanted diffuse reflectance of non-target materials. The warm-up times of the lamp and spectrometer were at least 30 minutes and the underlying plate of the sample dish showed a flat reflectance signal (~5%) over the whole recorded wavelength range. This was important as spectrally unsuitable background materials and light sources as well as insufficient warm-up times might cause unwanted effects on collected spectral data (see e.g. Jung et al. 2012, Götze et al. 2017). A Spectralon white reference panel of nearly 99% reflectivity was used for calibration purposes. Spectralon is made of polytetrafluoroethylene (PTFE) and shows Lambertian reflectance properties (e.g. Weidner and Hsia 1981, Bruegge et al. 1993, Stiegman et al. 1993).

The software RS³ (version 6.0), provided by ASD, was used for operating the FieldSpec Pro FR. The integration times, gain and offset-values of the individual detectors as well as the dark current were defined during the automatic optimisation process of the instrument to adjust the detectors to the current illumination conditions. Fifty measurements were internally averaged before saving each spectrum file. According to ASD (2002) and as mentioned in Jarmer (2005), increasing the number of internally averaged spectra will significantly increase the signal-to-noise level of the resulting spectrum. After saving three spectra per sample, the sample position was rotated by 90° before collecting another three spectra. This procedure was repeated three times

to acquire reflectance spectra for different sample positions, aiming to take possibly varying illumination and texture effects into account. Thus, twelve spectra were recorded in total for every sample (three spectra per each of the four sample positions).

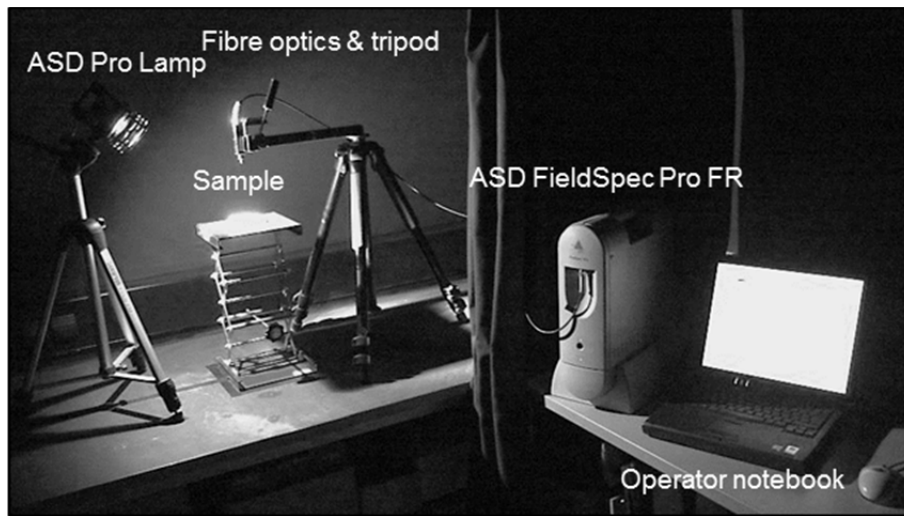


Fig. 4.5: Setup for the spectral laboratory measurements carried out with the ASD FieldSpec Pro FR.

4.6.1.2 Acquisition of Spectra in the Mid- and Longwave Infrared

To record reflectance properties of the samples in the mid-wave (MWIR) and longwave infrared (LWIR), an Agilent 4300 Handheld Fourier-transform infrared (FTIR) spectrometer was utilised. The instrument covers the wavelength range of ca. 2000 to 15400 nm with a spectral resolution of 16 cm^{-1} (Agilent 2017). In contrast to the measurements performed with the ASD FieldSpec Pro FR, the Agilent 4300 Handheld FTIR provides an internal energy source (ceramic heating element of 1000°C) and only contact measurements could be conducted utilising a diffuse reflectance sample interface. The saved spectra were based on 64 internally averaged measurements and three spectra were saved per sample. A gold reflector cap was utilised for calibrating the spectrometer. For further details on the basic principles of FTIR measurements and instruments as well as information on potential background contributors see for example Smith (1996), Marks (2009) and King et al. (2004a). The measurement set-up is presented in Figure 4.6. To assess the accuracy of the measurements, samples comprising minerals with distinct spectral features (e.g. quartz, gypsum) were measured. The results indicated good matches to reference spectra (see Appendix 4.2).



Fig. 4.6: Spectral measurements with the Agilent 4300 Handheld FTIR.

4.6.2 Spectroscopic Preprocessing

4.6.2.1 Basic Spectral Preprocessing

Spectra collected with the ASD FieldSpec Pro FR were preprocessed using the software ViewSpec Pro by ASD (version 6.0). Preprocessing encompassed the averaging of the twelve repetition spectra per sample as well as the correction of splices in the spectra. Such splices might occur at the transition zones between the detectors due to the different field of views of the individual fibres in the fibre optic cable (e.g. MacArthur et al. 2012, Hueni and Bialek 2017). After averaging and splice correction, the individual spectra were compiled into a digital spectral library file using the software ENVI (by Exelis Visual Information Solutions, Inc., a subsidiary of Harris Corporation; version 4.7-5.4.1). The spectral library was used as basis for subsequent qualitative and quantitative spectral analysis (see Chapter 4.7). The spectra recorded with the Agilent 4300 Handheld FTIR instrument were preprocessed using the software Spekwin32 (version 1.72.0, 06/2016, Menges 2016). The three repetition spectra per sample were averaged and all individual average spectra were compiled into one file. Afterwards, the spectra were transformed from wavenumber units (cm^{-1}) in nanometres (nm). The spectral library files compiled in ENVI and Spekwin32 were exported in common data formats like CSV for subsequent data analysis.

4.6.2.2 Spectral Smoothing

While major errors in spectroscopic measurements caused by external factors can be easily avoided by proper measurement set-ups (see for example Götze et al. 2017), spectroscopic data usually contains a certain amount of random noise caused by the instruments themselves (ASD 2002). Thus, various smoothing and filtering approaches are commonly applied, aiming at reducing random noise while maintaining the actual information contained in the spectral data (Maesschalck et al. 1999). Amongst the multitude of existing filtering and smoothing methods, e.g. moving average, median and Gaussian filtering, the approach developed by Savitzky and Golay (1964) is the most commonly used in chemometrics according to Maesschalck et al. (1999). Thus, the Savitzky-Golay filter was utilised for data smoothing within this thesis. This procedure encompasses the application of a polynomial function to a number of equidistant values to the left and to the right of the data point to be smoothed, to calculate a new data value (Savitzky and Golay 1964). Conservative filter-settings (widths 15, third degree polynomial function) were set for smoothing the VNIR/SWIR data to minimise changes in the original data and to prevent a loss of information. The smoothed VNIR/SWIR spectra were utilised solely for qualitative analysis and visualisation purposes. As the spectral resolution of the MWIR/LWIR spectra was significantly lower compared to the VNIR/SWIR data (585 data points for the range 2000-15400 nm compared to 2151 data points for the range 350-2500 nm), even conservative filter-settings lead to the loss of minor spectral features that might be relevant in terms of qualitative spectral analysis. Thus, no smoothing was applied to MWIR/LWIR spectra, although these spectra were considerably noisy at in the wavelength region > 12000 nm.

4.6.2.3 Spectral Normalisations and Transformations

According to Rinnan et al. (2009), spectroscopic data is often affected by unwanted non-linearities and baseline shifts caused by light scattering. Thus, preprocessing techniques are often applied to minimise such effects before utilising spectral data for chemometrical modelling approaches like PLSR (see Chapter 4.7.3, Rinnan et al. 2009). Preprocessing of the input data can potentially remove such non-linearities and provide more robust models (de Noord 1994). However, studies demonstrated that the results of PLSR modelling might differ depending on the type of preprocessing applied to the input spectra (e.g. Riedel et al. 2018). As such, no universal normalisation or transformation technique exists and identifying “the best” procedure is challenging and case-specific (Maesschalck et al. 1999, Rinnan et al. 2009).

Well-known normalisation and transformation procedures comprise the standard normal variate procedure (SNV, Barnes et al. 1989, Barnes et al. 1993) with subsequent de-trending as well as multiplicative scatter correction (MSC, Geladi et al. 1985, Isaksson and Næs 1988, Naes et al. 1990). While both methods aim at removing scatter effects, SNV is based on calculating the average value and the standard deviation of each spectrum, while MSC is performed by calculating the average spectrum based on a given set of spectra to generate a reference spectrum for the subsequent scatter correction of each individual spectrum (Kooistra et al. 2001, Rinnan et al. 2009). Another method to reduce non-linearities is the transformation of the original reflectance data into absorbance values (Maesschalck et al. 1999). A well-established technique in spectral analyses is called continuum removal (CR). This approach was originally introduced by Clark and Roush (1984) and is particularly useful for the analysis and parameterisation of mineral absorption characteristics (e.g. van der Meer 2004). The continuum represents a convex hull consisting of a number of segments, which fits the original spectrum at several local maxima. By transforming this convex hull against a baseline, even spurious absorption features that are barely visible otherwise, are highlighted (Clark and Roush 1984). This technique removes the influence of different reflectance intensities and allows the parameterisation of absorption features for subsequent analysis (see e.g. van der Meer 2004).

Within this thesis, aside from utilising the reflectance spectra, continuum removal was applied for absorption feature analyses. For this purpose, the continuum removal function as integrated in the software ENVI was applied. Furthermore, these spectra were utilised as input for the chemometrical modelling (see Chapter 4.7.2). In addition, the original reflectance spectra were transformed in absorbance spectra according to formula (4):

$$A = -\log_{10}(R) \quad (4)$$

4.7 Spectral Analysis

4.7.1 Separability Analyses and Classification

To initially assess the spectral separability of the different by-products, focus was put on methods that do not require prior knowledge about the spectral properties of these materials. Thus, generalised approaches were chosen, including principal component analysis (PCA) as described in Chapter 4.5. Furthermore, hierarchical cluster analysis (HCA) of the spectral and the chemical data was conducted in order to group spectrally (and chemically, respectively) similar materials in clusters that were subsequently compared. The hierarchical clustering requires the definition of a measure of distance for the characteristics of the individual objects to be clustered (e.g. Euclidian distance, Manhattan distance, etc.). Furthermore, a linkage criterion for determining the distance between sets of observations needs to be defined. Amongst others (e.g. complete- or single-linkage), the agglomerative, minimum variance method by Ward (1963) was used. The number of clusters in which the samples should be divided was determined by the number of different material types found within the sample pool. A support vector machine classification (SVMC) (see e.g. Boser et al. 1992, Cortes and Vapnik 1995) was conducted based on the R packages “e1071” (Meyer et al. 2017) and “caret” (Kuhn et al. 2017). SVMC is a machine learning approach, aiming to find hyperplanes for optimal separation of different classes. As linear functions are often not suitable for separation of the data, the original data is mapped in a new feature space using a kernel function in a way that the distance between the samples belonging to different classes is maximised. Samples at the “border” between two classes that are optimal for separating them form so-called support vectors (CAMO 2013, Hsu et al. 2016). The listed procedures (PCA, HCA, SVMC) were conducted based on the VNIR/SWIR and MWIR/LWIR spectra as well as on the combination of both ranges to assess the most suitable wavelength region for discriminating the different material types. For visualisation of the results, the R package “factoextra” (Kassambara and Mundt 2017) was utilised.

Other methods, like SAM and SFF (see the next chapter), are commonly utilised for matching unknown sample spectra with reference spectra, but typically require the definition of specific spectral characteristics or wavelength ranges for comparative purposes. Thus, no major focus was laid on these procedures, but they were applied using the complete VNIR/SWIR and MWIR/LWIR spectra to further assess the discriminability of the samples.

4.7.2 Qualitative Spectral Analyses

The major objective of the qualitative spectral analyses of the collected samples was to provide a comprehensive characterisation of the reflectance properties of typical iron- and steelworks by-products in the visible light, near and shortwave infrared as well as in the mid- and longwave infrared. For this purpose, the spectral properties of the collected samples were examined in terms of reflectance intensities, the general shape of the spectra as well as the presence and shape of the absorption features or reflectance maxima.

Determination and Parameterisation of Absorption Features

Absorption features in the spectra were identified and parameterised based on continuum removed spectra (see Chapter 4.6.2.3). Relevant parameters for characterising absorption features are: the wavelength position at the local absorption maximum; the absorption depth, which is the strength of an absorption in relation to the continuum hull; the width of the absorption, which

can be understood as the distance between the left and right shoulder; the area and asymmetry (e.g. van der Meer 1995, van der Meer 2004, Jarmer 2005, Fig. 4.7). For the VNIR/SWIR spectra, absorption features and the above-mentioned parameters were determined using ENVI and the IDL based tool DISPEC (version 3.6). DISPEC was developed by Harald van der Werff and kindly provided by the Faculty of Geo-Information Science and Earth Observation (ITC) of the University of Twente. Here, local maxima as well as inflection points were utilised to determine feature shoulder positions for applying the continuum removal normalisation and the subsequent feature characterisation. Feature positions and absorptions depths in the MWIR/LWIR spectra were determined empirically by applying continuum removal to specific wavelength intervals.

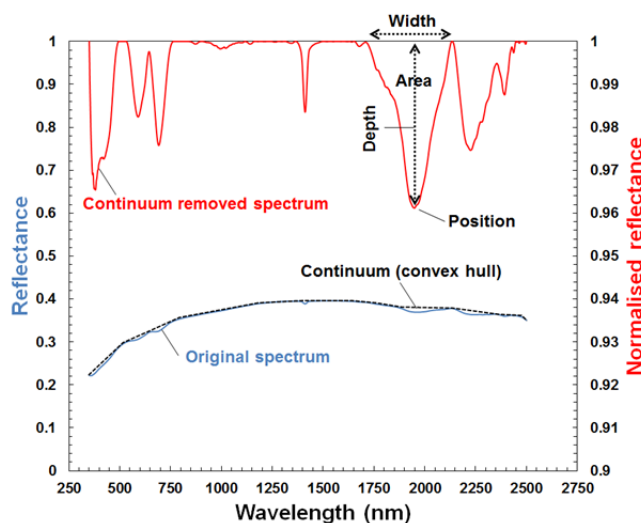


Fig. 4.7: Parameterisation of absorption features based on continuum removed spectra (after van der Meer 2004).

Spectral Identification of Mineral Phases

Spectral features identified in the spectra were interpreted in a semi-automated empirical approach using the XRD verified mineral phases (see Chapter 4.4) as reference. However, attention must be paid at this point as a known advantage of reflectance spectroscopy is that it is sensitive to crystalline as well as amorphous constituents in contrast to X-ray diffraction analysis (Clark 1999). Thus, spectra might indicate certain constituents not determined via XRD analysis. On the other hand, mineral phases determined with X-ray diffraction might not be spectrally active or cannot be determined due to overlapping or only weakly pronounced spectral features.

The algorithms Spectral Feature Fitting (SFF) and Spectral Angle Mapper (SAM) were supportingly utilised for the identification of mineral absorption features. Both methods are integrated in ENVI and represent established methods in the field of geological remote sensing (van der Meer et al. 2012). SFF is based on a least square fitting procedure to compare measured spectra to reference spectra (Clark et al. 1990a). SAM treats the spectra as vectors and compares the angle between them, where a smaller angle means more similar spectra (Kruse et al. 1993). SAM and SFF were additionally utilised to assess the spectral separability of the samples and to compare measured spectra with reference spectra from digital libraries provided with ENVI (e.g. Baldrige et al. 2009, Kokaly et al. 2017). However, the interpretation was mainly based on the information on spectral features given in the literature. These works encompassed e.g. the fundamental works of Hunt (1977), Hunt and Salisbury (1970, 1971), Hunt et al. (1971-1975), Clark et al. (1990b), Clark (1999), the spectra compilations in Hauff (2005, 2008) as well as the USGS (Clark et al. 2007, Kokaly et al. 2017) and ASTER spectral libraries (Baldrige et al. 2009).

4.7.3 Quantitative Spectral Analyses

The quantitative spectral analyses aimed at finding relationships between the spectral data and the chemical constituents. In a first step, correlations between the measured spectra and the chemical constituents were calculated. As described e.g. in Vohland et al. (2009), this approach is helpful for identifying spectrally sensitive wavelength ranges, which are directly or indirectly affected by or linked to the analysed chemical constituent. Furthermore, multivariate statistical models based on Partial Least Squares Regression (PLSR) were calculated on a defined calibration dataset and afterwards applied to a set of independent validation samples to predict chemical constituents. Afterwards, model performance and robustness were statistically assessed.

Creation of Calibration and Validation Datasets

There are different established methods for the selection of calibration and validation data in chemometrical modelling. In this context, Maesschalck et al. (1999) discussed amongst others: random sampling, the procedure developed by Kennard and Stone (1969), the cluster-based method introduced by Næs (1987) and the DUPLEX algorithm (Snee 1977). Within this thesis, the DUPLEX approach was selected. It is a modification of the Kennard-Stone procedure and an iterative process that starts by selecting two points that show the greatest distance to each other in a given data cluster (PC1 vs PC2 of the spectral data) for the calibration set. Afterwards, two of the remaining points that are again furthest away from each other are selected for validation samples. The next steps comprise the alternate selection of remaining points for the calibration as well as the validation set, which show again the greatest distance to the previously selected samples (Maesschalck et al. 1999). According to Maesschalck et al. (1999), this procedure “[...] selects representative calibration and test data sets of equal size” and can be considered as “[...] the best way to select representative calibration and test data sets in a validation context” (Maesschalck et al. 1999, p. 24). The DUPLEX algorithm was applied in R using the “prospectr” package by Sevents and Ramirez-Lopez (2014). In order to avoid that samples with extreme values of chemical constituents negatively affect the results of the latter conducted statistical modelling, they were initially removed utilising the “outliers” package for R by Komsta (2011) based on chi-squared scores and a probability threshold of 0.95.

Partial Least Squares Regression

Besides Principal Components Regression (PCR), Partial Least Squares Regression (PLSR) is one of the most used multivariate statistical approaches in spectroscopic modelling. Additionally to its original application in the field of chemometrics, it is also an established tool for quantitative analyses in the field of soil spectroscopy (e.g. Udelhoven et al. 2003, Siebielec et al. 2004, Viscarra Rossel et al. 2006, Vohland et al. 2009, Demattê et al. 2016, Kanning et al. 2016) as well as in mineralogical and geological spectroscopy (e.g. Goetz et al. 2009, Hecker et al. 2012). The procedure is suitable for analysis of complex data with potentially intercorrelated variables and is capable of handling missing or noisy data (Geladi and Kowalksi 1986, Wold et al. 2001). The main principle of PLSR is relating two data matrices, the depended or predictor variables and the independent response variables (Wold et al. 2001). Similar to Principal Component Analysis (PCA) (see e.g. Esbensen et al. 2012 for a comparison), PLSR transforms a large set of predictor variables into new, latent variables, so-called factors, and aims to explain the variation of the response variable(s) by using a certain number of weighted factors (Wold et al. 2001, Esbensen et

al. 2012). Even though several other regression techniques exist, e.g. Support Vector Regression (SVR) or Random Forest Regression (RFR), PLSR proved to be less susceptible to overfitting and outperformed other regression approaches depending on the chosen validation method in the study of Siegmann and Jarmer (2015).

For the PLSR approach, the VNIR/SWIR and the MWIR/LWIR spectra of sample material < 0.09 mm as well as a combination of both spectral ranges were utilised as predictor variables while the chemical constituents of the different iron- and steelworks by-products represented the response variables. Additionally, the spectra of unprepared samples with near *in situ* moisture as well as the spectra of unprepared but air-dried samples were utilised in order to assess the general impacts of *in situ* moisture and sample aggregation on the modelling results.

Chemical constituents with strongly asymmetric distributions are often normalised before calculating the PLSR Wold et al. (2001). However, PLSR does not require normally distributed data and initial model runs indicated that normalisation of the selected chemical constituents for modelling was not necessary. Thus, no normalisation or transformation of the chemical constituents was applied. The maximum number of latent variables for the calibration models was limited to 30 and calibration models were validated by leave-one-out cross-validation. The selection of calibration models for predicting chemical constituents for the test datasets was based on Akaike's Information Criterion (AIC, Akaike 1974). The calibration model providing the lowest AIC was selected for model validation. The AIC was calculated as given in formula 5:

$$AIC = n [\ln(RSS/n)] + 2k \quad (5)$$

Where N = the number of samples, k = the number of factors and RSS = Residual Sum of Squares. To assess the performance and robustness of the calibration models and the validation results, coefficients of determination (R^2), root mean square errors (RMSE) and residual prediction deviation (RPD) were calculated according to Martens and Næs (1989). As the residuals of PLSR models can be used for assessing model quality (Wold et al. 2001), the residuals (= observed values - predicted values) of the model validation were analysed for normal distribution using Shapiro-Wilk tests and two-tailed t-tests for analysing the mean of the residuals (which should ideally not significantly differ from zero). PLSR calculations were realised in R utilising the "pls" package by Mevik and Wehrens (2007).

There are different approaches for assessing influencing variables of PLSR models. Common are analyses of loading weights of the first factors used in a model as they are supposed to explain most of the variance occurring in the data (e.g. Rumpel et al. 2001, Forrester et al. 2015). Another approach is the analysis of regression coefficients as for example conducted by Viscarra Rossel et al. (2006), Eisele et al. 2012, Hecker et al (2012). Loading-weights explain the impact of individual wavelengths on specific factors and wavelength-specific regression coefficients represent the importance of the predictor variables for the entire model. In this thesis, another approach has been chosen and comprised the analysis of so-called VIP scores (variable importance in projection) as described by Chong et al. 2005 and implemented in R by Mevik (2007). VIP scores can be understood as the summed-up contribution of a variable across all model factors. They are calculated as weighted sum of squared correlations between the model factors and the original variable (e.g. Liu et al. 2014, Kawamura et al. 2017, Pinheiro et al. 2017).

5. Results and Discussion

5.1 Types of Iron- and Steelworks By-Products Analysed in this Study

The following chapter will address the typification of the collected samples, as these categories were used as reference for the subsequent spectral discrimination. Recent secondary products of the carbon steelmaking procedures of the Stahlwerk Thüringen GmbH (EAF and LF slag as well as mill scale) could be easily identified already *in situ* based on the knowledge of the local experts. Aside from these by-products, additional samples from recent high-alloy steelmaking procedures applied at other iron and steel plants that were not present at the Unterwellenborn dump site enriched the sample pool (stainless steel slag, EAF slag, AOD slag; see Chapter 4.2).

Apart from the selection of recent by-products, the sampling campaigns underlying this thesis focussed on by-products from past iron- and steelmaking processes applied at the Unterwellenborn site. Historical by-products that were still present in clearly delineated structures, like the converter (dedusting) sludge in various basins, or granulated blast furnace slag at the eastern part of the “Hochhalde”, can be regarded as relatively pure. However, a large number of the samples was not present at the dump surface and could only be accessed via excavator prospectings. In these prospectings, several relatively well distinguishable layers were found (see Fig. 4.3 and 4.4 in Chapter 4.2), but the unambiguous assignment of these materials to specific types of iron- and steelworks by-products was not possible in most cases *in situ*. Based on the mineralogical and chemical analyses and subsequent expert interpretation conducted by FEhS, the pool of samples was differentiated into four major by-product types: a) blast furnace slags, b) steelworks slags, c) dusts/sludges and d) other materials (see also Mrotzek-Blöß et al. 2016). If possible, these classes were further differentiated into subclasses within this thesis (see Tab. 5.1). These categories were used as the basis for the subsequent spectral-analytical approach for differentiation and classification of the samples. However, it must be taken into consideration that the samples from historical layers of the Unterwellenborn dump site that were assigned to these categories might contain impurities of other by-product types to a certain degree. This might be in particular the case for the “blast furnace slag” and “blast furnace flue dust”.

Tab. 5.1: Typification of the 102 samples in four major by-product classes and several sub-classes (the numbers in brackets represent the sample count for the specific material classes, + means a high probability of mixtures).

1 Blast furnace slag (29)	2 Steelworks slags (32)	3 Dusts/Sludges (19)	4 Others (22)
1.1 BFS+ (23) (either granulated or air cooled BFS or mixtures)	2.1 Thomas slag (14)	3.1 Blast furnace flue dust+ (2)	4.1 Mill scale (1)
1.2 Granulated BFS (6) (“slag sands”)	2.2 EAF slag (3) (carbon/low-alloy steelmaking)	3.2 Converter (dedusting) sludge (7)	4.2 Mixtures with high amounts of sand (7)
	2.3 EAF slag* (2) (medium-alloy steelmaking)	3.3 Unspecified dusts and sludges (10)	4.3 Limestone+sand (1)
	2.4 EAF slag* (1) (high-alloy steelmaking)		4.4 Unspecified other (13) (mixtures with sand, soil, fire- bricks, construction rubble, etc.)
	2.5 LF slag (3)		
	2.6 Unspecified sws (2)		
	2.7 Stainless steel slag* (5)		
	2.8 EAF foam slag* (1)		
	2.9 AOD slag* (1)		

* These materials were not present at the dump site of the Stahlwerk Thüringen GmbH and were provided by FEhS

The category “blast furnace slag” comprised 29 samples. While six samples collected at the surface at the eastern part of the “Hochhalde” could be identified as GBFS (“slag sands”), the majority of samples represented mixtures of air-cooled blast furnace slags, granulated blast furnace slags or comprised further materials that could not be clearly assigned. All BFS samples represent historic materials and might thus contain impurities. The samples collected at the “Canyon” could be clearly identified as by-products of the Thomas steelmaking procedure (Thomas slag, 14 samples) and were thus assigned to the steelworks slags. Each three samples of EAF and LF slag were recent by-products of the carbon steelmaking of the Stahlwerk Thüringen GmbH. Two further samples found at the Unterwellenborn dump site represented most likely steelworks slags that could not be clearly categorised. The additional samples constituting by-products from high-alloy steelmaking comprised EAF slags, AOD slag and five samples of stainless steel slag. Two samples are EAF slags from former medium-alloy steelmaking.

The category “dusts and sludges” encompassed seven samples of historical converter dedusting sludge. Two of these samples were collected in the eastern basin and five samples at the middle of the three basins at the northern slope of the “Hochhalde”. Two samples collected at the northern edge of the “Hochhalde” were supposed to contain BF flue dust. Ten further samples, which most likely represented not clearly specified dusts or sludges, were mainly found at the eastern part of the “Hochhalde”. The category “others” comprised one sample of mill scale, but also unspecified material mixtures, of which several samples might potentially contain construction rubble, soil or refractories to a certain degree. Seven samples showed high amounts of natural sand. One sample was identified as limestone.

5.2 Mineralogical Composition of the Samples

This chapter provides an overview of the results of the XRD analysis as provided by FEhS. Table 5.2 summarises the mineral phases (including the formulae) present in the by-product types considered relatively “pure” (see Tab. 5.1). The complete list of all mineral phases determined by XRD analysis for the 102 samples is given in Appendix 5.1. The following aspect is crucial: A plurality of samples contained X-ray amorphous components, including most of the (granulated) blast furnace slag samples, the converter dedusting sludge and several of the unspecified material mixtures found at the eastern part of the “Hochhalde”. These amorphous components of the samples - if present - were not quantified. This needs to be considered when interpreting the XRD results (Tab. 5.2) as especially the granulated blast furnace slag is mainly of glass-like structure. A brief description of the mineralogical composition of a selection of samples collected at the dump site of the Stahlwerk Thüringen GmbH is also given in Denk et al. (2015).

Carbonates

Calcite was present in the majority of samples as minor or major mineral constituent. It was found to be the dominant mineral phase in the crystalline part of the granulated blast furnace slag (GBFS). Calcite was not present in the mill scale and the EAF slag from the stainless steel production. The calcium carbonate modification vaterite was present in only few samples representing GBFS. While calcite is usually not found in fresh slags, it is formed by reaction of calcium silicates, calcium oxide or calcium hydroxides with moisture and CO₂ over time. This process is known as carbonatisation and causes the hardening of deposited by-products (see e.g.

Bialucha and Spanka 2014). The presence of calcite in the majority of samples collected at the dump site of the Stahlwerk Thüringen GmbH is thus an indicator for the relatively high age of these disposed by-products. Dolomite was determined in various samples, encompassing blast furnace slag collected at different excavator prospectings and was present in all converter dedusting sludge samples.

Oxides/Hydroxides

Brucite was present in only few samples collected at the “Sinterhang” excavator outcrop and in one sample collected at the outcrop at the plateau 274 as minor or spurious constituent. Goethite was found in only few samples, including the two samples supposed to contain blast furnace flue dust, in undefined material mixtures collected at the prospecting close to the “Sinterhang” and in samples from the eastern part of the “Hochhalde”. In contrast, hematite was present in 29 samples and was one of the major mineral phases of the red converter sludge and the mill scale.

Representatives of the spinel group (e.g. magnetite, jacobsonite or franklinite), were present in several samples as minor constituents, encompassing BFS samples collected at the prospectings at the plateaus 274 and 312 as well as in unspecified mixtures collected in the prospectings close to the “Sinterhang” and at the eastern part of the “Hochhalde”. Representatives of the spinel group were further present in the BF flue dust, the EAF slag from carbon steelmaking in Unterwellenborn, in the stainless steel slag and the EAF slag samples from the high-alloy steelmaking. Spinel was major constituents in the converter dedusting sludge and the mill scale.

Mayenite was present as a minor constituent in the stainless steel slag samples, the LFS and in the samples of the EAFS from medium-alloy steelmaking that were additionally added to the sample pool. Brownmillerite was found only in these two samples as minor constituent. Periclase was present e.g. in the LFS as minor constituent and in the stainless steel slag samples. Portlandite could be determined as minor component in the AODS, the samples from the stainless steel production and in the Thomas slag. Srebrodolskite was present in all of the collected Thomas slag samples as a minor mineralogical component, too. Wüstite constituted a minor phase in a large variety of the collected materials, including individual converter sludge and Thomas slag samples. Wüstite was a major component of the mill scale and the EAFS from carbon steelmaking.

Phosphates

Apatite was found to be one of the major mineral constituents of the Thomas slag samples and was further found in several samples collected at the eastern slope of the access ramp to the current slag disposal site at the Unterwellenborn dump. Besides apatite, silicocarnotite was another dominant mineral phase in all of the Thomas slag samples.

Silicates

The samples contained a variety of silicates, mainly nesosilicates (formed of insular SiO_4 groups) and sorosilicates (formed of isolated Si_2O_7 groups). The latter encompassed members of the melilite group, which are commonly found in BF and EAF slags (e.g. Drissen 2004) and which were present in the BF slag, stainless steel slag, EAF and LF slag samples in this thesis as well. Melilites were a major constituent of several unspecified samples collected at the eastern part of the “Hochhalde”. Rankinite was present in the stainless steel slag and was a major phase of the electric arc furnace slag from the stainless steel production.

5.2 Mineralogical Composition of the Samples

Tab. 5.2: Mineralogical composition of by-product classes considered relatively “pure” (x = major constituent, o = minor constituent, + = trace constituent, this rough semi-quantitative estimate refers exclusively to the crystalline part; yes = amorphous constituents present (not quantified). Light grey font indicates phases that were only observed in individual cases within the by-product classes. Mineralogical analyses were conducted and provided by FEHS.

Mineral phase (formula)	BFS+	GBFS	TS	EAFS				LFS	SSS	AODS	CDS	BFFD	MS
				cs	ma	ha	haf						
Andalusite Al ⁶ Al ⁵ [O]SiO ₄			o										
Anhydrite Ca[SO ₄]	+										+		
Apatite Ca ₅ [(F,Cl,OH) (PO ₄) ₃]			x										
Baryte Ba[SO ₄]	o	o											
Bredigite Ca ₇ Mg[SiO ₄] ₄				o/x									
Brownmillerite Ca ₂ (Al,Fe) ₂ O ₅					o								
Calcite Ca[CO ₃]	+/o/x	x	+/o/x	o	o		o	o	+	o	o/x	o	
Calcium-fluor-silicates									o	o			
Dolomite CaMg[CO ₃] ₂	+/o/x										o		
Ettringite Ca ₆ Al ₂ [(OH) ₁₂ (SO ₄) ₃]*(24+2)H ₂ O	+	o											
Feldspars	o		o										
Fluorite CaF ₂									+	o			
Free lime CaO													
Melilites	+/o/x			o/x		o	x	o	o	o		o	
Goethite α-FeOOH	+											o	
Gypsum Ca[SO ₄]*2H ₂ O	+/o										+/o		
Hematite Fe ₂ O ₃	+/o										x	o	x
Hydrogarnet Ca ₃ Al ₂ (OH) ₁₂			o										
Hydromagnesite Mg ₅ [(OH) ₂ (CO ₃) ₄]*4H ₂ O			o										
Iron (met.)	+										+		+
Larnite β-Ca ₂ [SiO ₄]			x	x	x			x	o				
Marcasite FeS ₂	o												
Mayenite Ca ₁₂ Al ₁₄ O ₃₃					o			o	o				
Merwinite Ca ₃ Mg[SiO ₄] ₂	+/o/x	x					o						
Micas	+												
Monticellite CaMg[SiO ₄]	o												
Periclase MgO					o			o	o				
Portlandite Ca(OH) ₂			o						+	o			
Potassium sulphate K ₂ SO ₄												o	
Quartz SiO ₂	o/x	+/o			o			+			+/o	x	
Rankinite Ca ₃ [Si ₂ O ₇]	x					x			o				
Silicocarnotite Ca ₅ (PO ₄) ₂ [SiO ₄]			x										
Spinel*	+/o		+	o	o	o	+		+	o	o/x	o	x
Srebrodolskite Ca ₂ Fe ₂ O ₅			+/o										
Wollastonite Ca ₃ [Si ₃ O ₉]						x			o				
Wüstite FeO	+		+/o	x	o	+		+			o		x
X-ray amorphous	yes	yes									yes		
γ-dicalcium silicate γ-Ca ₂ [SiO ₄]			o					x	o	x			

BFS+ = blast furnace slag (most likely not “pure”), GBFS = granulated blast furnace slag, TS = Thomas slag, EAFS = electric arc furnace slag (cs = carbon steelmaking, ma = medium-alloy steelmaking, ha = high-alloy steelmaking, haf = foamed EAF slag), LFS = ladle furnace slag, SSS = stainless steel slag, AODS = AOD slag, CDS = converter dedusting sludge, BFFD = blast furnace fume dust, MS = mill scale; *magnetite/franklinite/jacobsite

Nesosilicates comprised andalusite, which was found in four of the Thomas slag samples as minor constituent. Bredigite was present in the EAF slag from carbon steelmaking. Stainless steel slags typically contain β -dicalcium silicate (e.g. Drissen and Mudersbach 2012), which was present as Larnite in the stainless steel slag samples studied in this work as well. The mineral phase was further found in samples representing EAF slag from medium-alloy steel production. Larnite was a major constituent of few samples, encompassing LF slag and one sample each of Thomas slag and EAF slag found at the Unterwellenborn dump site.

γ -dicalcium silicate, which is typical for slags from secondary steelmaking (e.g. Drissen 2004), was present in the stainless steel slag and a major phase of the AOD slag. It was further present in the LF slag samples. Merwinite was a major constituent in individual “slag sand” samples and present in EAFS foam slag from high-alloy steelmaking.

A variety of other silicate mineral phases was determined within the sample pool. Feldspars (tectosilicates) were present as minor constituent in multiple samples, encompassing mainly historical blast furnace slag. Micas (phyllosilicates) were present as minor or trace component in several samples, of which most represented blast furnace slag collected at the prospecting at the plateau 312 and unspecified material mixtures collected close to the “Sinterhang”. Wollastonite (inosilicate) was found as a minor mineral phase in four of the stainless steel slag samples and as a major mineral phase in the EAF slag from high-alloy steelmaking.

Even though not a typical mineral phase of iron- and steelworks by-products, quartz (tectosilicate) was present in the majority of samples, ranging from a minor to a major mineral component. This is due to the anthropogenic nature of the dump site and the large variety of materials deposited during the long history of iron and steel production in Unterwellenborn. For example, the two samples considered to be blast furnace flue dust collected at the northern edge of the “Hochhalde” contained high amounts of quartz. The finding of quartz is related to the presence of natural sand, soil, demolition waste and other materials that were disposed of at the dump site. Thus, many of the historical by-products found at the Unterwellenborn dump cannot be considered “pure” but are material mixtures.

Sulfides and Sulphates

Anhydrite was present in two of the converter dedusting sludge samples. Half-hydrate was found in a variety of historical materials most likely representing granulated BFS or mixtures of BFS and other materials. Gypsum was present in multiple samples from the prospecting near the “Sinterhang“, in the converter dedusting sludge as well as in individual BFS samples. Ettringite was present in few samples, encompassing e.g. two GBFS samples. Baryte was found as a minor constituent only in few samples as well. Marcasite was present in four samples from the prospecting at the plateau 312 as a minor constituent. Minor amounts of potassium sulphate were present in the two samples containing blast furnace flue dust and jarosite was present in one sample from the eastern part of the “Hochhalde”.

Others

Metallic iron was present in several samples as minor or trace component, amongst the converter dedusting sludge samples and materials collected at the eastern part of the current slag disposal site. Fluorite was found only in the stainless steel slags and the AOD slag as minor or trace mineralogical constituent.

5.3 Chemical Composition of the Samples

5.3.1 Descriptive Statistics of the Chemical Composition of the Samples

The major chemical constituents of the 102 samples were (average values, see Tab. 5.3): CaO (26.6 m%), SiO₂ (21.1 m%), Fe_{total} (11.2 m%), TIC (8.6 m%), H₂O (7.8 m%), Al₂O₃ (6.7 m%), MgO (5.2 m%), P₂O₅ (3.0 m%), CaO_{free} (2.3 m%) and MnO (2.0 m%). For selected samples, iron was further differentiated into Fe₂O₃, FeO and Fe_{metallic}. These parameters were 11.0 m%, 3.6 m% and 1.6 m%, respectively, on average. The amounts of several metallic components (Mo, Ni, V, Zn, Al, Cr, Fe, Mn) were combined in a sum-parameter for assessing the overall metal content of the samples (10.2 m% on average). Due to budgetary restrictions, not all constituents could be determined for all samples. Furthermore, various constituents showed values below the detection limit or could not be precisely determined (e.g. < 0.05 m%). This explains the variation in “N”. The large variety of different by-product types within the sample ensemble is reflected by the variability of the chemical parameters and by the wide data ranges as given in Figure 5.1.

Tab. 5.3: Descriptive statistics of the major chemical constituents of the sample pool (average m% > 1) (chemical analyses by FEhS).

Parameter	N	Mean	SD	MD	Min	Max	Skew	SE	p***
Al ₂ O ₃	101	6.69	4.22	6.54	0.40	19.10	0.25	0.42	< 0.01
CaO	102	26.59	12.81	25.10	0.05	57.10	0.30	1.27	< 0.01
CaO _{free}	66	2.30	2.77	0.95	0.21	10.00	1.46	0.34	< 0.01
Fe ₂ O ₃	37	11.03	8.31	9.61	1.24	47.80	2.33	1.37	< 0.01
Fe _{metallic}	42	1.64	1.28	1.12	0.35	5.06	1.20	0.20	< 0.01
FeO	37	3.58	3.14	2.74	0.14	13.60	1.60	0.52	< 0.01
Fe _{total}	102	11.19	11.02	8.60	0.33	62.59	1.83	1.09	< 0.01
H ₂ O	100	7.78	4.92	6.80	0.10	23.60	1.08	0.49	< 0.01
LOI(CO ₂ , H ₂ O)*	102	16.23	10.43	14.65	0.18	61.60	0.96	1.03	< 0.01
MgO	101	5.16	3.01	5.25	0.80	17.40	0.80	0.30	< 0.01
MnO	102	2.04	1.61	1.46	0.13	9.85	1.79	0.16	< 0.01
P ₂ O ₅	93	2.96	4.87	0.86	0.01	16.80	1.75	0.50	< 0.01
SiO ₂	102	21.12	12.18	21.29	0.37	55.04	0.68	1.21	< 0.01
TIC	102	8.59	7.22	7.40	0.17	46.70	1.76	0.72	< 0.01
Σ(metals)**	44	10.17	8.17	8.95	1.06	39.30	1.22	1.23	< 0.01

*Loss on ignition, **Σ(Mo, Ni, V, Zn, Al, Cr, Fe, Mn), *** p-value of the Shapiro-Wilk test for normal distribution

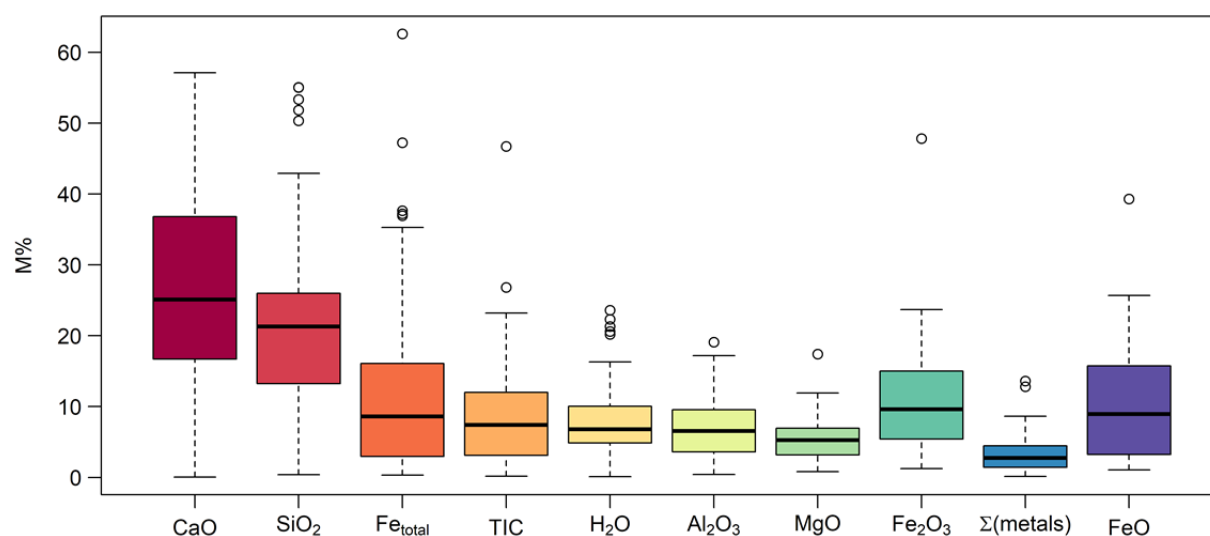


Fig. 5.1: Boxplots of the ten major chemical constituents of the sample ensemble (> 3 m% on average) (chemical analyses by FEhS).

The multitude of different iron- and steelworks by-products and the explorative character of the sampling campaigns led to unbalanced numbers of representative samples for each material class and is the reason for the skewed histograms (see Table 5.3). Except for Al_2O_3 , CaO and SiO_2 , which are relatively close to normal distributions, the skew for the other chemical components differed largely from zero and Shapiro-Wilk tests indicated that none of the parameters was normally distributed (see p-values in Table 5.3).

For CaO , Fe_{total} , SiO_2 and TIC , the constituent contents ranged between almost zero and up to nearly 60 m%. The constituents Al_2O_3 , H_2O , MgO and P_2O_5 (highest for the Thomas slag) varied between nearly zero and up to 20 m%, depending on the material type. Fe_2O_3 , FeO and $\text{Fe}_{\text{metallic}}$ reached nearly 48 m%, 14 m% and 5 m% in individual samples, respectively. The summed metal constituents varied between 1.1 and 39.3 m%.

The descriptive statistics of chemical constituents that were below one mass percent on average, but which reached maximum values of greater 0.5 to ca. 5 m%, are presented in Table 5.4 and in Figure 5.2. The p-values determined by Shapiro-Wilk tests indicate that again none of these parameters was normally distributed.

Tab. 5.4: Descriptive statistics of minor chemical constituents of the sample pool (max. m% > 0.5 - ~5) (chemical analyses by FEhS).

Parameter	N	Mean	SD	MD	Min	Max	Skew	SE	p**
$\text{Al}_{\text{metallic}}$	43	0.78	0.53	0.64	0.13	3.13	2.85	0.08	< 0.01
Cr_2O_3	83	0.81	1.27	0.11	0.01	5.24	2.07	0.14	< 0.01
$\text{Cr}_{\text{metallic}}$	43	0.13	0.14	0.07	0.01	0.55	1.60	0.02	< 0.01
Fluorite	28	0.16	0.15	0.08	0.02	0.55	1.28	0.03	< 0.01
K_2O	102	0.84	0.98	0.52	0.00	4.32	1.30	0.10	< 0.01
Na_2O	97	0.20	0.13	0.17	0.01	0.58	0.94	0.01	< 0.01
Pb	39	0.17	0.25	0.02	0.00	0.82	1.29	0.04	< 0.01
S_{total}	102	0.69	0.67	0.50	0.03	3.62	2.11	0.07	< 0.01
TiO_2	102	0.37	0.29	0.33	0.00	1.69	2.10	0.03	< 0.01
V_2O_5	101	0.11	0.14	0.04	0.00	0.65	1.93	0.01	< 0.01
Zn	98	0.61	1.02	0.04	0.00	4.13	1.90	0.10	< 0.01
ZnO	77	0.96	1.36	0.15	0.00	5.14	1.58	0.16	< 0.01

* p-value of the Shapiro-Wilk test for normal distribution

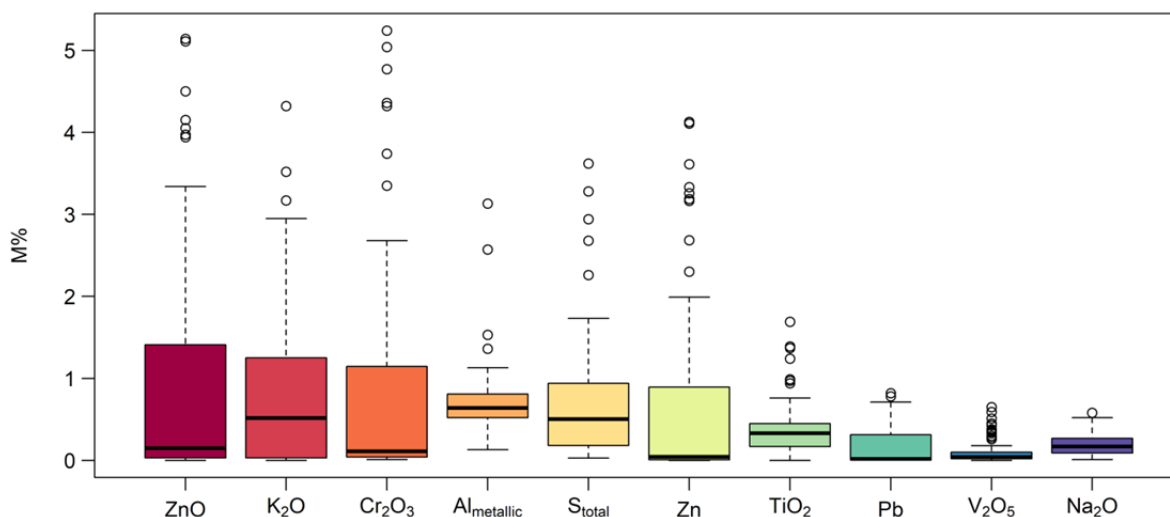


Fig. 5.2: Boxplots of ten minor chemical constituents of the sample ensemble (chemical analyses by FEhS).

The parameters Al_{metallic} , Cr_2O_3 , Fe_{metallic} , K_2O , S_{total} , Zn, ZnO reached maximum values of three to around five mass percent. The TiO_2 content was on average 0.4 m% but reached up to 1.7 m% in the stainless steel slag samples. Cr_{metallic} , Fluorite, Na_2O , Pb and V_2O_5 were < 1 m% in general.

A ternary plot based on the parameters SiO_2 , $CaO+MgO$ and $Al_2O_3+Fe_{\text{total}}+Cr_2O_3$ (see Fig. 5.3) gives a graphical overview of the chemical variety of the samples and allows the determination of potential material clusters. In this plot, the Thomas slag samples form an isolated cluster in the lower left due to relatively high $CaO+MgO$ contents in contrast to low SiO_2 as well as Al_2O_3 , Fe_{total} and Cr_2O_3 concentrations. Several samples representing unspecified material mixtures can be found in the top of the ternary plot as a result of their high amounts of natural sand (high quartz contents and subsequently high SiO_2 contents), while $CaO+MgO$ contents are low and the $Al_2O_3+Fe_{\text{total}}+Cr_2O_3$ contents are average.

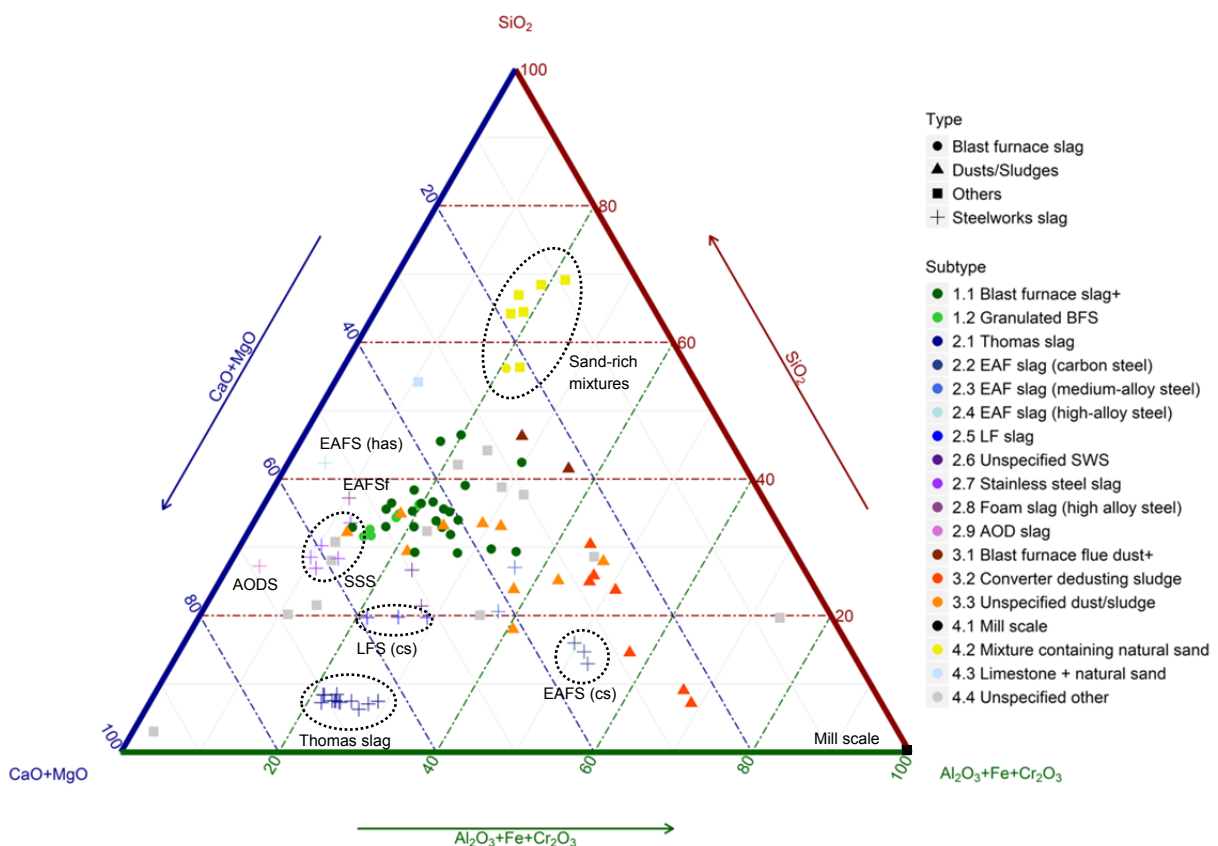


Fig. 5.3: Ternary plot of the chemical composition of the samples. It is important to consider that the given percentages do not represent absolute but relative constituent contents (chemical analyses by FEhS).

The EAFS and LFS samples from the carbon steel production conducted in the Stahlwerk Thüringen GmbH are located in the lower centre of the diagram and can be easily differentiated. While the SiO_2 contents of both types are comparable, the EAF slag samples show much higher total iron contents and can thus be found further to the right in the plot. The samples from the stainless steel production (stainless steel slag = SSS, EAF (foam) slag and AOD slag) can be found in the left of the ternary plot. These materials are characterised by (absolute) CaO contents of 40 to 50 m%, SiO_2 contents of 20 to 40 m% and low total iron contents (max. 1.5 m%). The left-centre of the plot is dominated by blast furnace slags, including air-cooled blast furnace slags, granulated blast furnace slags as well as mixtures of both types. The absolute CaO contents for the samples assigned to blast furnace slags ranged from ca. 13 to 35 m%, the SiO_2 contents from

16 to 34 m% and the total iron contents from 0.3 to 20 m%. The large ranges of these chemical constituents reflect the heterogeneity of this by-product class. The GBFS and most of the BFS samples found at the eastern part of the “Hochhalde” showed distinctively lower iron contents. The converter sludge samples are located in the lower right area of the plot as these materials showed relatively low CaO (ca. 11 to 14 m%) and SiO₂ contents (ca. 5 to 18 m%) but very high total iron contents of 20 to 38 m%. The only materials that showed even higher iron contents were the mill scale (basically free of CaO and SiO₂, Fe_{total} 63 m%), which is found on the far bottom right in the plot, and a sample that could not be unequivocally assigned to any specific by-product type (also in the right of the plot). The two samples representing blast furnace flue dust as well as further unspecified materials (most likely dusts or sludges) are located in the centre of the ternary plot. The extreme sample found to the far bottom left of the ternary plot showed the highest MgO content of all samples (17.4 m%). It could not be clearly typified but represents most likely a lime carrier (“Dolokalk”). Overall, the distribution of the samples in the ternary plot is in agreement with the results provided by other authors (Drissen 2004, Chiang and Pan 2017).

An overview of the chemical constituents Al₂O₃, CaO, Fe_{total} and SiO₂ for the individual by-product types is given in Table 5.5. More detailed information on the major, minor and trace chemical components of the samples grouped by by-product type are given in Appendix 5.2. Histograms, densities and normal fits for each parameter are provided in Appendix 5.3.

Tab. 5.5: Al₂O₃, CaO, Fe_{total} and SiO₂ contents (MN = mean, SD = standard deviation) of the 18 material types (the numbers in brackets represent the sample count for the specific material classes) (analyses by FEHS).

By-product type	CaO		SiO ₂		Al ₂ O ₃		Fe _{total}	
	MN	SD	MN	SD	MN	SD	MN	SD
BFS+ (23)	24.8	4.5	26.0	4.7	9.5	2.8	6.9	4.3
GBFS (6)	28.2	3.9	24.4	2.6	10.6	2.2	1.7	1.2
Thomas slag (14)	44.6	1.8	5.1	0.4	0.6	0.1	14.4	1.6
EAF slag (cs) (3)	24.9	0.6	12.4	1.1	5.5	0.3	35.6	1.0
EAF slag (mas) (2)	22.5	2.2	19.0	3.5	8.8	1.1	19.4	0.1
EAF slag (has) (1)	48.0	-	40.3	-	0.7	-	0.5	-
LF slag (3)	40.4	3.2	16.9	0.2	12.4	0.5	8.4	2.7
Unspecified sws (2)	35.1	4.0	19.5	6.1	10.3	12.4	9.6	10.9
Stainless steel slag (5)	46.6	4.1	26.6	2.4	4.1	0.6	1.4	0.6
Foam slag (1)	39.7	-	34.6	-	5.5	-	0.3	-
AOD slag (1)	57.1	-	23.6	-	1.4	-	2.5	-
Blast furnace flue dust (2)	14.2	2.8	32.0	4.2	6.6	1.4	16.4	4.3
Converter sludge (7)	12.8	0.9	11.4	5.1	4.5	1.7	27.3	6.8
Unsp. dust/sludge (10)	16.8	3.8	17.3	3.6	7.0	2.1	11.0	7.4
Mill scale (1)	0.1	-	0.4	-	< 0.01	-	62.6	-
Mixtures with sand (7)	9.7	2.9	50.2	4.9	10.7	1.0	4.6	1.5
Limestone+sand (1)	25.3	-	40.7	-	2.1	-	5.4	-
Unspecified other (13)	21.5	8.9	17.9	7.6	5.7	3.3	10.7	12.4

5.3.2 Inter-Correlations of the Chemical Constituents

As none of the chemical parameters was normally distributed, spearman rank correlations were calculated in order to assess possible inter-correlations between the individual components. A correlation matrix encompassing 23 major and minor chemical constituents is given in Figure 5.4.

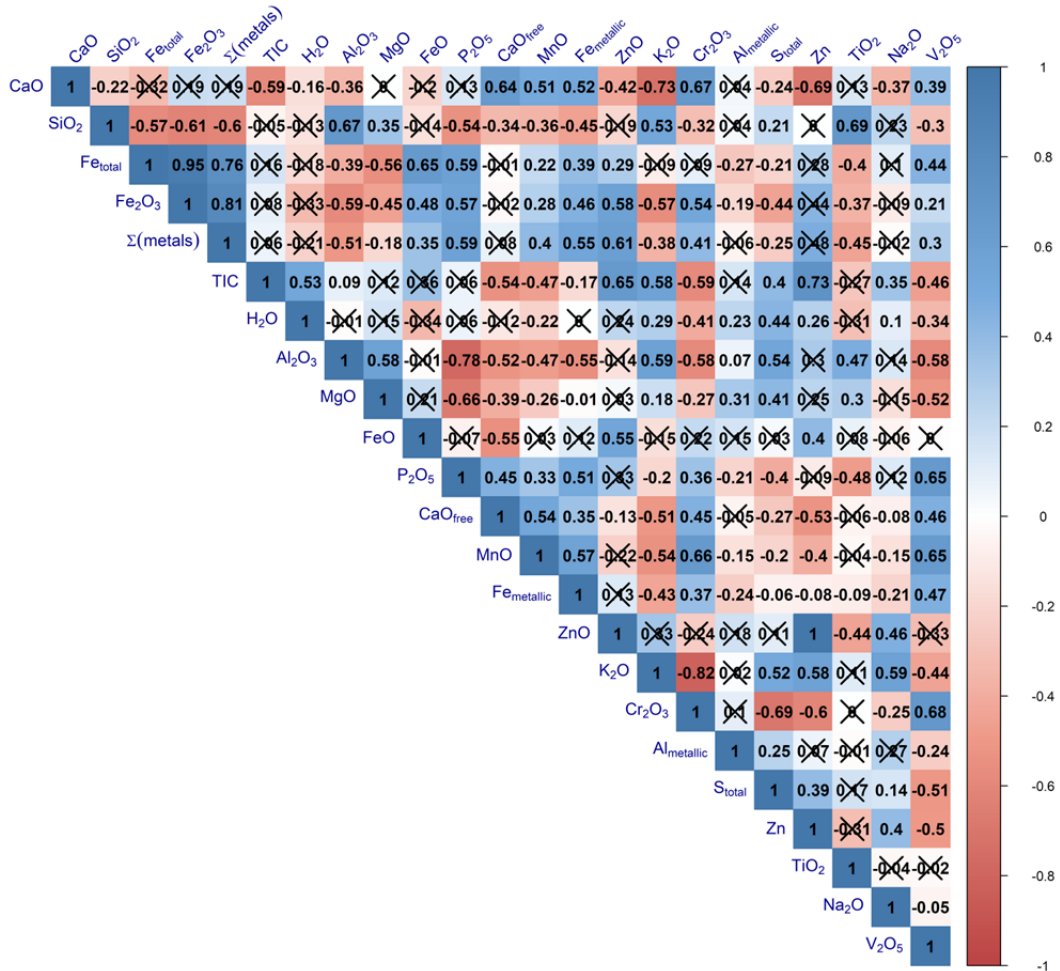


Fig. 5.4: Inter-correlations (Spearman rank correlation coefficients) between 23 major and minor components. Crossed-out numbers represent not significant correlations at the 0.05 significance level.

Strong positive correlations ($R > 0.7$) were found only in a few cases, encompassing a strong relationship between Fe_{total} and Fe_2O_3 ($R = 0.95$) as well as between Fe_{total} and the sum of metals ($R = 0.76$). Further strong correlations were present between the parameters Fe_2O_3 and the sum of metals ($R = 0.81$) and between TIC and Zn ($R = 0.73$). The observed strong correlations of Fe_{total} with other metal-parameters can be explained as Fe_{total} comprises iron contained in both Fe_2O_3 and FeO. Also, the sum parameter, which encompasses the metals Mo, Ni, V, Zn, Al, Cr, Fe, Mn, is obviously mainly driven by the general high total iron contents. ZnO is the oxidised form of Zn and thus explains the high rank correlation coefficient ($R = 1$).

Negative correlations were present between multiple chemical constituents, of which the strongest ($R = 0.7-0.9$) occurred between K_2O and Cr_2O_3 ($R = -0.82$), Al_2O_3 and P_2O_5 ($R = -0.78$) and CaO and K_2O ($R = -0.73$). Further moderately strong negative correlations were observed for Cr_2O_3 and S_{total} ($R = -0.69$), between CaO and Zn ($R = -0.69$) as well as between MgO and P_2O_5 ($R = -0.66$) (see Fig. 5.4). Moderate positive inter-correlations ($R > 0.5-0.7$) were observed

for a variety of chemical constituents comprising CaO and CaO_{free}; MnO and Fe_{metallic} as well as between MnO and Cr₂O₃; between SiO₂ and Al₂O₃; between K₂O and TiO₂; between Fe_{total} and FeO as well as P₂O₅; between Fe₂O₃ and P₂O₅, ZnO, Cr₂O₃, \sum (Mo, Ni, V, Zn, Al, Cr, Fe, Mn) showed moderate correlations with P₂O₅, Fe_{metallic} and ZnO. See Figure 5.4 for further details.

The observed inter-correlations reflect the variety of the different by-product types, which are associated with specific production processes and utilised additives. For example, the Thomas slag samples were the only samples containing higher amounts of P₂O₅ (ca. 13-15 m%) while showing also distinctively higher V₂O₅ contents (ca. 0.3-0.5 m%) compared to the majority of the samples. The Thomas slag samples further showed the lowest Al₂O₃ contents (< 1 m%) compared to the remaining sample ensemble, which explains the strong negative correlations between P₂O₅ and this constituent. The steelworks slags, encompassing the EAF slag samples and especially the stainless steel slags showed the highest Cr₂O₃ contents but relatively low S_{total} and very low K₂O contents at the same time, which can be considered as an explanation for the observed negative correlations.

5.3.3 Principal Component and Cluster Analysis of the Chemical Data

The results of a principal component analysis performed on 15 chemical constituents are given in Figure 5.5a (scatter plots of the principal component scores) and in Figure 5.5b (explained variance by the first 10 components as well as the contributions of the variables to each PC). The first principal component (PC) explained ca. 40% of the variance in the data, the second component ca. 19% and components three and four around 12% and 8%, respectively. The variables mainly contributing to PC1 were V₂O₅, P₂O₅ as well as Al₂O₃, SiO₂ and K₂O. While the first mentioned chemical constituents were highly concentrated in the Thomas slag, Al₂O₃, K₂O and SiO₂ contents were low in this by-product type. Consequently, the Thomas slag samples form a well-separated point cluster in the left part of the scatter plot of PCs 1 and 2 (and are also clearly visible in the scatter plots of PC 1/3 and 1/4). Samples relatively rich in SiO₂, K₂O, Na₂O and TiO₂ are found in the lower part of the lower right quadrant of the PC 1/2 scatter plot, while samples rich in Al₂O₃ are located in the upper part of this sector. The main contributors to PC2 were Zn, TIC and TiO₂. Samples rich in these constituents are visible in the right upper quadrant of the scatter plot of PCs 1/2. These materials mainly comprise several blast furnace slag samples as well as the converter dedusting sludge. The variables mostly contributing to PC3 were H₂O and S_{total}. Several samples rich in S_{total} were collected at the prospecting close to the "Sinterhang". These samples are visible as point cluster in the scatter plot of PC2 and PC3 (upper left quadrant). PC4 was characterised by high loadings of the Fe_{total} content and Na₂O. The scatter plot of PC1/4 thus highlights iron-rich samples in the lower left quadrant, encompassing EAF slag and the converter dedusting sludge collected at the dump site in Unterwellenborn.

5.3 Chemical Composition of the Samples

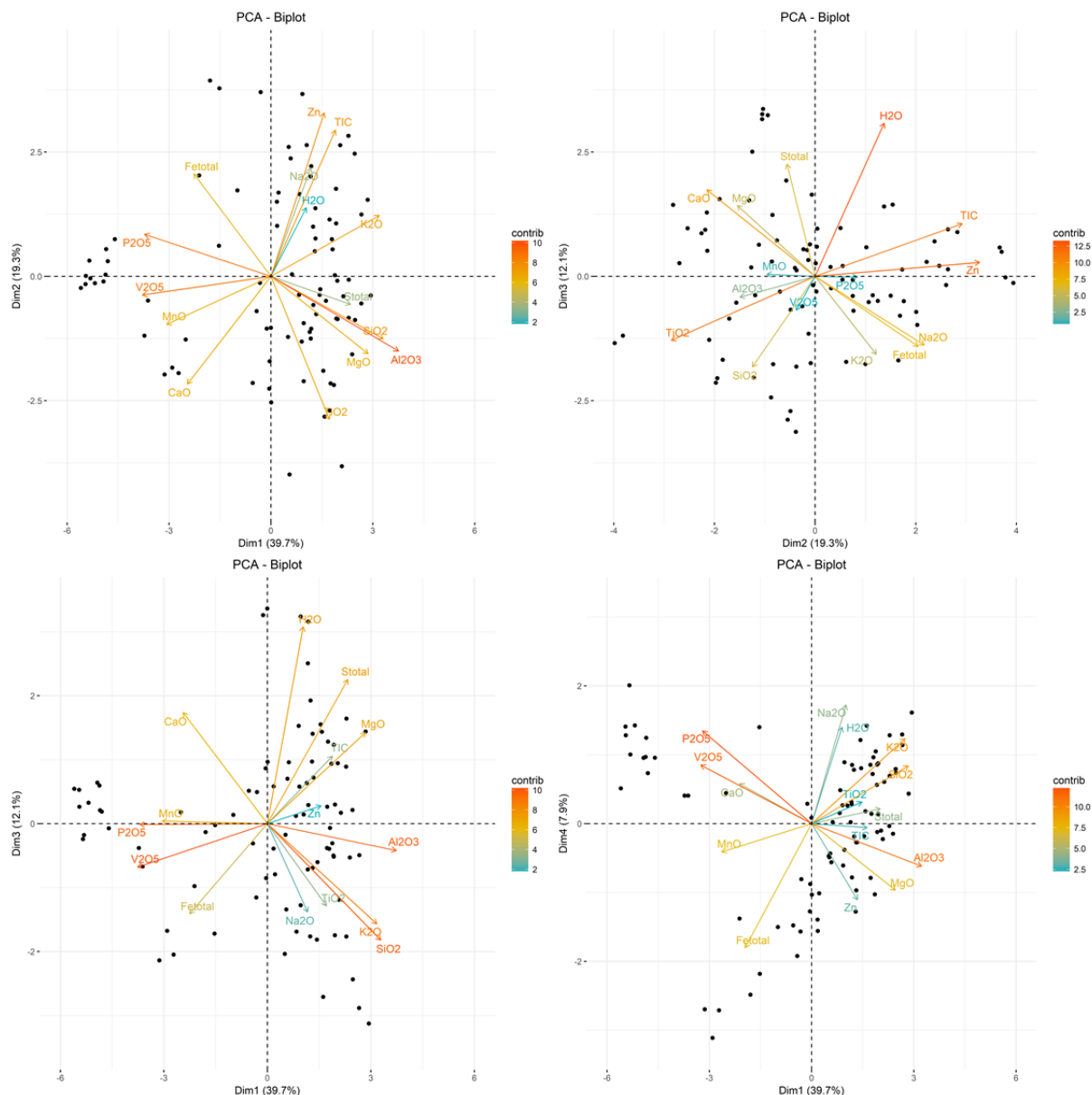


Fig. 5.5a: Results of the principal component analysis of 15 chemical constituents after square root adjustment of the sample ensemble ($N = 102$). The direction of the arrows indicates positive or negative correlations of the variables with the principal components (PC), the length of the arrows represents the strength of the correlation of the variables with the PC axes and the colours visualise the contribution of each variable to the PC.

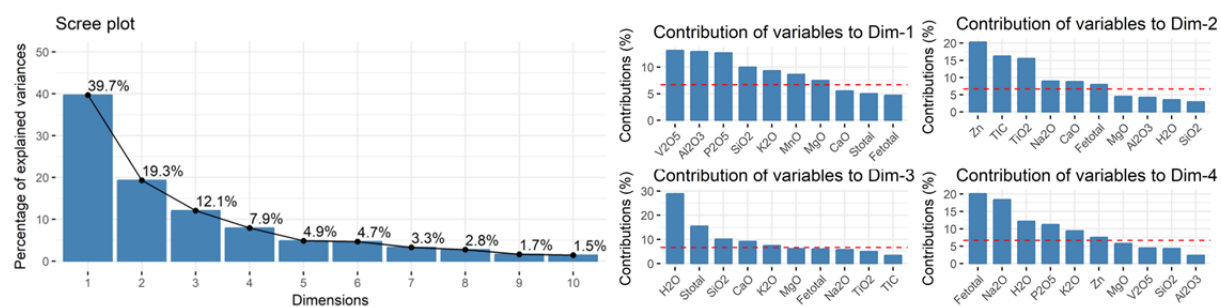


Fig. 5.5b: Explained variance of the first 10 components of the principal component analysis of 15 chemical constituents of the sample ensemble (left) and contributions of each variable to the first four PCs (right).

The dendrogram given in Figure 5.6 summarises the results from the chemical analyses and represents the variety in by-products types. Thomas slag as well as further slags from recent steel production, encompassing the various electric arc furnace slags from the carbon steel, medium- and high-alloy steelmaking, ladle furnace slag, stainless steel and AOD slags could be well separated based on their chemical composition. The converter dedusting sludges and certain unspecified dusts and sludges form another branch in the dendrogram. The mixtures with high amounts of natural sand form another distinctively separated cluster. Hence, the different samples collected within this thesis could be well-separated and grouped to specific clusters based on their chemical composition.

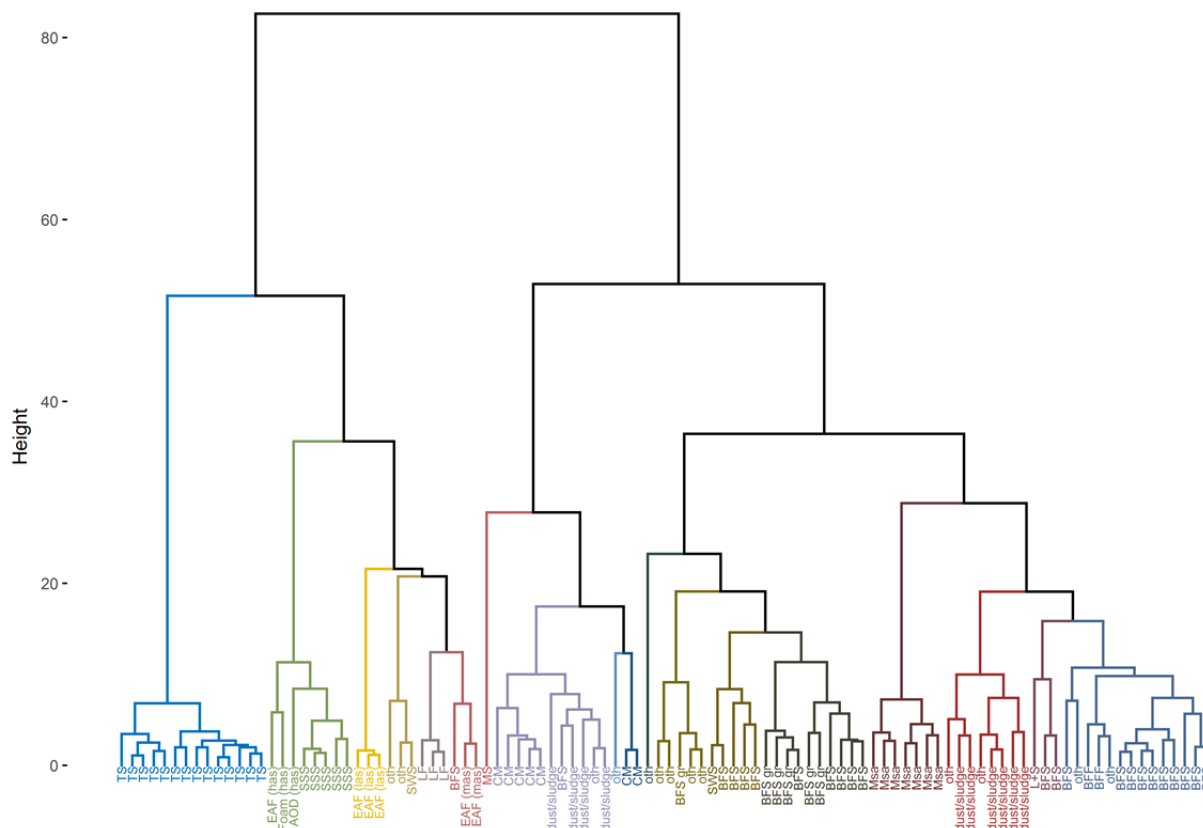


Fig. 5.6: Results of the hierarchical cluster analysis of 15 chemical constituents (Manhattan distances, Ward method, 18 clusters, square-root-normalised constituents). Samples are labelled according to their material type: AOD = argon oxygen decarburization slag, BFF = blast furnace flue dust, BFS = (unspecified) blast furnace slag, BFSgraN = granulated blast furnace slag (“slag sand”), CM = converter (dedusting) sludge, dust/sludge = unspecified dusts or sludges, EAF = Electric arc furnace slag (las = low-alloy/carbon steelmaking, mas = medium-alloy steelmaking, has = high-alloy steelmaking), Foam = foam slag, LF = ladle furnace slag, Mns = mixture containing high amounts of natural sand, MS = mill scale, Oth = unspecified material (including mixtures with soil, construction rubble, firebricks, etc.), SSS = stainless steel slag, SWS = unspecified steel work slag, TS = Thomas slag.

5.4 Spectral Separability Analysis of Iron- and Steelworks By-Products

Results of principal component analyses (PCA) conducted on the VNIR/SWIR, MWIR/LWIR and on the combination of both spectral ranges are presented in Ch. 5.4.1-5.4.3 to assess the general spectral separability of the different iron- and steelworks by-products. Scatterplots of the first principal components (PCs) are interpreted, as they typically explain most of the variance occurring in the data. Additional plots of further PCs are presented in App. 5.4.1-5.4.9 and axis loadings of the variables are given in App. 5.4.10-5.4.12. Besides the visual interpretation of PCA results, the outcomes of hierarchical cluster analysis (HCA) are presented and discussed in Ch. 5.4.5. Results of a support vector machine classification (SVMC) of a selection of major by-product types are shown in Ch. 5.4.6. The chosen PCA, HCA and SVMC approaches can be understood as unsupervised procedures that do not require pre-existing knowledge about the by-product-specific spectral properties. The results of assessing the spectral separability using SAM and SFF are given in App. 5.5.4. Summarising conclusions on this part are given in Ch. 5.4.7.

5.4.1 Spectral Separability based on PCA of VNIR/SWIR Spectra

Results of the principal component analyses of VNIR/SWIR reflectance, absorbance and continuum removed spectra are visualised in Fig. 5.7. The first two principal components of the reflectance data explained almost 99 % of the variance in the data (PC1: 93.6 %, PC2: 5.1 %). The scatter plot of these PCs (Fig. 5.7a) indicates a relatively good separability of the Thomas slag and the ladle furnace slag samples. Furthermore, the AOD slag sample can be clearly separated from the point cloud. The samples representing GBFS and stainless steel slag are found in the right part of the point cloud whereas the mill scale, samples representing materials associated with ironmaking (blast furnace slag, blast furnace flue dust, and several mixed materials), and the converter dedusting sludge samples are located in the left part of the point cloud as these materials showed negative loadings on the axis of PC2. The latter material types are characterised by (relatively) high iron contents and overall low reflectance (Ch. 5.5.1). However, a clear clustering of these material types within the point cloud of these PCs is hardly visible. The aforementioned GBFS, Thomas slag, ladle furnace slag and SSS show higher reflectance intensities.

Similar results can be observed by studying the scatter plot of the first components of the PCA based on absorbance spectra (Fig. 5.7b). Again, almost 99% of the variance occurring in the data is explained by the first two principal components (PC 1: 95.7%, PC2: 3.3%). The separability of the Thomas, EAF and LF slag samples is more distinct compared to the analysis based on reflectance data. In addition, the mill scale sample is clearly recognisable as individual point in the left part of the plot. Furthermore, the converter sludge samples and several samples most likely representing blast furnace slags with relatively high iron contents are more separated from the point cloud compared to the scatter plot of the principal components of the reflectance data. These materials can be better separated using the scatterplot of PC1 and PC3 (0.8% explained variance), in which they are located in the lower left quadrant (see Appendix 5.4.2).

The results of the PCA based on the continuum removed spectra (Fig. 5.7c) indicate that more principal components are needed for explaining the variations in material specific absorption feature characteristics compared to the variability in reflectance or absorption values. Here, the first two components explain 64.7% (PC1) and 9.9% (PC2) of the variance in the data. In

contrast to the results discussed before, the samples representing the converter dedusting sludge are clearly differing from the major point cloud in the score plot of PC1 and PC2 (Fig. 5.7c), while the majority of samples are staggered along PC1. The Thomas slag samples form a point cluster in the upper left quadrant in the scatter plot of PC1 and PC3 (7.4% explained variance, Fig. 5.7d). These two PCs further allow the differentiation of the GBFS samples (lower part of the plot) and the slags from high-alloy steel production are positively correlated with the PC2 axis. The remaining material types are clustered around the origin of the scatter plot and thus cannot be determined using these PCs of this spectra type (see also Appendix 5.4.3).

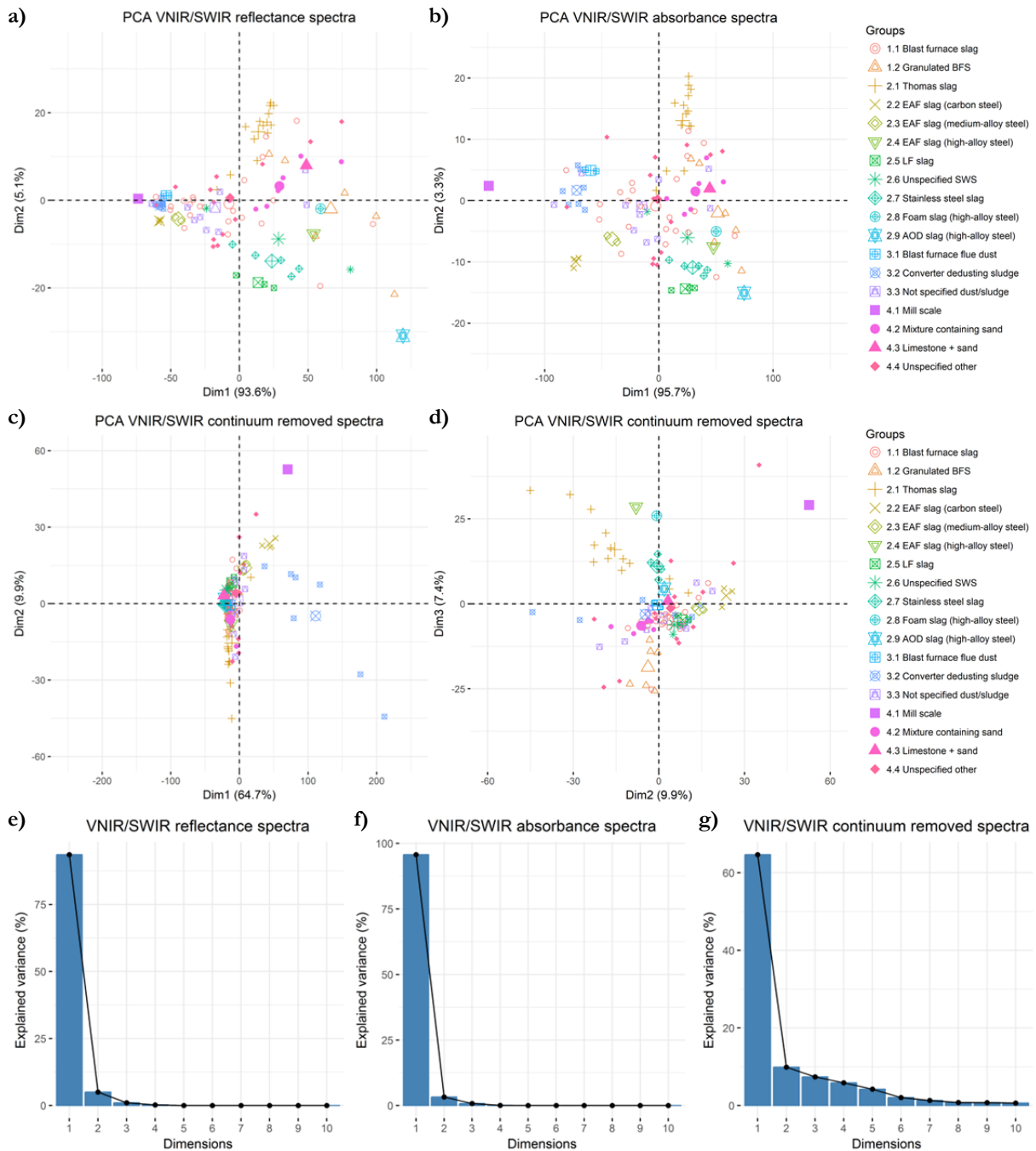


Fig. 5.7: Results of the PCA analysis of VNIR/SWIR spectra. Samples are grouped based on the by-product type (large symbols represent calculated cluster centres, Dim = principal component (PC)). Upper row: Scatterplots of PC scores based on reflectance (a) and absorbance spectra (b). Middle row: Scatterplots of PC scores based on continuum removed spectra (c, d). Bottom row: Explained variance by the PCs (e-g).

5.4.2 Spectral Separability based on PCA of MWIR/LWIR Spectra

The first two components of the MWIR/LWIR reflectance spectra explain 85.7% of the variance in the data (Figure 5.8e), which is less compared to the VNIR/SWIR reflectance spectra. The score plot of PC1 (60.3% explained variance) and PC2 (25.4% explained variance) shows a less clustered point cloud compared to the score plot of PC1/2 based on the VNIR/SWIR reflectance data and a distinct separation of specific by-product types is difficult (Fig. 5.8a). The slag samples from high-alloy steelmaking are located in the lower right part of the scatter plot, except for the AOD slag, which can be found in the upper right quadrant together with the GBFS samples. Several unspecified dusts and sludges as well as unspecified other materials are depicted in the upper left section. The iron-rich mill scale is represented in the lower left part of the scatter plot, as well as the EAF slag from carbon steelmaking, blast furnace flue dust and the converter dedusting sludge. However, the samples assigned to the mentioned by-product types as well as the remaining material types are generally located near the origin of the PCA plot and thus cannot be spectrally discriminated utilising these PCs. The Thomas slag samples can hardly be separated based on scatter plots of the scores of PC1 and PC2 but form a more distinct cluster when utilising PC4 (3.7% explained variance, see Appendix 5.4.4).

The score plot of the first two principal components of the MWIR/LWIR absorbance spectra (explained variance PC1: 58.8%, PC2 29.2%, Fig. 5.8b) shows a similar point distribution. In contrast, the scatter plots of PC1 and PC3 show a good separability of the EAF slag from the carbon steel production (left upper quadrant), the Thomas slag (right upper quadrant) and the samples containing high amounts of natural sand (lower right quadrant) as demonstrated in Appendix 5.4.5.

The principal components of the continuum removed spectra (Fig. 5.8c and 5.8d) provide a better separated point cloud compared to the reflectance and absorbance spectra. PC1 (67% explained variance) and PC2 (18% explained variance) allow a relatively good separation of the EAF slag (carbon steel production), the converter dedusting sludge, blast furnace flue dust and the mill scale from the remaining point cloud. These four by-product types can be found in the upper left quadrant of the scatter plot (Fig. 5.8c), as their spectral properties were negatively correlated with the axis of PC2 and positively with the axis of PC1. The third principal component of the continuum removed spectra explains 3.8% of the variance in the data. The LFS, stainless steel slag and AOD slag samples are present in the upper left sector of the scatter plot of PC2 and PC3 while the Thomas slag samples are located mainly in the lower left sector (Fig. 5.8d). The utilisation of PC1 and PC4 (2.1% explained variance) allows the distinct separation of the EAF slag samples from medium alloy-steelmaking and the EAF slag samples from carbon steelmaking are more distinctly clustered than before (see Appendix 5.4.6).

5.4 Spectral Separability Analysis of Iron- and Steelworks By-Products

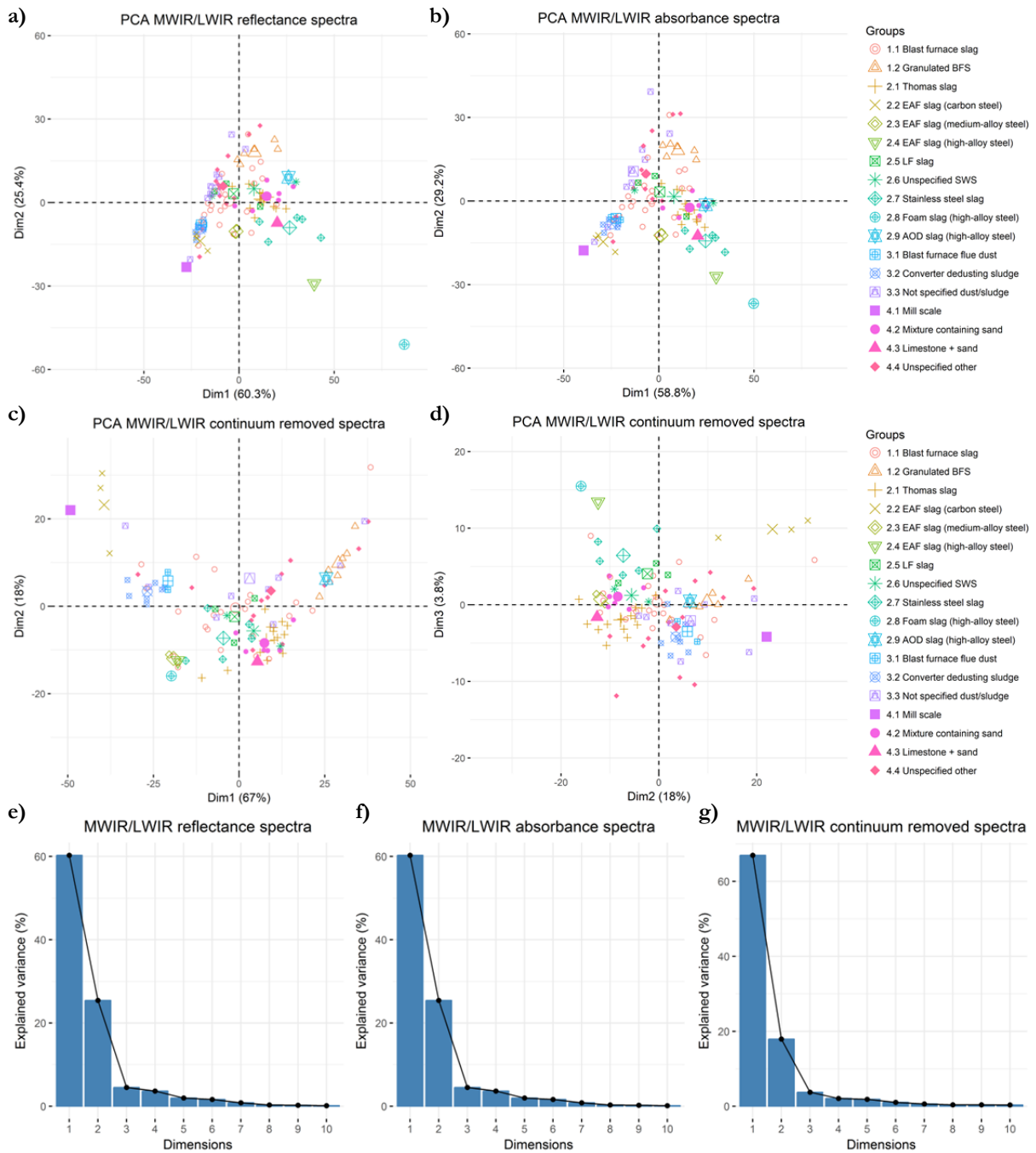


Fig. 5.8: Results of the PCA analysis of MWIR/LWIR spectra. Samples are grouped based on the by-product type (large symbols represent calculated cluster centres, Dim = principal component (PC)). Upper row: Scatterplots of PC scores based on reflectance (a) and absorbance spectra (b). Middle row: Scatterplots of PC scores based on continuum removed spectra (c, d). Bottom row: Explained variance by the PCs (e-g).

5.4.3 Spectral Separability based on PCA of VNIR-LWIR Spectra

The first two components of the VNIR-LWIR reflectance data explain ca. 92% of the variance of the data (Fig. 5.9e), which is less compared to the PCA of the VNIR/SWIR (ca. 99%) data but around 7% more than for the MWIR/LWIR data. The explained variance of the PCs based on absorbance spectra is very similar to the PCA outcomes based on reflectance data. The scatter plots of the first two PCs of the reflectance, and more distinct in case of the absorbance data, show that the slag samples related to high-alloy steelmaking (AODS, EAFs (foam), SSS) and the

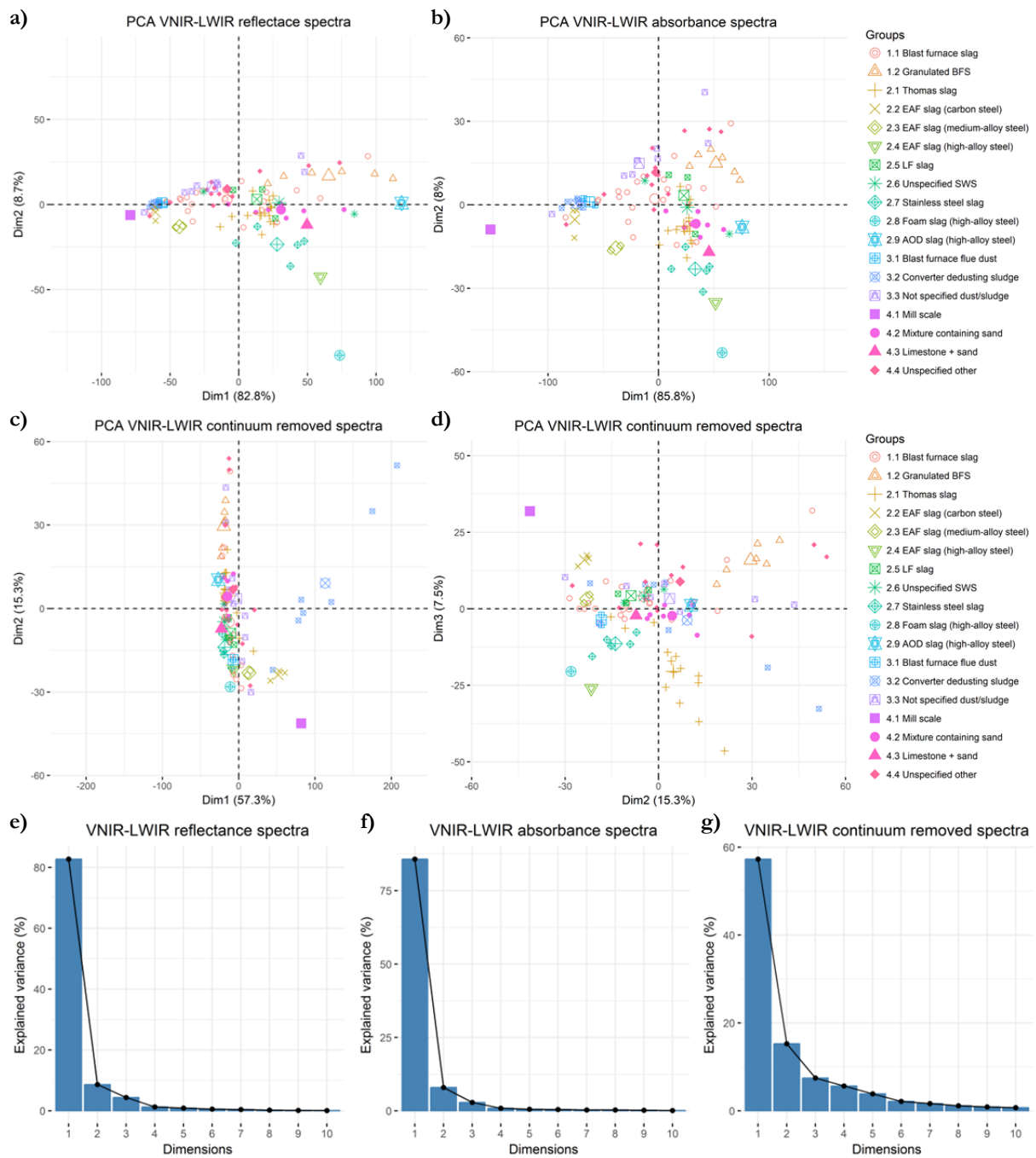


Fig. 5.9: Results of the PCA analysis MWIR/LWIR spectra. Samples are grouped based on the by-product type (large symbols represent calculated cluster centres, Dim = principal component (PC)). Upper row: Scatterplots of PC scores based on reflectance (a) and absorbance spectra (b). Middle row: Scatterplots of PC scores based on continuum removed spectra (c, d). Bottom row: Explained variance by the PCs (e-g).

sand-rich mixtures can be found mostly in the lower right part, granulated blast furnace slag in the upper right part and the mill scale, EAF slag, unspecified dusts and sludges and blast furnace slag are located on the right (Fig. 5.9a and 5.9b). Here, the spectral properties of the iron-rich material types were seemingly negatively correlated to the axis of PC2. The Thomas slag, LF slag and stainless steel slag can be more clearly differentiated from the point cloud by utilising the third principal component of the reflectance or absorbance data (see scatter plots of PC1 and PC3 as well as PC2 and PC 3 in Appendix 5.4.7). The EAF slag samples from the medium-alloy as well as from carbon steel production can be distinctively separated from the point cloud based on PC1 and PC4 (0.9% explained variance) of the absorbance spectra and form well-separated clusters in the upper left quadrant of the corresponding scatter plots (see App. 5.4.8).

The first two components of the continuum removed VNIR-LWIR data explain 57.3% and 15.3% of the variance in the spectra, respectively. While most of the data points are clumped along the axis of PC1, the mill scale, converter sludge and the EAF slag from carbon steelmaking can be more clearly identified in the lower and upper right quadrants of the scatter plot (Fig. 5.9c), meaning that the spectra properties of these iron-rich materials are positively correlated with the axis of PC1. The scatter plot of PC2 and PC3 (7.5% variance) allows a better separation of by-products from the stainless steel production (found in lower left quadrant), Thomas slag (lower right quadrant) and granulated blast furnace slags (upper right quadrant). Several material mixtures, the LF slag samples as well as the blast furnace slag are found close to the centre of this PCA plot (Fig. 5.9d) and thus cannot be spectrally discriminated using these two PCs.

5.4.4 PCA Results and Major Chemical Constituents

Based on the scatter plots of the PC1 and PC2 of the VNIR/SWIR absorbance spectra, which showed an overall good separability of several major by-product types, the major chemical constituents Al_2O_3 , CaO , Fe_{total} and SiO_2 were assigned as colour gradients to the point cloud instead of the by-product classes (Figure 5.10). The scatter plots show that the point distribution clearly corresponds to the chemical composition of the samples. The Thomas slag samples form a cluster in the VNIR/SWIR absorbance spectra in the upper right quadrant while the samples from secondary and stainless steelmaking (LF slag, stainless steel slag, AOD and EAF-foam slag) are found in the lower right quadrant (Fig. 5.10a). These material groups are characterised by the highest CaO contents in the sample pool. Samples with lower CaO contents are clustered along the axis of PC2 (Fig. 5.10a). The low SiO_2 content of the Thomas slag samples is clearly recognisable, while the majority of samples showing higher SiO_2 contents can be found relatively close to the positive part of the vertical axis indicating their strong correlation with PC1 (Fig. 5.10b). As Al_2O_3 and SiO_2 are moderately positively correlated (see Chapter 5.3.2), the colour pattern in the point cloud for Al_2O_3 is similar to SiO_2 , with clustered Thomas slag samples showing low Al_2O_3 contents in the upper right quadrant while samples with intermediate Al_2O_3 contents are found in the left part of the scatter plot. Samples with moderate to high Al_2O_3 contents are found in the right part of the point cloud (Fig. 5.10c).

The mill scale represents the sample with the highest Fe_{total} content and can be clearly identified as individual point in the left of the scatter plot in Figure 5.10d. The three EAF slag samples from the carbon steel fabrication in Unterwellenborn show high amounts of total iron as well and

form a cluster in the lower left quadrant. Samples with intermediate to high iron contents, encompassing blast furnace flue dust, converter dedusting sludge, several unspecified sludges and dusts as well as individual blast furnace slag samples are mainly presented in the left part of the point cloud. In contrast, by-products with low or very low total iron contents are located in the lower part of the upper right as well as in the lower right quadrant (Fig. 5.10d). The samples found there mainly represent by-product types from the stainless steel production (AODS, EAF-foam slag and stainless steel slag), LF slag as well as the granulated blast furnace slag.

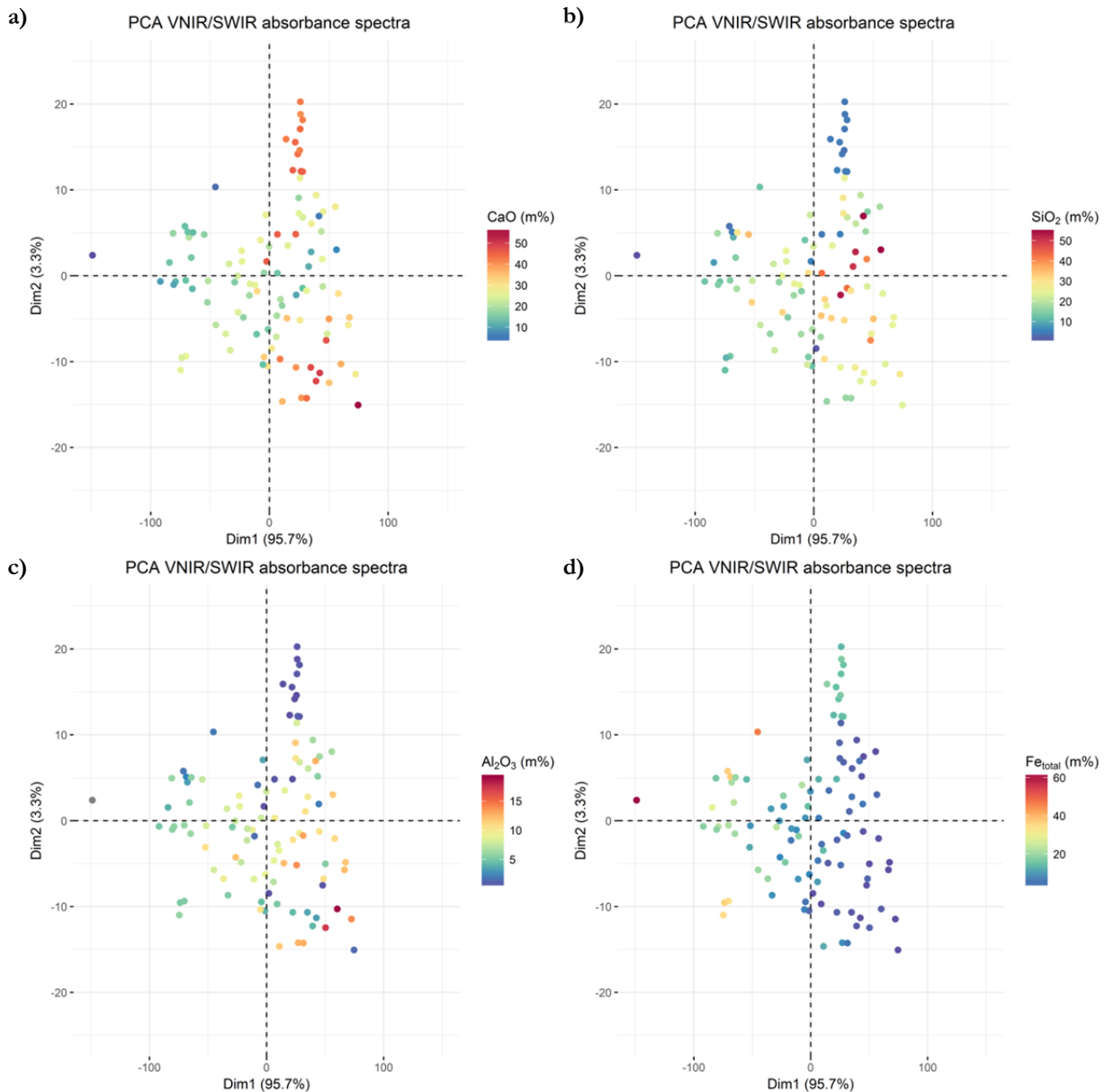


Fig. 5.10: Results of the PCA analysis of VNIR/SWIR absorbance spectra (PC1 and PC2) colour-coded based on the Al_2O_3 , CaO , Fe_{total} and SiO_2 contents of the samples.

5.4.5 Spectral Separability Analysis based on Hierarchical Cluster Analysis

The outcome of the hierarchical clustering of the spectral data supports the PCA results. Again, in agreement with the findings beforehand, the separation of individual by-product types was variable depending on the wavelength range and spectrum type used as input for the clustering

(blast furnace slag, granulated blast furnace slag, converter dedusting sludge, EAF and LF slag as well as stainless steel and Thomas slag) to analyse the capabilities for spectral classification of major iron- and steelworks by-product types. Unspecified material mixtures and by-product types for which less than three samples were available were excluded from this approach.

The results of the support vector machine classification are provided in Table 5.6. Solid results were attained for spectrally discriminating the selected iron- and steelworks by-products based on the VNIR/SWIR data. The best calibration results were achieved based on the continuum removed spectra (overall accuracy 89%), followed by absorbance (overall accuracy 79%) and reflectance spectra (73%). In contrast, the validation results were comparable for all spectra types (75-76% overall accuracy).

The calibration results for the classification based on the MWIR/LWIR spectra are slightly superior compared the VNIR/SWIR data. Again, the best calibration results were obtained utilising the continuum removed spectra (89% overall accuracy). The overall accuracies for the classification based on absorbance and reflectance data were identical (79%). The validation results for the SVM classification were best for the continuum removed spectra with an overall accuracy of 84%, which is better than the validation result based on the VNIR/SWIR continuum removed spectra. In contrast, the validation results for the classification of the MWIR/LWIR reflectance and absorbance spectra was slightly worse compared to the corresponding VNIR/SWIR spectra (76% and 72% respectively).

Tab. 5.6: SVM classification results for separability analysis of seven major by-product types.

Spectral range	Spectrum type	Accuracy _(cal) *	Accuracy _(val) *	N _{sv} **	Cost	Gamma
VNIR/SWIR	Reflectance	0.73	0.76	19	1	0.00047
	Absorbance	0.79	0.76	19	1	0.00047
	CR	0.89	0.75	19	1	0.00047
MWIR/LWIR	Reflectance	0.79	0.72	19	1	0.00173
	Absorbance	0.79	0.76	18	1	0.00173
	CR	0.89	0.84	19	1	0.001730
VNIR-LWIR	Reflectance	0.79	0.80	19	1	0.000391
	Absorbance	0.84	0.88	19	1	0.000391
	CR	0.89	0.88	19	1	0.000391

* By-product types and numbers of cal/val samples: Blast furnace slag (3/3), Converter sludge (3/4) EAF slag (low alloy steel production) (2/1), Ladle furnace slag (2/1), Thomas slag (3/11), GBFS (3/3), Stainless steel slag (3/2)

** Number of support vectors

Overall, the best classification results were achieved using the combination of the VNIR/SWIR and MWIR/LWIR data. The accuracies for the calibration based on the VNIR-LWIR reflectance, absorbance and continuum removed spectra were 79%, 84% and 89% and the corresponding results for the validation were 80%, 88% and 88%, respectively.

The described results indicate a high potential of VNIR/SWIR and MWIR/LWIR data for spectrally discriminating and classifying several types of iron- and steelworks by-products. However, the high number of support vectors in relation to the few training samples indicated a risk of overfitting of the SVM. Thus, no further tuning of the classifier was conducted. Hence, while the general spectral separability of the different by-product types has been successfully demonstrated, the transferability of the observed classification accuracies based on this selection of seven by-product types on larger datasets needs to be analysed in future studies.

5.4.7 Conclusions on the Spectral Separability Analyses

Based on visual interpretation of the PCA scatter plots, a good spectral separability was found for the Thomas slag, the EAF slag (from carbon steel, medium- and high-alloy steel production), the stainless steel slag, AODS, the GBFS, the converter dedusting sludge, the mil scale and sand-rich mixtures. The clear separation of the blast furnace slags was difficult, which is related to the more heterogeneous composition of this class compared to the before mentioned by-product types.

Following the PCA outcome, the spectral separability of most of the by-product types was more distinct based on the VNIR/SWIR spectral range compared to the MWIR/LWIR range. This indicates that most of the analysed by-products show an overall higher spectral dissimilarity in the visible light, near and shortwave infrared region compared to the mid- and longwave infrared. However, especially the EAF slag from medium-alloy steelmaking and the sand-rich mixtures could be more distinctively differentiated using the MWIR/LWIR range. The HCA of the spectral data provided sample clusters in high agreement with the by-product types derived from the chemical and mineralogical analyses. Again, the majority of by-products could be separated well based on the VNIR/SWIR data, except for the samples containing high amounts of sand and the EAF slag from medium-alloy steel production, which could be more clearly differentiated based on the MWIR/SWIR range. The results further imply that the spectral separability of the materials depends on the utilised spectral range and the spectrum type (reflectance, absorbance or continuum removed data). Thus, certain material types tend to be better separated from each other based on their reflectance or absorbance intensities while other by-product types show a better separability based on their specific absorption feature characteristics, which are highlighted by applying continuum removal normalisation. The continuum removed and absorbance spectra provided likewise a better separability of the by-product types than the reflectance spectra for the PCA and HCA. This observation was further confirmed by the results of the SVMC, which demonstrated the potential for spectrally classifying typical iron- and steelworks by-products based on supervised machine learning algorithms. Again, best classification results were achieved based on the continuum removed and absorbance spectra. Results obtained using Spectral Feature Fitting (SFF) and Spectral Angle Mapper (SAM) proved that reference spectra can be used for the successful detection of major by-product types (see Appendix 5.4). In agreement with the findings mentioned afore, differing results were obtained depending on the wavelength ranges with better results for the VNIR/SWIR spectra. Furthermore, varying results were achieved depending on the algorithm utilised.

When comparing the outcomes of the used approaches (PCA, HCA, SMVC; SFF and SAM, see App. 5.4) utilising the complete VNIR/SWIR and MWIR/LWIR spectra, one has to consider that the MWIR/LWIR covers a much wider wavelength range. Subsequently, the MWIR/LWIR by-product spectra contain a higher number of spectral characteristics compared to the VNIR/SWIR. These comprise features potentially shared by various by-product types while others might be unique for specific materials. Utilising all this information without defining “diagnostic” features or wavelength ranges might hamper the outcome. This is in agreement with the study conducted by Denk et al. (2015), who already demonstrated in a case study based on *in situ* spectral data that the differentiation and detection of various iron- and steelworks by-products based on SFF and SAM provided varying results for different by-product types and that the successful detection and differentiation of large pools of different by-product types requires the material-specific optimisation of detection procedures. Thus, the results do not mean that the

MWIR/LWIR data contains less relevant information for material discrimination, but highlights that a “closer look” at such spectra is required. This is realised in the following chapter.

The tanglegram in Fig. 5.12 summarises the observations described beforehand and links results from hierarchical cluster analyses based on chemical data and VNIR-LWIR continuum removed spectra. Groups of samples found in common sub-trees in both dendrograms are linked with parallel lines and well-matching clusters are obvious for the Thomas slag, EAF slag from carbon steel and medium-alloy steelmaking, the stainless steel slag, the LF slag, the granulated blast furnace slag and mixtures containing high amounts of natural sand.

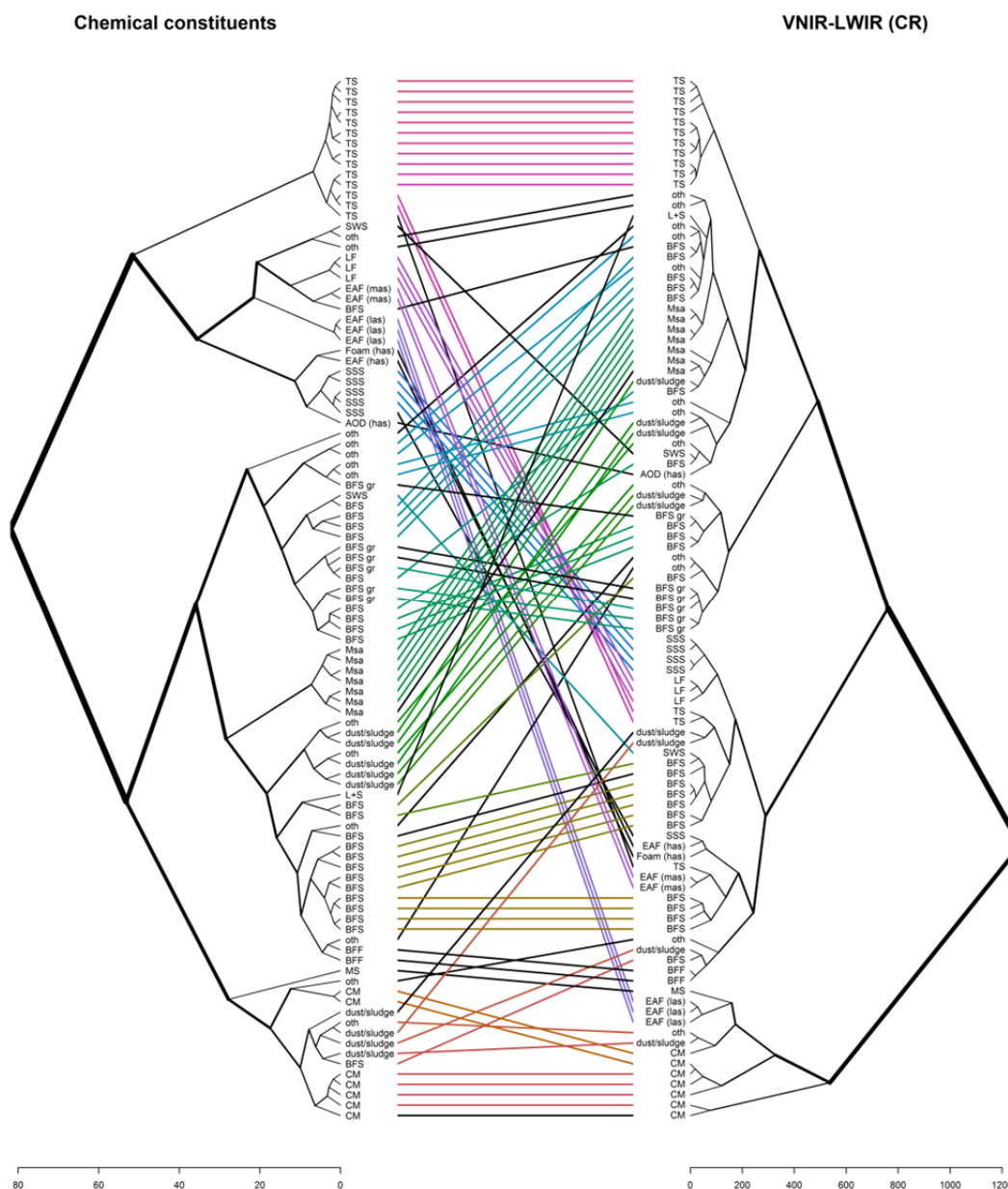


Fig. 5.12: Tanglegram of results from hierarchical cluster analysis (Manhattan dist., ward.D2 method, 18 classes) of VNIR-LWIR continuum removed spectra (right dendrogram) and chemical constituents after square root adjustment (left dendrogram). The samples are labelled according to the by-product type, whereas no-individual sample labels were assigned in order to highlight only the matching of by-product classes. Samples from identical material types are linked in both trees. Parallel lines connecting the samples on both sides indicate well matching clusters.

AOD = argon oxygen decarburization slag, BFS = blast furnace slag, BFSgr = granulated blast furnace slag, BFF = blast furnace flue dust, CM = converter dedusting sludge, EAF = Electric arc furnace slag (las/mas/has = carbon/medium-/high-alloy steelmaking), Foam = EAF foam slag, LF = ladle furnace slag, Msa = mixture containing high amounts of natural sand, MS = mill scale, Oth = unspecified material, dust/sludge = unspecified dusts or sludges, SSS = stainless steel slag, SWS = unspecified steel work slag, TS = Thomas slag.

5.5 Spectral Characteristics of Iron- and Steelworks By-products

5.5.1 Spectral Library (VNIR-LWIR) of Major By-Product Types

The following chapter will present the spectral characteristics of a selection of major iron- and steelworks by-products found within the sample ensemble of this thesis. Here, the spectra of representative samples of each by-product class considered relatively “pure” (see Chapter 5.1) are shown. The descriptions and plots cover the visible light, near and shortwave infrared (VNIR/SWIR) as well as the mid- and long-wave infrared (MWIR/LWIR). The spectra were acquired from material of $< 90 \mu\text{m}$ grain size, which was also used for the chemical and mineralogical analyses. The results of these analyses and photographs (dish diameter = 8.8 cm) of material in different grain sizes are supplementary provided for the representative samples following the example of other spectral libraries and compilations (e.g. Chukanov 2014, Chukanov and Chervonnyi 2016 and Kokaly et al. 2017). The chemical composition of these samples is supplementary shown as provided by FEhS. The results of the mineralogical analyses as conducted and provided by FEhS for the corresponding samples is given in Appendix. 5.1.

The individual by-product descriptions will focus on the reflectance intensities and list the observed spectral features. As many materials showed individual or multiple common spectral characteristics, a summing-up interpretation and discussion of the observed features is given in Chapter 5.5.2.2 to avoid redundancies in the descriptions. The spectra and supplementary photographs for all 102 samples are given in Appendix 5.6.

The following aspects must be considered:

- a) The presented spectra are representative of the by-product types within the sample pool analysed in this thesis. However, by-products collected at other dump sites or iron and steel plants might be of varying chemical and mineralogical composition, even if they are assigned to the same by-product type. This might result in differing spectral properties.
- b) Continuum removal (see Chapter 4.7.2) was applied on the whole VNIR/SWIR as well as on the MWIR/LWIR range for highlighting absorption features that might be hardly visible otherwise. As apparent in several plots, not every individual reflectance minimum could be successfully normalised using the so applied algorithm.
- c) The presented MWIR/LWIR spectra were cut at wavelengths $> 12000 \text{ nm}$, as the overall low reflectance, sensor noise and only few available data points hampered the spectral interpretation in this range. Features distinctively visible in the longer wavelengths not visible in the plots are discussed in Chapter 5.5.2.2. In some cases, the VNIR/SWIR spectra showed noise-induced artefacts in the wavelengths $> 2400 \text{ nm}$, which should not be confused with absorption features.
- d) Focus is put on highlighting present absorption features (reflectance minima). However, especially in the wavelength range $> 10000 \text{ nm}$, features related to e.g. silicates might be visible as reflectance maxima (see Chapter 2.2.2). Due to the general low reflectance observed in the range $> 9000 \text{ nm}$ and little contrast of the present spectral features, only prominent reflectance maxima were highlighted and will be addressed in Chapter 5.5.2.2. A list of all prominent reflectance maxima in the longwave infrared present in the reference samples is provided in Appendix 5.7.

5.5.1.1 Blast Furnace Slag (historic material, most likely not “pure”)

The VNIR/SWIR spectrum of the historic blast furnace slag sample (14-1) collected at the excavator prospecting at the “Plateau 312” is characterised by low reflectance of around 10%, which decreases towards the blue part of the visible light (Figure 5.13, left plot). The continuum removed spectrum exhibits a strong absorption near 400 nm and less distinct features at 1927 and 2225 nm. Minor absorption features are present at 873, 1027, 1294 and 1763 nm.

In the MWIR/LWIR (Fig. 5.13, right), the blast furnace slag also shows reflectance intensities of ~10%, which decrease in the longer wavelengths (> 9000 nm). In contrast to the VNIR/SWIR spectrum, more and stronger pronounced absorption features are present. Distinct features are located at 2872, 6097 and 6809 nm. Weaker features are present at 3981, 4808, 5566, 11368 and 11767 nm. Only faintly visible features are located at e.g. 3413, 9003 and 10995 nm.

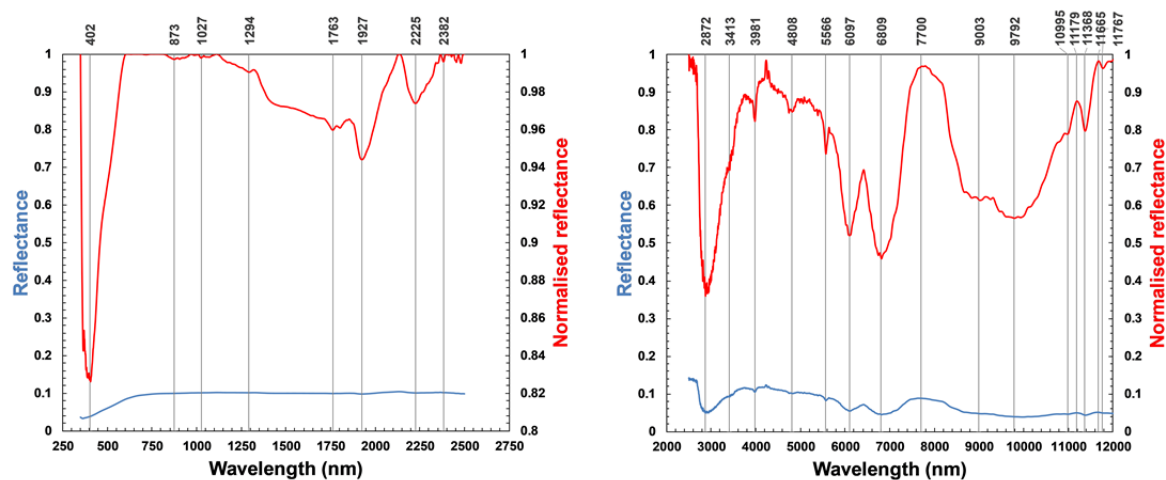


Fig. 5.13: Reflectance and continuum removed spectra of a historic blast furnace slag sample (14-1, < 90 μm) in the VNIR/SWIR (left) and MWIR/LWIR (right). The numbers presented on top of the plots highlight the wavelength position of reflectance minima or maxima.

Tab. 5.7: Chemical constituents (> 1 m%) and photographs of a blast furnace slag sample (14-1) (analyses by FEhS).

Constituent	m%	Sample photo (< 10 mm material)	Sample photo (< 90 μm material)
SiO ₂	21.8		
CaO	20.4		
TIC	14.5		
Fe _{total}	8.4		
Al ₂ O ₃	8.1		
H ₂ O	7.1		
MgO	5.5		
Zn	2.7		
FeO	2.6		
K ₂ O	2.4		
MnO	1.4		
CaO _{free}	1.3		
P ₂ O ₅	1.1		

5.5.1.2 Granulated Blast Furnace Slag (“Slag Sand”, historic by-product)

The sample representing granulated blast furnace slag, also known as “slag sand”, shows high reflectance intensities of around 60% in the VNIR/SWIR, but a strong drop of the reflectance values towards the shorter wavelengths in the visible part of the spectrum (Figure 5.14, left plot). Distinct absorption features are present at 396, 1434, 1928 and 2243 nm. Minor spectral features are visible at 519, 633 and 740 nm as well as at 1161, 1781 and 2476 nm.

The MWIR/LWIR spectrum (Fig. 5.14, right plot) shows relatively broad features at 2922, 6097, and 6809 nm, while sharp features are present at 3981 and 5566 nm. Weakly pronounced features are located at e.g. 3345, 3475 and 4674 nm. The range > 9000 nm appears nearly flat and shows only faintly pronounced features.

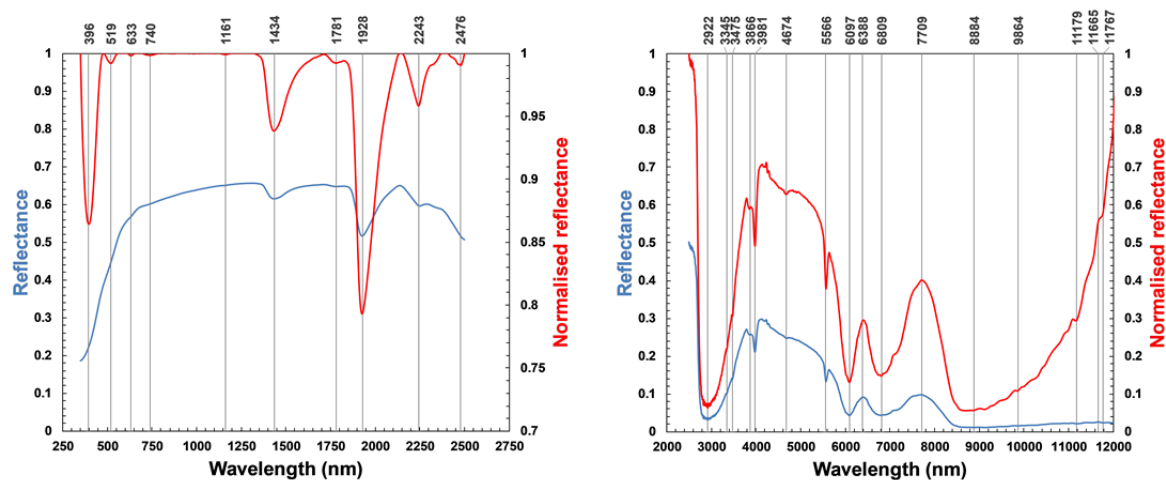


Fig. 5.14: Reflectance and continuum removed spectra of a historic granulated blast furnace slag sample (W2-21b, < 90 μm) in the VNIR/SWIR (left) and MWIR/LWIR (right). The numbers presented on top of the plots highlight the wavelength position of reflectance minima or maxima.

Tab. 5.8: Chemical constituents (> 1 m%) and photographs of a granulated blast furnace slag sample (W2-21b) (analyses by FEHS).

Constituent	m%	Sample photo (ca. < 10 mm material)	Sample photo (< 90 μm material)
CaO	28.60		
SiO ₂	28.21		
Al ₂ O ₃	14.00		
H ₂ O	11.00		
MgO	9.64		
TIC	6.30		
S _{total}	1.04		

5.5.1.3 Thomas Slag

The presented Thomas slag spectrum was recorded from a sample collected in the “Canyon” at the Unterwellenborn dump site, where all Thomas slag samples were found. The VNIR/SWIR spectrum shows a strong increase in reflectance from below 5% in the “blue wavelengths” to ca. 20% in the “red”, which further increases in the near (30%) and shortwave infrared (> 40%); Figure 5.15, left plot). Besides a strong absorption at 392 nm, further distinct features are visible at 711, 1152, 1416, 1767, 1946 and 2247 nm. Another weak feature can be found at 2397 nm.

The MWIR/LWIR spectrum exhibits common characteristics with the blast furnace slag with major features at 2948, 3980, 5566, 6097, 6809 and 8768 nm. Lesser pronounced absorptions are present at 3413, 3502 and 3844 nm. The three minor minima at 4707, 4860 and 5024 nm were only found in the Thomas slag samples. Furthermore, a distinct reflectance peak near 10200 nm and further minor features at e.g. 9251, 11368 and 11767 nm were observed (Fig. 5.15, left).

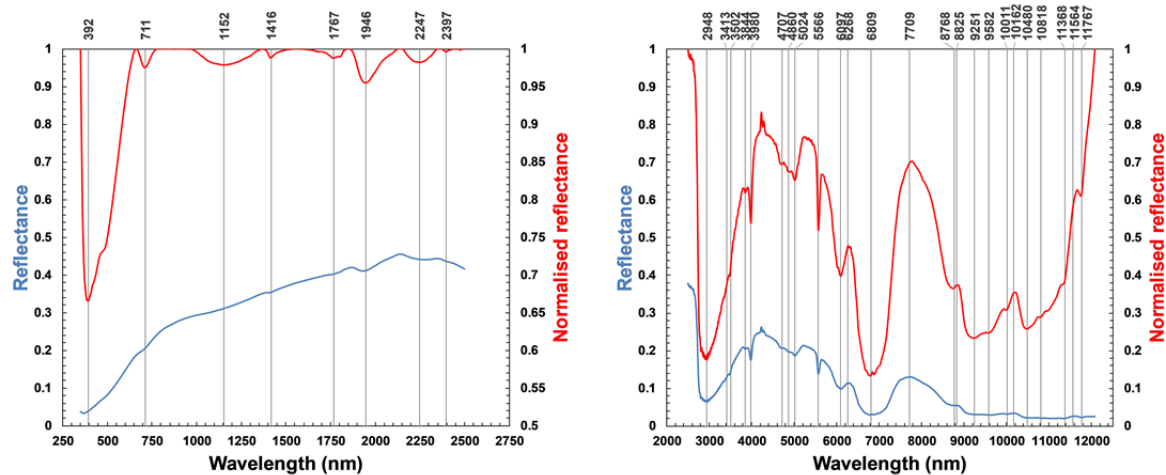


Fig. 5.15: Reflectance and continuum removed spectra of a Thomas slag sample (29-th, < 90 μm) in the VNIR/SWIR (left) and MWIR/LWIR (right). The numbers presented on top of the plots highlight the wavelength position of reflectance minima or maxima.

Tab. 5.9: Chemical constituents (> 1 m%) and photographs of a Thomas slag sample (29-th) (analyses by FEhS).

Constituent	m%	Sample photo (< 10 mm material)	Sample photo (< 90 μm material)
CaO	41		
F _{total}	16.7		
P ₂ O ₅	14		
TIC	5.4		
H ₂ O	4.98		
SiO ₂	4.67		
MnO	3.26		
CaO _{free}	2.3		
MgO	1.98		
Cr ₂ O ₃	1.14		

5.5.1.4 Electric Arc Furnace Slag (carbon steel production)

The VNIR/SWIR spectrum of an electric arc furnace slag (EAFS) sample from the recent carbon steel production of the Stahlwerk Thüringen GmbH is characterised by low reflectance intensities ($< 10\%$; Figure 5.16, left plot). However, the continuum removed spectrum indicates the presence of minor absorption features at 394, 493, 1774 and 1917 nm. A distinct absorption is present at 2217 nm.

In the mid- and longwave infrared (Fig. 5.16, right plot), the sample shows reflectance intensities of $< 10\%$ as well. The most dominant absorption feature is present at 6809 nm and another distinct feature is located at 2950 nm. Weakly pronounced spectral features are present at 5590 and 6125 nm. A multitude of minor minima and maxima can be found in the range > 8000 nm with maxima near 9600 and 11200 nm as well as minima at 9447, 10399, 11368 and 11767 nm.

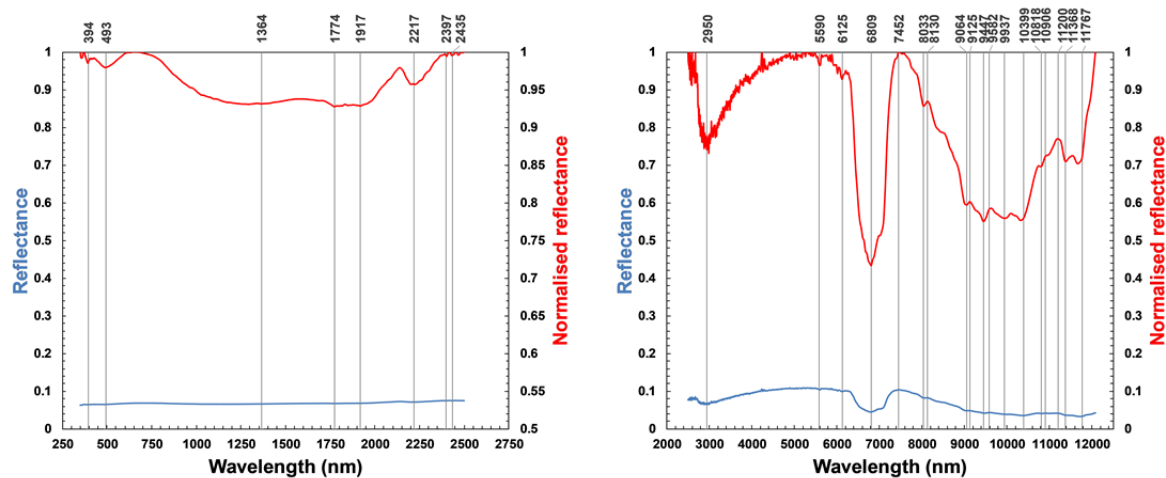




Fig. 5.16: Reflectance and continuum removed spectra of an EAFS sample from carbon steelmaking (sample EAFS-2, $< 90\ \mu\text{m}$) in the VNIR/SWIR (left) and MWIR/LWIR (right). The numbers presented on top of the plots highlight the wavelength position of reflectance minima or maxima.

Tab. 5.10: Chemical constituents ($> 1\ \text{m}\%$) and photos of an EAFS sample from carbon steelmaking (EAFS-2) (analyses by FEhS).

Constituent	m%	Sample photo	Sample photo ($< 90\ \mu\text{m}$ material)
Fe	36.93		
CaO	24.1		
SiO ₂	10.95		
MnO	5.89		
Al ₂ O ₃	5.22		
MgO	4.93		
TiC	3.92		
MnO	3.59		
H ₂ O	3.17		
Fe _{metallic}	1.73		
Cr ₂ O ₃	1.22		

5.5.1.5 Electric Arc Furnace Slag (medium-alloy steelmaking)

The EAF slag from medium-alloy steelmaking (mas) is similar to the EAF slag from carbon steelmaking (cs) in terms of the reflectance intensities ($\sim 10\%$) (Fig. 5.17, left plot). In contrast to the weakly pronounced absorptions in the visible light of the EAF slag (cs), two clearly recognisable features at 367 and 500 nm are present in this material type (and one barely visible feature at 630 nm). The features at 1401, 1929 and 2226 nm are similar to the EAFS (cs).

The slightly higher reflectance in the MWIR/LWIR for this sample compared to the VNIR-SWIR range is presumably caused by the different measurement procedures of the two instruments. In contrast to the EAF slag from carbon steelmaking, this sample shows more diversified spectral characteristics in the MWIR/LWIR. Distinct features can be observed at 2897 and 6741 nm while less deep but sharply shaped absorptions are present at 3981 and 5566 nm. Further features are located at 5005, 5344, 5566 and 6125 nm. A distinct reflectance maximum at 9251 nm is followed by a considerable absorption at 11368 nm (Fig. 5.17, right plot).

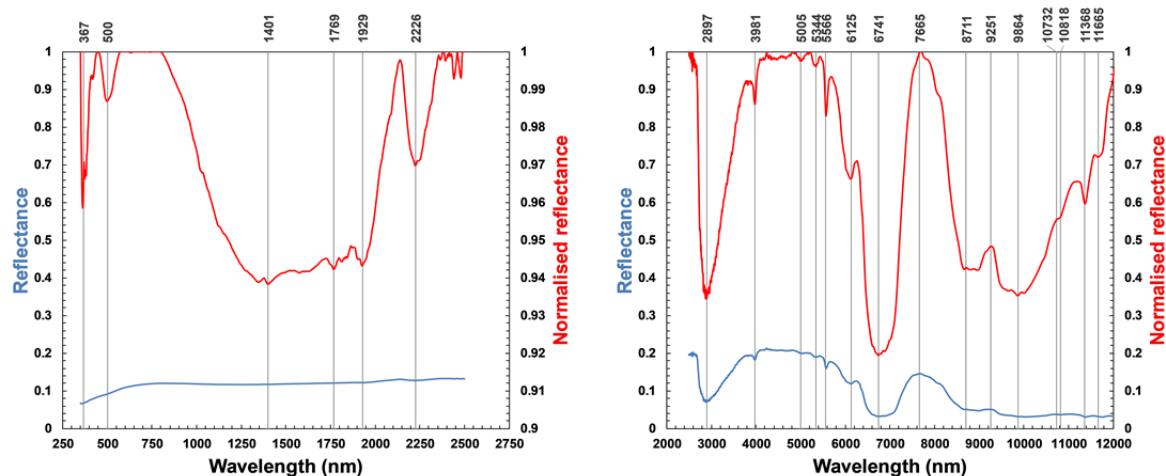


Fig. 5.17: Reflectance and continuum removed spectra of an EAFS sample from medium-alloy steelmaking (sample K1a, $< 90 \mu\text{m}$) in the VNIR/SWIR (left) and MWIR/LWIR (right). The numbers presented on top of the plots highlight the wavelength position of reflectance minima or maxima.

Tab. 5.11: Chemical constituents ($> 1 \text{ m}\%$) and photos of an EAFS sample from medium alloy steelmaking (K1a) (analyses by FEHS).

Constituent	m%	Sample photo (2-5 mm material)	Sample photo ($< 90 \mu\text{m}$ material)
CaO	24.0		
Fe	19.3		
SiO ₂	16.5		
MgO	9.54		
Al ₂ O ₃	9.54		
MgO	4.93		
Cr ₂ O ₃	2.36		

5.5.1.6 Electric Arc Furnace Slag (high-alloy steelmaking)

While the EAFS samples from the carbon and medium-alloy steelmaking show low reflectance intensities of ca. 10 %, the powdered EAFS sample from high-alloy steelmaking is characterised by reflectance values of ~25% in the visible light to nearly 50% in the SWIR (Fig. 5.18, left plot). The absorption characteristics are distinctively different to the two other EAF slag types analysed in this study and features are present at 449, 598, 706, 846, 1043, 1526, 1977 and 2226 nm.

The MWIR/LWIR spectrum exhibits strongly pronounced features at 2935 and 6809 nm. Minor minima can be observed - amongst others - at 3992, 5260, 5733, 6182, 10906 and 11767 nm. Between ca. 5300 and 6000 nm, numerous weakly prominent features were present, which might be related to noise to a certain degree. In contrast to the nearly flat spectra in the range > 8000 nm for many other material types, this sample shows distinct reflectance maxima near 8800, 10200 and 10400 nm (Fig. 5.18, right plot).

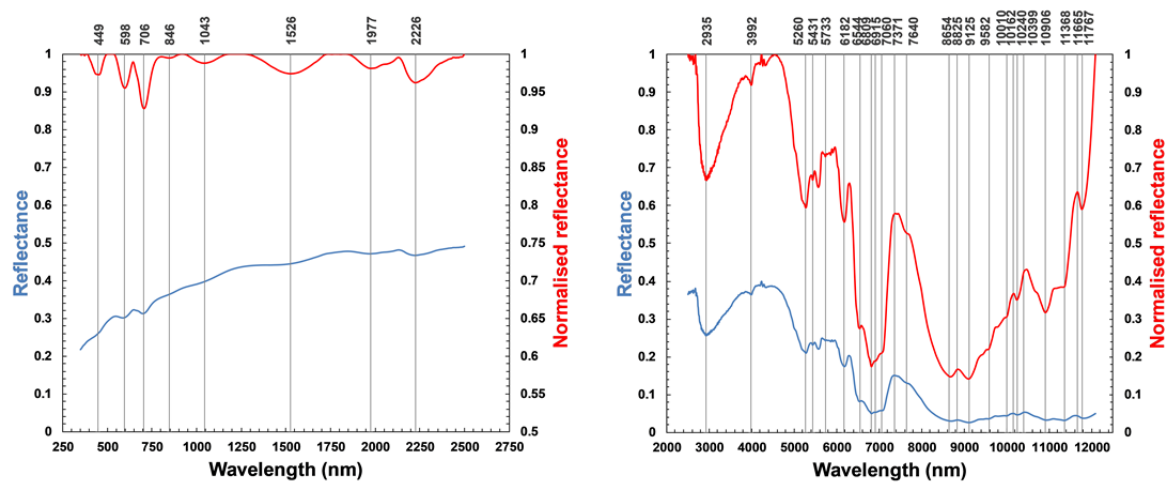




Fig. 5.18: Reflectance and continuum removed spectra of an EAFS sample from high-alloy steelmaking (T-EAFSn, < 90 μm) in the VNIR/SWIR (left) and MWIR/LWIR (right). The numbers presented on top of the plots highlight the wavelength position of reflectance minima or maxima.

Tab. 5.12: Chemical constituents (> 1 m%) and photos of an EAFS sample from high-alloy steelmaking (T-EAFSn) (analyses by FEhS).

Constituent	m%	Sample photo	Sample photo (< 90 μm material)
CaO	48.0		
SiO ₂	40.3		
Cr ₂ O ₃	3.35		
MnO	2.68		
MgO	2.35		

5.5.1.7 Foamed Electric Arc Furnace Slag (high-alloy steelmaking)

The powdered EAF foam slag from high-alloy steelmaking shows a reflectance of $\sim 30\%$ in the VIS and up to $\sim 55\%$ in the shortwave infrared (Fig. 5.19, left plot). Similar to the stainless steel slag (see 5.5.1.8), distinct absorption features are present at 432, 589, 698, 1007, 1957 and 2223 nm while weak absorptions can be located at 1412, 1680 and 2377 nm.

In the mid- and longwave infrared spectrum (Fig. 5.19, right), the foam slag shows the highest reflectance of the discussed samples in this chapter (50-60 % in the range 2000-4000 nm). Major absorption features are present at 2929, 5387, 6043 and 7023 nm. Minor features can be found at 3981, 5179 and 5566 nm. The wavelength range between 8000-11000 nm is characterised by the presence of multiple distinct minima (8943, 9514, 10011, 10399, 10906 and 11466 nm) and corresponding maxima (9251, 9762, 10162 and 10646 nm). These characteristics could not be observed in the same pronounced way for any other material in this thesis' sample ensemble.

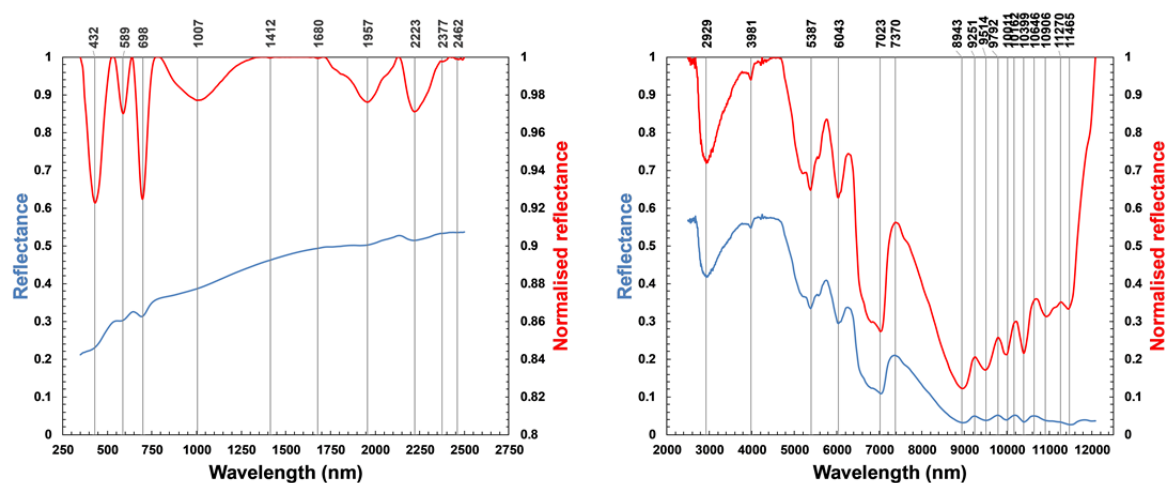
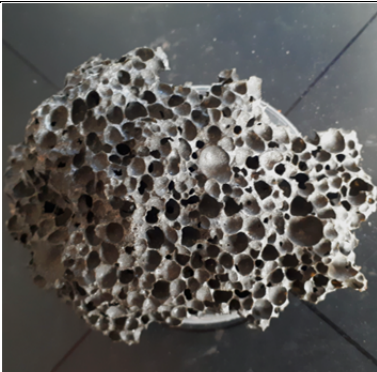



Fig. 5.19: Reflectance and continuum removed spectra of an EAF foam slag sample (T-EAFSf, $< 90 \mu\text{m}$) in the VNIR/SWIR (left) and MWIR/LWIR (right). The numbers presented on top of the plots highlight the wavelength position of reflectance minima or maxima.

Tab. 5.13: Chemical constituents ($> 1 \text{ m}\%$) and photographs of an EAF foam slag sample (T-EAFSf) (analyses by FEhS).

Constituent	m%	Sample photo ($< 10 \text{ mm}$ material)	Sample photo ($< 90 \mu\text{m}$ material)
CaO	39.7		
SiO ₂	34.59		
MgO	9.06		
Al ₂ O ₃	5.51		
Cr ₂ O ₃	3.74		
MnO	3.43		
TiO ₂	1.69		

5.5.1.8 Ladle Furnace Slag

The ladle furnace slag sample collected at the current slag disposal site of the Stahlwerk Thüringen GmbH shows a reflectance of ca. 20 % in the VNIR/SWIR (Figure 5.20, left plot). Minor absorptions in the spectrum are visible at 375, 524, 636, 1403, 1684, 1770 and 2461 nm, while stronger absorption features are present at 1934 and 2229 nm.

The reflectance intensities in the MWIR/LWIR continue at a level of ca. 15% and continuously decrease until < 5% in wavelength range >9000 nm (Fig. 5.20, right plot). Dominant features are found at 2872 and 6741 nm and less strong but sharply pronounced characteristics are present at 3981, 5566, 6125 nm. Minor maxima and minima can be determined in the longer wavelength infrared range, at which the feature at 11368 nm is the strongest pronounced absorption.

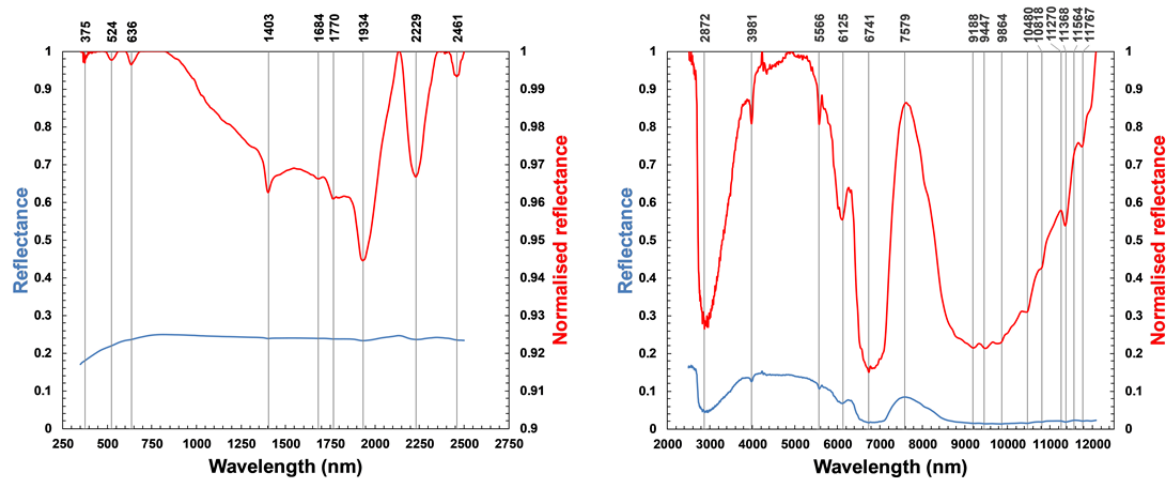


Fig. 5.20: Reflectance and continuum removed spectra of a ladle furnace slag sample (LFS-3, < 90 μm) in the VNIR/SWIR (left) and MWIR/LWIR (right). The numbers presented on top of the plots highlight the wavelength position of reflectance minima or maxima.

Tab. 5.14: Chemical constituents (> 1 m%) and photographs of a ladle furnace slag sample (LFS-3) (analyses by FEhS).

Constituent	m%	Sample photo (< 10 mm material)	Sample photo (< 90 μm material)
CaO	36.8		
SiO ₂	16.65		
Al ₂ O ₃	11.7		
Fe	11.69		
MgO	6.5		
H ₂ O	5.03		
MnO	2.66		
TiC	2.6		
Cr ₂ O ₃	1.04		

5.5.1.9 Stainless Steel Slag

The stainless steel slag shows an average reflectance of ~35% in the VNIR/SWIR range (Figure 5.21, left plot). Multiple distinct features are present in the visible light at 379, 418, 590 and 693 nm. Weakly pronounced features are located at 873 and 997 nm. Further, only faintly visible, features are present at 1130 and 1350 nm. A sharp absorption is seen at 1411 nm, a less pronounced one at 1679 nm and more distinct features are visible at 1948, 2225 and 2391 nm.

The MWIR/LWIR spectrum (Fig. 5.21, right plot) is characterised by relatively high reflectance values (~35% at 4500 nm) as well. Major absorption features are present at 2935, 3981, 5566, 6097, 6809 and 11368 nm. Minor features are located at 2543 nm and a sharp one at 2743 nm. Weakly pronounced features are located at 3345 and 3475 nm and at 3850, 4674 and 10818 nm.

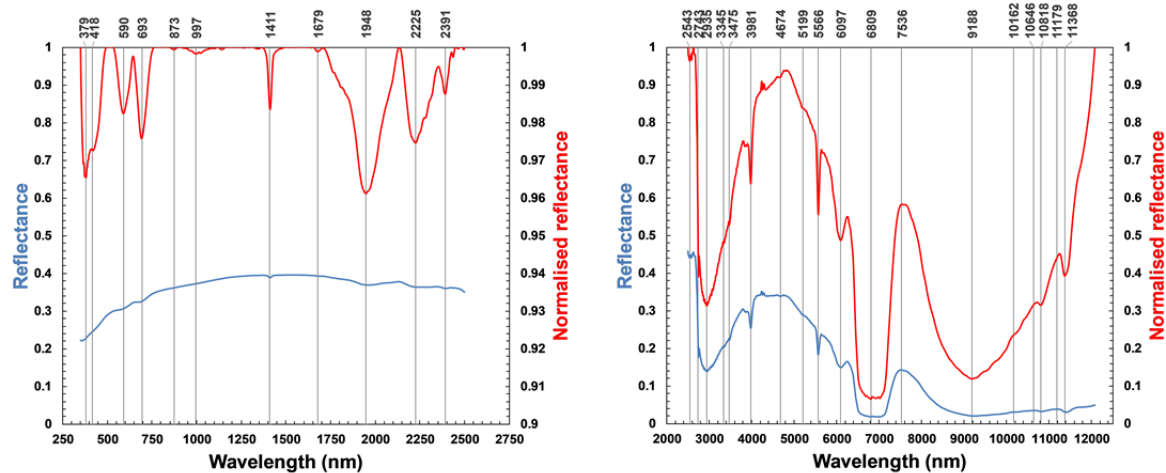


Fig. 5.21: Reflectance and continuum removed spectra of a stainless steel slag sample (T5, < 90 μm) in the VNIR/SWIR (left) and MWIR/LWIR (right). The numbers presented on top of the plots highlight the wavelength position of reflectance minima or maxima.

Tab. 5.15: Chemical constituents (> 1 m%) and photographs of a stainless steel slag sample (T5) (analyses by FEhS).

Constituent	m%	Sample photo (< 10 mm material)	Sample photo (< 90 μm material)
CaO	49.6		
SiO ₂	24.0		
MgO	5.46		
CaO _{free}	4.8		
Cr ₂ O ₃	4.32		
Al ₂ O ₃	4.2		
H ₂ O	3.7		
TIC	2.12		
Fe	1.51		
MnO	1.36		

5.5.1.10 AOD (Desulphurisation) Slag

The AOD desulphurisation slag sample, which had a whitish colour, shows the highest observed reflectance of all the introduced material types in the VNIR/SWIR (VNIR: 40-50%, SWIR ~60 %; Fig. 5.22, left plot). The continuum removed spectrum exhibits multiple features, of which the most prominent ones are located at 376, 431, 597, 709, 804, 966, 1066, 1411, 1680, 1797, 1937, 2214, 2310 and 2386 nm. Less pronounced features are visible at 966, 1006, 1680 and near 2310 nm.

Despite the highest reflectance in the VNIR/SWIR, the AODS sample (Fig. 5.22, right plot) is of lower reflectance in the MWIR/LWIR compared to the foam slag (5.5.1.9). The most prominent absorption features are located at 2545, 2824, 3992, 6125, 6741, 7799 and 11368 nm. Minor and partly sharply pronounced features are present at 2743, 3475, 5719, 5453, 5566, 5684 nm.

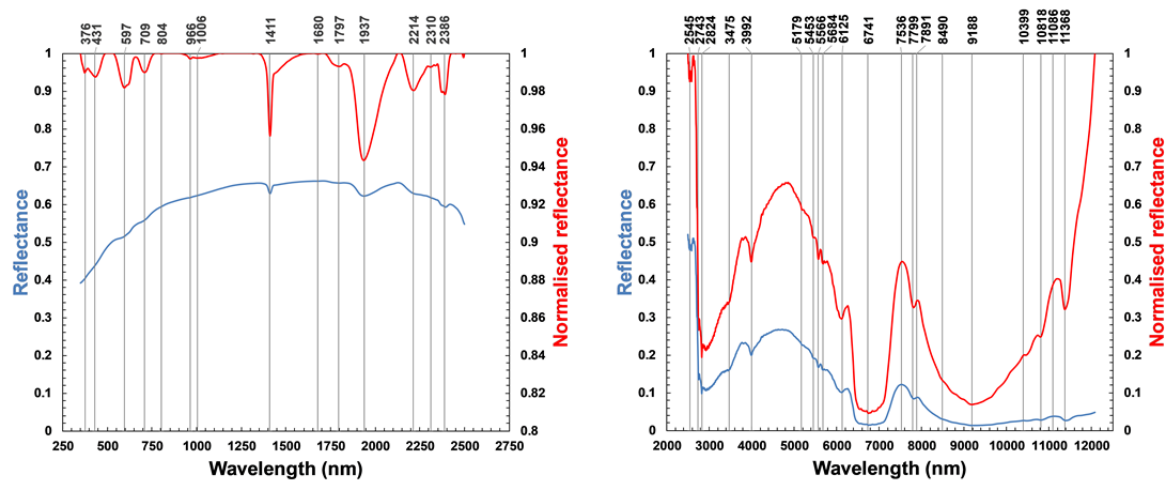




Fig. 5.22: Reflectance and continuum removed spectra of an AOD slag sample (T-AODS, < 90 μm) in the VNIR/SWIR (left) and MWIR/LWIR (right). The numbers presented on top of the plots highlight the wavelength position of reflectance minima or maxima.

Tab. 5.16: Chemical constituents (> 1 m%) and photographs of an AOD slag sample (T-AODS) (analyses by FEHS).

Constituent	m%	Sample photo	Sample photo (< 90 μm material)
CaO	57.1		
SiO ₂	23.62		
CaO _{free}	5.5		
H ₂ O	4.89		
TIC	3.5		
MgO	2.51		
Cr ₂ O ₃	1.45		
Al ₂ O ₃	1.39		

5.5.1.11 Blast Furnace Flue Dust (mixture, not “pure”)

The sample comprising blast furnace flue dust shows reflectance values of around 10% and similar spectral characteristics as the blast furnace slag (see Chapter 5.5.1.1) in the VNIR/SWIR (Figure 5.23, left plot). Differences are visible in the strong absorption in the visible range, which shows two maxima at 384 and 486 nm. Further distinct features are visible at 900, 1023, 1777, 1924 and 2217 nm. Faintly pronounced absorptions are located at 1292 and 1693 nm.

While the reflectance intensities in the MWIR/LWIR of this sample are again comparable to the blast furnace slag, distinct differences are visible in terms of the spectral features in this wavelength range (Fig. 5.23, right plot). Besides the prominent absorption bands located at 2910, 6125 and 6741 nm, two distinct reflectance peaks at 8180 and 9251 nm accompanied by an absorption at 8654 nm are visible. The spectrum further exhibits multiple, partially sharply shaped, features at 4987, 5344, 5566, 6950, 7098, 9721, 10818, 11179, 11368 and 11871 nm.

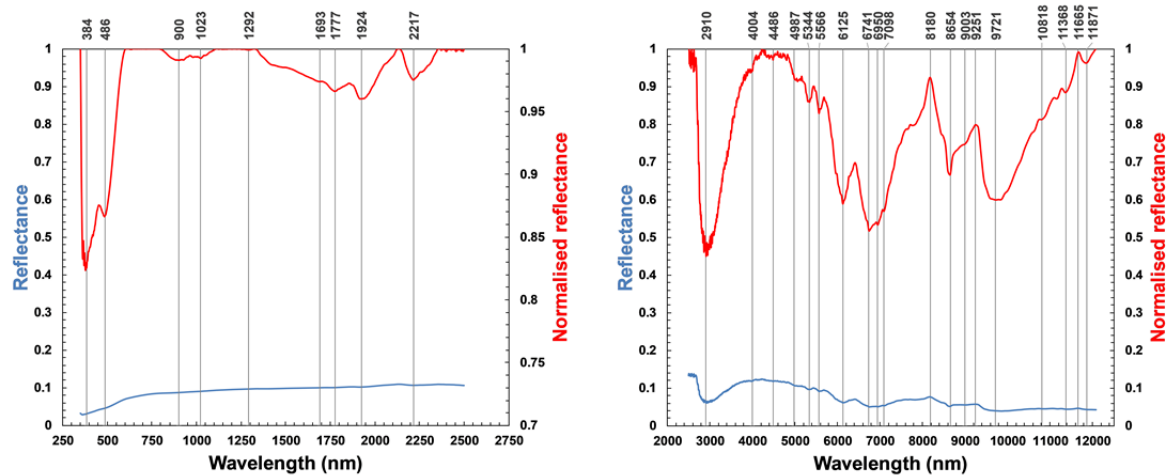


Fig. 5.23: Reflectance and continuum removed spectra of a blast furnace flue dust sample (24-A) in the VNIR/SWIR (left) and MWIR/LWIR (right). The numbers presented on top of the plots highlight the wavelength position of reflectance minima or maxima.

Tab. 5.17: Chemical constituents (> 1 m%) and photographs of a blast furnace flue dust sample (24-A) (analyses by FEhS).

Constituent	m%	Sample photo (< 10 mm material)	Sample photo (< 90 μm material)
SiO ₂	35		
CaO	16.2		
Fe _{total}	13.3		
TIC	9.3		
Al ₂ O ₃	7.57		
H ₂ O	5.66		
MgO	3.5		
FeO	2.59		
MnO	1.25		
CaO _{free}	1.1		
P ₂ O ₅	1.05		
ZnO	1.04		

5.5.1.12 Converter (Dedusting) Sludge

The reddish converter dedusting sludge sample shows generally low reflectance values in the VNIR/SWIR spectrum ($< 10\%$) with a prominent maximum near 750 nm (Fig. 5.24, left plot). The spectrum exhibits only few absorption features, of which a major feature at 488 nm as well as a broad feature with a maximum at 1481 nm can be assigned. Less pronounced characteristics are present at 1905, 2212 and close to 2450 nm.

In the MWIR/LWIR, the converter sludge sample shows reflectance values comparable to the VNIR/SWIR (ca. 10%; Fig. 5.24, right plot), but exhibits more spectral features. The most prominent absorptions are located at 2922, 6125, 6879 and 11368 nm. Less distinct features can be found at 3379, 3957, 5566, 8654, 9003, 9721, 10646, 10906 and 11767 nm.

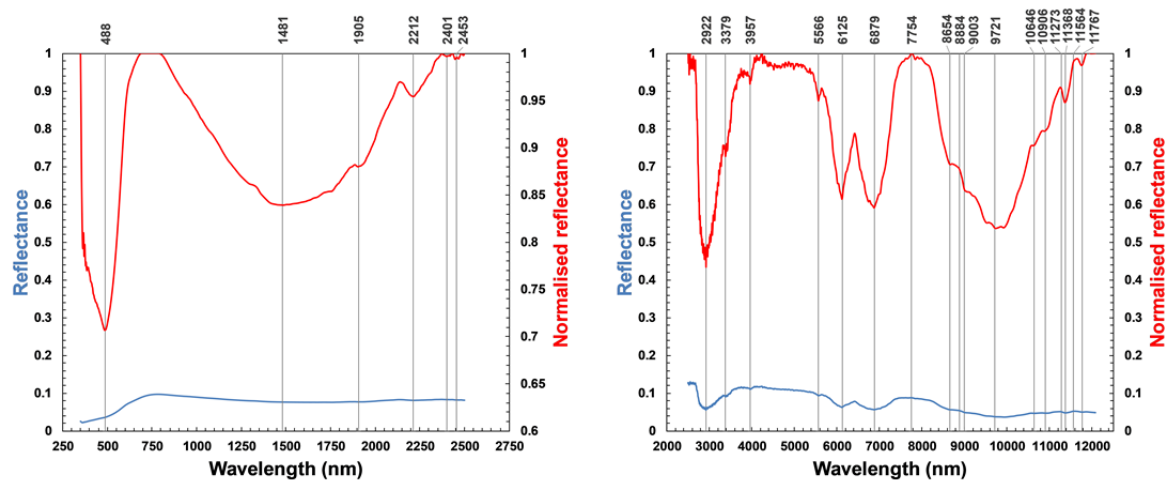


Fig. 5.24: Reflectance and continuum removed spectra of a converter dedusting sludge sample (27) in the VNIR/SWIR (left) and MWIR/LWIR (right). The numbers presented on top of the plots highlight the wavelength position of reflectance minima or maxima.

Tab. 5.18: Chemical constituents (> 1 m%) and photographs of a converter dedusting sludge sample (27) (analyses by FEhS).

Constituent	m%	Sample photo (< 10 mm material)	Sample photo (< 90 μ m material)
Fe	23.1		
TiC	18.6		
SiO ₂	15.33		
CaO	14.1		
H ₂ O	8.13		
FeO	7.61		
Al ₂ O ₃	5.57		
MgO	3.16		
ZnO	2.17		
P ₂ O ₅	1.362		

5.5.1.13 Mill Scale

The mill scale sample showed reflectance values $< 3\%$ in the whole VNIR/SWIR range. This was the lowest reflectance of all analysed samples (Figure 5.25, left plot). Due to the low reflectance, the spectrum is characterised by a relatively high amount of noise. However, the apparently flat reflectance curve exhibits a few absorption features, of which the strongest one is a broad absorption band covering the range ~ 700 to ~ 2100 nm with a maximum at 1224 nm. Further distinct features are located at 524 and 2216 nm. Further features were determined at 375 nm and between 2400 and 2500 nm, which are most likely related to noise.

The MWIR/LWIR spectrum is characterised by low reflectance values and a high noise level as well (Fig. 5.25, right plot). The spectrum is basically featureless with potential weak absorptions at 2950 and 6810 nm.

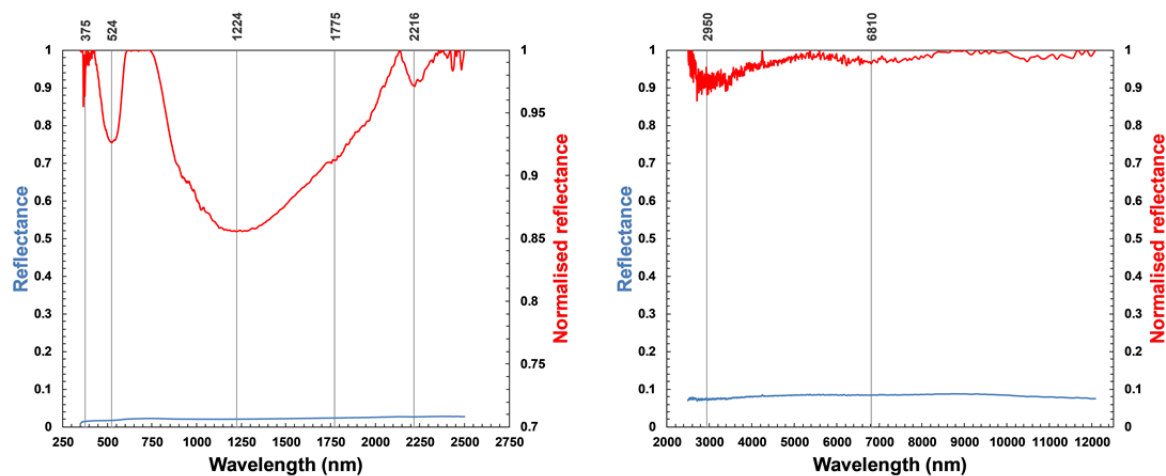




Fig. 5.25: Reflectance and continuum removed spectra of a mill scale sample (19) in the VNIR/SWIR (left) and MWIR/LWIR (right). The numbers presented on top of the plots highlight the wavelength position of reflectance minima or maxima.

Tab. 5.19: Chemical constituents (> 1 m%) and photographs of a mill scale sample (19) (analyses by FEhS).

Constituent	m%	Sample photo	Sample photo ($< 90 \mu\text{m}$ material)
Fe _{total}	62.59		
TIC	3.9		
H ₂ O	2.03		

5.5.2 Interpretation and Discussion of the Spectral Characteristics of the By-Products

5.5.2.1 Reflectance Intensities

The reflectance properties of the iron- and steelworks by-products described in the chapters beforehand were largely variable. In the VNIR/SWIR region, reflectance intensities ranged from < 10% for several by-product types (mill scale, EAF slag from carbon steel production, converter sludge) to nearly 60% for the AOD slag and “slag sand” samples. In general, samples of high reflectance in the VNIR/SWIR also exhibited a similar spectral behaviour in the MWIR. Noticeably, nearly all materials were of very low overall reflectance in the range > ~9000 nm.

Correlations calculated between the spectra and the contents of the four major chemical constituents (Al_2O_3 , CaO , Fe_{total} , SiO_2) highlight the impact of these parameters on the spectra (Fig. 5.26). As the chemical constituents were not normally distributed, these correlations are not statistically robust. It must further be considered that the sample pool is composed of a mixture of different by-products, which in turn are composed of different minerals, varying amounts of amorphous materials and partially contain opaque materials resulting in varying reflectivity and spectral features. Thus, the calculated correlation spectra indicate general trends and highlight relationships present within the sample pool, but are affected by extreme samples to a certain degree and do not necessarily reflect causalities.

Obviously, Al_2O_3 , CaO and SiO_2 are positively correlated with the reflectance values of the samples at the VNIR/SWIR wavelengths, meaning higher contents of these constituents are potentially associated with higher reflectance of the samples. Here, CaO showed the strongest impact also in the shortwave infrared. This is especially obvious for the CaO -rich stainless steel slag samples, which showed the highest reflectivity as well (see Ch. 5.5.1.9).

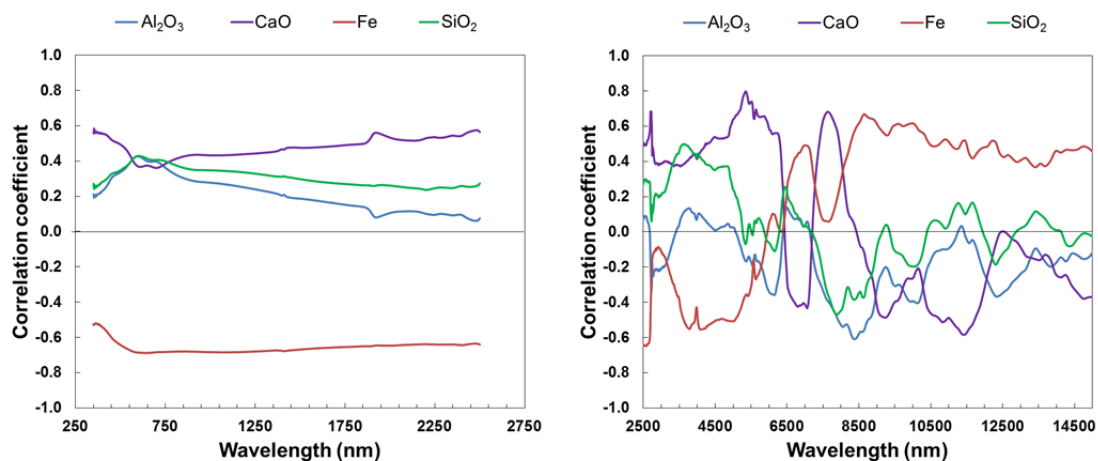


Fig. 5.26: Correlations between the VNIR/SWIR (left) and MWIR/LWIR (right) reflectance spectra of all samples ($N = 102$) and the content of the constituents Al_2O_3 , CaO , Fe_{total} and SiO_2 .

The by-product types with high or intermediate amounts of iron also showed the lowest reflectance intensities. This caused the strong negative correlation ($R \sim -0.7$) between the total iron content and the reflectance intensities of the samples as observed for the VNIR/SWIR range (Fig. 5.26, left plot) and is especially discernible for the mill scale sample, which showed the highest total iron, but also true for the EAF slag from carbon steel fabrication and the historic converter dedusting sludges. In contrast, the samples with the lowest iron contents tended to show the highest reflectance intensities (e.g. stainless steel slags, AOD and foam slag).

For the MWIR/LWIR, the correlations between the spectra and the chemical constituents are generally more diverse and challenging to interpret (Fig. 5.26, right plot, App. 5.8). The Al_2O_3 content was moderately negatively correlated with the spectra and the strongest relationships were found near the water absorption at 6100 nm and close to 8300, 10100 and 12400 nm, which are wavelengths at which silicate features occur (e.g. Hunt 1982; see Chapter 2.2.2). For CaO, positive correlations were observed in the range of 2500-6000 nm with distinct maxima near 2700, 5340 and 5780 nm, while moderately negative relationships occurred near 6800, 9300 and 11370 nm. The distinct drop in the correlation curve at 6880 nm to negative values and the subsequent increase to positive values towards 8000 nm as well as the minimum near 11400 nm are located at wavelengths known for the presence of vibrational features of the carbonate ion (see Chapter 2.2.2). A distinct reflectance maximum occurred in the sample spectra between 7300 and 8700 nm. The reflectance values at this wavelength were positively correlated with the CaO content. The Fe_{total} content negatively impacted reflectivity to ca. 6000 nm but was positively correlated with the longer wavelengths. SiO_2 showed a similar curve progression like the one for Al_2O_3 and was positively correlated to the wavelengths near 3500 nm and moderately negatively with the range of 7000-10000 nm. For further correlation spectra see Appendix 5.8.

To underline the relationship between the Fe_{total} content and the reflectivity of the samples, reflectance values at 1600 and 4500 nm (the samples showed high reflectance at these wavelengths) were determined for all samples and plotted against the total iron content (Fig. 5.27). No linear trends could be observed, but the samples rich in iron showed a distinctively lower reflectance. This effect was more pronounced at 1600 nm compared to 4500 nm, most likely due to the generally lower reflectance of the samples in the MWIR/LWIR.

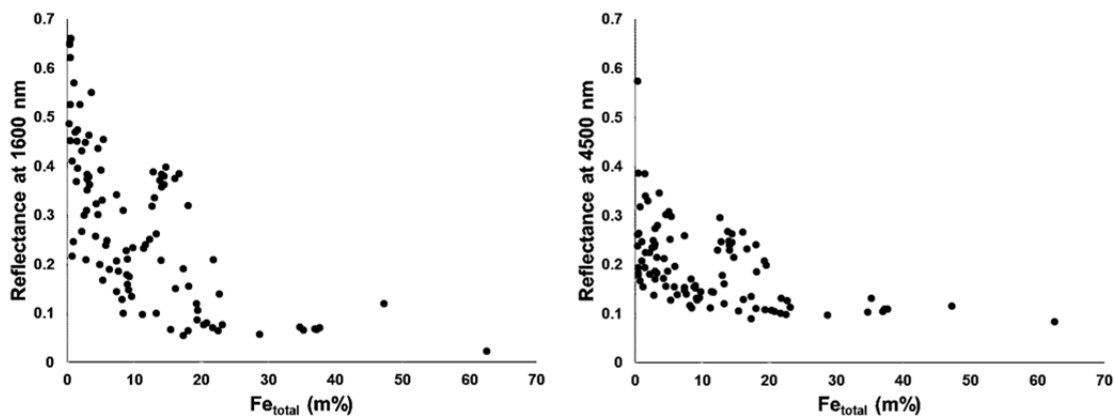


Fig. 5.27: Relation between the Fe_{total} content and the reflectivity of the samples determined at 1600 and 4500 nm.

Apart from Fe_{total} and the presence of specific mineral phases (e.g. magnetite), the low reflectance of the samples towards the wavelength range > 9000 nm is presumably related to opaque materials and metallic iron present in the samples, as such materials are known to cause very low reflectance (e.g. as described for meteorites in Salisbury 1993, Cooper et al. 2002). Furthermore, the fine grain size might distinctively contribute to the low reflectance (see Ch. 5.5.4). For sludges, the presence of amorphous carbon (see e.g. Miyamoto et al. 1981) might cause the low reflectivity to a certain degree. The drop in reflectance towards the “blue part” of the VIS as observed in all spectra, is related to the presence of iron (Hunt et al. 1971a). The constituents Cd, Pb and Zn were strongly negatively correlated with the VNIR/SWIR. Other metals (e.g. Cr_2O_3 , Ni) showed positive relations to the VNIR, emphasising that the sample reflectivity is the result of complex concurrences of the spectral behaviour of individual constituents (see App. 5.8).

5.5.2.2 Spectral Features

The major spectral features observed in the VNIR/SWIR as well as in the MWIR/LWIR spectra of the reference samples for each by-product class are schematically presented in the Figures 5.28 and 5.29 following the example of other authors (e.g. Drake 1995). These charts allow a better assessment of characteristics occurring in all spectra or of features that are unique for specific material types. While focussing on the absorption features, the positions of distinct reflectance maxima in MWIR/LWIR spectra are highlighted as well. Functional groups, which were thought to be causing the observed features, are provided and - if possible - specific minerals were assigned to the determined features. As mentioned before, all spectra showed very low reflectance intensities in the wavelength region exceeding 9000 nm with only few well pronounced features. Furthermore, the decreasing signal-to-noise ratio and resolution of the spectra towards the longer wavelengths additionally hampered the qualitative interpretation of the LWIR data. The XRD verified mineral phases (see Chapter 5.2) represented the basis for the analysis of the spectral identifiability of specific minerals. However, they only provide information on the crystalline components, but many samples contained amorphous constituents, which might also contain functional groups contributing to the observed features in the spectra.

Absorptions caused by electronic processes

Nearly all of the sample spectra exhibited distinct absorption features in the visible light and near infrared. This wavelength region is known to show features due to electronic processes in metal cations (see Chapter 2.2.2.1). The chemical analysis revealed that the samples contain multiple metal species (e.g. Cr, Fe, Mn, Ni, Pb, Ti, Zn, etc., see Chapter 5.3.1), of which various species might produce features at specific wavelengths. These in turn might shift in shape and position depending on the specific metal contents. Furthermore, features due to electronic processes occurring in different transition metals might produce features at similar wavelengths and consequently overlapping absorptions (e.g. Hunt 1977, Rossman 1988, Burns 2005). Thus, the specific assignment of all determined absorption features in the VNIR could not be unravelled with absolute certainty. However, several features appeared at wavelength positions that are typically assigned to specific constituents. As such, the absorptions at 700 and 870 nm observed in the blast furnace slag and the stainless steel slag spectra are most likely related to the presence of Fe^{3+} (e.g. Hunt et al. 1971a, Burns 2005, Gupta 2018). The AOD slag, stainless steel slag, LF slag and EAF slag from medium-alloy steelmaking exhibited features near 380 nm also due to the ferric iron (see e.g. Rossman 2014). Features occurring near 430, 450 and 520 nm in several samples were most likely related to Fe^{3+} as well (see e.g. Dematté et al. 2016). Furthermore, the features near 480 nm might be another indicator of Fe^{3+} (see e.g. Farrand et al. 2016). The spectra of the blast furnace slag, EAF slag from high-alloy steelmaking, the stainless steel slag, the foam and AOD slag as well as the blast furnace flue dust exhibited features near 1000 nm. Features at these wavelengths are often assigned to Fe^{2+} in the literature (e.g. Gupta 2018). Fe^{2+} might have also contributed to the distinct absorptions near 1920 nm as such contributions were reported e.g. for basalts (Anbazhagan and Arivazhagan 2009). Several of the features reported in the VNIR might be caused or contributed by Fe^{2+} as well (e.g. Gupta 2018). As mentioned, the multitude of different metals in the samples might contribute to one observed feature or produce overlapping features. For example, the features near 450 and 700 nm might also be affected by Mn^{3+} (Rossman 2014). Most samples from high-alloy steel production showed lower iron contents but higher Cr_2O_3 and TiO_2 contents compared to the majority of samples and their

spectra exhibited features near 590-600 nm. As features near 600 nm are potentially related to Ti^{3+} or $Fe^{2+}-Ti^{4+}$ interactions (Hunt 1977, Rossman 2014), it is possible that titanium contributed to these absorptions. In spinels, which were present in various samples, e.g. in the stainless steel slags, chromium might replace Fe^{3+} (Drissen 2004). The stainless steel slags also showed relatively high Cr_2O_3 contents and features at 410-450 nm. Thus, these features might be related to chromium, as chromium features at such wavelengths are described e.g. in Rossman (2014).

Besides the total iron content, the presence of specific iron oxides must be considered as an influencing factor on the general shape of the spectra. For example, magnetite was verified with XRD analysis for the mill scale, EAF slag from carbon steelmaking and the converter sludges. As described earlier, this mineral phase is known to show a nearly featureless spectrum and very low reflectance (e.g. Hunt et al. 1971a, see Chapter 2.2.2) and thus potentially masks absorption features that might be visible otherwise. Even though the converter dedusting sludge samples were found to comprise larger amounts of hematite, the typical feature pattern associated with this mineral was not found and the spectra were dominated by absorptions near 490 nm, a distinct reflectance peak at 770 nm, followed by a broad absorption feature ranging to ~ 2100 nm.

H₂O and OH features

Except for the mill scale, all of the studied major by-product classes exhibited absorption features between ca. 1900-1940 nm. This feature is most likely due to vibrational features of the water molecule (e.g. Hunt 1977, Hunt 1980, Hunt 1982, Clark 1999, Gupta 2018). As the samples were dried, moisture can be mostly excluded as impacting factor on the spectra, indicating that the observed features are related to water within the mineral lattice or impurities. The weak absorptions present in several spectra at 970 nm (e.g. in the AOD slag spectrum) as well as the minor features found at 1220 nm and close to 1770 nm are likely related to H_2O as well (e.g. Bowers and Smith 1972, Baumgardner et al. 1986). The minor absorption near 1150 nm found in the spectra of the Thomas slag and the GBFS are also due to combinations of H_2O vibrations (Hunt 1977). The relatively sharp absorptions near 1410 nm, which were distinctively present especially in the AOD and stainless steel slag spectra, are related to overtone vibrations of OH, while broader features near 1400 nm, as for example present in the GBFS spectrum, indicate the presence of water or combinations of OH and H_2O overtones (e.g. Hunt 1980). In the MWIR/LWIR, most of the samples showed distinct absorptions near 2900 and 6100 nm which are caused by H_2O vibrations (e.g. Hunt 1977, Prince et al. 2007, Marincea et al. 2011), of which the broad feature near 2900 nm is due to O-H stretching vibrations of water not fixed in the crystal lattice and the feature at 6100 nm due to H-O-H bending vibrations (Salisbury et al. 1987).

The distinct absorption that was basically present in all samples near 2220 nm is likely caused by combinations of metal-OH bends and OH-stretches, as they are known to produce features near 2200-2300 nm (Hunt 1977, Clark 1999, King et al. 2004b). Al-OH is known to produce features near 2200 nm (Gupta 2018), e.g. in form of doublets for example in kaolinite (see Baldridge et al. 2009, Kokaly et al. 2017), and features found near 2300 nm are typically related to Mg-OH (e.g. Gupta 2018). The observed features near 2220 nm might also be related to Si-OH as such features were found in other silica-rich materials (e.g. Rice et al. 2013). In studies on natural silica-rich glasses, features near 2200 nm were associated to water trapped in the material structure (e.g. Adams 1961). Thus, the observed feature near 2200 nm is most probably caused by OH and/or H_2O . The AOD and stainless steel slag showed sharp absorptions near 2740 nm, which are

interpreted as the OH fundamental vibrational feature (e.g. Hunt and Salisbury 1970). While the assignment of specific OH-bearing minerals based on the observed features was generally difficult, the presence of portlandite, which was determined as minor mineral phase in several samples (e.g. Thomas slag, stainless steel slag, EAF slag from carbon and medium-alloy steel fabrication), was clearly indicated by a feature near 2390 nm. Such a feature is also present in the portlandite spectrum of the USGS spectral library (Clark et al. 2007, Kokaly et al. 2017).

Carbonates

Although the XRD results confirmed that calcite is a constituent of the majority of samples (see Chapter 5.2) and this mineral is known to show several distinct features in the shortwave infrared (typically between 1800 and 2500 nm, e.g. Hunt and Salisbury 1971, van der Meer 1995; see Chapter 2.2.2.2), no distinct carbonate absorption features were found in the VNIR/SWIR spectra of the presented reference samples. For dolomite, which was found to be a minor mineral phase in individual samples (blast furnace slag, converter dedusting sludge) and which typically shows features similar to calcite with variations in the position of the absorption maxima (Hunt and Salisbury 1971, Clark 1999), no distinct absorptions could be determined either. The absence of carbonate features in the VNIR/SWIR might be related to the low grain size, as calcite spectra of fine-grained powders (see e.g. the examples in the ASTER spectral library; Baldridge et al. 2009) show weaker expressed characteristics. These features might be further suppressed in the homogenised powders, by (metallic) iron or due to the glass-like character of individual materials.

In contrast, the MWIR/LWIR spectra of the majority of samples showed characteristics due to vibrational features of the carbonate ion: the AOD and stainless steel slag showed minor absorptions near 2530 nm that are described for calcite (e.g. Gaffey 1986, Clark 1999, Baldridge et al. 2009). Various sample spectra exhibited sharp but only weakly expressed absorptions at 3345 and 3475 nm, representing a carbonate doublet feature (Salisbury et al. 1988). Nearly all samples showed distinct, sharp features at 3982 nm, which was in some cases present as a doublet, and at 5566 nm that are also present in a calcite spectrum of the USGS digital spectral library (Clark et al. 2007) and described by several authors for spectra of natural rocks and minerals as well as for slags (e.g. Salisbury et al. 1988, Prince et al. 2007, Setién et al. 2009, Bláhová et al. 2015). The distinct feature found at 6800 nm in nearly all samples corresponds to the fundamental vibration of the carbonate ion (degenerate antisymmetric C-O stretch, Hunt 1977, Clark 1999). Its position varied between ca. 6700-7300 nm. Furthermore, nearly every sample showed a minor feature at 11368 nm, which is most likely related to the out-of-plane bending mode of the carbonate ion (Hunt 1977, Clark 1999, Prince et al. 2007, Gupta 2018). The feature found near 11700 nm in a variety of sample spectra is present in a calcite reference spectrum in the USGS spectral library (Kokaly et al. 2017) as well and thus considered to be related to the carbonates. The features near 3980, 5560, 6800 and near 11400 nm present in the LF slag spectrum are in agreement with the findings in other studies on the spectral properties of such slags and are due to calcite (e.g. Setién et al. 2009). Diener (2006) also reported the broad feature between 6700-7400 nm due to C-O stretching vibrations of the carbonate ion as well as further carbonate features near 11360 and 14100 nm. At this point it must be strongly considered, that depending on the grain size, carbonate features in the LWIR might appear as reflectance maxima or minima (e.g. Zaini et al. 2012, Green and Schodlok 2016). Thus, the observed reflectance minima due to calcite in the longwave infrared might be visible as peaks in spectra of larger grain sizes.

Silicates

Except for the potential Si-OH feature near 2220 nm, no distinct spectral indicator in this wavelength region for silicates was found. In contrast, multiple features due to silicates – although only weakly expressed in most cases – were found in the longwave infrared region > 8000 nm, which is a region known to be dominated by silicate features (e.g. Hunt 1980, Gupta 2018). Also, silicate glasses are known to show features due to asymmetric stretching of Si-O bonds between 8000-12000 nm, overlapping with (Si, Al)-O stretchings near 9000 nm (e.g. King et al. 2004b). However, several authors found that the assignment of features occurring in this wavelength range to specific mineral species or functional groups is challenging for natural and technogenic glasses as well as for melts of small grain size (e.g. Mohassab and Sohn 2015, Morlok et al. 2016). This can be confirmed in this study. Here, the low reflectance of all samples and little contrast of spectral features in the LWIR hampered the qualitative spectral analysis. The most distinct silicate-related feature was found in the spectra of the samples comprising blast furnace flue dust. This spectrum showed a distinct reflectance peak at 8180 nm and an absorption feature at 8654 nm that are typical spectral indicators for the presence of quartz (e.g. Clark 1999, Baldrige et al. 2009, Kokaly et al. 2017). Quartz was verified as minor mineral phase with XRD analysis for this sample and considered an impurity. Such features were also present in the samples assigned to the category “mixtures with high amounts of natural sand” and are a possible explanation for the good spectral separability of these materials as observed in the PCA and cluster analyses (see Chapter 5.4; see Appendix 5.6 for spectra of these materials).

As mentioned, most of the studied by-product types showed either no clearly determinable or only weakly expressed features in the LWIR region. However, a variety of the minor maxima in this wavelength region might resemble weakly pronounced reststrahlen bands of silicates. Here minor reflectance maxima were observed in a variety of samples near 10100-10300 nm, e.g. in the Thomas slag and the EAF slag from carbon and stainless steelmaking. These maxima are interpreted as Si-O features as similar features were reported for different slags in the literature to be related to calcium silicates (e.g. Diener 2006). Minor reflectance maxima observed in several samples near 11000 nm might be due to Al-O vibrations. Again, similar features were reported for LF and EAF slag spectra (Diener 2006). The EAF slag from high-alloy steelmaking and the EAF foam slag showed a variety of well pronounced features in the LWIR range. For the EAF slag, a reflectance maximum near 10300 nm followed by a minor absorption near 10900 nm and a broad reflectance shoulder with a maximum near 13000 nm was observed (see Appendix 5.6 for the full spectra of the samples T-EAFSn and T-EAFSf). These characteristics exhibit similarities to the spectrum of wollastonite presented in several spectral libraries (Clark et al. 2007, Baldrige et al. 2009, Kokaly et al. 2017). Wollastonite was also confirmed as major mineral phase of the sample with XRD analysis. Of the entire sample spectra presented in Chapter 5.5.1, the foam slag spectrum was the only one showing a pattern of distinct minima at 8943, 9513, 10010 and 10399 nm (and corresponding maxima). Furthermore, the EAF foam slag was found to contain melilites (gehlenite-akermanite) as major mineral phase. It further contained merwinite as minor mineral phase, but other by-products containing merwinite as well did not exhibit such features. However, as other samples rich in gehlenite-akermanite showed the mentioned feature pattern (see samples 30-HOS, GPS, W3-Ref5, W3-Ref1-2, W3Ref-14, W3-Ref22 in App. 5.6), it is most likely that the observed features are related to this mineral phase.

Most silicates exhibit a well pronounced reflectance minimum near 8000 nm, which is known as the Christiansen feature (e.g. Hunt 1982, see Chapter 2.2.2.2). The position of the CF was found to be correlated with the silica content in several studies on silicate glasses and impactites, where the position of the CF shifted towards shorter wavelengths for minerals with high silica content (e.g. Logan et al. 1973, Lucey et al. 2017). The samples in this study did not show such a distinct minimum near 8000 nm but instead exhibited a broad reflectance maximum at this spectral range.

Others

The Thomas slag samples showed reflectance minima at 4674, 4878 and 5024 nm, which were found in a similar pattern in the USGS library spectrum for hydroxyl-apatite (Clark et al. 2007) and the apatite spectra in the ASTER spectral library (Baldrige et al. 2009). Furthermore, the minor absorption present in the Thomas slag spectra near 3844 nm as well as the feature at ca. 9200 nm also occur in the aforementioned (hydroxyl-)apatite reference spectra. Thus, the observed features indicate the presence of the phosphates apatite and/or silicocarnotite determined via XRD analysis for these samples. Furthermore, the USGS VNIR/SWIR spectrum for hydroxyl-apatite showed a distinct reflectance increase from the VNIR towards the SWIR, which was also observed in all Thomas slag spectra and interpreted as another potential spectral indicator for the presence of this phosphate-rich by-product type.

The spectra of most by-products showed small peaks between 4200 and 4300 nm (typically near 4230 nm). These features might be caused by CO₂ as this gas can produce sharp bands near 4300 nm when trapped as impurity (Salisbury et al. 1987). However, it is more likely that this effect is related to impacts of CO₂ as a potential background contributor (e.g. King et al. 2004a, Prince et al. 2007). As the FTIR measurements were conducted using a handheld instrument, it seems likely that exhaled air in the measurement surrounding contributed to these features.

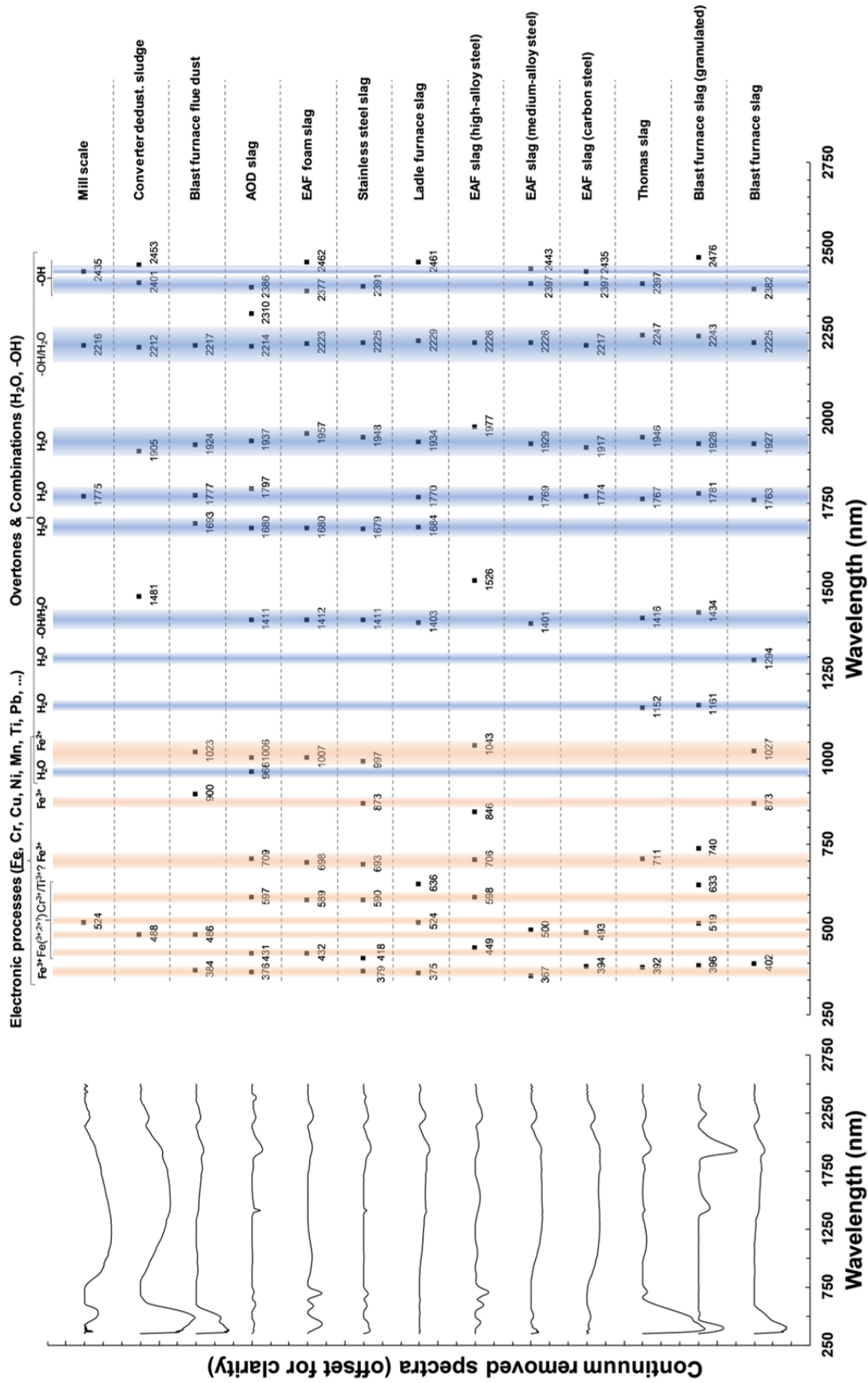


Fig. 5.28: Overview of spectral features found in the VNIR/SWIR spectra of the by-product samples presented in Chapter 5.5.1. Note: The assignment of specific metal cations to the features observed in the VNIR could not be fully unravelled as the multitude of different metal-constituents present in the samples might cause overlapping features or multiple contributions. The widths of the coloured columns only indicate an approximate correspondence to the actual feature width.

5.5.2.3 Relationships between Major Absorption Features and Chemical constituents

For dominant spectral features that were present in a larger number of samples, absorption characteristics were determined based on continuum removed spectral subsets and plotted against the contents of the chemical constituents in order to analyse potential quantitative relationships. As shown before, the absorption features occurring in the VNIR due to electronic processes were strongly variable for different by-product types and the number of samples with common features was limited. Thus, feature variations occurring in the visible light and near infrared will be discussed in more detail in Ch. 5.5.3 for specific by-product types. The following paragraph will focus on the variations of the absorptions at 1930 and 2230 nm (Fig. 5.30).

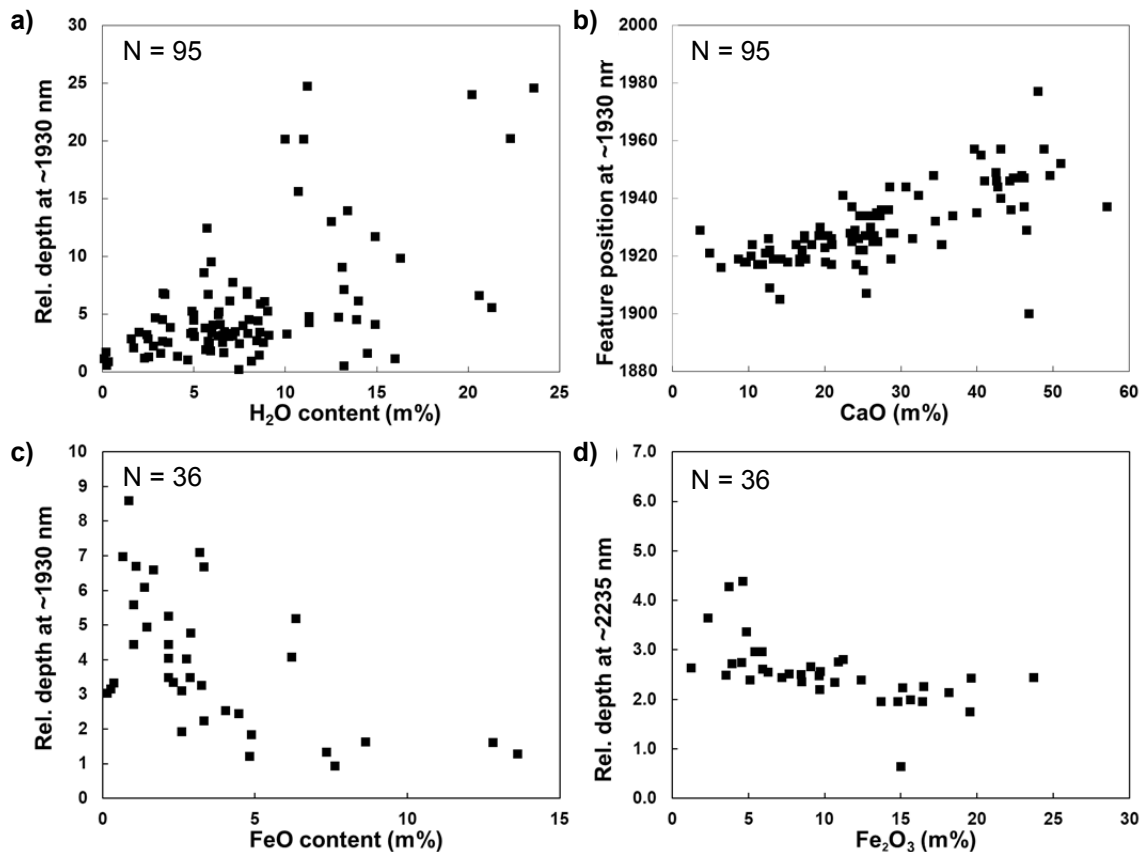


Fig. 5.30: Characteristics of dominant features in the VNIR/SWIR spectra versus contents of chemical constituents.

The feature found at 1930 nm is typically assigned to overtones of fundamental vibrations of the water molecule (e.g. Clark 1999, see Chapter 5.5.2.2). The relationship of the feature depths and the corresponding water contents is visualised in Figure 5.30a. While samples with higher water contents tended to show stronger absorption depths near 1930 nm, the relation was not very strong, and the point cloud clearly scattered. It was further found that the position of this feature tended to shift towards the longer wavelengths with increasing CaO content (Fig. 5.30b). Furthermore, the depths of the 1930 nm absorption feature decreased with higher FeO content of the samples (Fig. 5.30c). This indicates that Fe²⁺ is related to the characteristics of this feature. Basically, all sample spectra were characterised by a distinct feature near 2230 nm, which was most likely due to Si- or metal-OH overtones and combinations or due to H₂O (see Chapter 5.5.2.2). However, the depth of this feature showed only weak relations to the contents of the chemical constituents, as presented using the example of Fe₂O₃ (Fig. 5.30d) in the figure above.

The five most dominant absorptions present in the entirety of the MWIR/LWIR spectra were the features due to H₂O vibrational modes near 2930 and 6100 nm as well as the absorptions at 3980, 5560 and 6880 nm, which are related to vibrations of the carbonate ion (see Chapter 5.5.2.2). The H₂O content was moderately positively correlated to the strength of the absorptions near 2930 and 6100 nm ($R = 0.51$ and $R = 0.53$, respectively; Fig. 5.31a and 5.31b), which were already discussed as fundamental vibrational features of the water molecule (e.g. Hunt 1977). The depth of the sharp and well pronounced absorptions occurring at 3980 and 5560 nm showed no discernible relationship to the CaO ($R = 0.12$ and 0.13 , respectively) or the TIC content ($R = 0.23$ and $R = 0.1$), respectively. In contrast, the depth of the dominant absorption feature near 6880 nm that is known to be related to the fundamental vibration of the carbonate ion (e.g. Hunt 1980, Clark 1999) showed a strong positive correlation to the CaO content ($R = 0.77$, Fig. 5.31c), whereas the wavelength position of this feature was not distinctively correlated to any of the major chemical constituents. Also, the depth of the minor absorption near 11400 nm, which was interpreted to be related to carbonates too, showed a moderate relation to the CaO content ($R = 0.51$). Fe_{total} was moderately negatively correlated to the depth of most analysed features and the strongest relationship ($R = -0.59$) was found for the feature at 6100 nm (Fig. 5.31d).

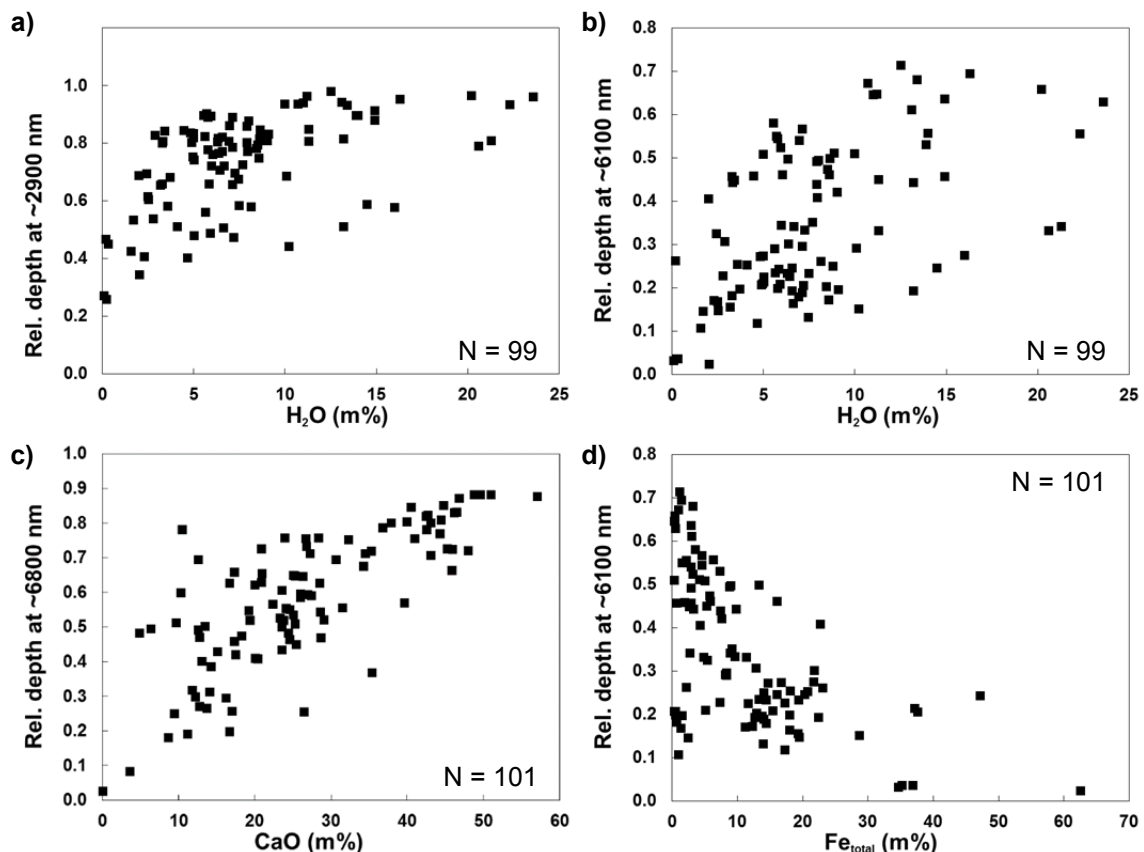


Fig. 5.31: Relative depths of features in the MWIR/LWIR versus contents of chemical constituents.

Overall, the observed relationships between characteristics of dominant features shared by the majority of samples and the chemical constituents were low or only moderate. This is interpreted as the result of the largely variable material composition within the sample pool. The example of the depth of the feature at 6100 nm and its relation to the H₂O and Fe_{total} contents demonstrated that chemical constituents might contribute opposingly to feature characteristics. Implications of this matter on the spectral quantification of by-product constituents are discussed in Ch. 5.6.4. Results of initial analyses conducted in this work did not indicate a strong relation between the calcite content from XRD analysis and the depth of absorptions related to the CO₃²⁻ ion.

5.5.3 Spectral Variations within By-Product Classes

For the iron- and steelworks by-product types for which at least five samples were available that could be explicitly assigned, the class-specific spectral variations were analysed both in terms of reflectance intensities and the absorption feature characteristics. As all samples were dried and homogenised, impacts of different grain sizes or moisture as explanation for the observed variations could be minimised. Thus, the occurring spectral deviations were considered to be mainly driven by differences in the mineralogical and chemical composition. In order to highlight wavelength ranges at which the largest variations both in reflectivity as well as in the absorption features occurred, the mean, minimum, maximum, standard deviation as well as the coefficient of variation were calculated for the reflectance and continuum removed spectra. Furthermore, absorption characteristics (e.g. position, depth, width, area and asymmetry) were determined for the VNIR/SWIR range (see also the tables provided in Appendix 5.9). For major features occurring in the MWIR/LWIR spectra, the relative absorption depths were determined as well. The majority of observed variations occurred at wavelengths associated with features caused by electronic processes (VNIR range), water (1400, 1900, 2900, 6100 nm), carbonates (near 3980, 5560, 6900 nm) or silicates (range > 8000 nm). The feature parameters, e.g. absorption depths, are expected to correspond to the amount of the absorbent following the Beer-Lambert-Law (see Chapter 2.2.1) and were plotted against the contents of chemical constituents found to be related to the observed variations (e.g. CaO, Fe_{total}, H₂O, TIC). While the low number of samples per by-product type prohibited statistical analyses, this approach aimed to highlight general trends in the feature-chemistry relationship and was conducted in similar way by e.g. Cloutis et al. (2004).

5.5.3.1 Blast Furnace Slag

The spectral variability of six samples defined as BFS, which were collected in the excavator prospecting at the “Plateau 312” and thus considered comparable, is presented in Fig. 5.32a and 5.32b. The coefficient of variation of the reflectance intensities (CV_{ref}) was consistent (25-30%) in the whole VNIR/SWIR. This is considered to be mainly driven by the differences in CaO content (MD= 22.6, SD = 3.1 m%) as this parameter was found to be strongly related to the reflectivity at all VNIR/SWIR wavelengths in similar intensity (see Ch. 5.5.2.1). In contrast, the CV curve of the continuum removed spectra (CV_{cr}) indicated only minor variability, for which the largest deviations (CV_{max} 5%) were occurring at the feature near 400 nm. While no distinct relationships of the depth of this feature to the total iron content could be observed, the weaker pronounced feature near 880 nm showed a discernible trend of increasing depth with increasing Fe_{total} content (MN= 9.8 m%, SD = 2.6 m%). Another trend was found between the variations in the depth of the 1930 nm feature and the H₂O content (MN = 7.0 m%, SD = 5.91 m%).

In the MWIR/LWIR, CV_{ref} and CV_{cr} were of larger variability (Fig. 5.32a). The variations occurring near 2900 and 6100 nm were found to be related to differences in the H₂O content (Fig. 5.32b). The variation in CV_{cr} at 2740 nm was interpreted to be related to the hydroxyl ion. The depth of the potential carbonate feature near 6880 nm showed a positive relationship to the variations in CaO content. It was further negatively correlated with the TIC content. High CV_{ref} and CV_{cr} values were determined in the range of 8000-12000 nm, which is typically referred to as the region dominated by silicate features (see 5.5.2.2) and thus likely related to variations in silicate minerals and/or in SiO₂ content (MN = 17.9 m%, SD = 2.4 m%) or other constituents.

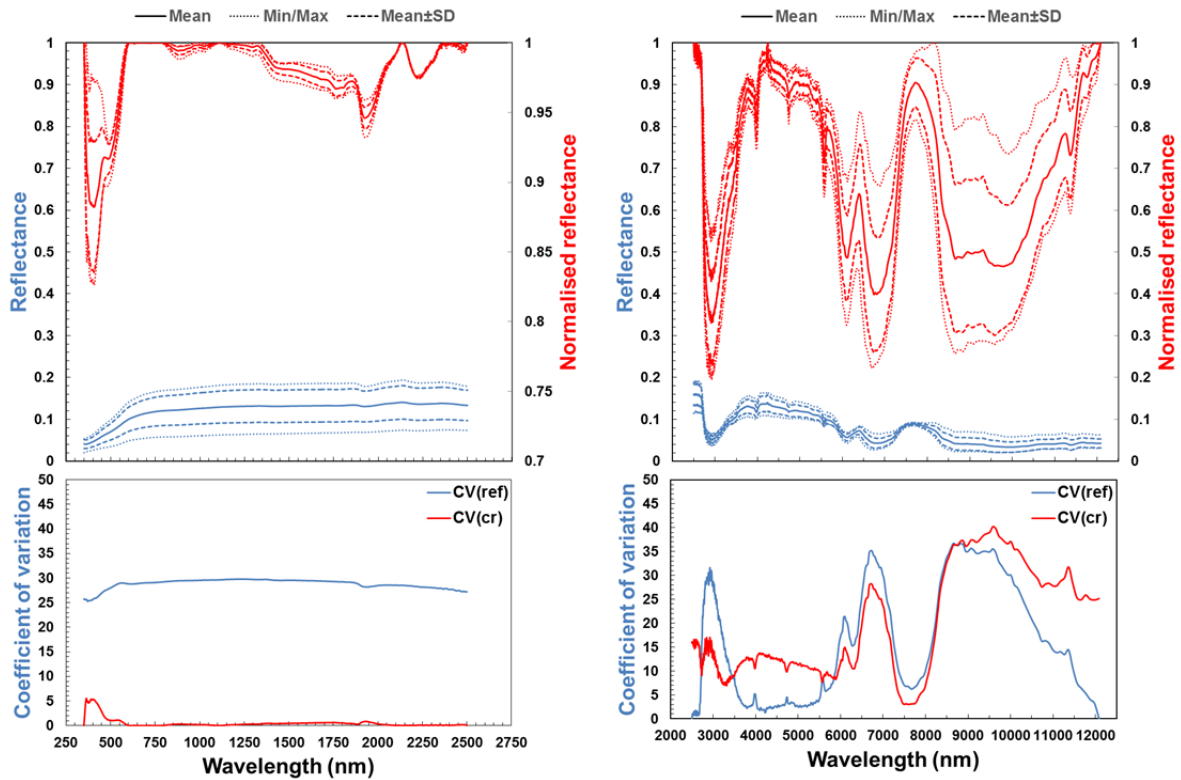


Fig. 5.32a: Variations in reflectance and continuum removed spectra of selected blast furnace slag samples ($N = 6$).

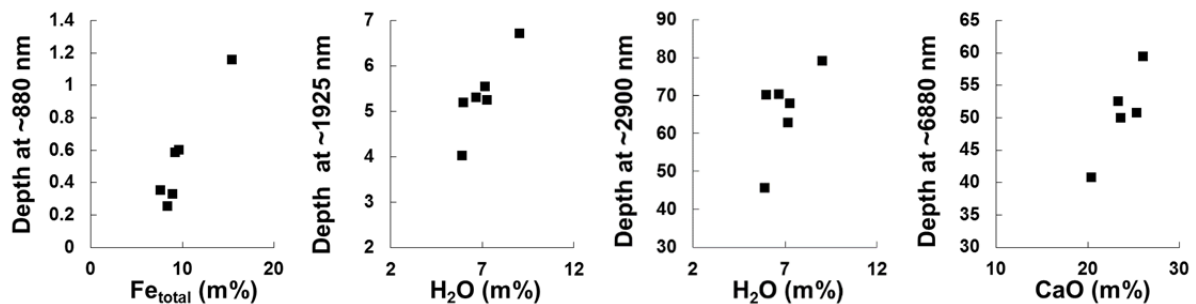


Fig. 5.32b: Spectral feature variations of blast furnace slag samples versus contents of chemical constituents ($N = 6$). Depicted feature depths are relative depths.

5.5.3.2 Granulated Blast Furnace Slag

In contrast to the blast furnace slag, the variations in the reflectance intensities for the samples identified as granulated blast furnace slag (“slag sand”) were not homogeneous over the whole VNIR/SWIR range but largest in the VNIR and decreasing towards the SWIR (Fig. 5.33a). The continuum removed spectra showed large deviations near 420 nm corresponding to the observed absorption features due to electronic processes. However, the feature depth at ca. 420 nm showed no discernible trend to the Fe_{total} content (MN = 1.7 m%, SD = 1.2 m%; Fig. 5.33b). The variations of the feature at 1930 nm were found to show no clear relation to the variability in water content (MN = 13.7 m%, SD = 4.2 m%) of the samples as well. In the MWIR/LWIR, the distinct sharp peaks in the CV_{ref} and CV_{cr} curves at 3980 and 5566 nm, which were assigned to carbonate features (Ch. 5.5.2.2), showed discernibly relations to the TIC content of the samples (MN = 8.7, SD = 3.3 m%). The deviations in the range > 8000 nm might be due to variations in SiO_2 content (MN = 24.4 m%, SD = 2.6 m%), CaO, Al_2O_3 or TIC (see Ch. 5.5.2.1, App. 5.8).

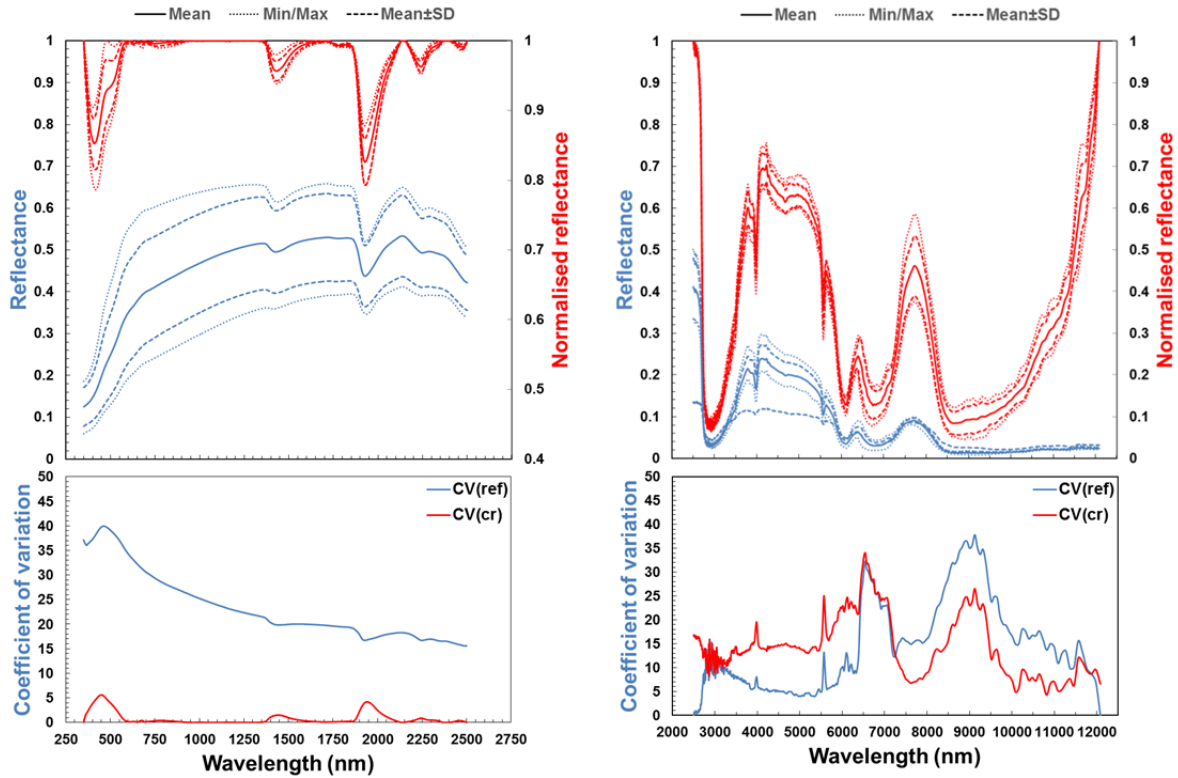


Fig. 5.33a: Variations in the reflectance and continuum removed spectra of selected GBFS samples (N = 6).

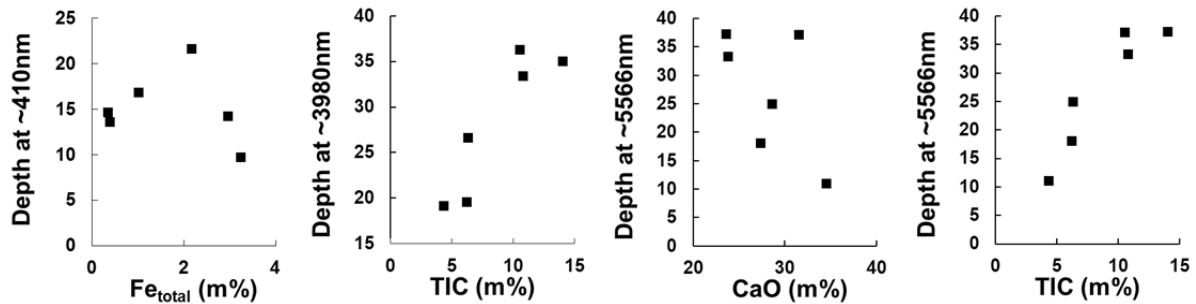


Fig. 5.33b: Spectral feature variations of selected GBFS samples versus contents of chemical constituents (N = 6). Depicted feature depths are relative depths.

5.5.3.3 Thomas Slag

The Thomas slag VNIR/SWIR spectra showed the strongest variations in reflectivity in the visible light and the CV_{cr} was highest at the broad absorption near 400 nm, at the minor feature near 710 nm and at ca. 1400 nm (Fig. 5.34a). Again, no clear relation of the absorption feature parameters near 400 nm to Fe_{total} was found. By trend, the width of the feature at 710 nm increased with higher Fe_{total} content (MN = 14.4 m%, SD = 1.6 m%; Fig. 5.34b). In the MWIR/LWIR, the CV of the reflectance and continuum removed spectra was consistently low (ca. 10%), except for the range near 6800 nm. Here, CV_{ref} and CV_{cr} increased up to nearly 60%. However, the depth of the 6800 nm feature did not show a clear relation to the CaO or TIC contents but a trend of increasing feature depth with increasing MnO (as well as Cr_2O_3) content. The little variable CaO and/or SiO_2 content (MN = 5.07 m%, SD = 0.42 m%) potentially explained the lower variability in the range > 8000 nm compared to the other by-product classes.

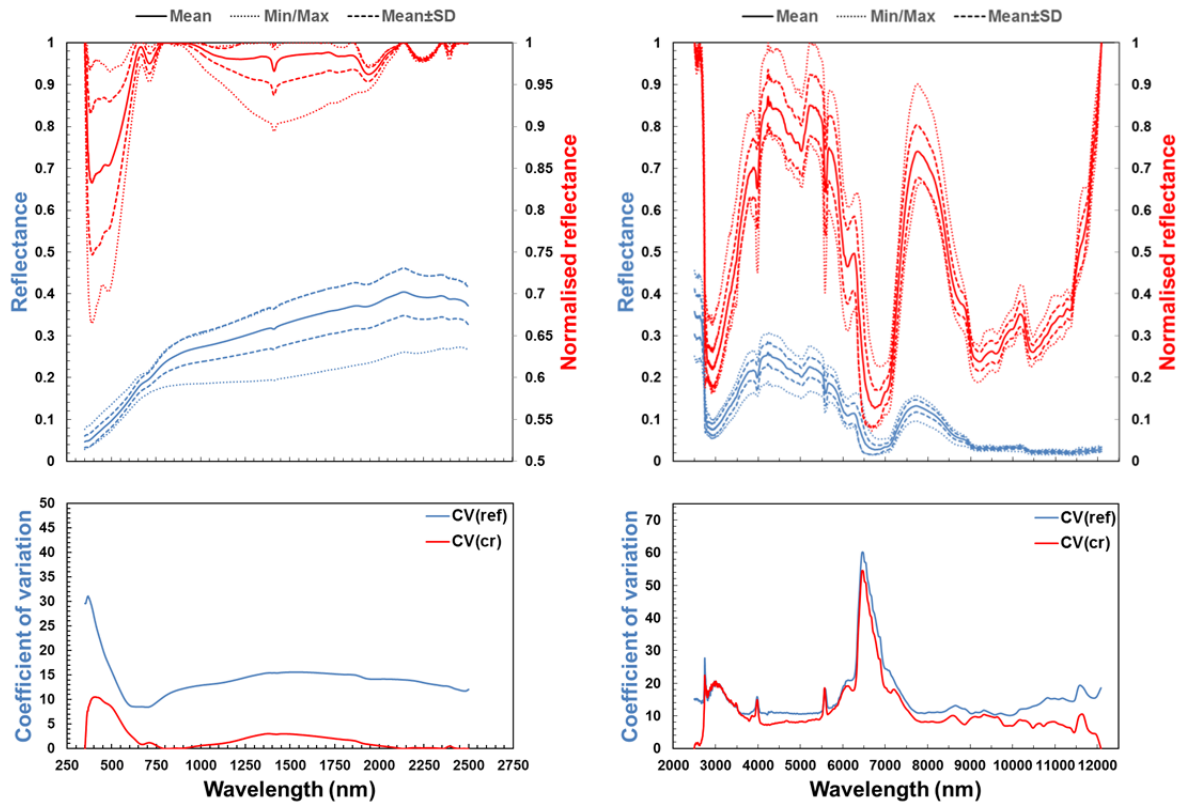


Fig. 5.34a: Variations in the reflectance and continuum removed spectra of the Thomas slag samples (N = 14).

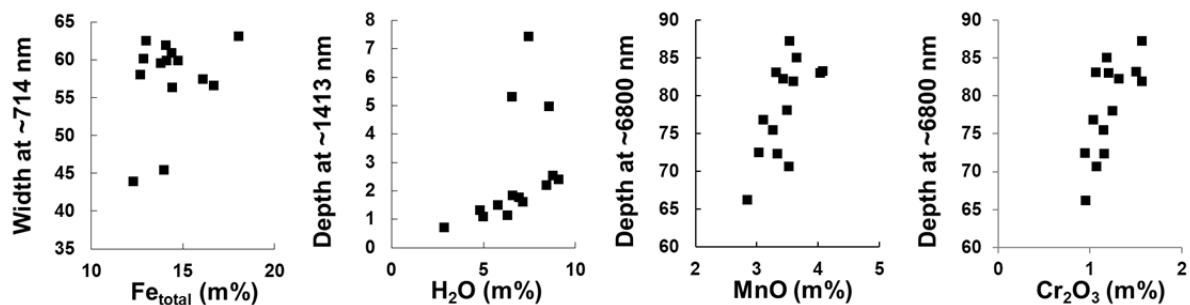


Fig. 5.34b: Spectral feature variations of Thomas slag samples versus contents of chemical constituents (N = 14). Depicted feature depths are relative depths.

5.5.3.4 Stainless Steel Slag

The reflectance spectra of the stainless steel slag samples showed nearly consistent CV_{ref} of ca. 10% in the VNIR/SWIR, again most likely related to minor variations in the CaO content (MN = 46.6 m%, SD = 4.1 m%, Fig. 5.35a). The CV_{cr} was generally very low (< 1%) and the variations in the features due to electronic processes showed no clear relationship to the Fe_{total} content, which was generally low (MN = 1.4 m%, SD = 0.6 m%). For the feature at 1400 nm, a trend of increasing depth with increasing water content (MN = 2.6 m%, SD = 0.8 m%) could be observed (Fig. 5.35b). In the MWIR/LWIR, spectral variations were considerably stronger. The depth of the broad absorption near 2930 nm could be related to the H_2O content and the depth of the sharp absorption at 5566 nm was found to be positively related to the TIC (and CaO) content. The absorption at 6900 nm was deeper for samples with higher TIC content as well. The variations occurring > 8000 nm are possibly due to variations in silicates and subsequently SiO_2 content (MN = 26.6 m%, SD = 2.4 m%).

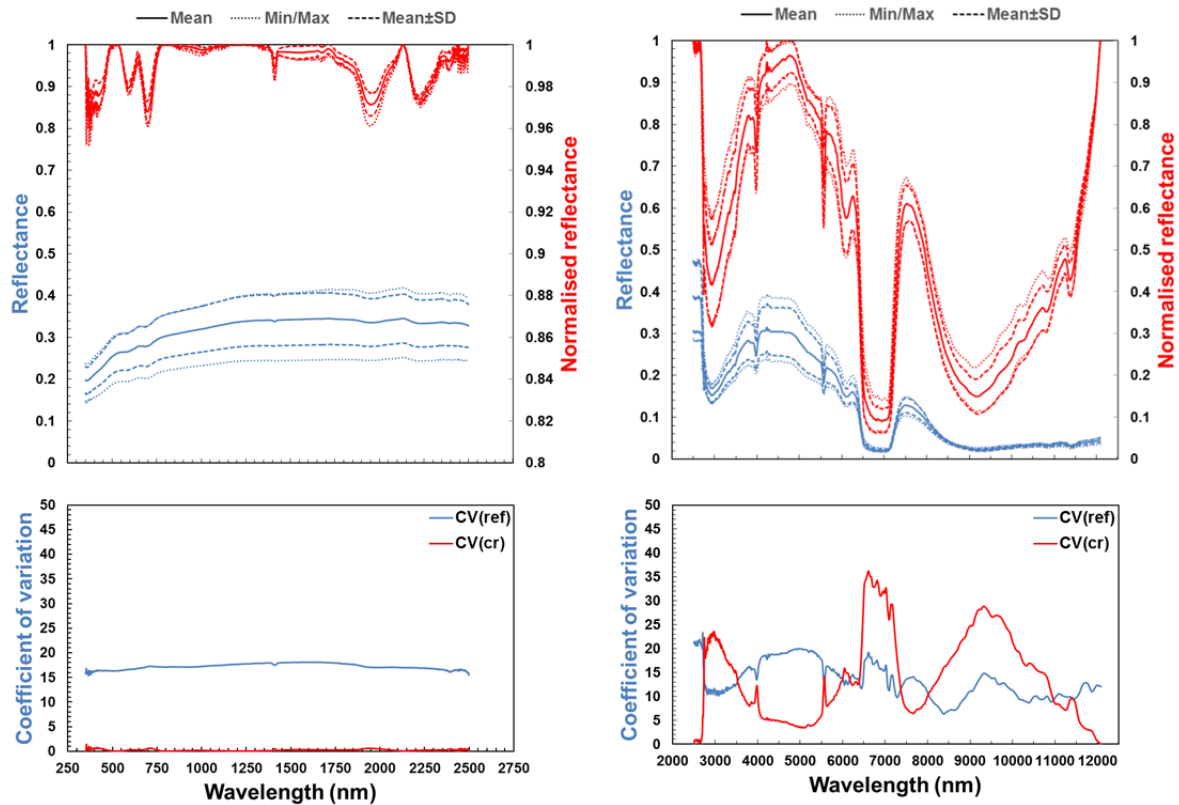


Fig. 5.35a: Variations in the reflectance and continuum removed spectra of the stainless steel slag samples (N = 5).

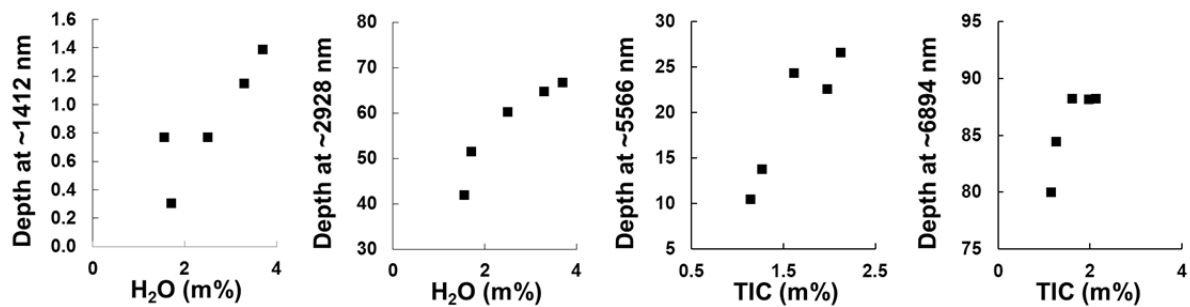


Fig. 5.35b: Spectral feature variations of stainless steel slag samples versus contents of chemical constituents (N = 5). Depicted feature depths are relative depths.

5.5.3.5 Converter Dedusting Sludge

The converter dedusting sludge samples were largely variable in their reflectivity in the VNIR, with CV_{ref} maxima near 490 nm and at the distinct reflectance peak near 750 nm (Fig. 5.36a). The coefficient of variation of the continuum removed spectra showed maxima near 490 nm, corresponding to the major absorption feature observed at these wavelengths. A further maximum in the CV_{cr} curve was observed near 1500 nm related to the large variability of the absorption maximum found at these wavelengths. The depths of these features were found to be strongly related with the total iron content (MN = 27.31 m%, SD = 6.84 m%; Fig. 5.36b). In the MWIR/SWIR spectra, the largest variations in the absorptions as well as in the reflectance intensities were observed for the water feature near 2900 nm, the reflectance minimum near 6900 nm and within the range > 8000 nm. However, the feature at 2925 nm showed no clear relation to the water content of the samples (MN = 10.6 m%, SD = 3.8 m%). The depth of the

absorption at 6870 nm was less strong in samples with higher TIC contents (MN = 20.3 m%, SD = 3.2 m%). In contrast to the other by-product types, the carbonate absorption feature near 11400 nm was stronger pronounced in the CV_{ref} and CV_{cr} , but the depth of this feature showed no discernible relation to the CaO or the TIC content.

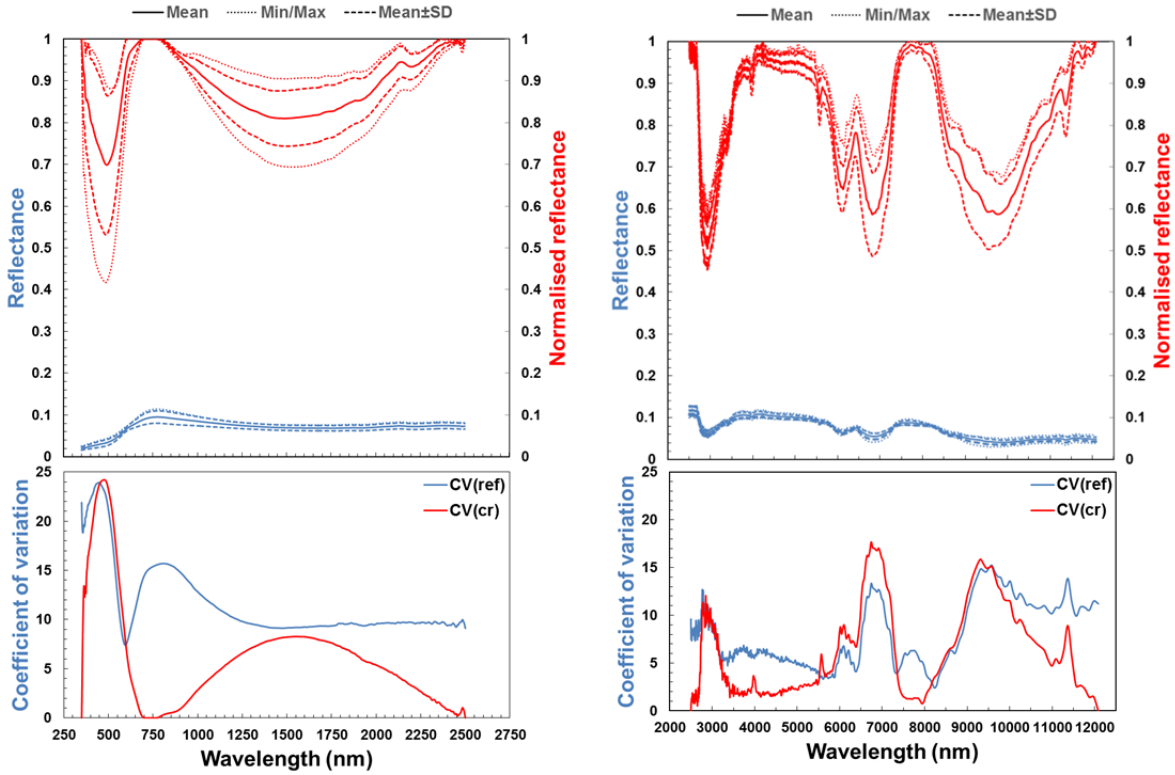


Fig. 5.36a: Variations in the reflectance and continuum removed spectra of the converter sludge samples (N = 7).

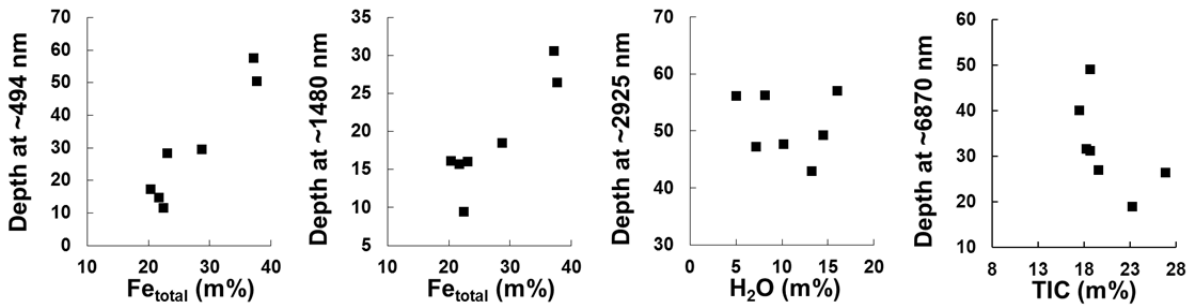


Fig. 5.36b: Spectral feature variations of converter sludge samples versus contents of chemical constituents (N = 5). Depicted feature depths are relative depths.

In summary: Relationships between specific chemical constituents and spectral characteristics present in the spectra of several by-product types could be observed. For example, between the Fe_{total} content and the strength of absorptions occurring in the VNIR spectra of the converter dedusting sludge and the blast furnace slag; between the H_2O content and the features occurring at 1400, 1900 and 2900 nm, as well as relations between TIC - and in some cases also for CaO - for the carbonate features near 3980, 5566 and 6800-6900 nm. In some cases, the observed negative intercorrelations between CaO and TIC (see Chapter 5.3.2) were also reflected by the variations occurring in feature depths. However, these trends were not linear and differ for the various by-product types. This confirms, as discussed in Ch. 5.5.2.1 (see also App. 5.8) and 5.5.2.3, the complex spectral interactions of the manifold components.

5.5.4 Impacts of Moisture and Sample Preparation

A comparison of VNIR/SWIR spectra of unprepared samples with near *in situ* moisture, of air-dried samples and of prepared samples with grain sizes of < 10 mm and $< 90 \mu\text{m}$ is provided in Figures 5.37 and 5.38 using the examples of selected by-products. In most cases, the drying and subsequent preparation of the samples led to changes in their spectral characteristics as known from literature. Here, most of the samples showed a distinctive increase in reflectance after air drying and less strong absorptions at the wavelengths near 1400 and 1900 nm. The lower reflectance of the moist material is related to the absorption of energy caused by water molecules and the mentioned features are the two major absorptions related to molecular water in the VNIR/SWIR (e.g. Hunt 1977, Gupta 2018). Although sample moisture was not quantified, the field observation indicated that the moisture was differing for individual samples. Consequently, the observed increases in reflectance after air drying of the material varied as well.

Crushing and sieving the samples distinctively increased the sample reflectance but decreased the depth of the absorption features. This is related to the increasing amount of surface scattering occurring in powders of small grain sizes compared to the higher amount of volume scattering at coarser particles (e.g. Salisbury et al. 1987, Salisbury et al. 1988, Hapke 2012). The presented blast furnace slag sample showed an increase in reflectance from ca. five to nearly ten percent after air drying (Figure 5.37a). Crushing this sample to a grain size < 10 mm led to a further increase in reflectance of twelve percent while the material $< 90 \mu\text{m}$ showed a reflectance comparable to the air-dried sample, most likely as a result of sample homogenisation. The absorptions at 1400 and 1900 nm were strongest for the moist and weakest for the powdered sample.

The moist GBFS sample showed a reflectance of around 28% at 1100 nm, ca. 20% at 1700 nm and 12% at 2200 nm (Fig. 5.37b). The reflectance partially increased to ca. 35% in the spectrum of the air-dried sample and to ca. 40% in the spectrum of the < 10 mm material. After crushing and sieving the sample to grain sizes $< 90 \mu\text{m}$, the reflectance further increased to overall ~60%, which is more than two times higher compared to the unprepared sample with *in situ* moisture. Again, distinct changes in the feature depths and widths were observed for the absorptions near 1400 and 1900 nm. In addition, the two minor features near 970 and 1200 nm that were present in the spectrum of the moist sample and related to H_2O absorptions (e.g. Bowers and Smith 1972, Baumgardner et al. 1986) disappeared in the spectra of the dried and prepared materials. Such features were also described in Denk et al. (2015) for a spectrum of a moist LF slag.

A Thomas slag sample (Fig. 5.37c) showed a systematic increase in reflectance from ca. ten percent on average for the moist sample to more than 40% for the spectra of the $< 90 \mu\text{m}$ powder. The most distinct changes in the shape of the absorption features were again related to the decrease in moisture during the drying process of the material. Apart from the features at 1400 and 1900 nm, the drying also affected the shape of the prominent feature in the visible light. The spectrum of the unprepared sample exhibited a much wider feature near 1400 nm compared to the relatively narrow feature in the spectrum of the air-dried and further prepared samples. Such effects are due to liquid water and might mask features visible in spectra of material of lower moisture content. Mulders (1987) described the masking effect of water on hydroxyl features in the SWIR of clay minerals in soils. This indicates that qualitative (e.g. the identifiability of mineral phases) as well as quantitative spectral analysis of iron- and steelworks by-products might be hampered when utilising spectra of material with relatively high *in situ* moisture.

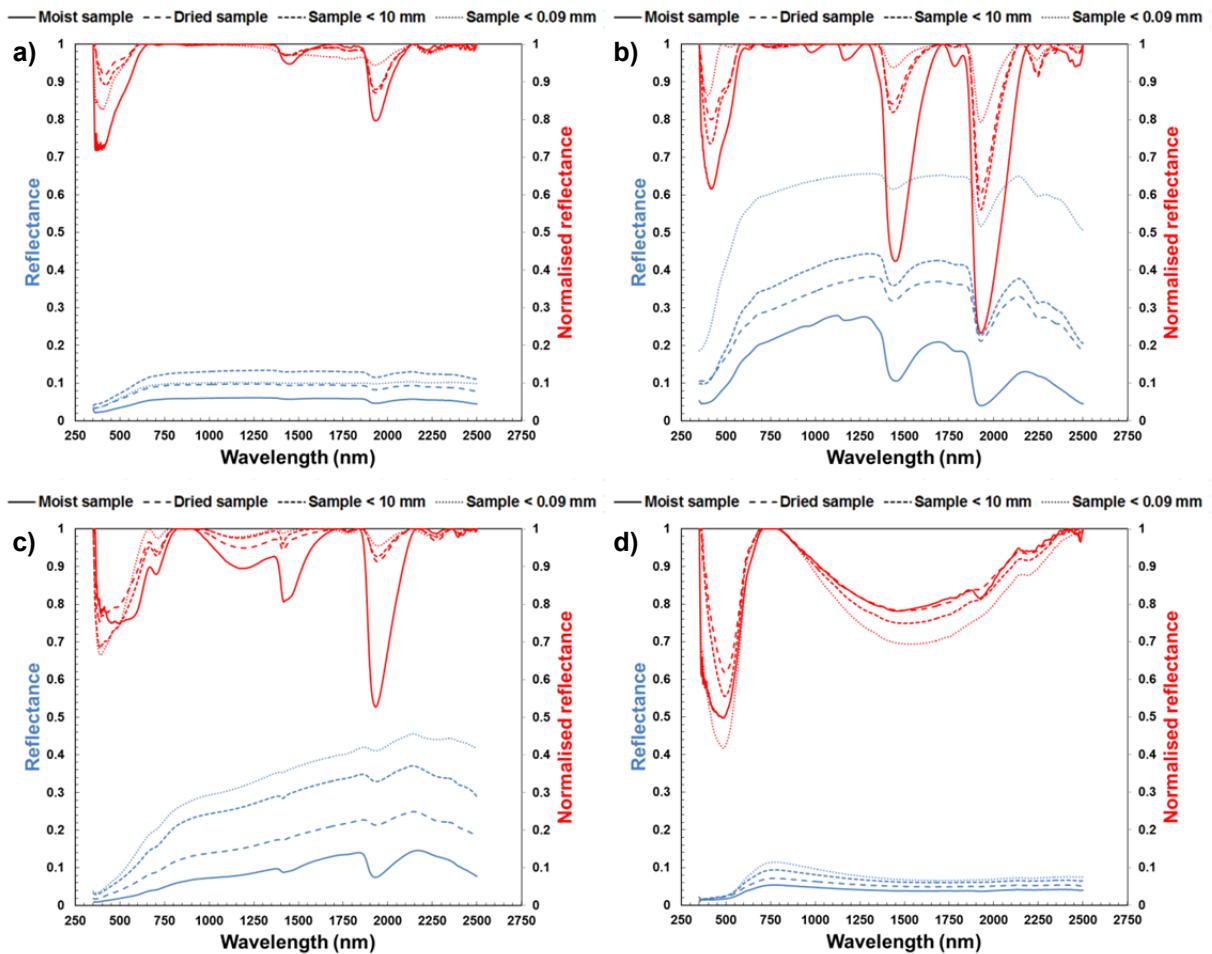


Fig. 5.37: Reflectance and continuum removed spectra of unprepared samples with in situ moisture, air-dried samples and samples < 10 mm and < 90 μm . a) Blast furnace slag, b) GBFS, c) Thomas slag, d) converter dedusting sludge.

The converter dedusting sludge sample (Fig. 5.37d) showed a consistent increase in reflectance after air-drying and subsequent sample homogenisation from ca. five percent to ca. ten percent at the distinct maximum at 750 nm. Except for the more pronounced water feature near 1900 nm in the spectrum of the moist sample, the general spectral shape and the characteristics of the absorption features remained mostly unchanged after drying and preparing the sample. While the powdered samples usually showed the highest reflectance and less deep absorptions, the spectrum of the material < 90 μm also showed the strongest absorptions. This might be explained as the iron-rich converter sludge might comprise opaque materials, which are known to show an opposite spectral behaviour compared to transparent materials (Irons et al. 1989).

For individual samples, a larger variety of grain size fractions was produced, allowing more comprehensive observations of the impact of differing grain sizes on the sample spectra. This is demonstrated for the example of a stainless steel slag sample. Again, the typical spectral behaviour was observed for the VNIR/SWIR region as discussed before and a consistent increase in reflectivity with decreasing grain size could be determined. The absorption features remained mainly unchanged. However, the feature near 600 nm was expressed as a doublet with minima near 590 and 620 nm in the spectra of larger grain size fractions but barely visible in the spectra of fine powdered material (see Fig. 5.38, left plot). As such, the 620 nm feature was hardly visible in the spectra of the prepared sample material < 90 μm presented in Chapter 5.5.1.9.

For the stainless steel slag, also MWIR/LWIR spectra could be acquired of the different grain size fractions (Fig. 5.38, right plot). The finer material was of higher reflectance in general, while only minimal differences could be observed for the wavelength region > 9000 nm. This finding is related to the mentioned wavelength specific effects of volume and surface scattering (Ch. 2.2.3).

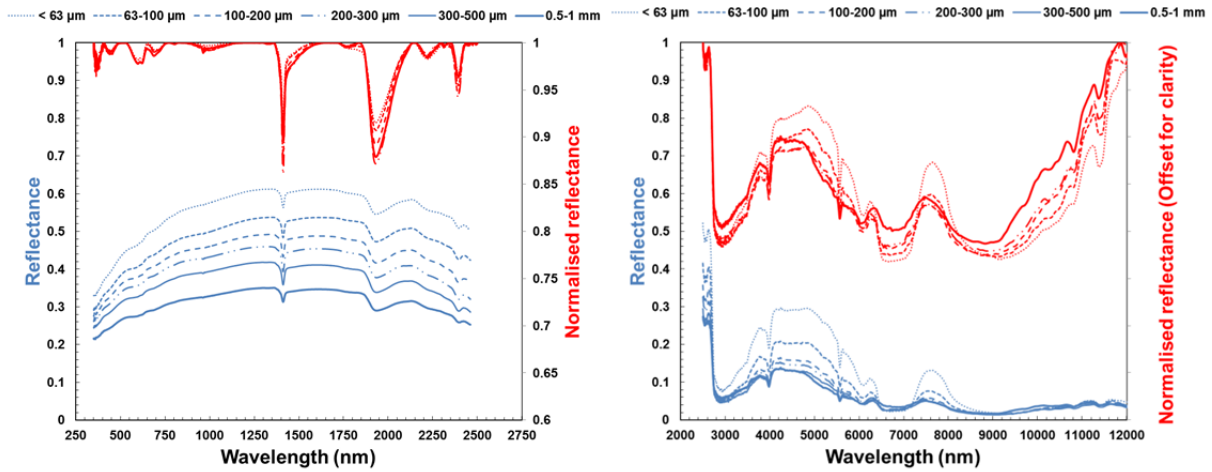


Fig. 5.38: VNIR/SWIR (left) and MWIR/LWIR (right) reflectance and continuum removed spectra of a stainless steel slag sample of different grain sizes.

In contrast to the examples described beforehand, individual samples showed a differing spectral behaviour after drying and sample preparation (Figure 5.39). For example, a sample collected at the excavator prospecting close to the ‘‘Sinterhang’’ at the ‘‘Plateau 272’’ of the Unterwellenborn dump, which most likely represents a mixture of blast furnace slag with other materials, showed a group of absorption features between 1400 and 1550 nm as well as between 2220 and 2270 nm that are caused by water vibrations and typical for gypsum (see e.g. Hunt et al. 1971b, Fig. 5.39a). These features are faintly visible in the spectrum of the moist sample and more pronounced in the spectrum of the air-dried sample. These distinct features are not visible in the spectrum of the < 90 μm material, although gypsum has been verified via XRD analysis to be a minor mineral phase of this sample (see Appendix 5.1 for XRD results, sample 21-3).

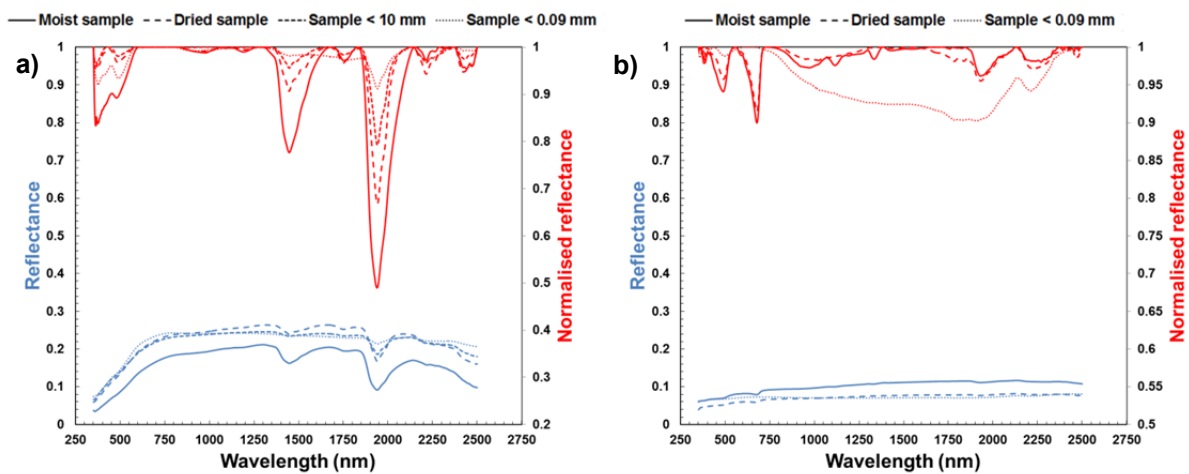


Fig. 5.39: Reflectance and continuum removed spectra of unprepared samples near *in situ* moisture, air-dried samples and crushed samples < 10 mm and < 90 μm . a) Sample most likely representing a mixture comprising blast furnace slag and other materials, b) EAF slag (carbon steelmaking).

This indicates that in individual cases, features of specific mineral phases present in the sample might be spectrally detectable in the unprepared samples but not in the homogenised samples. Possibly, gypsum was formed as a weathering product and formed a spectrally dominant coating that was destroyed by crushing the sample and thus spectrally less dominant in the homogenised powder. Noticeable observations were also made for the EAF slag from carbon steelmaking (Fig. 5.39b). The unprepared sample was of higher reflectance compared to the prepared samples, which might be related to the arrangement of the larger sample specimen and the illumination geometry. Furthermore, distinct changes in the absorption features were observed. The EAF slag exhibited a distinct feature at 680 nm most likely related to Fe^{3+} in the spectra of the moist and the air-dried sample. This feature was not present in the spectrum of the powdered sample anymore. Most likely, an oxide-crust covered the hand-samples, which was not spectrally detectable after sample preparation and homogenisation.

While the impact of weathering was not exhaustively studied within this work, effects of weathering crusts on spectral analyses of rocks and minerals were for example mentioned in Geerken (1991), who pointed out that such crusts might mask spectral characteristics that are visible in prepared samples. Zhou and Wang (2017) discussed weathering products of natural rocks and showed that weathering crusts might be similar or different to the spectral properties of a fresh rock. The examples provided in this chapter indicate that such findings are also true for anthropogenic materials found at iron- and steelworks disposal sites to a certain degree.

According to Salisbury et al. (1988), the spectral features of silicates tend to be nearly diminished at very fine grain sizes and only strong reststrahlen bands remain detectable. This might be a further explanation of the very low reflectance intensities observed for the wavelength range > 9000 nm and the low contrast of the spectral features in this range. However, as demonstrated in Figure 5.38, the general presence of the absorption features and their shape did not substantially change in the exemplarily studied sample at different grain sizes. As already mentioned earlier, spectral features might invert from reflectance peaks to troughs at specific grain sizes (Zaini et al. 2012). However, at least for the example described above, no such effects were observed.

The $< 90 \mu\text{m}$ material mainly used in this study granted an optimal comparability of the samples in terms of their grain size and allowed to optimally link the results of the spectral measurement to the results of the chemical and mineralogical analysis as both were conducted on the same material. However, the described observations imply that the grain size of $< 90 \mu\text{m}$ might not be preferable in every case for qualitative and thus potentially also for quantitative spectral analysis of iron- and steelworks by-products. Coarser fractions, e.g. the commonly used fraction > 2 mm in the case of soil spectroscopy, might be more suitable in certain situations. However, the specific impacts of moisture and grain size on the spectral identification of the mineral phases in iron- and steelworks by-products require further research. To assess the impact of moisture and sample aggregation for the quantification of chemical constituents in iron- and steelworks by-products, the spectra of unprepared and moist samples were additionally used as input for the PLSR model runs (see Chapter 5.6.6).

5.6 Spectral Quantification of Iron- and Steelworks By-Product Constituents

This chapter will present the PLSR results achieved using the VNIR/SWIR, MWIR/LWIR and VNIR-LWIR ranges. Among the plurality of chemical constituents, parameters were selected which were present in considerable amounts in all samples (> 3 m% on average) and for which at least 30 calibration as well as validation samples were available. These parameters comprised major constituents used to characterise iron- and steelworks by-products (e.g. Al₂O₃, CaO, Fe_{total}, MgO, H₂O, TIC). Additionally, Fe₂O₃, FeO and ∑(Mo, Ni, V, Zn, Al, Cr, Fe, Mn) were included, as these are parameters often analysed in spectral-geochemical studies or of potential relevance for assessing the raw material potential of iron- and steelworks by-products. For these constituents, fewer samples were available. The formation of the calibration and validation pools was realised using the DUPLEX sampling algorithm as described in Chapter 4.7.2.1. The mill scale sample was excluded from the PLSR modelling as this spectrum was basically flat, showed noticeable noise and caused outliers and unnecessary model complexity. The applied outlier removal procedure (see Ch. 4.7.2.1) further caused a minor decrease of the available samples compared to the numbers given in previous tables (e.g. Tab. 5.3 in Chapter. 5.3).

5.6.1 Modelling Results Based on VNIR/SWIR Spectra

Based on the VNIR/SWIR data, solid prediction results were obtained for CaO ($R^2_{\text{val}} = 0.78$), Fe_{total} ($R^2_{\text{val}} = 0.81$) and Fe₂O₃ ($R^2_{\text{val}} = 0.83$) (Tab. 5.33). The number of factors used in these models varied from seven to eight. Thus, the model complexity used for predicting these constituents was considered moderate. The RMSE_{val} for CaO was 5.85 m%, for Fe_{total} 3.14 m% and for Fe₂O₃ 2.79 m%. Regarding the ranges of the contents of these constituents (CaO = 54.46 m%, Fe_{total} = 46.90 m%, Fe₂O₃ = 46.56 m%), the achieved prediction errors were considered low. For MgO, the overall model performance was moderate. The validation outcomes for the remaining parameters did not indicate reliable prediction capabilities. Scatter plots showing the PLSR validation results for CaO, Fe_{total} and Fe₂O₃ are given in Fig. 5.40. The residuals of the predicted and observed values were normally distributed for all reliable models ($R^2_{\text{val}} > 0.6$), and the mean of the residuals did not significantly differ from zero. The only exception was CaO. Here, the scatter plot revealed that individual outliers caused this effect.

Tab. 5.20: PLSR results based on VNIR/SWIR spectra for 10 by-product constituents (cal = calibration, val = validation, NF = number of PLSR factors, CR = continuum removal). Residuals were evaluated using Shapiro-Wilk tests for normal distribution (see p_{sh} -values) and Student's t-test for mean analyses (see p_t -values).

	N		Preprocessing	R ²		RMSE		RPD		Residuals	
	N	NF		cal	val	cal	val	cal	val	p_{sh}	p_t
Al₂O₃	49	4	CR	0.53	0.44	3.96	2.80	1.47	1.29	0.74	0.73
CaO	50	8	Absorbance	0.75	0.78	7.37	5.85	2.03	2.01	0.40	0.02
Fe_{total}	47	7	Absorbance	0.76	0.81	4.45	3.14	2.07	2.20	0.38	0.09
Fe₂O₃	18	7	CR	0.70	0.83	4.68	2.79	1.87	2.13	0.34	0.03
FeO	17	4	CR	0.67	0.39	3.46	1.67	1.80	1.11	0.71	0.90
H₂O	47	4	Absorbance	0.27	0.17	3.52	3.71	1.18	1.05	0.00	0.21
MgO	49	4	CR	0.50	0.62	2.08	1.69	1.42	1.62	0.68	0.49
SiO₂	48	6	Reflectance	0.48	0.46	9.64	7.59	1.40	1.35	0.02	0.75
TIC	49	4	Absorbance	0.46	0.49	5.10	3.96	1.38	1.40	0.69	0.68
∑metals*	21	3	Absorbance	0.55	0.28	6.76	5.77	1.52	1.18	0.05	0.85

*∑(Mo, Ni, V, Zn, Al, Cr, Fe, Mn)

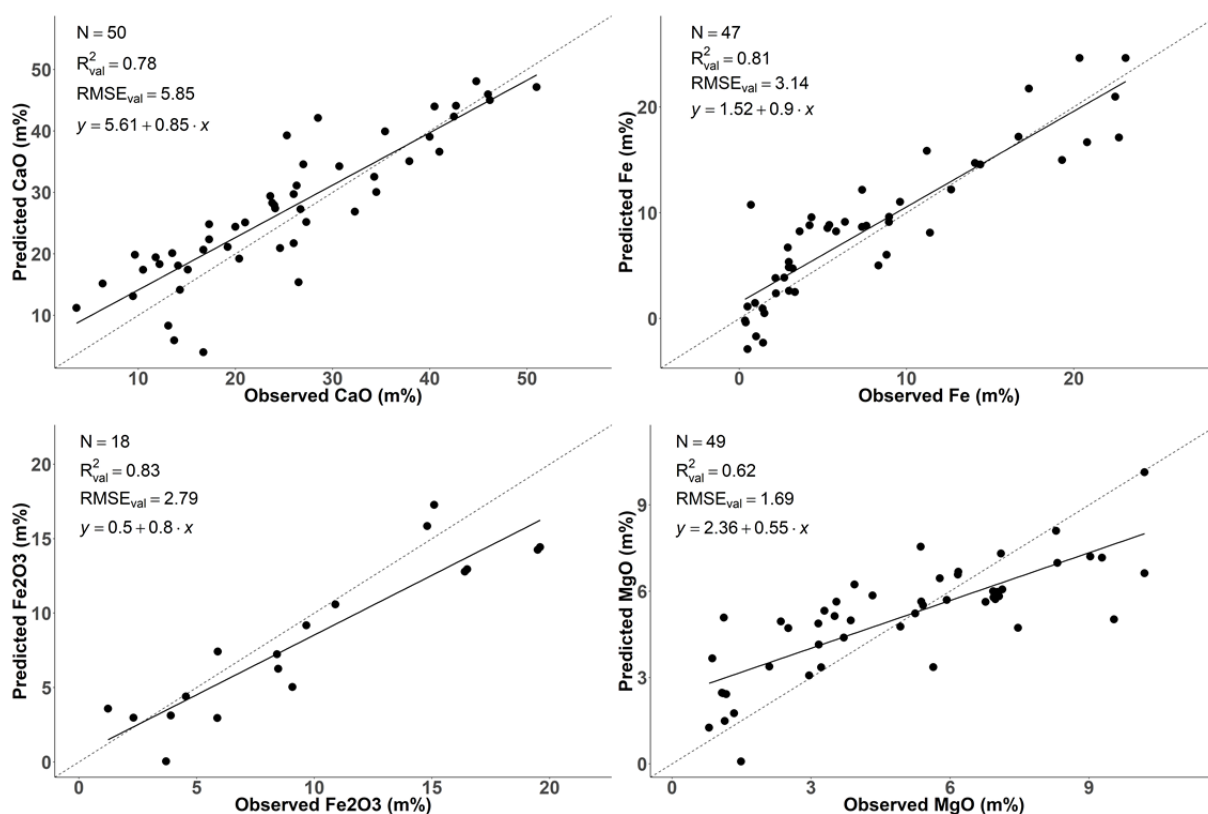


Fig. 5.40: PLSR results based on VNIR/SWIR spectra for selected iron- and steelworks by-product constituents.

5.6.2 Modelling Results Based on MWIR/LWIR Spectra

PLSR results obtained using the MWIR/LWIR spectra are provided in Table 5.34. In comparison to the VNIR/SWIR predictions, distinctively better validation results were observed for Al_2O_3 ($R_{val}^2 = 0.68$), SiO_2 ($R_{val}^2 = 0.82$), TIC ($R_{val}^2 = 0.77$) and $\sum(\text{Mo, Ni, V, Zn, Al, Cr, Fe, Mn})$ ($R_{val}^2 = 0.78$), indicating more powerful prediction capabilities of PLSR models based on the mid- and longwave infrared spectra for these constituents. The prediction results for CaO could be improved ($R_{val}^2 = 0.89$, $RMSE_{val} = 4.74 \text{ m}\%$), for which a less complex model (5 factors instead of 8) was required compared to the VNIR/SWIR range. For Al_2O_3 , an increase in model performance ($R_{val}^2 = 0.68$, $RMSE_{val} = 2.28 \text{ m}\%$) was obtained at the cost of a more complex PLSR model (8 factors instead of 4). The results for Fe_{total} were only slightly worse ($R_{val}^2 = 0.79$, $RMSE_{val} = 3.27 \text{ m}\%$) but fewer factors were necessary to build this prediction model. In contrast, the predictive capabilities for Fe_2O_3 were distinctively worse compared to the VNIR/SWIR spectra based PLSR models. Thus, most of the constituents could be more precisely estimated using MWIR/LWIR data, but individual components (Fe_2O_3) could be distinctively better estimated based on VNIR/SWIR data. Scatter plots for the six best prediction results obtained using the MWIR/LWIR range are given in Figure 5.41. For CaO, the trend and target lines nearly matched, indicating a well fitted and robust prediction model. For the other parameters the slope and offset of the trend lines showed larger deviations from the expected line. Comparable to the results obtained based on the VNIR/SWIR spectra driven PLSR models, the predicted values for samples with very low contents were negative in a few cases (Al_2O_3 , Fe_{total}), which is a result of the prediction uncertainty.

Tab. 5.21: PLSR results based on MWIR/LWIR spectra for 10 by-product constituents (cal = calibration, val = validation, NF = number of PLSR factors, CR = continuum removal). Residuals were evaluated using Shapiro-Wilk tests for normal distribution (see p_{sh} -values) and Student's t-test for mean analyses (see p_t -values).

	N		Preprocessing	R ²		RMSE		RPD		Residuals	
	N	NF		cal	val	cal	val	cal	val	p_{sh}	p_t
Al ₂ O ₃	49	8	Absorbance	0.74	0.68	2.53	2.28	1.98	1.72	0.06	0.88
CaO	49	5	Absorbance	0.88	0.89	9.31	4.04	2.93	2.91	0.72	0.60
Fe _{total}	47	5	Absorbance	0.70	0.79	5.27	3.27	1.86	2.12	0.59	0.13
Fe ₂ O ₃	18	4	Absorbance	0.71	0.28	3.57	5.78	1.90	1.00	0.35	0.04
FeO	17	2	CR	0.77	0.27	1.28	1.89	2.17	1.12	0.03	0.70
H ₂ O	46	2	Reflectance	0.46	0.39	3.33	2.98	1.37	1.28	0.77	0.77
MgO	48	6	Absorbance	0.65	0.50	2.04	1.97	1.70	1.30	0.02	0.03
SiO ₂	47	4	CR	0.70	0.82	7.11	4.44	1.83	2.33	0.54	0.54
TIC	48	6	Absorbance	0.72	0.77	3.54	3.00	1.92	2.00	0.03	0.07
∑metals*	21	3	CR	0.63	0.78	5.89	3.42	1.68	2.15	0.84	0.94

*∑(Mo, Ni, V, Zn, Al, Cr, Fe, Mn)

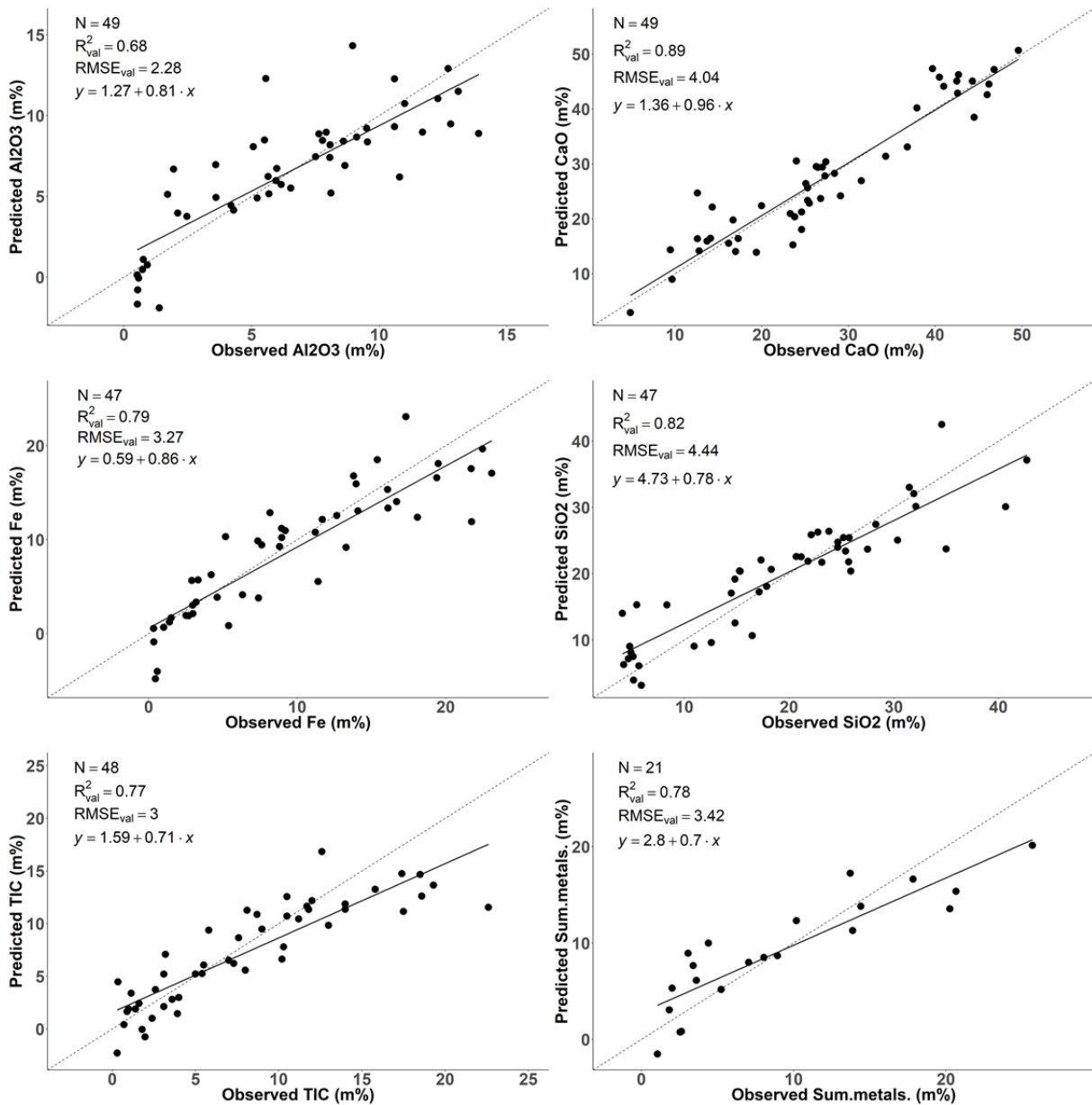


Fig. 5.41: PLSR results based on MWIR/LWIR spectra for selected iron- and steelworks by-product constituents.

5.6.3 Modelling Results Based on VNIR-LWIR Spectra

Table 5.35 provides the best PLSR modelling results obtained using the combined information of the VNIR/SWIR and the MWIR/LWIR range. The most solid prediction models were obtained for CaO ($R^2_{\text{val}} = 0.95$), Fe_{total} ($R^2_{\text{val}} = 0.90$), TIC ($R^2_{\text{val}} = 0.85$), SiO_2 ($R^2_{\text{val}} = 0.80$) and $\sum(\text{Mo, Ni, V, Zn, Al, Cr, Fe, Mn})$ ($R^2_{\text{val}} = 0.80$). Validation results with an R^2_{val} between 0.62 and 0.72 were achieved for the constituents Al_2O_3 , Fe_2O_3 and MgO. In contrast to the model performances for H_2O utilising either the VNIR/SWIR or the MWIR/LWIR range, the results from PLSR modelling based on the combined ranges lead to moderate results ($R^2_{\text{val}} = 0.56$). For FeO, the predictive performance could be improved as well. However, the validation results still did not indicate a robust prediction capacity. The number of factors (components) used for the models varied between one and nine, whereas higher numbers of factors indicate more complex models. The best CaO calibration model was slightly more complex (six factors) compared to the MWIR/LWIR based model (5 factors). Thus, the improvements in model performance for predicting individual constituents in the models using the combined wavelength ranges came at the cost of higher model complexity in some cases.

Tab. 5.22: PLSR results based on VNIR-LWIR spectra for 10 by-product constituents (cal = calibration, val = validation, NF = number of PLSR factors, CR = continuum removal). Residuals were evaluated using Shapiro-Wilk tests for normal distribution (see p_{sh} -values) and Student's t-test for mean analyses (see p_{t} -values).

	N		Preprocessing	R ²		RMSE		RPD		Residuals	
	N	NF		cal	val	cal	val	cal	val	p_{sh}	p_{t}
Al₂O₃	49	5	CR	0.71	0.67	3.47	2.29	1.88	1.72	0.24	0.13
CaO	49	6	Absorbance	0.91	0.95	6.21	2.82	3.44	4.54	0.65	0.94
Fe_{total}	47	5	Absorbance	0.76	0.90	4.79	2.21	2.06	3.08	0.20	0.33
Fe₂O₃	18	4	CR	0.86	0.72	3.58	2.65	2.72	1.86	0.63	0.24
FeO	17	1	Reflectance	0.53	0.47	1.29	2.46	1.50	1.02	0.21	0.01
H₂O	46	5	CR	0.54	0.56	3.21	2.57	1.50	1.46	0.17	0.06
MgO	48	9	Reflectance	0.61	0.62	2.56	1.76	1.62	1.43	0.17	0.57
SiO₂	47	9	Absorbance	0.86	0.80	7.89	4.07	2.67	2.25	0.20	0.50
TIC	48	7	CR	0.73	0.85	4.32	2.14	1.95	2.62	0.32	0.54
$\sum\text{metals}^*$	21	4	CR	0.71	0.80	4.73	3.26	1.90	2.20	0.38	0.27

* $\sum(\text{Mo, Ni, V, Zn, Al, Cr, Fe, Mn})$

For the PLSR models assumed to provide solid estimations ($R^2_{\text{val}} > \text{ca. } 0.8$), the root mean square errors (RMSE_{val} , see Table 5.35) were ca. 2 m% for TIC and Fe_{total} , and between ca. 2.8 and 4.1 m% for CaO, SiO_2 and $\sum(\text{Mo, Ni, V, Zn, Al, Cr, Fe, Mn})$. This is considered low and thus indicates suitable predictive capabilities for these constituents. In general, RPD values of 2-2.5 are assumed to provide suitable “approximate quantitative predictions”, models with RPD values of 2.5-3 can be considered as good and RPD values > 3 indicate high prediction capabilities (see Zornoza et al. 2008). According to this classification and regarding the calibration as well as the validation accuracies of the most promising results obtained in this set-up, the predictive capabilities of the formed PLSR models can be considered in the range of “moderate” (Fe_{total} , SiO_2 , TIC, $\sum(\text{Mo, Ni, V, Zn, Al, Cr, Fe, Mn})$) to very precise (CaO). It should be mentioned at this point that the utilisation of the RPD for assessing predictive performances of statistical models is critically discussed by individual authors (Minasny and McBratney 2013).

The scatterplots of predicted and observed values are provided in Figure 5.42. These plots indicate good fitted models for CaO, TIC and SiO₂, as the trend lines nearly fit the target lines. The outcome of the statistical analysis of the model residuals showed that all residuals were normally distributed and their mean value did not significantly differ from zero (see p_{sh} and p_t values in Tab. 5.35). This means, that the models do not contain systematic errors, e.g. systematic over- or underestimations, which confirms the robustness of the developed prediction models.

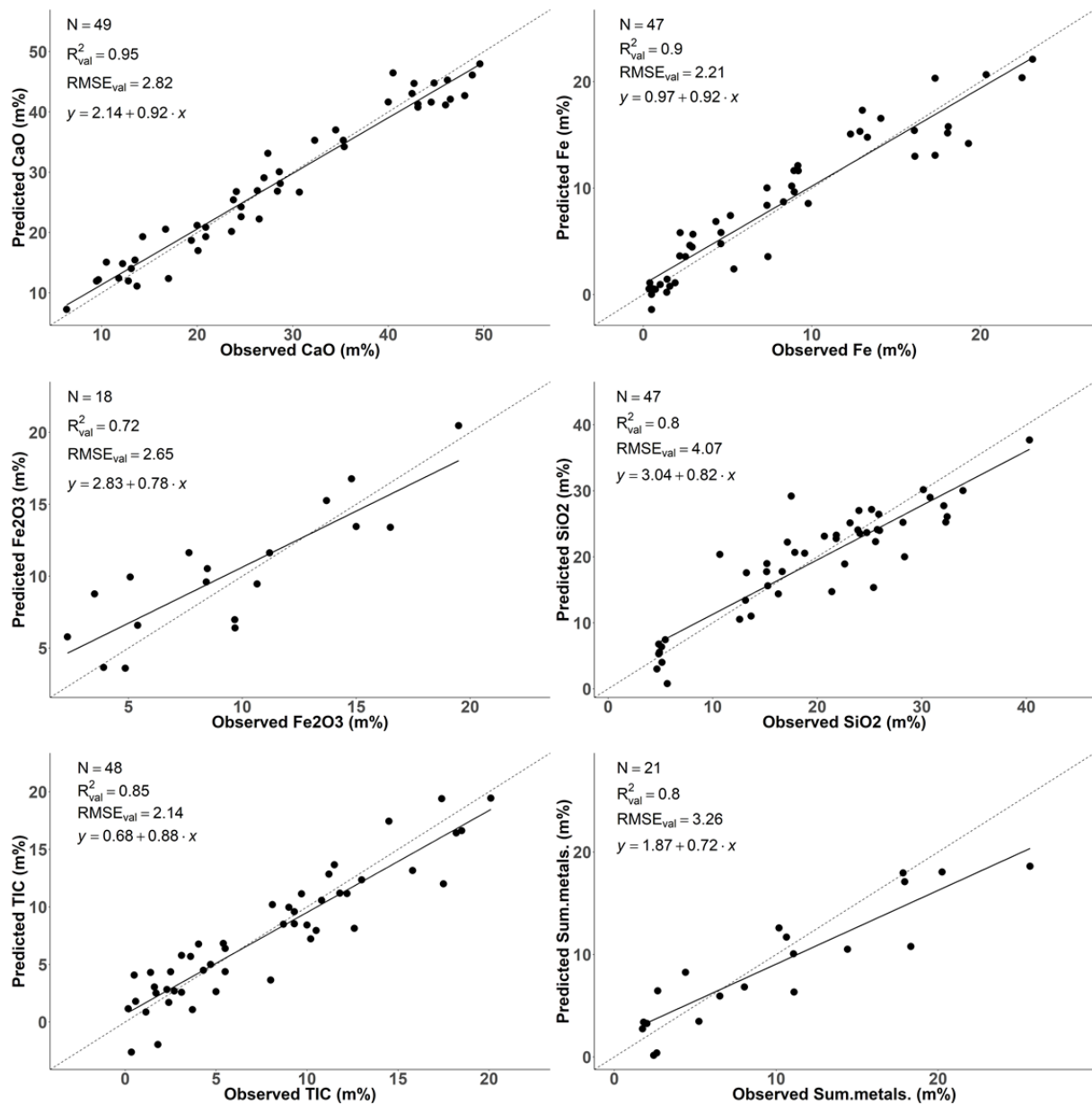


Fig. 5.42: PLSR results based on VNIR-LWIR spectra for selected iron- and steelworks by-product constituents. The spectral preprocessings correspond to Table 5.35.

5.6.4 Important Variables for the Prediction

This chapter will focus on the importance of the predictor variables (i.e. the wavelengths), for the PLSR models based on VIP scores (Variable Importance in Projection, see Chapter 4.7.3). As the complete analysis of the important variables for the entirety of all calculated PLSR models, considering all chemical constituents, preprocessings and wavelength ranges, is out of scope of this work, the following paragraphs will provide the VIP scores for a selection of relevant chemical parameters for which the best models were obtained per wavelength range (Fig. 5.43, see Appendix A5.13 for further plots). For orientation, a horizontal line at VIP scores of one is added to the plots, as this value is commonly used to separate important from less important variables for the prediction (see e.g. Liu et al. 2014, Kawamura et al. 2017, Pinheiro et al. 2017).

Among the plurality of different wavelength ranges found to be influential in the predictions of the various constituents, several wavelengths could be assigned to specific absorption features discussed earlier. As such, the absorption features near 1400 and 1900 nm, which are typically associated with OH and H₂O vibrations (e.g. Hunt 1980), respectively, were found to be largely influential in the VNIR/SWIR PLSR models for estimating Al₂O₃ and of less relevance for modelling CaO, Fe₂O₃ and SiO₂ (Fig. 5.43). These wavelengths were of subordinate relevance in the models calculated using the combined spectral ranges. The visible light (and partially the near infrared) was relevant for the prediction of Fe_{total}, Fe₂O₃ and $\sum(\text{Mo, Ni, V, Zn, Al, Cr, Fe, Mn})$. This is plausible as metals are known to show distinct absorptions due to electronic processes in the VNIR range or indirectly affect the VIS, e.g. the distinct drop in reflectance due to iron (see Chapter 2.2.2.1). As discussed earlier, it has to be considered that most of the samples contain a variety of different metals in larger quantities and the observed peaks in the VIP scores might reflect potentially overlapping features or contributions from various electronic processes, which hampers the assignment to individual metals. The PLSR predictions for the other parameters based on VNIR/SWIR spectra were mainly driven by VNIR wavelengths as well (see Fig. 5.43), indicating indirect relations of these chemical constituents to this spectral region.

The important wavelengths in the MWIR/LWIR were found to be much more variable compared to the VNIR/SWIR. In this range, distinct relations between peaks in the VIP scores and absorption features in the spectra were found as well. As such, the prominent H₂O features near 2900 and 6100 nm (e.g. Hunt 1977) were found to be influential for the prediction of various constituents (e.g. TIC). The sharp peak in the VIP-scores near 2740 nm resembles most likely the fundamental hydroxyl feature. Even though hardly visible in most of the sample spectra, the OH fundamental was interpreted to be of considerable relevance for the prediction of e.g. Fe₂O₃, TIC and the summed metal parameter. Minor maxima in the VIP scores near 3890 and 5560 nm, the broader maximum occurring near 7000 nm and the peak close to 11400 nm are corresponding to carbonate features (see Ch. 5.5.2.2). These wavelengths were relevant for predicting e.g. CaO and TIC, which are considered to be related to the carbonate content. The VIP scores indicated that the VNIR/SWIR range is of distinctly lower importance for the prediction of SiO₂ compared to the MWIR/LWIR range in the models using the combined wavelength ranges. This is plausible as silicates are known to show distinct features preferably in mid- and longwave infrared (see Chapters 2.2.2.2 and 5.5.2.2). In fact, the models for the prediction of SiO₂ were mainly driven by the wavelength range > 6000 nm. The PLSR predictions of Fe_{total} based on the MWIR/LWIR and VNIR-LWIR range were driven mainly by wavelengths near 6000 nm and between ca. 8000 and 10000 nm.

5.6 Spectral Quantification of Iron- and Steelworks By-Product Constituents

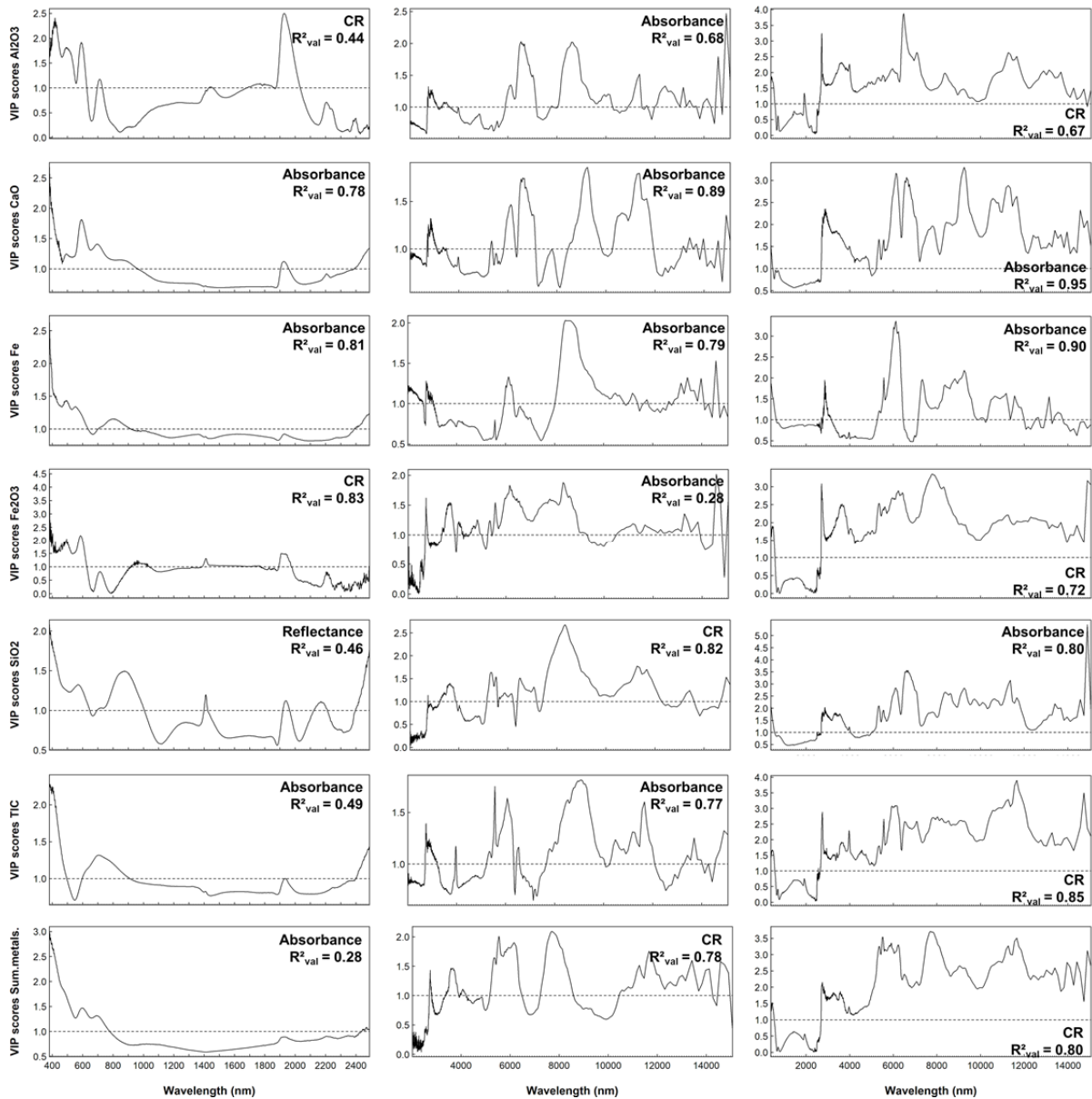


Fig. 5.43: VIP scores for the best PLSR models obtained for Al_2O_3 , CaO, Fe_{total} , Fe_2O_3 , SiO_2 , TIC and $\sum(Mo, Ni, V, Zn, Al, Cr, Fe, Mn)$ using VNIR/SWIR, MWIR/LWIR as well as VNIR-LWIR spectra. R^2_{val} values and the preprocessing type (CR = continuum removal) utilised for building the specific models are additionally provided.

Overall, the interpretation of the VIP scores emphasised the findings described earlier in this work. As such, only moderate correlations between the contents of the chemical constituents and the depths of spectral features, which were shared by the majority of samples, were found (Chapter 5.5.2.3). In some cases, distinct trends between feature characteristics and chemical constituents were noticeable while the variations of the same features could not be related to identical constituents for other by-products types (see Chapter 5.5.3). Thus, the VIP scores and as such the influential wavelengths for the prediction of the chemical constituents reflected the large heterogeneity of material types with varying spectral signatures and largely differing composition. Consequently, the influential wavelengths as determined using the VIP scores are not necessarily related to individual or multiple absorption features present in the spectra and might reflect purely statistical relationships to a certain degree. The VIP scores provide a basis for the selection of specific variables, i.e. wavelengths, for a subsequent model optimisation. However, the overall model complexity was already considered moderate (see Ch. 5.6.1-5.6.3).

PLSR is supposedly robust to noise and thus only the lower and upper wavelengths of the spectra were removed in order to use as much spectral information as possible. However, noise might have contributed to the models especially in the range > 12000 nm. It must be further considered that the VIP scores of the models are different depending on the preprocessing applied to the spectra, making the interpretation of important variables for the predictions more complex. In order to avoid altering the original spectral information recorded by two different spectrometers used in this work, no adjustment of the VNIR/SWIR and MWIR/LWIR data was conducted to match the border area of the spectra. While not observed in the VIP scores, these regions might have been influential for the prediction in individual cases. An adjustment of the spectra to match the reflectance values might reduce this effect but would alter the original data.

5.6.5 Summarised Model Assessment and Discussion

The predictive capabilities (R^2_{val} , RMSE_{val}) of the PLSR models based on the VNIR/SWIR, MWIR/LWIR or the VNIR-LWIR data are summarised in Table 5.36. The models based on VNIR/SWIR data showed a better performance for predicting Fe_{total} and Fe_2O_3 than the MWIR/LWIR models. This can be explained by the fact that metal ions are known to produce features due to electronic processes in the VNIR (see Chapters 2.2.2.2 and 5.5.2.2). The high influence of the VNIR wavelengths as visible in the VIP scores in VNIR/SWIR models (see Chapter 5.6.4) underlines this assumption. Distinctly better results with the MWIR/LWIR range were achieved for SiO_2 , TIC and the summed metal parameter. An explanation for the better predictive capabilities for the estimation of the SiO_2 content is that silicates are known to show distinct spectral characteristics mainly in the MWIR-LWIR (e.g. Hunt 1980). The superior performance of the models based on MWIR/LWIR data for predicting the TIC content is related to the presence of various carbonate absorption features in the MWIR/LWIR range. In contrast, the VNIR/SWIR spectra did not exhibit distinct characteristics related to carbonates (see Chapter 5.5.2.2). Less strong but still considerable improvements were achieved for predicting Al_2O_3 and CaO. The combination of the VNIR/SWIR and MWIR/LWIR ranges provided larger R^2_{val} in six cases and lower RMSE_{val} for seven of the 10 studied constituents. As mentioned earlier, this increase in prediction accuracy comes at the cost of higher model complexity in some cases, i.e. higher numbers of factors used in the PLSR models.

Tab. 5.23: R^2_{val} and RMSE_{val} of the PLSR models using VNIR/SWIR, MWIR/LWIR or VNIR-LWIR spectra.

Parameter	R^2_{val}			RMSE_{val} (m%)		
	VNIR/SWIR	MWIR/LWIR	VNIR-LWIR	VNIR/SWIR	MWIR/LWIR	VNIR-LWIR
Al_2O_3	0.44	0.68	0.67	2.80	2.28	2.29
CaO	0.78	0.89	0.95	5.85	4.04	2.82
Fe_{total}	0.81	0.79	0.90	3.14	3.27	2.21
Fe_2O_3	0.83	0.28	0.72	2.79	5.78	2.65
FeO	0.39	0.27	0.47	1.67	1.89	2.46
H_2O	0.17	0.39	0.56	3.71	2.98	2.57
MgO	0.62	0.50	0.62	1.69	1.97	1.76
SiO_2	0.46	0.82	0.80	7.59	4.44	4.07
TIC	0.49	0.77	0.85	3.96	3.00	2.14
$\sum \text{metals}^*$	0.28	0.78	0.80	5.77	3.42	3.26

* $\sum(\text{Mo, Ni, V, Zn, Al, Cr, Fe, Mn})$

The number of studies available on the quantitative prediction of chemical constituents of large heterogeneous pools of iron- and steelworks by-products utilising reflectance spectra covering different wavelength ranges is limited. Therefore, the observed results are briefly discussed

considering studies on soil parameters. Various studies found better predictions for metal constituents like Cd, Cu, Pb and Zn utilising MWIR/LWIR data compared to the VNIR/SWIR range, while for other parameters opposing results were obtained (e.g. Siebielec et al. 2004, Dong et al. 2011). In works of other authors, better capabilities for estimating the contents of metallic trace elements based on VNIR/SWIR spectra were found (e.g. Moros et al. 2009, Song et al. 2012). In Riedel et al. (2018), the prediction results for various metals were distinctively better in the models based on MWIR/LWIR spectra compared to the results achieved using VNIR/SWIR spectra in PLSR models. In this work, the results for $\sum(\text{Mo, Ni, V, Zn, Al, Cr, Fe, Mn})$ were more promising based on MWIR/LWIR spectra models, while Fe_{total} and Fe_2O_3 could be better predicted using the VNIR/SWIR data. In Eisele (2014), promising results for predicting SiO_2 and Al_2O_3 using MWIR/LWIR data were found, which was observed in this work as well. The solid results obtained for predicting CaO and MgO in this study are comparable to the results obtained in Picón et al. (2017), despite that study focussed solely on LF slag.

In summary, the outcome of the PLSR modelling conducted in this thesis demonstrated that attention must be paid when providing generalised recommendations on which wavelength range to use for the spectral estimation of chemical constituents typically found in iron- and steelworks by-products. It was found that the successful quantitative assessment of such parameters is dependent on the specific chemical constituent to be estimated. According to the observed results, the robust prediction of individual constituents requires MWIR/LWIR data, especially for SiO_2 , TIC and $\sum(\text{Mo, Ni, V, Zn, Al, Cr, Fe, Mn})$. In contrast, PLSR models based on the VNIR/SWIR spectra are suggested to be used for predicting Fe_2O_3 . For other constituents, e.g. CaO and Fe_{total} , reliable predictions can be achieved using either the VNIR/SWIR range or the MWIR/LWIR. For most of the studied chemical constituents, the highest prediction accuracies in terms of R^2_{val} and RMSE_{val} were obtained using the combined VNIR/SWIR and MWIR/LWIR data. However, while the differences in performance of the PLSR models based on either the VNIR/SWIR or the MWIR/LWIR data were substantial for various constituents, the observed improvements after combination of the two spectral ranges were less distinct.

The PLSR results further indicated that model outcomes vary not only depending on the utilised wavelength range but also on the preprocessing applied to the spectra. The models fitted to preprocessed spectra outperformed the PLSR models utilising the unmodified reflectance data in most cases. Here, different preprocessings provided differing results for the individual wavelength ranges. This can be explained, as one parameter might be better estimated based on the general reflectance or absorbance properties e.g. in the VNIR/SWIR, while continuum removal might highlight relevant spectral features in the MWIR/LWIR wavelength range. However, making generalised statements or recommendations for which preprocessing to use is difficult. These findings are in agreement with observations made in various studies focussing on the spectral quantification of soil parameters. Here, the modelling results varied depending on the spectral preprocessing and the wavelength range used as well (e.g. Kooistra et al. 2001, Moros et al. 2009, Riedel et al. 2018). The observations within the specific set-up applied in this work, comprising a heterogeneous sample pool and different wavelength ranges, indicated that the answer on the question “which preprocessing to choose” is case-dependent. The utilisation of absorbance and continuum removed spectra in addition to the unmodified reflectance spectra was found recommendable in order to assess the full potential of VNIR/SWIR and MWIR/LWIR data for quantifying typical constituents of iron- and steelworks by-products.

5.6.6 Modelling Results Based on Spectra of Unprepared Samples

This work focussed on the utilisation of VNIR/SWIR and MWIR/LWIR laboratory reflectance spectra of homogenised samples in order to provide a better understanding of the general potential of such data for quantifying chemical constituents of iron- and steelworks by-products. To assess the predictive capabilities of PLSR models based on spectra of materials closer to field conditions, model runs were conducted based on spectra of sample material with near *in situ* moisture as well as of air-dried but not further prepared material in addition to the models based on the spectra of homogenised powders < 90 µm. As MWIR/LWIR spectra could only be acquired of the powdered samples (see Chapter 4.6.1.2), this approach was realised solely on VNIR/SWIR spectra. Unprepared samples that were only present in form of larger unique specimen were excluded from this approach, resulting in partly lower numbers of samples compared to the models presented in Ch. 5.6.1-5.6.3. The focus was put on Al₂O₃, CaO, Fe_{total} and MgO, as these are relevant chemical constituents for characterising by-products associated with the iron and steel industry and moderate to promising prediction results for these constituents were achieved on the spectra of powdered sample material.

Based on the spectra of air-dried but not further prepared samples, solid modelling results could be obtained for CaO ($R^2_{\text{val}} = 0.76$; Table 5.37). For Al₂O₃ and MgO, the results were moderate to promising ($R^2_{\text{val}} = 0.57$ and $R^2_{\text{val}} = 0.67$, respectively). While promising calibration results were obtained for Fe_{total} ($R^2_{\text{cal}} = 0.60$), the validation results did not indicate reliable predictive capabilities ($R^2_{\text{val}} = 0.41$). Scatter plots for the two best results are given in Figure 5.44. The RMSE_{val} for CaO was 5.65 m%. This is nearly identical to the results achieved on the spectra of the < 90 µm material and indicates that reliable estimations for this constituent can also be made using spectra of air-dried but not further prepared material.

Tab. 5.24: PLSR results based on spectra of air-dried samples for selected chemical parameters (cal = calibration, val = validation, F = number of PLSR factors, CR = continuum removal). Residuals were evaluated using Shapiro-Wilk tests for normal distribution (see p_{sh} -values) and Student's t-test for mean analyses (see p_t -values).

	N		Preprocessing	R ²		RMSE		RPD		Residuals	
	N	F		cal	val	cal	val	cal	val	p_{sh}	p_t
Al ₂ O ₃	35	5	Absorbance	0.61	0.57	3.78	2.59	1.61	1.52	0.62	0.30
CaO	36	6	Absorbance	0.80	0.76	9.12	5.65	2.29	1.94	0.97	0.04
Fe _{total}	34	2	CR	0.60	0.41	4.65	5.74	1.61	1.30	0.01	0.39
MgO	35	6	CR	0.63	0.67	2.04	1.63	1.66	1.69	0.69	0.88

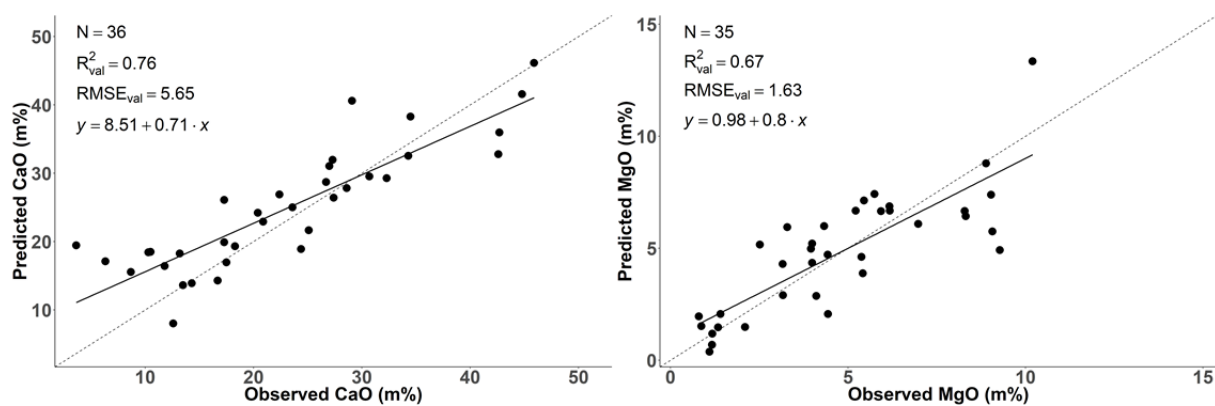


Fig. 5.44: PLSR results based on VNIR/SWIR spectra of air-dried samples for the constituents CaO and MgO. The spectral preprocessed correspond to Table 5.37.

The PLSR results based on spectra of unprepared material with near *in situ* moisture are given in Tab. 5.38 and Fig. 5.45. Again, the most reliable predictions were found for CaO ($R^2_{\text{val}} = 0.78$). The model statistics for the other parameters were comparable to the model outcomes using air-dried samples and are considered moderate. In relation to the model runs performed on the spectra of $< 90 \mu\text{m}$ material, the results for Fe_{total} were distinctly worse using the spectra of the unprepared sample material. Possible reasons are related to the smaller number of samples which might be not optimal for the applied sample division approach and the formation of weathering crusts that might mask features relevant for predicting Fe_{total} to a certain degree. Furthermore, the subsamples taken *in situ* from the bulk samples (which were used for homogenisation and subsequent chemical analysis) might have encompassed minor local variations in iron content. In contrast, the results for Al_2O_3 and MgO were on a similar level to the results obtained using the air-dried samples and comparable to the PLSR outcome based on spectra of $< 90 \mu\text{m}$ material.

Table 5.25: PLSR results based on spectra of samples with near *in situ* moisture (cal = calibration, val = validation, F = number of PLSR factors). Residuals were evaluated using Shapiro-Wilk tests for normal distribution (see p_{sh} -values) and Student's t-test for mean analyses (see p_{t} -values).

	N		Preprocessing	R^2		RMSE		RPD		Residuals	
	N	F		cal	val	cal	val	cal	val	p_{sh}	p_{t}
Al_2O_3	35	4	CR	0.53	0.57	3.14	2.72	1.49	1.55	0.40	0.83
CaO	36	6	Absorbance	0.78	0.78	9.21	5.84	2.14	2.04	0.06	0.25
Fe_{total}	34	1	CR	0.66	0.49	6.92	4.52	1.75	1.39	0.14	0.26
MgO	35	4	CR	0.64	0.68	2.27	1.46	1.69	1.74	0.05	0.15

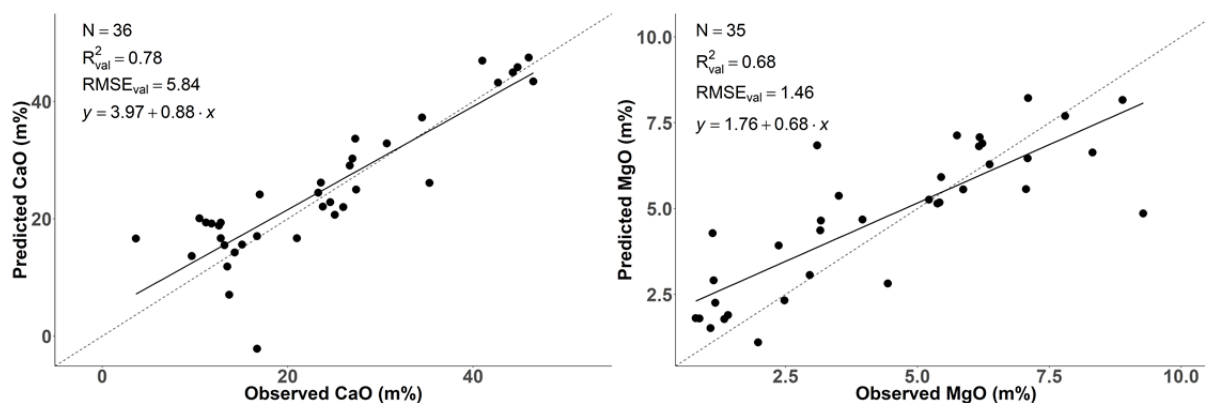


Fig. 5.45: PLSR results based on VNIR/SWIR spectra of unprepared samples for the constituents CaO and MgO. The spectral preprocessings correspond to Table 5.38.

The model outcomes obtained for CaO were not only comparable to the results observed for the prediction based on air-dried sample material, but on a similar level to the CaO prediction based on the VNIR/SWIR spectra of homogenised samples $< 90 \mu\text{m}$ as well. This was true in terms of R^2_{val} , RMSE_{val} as well as RPD_{val} . These findings are similar to results observed in a study on the PLSR-based prediction of the CaO content of limestone ore using spectra of wet and dry samples by Oh et al. (2017). These authors found that the most influential wavelengths for predicting CaO were 2350-2500 nm, which were less affected by moisture. In this thesis, the most influential wavelengths for predicting CaO using VNIR/SWIR spectra (of material $< 90 \mu\text{m}$, moist and air-dried samples) were found in the visible light and close to 2400 nm. These ranges were less affected by moisture as well. In summary, the obtained results demonstrate that for several chemical constituents typically used to characterise iron and steel industry by-products, especially CaO, reliable estimations can be achieved using VNIR/SWIR spectra of prepared samples as well as utilising spectra of material near *in situ* conditions.

6. Synthesis

6.1 Summary and Discussion of the Research Questions

As only few studies have focussed on this subject so far, this work contributes to extending the knowledge of reflectance properties of a variety of recent and historical iron- and steelworks by-products that might be found at dump sites. Reflectance spectra covering the visible light, near and shortwave infrared (VNIR-SWIR) as well as the mid- and longwave infrared (MWIR/LWIR) region were recorded utilising field-portable instruments typically used in remote sensing or industrial applications. These spectra were comprehensively characterised. This thesis further assessed the spectral separability of various iron- and steelworks by-products and analysed the feasibility of the spectral quantification of chemical constituents of such materials using the individual wavelength regions and the combination of both ranges.

The spectral analyses in this thesis relied on a heterogeneous pool of 102 samples representing a variety of recent and historic by-products of the iron and steel industry, encompassing blast furnace slag, granulated blast furnace slag, different electric arc furnace slags, ladle furnace slag, stainless steel slag as well as various dusts and sludges and material mixtures. This pool was formed based on multiple sampling campaigns conducted at the dump site of the today's Stahlwerk Thüringen GmbH and was extended by selected materials not present at this site. Mineralogical and chemical constituents were determined and provided the basis for the typification of the collected materials as well as for the qualitative and quantitative spectral analyses. Spectral measurements were realised in the laboratory on prepared sample material < 90 µm. Further spectra of unprepared samples with near *in situ* conditions (unprepared moist and air-dried material) were acquired in the VNIR/SWIR range.

The spectral analyses conducted in this thesis followed a deductive approach, which comprised three major objectives:

- 1) A generalised spectral separability analysis to assess the potential for spectral discrimination of the different by-product types. This was achieved utilising principal component analysis (PCA), hierarchical clustering (HCA) and a support vector machine classification (SVMC). Additionally, the spectral detectability of selected by-product types was assessed using Spectral Feature Fitting (SFF) and Spectral Angle Mapper (SAM).
- 2) The characterisation of the spectral properties of the major material types was conducted considering reflectance intensities, the presence of spectral features and the linking of parameters of these features to the chemical composition of the samples in order to assess potential relationships. This part further comprised the analyses of spectral variations occurring within by-product classes considered relatively pure and the analysis of impacts of moisture and sample preparation on the spectra.
- 3) The potential for spectrally quantifying chemical constituents of iron- and steelworks by-products was assessed in the last part of this thesis. It was realised using partial least squares regression (PLSR) after separating the sample pool in calibration and validation data. Important variables, i.e. wavelength ranges, for the predictions were assessed using VIP scores. In order to analyse the possibilities for predicting chemical constituents based on material near *in situ* conditions, further PLSR model runs were performed utilising spectra of moist and unprepared sample material as well as spectra of air-dried, but not further prepared samples.

In the following, the outcome of this work will be summarised by answering the initially posed research questions (see Chapter 1.2):

Objective I: Generalised spectral separability analysis of typical iron- and steelworks by-products

Ia Which potential does reflectance spectroscopy offer for discriminating iron- and steelworks by-products?

- Utilising PCA and HCA, the by-product types considered as relatively “pure” within the sample pool could be spectrally discriminated. The distinct separation of the blast furnace slag samples and several unspecified material mixtures was difficult, which is related to the more heterogeneous composition of these material types compared to the chemically and mineralogically (and spectrally) more homogeneous by-product classes (Ch. 5.4.1-5.4.3).
- The results of the HCA (Ch. 5.4.5 and App. 5.5.1-5.5.3) of the spectral data showed a high agreement with the by-product types derived from the chemical and mineralogical analyses. This indicates a large suitability of the spectral discrimination of such materials.
- SVMC results demonstrated the general classifiability of different iron- and steelworks by-products (Ch. 5.4.6). Results based on SFF and SAM indicated a high potential of spectrally detecting major by-product types out of a variety of heterogeneous materials (App. 5.5.4).

Ib Which spectral range and preprocessings are preferable?

- The separability was more distinct based on the VNIR/SWIR spectra compared to the MWIR/LWIR data for most by-product types (Ch. 5.4). This indicates that the analysed by-products showed a higher general spectral dissimilarity in the visible light, near and shortwave infrared region compared to the mid- and longwave infrared. In contrast, individual material types, e.g. the EAFS from medium-alloy steelmaking and sand-rich mixtures could be more clearly differentiated using the MWIR/LWIR range. Thus, it is recommendable to utilise both the VNIR/SWIR and MWIR/LWIR ranges for spectrally separating the large variety of materials potentially occurring at historic iron- and steelworks dump sites. However, a solid discrimination of the vast majority of different historical as well as recent by-products of iron- and steelmaking processes could be realised based only on the VNIR/SWIR range, which is covered by common field-portable spectrometers utilised in remote sensing applications.
- The apparently poorer discrimination results obtained using the MWIR/LWIR spectra compared to the VNIR/SWIR data should not be misinterpreted, taking into account that the MWIR/LWIR covers a much wider wavelength range (ca. 2000-15000 nm) compared to the VNIR/SWIR (350-2500 nm). Consequently, the MWIR/LWIR data potentially comprise more information, i.e. spectral characteristics, of which some might be shared by a variety of materials while others might be unique. Utilising all this information without defining wavelength ranges of interest or diagnostic spectral features might hamper the spectral discrimination utilising generalised approaches. Especially SFF and SAM results demonstrated that the group internal spectral variability in the MWIR/LWIR was larger compared to the VNIR/SWIR and that minor variations in chemistry and mineralogy were stronger reflected in the MWIR/LWIR range (App. 5.5.4). The large spectral variations occurring within one material type might “blur the lines” between different material types. Thus, the outcomes of the generalised separability approaches based on the MWIR/LWIR data observed in this work do not necessarily mean that this region contains less relevant spectral information for material discrimination but that variable selection might be required.

- Aside from the wavelength range, the spectral separability of the studied by-products was variable depending on the spectrum type (reflectance, absorbance or continuum removed). Thus, certain material types (e.g. Thomas slag, AOD and EAF-foam slag) could be better separated from each other based on their reflectance or absorbance intensities while other by-product types (e.g. the converter sludge, granulated blast furnace slag) showed a better separability based on their absorption features. Overall, the spectral separability was for most materials best based on CR spectra, followed by absorbance and reflectance data (Ch. 5.4).

Objective II: Building a spectral library for major iron- and steelworks by-products and characterising reflectance properties as well as major spectral features occurring in the spectra

IIa What are the spectral properties of common iron- and steelworks by-products?

- The reflectance of the different by-products varied strongly. Several material types showed reflectance intensities $< 10\%$ (e.g. the mill scale, the converter sludge, the EAF slag from carbon steelmaking). Other by-products, e.g. the GBFS and the slags from high-alloy steelmaking revealed high reflectance (up to $> 50\%$ in the VNIR/SWIR; Ch. 5.5.1).
- All samples were of low reflectance in the range > 9000 nm with only few well pronounced visible features. The low crystallinity of various material types, the presence of metallic iron and other opaque materials, and particularly the small grain size of the samples (< 90 μm) are likely to have contributed to this issue. In sludges, amorphous carbon is a further potential contributor to the overall low reflectivity (Ch. 5.5.2.1).
- The large variety of differing chemical constituents impacted the reflectance intensities of the studied by-products and - as also true for soils and natural rocks - the spectrum of the by-products is the result of the spectral properties of the individual constituents. For example, samples rich in CaO were found to show higher reflectance intensities than samples low in CaO. In contrast, Fe_{total} showed a strong negative impact on the sample reflectance and samples rich in iron were found to be of low reflectance, as especially obvious for the mill scale and the converter dedusting sludge (Ch. 5.5.2.1).
- The dominant features in the VNIR were due to electronic processes in transition metals. Absorptions occurring near 380, 480, 700 and 870 nm could be linked to Fe^{3+} and features occurring near 1000 nm to Fe^{2+} . The precise assignment of all observed absorptions was difficult due to the plurality of metals that potentially contribute to these features. Most spectra exhibited features near 1410 and 1920 nm related to OH and H_2O . A distinct absorption near 2220 nm was present in almost all samples and was interpreted as hydroxyl or H_2O feature. Although calcite was confirmed in the majority of samples via XRD analysis, no distinct carbonate features were found in the VNIR/SWIR (Ch. 5.5.2.2).
- The MWIR/LWIR spectra of most samples exhibited a variety of carbonate features (at 3980, 5560, 6800, 11360 and near 11700 nm). Minor carbonate features were present near 3345 and 3475 nm for individual samples. Dominant H_2O features were found in most sample spectra near 2900 and 6100 nm. Due to the low reflectance in the wavelength range > 9000 nm, the determination of features related to silicates was difficult. However, distinct patterns of reflectance maxima and absorption features could be assigned to wollastonite and gehlenite-akermanite. Quartz, which is considered an impurity, and which was found in several of the historic materials, could be identified based on a distinct reflectance maximum at 8180 nm and an absorption feature at 8654 nm. The spectra of the phosphate-rich Thomas slag samples showed features at 4674, 4878 and 5024 nm that were similar to features found in apatite reference spectra (Ch. 5.5.2.2).

IIb Which relationships between spectral features and chemical constituents can be observed?

- Analyses of dominant features shared by most samples indicated moderate relationships for the depth of the H₂O features at 1400, 1900, 2900 and 6100 nm and the H₂O (crystal water) content. The position of the feature near 1900 nm was further found to shift towards longer wavelengths with increasing CaO content. The dominant carbonate absorption feature near 6800 nm showed a distinct increase in depth with increasing CaO content. The Fe_{total} content negatively impacted the depth of the H₂O feature at 6100 nm (Ch. 5.5.2.3).
- Linking variations in spectral features observed within individual by-product classes to variations in their chemical composition provided strongly differing results. The strength of the VNIR absorptions present in selected blast furnace slag samples and the converter sludges showed positive relationships with the Fe_{total} content. For the H₂O features at 1400 and 1900 nm, a distinct increase in depth with increasing water content was found for the BFS and the stainless steel slag samples. The CaO content was positively related to the strength of the absorption near 6880 nm in the BFS. For the samples considered relatively “pure” historic GBFS, a positive relation between the depth of the feature at 3980 nm and the TIC content was observed. For the stainless steel slag samples, a positive relation was visible for the TIC content and the depths of the carbonate features near 5566 and 6900 nm. The variations in the major absorption features present in the spectra of the Thomas slag samples could not be clearly linked to variations in their chemistry (Ch. 5.5.3).
- The contrasting observations are interpreted as a result of varying sample mineralogy and the multitude of chemical constituents, which are present in the different by-product types in strongly varying amounts and which might have opposing effects on the spectra. Furthermore, the differences in the chemical constituents within individual by-product types might have been too small to be reflected in the absorption feature characteristics.
- The coefficients of variation of the reflectance and continuum removed spectra indicated a generally higher spectral variability in the MWIR/LWIR compared to the VNIR/SWIR. This affirms the findings of the spectral separability analyses, where a higher group-internal spectral variability is likely to have caused the worse discriminability using the complete mid- and longwave infrared spectra compared to the VNIR/SWIR data (Ch. 5.5.3).
- These findings indicate that a direct linking of absorption depths to contents of chemical constituents is not suitable for their quantification based on a very heterogeneous sample pool as utilised in this work. This underlines the necessity for the chosen multivariate approach in order to quantify chemical constituents based on the recorded spectral data.

IIc What is the impact of moisture and sample preparation on spectra of iron- and steelworks by-products?

- Air-drying and the subsequent decrease in sample moisture led to an increase in reflectance and to lesser depths of the water absorptions near 1400 and 1900 nm as known from the literature (e.g. Bowers and Hanks 1965, Baumgardner et al. 1986) (Ch. 5.5.4).
- Sample homogenisation and sieving to grain sizes < 90 µm caused a distinct increase in reflectance and a decrease in contrast of spectral features in both wavelength ranges due to shifts in the ratio of volume and surface scattering with decreasing grain size (Ch. 5.5.4).
- While the general shape of the spectra was not distinctly altered in most cases by air-drying or sample preparation, individual materials showed masking effects due to moisture and

spectral deviations after preparation. This has potential implications on qualitative and quantitative analyses of by-products based on field data (Ch. 5.5.4).

- The spectra of the homogenised materials < 90 µm allowed an optimal linkage of the chemical and spectral properties as identical materials were used for the chemical, mineralogical and spectral measurements. However, individual spectral features were more pronounced in the spectra of material of larger grain sizes and nearly diminished in the spectra of the powdered samples. For example, Si-O features in silicates are known to be “[...] greatly diminished and distorted in reflectance spectra of powdered rocks” (Salisbury et al. 1988). For carbonates, inversions of reflectance maxima to minima were observed with small grain sizes in the study by Zaini et al. 2012. This indicates that the < 90 µm fraction might not be ideal for spectral analyses in every case.
- The small grain size is likely to have contributed to the low reflectance intensities in the range > 9000 nm, as small grains cause micro-shadowing and the voids between the particles might induce a so-called cavity effect (Salisbury and Wald 1992; Ch. 5.5.4). However, spectra of individual samples of larger grain size indicated that the general presence and shape of features in the MWIR/LWIR did not substantially change for the different grain size fractions in this work (Ch. 5.5.4).

Objective III: Spectral quantification of constituents of iron- and steelworks by-products

IIIa Which chemical constituents of iron- and steelworks by-products can be spectrally predicted?

- For a variety of major iron- and steelworks by-product constituents, robust PLSR prediction results ($R^2_{\text{val}} = 0.8\text{--}0.9$) were obtained. These comprise: CaO, Fe_{total} , Fe_2O_3 , SiO_2 TIC and $\sum(\text{Mo, Ni, V, Zn, Al, Cr, Fe, Mn})$. For further parameters, including Al_2O_3 and MgO, promising PLSR results ($R^2_{\text{val}} = 0.6\text{--}0.7$) were achieved, indicating suitable spectral predictive capabilities for these constituents (Ch. 5.6.1-5.6.3).
- The RMSEs for the best validated prediction results ranged between ca. 2-3 m% for Al_2O_3 , CaO, Fe_{total} , Fe_2O_3 , MgO and TIC; and between ca. 3-4 m% for SiO_2 and $\sum(\text{Mo, Ni, V, Zn, Al, Cr, Fe, Mn})$. These prediction errors are considered low, which indicates a high suitability and promising accuracies of the spectral predictions for screening applications (Ch. 5.6).
- RPD values for the models ranged between ca. 2-3 for SiO_2 , TIC and Fe_{total} , and reached 4.5 for CaO. This implies a reliable model robustness and indicates a high potential for the utilisation of spectral predictions of these constituents (Ch. 5.6.1-5.6.3).

IIIb Which spectral range provides the best results for which constituent?

- For Fe_{total} and Fe_2O_3 , the PLSR models based on VNIR/SWIR spectra provided the best results. The MWIR/LWIR data provided better prediction capabilities for the other chemical constituents. However, for Al_2O_3 , CaO and MgO, promising predictions could be realised based on VNIR/SWIR data with relatively high accuracy as well (Ch. 5.6.1-5.6.5).
- The combination of both spectral ranges increased the R^2_{val} and decreased the RMSE_{val} for most of the parameters compared to the model results obtained using either the VNIR/SWIR or the MWIR/LWIR. However, these improvements in model performance were not as strong as between the individual wavelength ranges and came at the cost of higher model complexity in some cases (Ch. 5.6.1-5.6.5).

IIIc Which impacts do different preprocessings have on the model performance?

- Similar to the outcome of the spectral separability analyses, distinct differences in the PLSR model performance were observed depending on the spectral preprocessings and the chosen wavelength range as a result of the material-specific spectral properties (Ch. 5.6.1-5.6.5).
- In general, the application of continuum removal and absorbance preprocessing in addition to the utilisation of the unmodified spectra was found recommendable to assess the full potential of the spectral data for quantifying the chemical by-product constituents.

III d Which variables are important for the spectral prediction of chemical constituents?

- Individual or multiple wavelength regions associated with specific spectral features as well as wavelengths with no visible relation to absorption features or reflectance maxima contributed to the PLSR models, indicating indirect statistical relations (Ch. 5.6.4).
- Wavelengths associated with H₂O features near 2900 and 6100 nm were found to be relevant for the prediction of various constituents. The sharp peak in the VIP-scores near 2740 nm was interpreted to be related to the hydroxyl fundamental vibration and was of considerable relevance for the prediction of e.g. CaO, and SiO₂. The carbonate features at 3890, 5560, 7000 and near 11400 nm were relevant for predicting CaO and TIC. For predicting CaO and Fe_{total} using the VNIR/SWIR spectra, the VIS was of high relevance (Ch. 5.6.4).

III e Which prediction results can be obtained based on spectra of materials near in situ conditions?

- As discussed in IIc, sample preparation and *in situ* moisture had noticeable impacts on the spectra of the by-products with potential implications for quantification purposes.
- The prediction results for CaO, one of the most commonly used constituents to chemically characterise iron- and steelworks by-products, were found to be basically unaffected by moisture and sample preparation, both in terms of R²_{val} and RMSE_{val}. This indicates that robust predictions with relatively small errors that are comparable to laboratory experiments using homogenised sample material can also be achieved based on material near *in situ* conditions. Further promising results were obtained for Al₂O₃ and MgO. The results for Fe_{total} were less robust (Ch. 5.6.6).

6.2 Conclusions, Assessment of the Results and Possible Applications

General Conclusions

The outcome of this thesis indicates a high potential of reflectance spectroscopy covering the visible light to the longwave infrared for discriminating the heterogeneous materials potentially found at historic iron- and steelworks dump sites and for the quantification of a variety of chemical constituents typically used to characterise such materials. Thus, reflectance measurements and subsequent spectral analyses were found suitable tools for the qualitative as well as quantitative characterisation of iron- and steelworks by-products. The results demonstrated that different materials that are hardly distinguishable based on visual inspection can be spectrally grouped, typified and their chemical properties estimated with solid accuracies. Subsequently, such methods offer a large potential to assist the exploration of iron- and steelworks dump sites and landfills in terms of material discrimination, characterisation and the assessment of their geochemical properties. Considering that spectral measurements are non-invasive techniques that can be realised within minutes and estimations on the material type and chemical properties can be derived quickly, such methods provide a high capability for reducing the number of samples for cost- and labour-intensive chemical and mineralogical analyses for general material characterisation and in screening applications. The PLSR results demonstrated that this can be achieved using VNIR/SWIR spectra of prepared samples as well as spectra of material approximating field conditions for various constituents.

This work shows that the formation of statistical models for the estimation of certain chemical constituents can be realised based on a pool of relatively few samples of heterogeneous composition. The applied PLSR models indicate good predictive capabilities for various chemical constituents, encompassing Al_2O_3 , CaO , SiO_2 and TIC, which are typically used to characterise slags and other by-products (see Ch. 2.1.2). The results verify that these prediction models are suitable for screening applications, allowing a quick general chemical characterisation of materials.

The utilisation of the VNIR/SWIR and the MWIR/LWIR range was found recommendable for the spectral discrimination of different by-product types and for the quantification of most chemical constituents. However, the results of this work demonstrated that the spectral separation of different material types and the quantification of chemical constituents does not necessarily require both ranges. Hence, material typification and reliable estimations for several chemical parameters can be achieved either based on VNIR/SWIR or MWIR/LWIR data. This is of relevance as it cannot be assumed that field-portable instruments or imaging sensors covering both ranges are available for every research institution or company.

Relevance of spectral methods for assessing recent iron- and steelworks by-products

The outcome of this work is of considerable relevance for general laboratory analyses of iron- and steelworks by-products. The observed accuracies for the spectral prediction of e.g. CaO , Fe_{total} , SiO_2 and TIC as well as for other constituents allow the quick assessment of these properties, enhancing the assessment of the chemical and mineralogical properties of slags and other by-products. Other studies already demonstrated the applicability of (hyper)spectral methods for optimising the steel foundry process or for slag characterisation (Rodríguez et al. 2010, Gutiérrez et al. 2010, Picón et al. 2017). The established spectral library and knowledge base offers the potential to further optimise such procedures. Spectral methods might further be utilised as an alternative quality control technique for slags. A similar approach was proposed by

Zaini et al. (2016) for Portland cement-grade limestone. Thus, the achieved results are considered of promising relevance for such industrial applications. However, the by-products of recent iron- and steelmaking are very homogeneous due to the industrial-technogenic nature of these processes and the expected chemical variations occurring within slags might be small. Thus, while there is potential for laboratory analyses of recent materials, the main application is seen in the context of the (remote) exploration of historical iron- and steelworks dump sites.

Relevance of spectral methods for exploring anthropogenic secondary iron- and steelworks deposits

It can be assumed that the need for raw materials and the search for new deposits will further increase in the future. Thus, man-made secondary deposits will continue to play an important role in urban mining, meaning the detection, qualitative and quantitative characterisation of materials of economic interest and their subsequent reuse. This is reflected by the increasing number of calls for and programmes focussing on raw materials, which comprise among others the exploration of anthropogenic deposits (e.g. the R³ and R⁴ initiatives of the BMBF and the Strategic Implementation Plan of the European Innovation Partnership on Raw Materials/Horizon 2020). Furthermore, the high amounts of mining residuals (2012: > 700 MT, European Union 2016), the number of dump sites and landfills (in Germany > 1000, Mrotzek-Blöß et al. 2016) and generated industrial by-products (e.g. >400 MT of by-products from the iron and steel industry per year, World Steel Association 2016) can be assumed to further increase. Additionally, although recycling rates of recent by-products are high in western countries, lower reuse rates are found in other countries (Yi et al. 2012).

While reflectance spectroscopy and remote sensing certainly cannot replace established geochemical and mineralogical methods, the results of this work successfully demonstrated the high potential of spectral methods for the qualitative and quantitative characterisation of materials commonly found at anthropogenic deposits from the iron and steel industry. Thus, such methods may be applied beneficially in the exploration of historic dump sites. The formed knowledge base can be integrated into existing workflows and thus support the derivation of reliable information on different material types and the assessment of their general chemical properties. As initially discussed, one is confronted with a variety of challenges when exploring iron- and steelworks dump sites. Aside from the heterogeneous material deposition, dumped materials might be similar to the human eye despite them representing different material types. In other cases, materials might seem different but are actually identical, as minor variations e.g. in iron content can substantially change the colours of soils and other substrates (e.g. Schwertmann and Lentze 1966, Karmanova 1981, Cornell and Schwertmann 2003). As such, many historic materials are hardly distinguishable *in situ*, even by experts (see Fig. 6.1), and time-consuming sampling campaigns with subsequent laboratory analyses are required for chemical characterisation. Here, spectroscopy can quickly provide information on the similarity of materials (*in situ* or in the laboratory), allow the assignment of samples to specific classes and help assessing chemical properties. Apart from the utilisation of non-imaging spectrometers for material discrimination and assessment *in situ* or in the laboratory, the developed spectral library and gathered knowledge on the spectral separability can benefit spectral-based material-sorting applications in industrial contexts, as described e.g. by Picón et al. (2009, 2012); Gutiérrez et al. (2010) and Rodríguez et al. (2010) with relation to metals and by-products of the iron and steel industry, or as presented in Dalm et al. (2014) for copper ore.

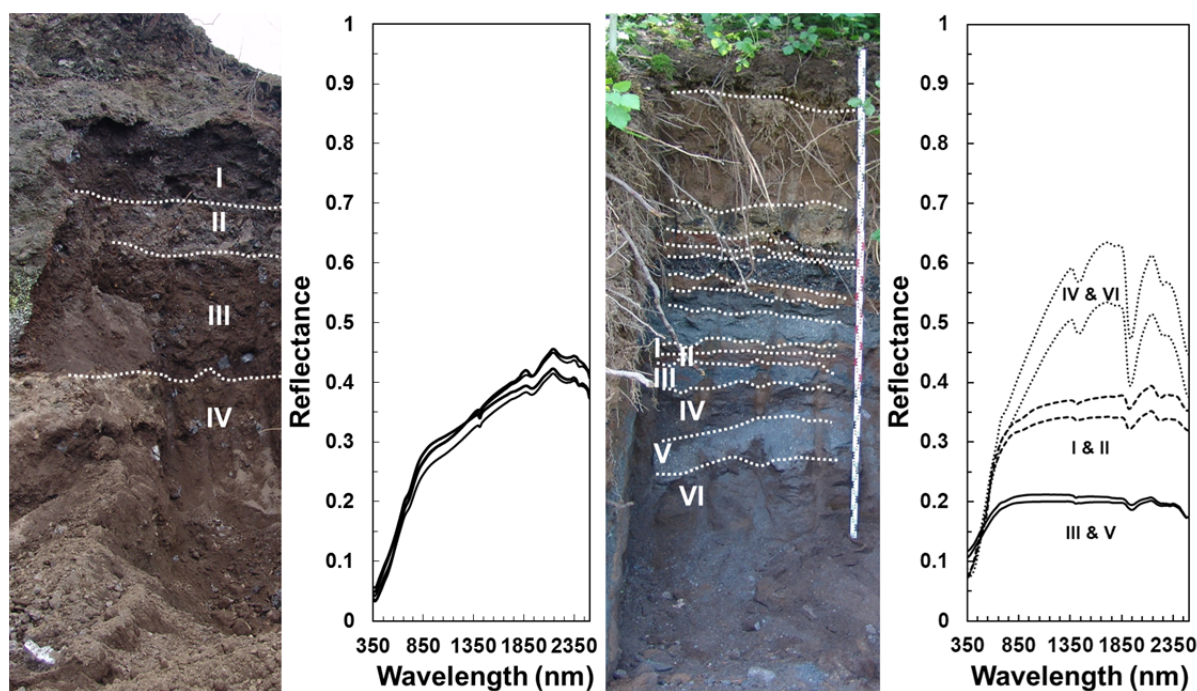


Fig. 6.1: Differences in visual material characterisation and application of spectral measurements. Left: The outcrop generated at the “Canyon” at the Unterwellenborn dump site. Based on expert information and *in situ* interpretation of visible differences in material colour, four layers supposed to comprise different materials were assigned, of which layer II was assumed to comprise Thomas slag. Spectral measurements shortly after sample collection indicated a high similarity of these materials and subsequent chemical analysis confirmed that all four layers actually were Thomas slag. Here, the compiled spectral library supports a quicker material identification. Right: Multiple layers of historical materials laid open at the excavator prospecting near the former “Sinterhang” at the Unterwellenborn dump site. Several greyish layers could be easily categorised in materials with similar or different spectral and subsequently chemical properties, which was barely possible based on visual interpretation. Here, a spectral library of these materials and the knowledge about the associated chemical properties help to identify such by-products at other sites of one dump site or at other dump sites.

Transferability of the results to other dump sites

The heterogeneous sample pool used in this thesis was supposed to represent a “real life situation”, comprising a variety of diverse materials that might be found in a similar way on other dump sites. However, the sample pool was obviously dominated by the chemical composition and the spectral properties of the specific materials present at the test dump site and did for example not include BOF slag. Thus, a general transferability of the results achieved in this study to other dump sites is assumed but deviations are expected for other sites with differing histories of iron- and steelmaking. Furthermore, although the dataset was separated into calibration and validation samples for the PLSR modelling, most of the samples were from the Unterwellenborn dump site and thus not completely independent. Here, it would be interesting to test the predictive capabilities of calibration models developed with this sample pool for estimating the composition of materials found at other dump sites. When exploring industrial deposits, a variety of legal obstacles might hamper the exploration of dump sites. However, these are general issues that are not specific for the proposed spectral approach (Mrotzek-Blöß et al. 2016).

Transferability of the results to (imaging) remote sensing data under field conditions

The analyses in this thesis were conducted at the laboratory scale, utilising mainly prepared and homogenised samples of very fine grain sizes. However, the potential of the used methods for field applications was addressed by utilising spectra of moist and air-dried samples without any

preparation for the PLSR model runs. Here, results showing suitable screening capabilities for assessing chemical characteristics of iron- and steelworks by-products were found as well, likewise indicating a high potential for field applications. These results were achieved based on VNIR/SWIR data. The predictive capability of PLSR models based on MWIR/LWIR spectra of material near field conditions remains to be tested.

For the transfer of the achieved results to imaging data under laboratory conditions, e.g. for material sorting using hyperspectral imaging as described earlier, no major impacts of atmospheric conditions are expected. In contrast, when using imaging sensors under field conditions, atmospheric bands have to be considered, i.e. wavelength ranges where radiation is absorbed by atmospheric gases and thus not available for remote sensing applications. The VIP scores of the built prediction models showed that regions near 1400, 1900, 2900 and between 5500-7500 nm were of relevance for the prediction of several constituents. Due to the nearly complete absorption of energy by H₂O or CO₂, these ranges are characterised by noise and do not provide useful information in remote sensing data. This does not necessarily mean that the achieved results cannot be transferred to field conditions, but deviations from the outcomes in this work are expected when utilising remote sensing data. However, the capabilities of terrestrial hyperspectral imaging for *in situ* discriminating different iron- and steelworks by-products were already successfully demonstrated in a case study conducted at the Unterwellenborn dump and hyperspectral airborne data allowed the spectral discrimination of various materials found at the dump surface as well (see Denk et al. 2015, Mrotzek-Blöß et al. 2016).

The measurements for covering the mid- and longwave infrared were realised as laboratory reflectance set-up in this thesis. These measurements were affected by “atmospheric” influences only to a minor degree (e.g. CO₂ peaks near 4300 nm) and the radiation for these measurements was provided by the powerful heating element in the instrument. In contrast, data recorded by thermal infrared imaging instruments in remote sensing applications is affected by atmospheric influences on a much stronger degree (atmospheric windows and bands, see the paragraph above) and typically emissivity or temperature information is derived from such data. The processing of such data is more complex compared to laboratory measurements and requires the removal of atmospheric influences (e.g. Kuenzer and Dech 2013). Thus, in contrast to the VNIR/SWIR data, the diffuse reflectance MWIR/LWIR data acquired using the handheld FTIR instrument in this thesis cannot be directly compared to (hyper)thermal remote sensing (emissivity) data but provide a comprehensive basis for various applications as well.

Proposed multi-scale contributions of (hyper)spectral methods for exploring iron- and steelworks dump sites

The great advantage of hyperspectral (or -thermal) remote sensing is that it allows the acquisition of spatial information for large areas. However, these methods are restricted to the reflected (or emitted) radiation by surfaces. As such, the manifold material types and the heterogeneous material composition at historic dump sites cannot be comprehensively assessed solely based on airborne (or spaceborne) data. Furthermore, vegetation cover might hamper the acquisition of comprehensive spectral information via airborne instruments. However, the spectral information of vegetation may be a useful indicator for the geochemical properties of the materials beneath. Additionally, factors like moisture, material mixtures, weathering products and vegetation lead to more complex spectra that are difficult to interpret (e.g. Siegal and Goetz 1977, Gupta 2018).

Thus, a multiscale approach for spectrally exploring iron- and steelworks dump sites is suggested as conducted in similar way in Mrotzek-Blöß et al. (2016) and as presented in Figure 6.2:

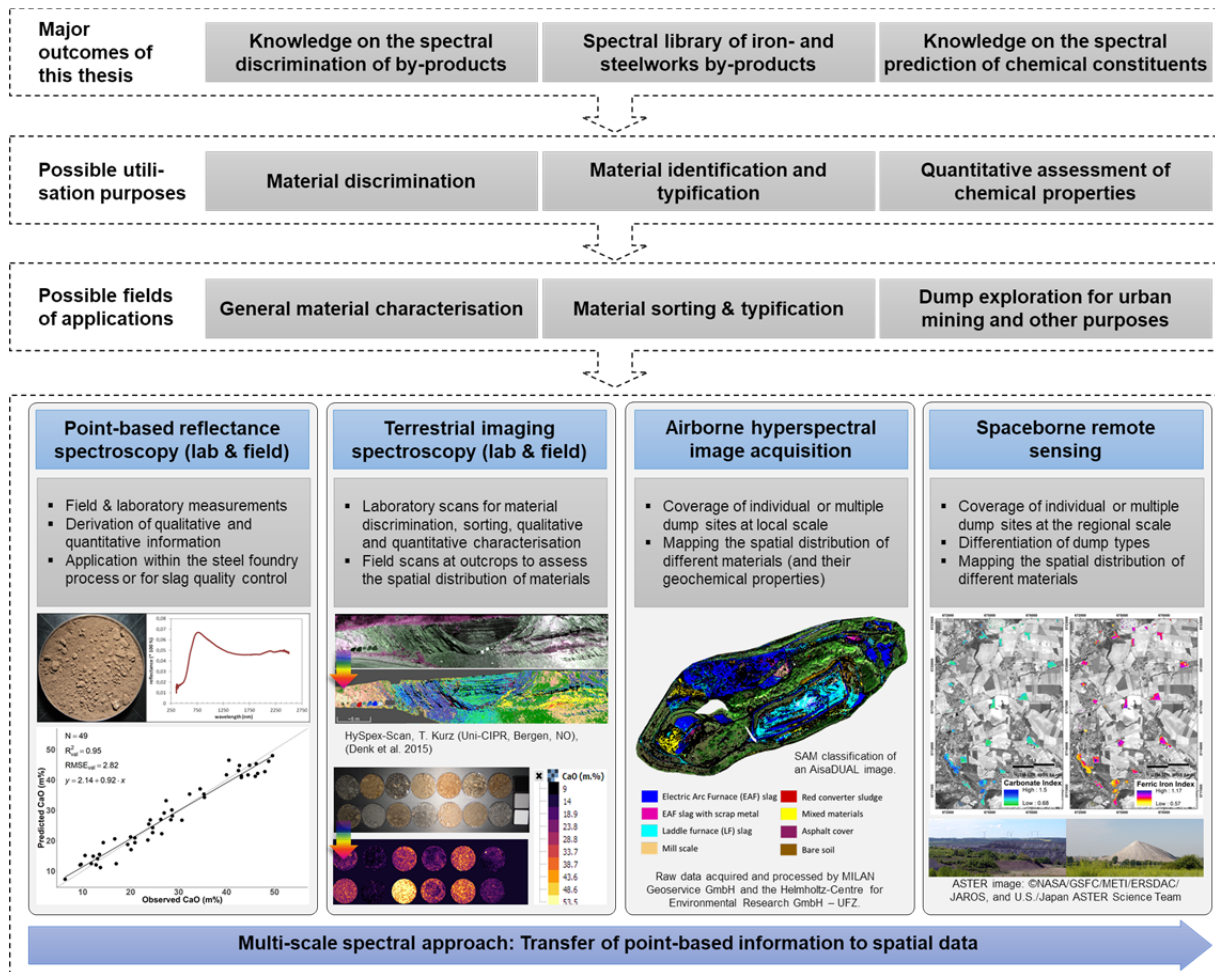


Fig. 6.2: Major outcomes of this thesis and potential application fields.

In detail, such an approach might comprise the following:

- Field and laboratory reflectance measurements using non-imaging portable instruments for spectrally assessing material types and chemical properties of iron- and steelworks by-products.
- Material sorting and classification (see e.g. Picón et al. 2009, 2012, Gutiérrez et al. 2010, Rodríguez et al. 2010), and determination of sample chemistry (similar to the study by Zaini et al. 2014 for carbonate rock chemistry) using laboratory-based hyperspectral imaging. This could also be applied for spectral analyses of drill cores acquired at dump sites.
- The application of terrestrial imaging spectroscopy at outcrops of a dump site for mapping the spatial distribution and chemical properties of materials of interest (see Denk et al. 2015).
- The utilisation of hyperspectral airborne (aircraft and/or UAV) or even spaceborne data of current multispectral or future hyperspectral missions (like EnMap) for analysing larger regions with multiple dump sites (as conducted in similar way in Mrotzek-Blöß et al. 2016).
- Furthermore, geophysical approaches in combination with hyperspectral measurements might provide relevant information suitable to support the exploration of iron- and steelworks dump sites (see e.g. Schulz et al. 2015, Günther and Martin 2016).

Such multi-scale information would allow the formation of more reliable deposit-models of the complex structure of historic dump sites of the iron and steel industry and thus benefit their exploration within urban mining applications.

6.3 Outlook

The outcome of this thesis represents a bridging function to further promote VNIR/SWIR as well as MWIR/LWIR reflectance spectroscopy to analyse iron- and steelworks by-products. Thus, this work subsequently promoted hyperspectral/hyperthermal remote sensing as promising tools to support the exploration of anthropogenic deposits in general and of historic iron- and steelworks dump sites and landfills in particular. Naturally, connection and optimisation possibilities arise, which are briefly described in the following section.

Material discrimination vs. identification

As discussed e.g. in Kirkland et al. (2002) and Hecker (2012), one has to consider the difference between discriminating different materials and identifying them. The analyses conducted in this work focussed on the spectral discrimination of various iron- and steelworks by-products but also indicated the possibility of their spectral identifiability among a plurality of heterogeneous materials. However, more research needs to be conducted on the detectability of such materials considering the presence of other materials (e.g. soil, natural rocks, other industrial by-products or other anthropogenic materials), which may occur at dump sites and might be recorded in remote sensing data of such areas. Here, the elaborated knowledge base of the spectral properties of the studied by-products is thought to be helpful for the selection of relevant features to be used within established mapping approaches, allow the development of decision trees or other approaches.

Spectral feature analyses

As presented in Chapter 5.5.2.2, most of the major absorption features identified in the spectra could be assigned to specific functional groups. However, especially the interpretation of the features present in the VNIR, which are due to electronic processes, was difficult. Here, future studies might provide more specific assignments. Furthermore, among the plurality of features observed in the MWIR/LWIR range, several of the minor reflectance maxima and minima described in this work are yet to be interpreted.

The limited number of samples per by-product class did not allow statistical analyses to find correlations between chemical constituents and spectral feature parameters and only general trends were reported. At this point, further studies might focus on the impact of chemical constituents or the mineral composition on spectral feature parameters using a higher number of samples per by-product type.

Optimisation of prediction models

The study of the influential wavelengths for the PLSR predictions (see Chapter 5.6.4) provides a basis for the selection of specific variables, i.e. wavelengths, for subsequent reduction of used variables leading to less complex and possibly more robust models. As the elaborated PLSR models utilised the full spectral ranges provided by the portable instruments, they also included wavelength ranges that are affected by absorptions by atmospheric gases, e.g. due to H₂O (near 1400, 1900 and between ca. 5500-7500 nm) and CO₂ (near 2900 and 4200 nm) (see e.g. Lillesand et al. 2008). While relevant information within these ranges can be acquired under laboratory conditions or using contact measurements in the field, they are not available in data of non-contact field measurements or in air- or spaceborne data. Hence, model runs should be performed excluding these ranges in order to assess possible restrictions.

Further topics for future research might be the quantification of minerals based on multivariate methods or the assessment of material types based on such procedures. The PLSR modelling in this work focussed on constituents > 3 m% on average. However, promising initial results were also found for a variety of other constituents, which were partly present in much lower contents, comprising Cr_2O_3 , K_2O , P_2O_5 and S_{total} . The potential for spectrally estimating such constituents could be evaluated in future studies. Furthermore, weak but noticeable relationships between the contents of constituents like As, Cd, Cu, Pb and Zn and the spectral data were observed. These constituents might be of relevance for studies focussing on environmental aspects at other sites and thus worthwhile to be studied in future research as well.

Impacts of moisture, grain size and sample preparation

In this study, the spectral discrimination, qualitative and quantitative spectral analyses were conducted based on spectra of materials < 90 μm . Furthermore, the general feasibility of PLSR predictions using spectra of material near *in situ* conditions could be successfully demonstrated. However, future work should focus on a larger variety of grain size fractions in order to assess impacts on spectral features and for qualitative as well as quantitative spectral analyses.

Transfer to imaging data

In addition to the few existing studies that successfully demonstrated the potential of terrestrial as well as airborne hyperspectral imaging methods for the *in situ* discrimination of iron- and steelworks by-products found at historic dump sites (Denk et al. 2015, Mrotzek-Blöß et al. 2016), further research is required to assess the full potential of such techniques for screening applications, including material detection as well as the quantification of chemical constituents. This may be applied at other dump sites following the proposed multi-scale approach shown in Figure 6.2. This may encompass measurements and analyses at the laboratory scale in terms of material sorting and assessment of chemical properties, *in situ* scans at already existing or artificially created cross-sections or the hyperspectral airborne exploration including the VNIR/SWIR range and the thermal infrared. Airborne remote sensing might comprise aircraft- but also UAV-carried sensors. UAV-based remote sensing might especially be helpful in acquiring information at steep slopes that are barely accessible and might not be properly covered in data from aircraft-carried sensors. Furthermore, UAVs are more flexible in terms of weather conditions. Thus, aside from heap volume estimations using e.g. lidar data or photogrammetrical approaches, UAV-based remote sensing is considered a promising tool for spectrally exploring iron- and steelworks dumps as well.

Concluding remarks

This work provides a basis for the aforementioned possible applications. Thus, it subsequently highlights hyperspectral and hyperthermal remote sensing as promising tools to support the exploration of anthropogenic deposits in general and of historic iron- and steelworks dump sites and landfills in particular. Considering the significance of urban mining for the sustainable use of resources, subsequent related research will become increasingly important in the future.

7. References

Books, Journal Articles, Reports, etc.

- Abrams, M. J., Ashley, R. P., Rowan, L. C., Goetz, A. F. H. & Kahle, A. B. (1977): Mapping of hydrothermal alteration in the Cuprite mining district, Nevada, using aircraft scanner images for the spectral region 0.46 to 2.36 μm , *Geology*, 5, (12), 713, [https://doi.org/10.1130/0091-7613\(1977\)5<713:MOHAIT>2.0.CO;2](https://doi.org/10.1130/0091-7613(1977)5<713:MOHAIT>2.0.CO;2).
- Adamczyk, B., Brenneis, R., Kühn, M. & Mudersbach, D. (2008): Verwertung von Edelstahlschlacken - Gewinnung von Chrom aus Schlacken als Rohstoffbasis. In: K. J. Thomé-Kozmiensky (Ed.), *Recycling und Rohstoffe* (143–160). Neuruppin: TK-Verl.
- Adams, R. V. (1961: Infrared absorption due to water in glasses, *Physics and Chemistry of Glasses*, 2, 39–49.
- Adler, H. H. & Kerr, P. F. (1962): Infrared study of aragonite and calcite, *The American Mineralogist*, 47, 700–717.
- Adler, H. H. & Kerr, P. F. (1963a): Infrared absorption frequency trends for anhydrous normal carbonates, *The American Mineralogist*, 48, 124–137.
- Adler, H. H. & Kerr, P. F. (1963b): Infrared spectra, symmetry and structure relations of some carbonate minerals, *The American Mineralogist*, 48, 839–853.
- Adler, H. H. & Kerr, P. F. (1965): Variations in infrared spectra, molecular symmetry and site symmetry of sulfate minerals, *The American Mineralogist*, 50, (1-2), 132–147.
- Agilent (2017): Agilent 4300 Handheld FTIR Spectrometer. Retrieved from https://www.agilent.com/cs/library/brochures/5991-4067EN_LR.pdf, 2018-03-23.
- Aimoto, M., Kanehashi, K. & Fujioka, Y. (2015): *Analytical Technologies for Steel Slag* (Nippon steel & sumitomo metal technical report No. 109).
- Akaike, H. (1974): A new look at the statistical model identification, *IEEE Transactions on Automatic Control*, 19, (6), 716–723, <https://doi.org/10.1109/TAC.1974.1100705>.
- Albertz, J. (2009): *Einführung in die Fernerkundung: Grundlagen der Interpretation von Luft- und Satellitenbildern*, (4. aktualisierte Aufl.), Darmstadt: WBG, (4. aktualisierte Aufl.), 254, 978-3-534-23150-8.
- Allmann, R. (2003): *Röntgen-Pulverdiffraktometrie*, Berlin, Heidelberg: Springer Berlin Heidelberg, 278, 978-3-540-43967-7.
- Anbazhagan, S. & Arivazhagan, S. (2009): Reflectance spectra of analog basalts; implications for remote sensing of lunar geology, *Planetary and Space Science*, 57, (12), 1346–1358, <https://doi.org/10.1016/j.pss.2009.06.020>.
- Anderson, M. S., Andringa, J. M., Carlson, R. W., Conrad, P., Hartford, W., Shafer, M., Hand, K. (2005): Fourier transform infrared spectroscopy for Mars science, *Review of Scientific Instruments*, 76, (3), 34101, <https://doi.org/10.1063/1.1867012>.
- Anderson, J. E. & Robbins, E. I. (1998): Spectral reflectance and detection of iron-oxide precipitates associated with acidic mine drainage, *Photogrammetric Engineering and Remote Sensing*, 64, (12), 1201–1208.
- Arndt, N., Kesler, S. & Ganino, C. (2015): *Metals and Society: An Introduction to Economic Geology*, Cham: Springer International Publishing, 162, 978-3-319-17231-6.

- Arnold, G. & Wagner, C. (1988): Grain-size influence on the mid-infrared spectra of the minerals, *Earth, Moon and Planets*, 41, (2), 163–171, <https://doi.org/10.1007/BF00056401>.
- ASD - Analytical Spectral Devices, Inc. (2002): *FieldSpec Pro User's Guide*.
- Baldrige, A. M., Hook, S. J., Grove, C. I. & Rivera, G. (2009): The ASTER spectral library version 2.0, *Remote Sensing of Environment*, 113, (4), 711–715, <https://doi.org/10.1016/j.rse.2008.11.007>.
- Barnes, R. J., Dhanoa, M. S. & Lister, S. J. (1989): Standard Normal Variate Transformation and De-Trending of Near-Infrared Diffuse Reflectance Spectra, *Applied Spectroscopy*, 43, (5), 772–777, <https://doi.org/10.1366/0003702894202201>.
- Barnes, R. J., Dhanoa, M. S. & Lister, S. J. (1993): Correction to the Description of Standard Normal Variate (SNV) and De-Trend (D'T) Transformations in Practical Spectroscopy with Applications in Food and Beverage Analysis—2nd Edition, *Journal of Near Infrared Spectroscopy*, 1, (3), 185–186.
- Bartusch, H., Fernández Alcalde, A. M. & Fröhling, M. (2013): *Erhöhung der Energie- und Ressourceneffizienz und Reduzierung der Treibhausgasemissionen in der Eisen-, Stahl- und Zinkindustrie (ERESTRE). Produktion und Energie: Vol. 2*, Karlsruhe: KIT Scientific Publishing, 161, 978-3-86644-857-5.
- Baumgardner, M. F., Silva, L. F., Biehl, L. L. & Stoner, E. R. (1986): Reflectance Properties of Soils. In: *Advances in Agronomy. Advances in Agronomy*. (Vol. 38, 1–44). Elsevier, [https://doi.org/10.1016/S0065-2113\(08\)60672-0](https://doi.org/10.1016/S0065-2113(08)60672-0).
- Beer, J. de, Worrell, E. & Blok, K. (1998): Future technologies for energy-efficient iron and steel making, *Annual Review of Energy and the Environment*, 23, (1), 123–205, <https://doi.org/10.1146/annurev.energy.23.1.123>.
- Ben-Dor, E., Chabrilat, S., Demattê, J., Taylor, G. R., Hill, J., Whiting, M. L. & Sommer, S. (2009): Using Imaging Spectroscopy to study soil properties, *Remote Sensing of Environment*, 113, 38-55, <https://doi.org/10.1016/j.rse.2008.09.019>.
- BGR - Bundesanstalt für Geowissenschaften und Rohstoffe in Zusammenarbeit mit den Staatlichen Geologischen Diensten. (2005): *Bodenkundliche Kartieranleitung KA5: Mit 103 Tabellen*, (5th ed.), Stuttgart: Schweizerbart, (5th ed.), 438, 978-3-510-95920-4.
- BGR - Bundesanstalt für Geowissenschaften und Rohstoffe (BGR, in Zusammenarbeit mit den Staatlichen Geologischen Diensten (SGD) der Bundesländer im Blattschnitt der Topographischen Übersichtskarte (2015): Bodenübersichtskarte 1:200.000 (BÜK200) - CC5534 Zwickau.
- BGR – Bundesanstalt für Geowissenschaften und Rohstoffe (2017): Deutschland – Rohstoffsituation 2016, Retrieved from https://www.bgr.bund.de/DE/Themen/Min_rohstoffe/Downloads/rohsit-2016.pdf?__blob=publicationFile&v=2*, 2018-03-14.
- Bialucha, R. & Spanka, M. (2014): Zeitliche Entwicklung der Karbonatisierung von Stahlwerksschlacken und Auswirkung auf die Löslichkeit umweltrelevanter Bestandteile, *FEbS Report*, 21, (1), 1–7.
- Bláhová, L., Mucha, M., Navrátilová, Z. & Gorošová, S. (2015): Sorption Properties of Slags, *Inženýrská Mineralna*, 2, 89–94.

- Boesche, N., Rogass, C., Lubitz, C., Brell, M., Herrmann, S., Mielke, C., Kaufmann, H. (2015): Hyperspectral REE (Rare Earth Element) Mapping of Outcrops—Applications for Neodymium Detection, *Remote Sensing*, 7, (12), 5160–5186, <https://doi.org/10.3390/rs70505160>.
- Boser, B. E., Guyon, I. M. & Vapnik, V. N. (1992) A training algorithm for optimal margin classifiers. In: D. Haussler (Ed.), *Proceedings of the fifth annual workshop on Computational learning theory - COLT '92* (144–152). New York, New York, USA: ACM Press, <https://doi.org/10.1145/130385.130401>.
- Bowers, S. A. & Hanks, R. J. (1965): Reflection of radiant energy from soils., *Soil Science*, 100, (2), 130–138.
- Bowers, S. A. & Smith, S. J. (1972): Spectrophotometric Determination of Soil Water Content¹, *Soil Science Society of America Journal*, 36, (6), 978, <https://doi.org/10.2136/sssaj1972.03615995003600060045x>.
- Bragg, W. H. & Bragg, W. L. (1913): The Reflection of X-rays by Crystals, *Proceedings of the Royal Society A: Mathematical, Physical and Engineering Sciences*, 88, (605), 428–438, <https://doi.org/10.1098/rspa.1913.0040>.
- Brenner, I. B. & Taylor, H. E. (1992): A Critical Review of Inductively Coupled Plasma-Mass Spectrometry for Geoanalysis, Geochemistry, and Hydrology. Part I. Analytical Performance, *Critical reviews in analytical chemistry*, 23, (5), 355–367, <https://doi.org/10.1080/10408349208051650>.
- Bruegge, C. J., Stiegman, A. E., Rainen, R. A. & Springsteen, A. W. (1993): Use of Spectralon as a diffuse reflectance standard for in-flight calibration of earth-orbiting sensors, *Optical Engineering*, 32, (4), 805, <https://doi.org/10.1117/12.132373>.
- Bunaciu, A. A., Udriștișoiu, E. G. & Aboul-Enein, H. Y. (2015): X-ray diffraction: Instrumentation and applications, *Critical reviews in analytical chemistry*, 45, (4), 289–299, <https://doi.org/10.1080/10408347.2014.949616>.
- Bundesministerium für Umwelt, Naturschutz, Bau und Reaktorsicherheit (BMUB) (2015): Deutsches Ressourceneffizienzprogramm (ProgRess): Programm zur nachhaltigen Nutzung und zum Schutz der natürlichen Ressourcen, Retrieved from https://www.bmub.bund.de/fileadmin/Daten_BMU/Pool/Broschueren/progress_broschue_de_bf.pdf, 2018-02-23.
- Bundesministerium für Umwelt, Naturschutz, Bau und Reaktorsicherheit (BMUB) (2016): Deutsches Ressourceneffizienzprogramm II: Programm zur nachhaltigen Nutzung und zum Schutz der natürlichen Ressourcen, Retrieved from http://www.bmub.bund.de/fileadmin/Daten_BMU/Pool/Broschueren/progress_ii_broschue_bf.pdf, 2018-23-02.
- Bundesministerium für Wirtschaft und Technologie (BMWi) (2010): Rohstoffstrategie der Bundesregierung: Sicherung einer nachhaltigen Rohstoffversorgung Deutschlands mit nicht-energetischen mineralischen Rohstoffen, Retrieved from <http://www.rohstoffwissen.org/fileadmin/downloads/160720.rohstoffstrategie-der-bundesregierung.pdf>, 2018-03-14.
- Burns, R. G. (1970): *Mineralogical applications of crystal field theory*, Cambridge: University Press, XII, 224, 0-521-07610-2.

- Burns, R. G. (2005): *Mineralogical applications of crystal field theory*, (2nd ed.). *Cambridge topics in mineral physics and chemistry: Vol. 5*, Cambridge: Cambridge University Press, (2nd ed.), xxiii, 551, 978-0521017855.
- Buzzi, J., Riaza, A., García-Meléndez, E., Weide, S. & Bachmann, M. (2014): Mapping Changes in a Recovering Mine Site with Hyperspectral Airborne HyMap Imagery (Sotiel, SW Spain), *Minerals*, 4, (4), 313–329, <https://doi.org/10.3390/min4020313>.
- CAMO Software (2013): *Unscrambler documentation*.
- Chiang, P.-C. & Pan, S.-Y. (2017): *Carbon Dioxide Mineralization and Utilization*, Singapore: Springer Singapore, 452, 978-981-10-3267-7.
- Chong, I.-G. & Jun, C.-H. (2005): Performance of some variable selection methods when multicollinearity is present, *Chemometrics and Intelligent Laboratory Systems*, 78, (1-2), 103–112, <https://doi.org/10.1016/j.chemolab.2004.12.011>.
- Chukanov, N. V. (2014): *Infrared spectra of mineral species*, Dordrecht: Springer Netherlands, 1726, 978-94-007-7127-7.
- Chukanov, N. V. & Chervonnyi, A. D. (2016): *Infrared Spectroscopy of Minerals and Related Compounds*, Cham: Springer International Publishing, 1109, 978-3-319-25347-3.
- Clark, R. N. (1999): Spectroscopy of Rocks and Minerals, and Principles of Spectroscopy. In: A. N. Rencz (Ed.), *Manual of Remote Sensing: Volume 3, Remote Sensing for the Earth Sciences* (3–58). New York: John Wiley and Sons.
- Clark, R. N. (2004): Spectroscopy of rocks and minerals, and principles of spectroscopy. In: P. King, M. Ramsey, & G. Swayze (Eds.), *Short course series: Vol. 33. Infrared spectroscopy in geochemistry, exploration geochemistry and remote sensing* (17–55). Ottawa: Mineralogical Association of Canada.
- Clark, R. N., Gallagher, A. J. & Swayze G. A. (1990a): Material Absorption Band Depth Mapping of Imaging Spectrometer Data Using a Complete Band Shape Least-Squares Fit with Library Reference Spectra, *Proceedings of the Second Airborne Visible/Infrared Imaging Spectrometer (AVIRIS) Workshop, JPL Publication, 90*, (54).
- Clark, R. N., King, T. V. V., Klejwa, M., Swayze, G. A. & Vergo, N. (1990b): High spectral resolution reflectance spectroscopy of minerals, *Journal of Geophysical Research*, 95, (B8), 12653, <https://doi.org/10.1029/JB095iB08p12653>.
- Clark, R. N. & Roush, T. L. (1984): Reflectance spectroscopy: Quantitative analysis techniques for remote sensing applications, *Journal of Geophysical Research*, 89, (B7), 6329–6340, <https://doi.org/10.1029/JB089iB07p06329>.
- Clark, R. N., Swayze, G. A., Livo, K. E., Kokaly, R. F., Sutley, S. J., Dalton, J. B., Gent, C. A. (2003): Imaging spectroscopy: Earth and planetary remote sensing with the USGS Tetracorder and expert systems, *Journal of Geophysical Research*, 108, (E12), 16, <https://doi.org/10.1029/2002JE001847>.
- Clark, R. N., Swayze, G. A., Wise, R., Livo, E., Hoefen, T., Kokaly, R., & Sutley, S. J. (2007): USGS digital spectral library splib06a, Retrieved from http://speclab.cr.usgs.gov/spectral.lib06.*, 2017-07-12.
- Cloutis, E. A. (1996): Hyperspectral geological remote sensing: evaluation of analytical techniques, *International Journal of Remote Sensing*, 17, (12), 2212–2242.

- Cloutis, E. A. (2002): Pyroxene reflectance spectra: Minor absorption bands and effects of elemental substitutions, *Journal of Geophysical Research*, 107, (E6), 293, <https://doi.org/10.1029/2001JE001590>.
- Cloutis, E. A. & Bell, J. F. (2004): Mafic silicate mapping on Mars: Effects of palagonitic material, multiple mafic silicates, and spectral resolution, *Icarus*, 172, (1), 233–254, <https://doi.org/10.1016/j.icarus.2004.06.002>.
- Cloutis, E. A., Craig, M. A., Kruzelecky, R. V., Jamroz, W. R., Scott, A., Hawthorne, F. C. & Mertzman, S. A. (2008): Spectral reflectance properties of minerals exposed to simulated Mars surface conditions, *Icarus*, 195, (1), 140–168, <https://doi.org/10.1016/j.icarus.2007.10.028>.
- Cloutis, E. A. & Gaffey, M. J. (1993): The Constituent Minerals in Calcium-Aluminum Inclusions: Spectral Reflectance Properties and Implications for CO Carbonaceous Chondrites and Asteroids, *Icarus*, 105, (2), 568–579, <https://doi.org/10.1006/icar.1993.1150>.
- Cloutis, E. A., Gaffey, M. J., Smith, D. G. & Lambert, R. S. J. (1990): Reflectance spectra of mafic silicate-opaque assemblages with applications to meteorite spectra, *Icarus*, 84, (2), 315–333, [https://doi.org/10.1016/0019-1035\(90\)90041-7](https://doi.org/10.1016/0019-1035(90)90041-7).
- Cloutis, E. A., Hardersen, P. S., Bish, D. L., Bailey, D. T., Gaffey, M. J. & Craig, M. A. (2010): Reflectance spectra of iron meteorites: Implications for spectral identification of their parent bodies, *Meteoritics & Planetary Science*, 45, (2), 304–332, <https://doi.org/10.1111/j.1945-5100.2010.01033.x>.
- Cloutis, E. A., Sunshine, J. M. & Morris, R. V. (2004): Spectral reflectance-compositional properties of spinels and chromites: Implications for planetary remote sensing and geothermometry, *Meteoritics & Planetary Science*, 39, (4), 545–565, <https://doi.org/10.1111/j.1945-5100.2004.tb00918.x>.
- Cooper, B. L., Salisbury, J. W., Killen, R. M. & Potter, A. E. (2002): Midinfrared spectral features of rocks and their powders, *Journal of Geophysical Research*, 107, (E4), 1787, <https://doi.org/10.1029/2000JE001462>.
- Cornell, R. M. & Schwertmann, U. (2003): *The iron oxides: Structure, properties, reactions, occurrences and uses*, (2., completely rev. and extended ed.), Weinheim: Wiley-VCH, , 664, 9783527602094.
- Conel, J. E. (1969): Infrared emissivities of silicates: Experimental results and a cloudy atmosphere model of Spectral emission from condensed particulate mediums, *Journal of Geophysical Research*, 74, (6), 1614-1634, <https://doi.org/10.1029/JB074i006p01614>.
- Cortes, C. & Vapnik, V. (1995): Support-vector networks, *Machine Learning*, 20, (3), 273–297, <https://doi.org/10.1007/BF00994018>.
- Dalm, M., Buxton, M. W., van Ruitenbeek, F. J. & Voncken, J. H. (2014): Application of near-infrared spectroscopy to sensor-based sorting of a porphyry copper ore, *Minerals Engineering*, 58, 7–16, <https://doi.org/10.1016/j.mineng.2013.12.016>.
- Das, R., Ali, M. E. & Hamid, S. (2014): Current applications of x-ray powder diffraction - A review, *Reviews on advanced materials science*, 38, (2), 95–109.
- Das, B., Prakash, S., Reddy, P., Biswal, S. K., Mohapatra, B. K. & Misra, V. N. (2002): Effective Utilization of Blast Furnace Flue Dust of Integrated Steel Plants, *The European journal of Mineral Processing and Environmental Protection*, 2, (2), 61–68.
- Das, B., Prakash, S., Reddy, P. & Misra, V. N. (2007): An overview of utilization of slag and sludge from steel industries, *Resources, Conservation and Recycling*, 50, (1), 40–57, <https://doi.org/10.1016/j.resconrec.2006.05.008>.

- Decker, H. & Rüger, F. (1991): Der Kamsdorfer Bergbau und seine Mineralien., *Mineralien, Geologie und Bergbau in Ostthüringen*, 80–88.
- Demattê, J., Morgan, C., Chabrilat, S., Rizzo, R., Franceschini, M., Terra, F. S., Wetterlind, J. (2016): Spectral sensing from ground to space in soil science: state of the art, applications, potential, and perspectives. In: P. S. Thenkabail (Ed.), *Remote sensing handbook: Land resources monitoring, modeling, and mapping with remote sensing (Vol. 2)* (661–732). Boca Raton, FL: CRC Press.
- Denk, M., Gläßer, C., Kurz, T. H., Buckley, S. J. & Drissen, P. (2015): Mapping of iron and steelwork by-products using close range hyperspectral imaging: A case study in Thuringia, Germany, *European Journal of Remote Sensing*, 48, (1), 489–509, <https://doi.org/10.5721/EuJRS20154828>.
- Diener, S. (2006): Mineral phases of steel industry slags used in a landfill cover construction (Master's Thesis). Technische Universität Dresden, Dresden.
- Diener, S., Andreas, L., Herrmann, I. & Lagerkvist, A. Mineral transformations in steel slag used as landfill cover liner. In: *Proceedings Sardinia 2007, Eleventh International Waste Management and Landfill Symposium, S. Margherita di Pula, Cagliari, Italy; 1 - 5 October 2007*.
- Dippenaar, R. (2004): Industrial uses of slag—The use and re-use of iron and steelmaking slags. In: *VII International Conference on Molten Slags Fluxes and Salts* (37–69).
- Dohlen, M. & Steinweg, B. (2009): Aschen und Schlacken: Identifizierung und Charakterisierung in der bodenkundlichen Praxis., *Altlasten-Spektrum*, 5, 243–251.
- Dong, Y.-W., Yang, S.-Q., Xu, C.-Y., Li, Y.-Z., Bai, W., Fan, Z.-N. & Li, Q.-Z. (2011): Determination of Soil Parameters in Apple-Growing Regions by Near- and Mid-Infrared Spectroscopy, *Pedosphere*, 21, (5), 591–602, [https://doi.org/10.1016/S1002-0160\(11\)60161-6](https://doi.org/10.1016/S1002-0160(11)60161-6).
- Dormann, C. F. (2017): *Parametrische Statistik*, Berlin, Heidelberg: Springer Berlin Heidelberg, 350, 978-3-662-54683-3.
- Drake, N. A. (1995): Reflectance spectra of evaporite minerals (400-2500 nm): Applications for remote sensing, *International Journal of Remote Sensing*, 16, (14), 2555–2571, <https://doi.org/10.1080/01431169508954576>.
- Drissen, P. (2004): Eisenhüttenschlacken – industrielle Gesteine, *FEhS Report*, 11, (1), 4–9.
- Drissen, P. (2011): Aufkommen und Nutzung von Stäuben, Schlämmen und Walzzunder, *FEhS Report*, 18, (1), 1-3.
- Drissen, P. (2012): Ressourceneffiziente Herstellung von Dünger aus Stahlwerksschlacke und P₂O₅-haltigen Reststoffen, *FEhS Report*, 19, (2), 1–4,
- Drissen, P. & Algermissen, D. (2016): Verfestigung von Schlämmen aus Nassentstaubungsanlagen der Eisen- und Stahlindustrie, *FEhS Report*, 23, (1), 1–8,
- Drissen, P. & Arlt, K. (2000): Entstehung feinkörniger Pfannenschlacken, *FEhS Report*, 7, (2), 12-16.
- Drissen, P. & Mudersbach, D. (2012): Entwicklung von Baustoffen aus Edelstahlschlacken für Flächensanierung und Deponiebau, *FEhS Report*, 19, (1), 1–6.
- Drissen, P., Mudersbach, D., Schulbert, K. & Zehn, T. (2012): Stabilisierung sekundärmetallurgischer Schlacken aus der Qualitätsstahlerzeugung, *FEhS Report*, 19, (1), 10-14.

- Drobe, M., & Killiches, F. (2014): Vorkommen und Produktion mineralischer Rohstoffe - ein Ländervergleich: Rohstoffwirtschaftliche Einordnung aller Länder nach Reserven, Ressourcen, Bergbauproduktion und Raffinadeproduktion im weltweiten Vergleich, in Bezug auf die Bedeutung für Deutschland und für die jeweilige nationale Wirtschaft, Retrieved from https://www.bgr.bund.de/DE/Themen/Min_rohstoffe/Downloads/studie_rohstoffwirtschaftliche_einordnung_2014.pdf?__blob=publicationFile&v=4, 2018-03-14.
- Dürkoop, A., Gräbe, G., Brandstetter, C. & Rentsch, L. (Eds.). (2016): *Innovative Technologien für Ressourceneffizienz - Strategische Metalle und Mineralien: Mit CD-ROM. Ergebnisse der Fördermaßnahme r3*, Stuttgart: Fraunhofer Verlag, 440, 978-3-8396-1102-9.
- DWD - Deutscher Wetterdienst (2015): Niederschlag: langjährige Mittelwerte 1981 - 2010: Station 4332 Saalfed, Retrieved from https://www.dwd.de/DE/leistungen/klimadatendeutschland/mittelwerte/nieder_8110_akt.html.html?view=na&nn=16102*, 2018-02-27.
- Dyck, A. (2004): *Abschlussbericht Monitoring "Setzungsmessungen" Halde Maxhütte Untervellenborn "Gichtfeinschlammbecken"*. Archiv der Thüringer Landesanstalt für Umwelt und Geologie, Signatur II2 5334-510/2004.
- Eckey, H.-F., Kosfeld, R. & Rengers, M. (2002): *Multivariate Statistik: Grundlagen - Methoden - Beispiele*, Wiesbaden: Gabler, 442, 978-3-409-11969-6.
- Efimov, A. M. (1995): *Optical constants of inorganic glasses. The CRC Press laser and optical science and technology series*, Boca Raton: CRC Press, 202, 0-8493-3783-6.
- Efimov, A. M., Pogoreva, V. G. & Shashkin, A. V. (2003): Water-related bands in the IR absorption spectra of silicate glasses, *Journal of Non-Crystalline Solids*, 332, (1-3), 93–114, <https://doi.org/10.1016/j.jnoncrysol.2003.09.020>.
- Ehrenberg, A. (2006a): Hüttensand - Ein leistungsfähiger Baustoff mit Tradition und Zukunft Teil 1, *Beton-Informationen*, (4), 35–63.
- Ehrenberg, A. (2006b): Hüttensand - Ein leistungsfähiger Baustoff mit Tradition und Zukunft Teil 2, *Beton-Informationen*, (5), 67–95.
- Eisele, A. (2014): Möglichkeiten der Nutzung thermal-infraroter Wellenlängen zur fernerkundlichen Erfassung/Quantifizierung von Bodenparametern in semiariden Agrarregionen – eine vergleichende Studie der spektralen Bereiche des LWIR und des VNIR-SWIR auf der Basis von Labormessungen. Humboldt-Universität zu Berlin, Berlin.
- Eisele, A., Chabrilat, S., Hecker, C., Hewson, R., Lau, I. C., Rogass, C., Kaufmann, H. (2015): Advantages using the thermal infrared (TIR) to detect and quantify semi-arid soil properties, *Remote Sensing of Environment*, 163, 296–311, <https://doi.org/10.1016/j.rse.2015.04.001>.
- Eisele, A., Lau, I., Hewson, R., Carter, D., Wheaton, B., Ong, C. & Kaufmann, H. (2012): Applicability of the Thermal Infrared Spectral Region for the Prediction of Soil Properties Across Semi-Arid Agricultural Landscapes, *Remote Sensing*, 4, (12), 3265–3286, <https://doi.org/10.3390/rs4113265>.
- EPC GmbH (1996): *Historische Recherche zur Industriebalde (unpublished)*.
- Esbensen, K., Guyot, D., Westad, F. & Houmoller, L. P. (2012): *Multivariate data analysis-in practice: An introduction to multivariate data analysis and experimental design*, (5th ed.), Oslo: CAMO, (5th ed.), 598, 82-993330-3-2.
- Estep-Barnes, P. A. (1977): Infrared Spectroscopy. In: J. Zussman (Ed.), *Physical methods in determinative mineralogy* (529–603). London: Academic Press.

- European Union. (2016): *Energy, transport and environment indicators*, (2016 ed.). *Energy, transport and environment indicators, Data*, Luxembourg: Publications Office of the European Union, (2016 ed.), Retrieved from <http://ec.europa.eu/eurostat/documents/3217494/7731525/KS-DK-16-001-EN-N.pdf/cc2b4de7-146c-4254-9521-dcbd6e6fafa6>, 231 str., 978-92-79-60138-5.
- Farmer, V. C. (1974): *The Infrared Spectra of Minerals*, London: Mineralogical Society of Great Britain and Ireland, 539, 9780903056052.
- Farrand, W. H., Wright, S. P., Rogers, A. D. & Glotch, T. D. (2016): Basaltic glass formed from hydrovolcanism and impact processes: Characterization and clues for detection of mode of origin from VNIR through MWIR reflectance and emission spectroscopy, *Icarus*, 275, 16–28, <https://doi.org/10.1016/j.icarus.2016.03.027>.
- Faulques, E., Fritsch, E. & Ostroumov, M. (2001): Spectroscopy of natural silica-rich glasses, *Journal of Mineralogical and Petrological Sciences*, 96, (3), 120–128, <https://doi.org/10.2465/jmps.96.120>.
- Feely, K. C. & Christensen, P. R. (1999): Quantitative compositional analysis using thermal emission spectroscopy: Application to igneous and metamorphic rocks, *Journal of Geophysical Research*, 104, (E10), 24195–24210, <https://doi.org/10.1029/1999JE001034>.
- Feng, C., Chu, M., Tang, J., Tang, Y. & Liu, Z. (2016): Effect of CaO/SiO₂ and Al₂O₃ on Viscous Behaviors of the Titanium-Bearing Blast Furnace Slag, *steel research international*, 87, (10), 1274–1283, <https://doi.org/10.1002/srin.201500355>.
- Fernandes, G. W., Goulart, F. F., Ranieri, B. D., Coelho, M. S., Dales, K., Boesche, N. & Soares-Filho, B. (2016): Deep into the mud: Ecological and socio-economic impacts of the dam breach in Mariana, Brazil, *Natureza & Conservação*, 14, (2), 35–45, <https://doi.org/10.1016/j.ncon.2016.10.003>.
- Fernández-González, D., Ruiz-Bustinza, I., Mochón, J., González-Gasca, C. & Verdeja, L. F. (2017): Iron Ore Sintering: Process, *Mineral Processing and Extractive Metallurgy Review*, 38, (4), 215–227, <https://doi.org/10.1080/08827508.2017.1288115>.
- Forrester, S. T., Janik, L. J., Soriano-Disla, J. M., Mason, S., Burkitt, L., Moody, P., McLaughlin, M. J. (2015): Use of handheld mid-infrared spectroscopy and partial least-squares regression for the prediction of the phosphorus buffering index in Australian soils, *Soil Research*, 53, (1), 67, <https://doi.org/10.1071/SR14126>.
- Förderverein Schaudenkmal Gaszentrale Unterwellenborn e.V.: <http://www.gmzuborn.de/seite01.htm>, 2018-03-23.
- Gaffey, S. J. (1986): Spectral reflectance of carbonate minerals in the visible and near infrared (0.35 - 2.55 microns), *American Mineralogist*, 71, 151–162.
- Gannouni, S., Rebai, N. & Abdeljaoued, S. (2012): A Spectroscopic Approach to Assess Heavy Metals Contents of the Mine Waste of Jalta and Bougrine in the North of Tunisia, *Journal of Geographic Information System*, 04, (03), 242–253, <https://doi.org/10.4236/jgis.2012.43029>.
- Gara, S. & Schrimpf, S. (1998): *Behandlung von Reststoffen und Abfällen in der Eisen- und Stahlindustrie. Monographien / Umweltbundesamt: Bd. 92*, Wien: Umweltbundesamt, 114, 3-85457-394-4.
- Geerken, R. (1991): Informationspotential von spektral hochauflösenden Fernerkundungsdaten für die Identifizierung von Mineralen und Gesteinen: Laborversuche und Anwendungsbeispiele in der Geologie (Ph.D. thesis). University of Karlsruhe, Karlsruhe.

- Geiseler, J. (1996): Use of steelworks slag in Europe, *Waste Management*, 16, (1-3), 59–63, [https://doi.org/10.1016/S0956-053X\(96\)00070-0](https://doi.org/10.1016/S0956-053X(96)00070-0).
- Geladi, P. & Kowalski, B. R. (1986): Partial least-squares regression: A tutorial, *Analytica Chimica Acta*, 185, 1–17, [https://doi.org/10.1016/0003-2670\(86\)80028-9](https://doi.org/10.1016/0003-2670(86)80028-9).
- Geladi, P., MacDougall, D. & Martens, H. (1985): Linearization and Scatter-Correction for Near-Infrared Reflectance Spectra of Meat, *Applied Spectroscopy*, 39, (3), 491–500, <https://doi.org/10.1366/0003702854248656>.
- Geschichtsverein Maximilianshütte/Maxhütte e.V. (1997): *Die Maxhütte Unterwellenborn vor 1873 bis 1920 (Teil I): Aus alten Traditionen wächst ein neues Werk*, Unterwellenborn.
- Geschichtsverein Maximilianshütte/Maxhütte e.V. (1998): *Die Maxhütte Unterwellenborn 1921 bis 1945 (Teil II): Der metallurgische Großbetrieb im Thüringer Land*, Unterwellenborn.
- Geschichtsverein Maximilianshütte/Maxhütte e.V. (2004): *Die Maxhütte Unterwellenborn 1945 bis 1950 (Teil III): Vom schweren Anfang zum VEB Maxhütte*, Unterwellenborn: Geschichtsverein Maximilianshütte/Maxhütte, 196, 3-9809410-3-5.
- Geschichtsverein Maximilianshütte/Maxhütte e.V. (2005): *Die Maxhütte Unterwellenborn 1951 bis 1965 (Teil IV): Nach den schweren Nachkriegsjahren neue Zuversicht für den weiteren Ausbau des Werkes*, 3-9809410-4-3.
- Geschichtsverein Maximilianshütte/Maxhütte e.V. (2011): *Die Maxhütte Unterwellenborn 1966 bis 1989 (Teil V): Nach Jahren der Stagnation die Modernisierung der metallurgischen Stufen einschließlich des Großvorhabens Kombinierte Formstahlstraße*, 3-980 9410-5-6.
- Geschichtsverein Maximilianshütte/Maxhütte e.V. (2012): *Die Maxhütte Unterwellenborn GmbH von 1990 bis 30. Juni 1992 und die Entwicklung der Stahlwerk Thüringen GmbH von der Gründung am 1. Juli 1992 bis 31. Dezember 2006 (Teil VI): Stahlwerk Thüringen GmbH - eine erfolgreiche Privatisierung in der Stahlindustrie der ehemaligen DDR*, 3-9809410-7-8.
- Ghosh, S. N. & Chatterjee, A. K. (1974): Absorption and reflection infra-red spectra of major cement minerals, clinkers and cements, *Journal of Materials Science*, 9, (10), 1577–1584, <https://doi.org/10.1007/BF00540754>.
- Ghosh, A. & Chatterjee, A. (2008): *Ironmaking and steelmaking: Theory and practice*, New Delhi: Prentice-Hall of India, 472, 9788120332898.
- Ghosh, S., Prasanna, V. L., Sowjanya, B., Srivani, P., Alagaraja, M. & Banji, D. (2013): Inductively Coupled Plasma –Optical Emission Spectroscopy: A Review, *Asian Journal of Pharmaceutical Analysis*, 3, (1), 24–33,
- Glanville, K. & Chang, H.-C. (2015): Remote Sensing Analysis Techniques and Sensor Requirements to Support the Mapping of Illegal Domestic Waste Disposal Sites in Queensland, Australia, *Remote Sensing*, 7, (12), 13053–13069, <https://doi.org/10.3390/rs71013053>.
- Gläßer, C. (2004): *Nachhaltige Entwicklung von Folgelandschaften des Braunkohlebergbaus: Stand und Perspektiven in Wissenschaft und Praxis*, (1. Aufl.). *Zeitschrift für angewandte Umweltforschung. Sonderheft: Vol. 14*, Berlin: Analytica-Verl., (1. Aufl.), 312, 978-3929342765.
- Gläßer, C., Groth, D. & Frauendorf, J. (2011): Monitoring of hydrochemical parameters of lignite mining lakes in Central Germany using airborne hyperspectral casi-scanner data, *International Journal of Coal Geology*, 86, (1), 40–53, <https://doi.org/10.1016/j.coal.2011.01.007>.

- Goetz, A. F. (2009): Three decades of hyperspectral remote sensing of the Earth: A personal view, *Remote Sensing of Environment*, 113, S5-S16, <https://doi.org/10.1016/j.rse.2007.12.014>.
- Goetz, A. F., Curtiss, B. & Shiley, D. A. (2009): Rapid gangue mineral concentration measurement over conveyors by NIR reflectance spectroscopy, *Minerals Engineering*, 22, (5), 490–499, <https://doi.org/10.1016/j.mineng.2008.12.013>.
- Goetz, A. F. H., Rock, B. N. & Rowan, L. C. (1983): Remote sensing for exploration; an overview, *Economic Geology*, 78, (4), 573–590, <https://doi.org/10.2113/gsecongeo.78.4.573>.
- Goetz, A. F. & Rowan, L. C. (1981): Geologic remote sensing, *Science*, 211, (4484), 781–791, <https://doi.org/10.1126/science.211.4484.781>.
- Goguen, J. D. (1981): A theoretical and experimental investigation of the photometric functions of particulate surfaces (Ph.D. thesis). Cornell University.
- Gomes, C. E. M. & Ferreira, O. P. (2005): Analyses of microstructural properties of VA/VeoVA copolymer modified cement pastes, *Polímeros*, 15, (3), 193–198, <https://doi.org/10.1590/S0104-14282005000300009>.
- Goodwin, D. G. & Mitchner, M. (1986): Measurements of the near infrared optical properties of coal slags, *Chemical Engineering Communications*, 44, (1-6), 241–255, <https://doi.org/10.1080/00986448608911358>.
- Götze, C., Beyer, F. & Gläßer, C. (2016): Pioneer vegetation as an indicator of the geochemical parameters in abandoned mine sites using hyperspectral airborne data, *Environmental Earth Sciences*, 75, (7), 37, <https://doi.org/10.1007/s12665-016-5367-1>.
- Götze, C., Denk, M., Riedel, F. & Gläßer, C. (2017): Interlaboratory Comparison of Spectrometric Laboratory Measurements of a Chlorite Rock Sample, *PFG – Journal of Photogrammetry, Remote Sensing and Geoinformation Science*, 85, (5), 307–316, <https://doi.org/10.1007/s41064-017-0031-2>.
- Graedel, T. E. (2009): *Metal stocks in society: Scientific synthesis*, Paris: UNEP DTIE, 48, 978-92-807-3082-1.
- Green, D. & Schodlok, M. (2016): Characterisation of carbonate minerals from hyperspectral TIR scanning using features at 14 000 and 11 300 nm, *Australian Journal of Earth Sciences*, 71, 1–7, <https://doi.org/10.1080/08120099.2016.1225601>.
- Großtagebau Kamsdorf GmbH. <http://www.tagebau-kamsdorf.de/>. 2018-02-26.
- Grundmann, L. (2001): *Saalfeld und das Thüringer Schiefergebirge: Eine landeskundliche Bestandsaufnahme im Raum Saalfeld, Leutenberg und Lauenstein. Werte der deutschen Heimat: Vol. 62*, Köln: Böhlau, 293, 3-412-10800-6.
- Guldan, D. (2013): Aufbereitung von Edelstahlschlacken. In: K. J. Thomé-Kozmiensky (Ed.), *Aschen-Schlacken-Stäube: Aus Abfallverbrennung und Metallurgie* (565–586). Neuruppin: TK.
- Günther, T. & Martin, T. (2016): Spectral two-dimensional inversion of frequency-domain induced polarization data from a mining slag heap, *Journal of Applied Geophysics*, 135, 436–448, <https://doi.org/10.1016/j.jappgeo.2016.01.008>.
- Gupta, P. K. (1996): Non-crystalline solids: Glasses and amorphous solids, *Journal of Non-Crystalline Solids*, 195, (1-2), 158–164, [https://doi.org/10.1016/0022-3093\(95\)00502-1](https://doi.org/10.1016/0022-3093(95)00502-1).
- Gupta, R. P. (2018): *Remote Sensing Geology*, Berlin, Heidelberg: Springer Berlin Heidelberg, 428, 978-3-662-55874-4.

- Gutiérrez J.A., Picon A., Rodríguez S. & Girbau I. (2010): The application of hyperspectral image processing to the steel foundry process. In: *Proceedings of the International Surface Inspection Summit*.
- Hall, G. (1992): Inductively coupled plasma mass spectrometry in geoanalysis, *Journal of Geochemical Exploration*, 44, (1-3), 201–249, [https://doi.org/10.1016/0375-6742\(92\)90051-9](https://doi.org/10.1016/0375-6742(92)90051-9).
- Hapke, B. (1981): Bidirectional reflectance spectroscopy: 1. Theory, *Journal of Geophysical Research*, 86, (B4), 3039–3054, <https://doi.org/10.1029/JB086iB04p03039>.
- Hapke, B. (2012): *Theory of reflectance and emittance spectroscopy*, (2. ed.), Cambridge, New York: Cambridge University Press, (2. ed.), 513, 978-0521883498.
- Hauff, P. L. (2005): *Applied reflectance spectroscopy: With emphasis on data collection and data interpretation using field spectrometers*.
- Hauff, P. L. (2008): An overview of VIS-NIR-SWIR field spectroscopy as applied to precious metals exploration, Retrieved from <http://www.spectral-international.com/files/50329239.pdf>, 2018-03-14.
- Hecker, C. A. (2012): Mapping Feldspars from Above — a Thermal Infrared and Partial Least Squares-based Approach (Ph.D. thesis). University of Twente, Enschede.
- Hecker, C., Dilles, J. H., van der Meijde, M. & van der Meer, F. D. (2012): Thermal infrared spectroscopy and partial least squares regression to determine mineral modes of granitoid rocks, *Geochemistry, Geophysics, Geosystems*, 13, (3), 1-15, <https://doi.org/10.1029/2011GC004004>.
- Hecker, C., Hook, S., van der Meijde, M., Bakker, W., van der Werff, H., Wilbrink, H., van der Meer, F. (2011): Thermal infrared spectrometer for Earth science remote sensing applications-instrument modifications and measurement procedures, *Sensors (Basel, Switzerland)*, 11, (11), 10981–10999, <https://doi.org/10.3390/s111110981>.
- Hecker, C., van der Meijde, M. & van der Meer, F. D. (2010): Thermal infrared spectroscopy on feldspars - Successes, limitations and their implications for remote sensing, *Earth-Science Reviews*, 103, (1-2), 60-70, <https://doi.org/10.1016/j.earscirev.2010.07.005>.
- Heite, W. (2015): Konzeption der mechanischen Aufbereitung von Haldenmaterialien aus der Eisen- und Stahlindustrie als Teil der Prozesskette zur Wertstoffgewinnung (Master's Thesis). Ruhr-Universität Bochum.
- Herrmann, I., Andreas, L., Diener, S. & Lind, L. (2010): Steel slag used in landfill cover liners: Laboratory and field tests, *Waste management & research: the journal of the International Solid Wastes and Public Cleansing Association, ISWA*, 28, (12), 1114–1121, <https://doi.org/10.1177/0734242X10365095>.
- Heußen, M. & Markus, H. P. (2013): Ressourcenmanagement eines Elektrostahlwerks. In: K. J. Thomé-Kozmiensky (Ed.), *Aschen-Schlacken-Stäube: Aus Abfallverbrennung und Metallurgie* (485–505). Neuruppin: TK.
- Hiekel, W., Fritzlar, F., Nöllert, A., Westhus & W. (2004): Die Naturräume Thüringen, *Naturschutzreport*, 21.
- Hirschmugl, C. (2004): An introduction to infrared spectroscopy for geochemistry and remote sensing. In: P. King, M. Ramsey & G. Swayze (Eds.), *Short course series: Vol. 33. Infrared spectroscopy in geochemistry, exploration geochemistry and remote sensing* (1–16). Ottawa: Mineralogical Association of Canada.
- Horgan, B. & Bell, J. F. (2012): Widespread weathered glass on the surface of Mars, *Geology*, 40, (5), 391–394, <https://doi.org/10.1130/G32755.1>.

- Horgan, B. H., Cloutis, E. A., Mann, P. & Bell, J. F. (2014): Near-infrared spectra of ferrous mineral mixtures and methods for their identification in planetary surface spectra, *Icarus*, 234, 132–154, <https://doi.org/10.1016/j.icarus.2014.02.031>.
- Horgnies, M., Chen, J. J. & Bouillon, C. (2013) Overview about the use of Fourier Transform Infrared spectroscopy to study cementitious materials. In: C. A. Brebbia, A. Mammoli, & A. Klemm (Eds.): *WIT Transactions on Engineering Sciences* (251–262). WIT Press Southampton, UK, <https://doi.org/10.2495/MC130221>.
- Hotelling, H. (1933): Analysis of a complex of statistical variables into principal components, *Journal of Educational Psychology*, 24, (6), 417–441, <https://doi.org/10.1037/h0071325>.
- Hsu, C.-W., Chang, C.-C. & Lin, C.-J. (2016): A Practical Guide to Support Vector Classification, Retrieved from <https://www.csie.ntu.edu.tw/~cjlin/papers/guide/guide.pdf>, 2018-03-14.
- Huaiwei, Z. & Xin, H. (2011): An overview for the utilization of wastes from stainless steel industries, *Resources, Conservation and Recycling*, 55, (8), 745–754, <https://doi.org/10.1016/j.resconrec.2011.03.005>.
- Hubbart, C. R & Snyder, R. L. (1988): RIR - Measurement and Use in Quantitative XRD. *Powder Diffraction*, 3, 2, 74-77, <https://doi.org/10.1017/S0885715600013257>.
- Hueni, A. & Bialek, A. (2017): Cause, Effect, and Correction of Field Spectroradiometer Interchannel Radiometric Steps, *IEEE Journal of Selected Topics in Applied Earth Observations and Remote Sensing*, 10, (4), 1542–1551, <https://doi.org/10.1109/JSTARS.2016.2625043>.
- Hunt, G. R. (1977): Spectral signatures of particulate minerals in the visible and near infrared, *Geophysics*, 42, (3), 501–513, <https://doi.org/10.1190/1.1440721>.
- Hunt, G. R. (1980): Electromagnetic radiation: The communication link in remote sensing. In: B. S. Siegal & A. R. Gillespie (Eds.), *Remote sensing in geology* (5–45). New York: Wiley.
- Hunt, G. R. (op. 1982): Spectroscopic properties of rocks and minerals. In: R. S. Carmichael (Ed.), *Handbook of physical properties of rocks* (295–385). Boca Raton: CRC Press.
- Hunt, G. R. & Salisbury, J. W. (1970): Visible and near-infrared spectra of minerals and rocks: I. Silicate minerals, *Modern Geology*, 1, 283–300.
- Hunt, G. R. & Salisbury, J. W. (1971): Visible and near-infrared spectra of minerals and rocks: II. Carbonates, *Modern Geology*, 2, 23–30.
- Hunt, G. R. & Salisbury, J. W. (1976a): Visible and near-infrared spectra of minerals and rocks: XI. Sedimentary rocks, *Modern Geology*, 5, 211–217.
- Hunt, G. R. & Salisbury, J. W. (1976b): Visible and near-infrared spectra of minerals and rocks: XII. Metamorphic rocks, *Modern Geology*, 5, 219–228.
- Hunt, G. R., Salisbury, J. W. & Lenhoff, C. J. (1971a): Visible and near-infrared spectra of minerals and rocks: III. Oxides and hydroxides, *Modern Geology*, 2, 195–205.
- Hunt, G. R., Salisbury, J. W. & Lenhoff, C. J. (1971b): Visible and near-infrared spectra of minerals and rocks: IV. Sulphides and sulphates, *Modern Geology*, 3, 1–14.
- Hunt, G. R., Salisbury, J. W. & Lenhoff, C. J. (1972): Visible and near-infrared spectra of minerals and rocks: V. Halides, arsenates, vanadates, and borates, *Modern Geology*, 3, 121–132.
- Hunt, G. R., Salisbury, J. W. & Lenhoff, C. J. (1973a): Visible and near-infrared spectra of minerals and rocks: VI. Additional silicates, *Modern Geology*, 4, 85–106.
- Hunt, G. R., Salisbury, J. W. & Lenhoff, C. J. (1973b): Visible and near-infrared spectra of minerals and rocks: VII. Acidic igneous rocks, *Modern Geology*, 4, 217–224.

- Hunt, G. R., Salisbury, J. W. & Lenhoff, C. J. (1973c): Visible and near-infrared spectra of minerals and rocks: VIII. Intermediate igneous rocks, *Modern Geology*, 4, 237–244.
- Hunt, G. R., Salisbury, J. W. & Lenhoff, C. J. (1974): Visible and near-infrared spectra of minerals and rocks: IX. Basic and ultrabasic igneous rocks, *Modern Geology*, 5, 15–22.
- Hunt, G. R., Salisbury, J. W. & Lenhoff, C. J. (1975): Visible and near-infrared spectra of minerals and rocks: X. Stony meteorites, *Modern Geology*, 5, 115–126.
- Hunt, J. M. & Turner, D. S. (1953): Determination of Mineral Constituents of Rocks by Infrared Spectroscopy, *Analytical Chemistry*, 25, (8), 1169–1174, <https://doi.org/10.1021/ac60080a007>.
- Intera Kenting Ltd. (1992): *Remote sensing to monitor uranium tailing sites - a review (AECB Project No. 5.142.1): A research report prepared for the Atomic Energy Control Board Ottawa, Canada*.
- IPCC, 2007: Climate Change 2007: Mitigation. Contribution of Working Group III to the Fourth Assessment Report of the Intergovernmental Panel on Climate Change [B. Metz, O.R. Davidson, P.R. Bosch, R. Dave, L.A. Meyer (eds)], Cambridge University Press, Cambridge, United Kingdom and New York, NY, USA, Retrieved from https://www.ipcc.ch/pdf/assessment-report/ar4/wg3/ar4_wg3_full_report.pdf, 2018-03-14.
- Irons, J. R., Weismiller, R. A. & Weismiller, W., Petersen, G. (1989): Soil reflectance. In: G. Asrar (Ed.), *Wiley series in remote sensing. Theory and applications of optical remote sensing*. New York: Wiley.
- Isaksson, T. & Næs, T. (1988): Effect of multiplicative scatter correction (MSC) and linearity improvement in NIR spectroscopy, *Applied Spectroscopy*, 42, (7), 1273–1284.
- Izawa, M., Cloutis, E. A., Rhind, T., Mertzman, S. A., Poitras, J., Applin, D. M. & Mann, P. (2018): Spectral reflectance (0.35–2.5 µm) properties of garnets: Implications for remote sensing detection and characterization, *Icarus*, 300, 392–410, <https://doi.org/10.1016/j.icarus.2017.09.005>.
- Jandewerth, M., Denk, M., Gläßer, C., Mrotzek, A. & Teuwsen, S. (2013): Fraunhofer-Gesellschaft Reduktion von Rohstoffimporten durch Wertstoffgewinnung aus Hüttenhalden - Entwicklung eines multiskalaren Ressourcenkatasters für Hüttenhalden. In: K. J. Thomé-Kozmiensky (Ed.), *Aschen-Schlacken-Stäube: Aus Abfallverbrennung und Metallurgie* (639–660). Neuruppin: TK.
- Jansen, D., Stabler, Ch., Goetz-Neunhoeffler, F., Dittrich, S. & Neubauer, J. (2011): Does Ordinary Portland Cement contain amorphous phase? A quantitative study using an external standard method. *Powder Diffraction*, 26, 1, 31–38, <https://doi.org/10.1154/1.3549186>.
- Jarmer, T. (2005): Der Einsatz von Reflexionsspektrometrie und Satellitenbilddaten zur Erfassung pedochemischer Eigenschaften in semi-ariden und ariden Gebieten Israels (Ph.D. thesis). University of Trier, Trier.
- Jolliffe, I. T. (2002): *Principal Component Analysis*, New York: Springer-Verlag, 488, 0-387-95442-2.
- Juhart, M., Peter, M. & Koch, K. (2001): Schaumschlacken in der Stahl-Metallurgie, *TUContact*, (9), 38–41.
- Jung, A., Götze, C. & Glässer, C. (2012): Overview of Experimental Setups in Spectroscopic Laboratory Measurements – the SpecTour Project, *Photogrammetrie - Fernerkundung - Geoinformation*, 2012, (4), 433–442, <https://doi.org/10.1127/1432-8364/2012/0129>.
- Kanning, M., Siegmann, B. & Jarmer, T. (2016): Regionalization of Uncovered Agricultural Soils Based on Organic Carbon and Soil Texture Estimations, *Remote Sensing*, 8, (12), 927, <https://doi.org/10.3390/rs8110927>.

- Karmanova, A. (1981): Effect of various iron compounds on the spectral reflectance and color of soils., *Soviet Soil Science*, *9*, 53–60.
- Kawamura, K., Tsujimoto, Y., Rabenarivo, M., Asai, H., Andriamananjara, A. & Rakotoson, T. (2017): Vis-NIR Spectroscopy and PLS Regression with Waveband Selection for Estimating the Total C and N of Paddy Soils in Madagascar, *Remote Sensing*, *9*, (12), 1081, <https://doi.org/10.3390/rs9101081>.
- Kemper, T. & Sommer, S. (2002): Estimate of Heavy Metal Contamination in Soils after a Mining Accident Using Reflectance Spectroscopy, *Environmental science & technology*, *36*, (12), 2742–2747, <https://doi.org/10.1021/es015747j>.
- Kennard, R. W. & Stone, L. A. (1969): Computer aided design of experiments, *Technometrics*, *11*, (1), 137–148.
- King, P., Ramsey, M., McMillan, P. F. & Swayze, G. (2004a): Laboratory Fourier transform infrared spectroscopy methods for geologic samples. In: P. King, M. Ramsey, & G. Swayze (Eds.), *Short course series: Vol. 33. Infrared spectroscopy in geochemistry, exploration geochemistry and remote sensing* (57–91). Ottawa: Mineralogical Association of Canada.
- King, P., McMillan, P. F. & Moore, G. M. (2004b): Infrared spectroscopy of silicate glasses with application to natural systems. In P. King, M. Ramsey, & G. Swayze (Eds.), *Short course series: Vol. 33. Infrared spectroscopy in geochemistry, exploration geochemistry and remote sensing* (93–133). Ottawa: Mineralogical Association of Canada.
- Kirkland, L., Herr, K., Keim, E., Adams, P., Salisbury, J., Hackwell, J. & Treiman, A. (2002): First use of an airborne thermal infrared hyperspectral scanner for compositional mapping, *Remote Sensing of Environment*, *80*, (3), 447–459, [https://doi.org/10.1016/S0034-4257\(01\)00323-6](https://doi.org/10.1016/S0034-4257(01)00323-6).
- Klinglmair, M. & Fellner, J. (2010): Urban Mining in Times of Raw Material Shortage, *Journal of Industrial Ecology*, *14*, (4), 666–679, <https://doi.org/10.1111/j.1530-9290.2010.00257.x>.
- Koerting, F., Rogass, C., Kaempf, H., Lubitz, C., Harms, U., Schudack, M., Altenberger, U. (2015): Drill core mineral analysis by means of the hyperspectral imaging spectrometer hypex, xrd and asd in proximity of the mýtina maar, czech republic, *ISPRS - International Archives of the Photogrammetry, Remote Sensing and Spatial Information Sciences, XL-1-W5*, 417–424, <https://doi.org/10.5194/isprsarchives-XL-1-W5-417-2015>.
- Kokaly, R.F., Clark, R.N., Swayze, G.A., Livo, K.E., Hoefen, T.M., Pearson, N.C., Wise, R.A., Benzel, W.M., Lowers, H.A. (Ed.). (2017): USGS Spectral Library Version 7 [Special issue], *U.S. Geological Survey Data Series*, (1035).
- Kooistra, L., Wehrens, R., Leuven, R. & Buydens, L. (2001): Possibilities of visible–near-infrared spectroscopy for the assessment of soil contamination in river floodplains, *Analytica Chimica Acta*, *446*, (1-2), 97–105, [https://doi.org/10.1016/S0003-2670\(01\)01265-X](https://doi.org/10.1016/S0003-2670(01)01265-X).
- Kotthaus, S., Smith, T. E., Wooster, M. J. & Grimmond, C. (2014): Derivation of an urban materials spectral library through emittance and reflectance spectroscopy, *ISPRS Journal of Photogrammetry and Remote Sensing*, *94*, 194–212, <https://doi.org/10.1016/j.isprsjprs.2014.05.005>.
- Kraft, G. & Fischer, J. (1963): Die Bestimmung von metallischem, zweiwertigem und dreiwertigem Eisen nebeneinander in Eisenhüttenprodukten, *Fresenius' Zeitschrift für analytische Chemie*, *197*, (2), 217–221.

- Krivsky, W. A. (1973): The linde argon-oxygen process for stainless steel; A case study of major innovation in a basic industry, *Metallurgical transactions*, *4*, 1439–1447.
- Krook, J. & Baas, L. (2013): Getting serious about mining the technosphere: A review of recent landfill mining and urban mining research, *Journal of Cleaner Production*, *55*, 1–9, <https://doi.org/10.1016/j.jclepro.2013.04.043>.
- Kruse, F. A., Lefkoff, A. B., Boardman, J. W., Heidebrecht, K. B., Shapiro, A. T., Barloon, P. J. & Goetz, A. (1993): The spectral image processing system (SIPS)—interactive visualization and analysis of imaging spectrometer data, *Remote Sensing of Environment*, *44*, (2-3), 145–163, [https://doi.org/10.1016/0034-4257\(93\)90013-N](https://doi.org/10.1016/0034-4257(93)90013-N).
- Kuenzer, C. & Dech, S. (2013): *Thermal Infrared Remote Sensing*, (Vol. 17), Dordrecht: Springer Netherlands, 537, 978-94-007-6638-9.
- Kurz, T. H., Buckley, S. J. & Howell, J. A. (2013): Close-range hyperspectral imaging for geological field studies: Workflow and methods, *International Journal of Remote Sensing*, *34*, (5), 1798–1822, <https://doi.org/10.1080/01431161.2012.727039>.
- Kurz, T. H., Dewit, J., Buckley, S. J., Thurmond, J. B., Hunt, D. W. & Swennen, R. (2012): Hyperspectral image analysis of different carbonate lithologies (limestone, karst and hydrothermal dolomites): The Pozalagua Quarry case study (Cantabria, North-west Spain), *Sedimentology*, *59*, (2), 623–645, <https://doi.org/10.1111/j.1365-3091.2011.01269.x>.
- Launer, P. J. (1952): Regularities in the infrared absorption spectra of silicate minerals., *American Mineralogist*, *37*, 764–784.
- Lillesand, T. M., Kiefer, R. W. & Chipman, J. W. (repr. 2013, 2008): *Remote sensing and image interpretation*, (6th ed.), Hoboken, NJ: John Wiley & Sons, (6th ed.), 756, 978-0-470-05245-7.
- Liu, C., Guo, M., Blanpain, B. & Huang, S. (2017): Effect of Al₂O₃ addition on the crystallisation of a high basicity BOF slag: perspective of glass forming ability for slag valorisation, *Proceedings of the 5th International Slag Valorisation Symposium, Leuven*, 121–124.
- Liu, Y., Jiang, Q., Fei, T., Wang, J., Shi, T., Guo, K. & Chen, Y. (2014): Transferability of a Visible and Near-Infrared Model for Soil Organic Matter Estimation in Riparian Landscapes, *Remote Sensing*, *6*, (12), 4305–4322, <https://doi.org/10.3390/rs6054305>.
- Liukkonen, M., Penttilä, K. & Koukkari, P. *A compilation of slag foaming phenomenon research: Theoretical studies, industrial experiments and modelling*, 2012: VTT Technology 63, 128, 978-951-38-7897-9.
- Logan, L. M., Hunt, G. R., Salisbury, J. W. & Balsamo, S. R. (1973): Compositional implications of Christiansen frequency maximums for infrared remote sensing applications, *Journal of Geophysical Research*, *78*, (23), 4983–5003, <https://doi.org/10.1029/JB078i023p04983>.
- Lucey, P. G., Greenhagen, B. T., Song, E., Arnold, J. A., Lemelin, M., Hanna, K. D. & Paige, D. A. (2017): Space weathering effects in Diviner Lunar Radiometer multispectral infrared measurements of the lunar Christiansen Feature: Characteristics and mitigation, *Icarus*, *283*, 343–351, <https://doi.org/10.1016/j.icarus.2016.05.010>.
- Lumme, K. & Bowell, E. (1981): Radiative transfer in the surfaces of atmosphereless bodies. I - Theory. II - Interpretation of phase curves, *The Astronomical Journal*, *86*, 1694, <https://doi.org/10.1086/113054>.
- Lyon, R. J. P. (1965): Analysis of rocks by spectral infrared emission (8 to 25 microns), *Economic Geology*, *60*, (4), 715–736, <https://doi.org/10.2113/gsecongeo.60.4.715>.

- Lyon, R. J. P. & Burns, E. A. (1963): Analysis of rocks and minerals by reflected infrared radiation, *Economic Geology*, *58*, (2), 274–284, <https://doi.org/10.2113/gsecongeo.58.2.274>.
- Mac Arthur, A., MacLellan, C. J. & Malthus, T. (2012): The Fields of View and Directional Response Functions of Two Field Spectroradiometers, *IEEE Transactions on Geoscience and Remote Sensing*, *50*, (10), 3892–3907, <https://doi.org/10.1109/TGRS.2012.2185055>.
- Madsen, I. C., Scarlett N. V. Y., Cranswick L. M. D. & Lwin, T. (2001): Outcomes of the International Union of Crystallography Commission on Powder Diffraction Round Robin on Quantitative Phase Analysis: samples 1 a to 1 h. *Journal of Applied Crystallography*, *34*, 4, 409–426, <https://doi.org/10.1107/S0021889801007476>.
- Maesschalck, R. de, Estienne, F., Verdú-Andrés, J., Candolfi, A., Centner, V., Despagne, F., Vandeginste, B. (1999): The development of calibration models for spectroscopic data using principal component regression, tutorial, retrieved from: https://www.researchgate.net/publication/237417119_The_development_of_calibration_models_for_spectroscopic_data_using_principal_component_regression. 2018-03-27.
- Malinina, G. A. & Stefanovsky, S. V. (2014): Structure and Vibrational Spectra of Slags Produced from Radioactive Waste, *Journal of Applied Spectroscopy*, *81*, (2), 200–204, <https://doi.org/10.1007/s10812-014-9910-0>.
- Marincea, S., Dumitras, D.-G., Ghinet, C., Fransolet, A.-M., Hatert, F. & Rondeaux, M. (2011): Gehlenite from three occurrences of high-temperature skarns, Romania: New mineralogical data, *The Canadian Mineralogist*, *49*, (4), 1001–1014, <https://doi.org/10.3749/canmin.49.4.1001>.
- Marks, R. J. (2009): *Handbook of Fourier analysis & its applications*, Oxford, New York: Oxford University Press, 772, 978-0-19-533592-7.
- Martens, H. & Næs, T. (1989): *Multivariate calibration*, ([Reprinted]), Chichester: J. Wiley & Sons, ([Reprinted]), 419, 0-471-90979-3.
- Mausbach, K., Nowack, N. & Schlegelmilch, F. (1997a): Infrared emission spectra (FTIR) and crystallisation studies of the glassy CaO·MgO·2SiO₂ -slag (900 - 1200°C), *Steel Research*, *68*, (8), 355–358, <https://doi.org/10.1002/srin.199700565>.
- Mausbach, K., Nowack, N. & Schlegelmilch, F. (1997b): UV/VIS-spectroscopy of aluminates in liquid and solid oxide slags, *Steel Research*, *68*, (9), 392–397, <https://doi.org/10.1002/srin.199700572>.
- McClure, D. S. (1957): The distribution of transition metal cations in spinels, *Journal of Physics and Chemistry of Solids*, *3*, (3-4), 311–317, [https://doi.org/10.1016/0022-3697\(57\)90034-3](https://doi.org/10.1016/0022-3697(57)90034-3).
- Menges, F. Spekwin32 - optical spectroscopy software: version 1.72.0, 06/2016, Retrieved from <http://www.ffmpeg2.de/spekwin/>.
- Merkel, T. (2014): Erhebungen zu Produktion und Einsatz in Hoch- und Stahlwerksschlacke., *FEbS Report*, *21*, (1), 18.
- Merkel, T. (2017): Erzeugung und Nutzung von Eisenhüttenschlacken 2016, *FEbS Report*, *24*, (1), 15.
- Metternicht, G. I. & Zinck, J. A. (2009): *Remote sensing of soil salinization: Impact on land management*, Boca Raton: CRC Press, 377, 9781420065022.
- Mielke, C., Rogaß, C., Bösch, N., Kaufmann, H. & Guanter, L. (2014): Anwendung der Fernerkundung in der Exploration und im Haldenmonitoring im südlichen Afrika, *System Erde*, *4*, (2), <https://doi.org/10.2312/GFZ.syserde.04.02.8>.

- Mielke, C., Rogass, C., Boesche, N., Segl, K. & Altenberger, U. (2016): EnGeoMAP 2.0—Automated Hyperspectral Mineral Identification for the German EnMAP Space Mission, *Remote Sensing*, 8, (2), 127, <https://doi.org/10.3390/rs8020127>.
- Minasny, B. & McBratney, A. (2013): Why you don't need to use RPD, *Pedomtron - The Newsletter of the Pedometrics Commission of the IUSS*, (33), 14–15.
- Miyamoto, M., Mito, A., Takano, Y. & Fujii, N. (1981): Spectral reflectance (0.25-2.5 / μm) of powdered olivines and meteorites, and their bearing on surface materials of asteroids. *Mere. Natl. Inst. Polar Res. Spec. Iss.* 20, 345-361.
- Miyamoto, M., Mito, A. & Takano, Y. (1982): An attempt to reduce the effects of black material from the spectral reflectance of meteorites or asteroids. In: *Symposium on Antarctic Meteorites, 7th, Tokyo, Japan, Feb. 19, 20, 1982 National Institute of Polar Research, Memoirs, Special Issue* (291–307).
- Moenke, H. (1962): *Mineralspektren (aufgenommen mit dem Jenaer Spektrometer UR 10): Die Ultrarotabsorption der häufigsten und wirtschaftlich wichtigsten Halogenid-, Oxyd-, Hydroxyd-, Carbonat-, Nitrat-, Borat-, Sulfat-, Chromat-, Wolfram-, Molybdat-, Phosphat-, Arsenat-, Vanadat- und Silikatminerale im Spektralbereich 400-4000 cm⁻¹*, Berlin: Akademie-Verlag, 42.
- Mohassab, Y. & Sohn, H. Y. (2015): Analysis of Slag Chemistry by FTIR-RAS and Raman Spectroscopy: Effect of Water Vapor Content in H₂-H₂O-CO-CO₂ Mixtures Relevant to a Novel Green Ironmaking Technology, *steel research international*, 86, (7), 740–752, <https://doi.org/10.1002/srin.201400186>.
- Montero S., I. C., Brimhall, G. H., Alpers, C. N. & Swayze, G. A. (2005): Characterization of waste rock associated with acid drainage at the Penn Mine, California, by ground-based visible to short-wave infrared reflectance spectroscopy assisted by digital mapping, *Chemical Geology*, 215, (1-4), 453–472, <https://doi.org/10.1016/j.chemgeo.2004.06.045>.
- Morlok, A., Stojic, A., Weber, I., Hiesinger, H., Zanetti, M. & Helbert, J. (2016): Mid-infrared bi-directional reflectance spectroscopy of impact melt glasses and tektites, *Icarus*, 278, 162–179, <https://doi.org/10.1016/j.icarus.2016.06.013>.
- Moros, J., Fdez-Ortiz De Vallejuelo, S., Gredilla, A., Diego, A. de, Madariaga, J. M., Garrigues, S. & La Guardia, M. de. (2009): Use of reflectance infrared spectroscopy for monitoring the metal content of the estuarine sediments of the Nerbioi-Ibaizabal River (Metropolitan Bilbao, Bay of Biscay, Basque Country), *Environmental science & technology*, 43, (24), 9314–9320, <https://doi.org/10.1021/es9005898>.
- Motz, H. & Geiseler, J. (2001): Products of steel slags an opportunity to save natural resources, *Waste Management*, 21, (3), 285–293, [https://doi.org/10.1016/S0956-053X\(00\)00102-1](https://doi.org/10.1016/S0956-053X(00)00102-1).
- Mrotzek-Blöß, A., Nühlen, J., Jandewerth, M., Gläßer, C., Denk, M., Mudersbach, D., Algermissen, D., Teuwsen, S. (2016): *Schlussbericht zum Projekt „Konzeption und Entwicklung eines Ressourcenkatasters für Hüttenbalden durch Einsatz von Geoinformationstechnologien und Strategieentwicklung zur Wiedergewinnung von Wertstoffen“ (REStrateGIS, FKZ: 033R103)*.
- Mshiu, E. E., Gläßer, C. & Borg, G. (2015): Identification of hydrothermal paleofluid pathways, the pathfinders in the exploration of mineral deposits: A case study from the Sukumaland Greenstone Belt, Lake Victoria Gold Field, Tanzania, *Advances in Space Research*, 55, (4), 1117–1133, <https://doi.org/10.1016/j.asr.2014.11.024>.
- Mulders, M. A. (1987): *Remote sensing in soil science*, Amsterdam: Elsevier, x, 379, 0-444-42783-X.

- Murphy, R. J. & Monteiro, S. T. (2013): Mapping the distribution of ferric iron minerals on a vertical mine face using derivative analysis of hyperspectral imagery (430–970nm), *ISPRS Journal of Photogrammetry and Remote Sensing*, 75, 29–39, <https://doi.org/10.1016/j.isprsjprs.2012.09.014>.
- Næs, T. (1987): The design of calibration in near infra-red reflectance analysis by clustering, *Journal of Chemometrics*, 1, (2), 121–134, <https://doi.org/10.1002/cem.1180010207>.
- Naes, T., Isaksson, T. & Kowalski, B. (1990): Locally weighted regression and scatter correction for near-infrared reflectance data, *Analytical Chemistry*, 62, (7), 664–673, <https://doi.org/10.1021/ac00206a003>.
- Nash, D. B., Salisbury, J. W., Conel, J. E., Lucey, P. G. & Christensen, P. R. (1993): Evaluation of infrared emission spectroscopy for mapping the moon's surface composition from lunar orbit, *Journal of Geophysical Research*, 98, (E12), 23535, <https://doi.org/10.1029/93JE02604>.
- Nicodemus, F. E. (1965): Directional Reflectance and Emissivity of an Opaque Surface, *Applied optics*, 4, (7), 767, <https://doi.org/10.1364/AO.4.000767>.
- Noord, O. E. de. (1994): The influence of data preprocessing on the robustness and parsimony of multivariate calibration models, *Chemometrics and Intelligent Laboratory Systems*, 23, (1), 65–70, [https://doi.org/10.1016/0169-7439\(93\)E0065-C](https://doi.org/10.1016/0169-7439(93)E0065-C).
- Nowack, N., Okretic, S., Pfeifer, F. & Zebger, I. (2001): Ultraviolet/visible spectroscopy of molten slags and glasses (up to 1600°C), *Journal of Non-Crystalline Solids*, 282, (1), 30–40, [https://doi.org/10.1016/S0022-3093\(01\)00326-X](https://doi.org/10.1016/S0022-3093(01)00326-X).
- Nowack, N., Zebger, I., Pfeifer, F. & Rheindorf, A. (2007): Application of UV/VIS-Reflection Spectroscopy for Determination of the Oxidation State of Liquid Slags with High Fe 3+ - Contents, *steel research international*, 78, (9), 685–692, <https://doi.org/10.1002/srin.200706270>.
- Nühlen, J., Mrotzek-Blöß, A., Jandewerth, M., Denk, M., Gläßer, C., Algermissen, D., Mütterthies, A. (2016a): REStrateGIS - Konzeption und Entwicklung eines Ressourcenkatalogs für Hüttenhalden durch Einsatz von Geoinformationstechnologien und Strategieentwicklung zur Wiedergewinnung von Wertstoffen. In: A. Dürkoop, G. Gräbe, C. Brandstetter & Rentsch, L. (Eds.), *Innovative Technologien für Ressourceneffizienz - Strategische Metalle und Mineralien: Mit CD-ROM. Ergebnisse der Fördermaßnahme r3* (311–328). Stuttgart: Fraunhofer Verlag.
- Nühlen, J., Denk, M., Gläßer, C., Teuwsen, S. & Algermissen, D. (2016b): Sekundärrohstoffe in Hüttenhalden – Strategien zur Haldendetektion und -analyse auf Basis von Geoinformationstechnologien. In: K. J. Thomé-Kozmiensky (Ed.), *Mineralische Nebenprodukte und Abfälle: Aschen, Schlacken, Stäube und Baurestmassenn* (359–382).
- Nühlen, J., Denk, M., Gläßer, C., Teuwsen, S. & Algermissen, D. (2016c): Sekundärrohstoffe in Hüttenhalden. Das Projekt REStrateGIS zeigt neue Strategien zur Haldendetektion und –analyse auf Basis von Geoinformationstechnologien auf, *ReSource – Abfall, Rohstoff, Energie. Fachzeitschrift für nachhaltiges Wirtschaften*, 29, (3), 4–15.
- Oh, S., Hyun, C.-U. & Park, H.-D. (2017): Near-Infrared Spectroscopy of Limestone Ore for CaO Estimation under Dry and Wet Conditions, *Minerals*, 7, (12), 193, <https://doi.org/10.3390/min7100193>.
- Park, J. H., Min, D. J. & Song, H. S. (2002): FT-IR Spectroscopic Study on Structure of CaO-SiO₂ and CaO-SiO₂-CaF₂ Slags, *ISIJ International*, 42, (4), 344–351, <https://doi.org/10.2355/isijinternational.42.344>.

- Park, J.-Y., Park, S.-J., Chang, W.-S., Sohn, I. & Rigaud, M. (2012): Effect of FeO Content and CaO/SiO₂ Ratio on Hydrogen Dissolution in CaF₂-CaO-SiO₂-Based Welding Fluxes, *Journal of the American Ceramic Society*, 95, (5), 1756–1763, <https://doi.org/10.1111/j.1551-2916.2012.05173.x>.
- Pearson, K. (1901): On lines and planes of closest fit to systems of points in space, *The London, Edinburgh, and Dublin Philosophical Magazine and Journal of Science*, 2, (11), 559–572, <https://doi.org/10.1080/14786440109462720>.
- Pichler, C., Unger, A. & Antrekowitsch, J. (2013): Rückgewinnung von Wertmetallen aus Stahlwerksstäuben durch ein reduzierendes Metallbad. In: K. J. Thomé-Kozmiensky (Ed.), *Aschen-Schlacken-Stäube: Aus Abfallverbrennung und Metallurgie* (587–598). Neuruppin: TK.
- Picón, A. (2012): Real-time hyperspectral processing for automatic nonferrous material sorting, *Journal of Electronic Imaging*, 21, (1), 13018, <https://doi.org/10.1117/1.JEI.21.1.013018>.
- Picón, A., Ghita, O., Whelan, P. F. & Iriondo, P. M. (2009): Fuzzy Spectral and Spatial Feature Integration for Classification of Nonferrous Materials in Hyperspectral Data, *IEEE Transactions on Industrial Informatics*, 5, (4), 483–494, <https://doi.org/10.1109/TII.2009.2031238>.
- Picón, A., Vicente, A. V., Rodríguez-Vaamonde, S., Armentia, J., Arteche, J. A. & Macaya, I. (2017): Ladle furnace slag characterization through hyperspectral reflectance regression model for secondary metallurgy process optimization, *IEEE Transactions on Industrial Informatics*, 1, <https://doi.org/10.1109/TII.2017.2773068>.
- Pinheiro, É., Ceddia, M., Clingensmith, C., Grunwald, S. & Vasques, G. (2017): Prediction of Soil Physical and Chemical Properties by Visible and Near-Infrared Diffuse Reflectance Spectroscopy in the Central Amazon, *Remote Sensing*, 9, (12), 293, <https://doi.org/10.3390/rs9040293>.
- Pontikes, Y., Jones, P. T., Geysen, D. & Blanpain, B. (2010): Options to Prevent Dicalcium Silicate-Driven Disintegration of Stainless Steel Slags, *Archives of Metallurgy and Materials*, 55, (4), 1167–1172, <https://doi.org/10.2478/v10172-010-0020-6>.
- Priester, M. & Dolega, P. (2015): *Bergbauliche Reststoffe – Teilprojektbericht ÖkoRes.*, Berlin, 76.
- Prince, A. P., Kleiber, P., Grassian, V. H. & Young, M. A. (2007): Heterogeneous interactions of calcite aerosol with sulfur dioxide and sulfur dioxide-nitric acid mixtures, *Physical chemistry chemical physics: PCCP*, 9, (26), 3432–3439, <https://doi.org/10.1039/b703296j>.
- Radenović, A., Malina, J. & Sofilić, T. (2013): Characterization of Ladle Furnace Slag from Carbon Steel Production as a Potential Adsorbent, *Advances in Materials Science and Engineering*, 2013, (6), 1–6, <https://doi.org/10.1155/2013/198240>.
- Ramachandran, V. S., Sereda, P. J. & Feldman, R. F. (1964): Mechanism of Hydration of Calcium Oxide, *Nature*, 201, (4916), 288–289, <https://doi.org/10.1038/201288a0>.
- Ramírez-Santos, Á. A., Castel, C. & Favre, E. (2017): Utilization of blast furnace flue gas: Opportunities and challenges for polymeric membrane gas separation processes, *Journal of Membrane Science*, 526, 191–204, <https://doi.org/10.1016/j.memsci.2016.12.033>.
- Ramsey, M. (2004): Quantitative geological surface processes extracted from infrared spectroscopy and remote sensing. In: P. King, M. Ramsey, & G. Swayze (Eds.), *Short course series: Vol. 33. Infrared spectroscopy in geochemistry, exploration geochemistry and remote sensing* (197–213). Ottawa: Mineralogical Association of Canada.

- Ramsey, M. S. & Fink, J. H. (1999): Estimating silicic lava vesicularity with thermal remote sensing: A new technique for volcanic mapping and monitoring, *Bulletin of Volcanology*, 61, (1-2), 32–39, <https://doi.org/10.1007/s004450050260>.
- Rashed, T. & Jürgens, C. (2010): *Remote Sensing of Urban and Suburban Areas*, (Vol. 10), Dordrecht: Springer Netherlands, 978-1-4020-4371-0.
- Rekersdrees, T., Schliephake, H. & Schulbert, K. (2014): Aufbau und Prozessführung des Lichtbogenofens unter besonderer Berücksichtigung des Schlackenmanagements. In: K. J. Thomé-Kozmiansky (Ed.), *Mineralische Nebenprodukte und Abfälle: Aschen, Schlacken, Stäube und Baurestmassen* (305–326). Nietwerder: TK-Vlg.
- Remus, R., Monsonet, M., Roudier, S. & Sancho, L. D. (2013): *Best available techniques (BAT) reference document for iron and steel production: Industrial emissions directive 2010/75/EU (integrated pollution prevention and control)*. Scientific and technical research series: Vol. 25521, Luxembourg: Publications Office of the European Union, Retrieved from <http://bookshop.europa.eu/en/best-available-techniques-bat-reference-document-for-iron-and-steel-production-pbLFNA25521/>, 17, 9789279264764.
- Riaza, A. & Müller, A. (2010): Hyperspectral remote sensing monitoring of pyrite mine wastes: A record of climate variability (Pyrite Belt, Spain), *Environmental Earth Sciences*, 61, (3), 575–594, <https://doi.org/10.1007/s12665-009-0368-y>.
- Rice, M. S., Cloutis, E. A., Bell, J. F., Bish, D. L., Horgan, B. H., Mertzman, S. A., Mountain, B. (2013): Reflectance spectra diversity of silica-rich materials: Sensitivity to environment and implications for detections on Mars, *Icarus*, 223, (1), 499–533, <https://doi.org/10.1016/j.icarus.2012.09.021>.
- Riedel, F., Denk, M., Müller, I., Barth, N. & Gläßer, C. (2018): Prediction of soil parameters using the spectral range between 350 and 15,000 nm: A case study based on the Permanent Soil Monitoring Program in Saxony, Germany, *Geoderma*, 315, 188–198, <https://doi.org/10.1016/j.geoderma.2017.11.027>.
- Rietveld, H. M. (1969): A profile refinement method for nuclear and magnetic structures. *Journal of Applied Crystallography*, 2, 2, 65-71, <https://doi.org/10.1107/S0021889869006558>.
- Rinnan, Å., van den Berg, F. & Engelsen, S. B. (2009): Review of the most common pre-processing techniques for near-infrared spectra, *TrAC Trends in Analytical Chemistry*, 28, (10), 1201–1222, <https://doi.org/10.1016/j.trac.2009.07.007>.
- Roberts, D. A. & Herold, M. (2004): Imaging spectrometry for urban materials. In: P. King, M. Ramsey, & G. Swayze (Eds.), *Short course series: Vol. 33. Infrared spectroscopy in geochemistry, exploration geochemistry and remote sensing* (155–180). Ottawa: Mineralogical Association of Canada.
- Rodriguez, S., Picon, A., Gutierrez, J. A., Bereciartua, A. & Iriondo, P. (2010) Automatic slag characterization based on hyperspectral image processing. In: *2010 IEEE 15th Conference on Emerging Technologies & Factory Automation (ETFA 2010)* (1–4). IEEE, <https://doi.org/10.1109/ETFA.2010.5641225>.
- Roessner, S., Segl, K., Bochow, M., Heiden, U., Heldens, W. & Kaufmann, H. (2011): Potential of hyperspectral remote sensing for analyzing the urban environment. In: X. Yang (Ed.), *Urban remote sensing: Monitoring, synthesis and modeling in the urban environment* (49–60). Chichester West Sussex, Hoboken NJ: Wiley-Blackwell.

- Rossmann, G. R. (1996): Studies of OH in nominally anhydrous minerals, *Physics and Chemistry of Minerals*, 23, (4-5), 299–304.
- Rossmann, G. R. (2014): Optical Spectroscopy, *Reviews in Mineralogy and Geochemistry*, 78, (1), 371–398, <https://doi.org/10.2138/rmg.2014.78.9>.
- Rossmann, G. R. (1988): Optical Spectroscopy. In: F. C. Hawthorne & G. E. Brown (Eds.), *Reviews in mineralogy: v. 18. Spectroscopic methods in mineralogy and geology* (207–254). Washington, D.C.: Mineralogical Society of America.
- Ruff, S. W., Christensen, P. R., Barbera, P. W. & Anderson, D. L. (1997): Quantitative thermal emission spectroscopy of minerals: A laboratory technique for measurement and calibration, *Journal of Geophysical Research*, 102, (B7), 14899–14913, <https://doi.org/10.1029/97JB00593>.
- Ruge, J. (1987): *Technologie der Werkstoffe*, Wiesbaden: Vieweg+Teubner Verlag, 236, 978-3-663-00069-3.
- Ruge, J. & Wohlfahrt, H. (2013): *Technologie der Werkstoffe: Herstellung, Verarbeitung, Einsatz*, (9th ed.), Wiesbaden: Springer Fachmedien Wiesbaden; Imprint; Springer Vieweg, (9th ed.), 385, 978-3-658-01881-8.
- Rüger, F. & Decker, M. (1992): Bergbaugeschichte, Geologie und Mineralien des Saalfeld-Kamisdorfer Bergbaureviers in Ostthüringen, *Emser Hefte*, 13, (4), 7–70.
- Rumpel, C., Janik, L. J., Skjemstad, J. O. & Kögel-Knabner, I. (2001): Quantification of carbon derived from lignite in soils using mid-infrared spectroscopy and partial least squares, *Organic Geochemistry*, 32, (6), 831–839, [https://doi.org/10.1016/S0146-6380\(01\)00029-8](https://doi.org/10.1016/S0146-6380(01)00029-8).
- Rütten, J. (2006): Application of the Waelz technology on resource-recycling of steel mill dust, *SEALSI Quarterly*, 35, (4), 13–19.
- Sadeghi, M., Borg, G. & Gläßer, C. (2008): Relationship between large-scale ring structures and lineaments with big porphyry copper deposits in Iran, *Geosciences*, 17, (1), 198–205.
- Salisbury, J. W. (1992): *Infrared (2.1-25µm) spectra of minerals*: Johns Hopkins University Press, 267, 0-8018-4423-1.
- Salisbury, J. W. (1993): Mid-infrared spectroscopy: Laboratory data, *Remote Geochemical Analysis*, edited by C. Pieters and P. Englert, chap. 4, (79–98), Cambridge Univ. Press, New York.
- Salisbury, J. W. & D'Aria, D. M. (1992): Emissivity of terrestrial materials in the 8–14 µm atmospheric window, *Remote Sensing of Environment*, 42, (2), 83–106, [https://doi.org/10.1016/0034-4257\(92\)90092-X](https://doi.org/10.1016/0034-4257(92)90092-X).
- Salisbury, J. W. & D'Aria, D. M. (1992): Infrared (8–14 µm) remote sensing of soil particle size, *Remote Sensing of Environment*, 42, (2), 157–165, [https://doi.org/10.1016/0034-4257\(92\)90099-6](https://doi.org/10.1016/0034-4257(92)90099-6).
- Salisbury, J. W., D'Aria, D. M. & Jarosewich, E. (1991): Midinfrared (2.5–13.5 µm) reflectance spectra of powdered stony meteorites, *Icarus*, 92, (2), 280–297, [https://doi.org/10.1016/0019-1035\(91\)90052-U](https://doi.org/10.1016/0019-1035(91)90052-U).
- Salisbury, J. W. & Wald, A. (1992): The role of volume scattering in reducing spectral contrast of reststrahlen bands in spectra of powdered minerals, *Icarus*, 96, (1), 121–128, [https://doi.org/10.1016/0019-1035\(92\)90009-V](https://doi.org/10.1016/0019-1035(92)90009-V).
- Salisbury, J. W., Walter, L. S., & Vergo, N. (1987): *Mid-Infrared (2.1-25 µm) Spectra of Minerals: First Edition: USGS Open-File Report 87-263*.

- Salisbury, J. W., Walter, L. S., & D'Aria, D. (1988): *Mid-Infrared (2.5 to 13.5 μm) Spectra of Igneous Rocks: USGS Open-File Report 88-686*.
- Savitzky, A. & Golay, M. J. E. (1964): Smoothing and Differentiation of Data by Simplified Least Squares Procedures, *Analytical Chemistry*, 36, (8), 1627–1639, <https://doi.org/10.1021/ac60214a047>.
- Schaefer, C., Bormuth, C. & Matossi, F. (1926): Das ultrarote Absorptionsspektrum der Carbonate, *Zeitschrift für Physik*, 39, (9), 648–659, <https://doi.org/10.1007/BF01322127>.
- Schläfer, H. L. & Gliemann, G. (1980): *Einführung in die Ligandenfeldtheorie*, (2. Aufl., unveränd. Nachdr. d. 1. Aufl.), Wiesbaden: Akademische Verlagsgesellschaft, 535, 9783400004083.
- Schmetzer, K. (1982): Absorption spectroscopy and colour of V³⁺-bearing natural oxides and silicates - a contribution to the crystal chemistry of vanadium, *Neues Jahrbuch für Mineralogie - Abhandlungen*, 144, (1), 73–106.
- Schmidt, H. & Glaesser, C. (1998): Multitemporal analysis of satellite data and their use in the monitoring of the environmental impacts of open cast lignite mining areas in Eastern Germany, *International Journal of Remote Sensing*, 19, (12), 2245–2260, <https://doi.org/10.1080/014311698214695>.
- Schodlok, M. C. (2004): Quantitative Analysen magmatischer Gesteine mittels reflexionsspektroskopischer Infrarot-Messungen (Ph.D. thesis). University of Potsdam, Potsdam.
- Schodlok, M. C., Green, A. & Huntington, J. (2016): A reference library of thermal infrared mineral reflectance spectra for the HyLogger-3 drill core logging system, *Australian Journal of Earth Sciences*, 98, 1–9, <https://doi.org/10.1080/08120099.2016.1234508>.
- Schulz, R., Denk, M., Gläßer, C., Kurz, T.H., Buckley, S.J., Drissen, P. & Paasche, H. (2015): Geophysikalische und reflexionsspektrometrische Untersuchung eines Haldenkörpers aus der Eisen- und Stahlindustrie: Eine Multisensor-Fallstudie in Thüringen. 75. Jahrestagung der Deutschen Geophysikalischen Gesellschaft, 23. – 26.03.2015, Hannover.
- Schüler, S., Algermissen, D., Markus, H., Mudersbach, D. & Drissen, P. (2016): Metallurgische Maßnahmen zur Einstellung der Nachhaltigkeit von Elektroofenschlacke: Kreislaufwirtschaft stabil weiterentwickeln. In: K. J. Thomé-Kozmiensky (Ed.), *Mineralische Nebenprodukte und Abfälle: Aschen, Schlacken, Stäube und Baurestmassenn* (259–277).
- Schwertmann, U. & Lentze, W. (1966): Bodenfarbe und Eisenoxidform, *Zeitschrift für Pflanzenernährung, Düngung, Bodenkunde*, 115, (3), 209–214, <https://doi.org/10.1002/jpln.19661150307>.
- Seidel, G. (Ed.). (2003): *Geologie von Thüringen: Mit 34 Tabellen*, (2nd ed.), Stuttgart: E. Schweizerbart'sche Verlagsbuchhandlung (Nägele u. Obermiller), 2, 601, 3510652053.
- Setién, J., Hernández, D. & González, J. J. (2009): Characterization of ladle furnace basic slag for use as a construction material, *Construction and Building Materials*, 23, (5), 1788–1794, <https://doi.org/10.1016/j.conbuildmat.2008.10.003>.
- Shi, C. (2002): Characteristics and cementitious properties of ladle slag fines from steel production, *Cement and Concrete Research*, 32, (3), 459–462, [https://doi.org/10.1016/S0008-8846\(01\)00707-4](https://doi.org/10.1016/S0008-8846(01)00707-4).

- Shimoda, K., Tobu, Y., Kanehashi, K., Nemoto, T. & Saito, K. (2008): Total understanding of the local structures of an amorphous slag: Perspective from multi-nuclear (²⁹Si, ²⁷Al, ¹⁷O, ²⁵Mg, and ⁴³Ca) solid-state NMR, *Journal of Non-Crystalline Solids*, *354*, (10-11), 1036–1043, <https://doi.org/10.1016/j.jnoncrysol.2007.08.010>.
- Siebielec, G., McCarty, G. W., Stuczynski, T. I. & Reeves, J. B. (2004): Near- and Mid-Infrared Diffuse Reflectance Spectroscopy for Measuring Soil Metal Content, *Journal of Environment Quality*, *33*, (6), 2056, <https://doi.org/10.2134/jeq2004.2056>.
- Siegal, B. S. & Goetz, A. F. H. (1977): Effect of vegetation on rock and soil type discrimination, *Photogrammetric Engineering and Remote Sensing*, *2*, (2), 191–196.
- Siegmann, B. & Jarmer, T. (2015): Comparison of different regression models and validation techniques for the assessment of wheat leaf area index from hyperspectral data, *International Journal of Remote Sensing*, *36*, (18), 4519–4534, <https://doi.org/10.1080/01431161.2015.1084438>.
- Singh, G. P., Sundeep, Choudhary, R. P., Vardhan, H., Aruna, M. & Akolkar, A. B. (2015): Iron Ore Pelletization Technology and its Environmental Impact Assessment in Eastern Region of India – A Case Study, *Procedia Earth and Planetary Science*, *11*, 582–597, <https://doi.org/10.1016/j.proeps.2015.06.060>.
- Smith, B. C. (1996): *Fundamentals of fourier transform infrared spectroscopy*, Boca Raton: CRC Press, 202, 0-8493-2461-0.
- Smith, R. J., Horgan, B. H. N., Mann, P., Cloutis, E. A. & Christensen, P. R. (2017): Acid weathering of basalt and basaltic glass: 2. Effects of microscopic alteration textures on spectral properties, *Journal of Geophysical Research: Planets*, *122*, (1), 203–227, <https://doi.org/10.1002/2016JE005112>.
- Snee, R. D. (1977): Validation of regression models: methods and examples, *Technometrics*, *19*, (4), 415–428.
- Snyder, R. L. (1992): The Use of Reference Intensity Ratios in X-Ray Quantitative Analysis, *Powder Diffraction*, *7*, (04), 186–193, <https://doi.org/10.1017/S0885715600018686>.
- Soil Survey Staff (2009): *Soil Survey Field and Laboratory Methods Manual*. Soil Survey Investigations Report No. 51, Version 1.0. R. Burt (ed.). U.S. Department of Agriculture, Natural Resources Conservation Service.
- Song, Y., Li, F., Yang, Z., Ayoko, G. A., Frost, R. L. & Ji, J. (2012): Diffuse reflectance spectroscopy for monitoring potentially toxic elements in the agricultural soils of Changjiang River Delta, China, *Applied Clay Science*, *64*, 75–83, <https://doi.org/10.1016/j.clay.2011.09.010>.
- Song, K., Park, S., Kim, W., Jeon, C. & Ahn, J.-W. (2017): Effects of Experimental Parameters on the Extraction of Silica and Carbonation of Blast Furnace Slag at Atmospheric Pressure in Low-Concentration Acetic Acid, *Metals*, *7*, (12), 199, <https://doi.org/10.3390/met7060199>.
- Sonntag, M. (2011): DDR-Arbeitslager in Thüringen 1949–1989, *Thüringen: Blätter zur Landeskunde*, (85), Retrieved from http://zs.thulb.uni-jena.de/receive/jportal_jpvolume_00199350.
- Spieß, L., Teichert, G., Schwarzer, R., Behnken, H. & Genzel, C. (2009): *Moderne Röntgenbeugung: Röntgendiffraktometrie für Materialwissenschaftler, Physiker und Chemiker*, (2nd ed.). *Studium*, Wiesbaden: Vieweg + Teubner, (2nd ed.), 564, 978-3-8351-0166-1.

- Sprague, A. L., Deutsch, L. K., Hora, J., Fazio, G. G., Ludwig, B., Emery, J. & Hoffmann, W. F. (2000): Mid-Infrared (8.1–12.5 μm) Imaging of Mercury, *Icarus*, 147, (2), 421–432, <https://doi.org/10.1006/icar.2000.6447>.
- Stahlwerk Thüringen GmbH (SWT). <https://www.stahlwerk-thueringen.de/>. 2018-02-24.
- Stebbins, J. F., McMillan, P. F. & Dingwell, D. B. (1995): *Structure, dynamics and properties of silicate melts. Reviews in mineralogy: Vol. 32*, Washington: Mineralogical Society of America, 616, 978-0-939950-39-3.
- Stiegman, A. E., Bruegge, C. J. & Springsteen, A. W. (1993): Ultraviolet stability and contamination analysis of Spectralon diffuse reflectance material, *Optical Engineering*, 32, (4), 799, <https://doi.org/10.1117/12.132374>.
- Sun, D.-W. (2010): *Hyperspectral imaging for food quality analysis and control*, London: Academic, 477, 9780080886282.
- Swayze, G. A., Smith, K. S., Clark, R. N., Sutley, S. J., Pearson, R. M., Vance, J. S., Roth, S. (2000): Using Imaging Spectroscopy to Map Acidic Mine Waste, *Environmental science & technology*, 34, (1), 47–54, <https://doi.org/10.1021/es990046w>.
- Tang, H. & Li, Z.-L. (2014): *Quantitative Remote Sensing in Thermal Infrared*, Berlin, Heidelberg: Springer Berlin Heidelberg, 281, 978-3-642-42026-9.
- Tatzer, P., Wolf, M. & Panner, T. (2005): Industrial application for inline material sorting using hyperspectral imaging in the NIR range, *Real-Time Imaging*, 11, (2), 99–107, <https://doi.org/10.1016/j.rti.2005.04.003>.
- Thenkabail, P. S., Lyon, J. G. & Huete, A. (2012): *Hyperspectral remote sensing of vegetation*, Boca Raton, Fla.: CRC Press, 782, 9781439845370.
- Tinz, U. (2006): *Erkundungsbohrungen im Bereich der östlichen Hochbalde mit Untersuchung von entnommenen Materialproben (unpublished)*. Verfahrenstechnisches Institut Saalfeld GmbH, No. 037/06, Saalfeld.
- Tinz, U. & Stamm, K. (1996): *Rekultivierungskonzept "Rotschlammbecken" (unpublished)*. Verfahrenstechnisches Institut Saalfeld GmbH, No. 030/96-453-3.2, Saalfeld.
- Tinz, U., Bartzsch, K., Stamm, K. (1996): *Altlastenuntersuchung und Gefährdungseinschätzung Teilbereich Maxhüttenbalden (unpublished)*. Verfahrenstechnisches Institut Saalfeld GmbH, No. 123/95-453-3, Saalfeld.
- Tinz, U. & Stamm, K. (1998a): *Rekultivierungsplanung „Gichtfein-schlammdeponie“ (unpublished)*. Verfahrenstechnisches Institut Saalfeld GmbH, No. 072/97-394-3, Saalfeld.
- Tinz, U. & Stamm, K. (1998b): *Rekultivierungsplanung „Teich-Teich“ (unpublished)*. Verfahrenstechnisches Institut Saalfeld GmbH, No. 073/97-394-3, Saalfeld.
- TLS - Thüringer Landesamt für Statistik (2018): Gemeinde Unterwellenborn. Bevölkerung nach Geschlecht. Retrieved from <https://statistik.thueringen.de/datenbank/portrait.asp?TabelleID=GG000102&auswahl=gem&nr=73111&Aevas2=Aevas2&tit2=&TIS=&SZDT=>, 2018-03-23.
- TLUG - Thüringer Landesanstalt für Umwelt und Geologie (Puff, P., Steinmüller, A. & Wucher, K.) (2001): *Geologische Karte von Thüringen 1:25.000. Blatt 5334 Saalfeld (Saale)*.
- TLUG - Thüringer Landesanstalt für Umwelt und Geologie (2005): *Thüringen Untertage: Ein Exkurs zu Schauhöhlen, Besucherbergwerken und GeoMuseen*, Jena: Thüringer Landesanstalt für Umwelt und Geologie, 317, 3-9806811-4-9.

- TLUGa -Thüringer Landesanstalt für Umwelt und Geologie. Klima, Retrieved from http://www.tlug-jena.de/uw_raum/umweltregional/slf/slf09.html, 2018-02-27.
- TLUGb -Thüringer Landesanstalt für Umwelt und Geologie. Die vier Thüringer Klimabereiche und ihre klimacharakteristischen Merkmale, Retrieved from http://www.tlug-jena.de/uw_raum/umweltregional/thueringen/09_klimabereiche.html, 2018-02-27.
- Torrance, K. E. & Sparrow, E. M. (1967): Theory for Off-Specular Reflection from Roughened Surfaces, *Journal of the Optical Society of America*, 57, (9), 1105, <https://doi.org/10.1364/JOSA.57.001105>.
- Tossavainen, M., Engstrom, F., Yang, Q., Menad, N., Lidstrom Larsson, M. & Bjorkman, B. (2007): Characteristics of steel slag under different cooling conditions, *Waste management (New York, N.Y.)*, 27, (10), 1335–1344, <https://doi.org/10.1016/j.wasman.2006.08.002>.
- Udelhoven, T., Emmerling, C. & Jarmer, T. (2003): Quantitative analysis of soil chemical properties with diffuse reflectance spectrometry and partial least-square regression: A feasibility study, *Plant and Soil*, 251, (2), 319–329.
- Ullrich, W. (2005): *Untersuchung von Stützenproben (unpublished)*. FCB Fachbüro für Consulting und Bodenmechanik GmbH, Espenhain.
- van der Meer, F. (1995): Spectral reflectance of carbonate mineral mixtures and bidirectional reflectance theory: Quantitative analysis techniques for application in remote sensing, *Remote Sensing Reviews*, 13, (1-2), 67–94, <https://doi.org/10.1080/02757259509532297>.
- van der Meer, F. (2004): Analysis of spectral absorption features in hyperspectral imagery, *International Journal of Applied Earth Observation and Geoinformation*, 5, (1), 55–68, <https://doi.org/10.1016/j.jag.2003.09.001>.
- van der Meer, F. D., van der Werff, H. M., van Ruitenbeek, F. J., Hecker, C. A., Bakker, W. H., Noomen, M. F., Woldai, T. (2012): Multi- and hyperspectral geologic remote sensing: A review, *International Journal of Applied Earth Observation and Geoinformation*, 14, (1), 112–128, <https://doi.org/10.1016/j.jag.2011.08.002>.
- Vaughan, R., Calvin, W. M. & Taranik, J. V. (2003): SEBASS hyperspectral thermal infrared data: Surface emissivity measurement and mineral mapping, *Remote Sensing of Environment*, 85, (1), 48–63, [https://doi.org/10.1016/S0034-4257\(02\)00186-4](https://doi.org/10.1016/S0034-4257(02)00186-4).
- Vaughan, R. G., Hook, S. J., Calvin, W. M. & Taranik, J. V. (2005): Surface mineral mapping at Steamboat Springs, Nevada, USA, with multi-wavelength thermal infrared images, *Remote Sensing of Environment*, 99, (1-2), 140–158, <https://doi.org/10.1016/j.rse.2005.04.030>.
- VDEh -Verein Deutscher Eisenhüttenleute. (1995): *Slag atlas*, (2. ed., Repr. without change), Düsseldorf: Verl. Stahleisen, 616, 3-514-00457-9.
- VDEh -Verein Deutscher Eisenhüttenleute. (2015): *Steel manual*, Düsseldorf: Stahlinstitut VDEh, 219, 978-3-514-00817-5.
- VDEh -Verein Deutscher Eisenhüttenleute. (2016): *Jahrbuch Stahl 2017*, Düsseldorf: Stahleisen, 964, 9783514008250.
- Vincent, R. K. & Hunt, G. R. (1968): Infrared reflectance from mat surfaces, *Applied optics*, 7, (1), 53–59, <https://doi.org/10.1364/AO.7.000053>.

- Viscarra Rossel, R. A., Walvoort, D., McBratney, A. B., Janik, L. J. & Skjemstad, J. O. (2006): Visible, near infrared, mid infrared or combined diffuse reflectance spectroscopy for simultaneous assessment of various soil properties, *Geoderma*, 131, (1-2), 59–75, <https://doi.org/10.1016/j.geoderma.2005.03.007>.
- Vohland, M., Bossung, C. & Fründ, H.-C. (2009): A spectroscopic approach to assess trace-heavy metal contents in contaminated floodplain soils via spectrally active soil components, *Journal of Plant Nutrition and Soil Science*, 172, (2), 201–209, <https://doi.org/10.1002/jpln.200700087>.
- VTI - Verfahrenstechnisches Institut Saalfeld GmbH (1997): *Studie/Vorplanung Versickerungsanlage Rotschlammbecken: Erläuterungsbericht (unpublished)*, Saalfeld.
- Wagenbreth, O. & Steiner, W. (2015): *Geologische Streifzüge*, Berlin, Heidelberg: Springer Berlin Heidelberg, 204, 978-3-662-44727-7.
- Ward, J. H. (1963): Hierarchical Grouping to Optimize an Objective Function, *Journal of the American Statistical Association*, 58, (301), 236–244.
- Waseda, Y., Matsubara, E. & Shinoda, K. (2011): *X-Ray Diffraction Crystallography*, Berlin, Heidelberg: Springer Berlin Heidelberg, 978-3-642-16634-1.
- Waseda, Y. & Toguri, J. M. (1998): *The structure and properties of oxide melts: Application of basic science to metallurgical processing*, Singapore, River Edge, NJ: World Scientific, 236, 978-981-02-3317-4.
- Weidner, V. R. & Hsia, J. J. (1981): Reflection properties of pressed polytetrafluoroethylene powder, *Journal of the Optical Society of America*, 71, (7), 856, <https://doi.org/10.1364/JOSA.71.000856>.
- Westphal, T. (2007): Quantitative Rietveld-Analyse von amorphen Materialien am Beispiel von Hochofenschlacken und Flugaschen (Ph.D. thesis). Martin Luther University Halle-Wittenberg, Halle.
- Williams, D. J., Bigham, J. M., Cravotta III, C. A., Trainaa, S. J., Anderson, J. E. & Lyon, J. G. (2002): Assessing mine drainage pH from the color and spectral reflectance of chemical precipitates, *Applied Geochemistry*, 17, (10), 1273–1286, [https://doi.org/10.1016/S0883-2927\(02\)00019-7](https://doi.org/10.1016/S0883-2927(02)00019-7).
- Wittmer, D. M. A. G. (2006): *Kupfer im regionalen Ressourcenhaushalt: Ein methodischer Beitrag zur Exploration urbaner Lagerstätten*, Zürich: vdf, Hochsch.-Verl. an der ETH, 81, 3-7281-3047-8.
- Wold, S., Sjöström, M. & Eriksson, L. (2001): PLS-regression: A basic tool of chemometrics, *Chemometrics and Intelligent Laboratory Systems*, 58, (2), 109–130, [https://doi.org/10.1016/S0169-7439\(01\)00155-1](https://doi.org/10.1016/S0169-7439(01)00155-1).
- Wong, J. & Angell, C. A. (1970): Applications of Spectroscopy in the Study of Glassy Solids Part I. Introduction, γ -Ray Spectroscopy (Mössbauer Effect), X-Ray Absorption Fine Structure, UV Absorption, and Visible Spectra, *Applied Spectroscopy Reviews*, 4, (1), 97–153, <https://doi.org/10.1080/05704927008081696>.
- Wong, J. & Angell, C. A. (1971): Application of Spectroscopy in the Study of Glassy Solids, Part II. Infrared, Raman, EPR, and NMR Spectral Studies, *Applied Spectroscopy Reviews*, 4, (2), 155–232, <https://doi.org/10.1080/05704927108082604>.
- World Steel Association. (2012): *The white book of steel*, Brussels: World Steel Association, 49, 978-2-930069-67-8.
- World Steel Association (2016): Fact Sheet: Steel industry by-products, Retrieved from https://www.worldsteel.org/en/dam/jcr:1b916a6d-06fd-4e84-b35d-c1d911d18df4/Fact_By-products_2016.pdf, 2018-02-26.

- World Steel Association (2017): World Steel in Figures 2017, Retrieved from <https://www.worldsteel.org/en/dam/jcr:0474d208-9108-4927-ace8-4ac5445c5df8/World+Steel+in+Figures+2017.pdf>, 2018-03-14.
- World Steel Association (2018): Fact sheet: Steel and raw materials, Retrieved from https://www.worldsteel.org/en/dam/jcr:16ad9bcd-dbf5-449f-b42c-b220952767bf/fact_raw+materials_2018.pdf, 2018-02-26.
- Yan, P., Huang, S., van Dyck, J., Guo, M. & Blanpain, B. (2014): Desulphurisation and Inclusion Behaviour of Stainless Steel Refining by Using CaO–Al₂O₃ Based Slag at Low Sulphur Levels, *ISIJ International*, 54, (1), 72–81, <https://doi.org/10.2355/isijinternational.54.72>.
- Yang, X. (Ed.). (2011): *Urban remote sensing: Monitoring, synthesis and modeling in the urban environment*, Chichester West Sussex, Hoboken NJ: Wiley-Blackwell, 388, 047074958X.
- Yi, H., Xu, G., Cheng, H., Wang, J., Wan, Y. & Chen, H. (2012): An Overview of Utilization of Steel Slag, *Procedia Environmental Sciences*, 16, 791–801, <https://doi.org/10.1016/j.proenv.2012.10.108>.
- Yildirim, I. Z. & Prezzi, M. (2011): Chemical, Mineralogical, and Morphological Properties of Steel Slag, *Advances in Civil Engineering*, 2011, (2), 1–13, <https://doi.org/10.1155/2011/463638>.
- Zabcic, N., Rivard, B., Ong, C. & Mueller, A. (2014): Using airborne hyperspectral data to characterize the surface pH and mineralogy of pyrite mine tailings, *International Journal of Applied Earth Observation and Geoinformation*, 32, 152–162, <https://doi.org/10.1016/j.jag.2014.04.008>.
- Zaini, N., van der Meer, F. & van der Werff, H. (2012): Effect of Grain Size and Mineral Mixing on Carbonate Absorption Features in the SWIR and TIR Wavelength Regions, *Remote Sensing*, 4, (12), 987–1003, <https://doi.org/10.3390/rs4040987>.
- Zaini, N., van der Meer, F. & van der Werff, H. (2014): Determination of Carbonate Rock Chemistry Using Laboratory-Based Hyperspectral Imagery, *Remote Sensing*, 6, (5), 4149–4172, <https://doi.org/10.3390/rs6054149>.
- Zaini, N., van der Meer, F., van Ruitenbeek, F., Smeth, B. d., Amri, F. & Lievens, C. (2016): An Alternative Quality Control Technique for Mineral Chemistry Analysis of Portland Cement-Grade Limestone Using Shortwave Infrared Spectroscopy, *Remote Sensing*, 8, (12), 950, <https://doi.org/10.3390/rs8110950>.
- Zhao, D., Zhang, Z., Tang, X., Liu, L. & Wang, X. (2014): Preparation of Slag Wool by Integrated Waste-Heat Recovery and Resource Recycling of Molten Blast Furnace Slags: From Fundamental to Industrial Application, *Energies*, 7, (12), 3121–3135, <https://doi.org/10.3390/en7053121>.
- Zhou, K.-F. & Wang, S.-S. (2017): Spectral properties of weathered and fresh rock surfaces in the Xiemisitai metallogenic belt, NW Xinjiang, China, *Open Geosciences*, 9, (1), 173, <https://doi.org/10.1515/geo-2017-0027>.
- Zornoza, R., Guerrero, C., Mataix-Solera, J., Scow, K. M., Arcenegui, V. & Mataix-Beneyto, J. (2008): Near infrared spectroscopy for determination of various physical, chemical and biochemical properties in Mediterranean soils, *Soil biology & biochemistry*, 40, (7), 1923–1930, <https://doi.org/10.1016/j.soilbio.2008.04.003>.
- Zündorf, H.-J., Günther, K.-F., Korsch, H. & Westhus, W. (Eds.) (2006): *Flora von Thüringen: Die wildwachsenden Farn- und Blütenpflanzen Thüringens*, Jena: Weissdorn-Verl., 764, 3936055092.

R and R Packages

- Hamilton, N. (2017). ggtern: An Extension to 'ggplot2', for the Creation of Ternary Diagrams. R package version 2.2.1. Available from <https://CRAN.R-project.org/package=ggtern>.
- Kassambara, A. & Mundt, F. (2017): factoextra: Extract and Visualize the Results of Multivariate Data Analyses. R package version 1.0.5. Available from <https://CRAN.R-project.org/package=factoextra>.
- Komsta, L. (2011): outliers: Tests for outliers. R package version 0.14. Available from <https://CRAN.R-project.org/package=outliers>.
- Kuhn, M., with contributions from Wing, J., Weston, S., Williams, A., Keefer, C., Engelhardt, A., Cooper, T., Mayer, Z., Kenkel, B., the R Core Team, Benesty, M., Lescarbeau, R., Ziem, A., Scrucca, L., Tang, Y., Candan, C. & Hunt, T. (2017): caret: Classification and Regression Training. R package version 6.0-77. Available from <https://CRAN.R-project.org/package=caret>.
- Mevik, B.H., Wehrens, R. & Liland, K.H. (2016): pls: Partial Least Squares and Principal Component Regression. R package version 2.6-0. Available from <https://CRAN.R-project.org/package=pls>.
- Meyer, D., Dimitriadou, E., Hornik, K., Weingessel, A. & Leisch, F. (2017): e1071: Misc Functions of the Department of Statistics, Probability Theory Group (Formerly: E1071), TU Wien. R package version 1.6-8. Available from <https://CRAN.R-project.org/package=e1071>.
- R Core Team (2017). R: A language and environment for statistical computing. R Foundation for Statistical Computing, Vienna, Austria. Available from <https://www.R-project.org/>.
- Revelle, W. (2017) psych: Procedures for Personality and Psychological Research, Northwestern University, Evanston, Illinois, USA, Available from <https://CRAN.R-project.org/package=psych> Version = 1.7.5.
- RStudio Team (2017): RStudio: Integrated Development for R. RStudio, Inc., Boston, MA URL Available from <http://www.rstudio.com/>.
- Stevens, A. & Ramirez-Lopez, L. (2013): An introduction to the prospectr package. R package Vignette R package version 0.1.3.
- Venables, W. N. & Ripley, B. D. (2002): Modern Applied Statistics with S. Fourth Edition. Springer, New York. ISBN 0-387-95457-0.
- Wickham, H. (2009): ggplot2: Elegant Graphics for Data Analysis. Springer-Verlag New York.
- Wie, T. & Simko, V. (2017): R package "corrplot": Visualization of a Correlation Matrix (Version 0.84). Available from <https://github.com/taiyun/corrplot>.

DIN, EN and other Norms

BS EN 13656:2002- Characterization of waste. Microwave assisted digestion with hydrofluoric (HF), nitric (HNO₃), and hydrochloric (HCl) acid mixture for subsequent determination of elements, 2002-10.

DIN EN 932-1:1996-11 - Test for general properties of aggregates - Part 1: Methods for sampling; German version EN 932-1:1996, 1996-11.

DIN EN 12457-4:2003-01 - Characterization of waste - Leaching; Compliance test for leaching of granular waste materials and sludges - Part 4: One stage batch test at a liquid to solid ratio of 10 l/kg for materials with particle size below 10 mm (without or with limited size reduction); German version EN 12457-4:2002, 2003-01.

DIN EN 1744-1:2013-03 - Tests for chemical properties of aggregates - Part 1: Chemical analysis; German version EN 1744-1:2009+A1:2012, 2013-03.

DIN EN 196-2:2013-10 - Method of testing cement - Part 2: Chemical analysis of cement; German version EN 196-2:2013, 2013-10.

DIN 51084:1990-07 - Testing of oxidic raw and basic materials for ceramic, glass and glazes - Determination of fluoride content, 2008-11.

DIN EN 12879:2001-02 - Characterization of sludges - Determination of the loss on ignition of dry mass; German version EN 12879:2000, 2001-02.

DIN EN 15936:2012-11 - Sludge, treated biowaste, soil and waste - Determination of total organic carbon (TOC) by dry combustion; German version EN 15936:2012, 2012-11.

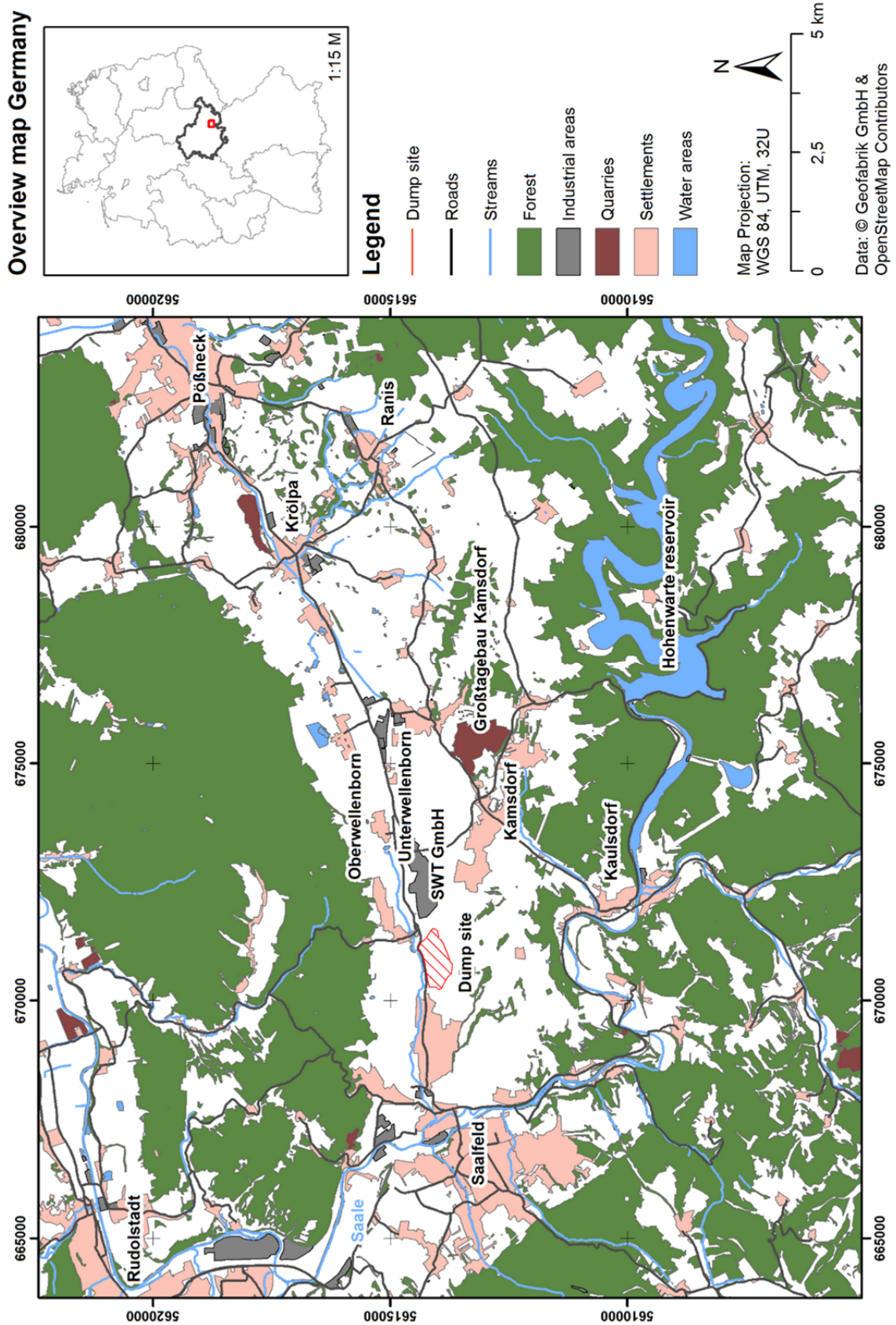
DIN EN ISO 11885:2009-09 - Water quality - Determination of selected elements by inductively coupled plasma optical emission spectrometry (ICP-OES) (ISO 11885:2007); German version EN ISO 11885:2009, 2009-09.

**Qualitative and quantitative spectral characterisation of iron-
and steelworks by-products - Combining information from
the visible light to the longwave infrared**

Appendix

8. Appendix

Appendices Chapter 3



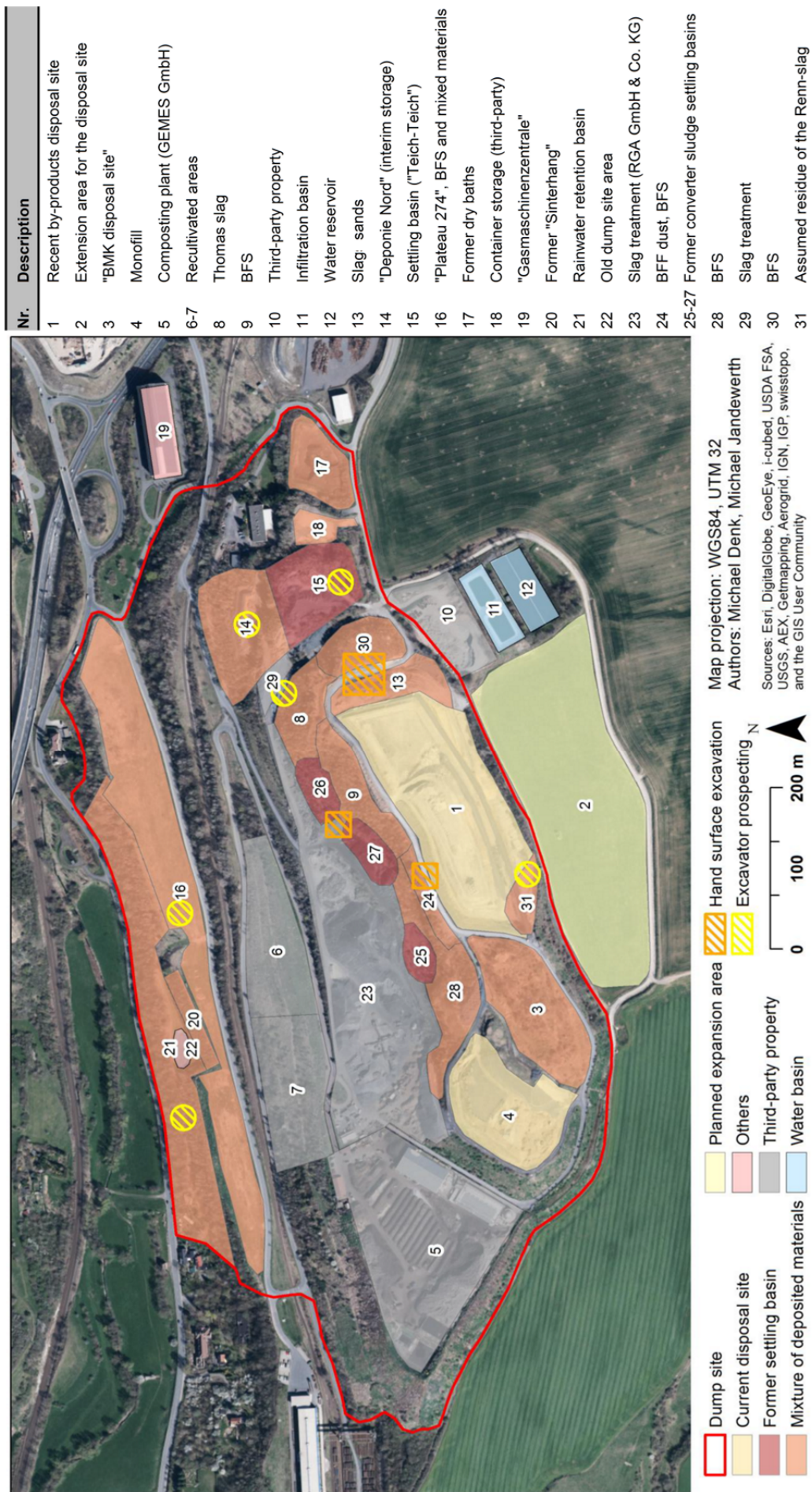
A3.1: Large-scale overview map of Unterwellenborn in southern Thuringia.

A3.2: Stratigraphy of the Saalfeld-Kamsdorf deposit (Rüger & Decker 1992)

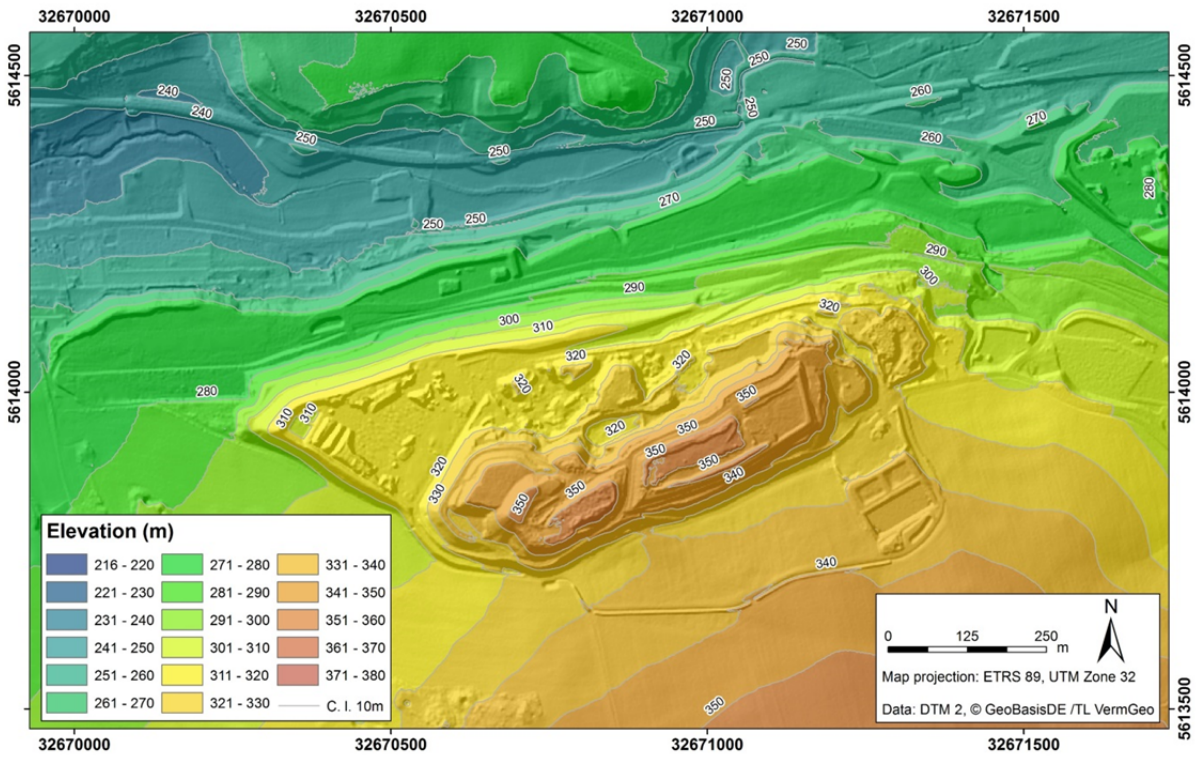
Series	Layers	Thickness (m)
Zechstein 1	Middle Werra Clay	6-8
	Werra Dolomite/Riff Dolomite	20-30
	Upper Zechstein Limestone	18-23
	Upper Slate	0.3-0.6
	Lower Zechstein Limestone	2-55
	Lower Slate (Kupferschiefer)	0-3.5
	“Mutterflöz”, dolomitic limestone	0-4
Permian	Rotliegend conglomerate	0-10
Carboniferous	Argillaceous slate and greywacke	-

A3.3 Utilisation of the iron- and steelmaking by-products of the Maxhütte in the 1950s (after Mrotzek-Blöß et al. 2016, data from Geschichtsverein Maxhütte e.V. 2005)

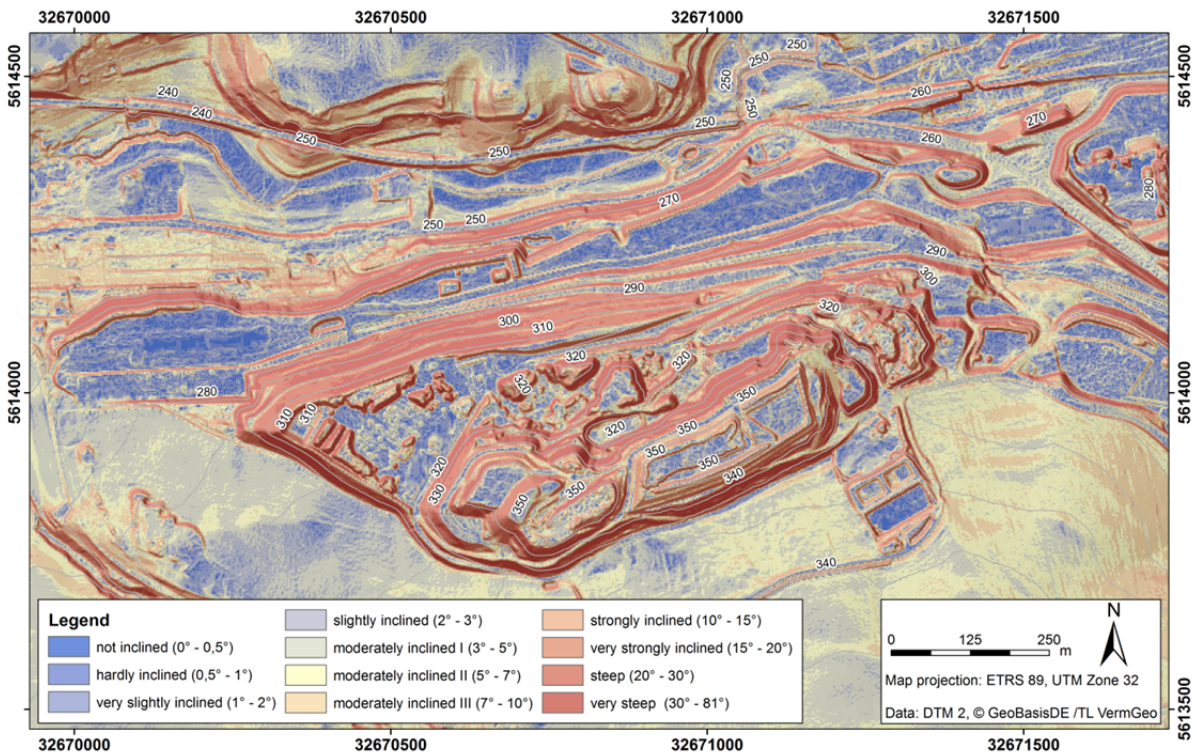
Process	Type of Usage	Amount used (1955)
Blast furnace	The blast furnace slag was almost completely used for the cement industry and slag block stone production	155040 t cement industry 56000 t slag block stones
Low shaft furnace	Most of the slag was deposited, only minor amounts used for slag wool production	2435 t slag wool
Renn furnace	Most of the slag was deposited; partial rebuild of the dump site and material reuse for the production of building materials starting in the 1970s	328460 t were used as construction material and for sale
Thomas steelmaking	Thomas phosphate was used as fertiliser	65100 ton
Electric steelmaking	Most of the slag was deposited	-



A3.4: Overview map of the dump site of the Stahlwerk Thüringen GmbH with relevant structural areas and highlighted sampling locations (Modified after Mrotzek-Bilöß et al. 2016).



A3.5: Differences in altitude occurring at the dump site of the Stahlwerk Thüringen GmbH.



A3.6: Differences in slope occurring at the dump site of the Stahlwerk Thüringen GmbH.

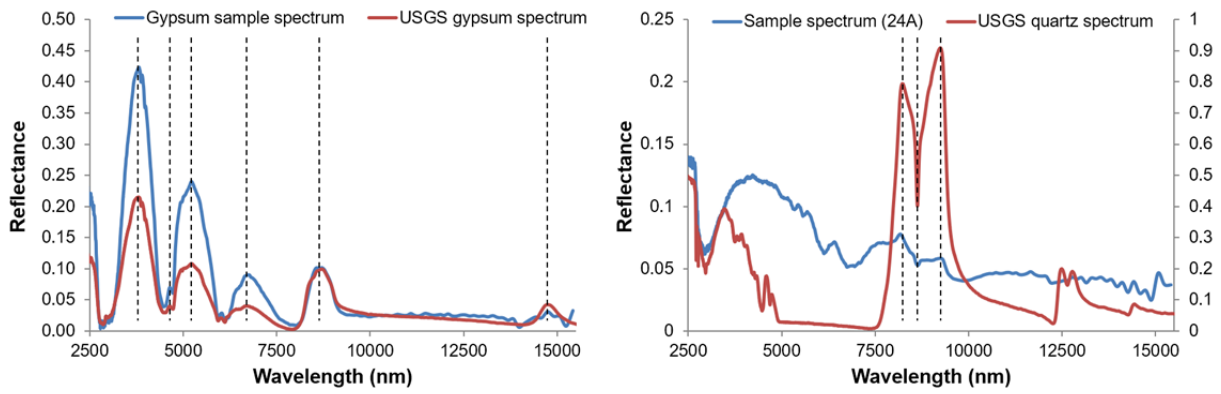
Appendices Chapter 4

A4.1: Instrumental parameters of the XRD measurements as conducted by FEhS.

Parameters	Values
Goniometer radius	240 mm
Radiation	Copper (Cu K α)
Power, Amperage	45 kV, 40 mA
Geometry	θ/θ diffractometer
Detector	Proportional counter

A4.2: DIN standards utilised for analysing the different chemical constituents by FEhS.

Constituent	DIN/Procedure
Aluminium metallic	Handbuch Eisenhüttenlabor, Bd. 1A
Aluminium oxide	ICP-OES EN ISO 11885 (2009-09)
Arsenic	ICP-OES EN ISO 11885 (2009-09)
Lead	ICP-OES EN ISO 11885 (2009-09)
Cadmium	ICP-OES EN ISO 11885 (2009-09)
Calcium oxide	ICP-OES EN ISO 11885 (2009-09)
Chromium metallic	Handbuch Eisenhüttenlabor, Bd. 1A
Chromium (III) oxide	ICP-OES EN ISO 11885 (2009-09)
Iron_{total}	DIN 51418-2 [2015-03]; DIN EN ISO 12677 [2013-02]
Iron metallic	Handbuch Eisenhüttenlabor, Bd. 1A
Iron (II) oxide	ICP-OES EN ISO 11885 (2009-09)
Iron (III) oxide	ICP-OES EN ISO 11885 (2009-09)
Fluoride	DIN 51084 (1990-07)
Free lime	DIN EN 1744-1: 2009 + A1: 2012
Total inorganic carbon (TIC)	DIN EN 15936 (2012-11)
Loss on ignition (550 °C)	DIN EN 12879: 2000
Loss on ignition (CO₂ + H₂O)	Berechnung Hausmethode
Potassium oxide	ICP-OES EN ISO 11885 (2009-09)
Copper	ICP-OES EN ISO 11885 (2009-09)
Copper oxide	ICP-OES EN ISO 11885 (2009-09)
Lithium oxide	ICP-OES EN ISO 11885 (2009-09)
Magnesium oxide	ICP-OES EN ISO 11885 (2009-09)
Manganese (II) oxide	ICP-OES EN ISO 11885 (2009-09)
Molybdenum	ICP-OES EN ISO 11885 (2009-09)
Molybdenum metallic	Handbuch Eisenhüttenlabor, Bd. 1A
Sodium oxide	ICP-OES EN ISO 11885 (2009-09)
Nickel	ICP-OES EN ISO 11885 (2009-09)
Nickel metallic	Handbuch Eisenhüttenlabor, Bd. 1A
Phosphorus pentoxide	ICP-OES EN ISO 11885 (2009-09)
Sulphur, total	DIN EN 1744-1: 2009 + A1: 2012
Selenium	ICP-OES EN ISO 11885 (2009-09)
Silver	ICP-OES EN ISO 11885 (2009-09)
Silicon oxide	DIN EN 196-2 (2013-10)
Titanium oxide	ICP-OES EN ISO 11885 (2009-09)
Vanadium	ICP-OES EN ISO 11885 (2009-09)
Vanadium pentoxide	ICP-OES EN ISO 11885 (2009-09)
Water	haus eigene PA
Wolfram	ICP-OES EN ISO 11885 (2009-09)
Zinc	ICP-OES EN ISO 11885 (2009-09)
Zinc oxide	ICP-OES EN ISO 11885 (2009-09)



A4.3: Comparison of MWIR/LWIR spectra recorded with the Agilent 4300 Handheld FTIR spectrometer of samples showing distinct diagnostic spectral features with corresponding reference spectra from Kokaly et al. (2017).
 Left: Gypsum, Right: Quartz-rich sample.

Appendices Chapter 5

A5.1: Mineralogical composition of the samples, sorted by by-product class (x = major constituent, o = minor constituent, + = trace constituent, this semi-quantitative information refers exclusively to the crystalline part; yes = amorphous constituents present (not quantified). Mineralogical analyses were conducted and provided by FEhS.

A5.1.1: Mineralogical composition of the “BFS+” samples (historical material, not pure) (I) (analyses by FEhS).

Mineral	14-1	14-2	14-3	14-4	14-5	14-6	30-ho	31-1	31-2	16-4	16-5
Anhydrite											
Baryte											
Calcite	x	x	x	x	x	o	+	x	o	o	+
Dolomite	o	o		o	o	x		o	x	o	o
Iron (met.)										+	
Ettringite					o					+	+
Feldspars			o		o					o	o
Melilites*	x	x	o	x	o	o	x	+	+	+	
Gypsum		o									
Micas								+		+	+
Goethite								+			
Hematite	o	o	o	o	o	o			+	+	
Spinels**	o				o	o	o	+	+	+	
Marcasite	o		o	o	o						
Merwinite								+	+		
Monticellite							o				
Quartz	x	x	x	x	x	x	o	o	x	x	x
Rankinite			x								
X-ray amorphous	yes	yes	yes	yes	yes	yes		yes	yes		
Vertumnite								+			
Wüstite									+		

*Gehlenite-Akermanite system, **Magnetite/Jacobsite/Franklinite

A5.1.1: Mineralogical composition of the “BFS+” samples (historical material, not pure) (II) (analyses by FEhS).

Mineral	16-6	16-7	21-3	W3-R3	W3-R5	W3-R1-2	W3-R14	W3-R16	W3-R20	W3-R21	W3-R22	W3-R23
Anhydrite			+						+			
Baryte				o				o	o	o		
Calcite	x	o	x	x	o	o		x	x	x	o	x
Dolomite	+	o										
Iron (met.)								+				
Ettringite	+											
Feldspars	o	o	o	o								
Melilites*					x	x	x				x	x
Gypsum			o		o						o	
Micas	+	+						o				
Goethite												
Hematite	+											
Spinels**	+										o	
Marcasite												
Merwinite					o		o			x		
Monticellite						o	o					
Quartz	o	x	o	x	o	o		x	o	o	o	
Rankinite												
X-ray amorphous			yes					yes	yes	yes		yes
Vertumnite												
Wüstite					+							

*Gehlenite-Akermanite system, **Magnetite/Jacobsite/Franklinite

A5.1.2: Mineralogical composition of the “granulated blast furnace slag” samples (analyses by FEhS).

Mineral	W2-20a	W2-20b	W2-21a	W2-21b	W2-22a	W2-22b
Baryte					o	o
Calcite	x	x	x	x	x	x
CSH phases		+				
Ettringite		o				o
Merwinite		x				x
Quartz	+		o		o	o
X-ray amorphous	yes	yes	yes	yes	yes	yes

A5.1.3: Mineralogical composition of the “converter dedusting sludge” samples (analyses by FEhS).

Mineral	26	27	17	18a	18b	18c	18d
Anhydrite				+	+		
Calcite		x	x	x	o	o	x
Dolomite		o	o	o	o	o	o
Iron (met.)		+	+	+	+	+	+
Gypsum			o	+	o	o	o
Hematite		x	o	x	x	x	x
Spinel**		x	o	x	o	o	o
Quartz		+	o	+	o	o	o
X-ray amorphous			yes	yes	yes	yes	yes
Wüstite			o	o	o	o	o

*Gehlenite-Akermanite system, **Magnetite/Jacobsite/Franklinite

A5.1.4: Mineralogical composition of the “stainless steel slag” samples (analyses by FEhS).

Mineral	T1	T2	T3	T4	T5
β -dicalcium silicate	o	o	o	o	o
Calcite	+	+	+	+	+
Calcium-Fluor-Silicate	o	o			o
Fluorite	+	+	+	+	+
Melilites*	o	o	o	o	o
Mayenite	o	o	o	+	o
Periclase	o	o	o	x	o
Portlandite	+	+	+	+	+
Quartz				+	
Rankinite	o	o	o	o	o
Spinel**	+	+	+	+	+
Wollastonite	o		o	o	o
γ -dicalcium silicate	o	o	o	o	o

*Gehlenite-Akermanite system, **Magnetite/Franklinite/Jacobsite

A5.1.5: Mineralogical composition of the “EAFS (carbon steel)” samples (analyses by FEhS).

Mineral	EAFS-1	EAFS-2	EAFS-3
Bredigite	x	o	x
Calcite	+	o	o
Melilites*	x	o	x
Larnite		x	
Spinel**	o	o	o
Wüstite	x	x	x

*Gehlenite-Akermanite system, **Magnetite/Jacobsite/Franklinite

A5.1.6: Mineralogical composition of the “ladle furnace slag” samples (analyses by FEhS).

Mineral	LFS-1	LFS-2	LFS-3
Calcite	o	o	o
Melilites*	o	o	o
Larnite	x	x	x
Mayenite	o	o	o
Periclase	o	o	o
Quartz	+	+	+
Wüstite	+	+	+
γ -dicalcium silicate	x	x	x

*Gehlenite-Akermanite system, **Magnetite/Jacobsite/Franklinite

A5.1.7: Mineralogical composition of the “EAFS (medium-alloy steel)” samples (analyses by FEhS).

Mineral	K1a	K2a
β -dicalcium silicate	x	x
Browmillerite	o	o
Calcite	o	o
Cristobalit		+
Mayenite	o	o
Periclase	o	o
Quartz	o	o
Spinel**	o	o
Wüstite	o	o

*Gehlenite-Akermanite system, **Magnetite/Jacobsite/Franklinite

A5.1.8: Mineralogical composition of the “EAFS (high-alloy steel)” samples (analyses by FEhS).

Mineral	T-EAFS-n
Melilites*	o
Spinel**	o
Rankinite	x
Wollastonite	x
Wüstite	+

*Gehlenite-Akermanite system, **Magnetite/Jacobsite/Franklinite

A5.1.9: Mineralogical composition of the “EAF foam slag” sample (analyses by FEhS).

Mineral	T-EAFS-f
Calcite	o
Melilites*	x
Spinel**	+
Merwinite	o

*Gehlenite-Akermanite system, **Magnetite/Jacobsite/Franklinite

A5.1.10: Mineralogical composition of the “AOD slag” sample (analyses by FEhS).

Mineral	T-AODS
Calcite	o
Calcium-Fluor-Silicate	o
Fluorite	o
Melilites*	o
Portlandite	o
γ -dicalcium silicate	x

*Gehlenite-Akermanite system

A5.1.11: Mineralogical composition of the “unspecified steelworks slag” samples (analyses by FEhS).

Mineral	21-9	GPS
Brucite	+	
Calcite	x	o
Ettringite	+	
Melilites*		x
Hydrotalcite	+	
Spinel**	+	
Merwinite	o	x
Periclase		+
Portlandite	o	
Quartz	o	

*Gehlenite-Akermanite system, **Magnetite/Jacobsite/Franklinite

A5.1.12: Mineralogical composition of the “blast furnace flue dust” samples (analyses by FEhS).

Mineral	24-A	24-B
Calcite	o	o
Melilites*	o	o
Goethite	o	o
Hematite	o	o
Potassium sulphate	o	o
Spinel**	o	o
Quartz	x	x

*Gehlenite-Akermanite system, **Magnetite/Jacobsite/Franklinite

A5.1.13: Mineralogical composition of the “Thomas slag” samples (I) (analyses by FEhS).

Mineral	29-ho	29-hu	29-bg	29-th	W1-R1	W1-R3s	W1-R3b	W1-R3g
Andalusite								o
Apatite	x	x	x	x	x	x	x	x
Calcite	+	o	o	o				
Hydrogarnet	o	o	o	o	o			
Hydromagnesite							o	o
Larnite								o
Portlandite	o	o	o	o	o	o	o	o
Quartz	+							
Silicocarnotite	x	x	x	x	x	x	x	x
Srebrodolskite	o	o	o	o	o	+	o	o
Wüstite	o	+	o	+	o	+		+

A5.1.13: Mineralogical composition of the “Thomas slag” samples (II) (analyses by FEhS).

Mineral	W1-R5	W1-R6	W1-R7o	W1-RV7m	T-VK	W1-R7u
Andalusite		o			o	o
Apatite	x	x	x	x	o	x
Calcite	o				x	o
Hydrogarnet						
Hydromagnesite		o	o	o		
Larnite						
Spinels**						+
Portlandite	o	o	o	o	o	o
Quartz						
Silicocarnotite	x	x	x	x	x	x
Srebrodolskite	o	o	o	o		o
Wüstite			o	+		+
γ -dicalcium silicate					o	

**Magnetite/Jacobsite/Franklinite

A5.1.14: Mineralogical composition of the “mill scale” sample (analyses by FEhS).

Mineral	19
Iron (met.)	+
Hematite	o
Spinels**	x
Wüstite	x

**Magnetite/Jacobsite/Franklinite

A5.1.15: Mineralogical composition of the “mixtures with high amounts of sand” samples (analyses by FEhS).

Mineral	16-3	21-10	21-11	21-4	21-5	21-7	W3-R19
Calcite	o	+	+	+	+	+	o
Dolomite	o	+	+		+	o	
Ettringite	+						
Feldspars	o	o	o	o	o	o	o
Gypsum				+	+	+	
Micas	+	+	+	+	+	+	+
Hematite			+				
Spinel**		+	+			+	
Quartz	x	x	x	x	x	x	x
Rankinite		+					

*Gehlenite-Akermanite system, **Magnetite/Franklinite/Jacobsite

A5.1.16: Mineralogical composition of the “unspecified dusts and sludges” samples (analyses by FEhS).

Mineral	W3-R10	W3-R11	W3-R12	W3-R13	W3-R15	W3-R18	W3-R2	W3-R4	W3-R6	15
Apatite	x			o						x
Calcite	x	o	x	x	x	x		x	x	o
Dolomite		o		o	o		x	o		x
Iron (met.)					+	o				
Feldspars							+			
Half-hydrate			o			o				
Goethite						o				
Hematite	o		o		o	o		o		o
Hydrotalcite				o						
Spinel**						o		o	o	o
Mulite		x								
Quartz	o	x	o	o	x	x	o	o	+	o
X-ray amorphous	yes	yes	yes	yes	yes	yes	yes	yes	yes	
Wüstite		o								o

**Magnetite/Franklinite/Jacobsite

A5.1.17: Mineralogical composition of the “unspecified others” samples (analyses by FEhS).

Mineral	30-df	21-12	21-13	21-14	21-15	21-6	21-8	DK	W3-R8	W3-R9	W3-R1	W3-R17	W3-R7
Alabandite													o
Alumohydrocalcite													+
Apatite	o			+						x			
Baryte		o	o		x								
Brucite		o		o									
Calcite	x	o	x	o	x	o	x	x	x	x	o	o	x
Iron (met.)	o												o
Ettringite		+		+	+								
Feldspars										o			o
Melilites*						+					x		
Gypsum			o	+									
Goethite							+						o
Half-hydrate												o	
Hematite	o									o	o		
Hydrogarnet													
Hydromagnesite									o				
Hydrotalcite					+		+						o
Spinel**							+	+		o	o	o	
Merwinite						o	o						
Portlandite		x		x									
Quartz	x	+		o		o	o		x	o	x	x	x
Rapidcreekite		o											
X-ray amorphous	yes		yes	yes	yes	yes			yes	yes		yes	yes
Sillimanite	o												
Wüstite													o

*Gehlenite-Akermanite system, **Magnetite/Franklinite/Jacobsite

A5.1.18: Mineralogical composition of the “limestone+natural sand” sample (analyses by FEhS).

Mineral	W1-R3r
Calcite	o
Feldspars	o
Micas	+
Hydromagnesite	o
Portlandite	+
Quartz	x
Silicocarnotite	o
Srebrodolskite	o

A5.2: Statistics on the chemical composition (m%) of the major by-product classes (I).*

	Bast furnace slag (+) (N = 23)				Granulated BFS (N =6)				Thomas slag (N =14)			
	Mean	Max	Min	SD	Mean	Max	Min	SD	Mean	Max	Min	SD
CaO	24.813	35.400	17.000	4.543	28.217	34.500	23.600	3.917	44.564	46.800	41.000	1.794
SiO₂	26.033	33.940	17.520	4.673	24.385	28.210	21.000	2.625	5.065	5.900	4.220	0.424
MgO	6.267	10.200	3.290	1.535	7.867	9.640	5.930	1.401	1.266	2.100	0.870	0.351
Al₂O₃	9.508	17.200	5.330	2.778	10.545	14.000	7.640	2.211	0.637	0.920	0.400	0.134
Fe	6.884	18.100	0.474	4.289	1.690	3.239	0.350	1.169	14.371	18.060	12.300	1.561
FeO	2.985	4.880	1.370	0.985					0.442	1.010	0.140	0.337
Fe₂O₃	8.278	15.100	3.911	3.281					16.300	19.500	13.700	2.092
MnO	1.628	4.430	0.210	1.033	1.422	2.800	0.380	0.838	3.440	4.070	2.840	0.331
Cr₂O₃	0.098	0.500	0.010	0.128	0.037	0.040	0.030	0.005	1.206	1.560	0.940	0.201
TiO₂	0.504	1.370	0.270	0.224	0.410	0.530	0.320	0.075	0.160	0.190	0.130	0.019
Fe_{metallic}	1.391	4.430	0.410	1.153					2.928	3.740	2.230	0.538
Al_{metallic}	0.851	3.130	0.130	0.669					0.495	0.640	0.370	0.099
Cr_{metallic}	0.059	0.140	0.011	0.034		0.000	0.000		0.323	0.390	0.210	0.075
K₂O	1.238	2.950	0.290	0.778	0.543	0.970	0.280	0.245	0.027	0.050	0.010	0.011
CuO	0.026	0.050	0.010	0.011	0.010	0.010	0.010	0.000	0.003	0.010	0.000	0.004
Li₂O	0.024	0.050	0.010	0.012	0.038	0.060	0.030	0.011		0.000	0.000	
Na₂O	0.247	0.490	0.070	0.139	0.092	0.150	0.070	0.029	0.186	0.400	0.060	0.081
P₂O₅	0.613	1.620	0.100	0.386	0.108	0.140	0.080	0.025	14.014	16.800	12.900	1.185
V₂O₅	0.043	0.100	0.010	0.029	0.013	0.020	0.010	0.005	0.371	0.510	0.260	0.072
ZnO	0.542	3.340	0.020	0.764	0.128	0.250	0.050	0.075	0.010	0.010	0.010	0.000
CaO_{free}	0.814	1.300	0.440	0.297	0.655	1.000	0.310	0.345	5.616	10.000	0.920	2.784
CO₂+H₂O	16.711	35.900	0.700	8.398	22.400	28.900	14.300	5.412	9.798	13.200	6.770	1.655
TIC	10.391	22.600	0.500	5.768	8.683	14.000	4.300	3.344	3.054	10.300	0.580	2.645
H₂O	6.297	13.200	0.200	3.089	13.713	22.300	9.980	4.196	6.734	9.100	2.870	1.681
Fluorite	0.116	0.310	0.050	0.064								
S_{total}	1.135	3.620	0.217	0.737	1.036	1.380	0.649	0.248	0.180	0.254	0.134	0.029
As	0.004	0.008	0.002	0.002					0.001	0.001	0.001	0.000
Cd	0.003	0.016	0.000	0.004					0.000	0.000	0.000	0.000
Cu	0.020	0.042	0.007	0.009					0.004	0.006	0.004	0.001
Mo	0.001	0.003	0.000	0.001					0.004	0.006	0.003	0.001
Ni	0.005	0.010	0.002	0.002					0.001	0.002	0.001	0.000
V	0.030	0.055	0.012	0.015					0.207	0.239	0.168	0.026
W	0.024	0.086	0.008	0.026					0.000	0.000	0.000	0.000
Pb	0.263	0.819	0.005	0.287					0.002	0.004	0.001	0.001
Zn	0.436	2.685	0.017	0.615	0.069	0.203	0.001	0.069	0.004	0.009	0.001	0.002
Ag	0.001	0.002	0.001	0.000	0.001	0.001	0.001	0.000	0.004	0.005	0.001	0.001
Σ(metals)	7.497	17.277	2.001	4.795					18.486	20.258	17.846	1.024

*Chemical analyses by FEhS

A5.2: Statistics on the chemical composition (m%) of the major by-product classes (II).*

	EAFS (carbon steelm.) (N = 3)				EAFS (med.-alloy steelm.) (N = 2)				EAFS (high-alloy st.) (N = 1)
	Mean	Max	Min	SD	Mean	Max	Min	SD	
CaO	24.900	25.500	24.100	0.589	22.450	24.000	20.900	1.550	48.000
SiO₂	12.407	13.680	10.950	1.122	18.950	21.400	16.500	2.450	40.300
MgO	4.303	4.930	3.940	0.445	8.770	9.540	8.000	0.770	2.350
Al₂O₃	5.523	5.990	5.220	0.335	8.775	9.540	8.010	0.765	0.650
Fe	35.633	36.930	34.700	0.946	19.400	19.500	19.300	0.100	0.498
FeO		0.000	0.000		13.200	13.600	12.800	0.400	
Fe₂O₃		0.000	0.000		11.050	11.200	10.900	0.150	
MnO	6.117	6.700	5.760	0.416	3.430	3.590	3.270	0.160	2.680
Cr₂O₃	2.443	2.680	2.290	0.170	1.235	1.250	1.220	0.015	3.350
TiO₂	0.383	0.430	0.340	0.037	0.290	0.300	0.280	0.010	0.220
Fe_{metallic}					1.395	1.730	1.060	0.335	
Al_{metallic}					1.025	1.360	0.690	0.335	
Cr_{metallic}					0.085	0.090	0.080	0.005	
K₂O	0.020	0.020	0.020	0.000	0.150	0.180	0.120	0.030	0.010
CuO	0.033	0.040	0.030	0.005	0.010	0.010	0.010	0.000	
Li₂O		0.000	0.000		0.260	0.270	0.250	0.010	
Na₂O	0.073	0.090	0.050	0.017	0.250	0.300	0.200	0.050	0.010
P₂O₅	0.480	0.550	0.430	0.051	0.215	0.220	0.210	0.005	
V₂O₅	0.133	0.180	0.110	0.033	0.130	0.130	0.130	0.000	0.050
ZnO	0.017	0.020	0.010	0.005	0.955	1.210	0.700	0.255	
CaO_{free}					0.460	0.540	0.380	0.080	
CO₂+H₂O	0.563	0.670	0.450	0.090	6.830	7.090	6.570	0.260	0.180
TIC	0.353	0.360	0.350	0.005	3.980	4.040	3.920	0.060	0.170
H₂O	0.210	0.320	0.100	0.090	2.850	3.170	2.530	0.320	
Fluorite									
S_{total}	0.156	0.175	0.145	0.013	0.415	0.530	0.300	0.115	0.086
As									
Cd					0.000	0.001	0.000	0.000	
Cu					0.017	0.018	0.017	0.001	
Mo					0.006	0.006	0.006	0.000	
Ni					0.017	0.018	0.015	0.001	
V					0.029	0.054	0.004	0.025	
W					0.036	0.038	0.033	0.003	
Pb					0.032	0.044	0.020	0.012	
Zn	0.015	0.018	0.011	0.003	1.033	1.267	0.799	0.234	
Ag					0.001	0.001	0.001	0.000	
Σ(metals)					25.113	25.686	24.540	0.573	

*Chemical analyses by FEhS

A5.2: Statistics on the chemical composition (m%) of the major by-product classes (III).*

	LF slag (N = 3)				Unspecified SWS (N = 2)				Stainless steel slag (N = 5)			
	Mean	Max	Min	SD	Mean	Max	Min	SD	Mean	Max	Min	SD
CaO	40.433	44.500	36.800	3.158	35.100	37.900	32.300	2.800	46.600	51.000	40.500	4.066
SiO₂	16.897	17.150	16.650	0.204	19.490	23.810	15.170	4.320	26.640	30.800	24.000	2.365
MgO	6.737	6.940	6.500	0.181	5.250	6.510	3.990	1.260	6.604	11.300	4.490	2.436
Al₂O₃	12.367	12.800	11.700	0.478	10.305	19.100	1.510	8.795	4.100	5.120	3.270	0.636
Fe	8.398	11.690	5.179	2.659	9.606	17.320	1.892	7.714	1.420	2.510	0.730	0.615
FeO					6.190	6.190	6.190	0.000				
Fe₂O₃					10.650	10.650	10.650	0.000				
MnO	1.950	2.660	1.530	0.505	2.925	5.590	0.260	2.665	1.810	2.320	1.360	0.321
Cr₂O₃	0.760	1.040	0.600	0.199	0.570	0.570	0.570	0.000	4.746	5.240	4.320	0.364
TiO₂	0.330	0.330	0.330	0.000	0.440	0.580	0.300	0.140	1.106	1.390	0.940	0.178
Fe_{metallic}					5.060	5.060	5.060	0.000	1.398	2.490	0.700	0.623
Al_{metallic}					0.540	0.540	0.540	0.000	0.824	1.130	0.460	0.220
Cr_{metallic}					0.120	0.120	0.120	0.000	0.400	0.550	0.280	0.102
K₂O	0.033	0.040	0.030	0.005	0.195	0.230	0.160	0.035	0.018	0.030	0.010	0.007
CuO	0.010	0.010	0.010	0.000	0.020	0.020	0.020	0.000	0.010	0.010	0.010	0.000
Li₂O						0.000	0.000		0.156	0.210	0.120	0.032
Na₂O	0.080	0.080	0.080	0.000	0.070	0.080	0.060	0.010				
P₂O₅	0.097	0.120	0.080	0.017	3.855	7.650	0.060	3.795	0.010	0.010	0.010	0.000
V₂O₅	0.047	0.060	0.040	0.009	0.325	0.650	0.000	0.325	0.084	0.100	0.070	0.012
ZnO	0.027	0.030	0.020	0.005	0.160	0.160	0.160	0.000				
CaO_{free}	0.493	0.540	0.440	0.041	2.255	3.700	0.810	1.445	3.420	5.300	1.800	1.423
CO₂+H₂O	7.780	8.330	7.410	0.397	11.610	14.100	9.120	2.490	4.172	5.820	2.700	1.179
TIC	2.567	2.700	2.400	0.125	6.150	7.600	4.700	1.450	1.620	2.120	1.140	0.383
H₂O	5.203	5.620	4.960	0.296	5.445	6.440	4.450	0.995	2.552	3.700	1.560	0.844
Fluorite												
S_{total}	0.679	0.754	0.595	0.065	0.583	0.884	0.282	0.301	0.142	0.170	0.100	0.028
As					0.003	0.003	0.003	0.000	0.001	0.002	0.001	0.000
Cd					0.000	0.000	0.000	0.000	0.000	0.000	0.000	0.000
Cu					0.015	0.015	0.015	0.000	0.005	0.009	0.003	0.002
Mo					0.000	0.000	0.000	0.000	0.019	0.032	0.009	0.009
Ni					0.007	0.007	0.007	0.000	0.115	0.204	0.039	0.060
V					0.365	0.365	0.365	0.000	0.037	0.047	0.030	0.006
W					0.011	0.011	0.011					
Pb					0.003	0.003	0.003					
Zn	0.023	0.026	0.020	0.002	0.066	0.127	0.005	0.061	0.003	0.004	0.002	0.001
Ag					0.002	0.002	0.002					
Σ(metals)					10.873	10.873	10.873	0.000	7.550	8.936	6.526	0.847

*Chemical analyses by FEhS

A5.2: Statistics on the chemical composition (m%) of the major by-product classes (IV).*

	Foam slag (high-alloy steelm.) (N = 1)	AODS (high- alloy steelm.) (N = 1)	Blast furnace flue dust (N = 2)				Converter dedusting sludge (N = 7)			
			Mean	Max	Min	SD	Mean	Max	Min	SD
CaO	39.700	57.100	14.200	16.200	12.200	2.000	12.757	14.100	11.200	0.939
SiO₂	34.590	23.620	32.005	35.000	29.010	2.995	11.433	18.280	4.100	5.055
MgO	9.060	2.510	3.525	3.550	3.500	0.025	2.553	3.380	1.180	0.818
Al₂O₃	5.510	1.390	6.610	7.570	5.650	0.960	4.523	6.160	1.850	1.648
Fe	0.327	0.579	16.350	19.400	13.300	3.050	27.314	37.630	20.350	6.835
FeO			3.520	4.450	2.590	0.930	5.890	7.610	4.170	1.720
Fe₂O₃			14.450	16.500	12.400	2.050	35.750	47.800	23.700	12.050
MnO	3.430	0.910	1.210	1.250	1.170	0.040	1.089	1.510	0.870	0.233
Cr₂O₃	3.740	1.450	0.110	0.130	0.090	0.020	0.137	0.240	0.090	0.051
TiO₂	1.690	0.470	0.415	0.440	0.390	0.025	0.167	0.240	0.060	0.070
Fe_{metallic}			3.490	4.360	2.620	0.870	0.550	0.570	0.530	0.020
Al_{metallic}			0.575	0.590	0.560	0.015	0.755	0.810	0.700	0.055
Cr_{metallic}			0.073	0.090	0.055	0.018	0.030	0.040	0.020	0.010
K₂O	0.020	0.010	1.100	1.210	0.990	0.110	0.513	0.920	0.150	0.259
CuO			0.035	0.040	0.030	0.005	0.053	0.080	0.040	0.012
Li₂O				0.000	0.000			0.000	0.000	
Na₂O	0.050	0.020	0.530	0.580	0.480	0.050	0.267	0.410	0.130	0.099
P₂O₅			1.160	1.270	1.050	0.110	1.376	2.230	1.150	0.357
V₂O₅	0.090	0.030	0.045	0.050	0.040	0.005	0.036	0.060	0.030	0.010
ZnO			0.965	1.040	0.890	0.075	2.950	4.500	1.410	1.170
CaO_{free}		5.500	1.100	1.100	1.100	0.000	0.398	0.520	0.290	0.084
CO₂+H₂O	0.310	8.340	17.250	19.500	15.000	2.250	30.943	37.000	23.700	5.359
TIC	0.300	3.500	10.650	12.000	9.300	1.350	20.329	26.800	17.400	3.160
H₂O		4.890	6.575	7.490	5.660	0.915	10.609	16.000	5.030	3.779
Fluorite			0.325	0.390	0.260	0.065	0.475	0.550	0.400	0.075
S_{total}	0.077	0.205	0.402	0.510	0.294	0.108	0.604	0.939	0.146	0.299
As			0.003	0.003	0.002	0.001	0.003	0.003	0.003	0.000
Cd			0.008	0.009	0.008	0.000	0.017	0.017	0.017	0.000
Cu			0.027	0.031	0.023	0.004	0.051	0.066	0.036	0.015
Mo			0.003	0.005	0.002	0.001	0.002	0.002	0.002	0.000
Ni			0.017	0.019	0.015	0.002	0.024	0.030	0.018	0.006
V			0.025	0.029	0.020	0.004	0.020	0.025	0.015	0.005
W			0.000	0.000	0.000	0.000	0.000	0.000	0.000	0.000
Pb			0.219	0.262	0.176	0.043	0.465	0.565	0.364	0.101
Zn	0.000	0.002	0.776	0.833	0.719	0.057	2.370	3.612	1.135	0.938
Ag			0.000	0.000	0.000	0.000	0.003	0.006	0.002	0.002
Σ(metals)	39.700	57.100	16.103	18.326	13.881	2.223	29.980	39.297	20.664	9.317

*Chemical analyses by FEHS

A5.2: Statistics on the chemical composition (m%) of the major by-product classes (V).*

	Not specified dust/sludge (N = 10)				Mill scale (N =1)	Mixture containing sand (N = 7)			
	Mean	Max	Min	SD		Mean	Max	Min	SD
CaO	16.828	21.000	8.680	3.819	0.050	9.683	13.500	4.870	2.890
SiO₂	17.248	23.140	10.690	3.644	0.370	50.167	55.040	42.710	4.908
MgO	7.191	10.600	3.100	2.344		3.431	4.110	2.370	0.551
Al₂O₃	6.945	10.500	3.300	2.061		10.714	12.700	9.510	1.040
Fe	10.991	22.700	1.208	7.362	62.590	4.637	7.400	2.907	1.522
FeO	7.330	7.330	7.330	0.000		1.583	3.310	0.650	0.911
Fe₂O₃	19.600	19.600	19.600	0.000		4.465	5.887	2.323	1.173
MnO	0.988	1.350	0.630	0.251	0.830	0.874	1.620	0.290	0.386
Cr₂O₃	0.030	0.070	0.020	0.018	0.090	0.038	0.060	0.010	0.020
TiO₂	0.142	0.220	0.030	0.056	0.000	0.446	0.600	0.380	0.073
Fe_{metallic}	1.430	1.430	1.430			0.572	0.840	0.350	0.164
Al_{metallic}	0.550	0.550	0.550			0.595	0.870	0.350	0.176
Cr_{metallic}	0.007	0.007	0.007	0.000		0.080	0.120	0.051	0.023
K₂O	1.334	2.850	0.360	0.719	0.000	3.024	4.320	2.340	0.660
CuO	0.025	0.050	0.010	0.011	0.300	0.010	0.010	0.010	0.000
Li₂O	0.108	0.230	0.010	0.076		0.012	0.020	0.010	0.004
Na₂O	0.192	0.320	0.080	0.095	0.010	0.261	0.430	0.170	0.089
P₂O₅	1.229	3.820	0.300	0.964	0.220	0.486	0.890	0.190	0.246
V₂O₅	0.026	0.040	0.000	0.012	0.010	0.044	0.080	0.010	0.022
ZnO	2.661	5.140	0.830	1.497	0.030	0.040	0.110	0.010	0.039
CaO_{free}	0.584	1.300	0.210	0.340		0.537	0.750	0.340	0.168
CO₂+H₂O	23.560	31.400	16.200	5.013	5.930	10.666	15.400	6.520	2.593
TIC	13.540	20.100	9.000	3.271	3.900	4.729	9.300	2.700	2.099
H₂O	10.023	16.300	4.090	3.805	2.030	5.930	7.930	3.290	1.511
Fluorite	0.380	0.380	0.380			0.058	0.071	0.044	0.009
S_{total}	0.676	1.450	0.173	0.361	0.028	0.377	0.523	0.173	0.119
As	0.005	0.005	0.005			0.002	0.003	0.001	0.001
Cd	0.007	0.007	0.007			0.000	0.000	0.000	0.000
Cu	0.026	0.026	0.026			0.006	0.011	0.001	0.003
Mo	0.003	0.003	0.003			0.000	0.000	0.000	0.000
Ni	0.013	0.013	0.013			0.004	0.005	0.002	0.001
V	0.018	0.018	0.018			0.027	0.046	0.015	0.011
W						0.015	0.020	0.009	0.004
Pb	0.557	0.557	0.557			0.009	0.021	0.003	0.006
Zn	2.138	4.128	0.667	1.203	0.025	0.032	0.090	0.008	0.031
Ag	0.005	0.008	0.002	0.002					
Σ(metals)	17.077	17.077	17.077			2.046	2.632	1.060	0.556

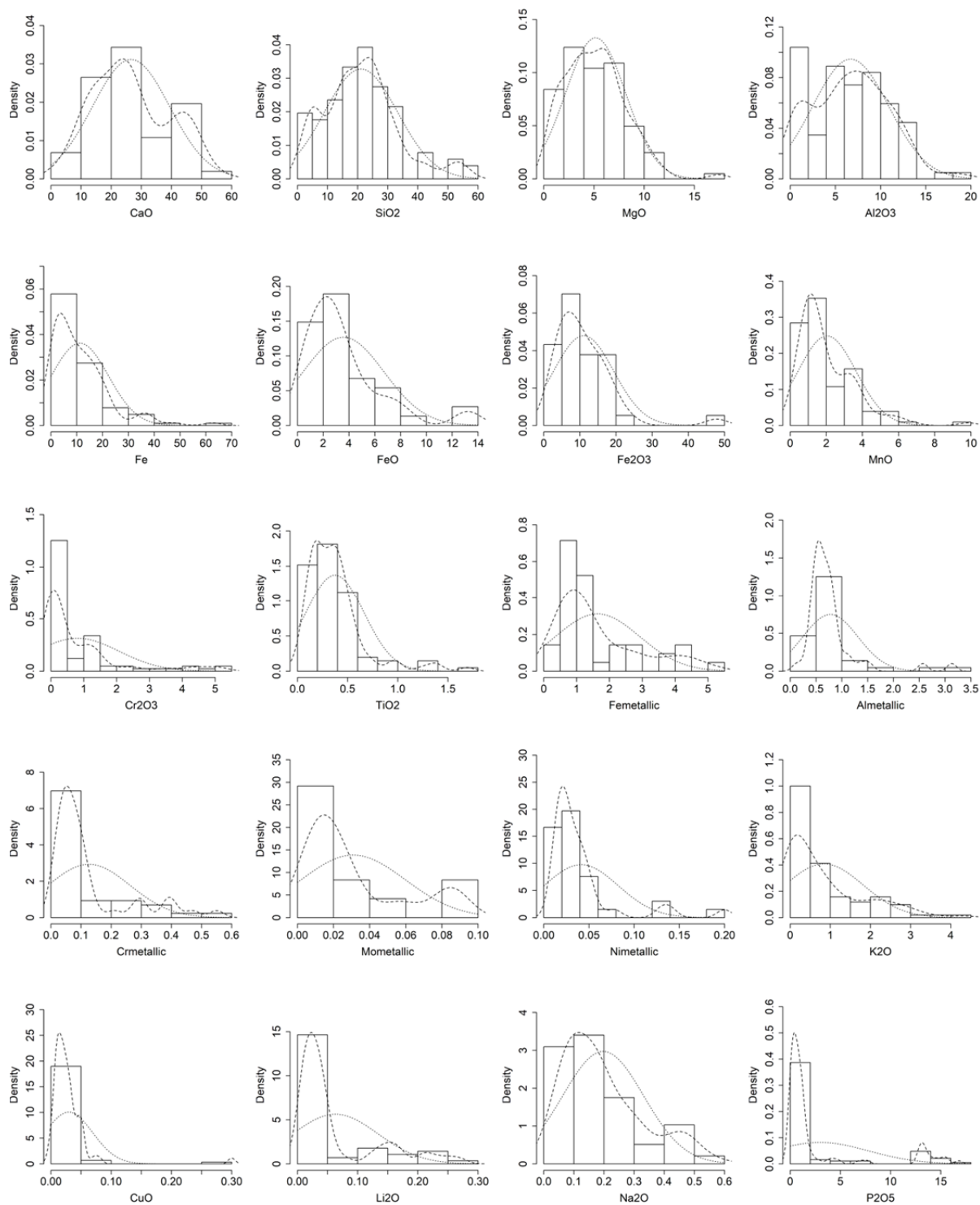
*Chemical analyses by FEhS

A5.2: Statistics on the chemical composition (m%) of the major by-product classes (VI).*

	Limestone+sand (N =1)	Unspecified other (N = 13)			
		Mean	Max	Min	SD
CaO	25.300	21.539	34.300	3.640	8.913
SiO₂	40.680	17.923	30.370	1.470	7.547
MgO	1.120	6.325	17.400	0.800	4.199
Al₂O₃	2.110	5.673	11.600	0.570	3.266
Fe	5.384	10.710	47.230	0.450	12.419
FeO		4.100	8.620	1.010	2.912
Fe₂O₃		9.470	18.129	1.237	6.429
MnO	1.240	2.512	9.850	0.130	2.568
Cr₂O₃	0.440	0.130	0.460	0.010	0.170
TiO₂	0.100	0.287	0.540	0.020	0.154
Fe_{metallic}		1.958	4.150	1.000	1.212
Al_{metallic}		1.015	2.570	0.460	0.791
Cr_{metallic}		0.055	0.100	0.013	0.032
K₂O	0.740	0.898	2.910	0.030	0.936
CuO		0.023	0.070	0.010	0.017
Li₂O		0.062	0.170	0.010	0.056
Na₂O	0.230	0.168	0.520	0.050	0.151
P₂O₅	4.810	1.794	6.910	0.060	1.928
V₂O₅	0.150	0.109	0.590	0.000	0.167
ZnO	0.010	0.770	3.970	0.000	1.181
CaO_{free}	0.380	2.646	9.100	0.230	3.375
CO₂+H₂O	12.200	25.231	61.600	13.100	12.051
TIC	9.700	11.931	46.700	5.500	10.208
H₂O	2.420	13.295	23.600	5.860	6.178
Fluorite		0.135	0.490	0.023	0.178
S_{total}	0.076	1.173	3.280	0.090	0.996
As		0.003	0.007	0.001	0.002
Cd		0.001	0.001	0.000	0.001
Cu		0.008	0.020	0.001	0.007
Mo		0.001	0.001	0.000	0.000
Ni		0.005	0.011	0.001	0.003
V		0.096	0.330	0.004	0.115
W		0.008	0.015	0.002	0.004
Pb		0.107	0.712	0.002	0.247
Zn	0.012	0.571	3.188	0.004	0.925
Ag	0.001	0.001	0.001	0.001	0.000
Σ(metals)		6.892	13.720	1.821	4.147

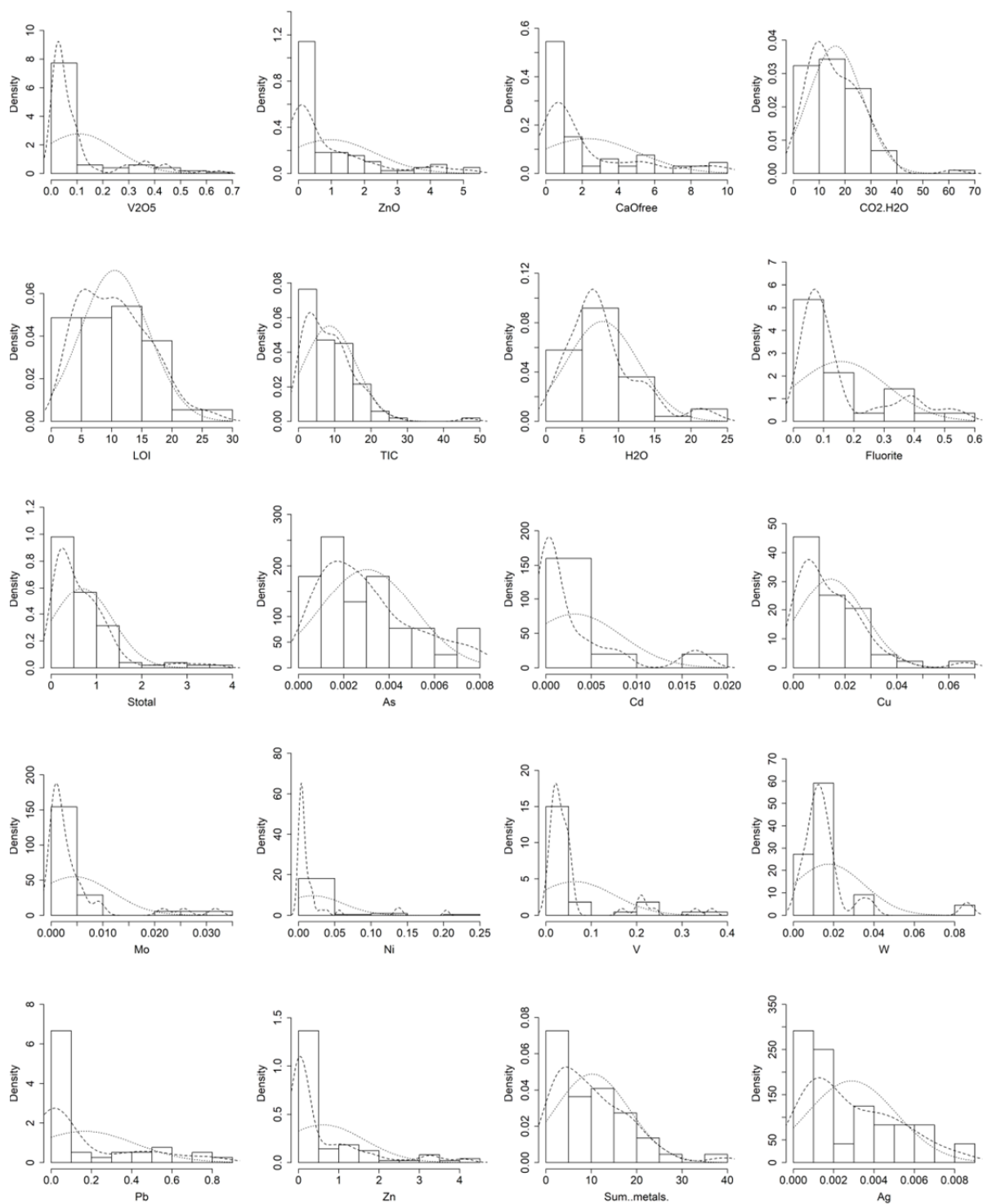
*Chemical analyses by FEhS

A5.3: Histograms, density and normal fits for the analysed chemical constituents (I).*

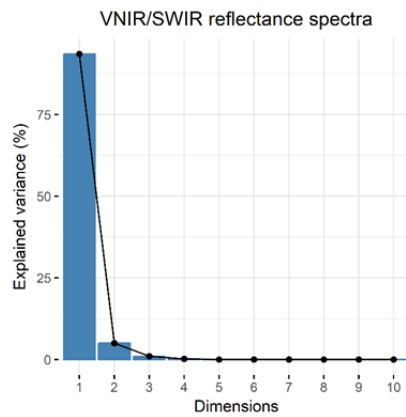
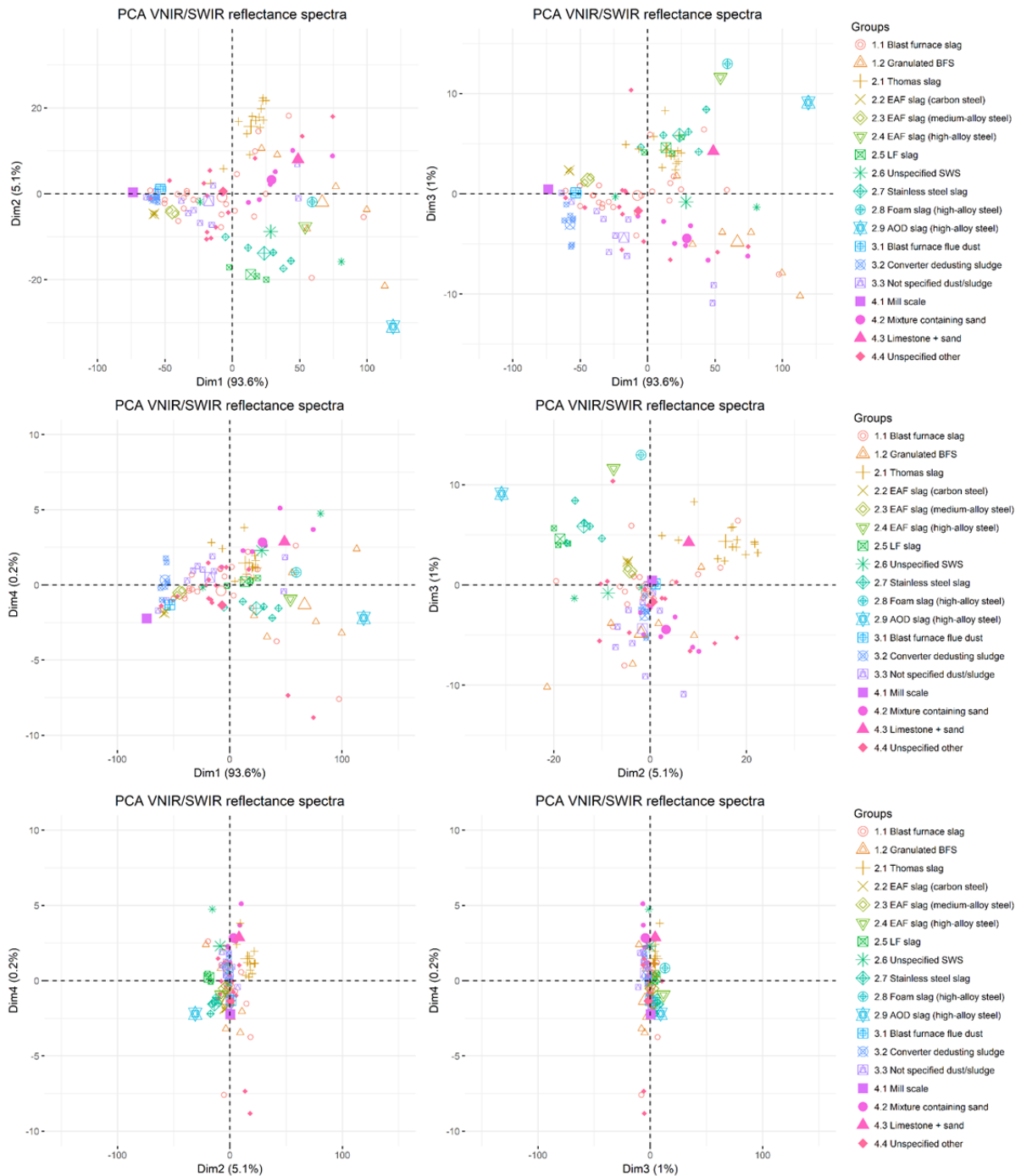


*Chemical analyses by FEHS

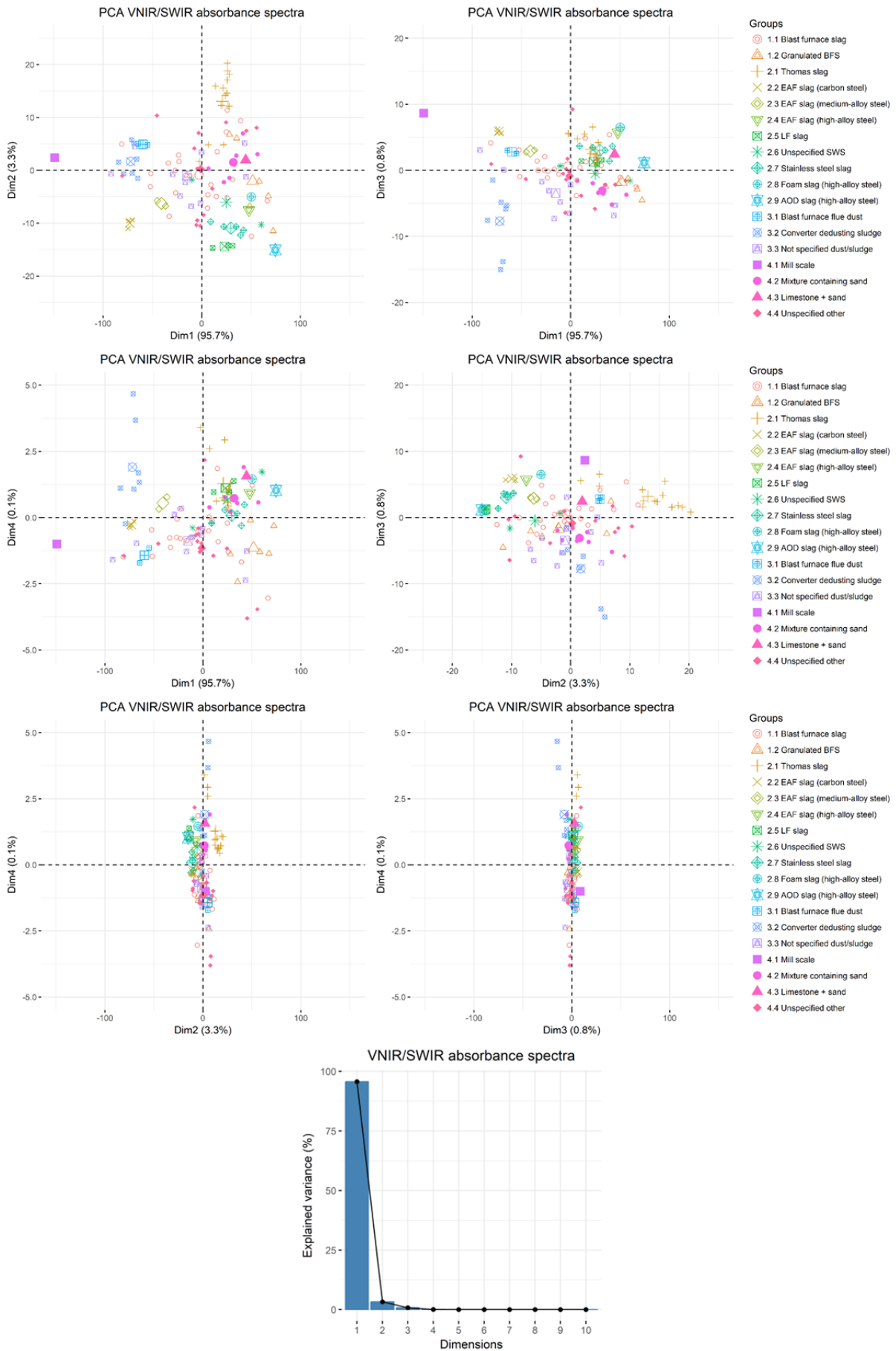
A5.3: Histograms, density and normal fits for the analysed chemical constituents (II).*



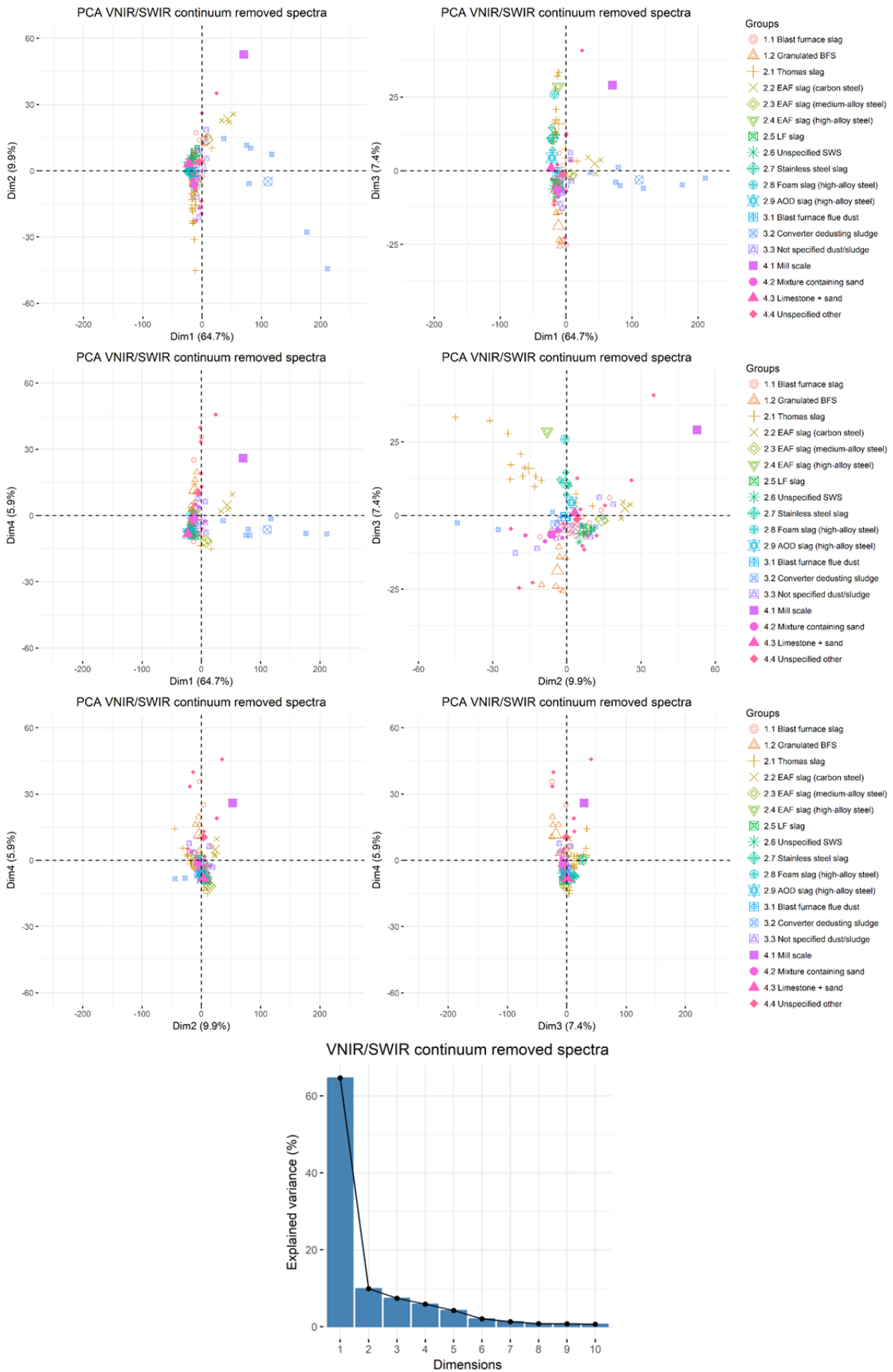
*Chemical analyses by FEHS



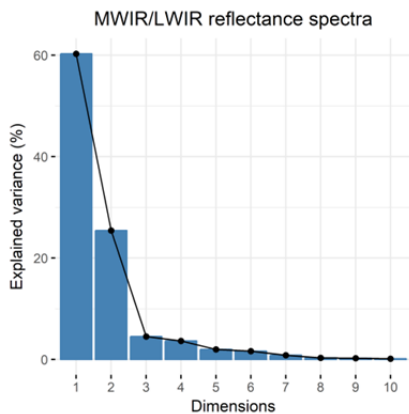
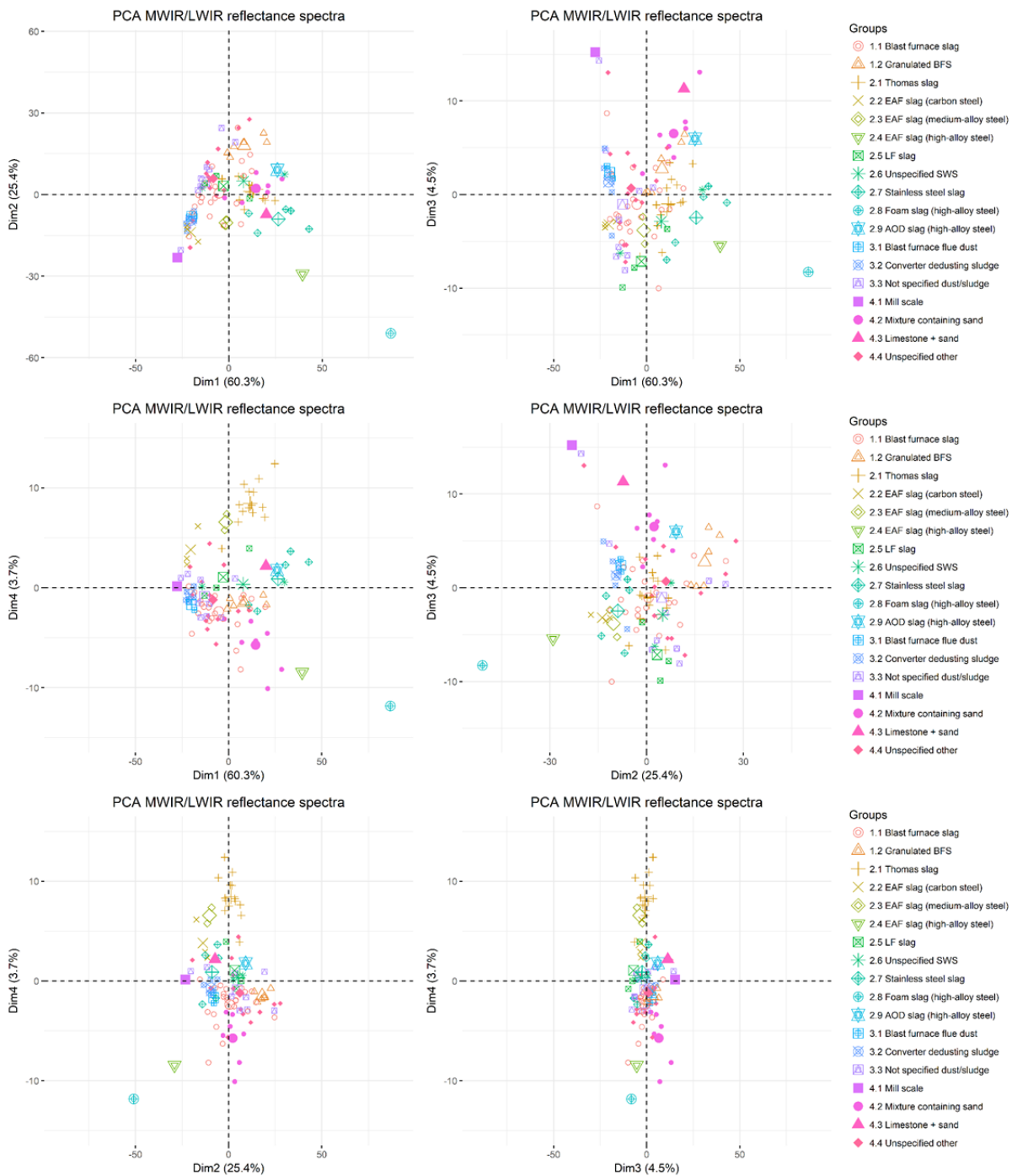
A5.4.1: Results of the PCA of VNIR/SWIR reflectance spectra.



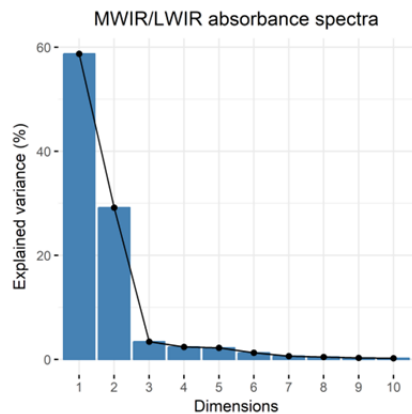
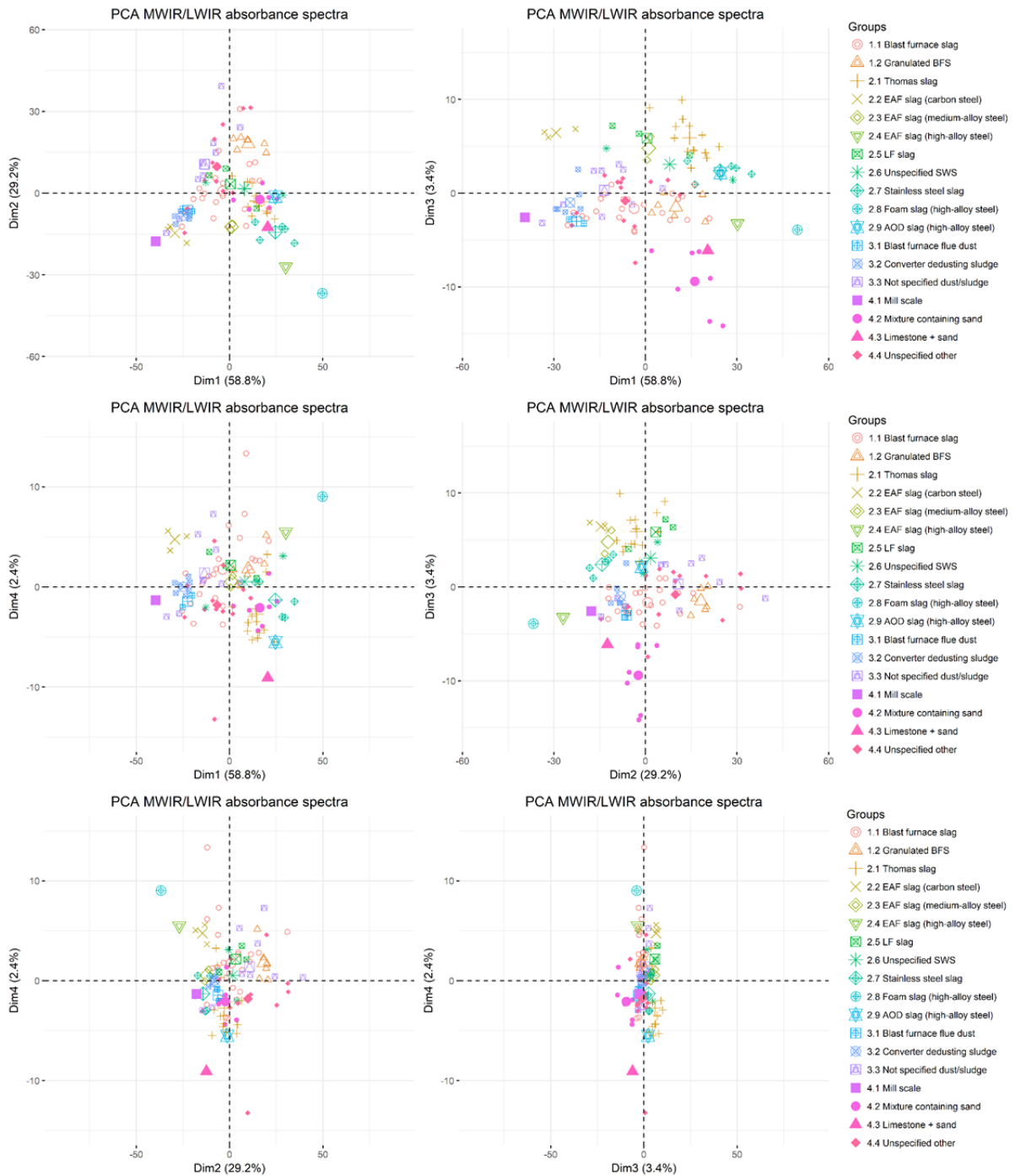
A5.4.2: Results of the PCA of VNIR/SWIR absorbance spectra.



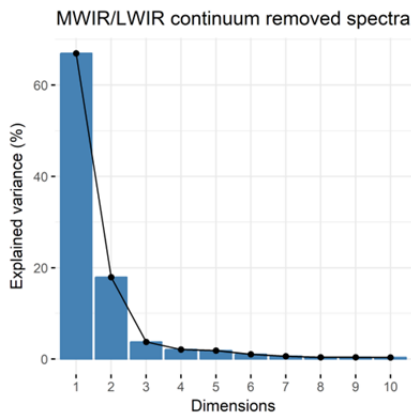
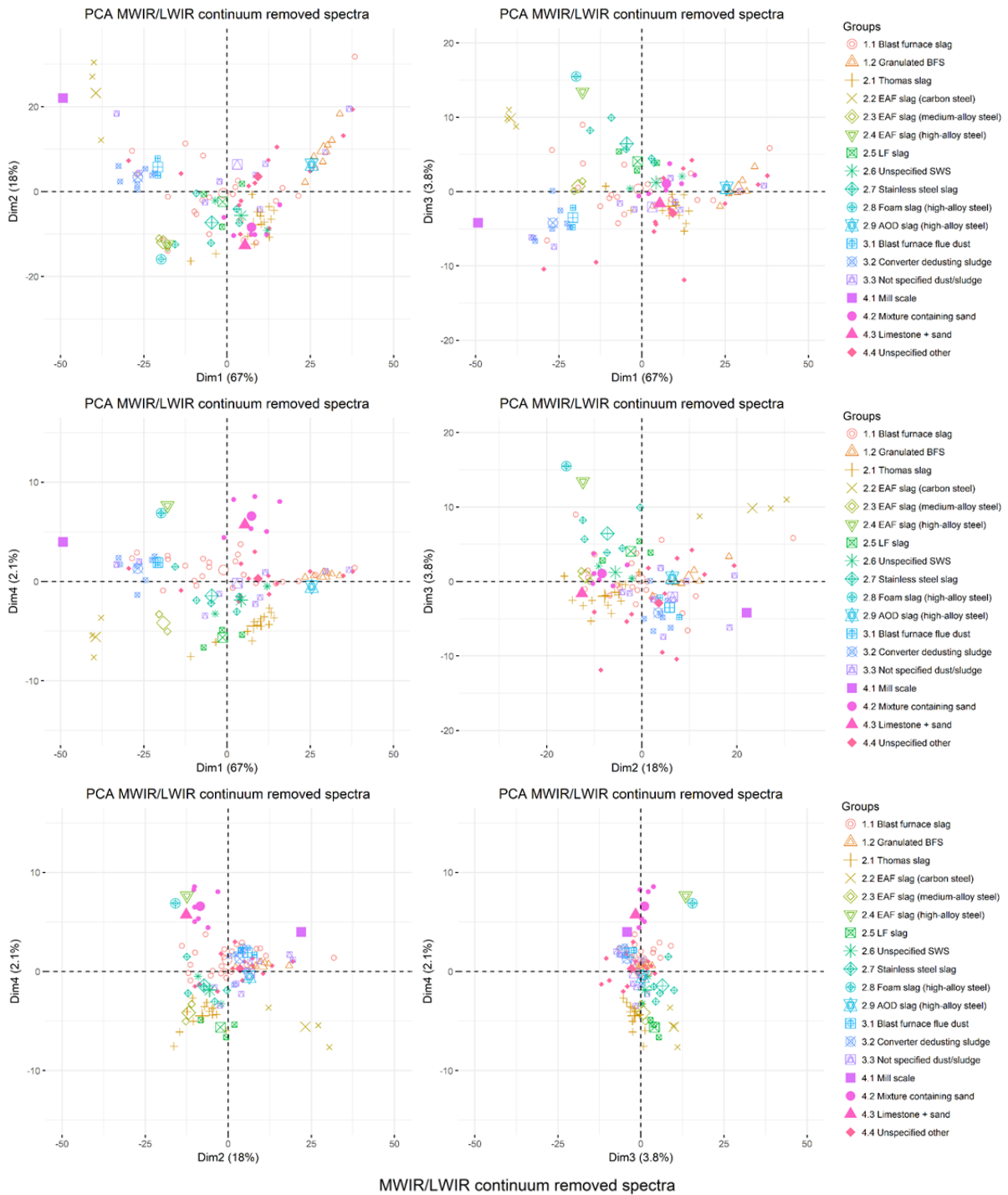
A5.4.3: Results of the PCA of VNIR/SWIR continuum removed spectra.



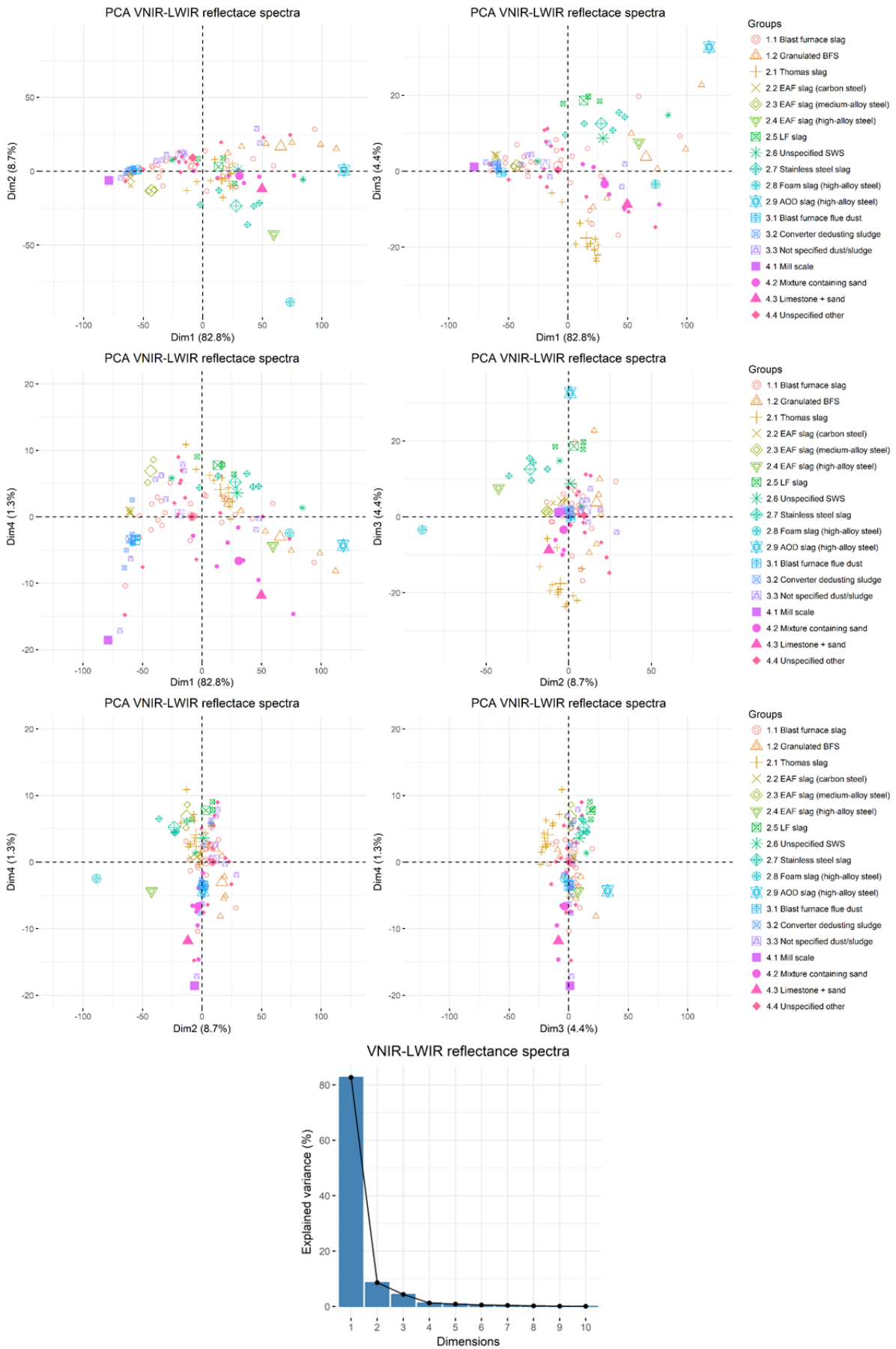
A5.4.4: Results of the PCA of MWIR/LWIR reflectance spectra.



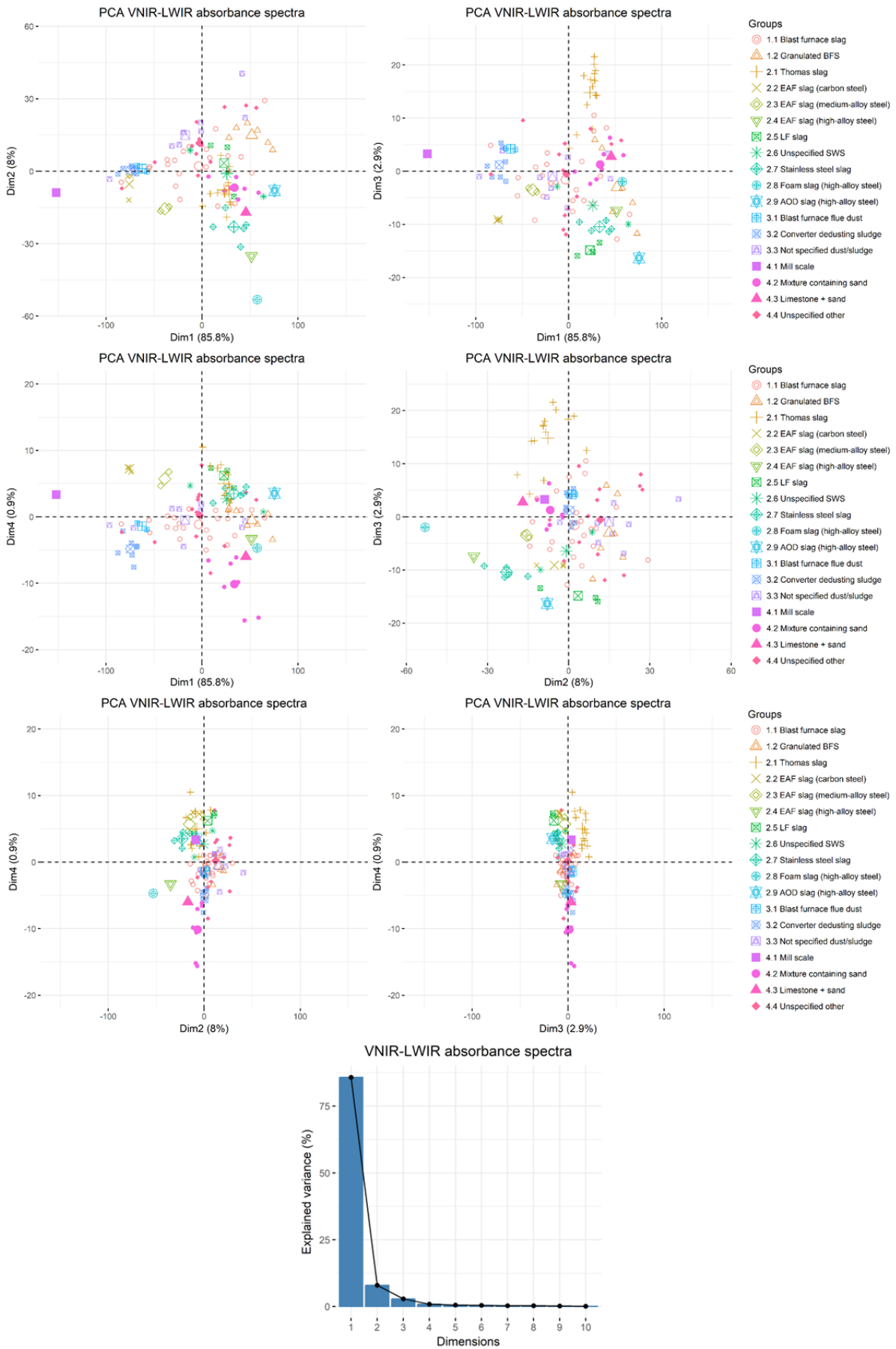
A5.4.5: Results of the PCA of MWIR/LWIR absorbance spectra.



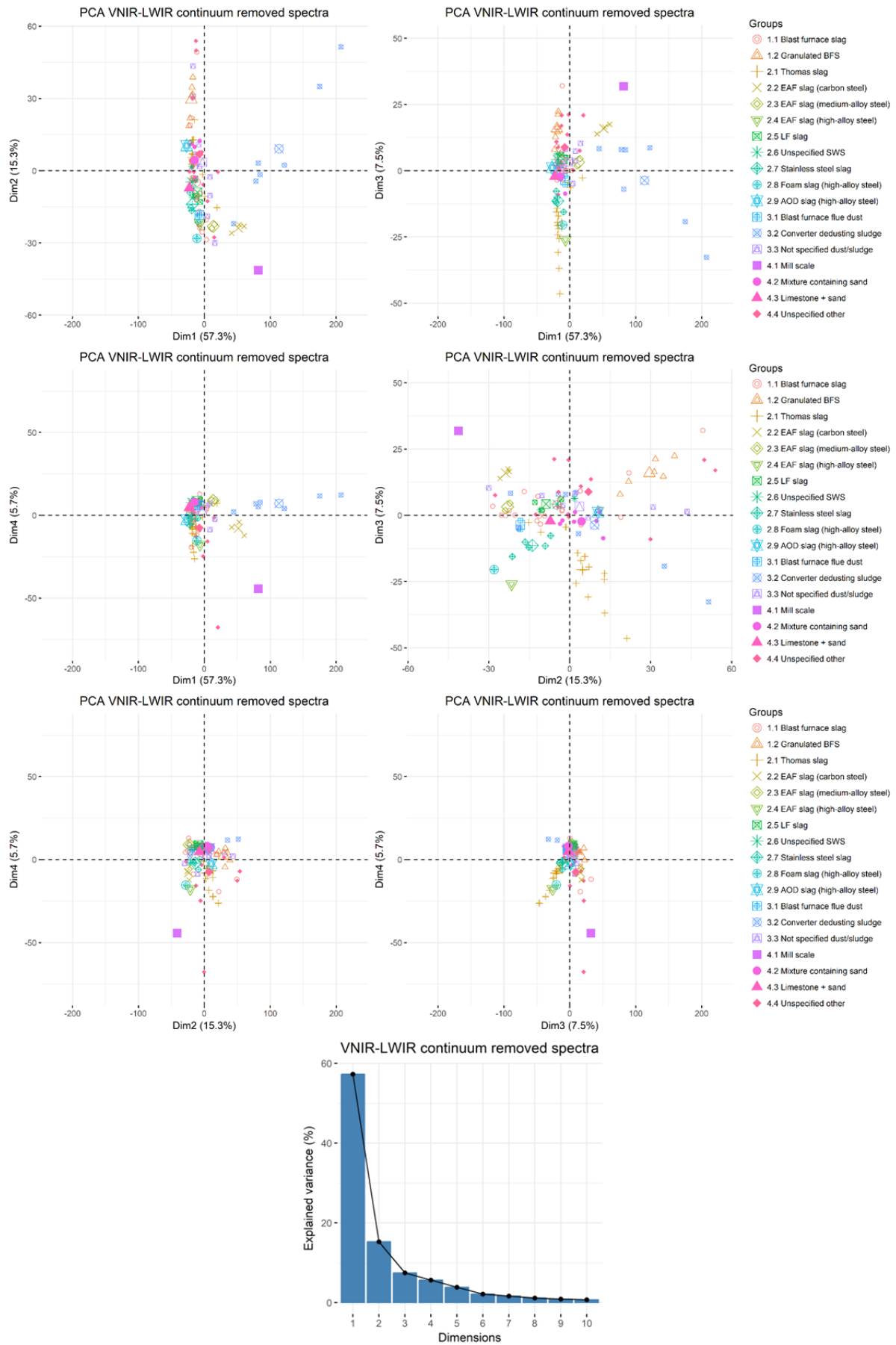
A5.4.6: Results of the PCA of MWIR/LWIR continuum removed spectra.



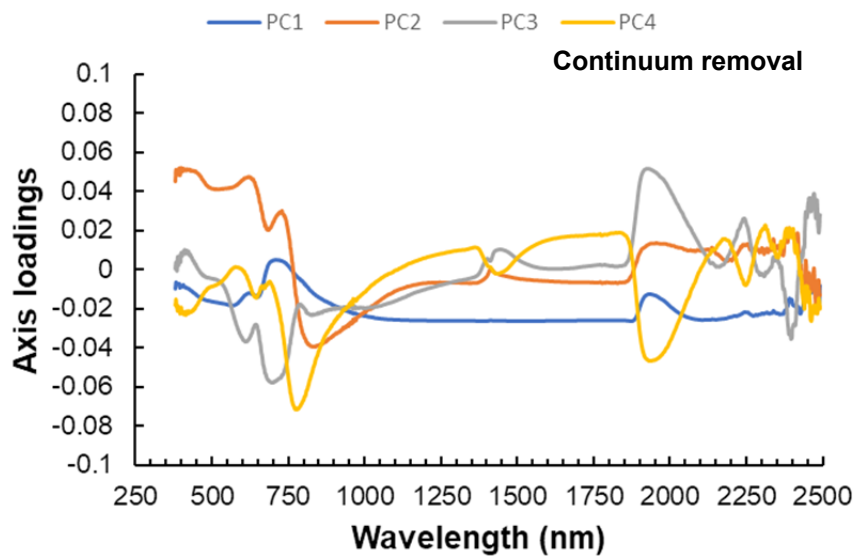
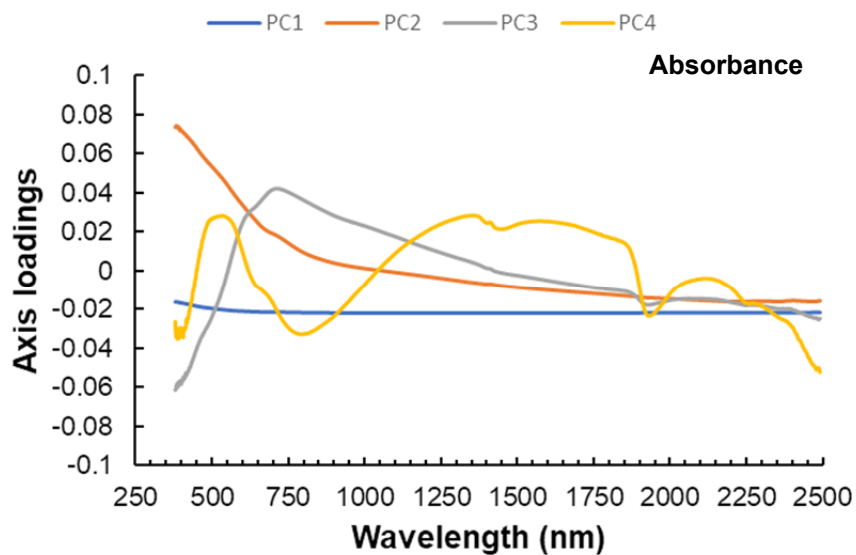
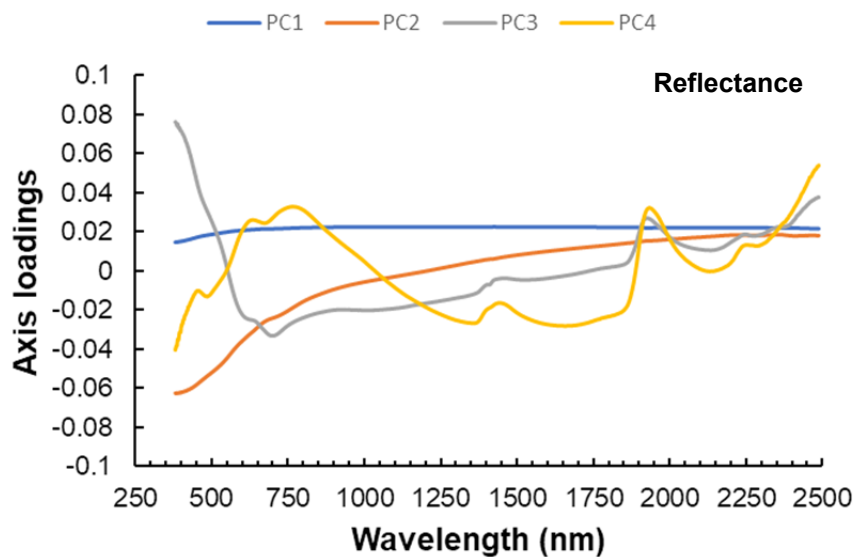
A5.4.7: Results of the PCA of VNIR-LWIR reflectance spectra.



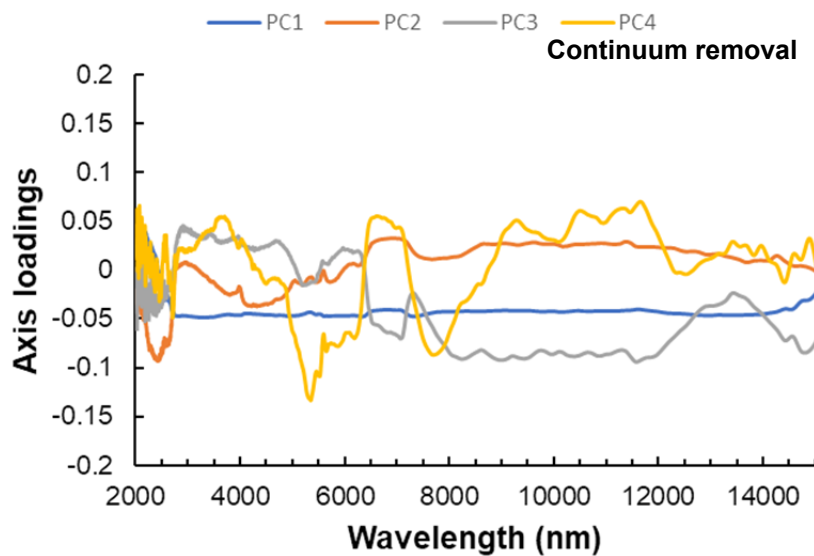
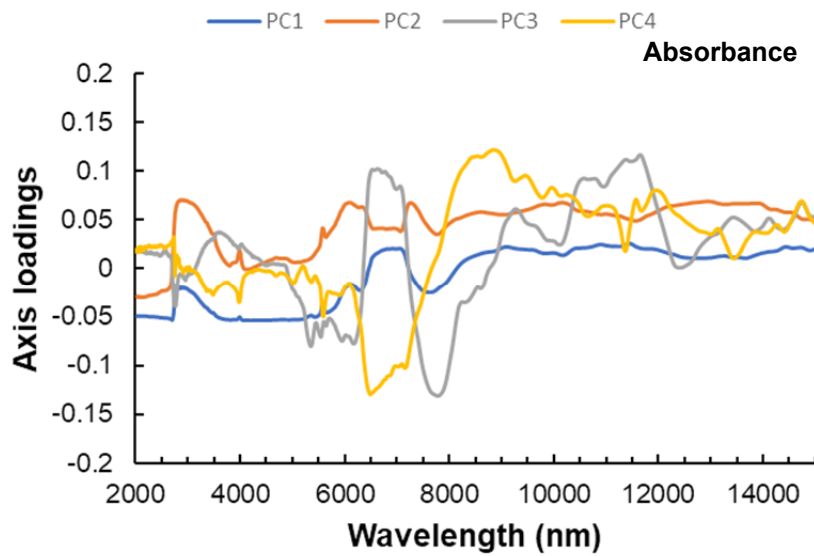
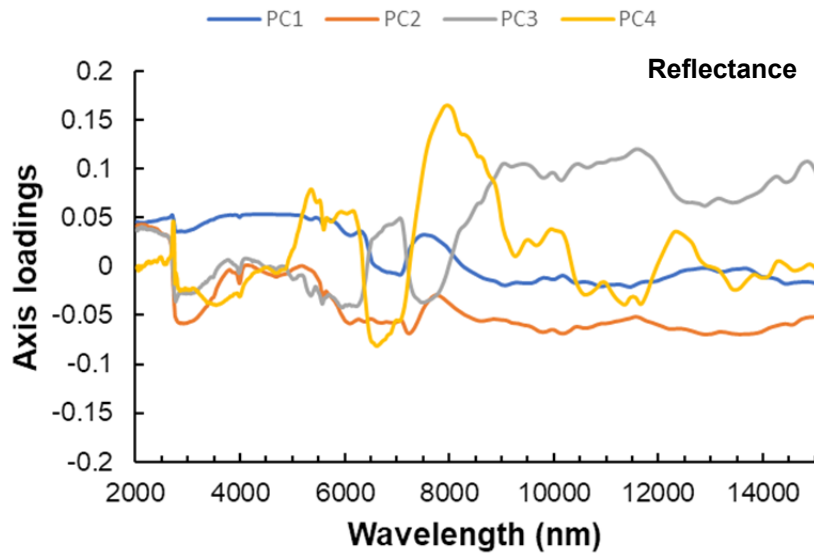
A5.4.8: Results of the PCA of VNIR-LWIR absorbance spectra.



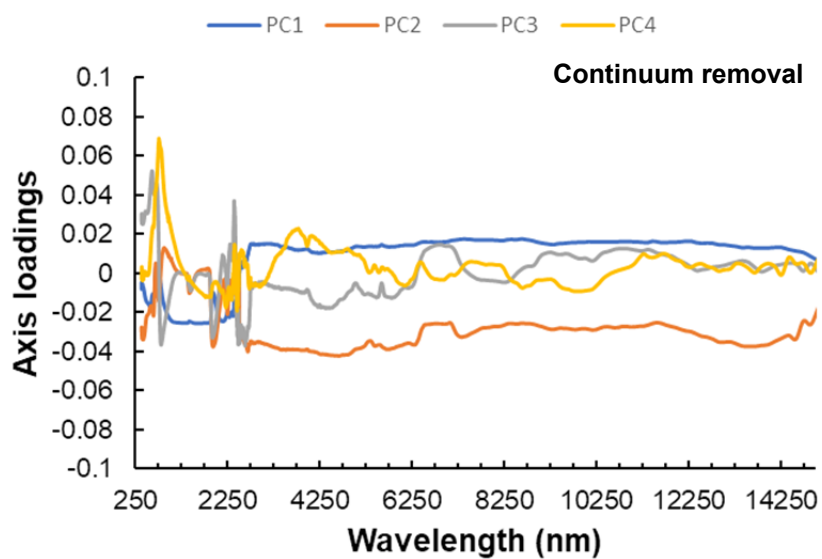
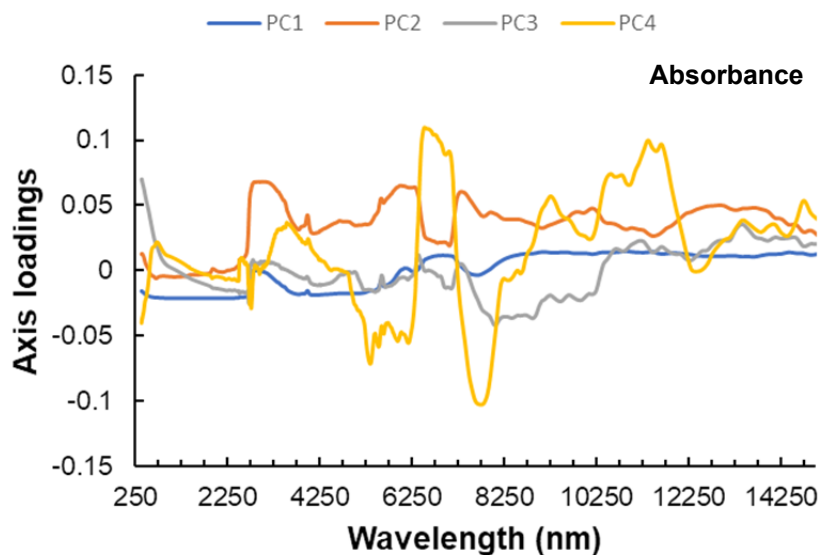
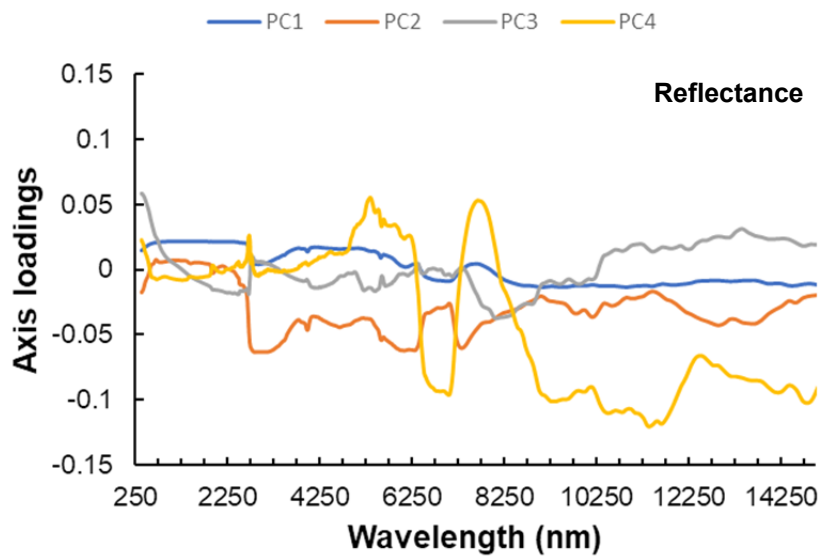
A5.4.9: Results of the PCA of VNIR-LWIR continuum removed spectra.



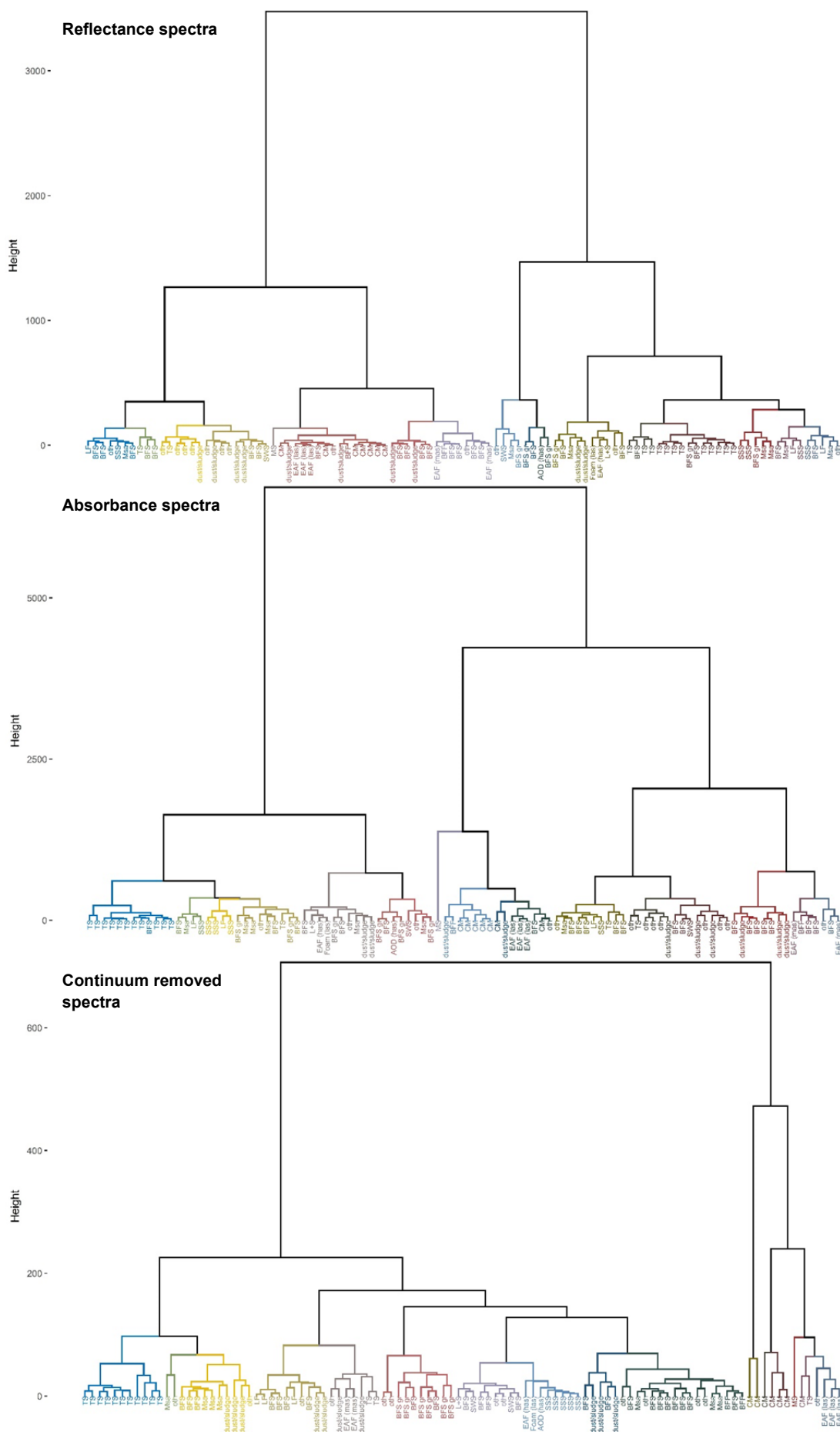
A5.4.10: Axis loadings of the PCA based on VNIR/SWIR spectra.



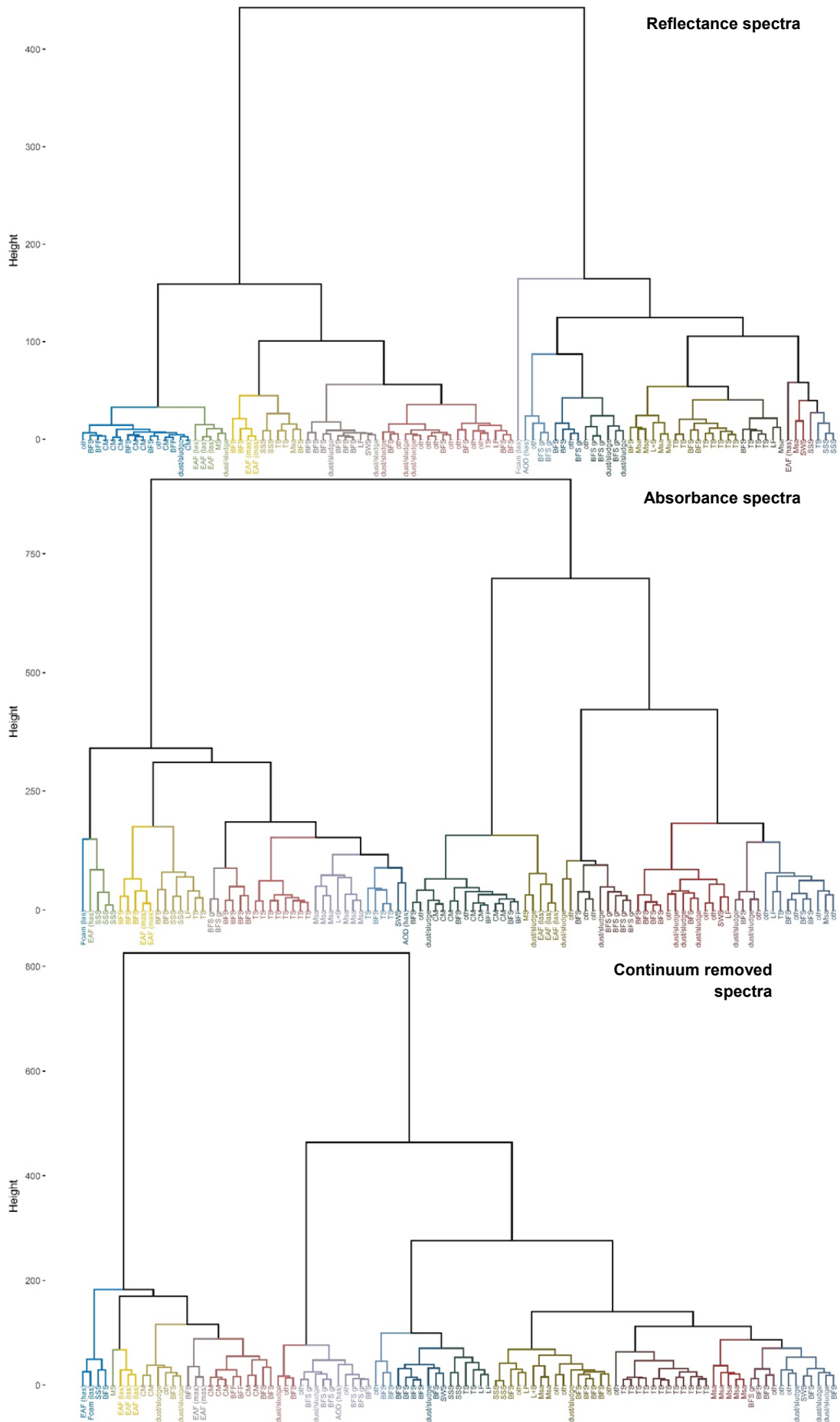
A5.4.11: Axis loadings of the PCA based on MWIR/LWIR spectra.



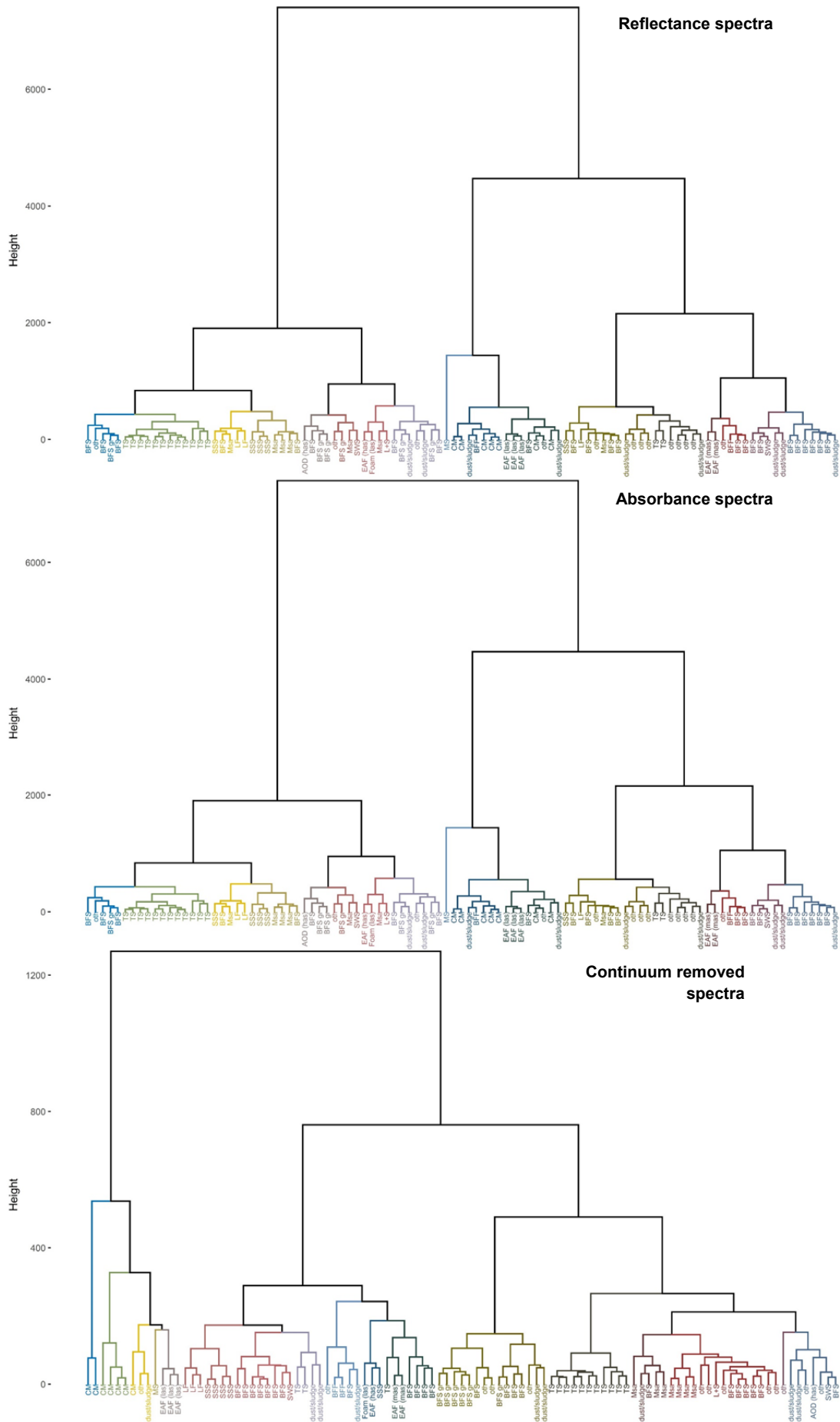
A5.4.12: Axis loadings of the PCA based on VNIR-LWIR spectra.



A5.5.1: Results of the HCA based on VNIR/SWIR spectra (Manhattan distance, ward.D2 method).



A5.5.2: Results of the HCA based on MWIR/LWIR spectra (Manhattan distance, ward.D2 method).



A5.5.3: Results of the HCA based on VNIR-LWIR spectra (Manhattan distance, ward.D2 method).

A5.5.4 Results obtained using Spectral Feature Fitting (SFF) and Spectral Angle Mapper (SAM).

For five relatively “pure” material classes, reference spectra were defined, which were afterwards compared with the complete spectral library of all samples (N = 102) using SFF and SAM. For each sample and for each algorithm, a similarity score was calculated, for which a higher score means a higher similarity to the defined reference spectrum (maximum = 1, minimum = 0). Based on the results of both methods (weight 1:1), a summed total similarity score was calculated. For this initial approach, the complete spectra were utilised., i.e. no specific spectral region for the comparison was defined. The resulting scores of the first 10 samples (20 in case of the Thomas slag) are presented in the following tables. Ideally, all samples belonging to one material type would show the highest similarity to the reference sample and samples related to other material types distinctly lower scores. This was the case using the VNIR/SWIR spectra, where all sample spectra related to one material type showed the highest similarity scores to the defined reference spectrum for this class (except for three of the 14 Thomas slag samples). This indicates a high potential for spectrally detecting the studied by-product types out of a variety of other material types. Based on the MWIR/LWIR spectra, the assignment of the sample spectra to the reference spectrum was not as clear as using the VNIR/SWIR spectra and the similarity scores were generally lower. This means that the overall spectral variability in the MWIR/LWIR within specific by-product types is distinctly larger compared to the VNIR/SWIR. Obviously, even minor differences in mineralogy and chemistry are stronger reflected in the MWIR/LWIR compared to the VNIR/SWIR and cause spectral deviations that hamper the precise spectral assignment of samples to one material type. As such, when utilising the complete spectra, material discrimination and detection is more promising using the VNIR/SWIR. However, usually specific wavelength ranges or individual spectral features are defined for such approaches.

A5.5.4.1: SFF and SAM scores of the converter dedusting sludge spectra (N = 7, in italics: sample of differing type).

VNIR/SWIR				MWIR/LWIR			
Sample spectra	Scores			Sample spectra	Scores		
Reference 18a	Total	SAM	SFF	Reference 18a	Score	SAM	SFF
18a	2	1	1	18a	2	1	1
18c	1.442	0.679	0.763	18b	1.149	0.502	0.647
18d	1.403	0.629	0.774	<i>14-6</i>	<i>1.105</i>	<i>0.493</i>	<i>0.612</i>
27	1.28	0.567	0.713	<i>15</i>	<i>0.865</i>	<i>0.281</i>	<i>0.584</i>
17	1.054	0.239	0.815	<i>30df</i>	<i>0.858</i>	<i>0.354</i>	<i>0.504</i>
18b	1.004	0.211	0.793	18d	0.676	0.038	0.638
26	0.781	0.027	0.754	27	0.653	0	0.653
<i>W3-R4</i>	<i>0.688</i>	<i>0.172</i>	<i>0.515</i>	17	0.595	0.01	0.584
<i>W1-R3s</i>	<i>0.551</i>	<i>0</i>	<i>0.551</i>	18c	0.594	0	0.594
<i>W1-R1</i>	<i>0.518</i>	<i>0</i>	<i>0.518</i>	<i>24B</i>	<i>0.527</i>	<i>0</i>	<i>0.527</i>

A5.5.4.2: SFF and SAM scores of the stainless steel slag spectra (N = 5, in italics: sample of differing type).

VNIR/SWIR				MWIR/LWIR			
Sample spectra	Scores			Sample spectra	Scores		
Reference T1	Total	SAM	SFF	Reference T1	Score	SAM	SFF
T1	2	1	1	T1	2	1	1
T3	1.857	0.89	0.967	T4	0.954	0.375	0.579
T2	1.857	0.89	0.967	T5	0.842	0.345	0.496
T4	1.824	0.851	0.973	T2	0.809	0.336	0.473
T5	1.64	0.669	0.971	<i>W3-R1-2</i>	<i>0.493</i>	<i>0.219</i>	<i>0.273</i>
<i>T-AODS</i>	<i>1.589</i>	<i>0.67</i>	<i>0.919</i>	<i>LFS-2</i>	<i>0.414</i>	<i>0.087</i>	<i>0.327</i>
<i>31-1</i>	<i>1.392</i>	<i>0.487</i>	<i>0.905</i>	T3	0.307	0	0.307
<i>W3-R5</i>	<i>1.385</i>	<i>0.467</i>	<i>0.918</i>	<i>31-1</i>	<i>0.255</i>	<i>0</i>	<i>0.255</i>
<i>31-2</i>	<i>1.36</i>	<i>0.466</i>	<i>0.894</i>	<i>21-9</i>	<i>0.239</i>	<i>0.102</i>	<i>0.137</i>
<i>21-14</i>	<i>1.351</i>	<i>0.432</i>	<i>0.918</i>	<i>W3-R22</i>	<i>0.193</i>	<i>0</i>	<i>0.193</i>

A5.5.4.3: SFF and SAM scores of the EAFS from carbon steelm. spectra (N = 3, in italics: sample of differing type).

VNIR/SWIR				MWIR/LWIR			
Sample spectra	Scores			Sample spectra	Scores		
Reference EAFS-1	Total	SAM	SFF	Reference EAFS-1	Score	SAM	SFF
EAFS-1	2	1	1	EAFS-1	2	1	1
EAFS-2	1.767	0.851	0.916	EAFS-3	0.981	0.507	0.474
EAFS-3	1.652	0.691	0.961	EAFS-2	0.777	0.24	0.537
<i>LFS-3</i>	<i>1.287</i>	<i>0.462</i>	<i>0.826</i>	<i>26</i>	<i>0.007</i>	<i>0</i>	<i>0.007</i>
<i>LFS-2</i>	<i>1.125</i>	<i>0.39</i>	<i>0.735</i>	<i>19</i>	<i>0</i>	<i>0</i>	<i>0</i>
<i>K1a</i>	<i>1.092</i>	<i>0.254</i>	<i>0.839</i>				
<i>LFS-1</i>	<i>1.039</i>	<i>0.309</i>	<i>0.73</i>				
<i>K2a</i>	<i>0.993</i>	<i>0.191</i>	<i>0.802</i>				
<i>DK</i>	<i>0.762</i>	<i>0</i>	<i>0.762</i>				
<i>31-21</i>	<i>0.761</i>	<i>0</i>	<i>0.761</i>				

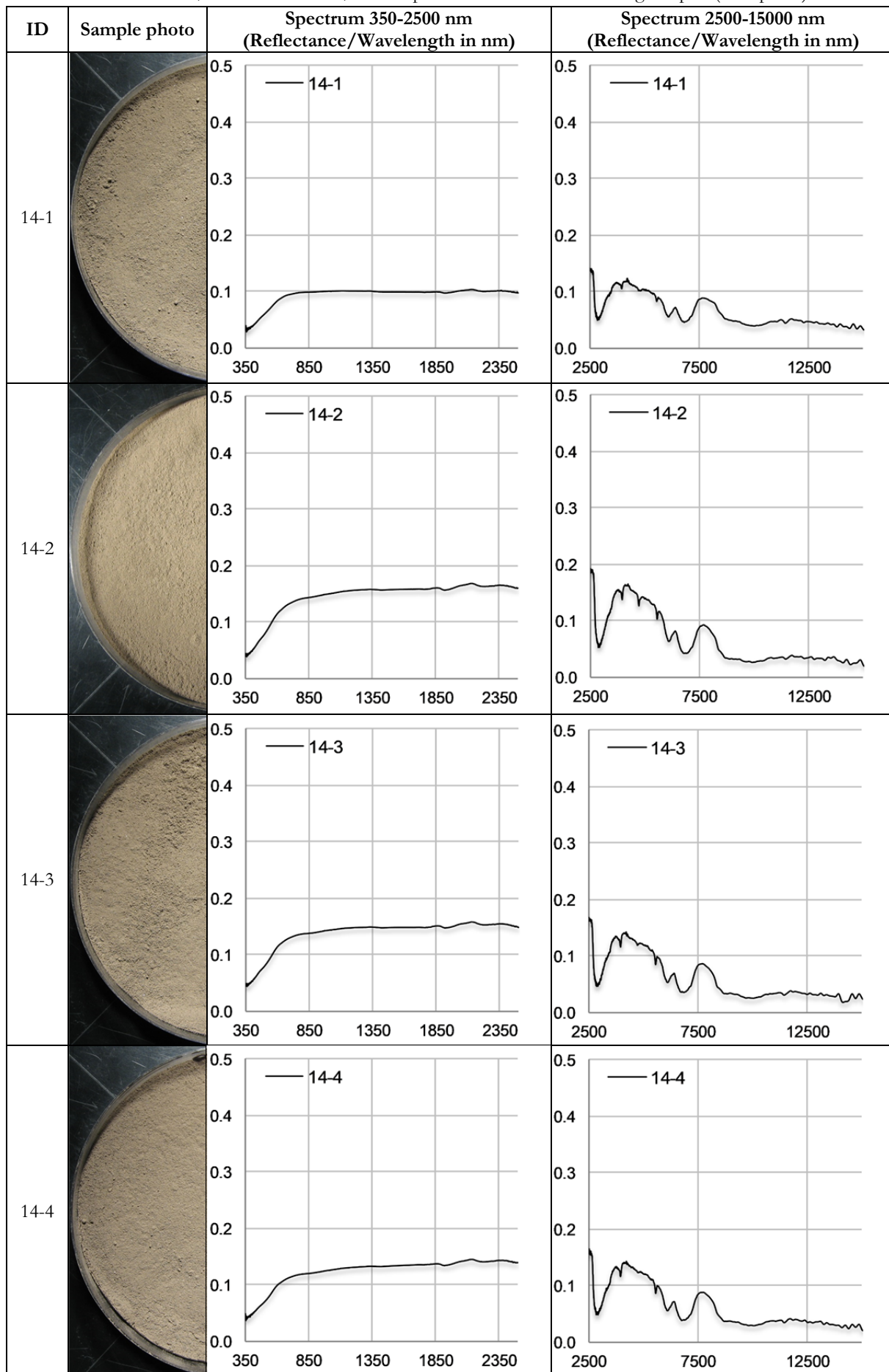
A5.5.4.4: SFF and SAM -scores of the LFS spectra (N = 3, in italics: sample of differing type).


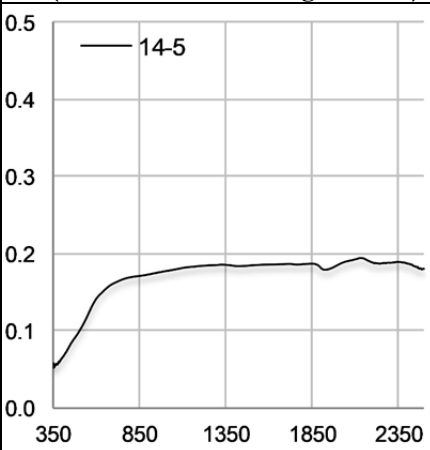
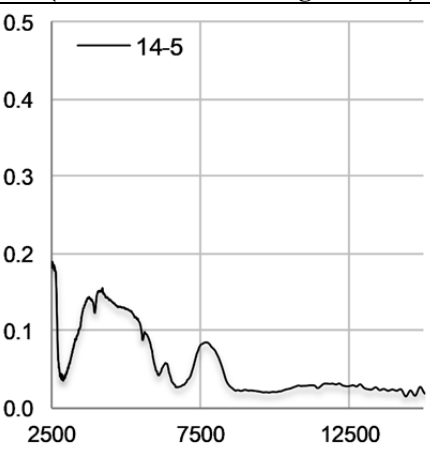

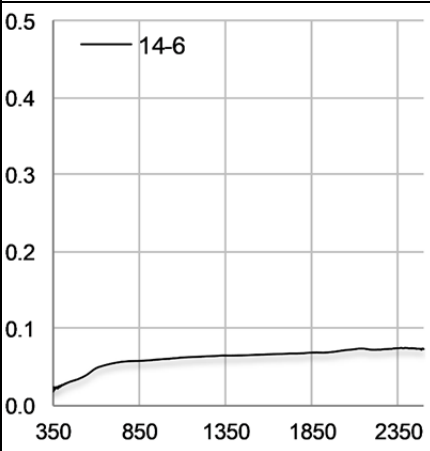
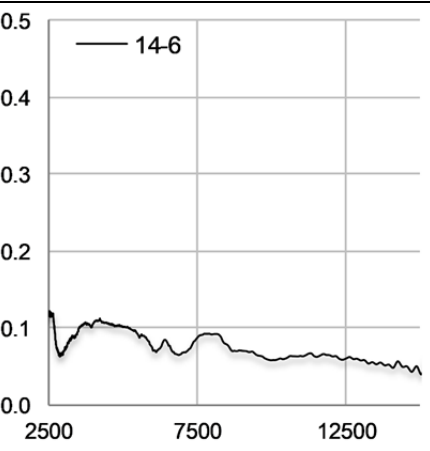

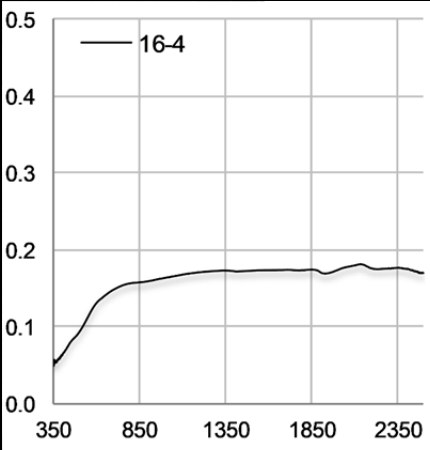
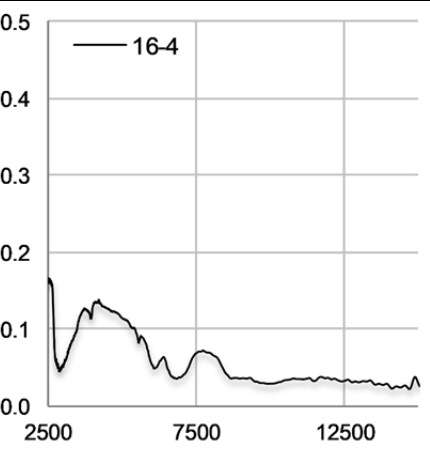

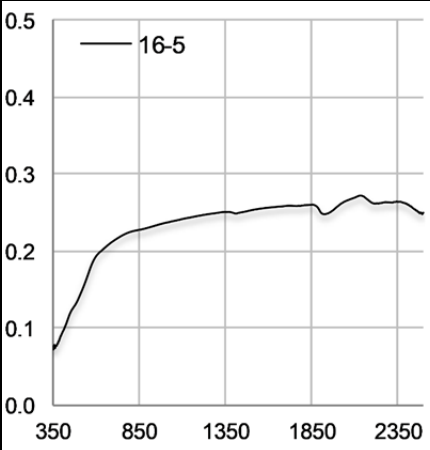
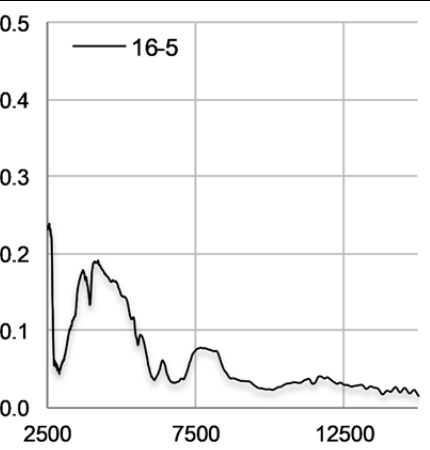
VNIR/SWIR				MWIR/LWIR			
Sample spectra	Scores			Sample spectra	Scores		
Reference LFS-1	Total	SAM	SFF	Reference LFS-1	Score	SAM	SFF
LFS-1	2	1	1	LFS-1	2	1	1
LFS-2	1.849	0.863	0.986	LFS-2	1.027	0.47	0.557
LFS-3	1.718	0.763	0.955	<i>14-5</i>	<i>0.793</i>	<i>0.286</i>	<i>0.507</i>
<i>16-6</i>	<i>1.582</i>	<i>0.661</i>	<i>0.922</i>	<i>21-6</i>	<i>0.767</i>	<i>0.324</i>	<i>0.444</i>
<i>21-14</i>	<i>1.545</i>	<i>0.645</i>	<i>0.9</i>	<i>W3-R22</i>	<i>0.761</i>	<i>0.337</i>	<i>0.424</i>
<i>21-12</i>	<i>1.542</i>	<i>0.655</i>	<i>0.888</i>	<i>21-14</i>	<i>0.658</i>	<i>0.251</i>	<i>0.407</i>
<i>W3-R5</i>	<i>1.437</i>	<i>0.54</i>	<i>0.897</i>	<i>W1-R3bg</i>	<i>0.645</i>	<i>0.256</i>	<i>0.389</i>
<i>T-AODS</i>	<i>1.397</i>	<i>0.525</i>	<i>0.872</i>	<i>GPS</i>	<i>0.641</i>	<i>0.143</i>	<i>0.498</i>
<i>T5</i>	<i>1.359</i>	<i>0.501</i>	<i>0.858</i>	<i>W3-R15</i>	<i>0.584</i>	<i>0.152</i>	<i>0.431</i>
<i>K2a</i>	<i>1.329</i>	<i>0.43</i>	<i>0.899</i>	<i>W3-R10</i>	<i>0.582</i>	<i>0.177</i>	<i>0.405</i>

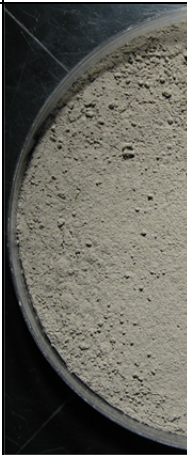
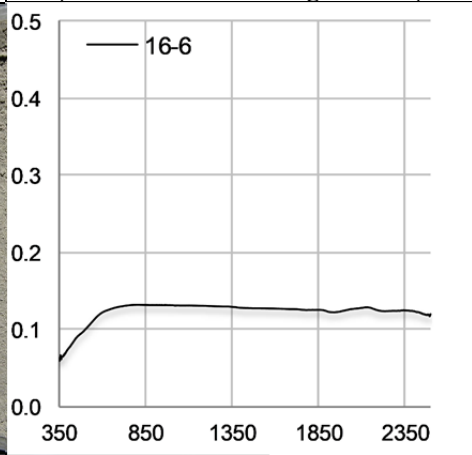
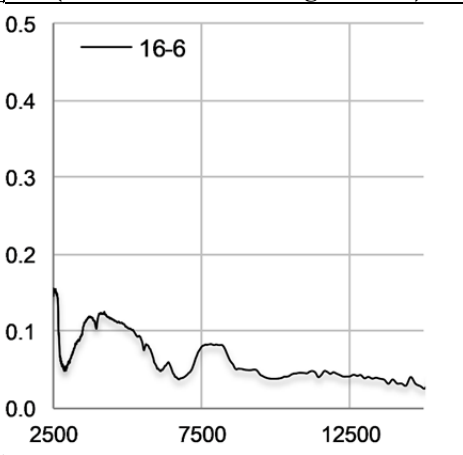

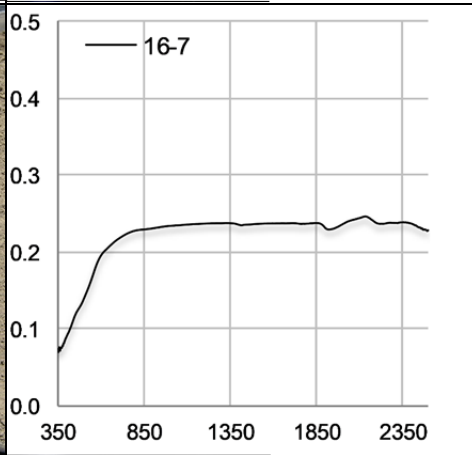
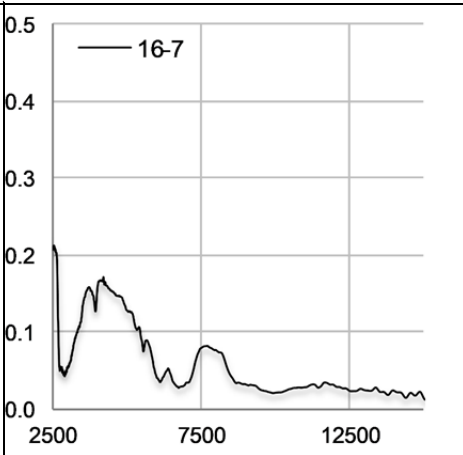
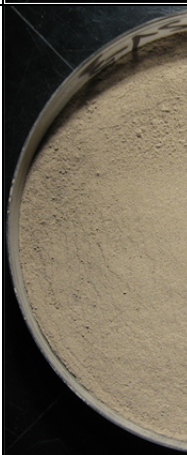
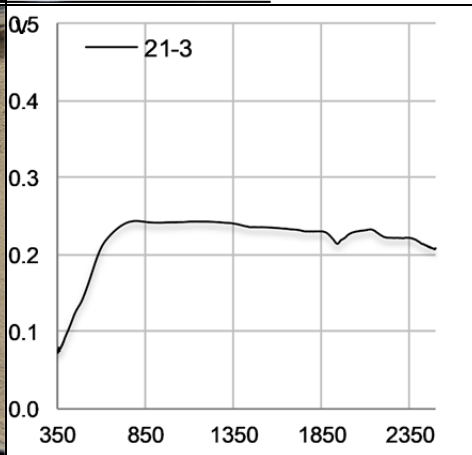
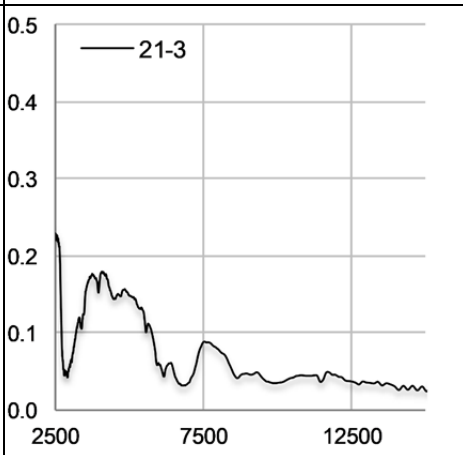

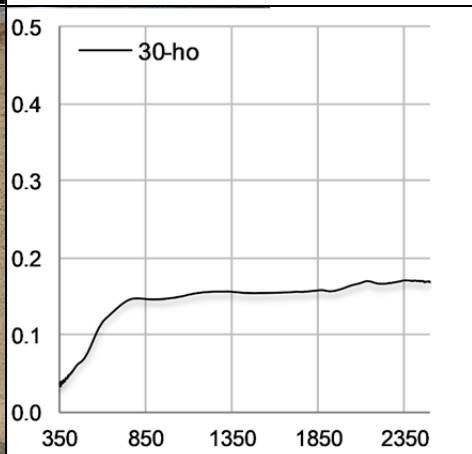
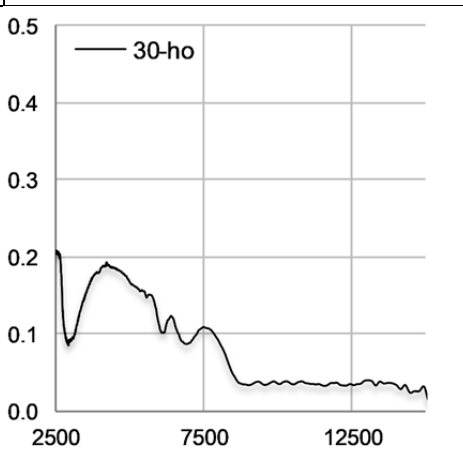
A5.5.4.5: SFF and SAM scores of the Thomas slag spectra (N = 14, in italics: sample of differing type).


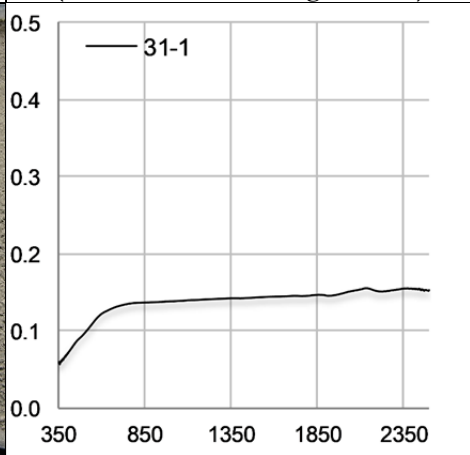
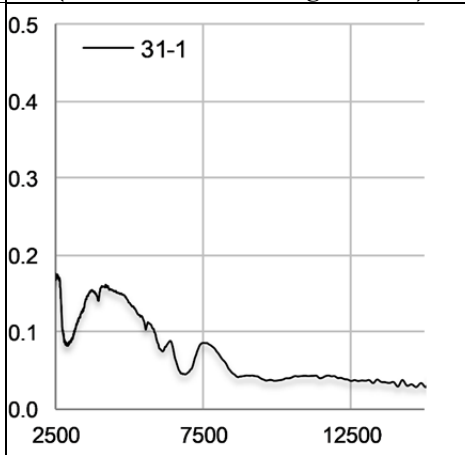

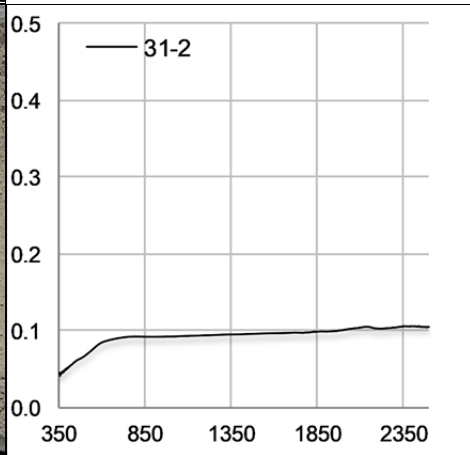
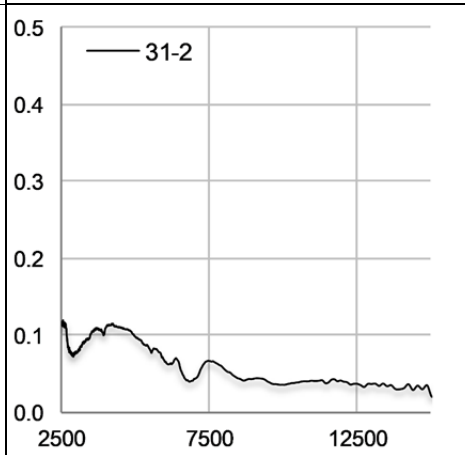

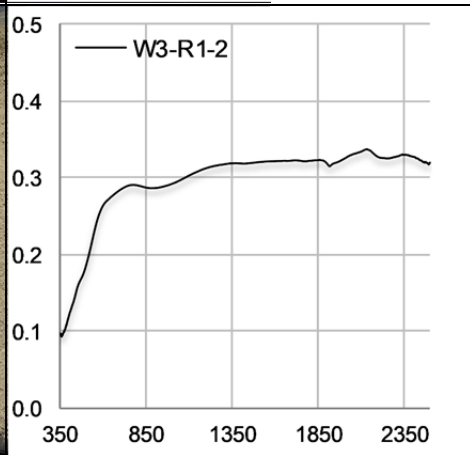
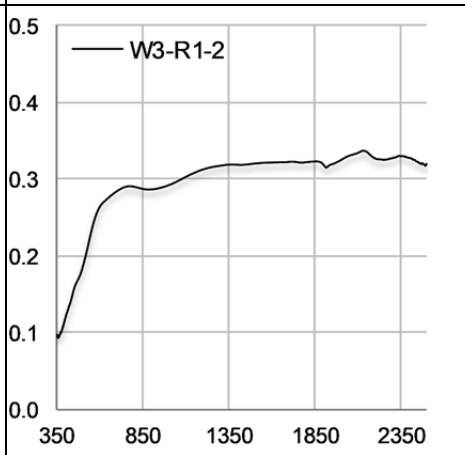

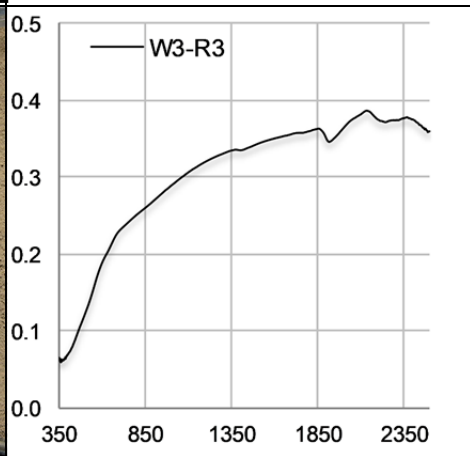
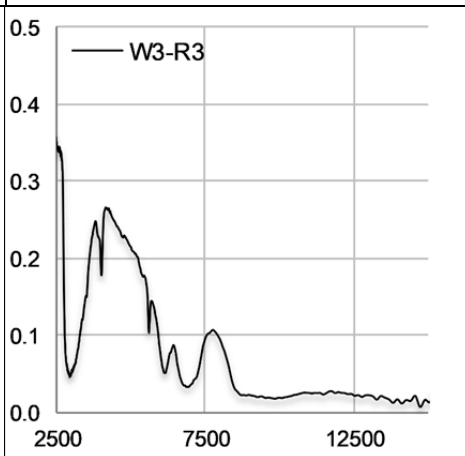
VNIR/SWIR				MWIR/LWIR			
Sample spectra	Scores			Sample spectra	Scores		
Reference 29-Th	Total	SAM	SFF	Reference 29-Th	Score	SAM	SFF
29-Th	2	1	1	29-Th	2	1	1
W1-R7u	1.766	0.872	0.894	W1-R7u	1.35	0.694	0.656
29-bg	1.742	0.832	0.91	W1-R5a	1.287	0.623	0.665
W1-R5	1.625	0.737	0.888	W1-VK	1.202	0.596	0.606
W1-R7o	1.621	0.795	0.826	29-bg	1.138	0.475	0.662
29-Ho	1.615	0.724	0.892	W1-R1	0.941	0.379	0.562
W1-VK	1.589	0.772	0.817	W1-R7m	0.918	0.457	0.46
W1-R3-b	1.552	0.713	0.839	W1-R3b	0.883	0.4	0.482
W1-R7m	1.543	0.741	0.802	29-Ho	0.779	0.336	0.443
29-Hu	1.367	0.504	0.863	29-Hu	0.663	0.209	0.454
W1-R3g	1.259	0.49	0.769	W1-R7o	0.658	0.237	0.421
<i>W3-R21</i>	<i>1.082</i>	<i>0.345</i>	<i>0.736</i>	<i>21-8</i>	<i>0.639</i>	<i>0.088</i>	<i>0.552</i>
<i>W3-R20</i>	<i>0.864</i>	<i>0.36</i>	<i>0.505</i>	W1-R3b	0.614	0.24	0.374
<i>W3-R3</i>	<i>0.85</i>	<i>0.114</i>	<i>0.736</i>	<i>W3-R16</i>	<i>0.6</i>	<i>0.19</i>	<i>0.41</i>
<i>W3-R7</i>	<i>0.792</i>	<i>0</i>	<i>0.792</i>	<i>W3-R13</i>	<i>0.576</i>	<i>0.211</i>	<i>0.366</i>
<i>21-4</i>	<i>0.767</i>	<i>0</i>	<i>0.767</i>	<i>21-14</i>	<i>0.537</i>	<i>0.155</i>	<i>0.382</i>
<i>21-5</i>	<i>0.764</i>	<i>0</i>	<i>0.764</i>	<i>W3-R15</i>	<i>0.513</i>	<i>0.165</i>	<i>0.347</i>
<i>21-11</i>	<i>0.74</i>	<i>0</i>	<i>0.74</i>	<i>W3-R21</i>	<i>0.501</i>	<i>0.05</i>	<i>0.45</i>
<i>W3-R17</i>	<i>0.729</i>	<i>0</i>	<i>0.729</i>	<i>W3-R</i>	<i>0.473</i>	<i>0.158</i>	<i>0.315</i>
<i>21-7</i>	<i>0.728</i>	<i>0</i>	<i>0.728</i>	<i>22a</i>	<i>0.399</i>	<i>0</i>	<i>0.399</i>

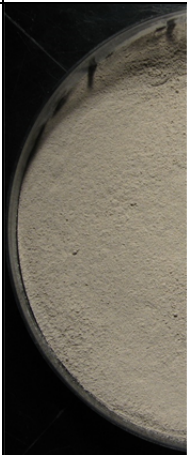
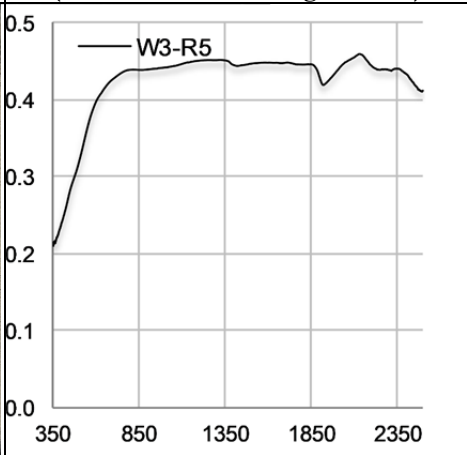
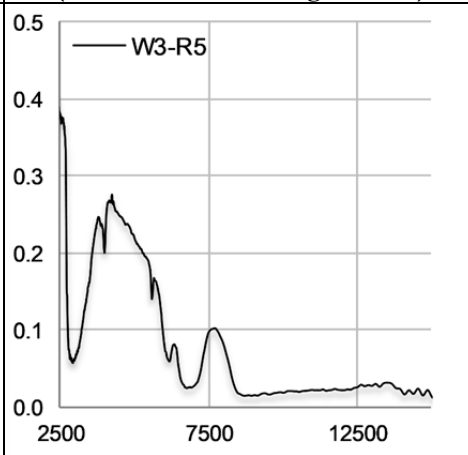

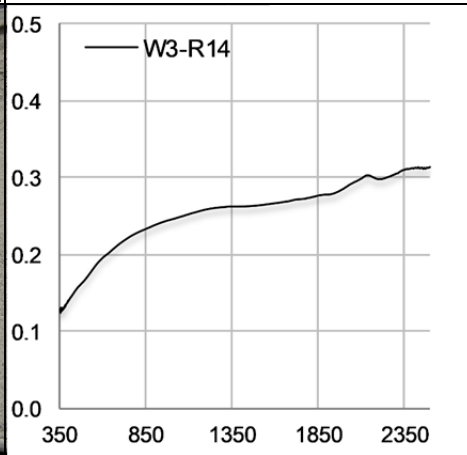
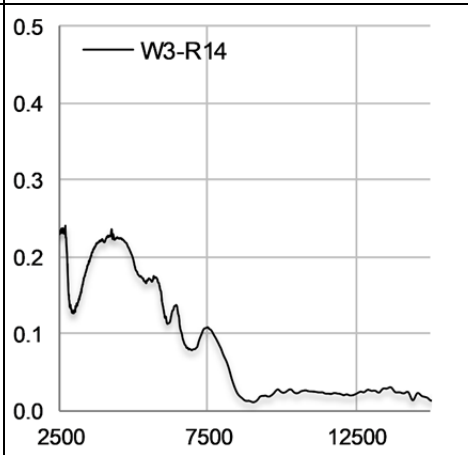

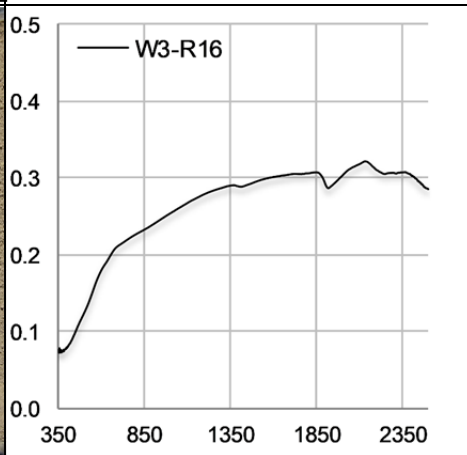
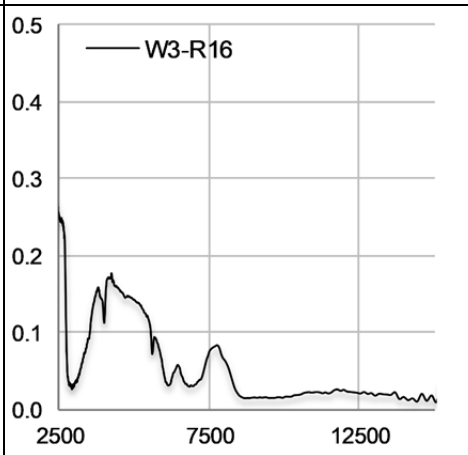

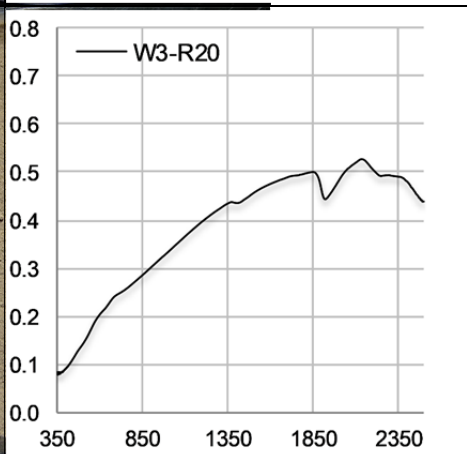
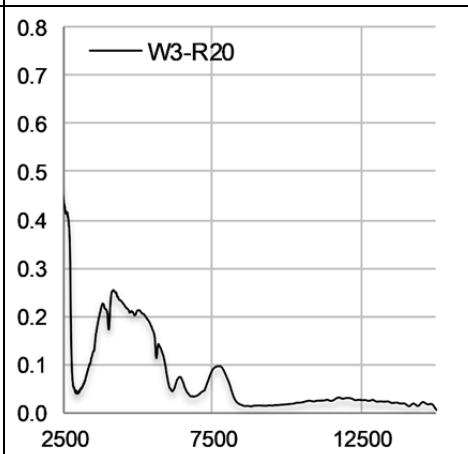
A5.6.1: VNIR/SWIR and MWIR/LWIR spectra of the blast furnace slag samples (not “pure”).


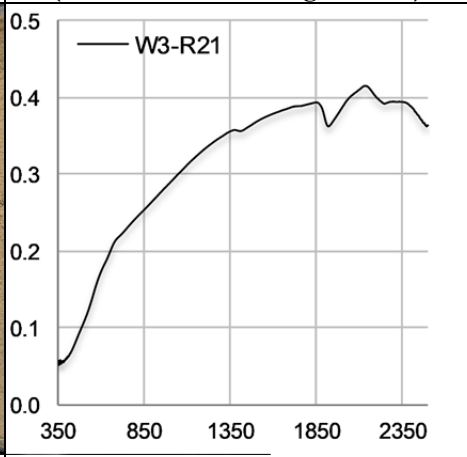
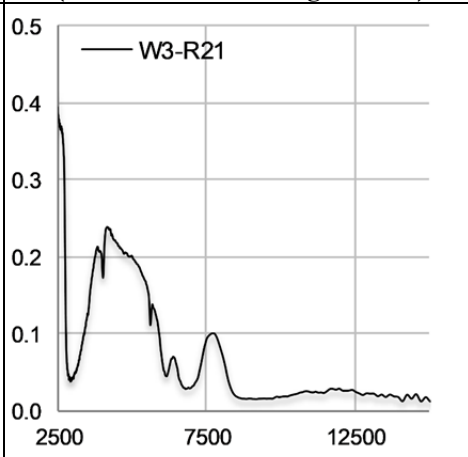

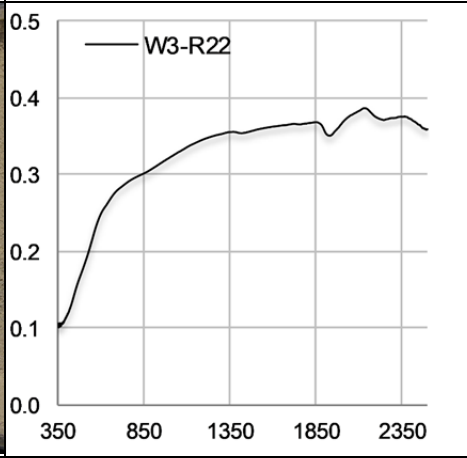
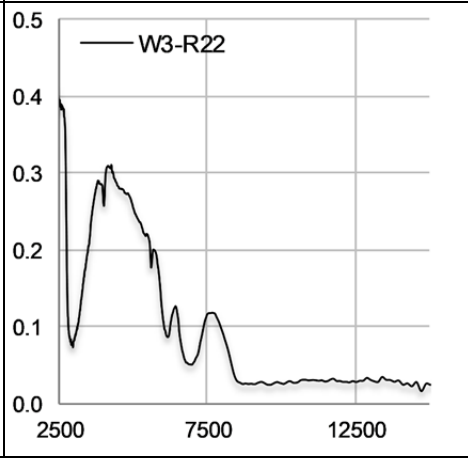

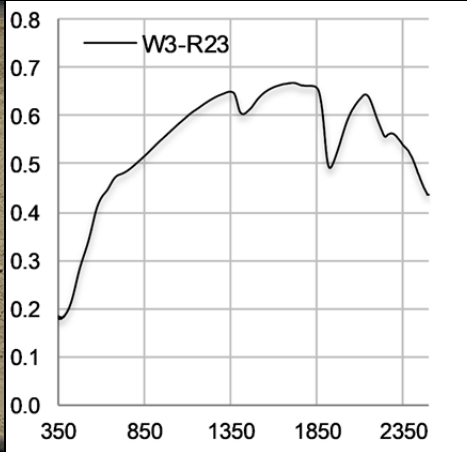
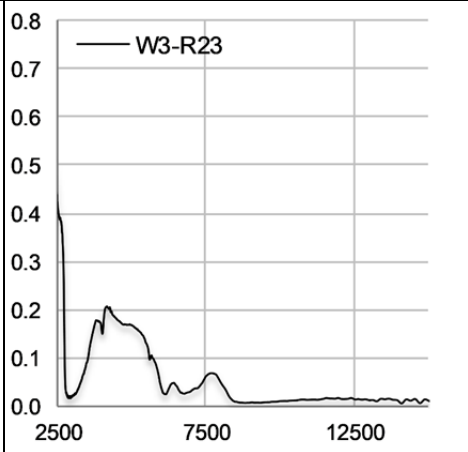


ID	Sample photo	Spectrum 350-2500 nm (Reflectance/Wavelength in nm)	Spectrum 2500-15000 nm (Reflectance/Wavelength in nm)
14-5			
14-6			
16-4o			
16-5			


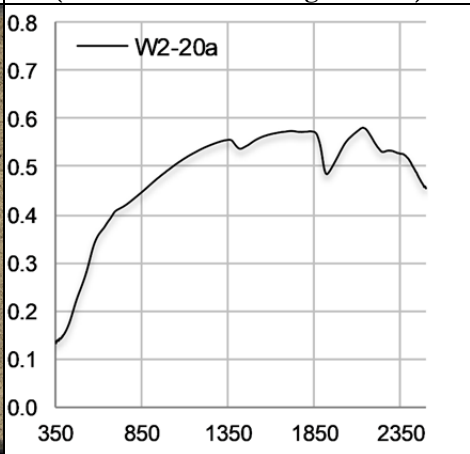
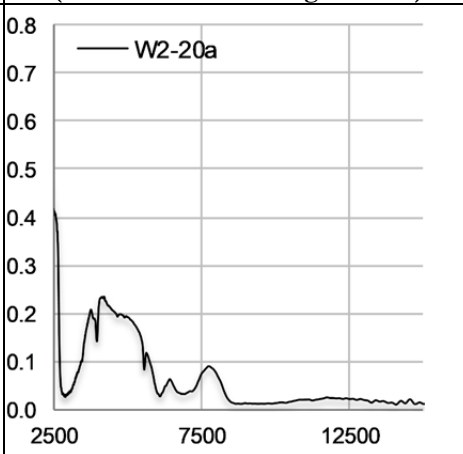

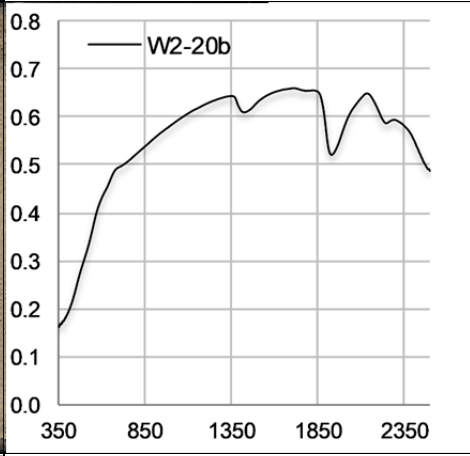
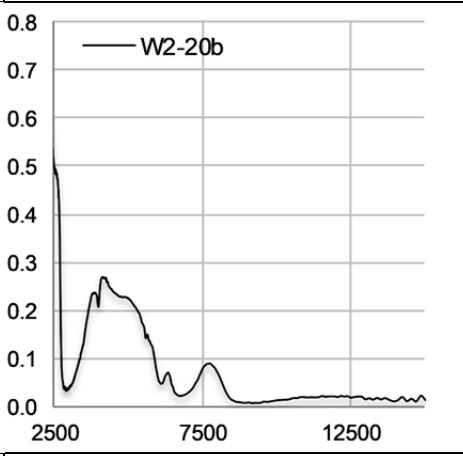

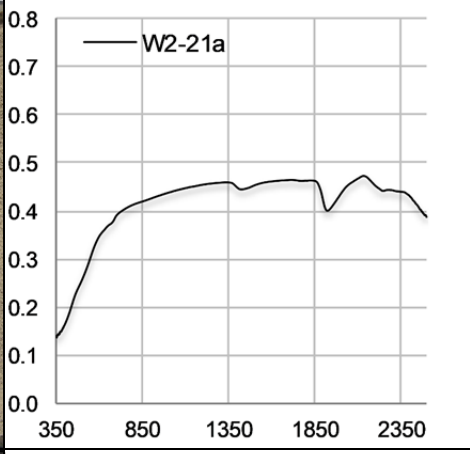
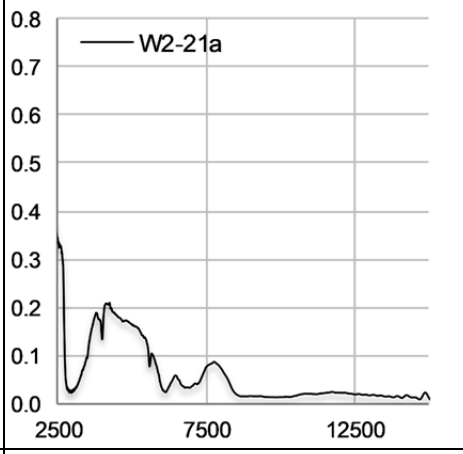

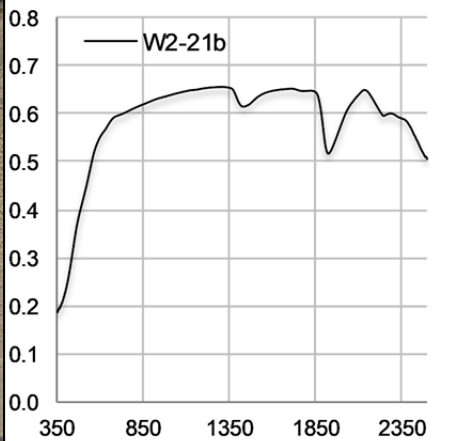
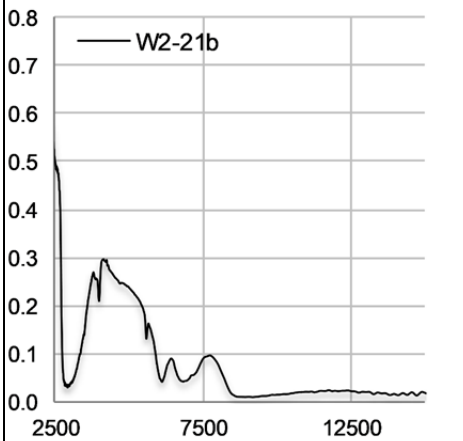
ID	Sample photo	Spectrum 350-2500 nm (Reflectance/Wavelength in nm)	Spectrum 2500-15000 nm (Reflectance/Wavelength in nm)
16-6			
16-7			
21-3			
30-ho			


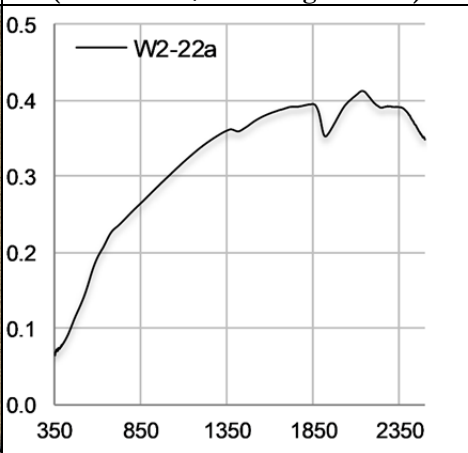
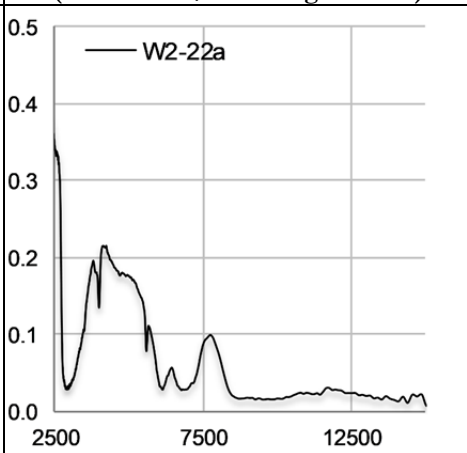

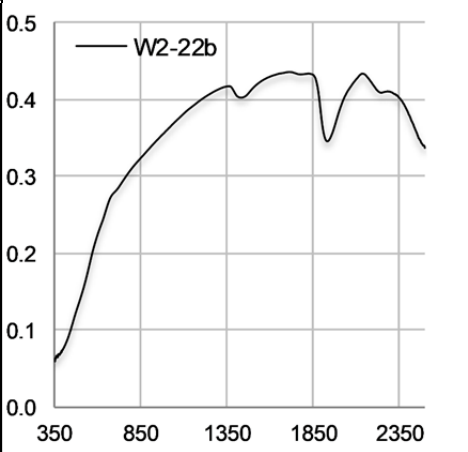
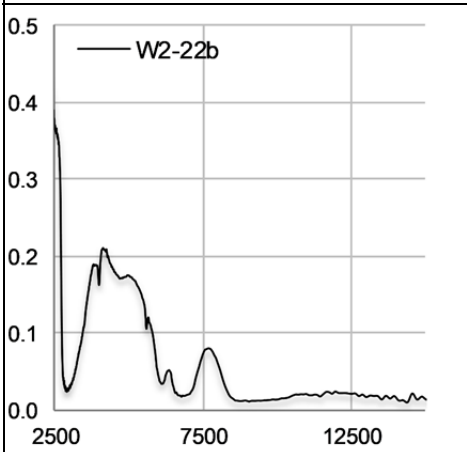
ID	Sample photo	Spectrum 350-2500 nm (Reflectance/Wavelength in nm)	Spectrum 2500-15000 nm (Reflectance/Wavelength in nm)
31-1			
31-2			
W3-R1-2			
W3-R3			

ID	Sample photo	Spectrum 350-2500 nm (Reflectance/Wavelength in nm)	Spectrum 2500-15000 nm (Reflectance/Wavelength in nm)
W3-R5			
W3-R14			
W3-R16			
W3-R20			

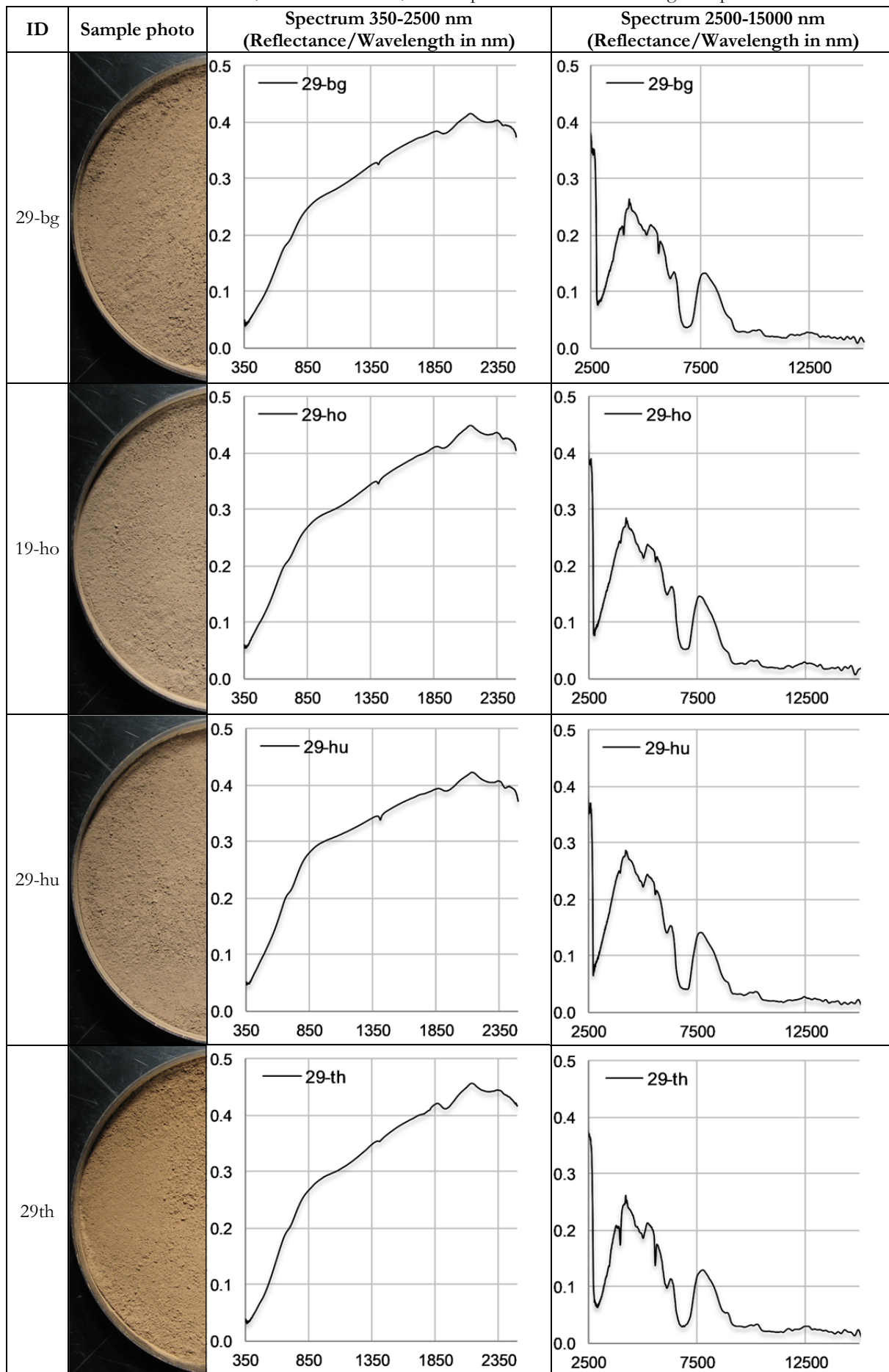
ID	Sample photo	Spectrum 350-2500 nm (Reflectance/Wavelength in nm)	Spectrum 2500-15000 nm (Reflectance/Wavelength in nm)
W3-R21			
W3-R22			
W3-R23			


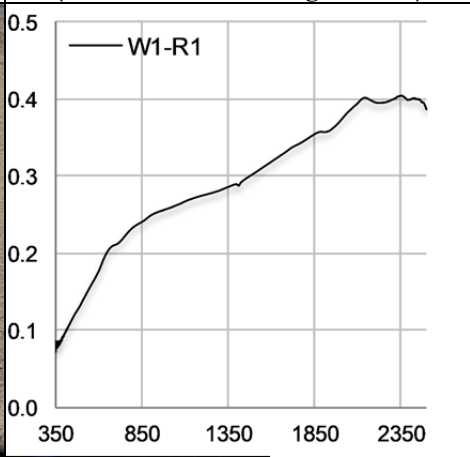
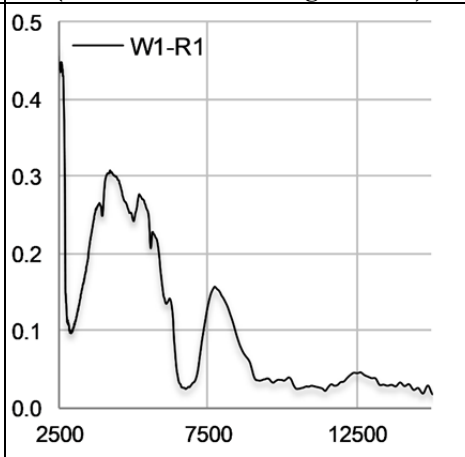

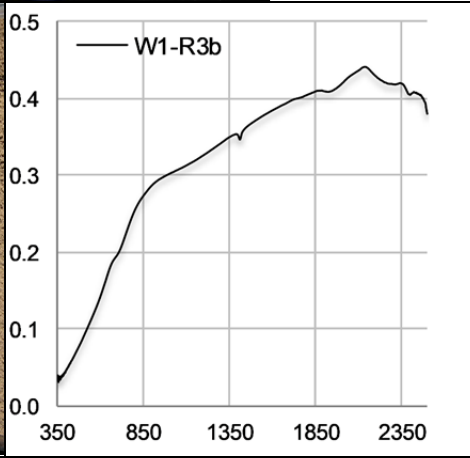
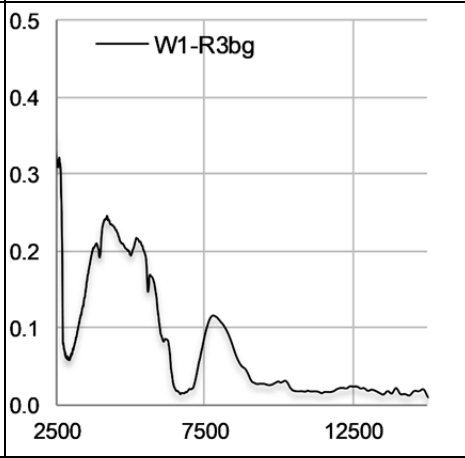

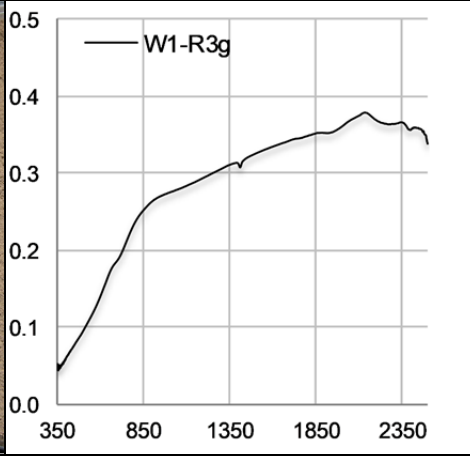
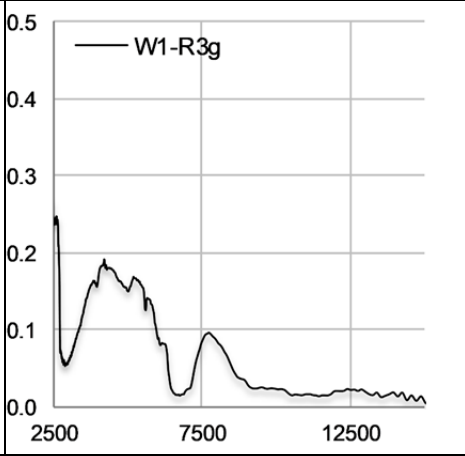

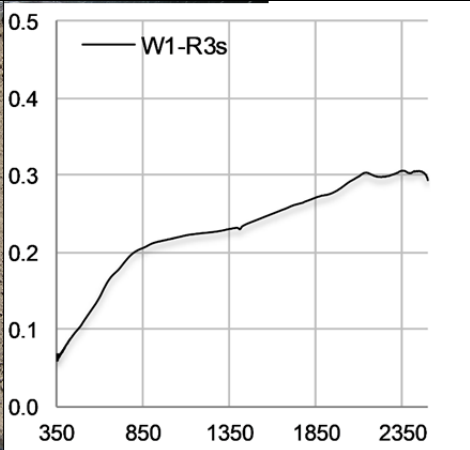
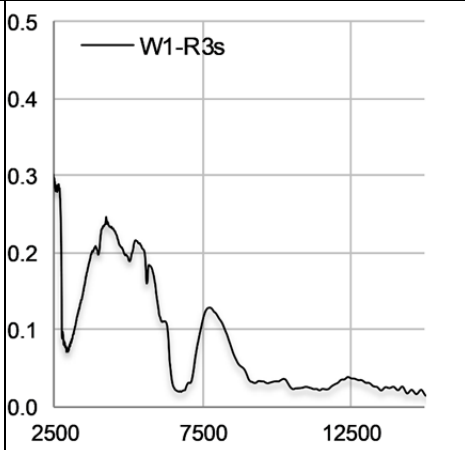
A5.6.2: VNIR/SWIR and MWIR/LWIR spectra of the “granulated blast furnace slag” samples.


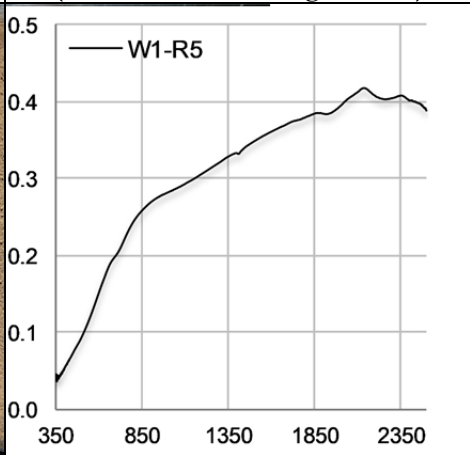
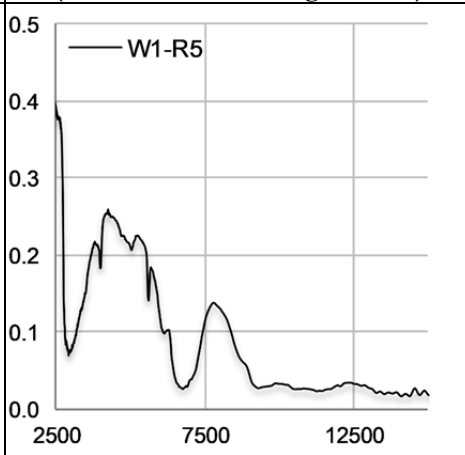

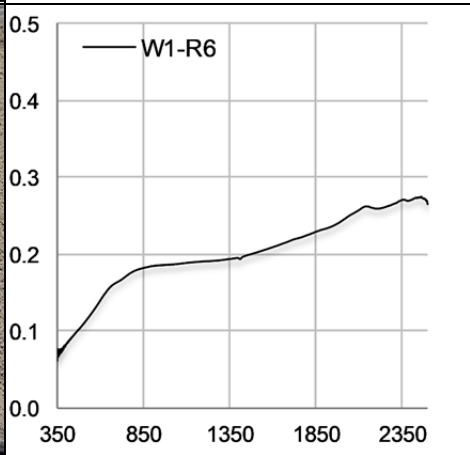
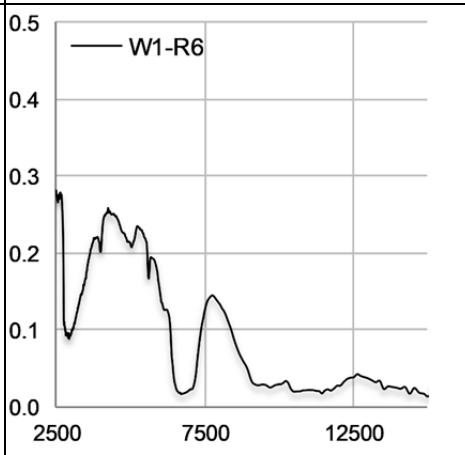

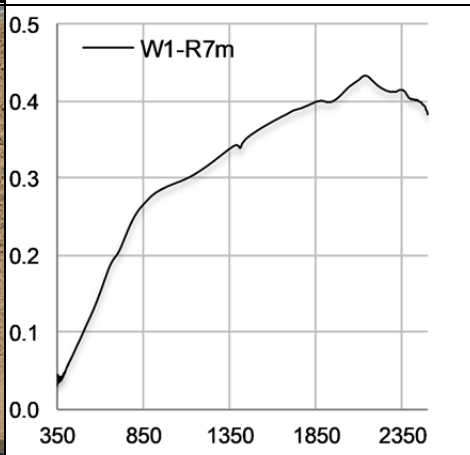
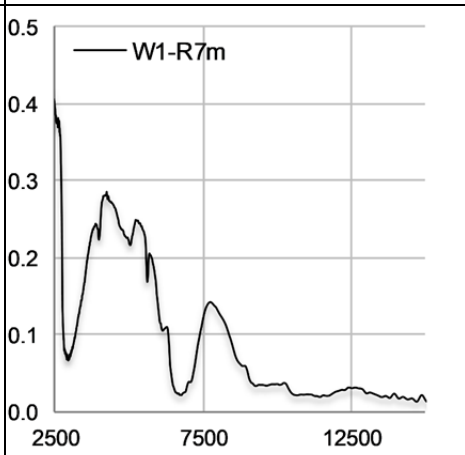

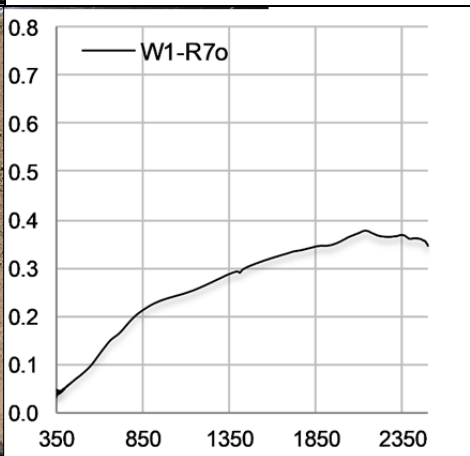
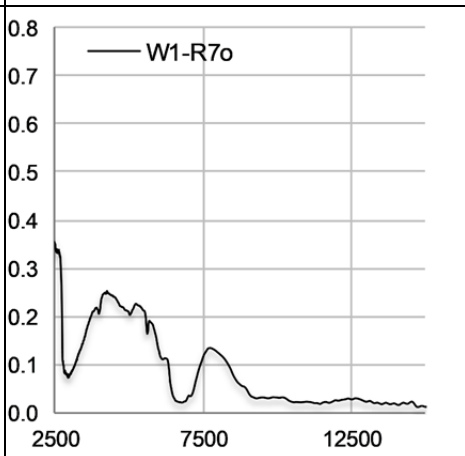
ID	Sample photo	Spectrum 350-2500 nm (Reflectance/Wavelength in nm)	Spectrum 2500-15000 nm (Reflectance/Wavelength in nm)
W2-20a			
W2-20b			
W2-21a			
W2-21b			

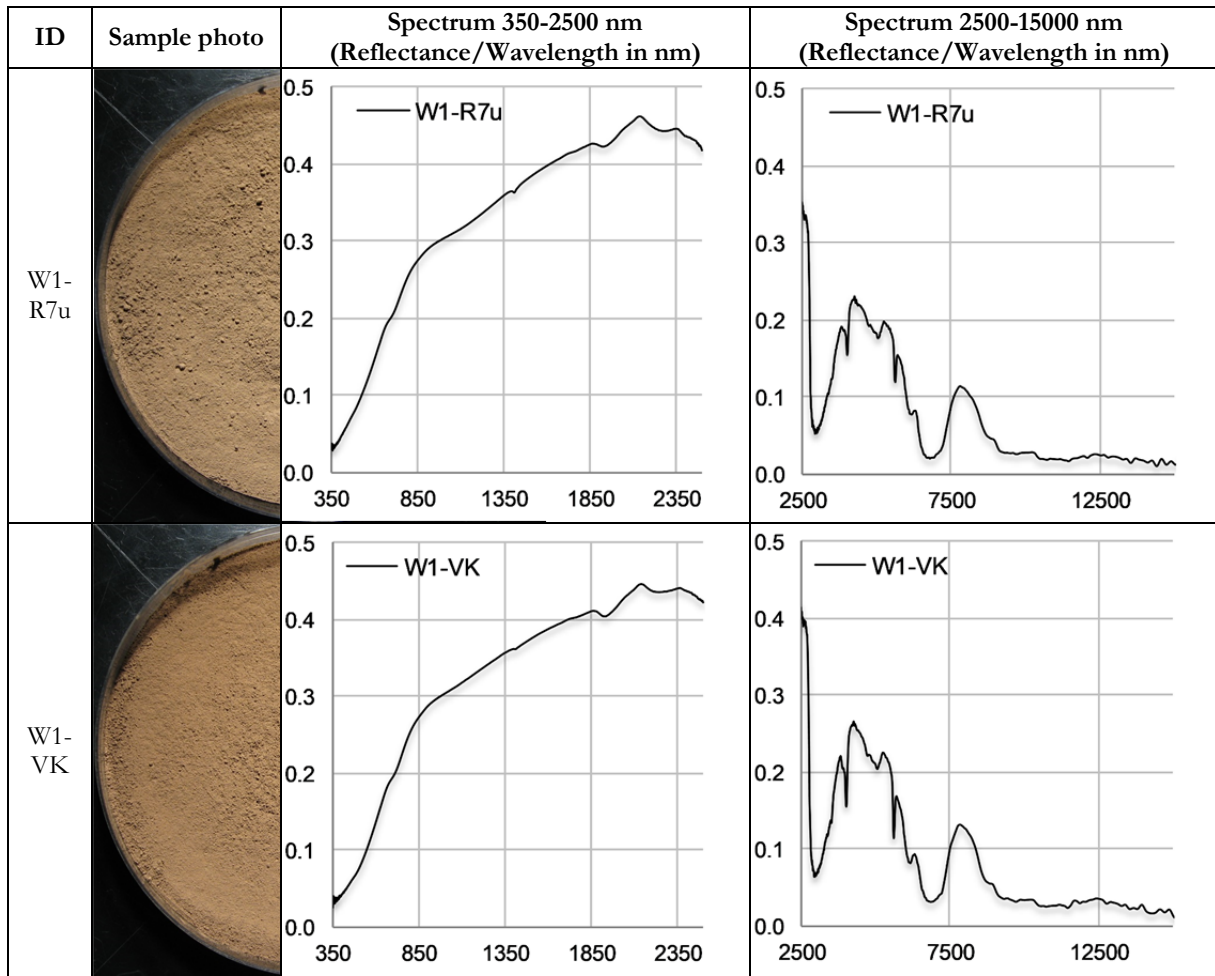
ID	Sample photo	Spectrum 350-2500 nm (Reflectance/Wavelength in nm)	Spectrum 2500-15000 nm (Reflectance/Wavelength in nm)
W2-22a			
W2-22b			

A5.6.3: VNIR/SWIR and MWIR/LWIR spectra of the “Thomas slag” samples.

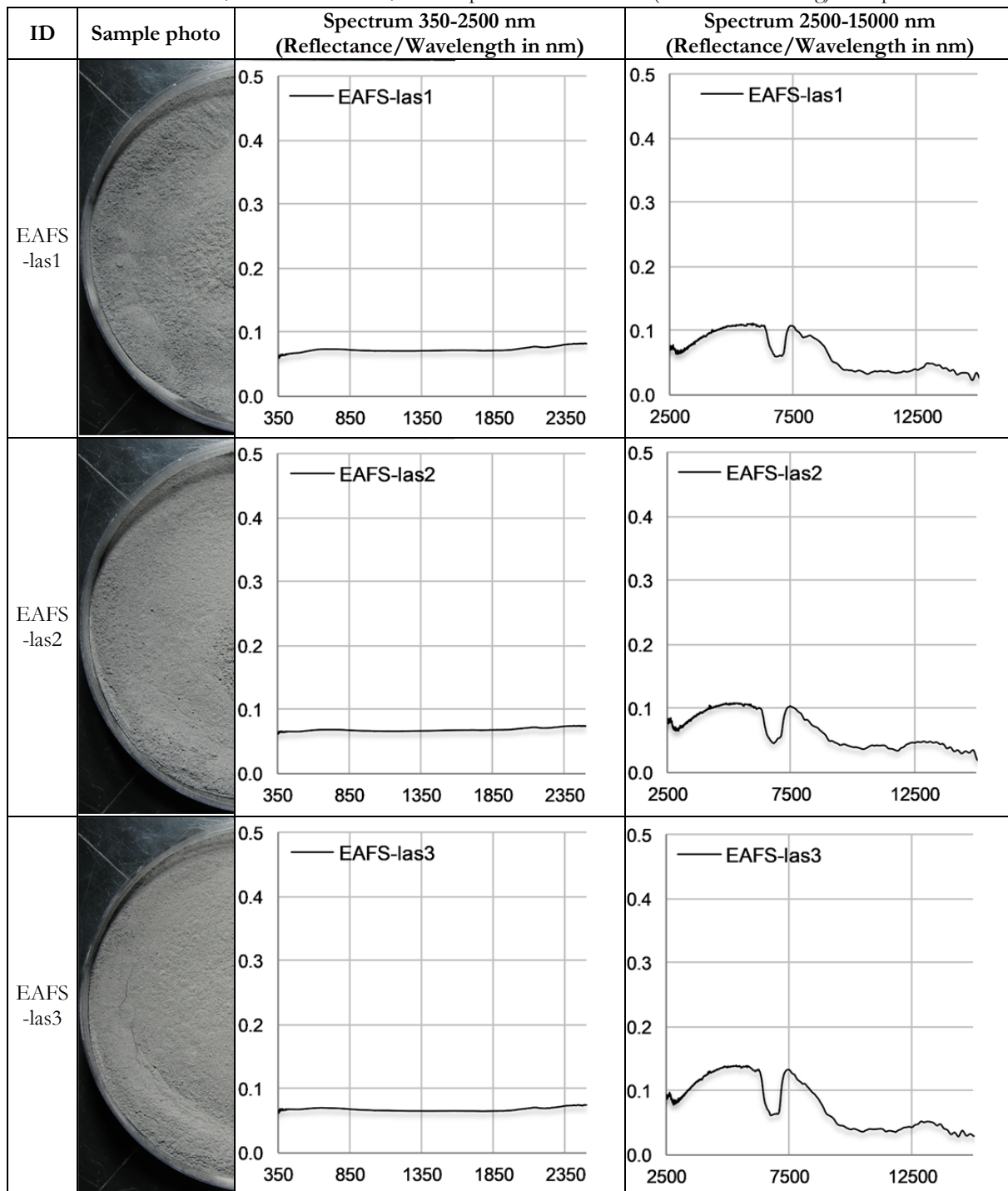


ID	Sample photo	Spectrum 350-2500 nm (Reflectance/Wavelength in nm)	Spectrum 2500-15000 nm (Reflectance/Wavelength in nm)
W1-R1			
W1-R3b			
W1-R3g			
W1-R3s			

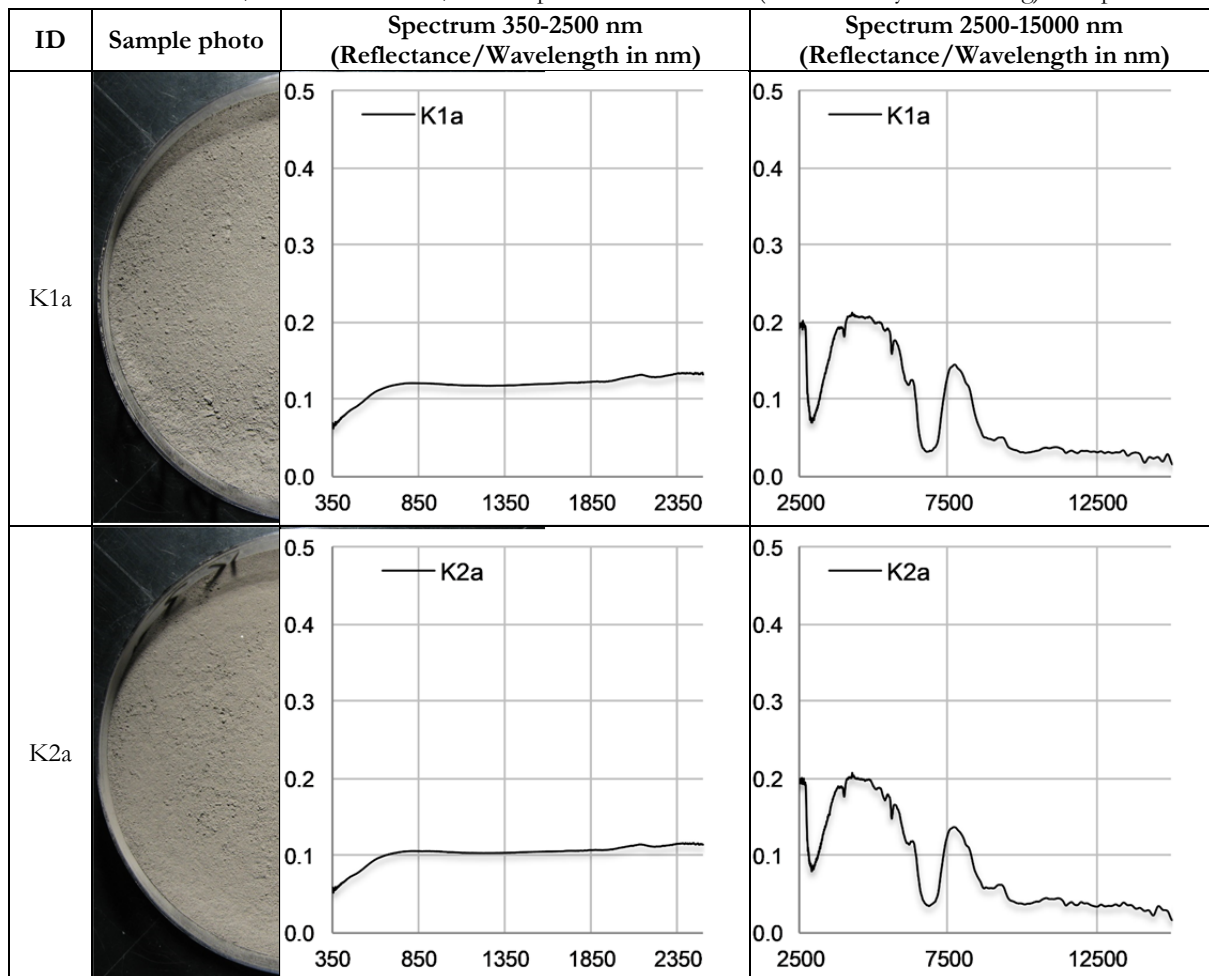
ID	Sample photo	Spectrum 350-2500 nm (Reflectance/Wavelength in nm)	Spectrum 2500-15000 nm (Reflectance/Wavelength in nm)
W1-R5			
W1-R6			
W1-R7m			
W1-R7o			



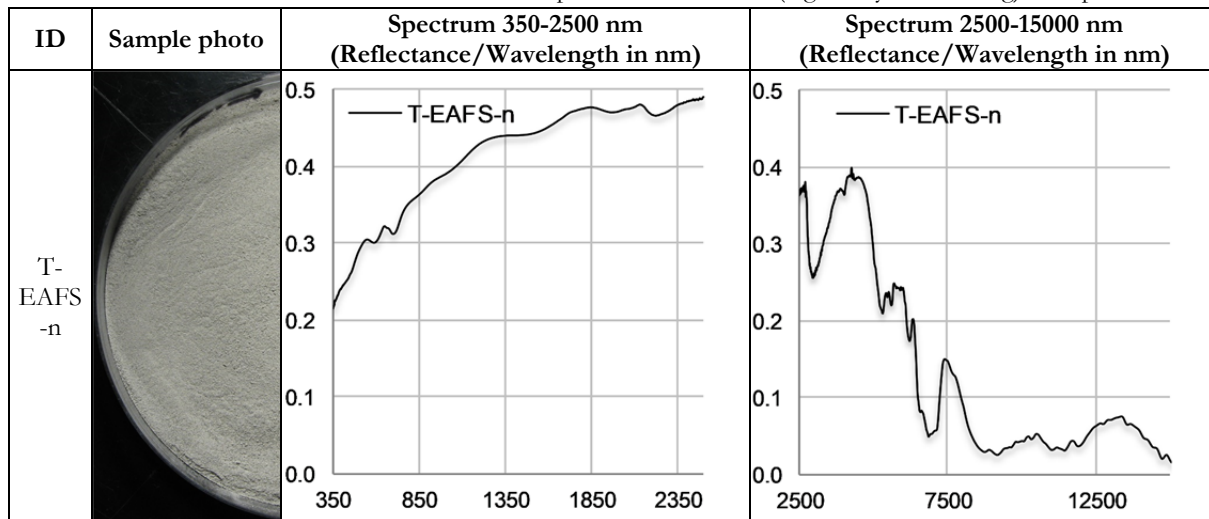
A5.6.4: VNIR/SWIR and MWIR/LWIR spectra of the “EAFS (carbon steelmaking)” samples.



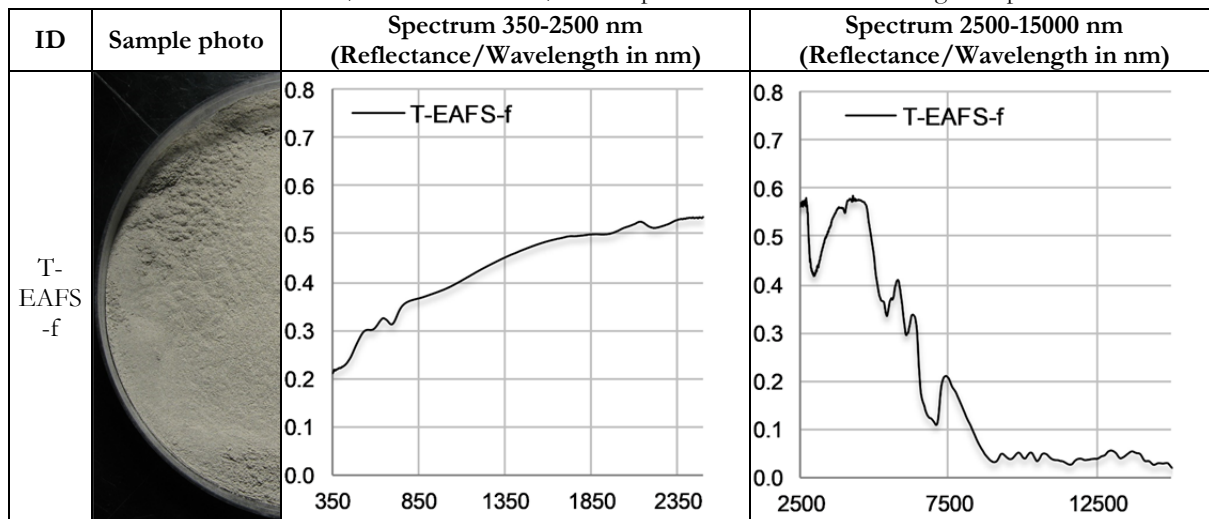
A5.6.5: VNIR/SWIR and MWIR/LWIR spectra of the “EAFS (medium-alloy steelmaking)” samples.



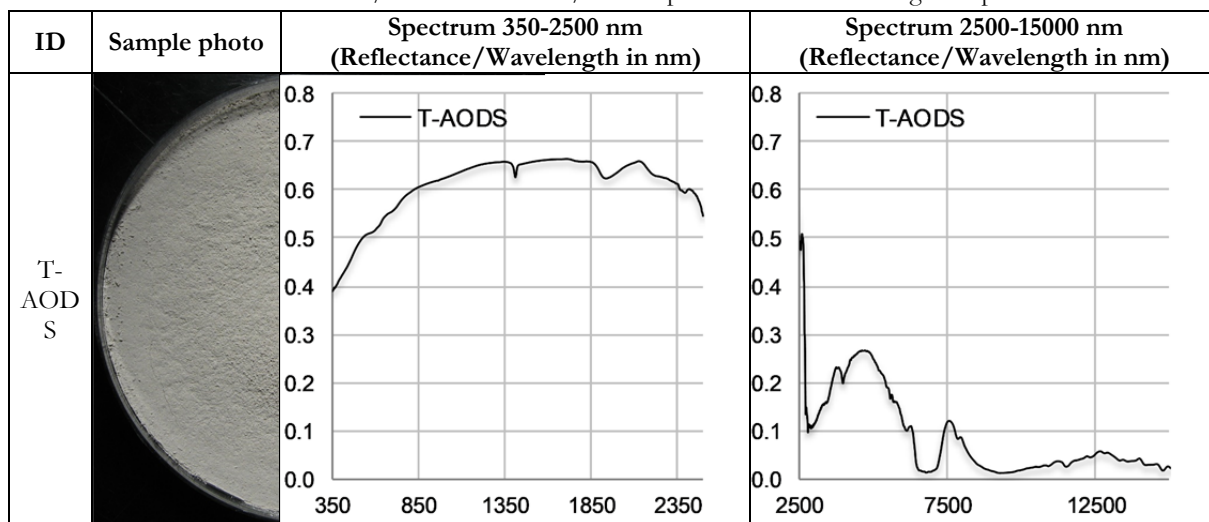
A5.6.6: VNIR/SWIR and MWIR/LWIR spectra of the “EAFS (high-alloy steelmaking)” samples.



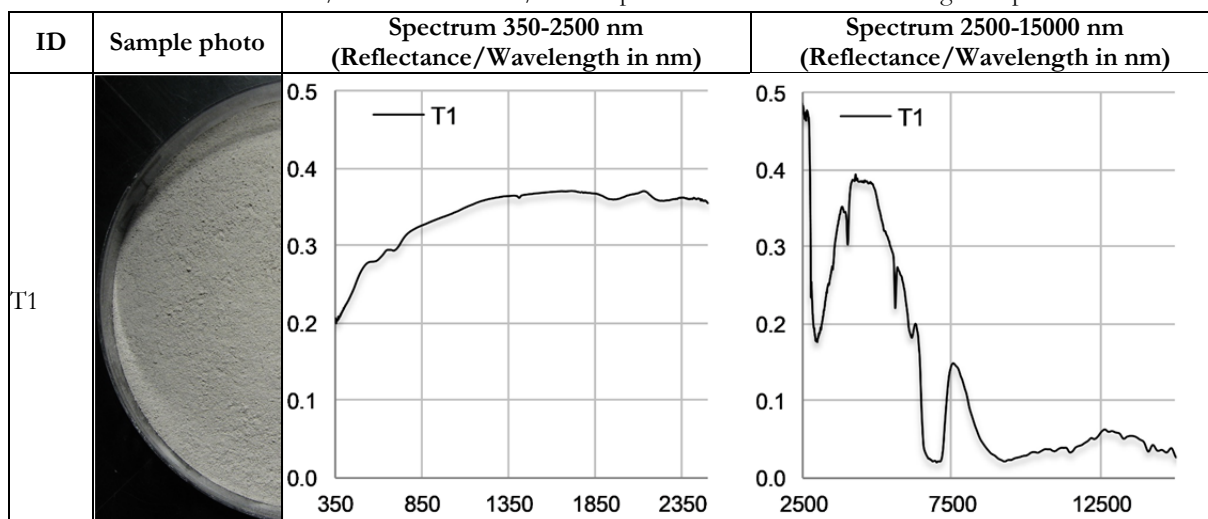
A5.6.7: VNIR/SWIR and MWIR/LWIR spectra of the “EAF foam slag” sample.

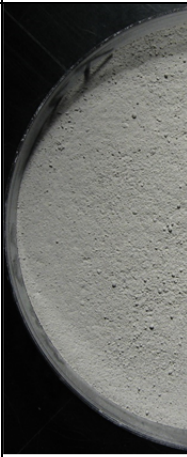
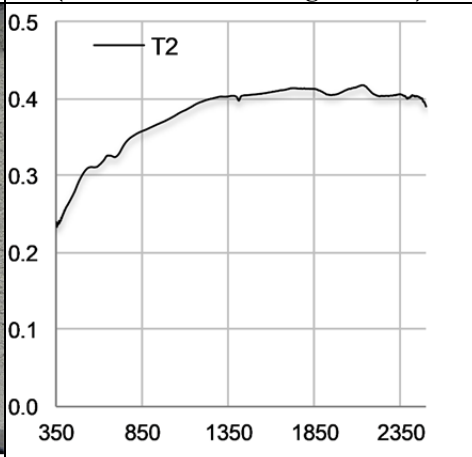
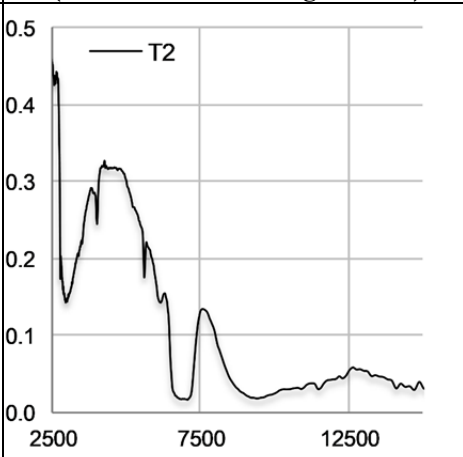
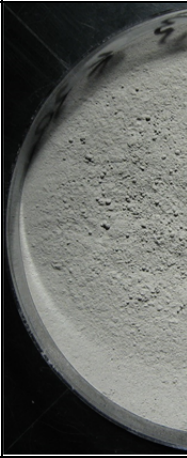
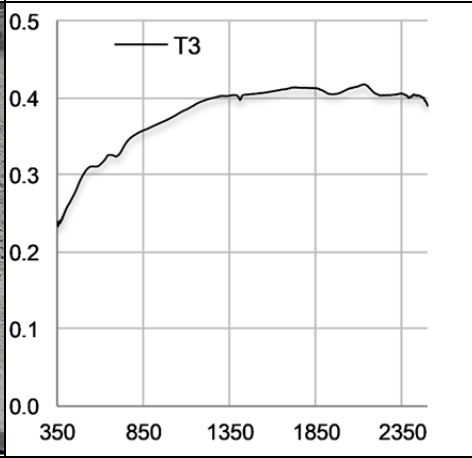
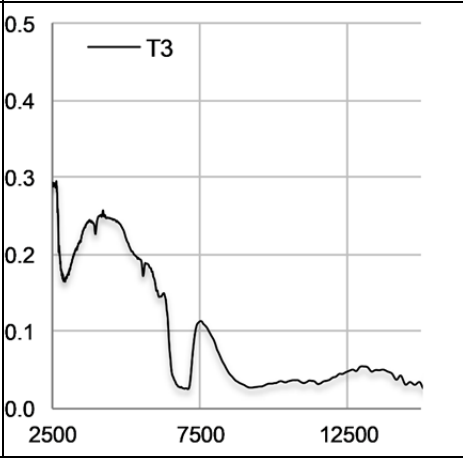

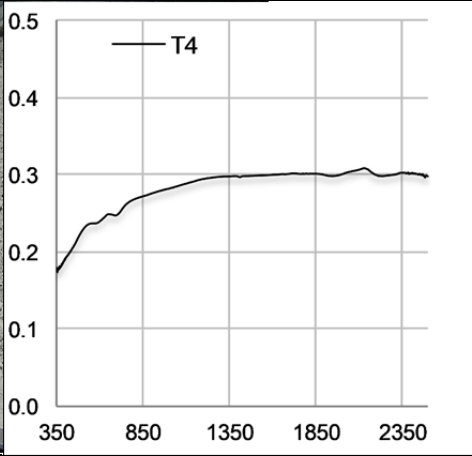
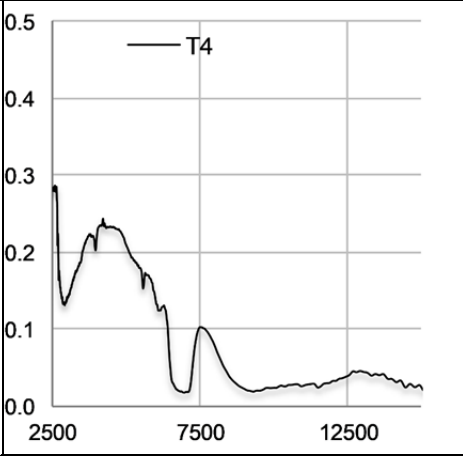
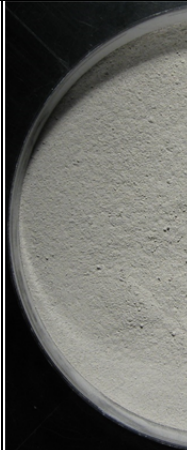
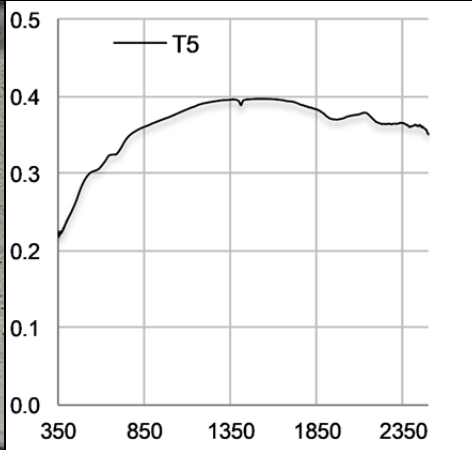
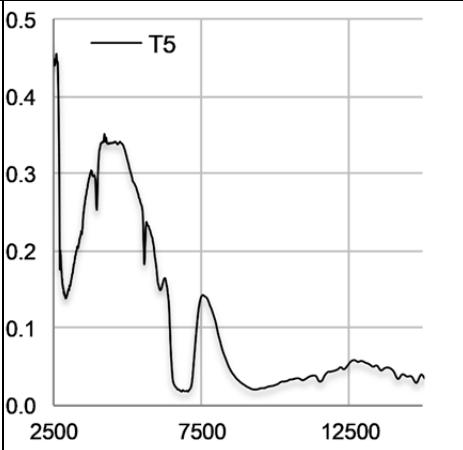


A5.6.8: VNIR/SWIR and MWIR/LWIR spectra of the “AOD slag” sample.

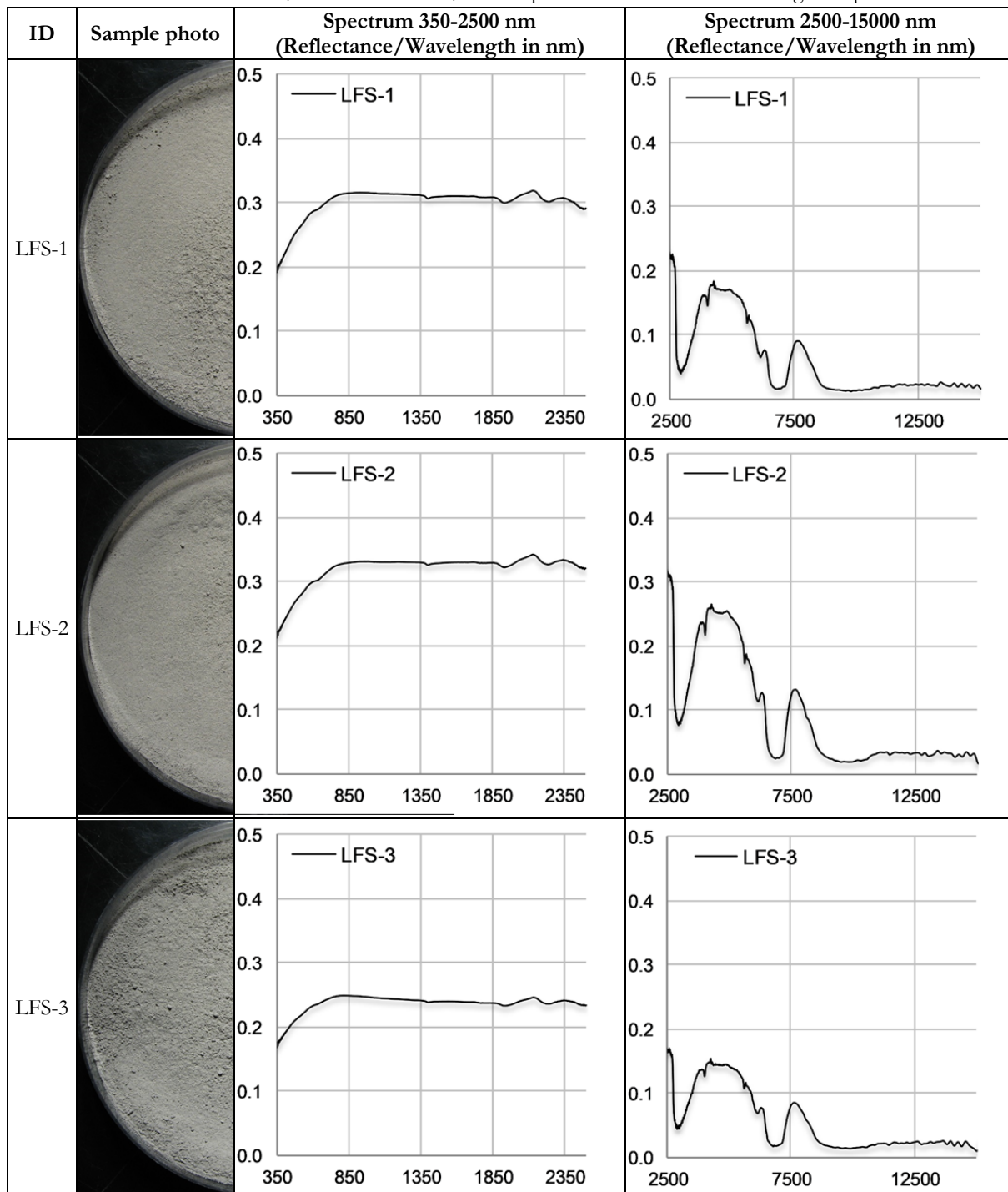


A5.6.9: VNIR/SWIR and MWIR/LWIR spectra of the “stainless steel slag” sample.


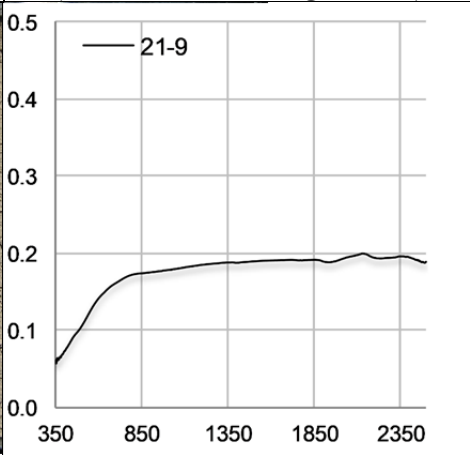
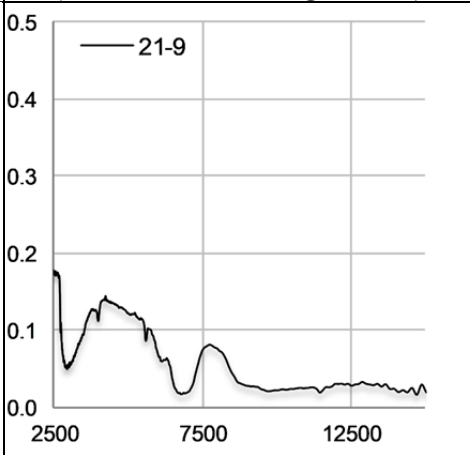

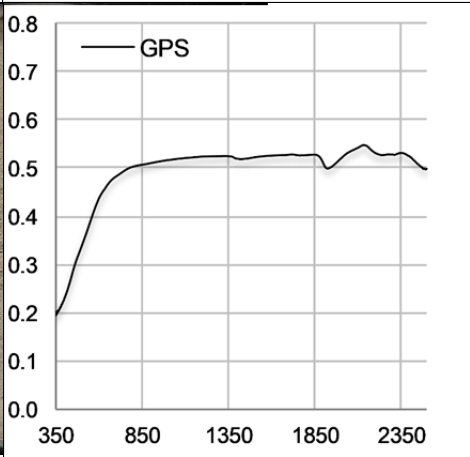
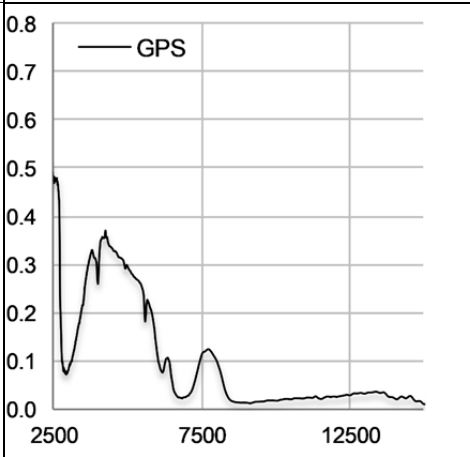


ID	Sample photo	Spectrum 350-2500 nm (Reflectance/Wavelength in nm)	Spectrum 2500-15000 nm (Reflectance/Wavelength in nm)
T2			
T3			
T4			
T5			


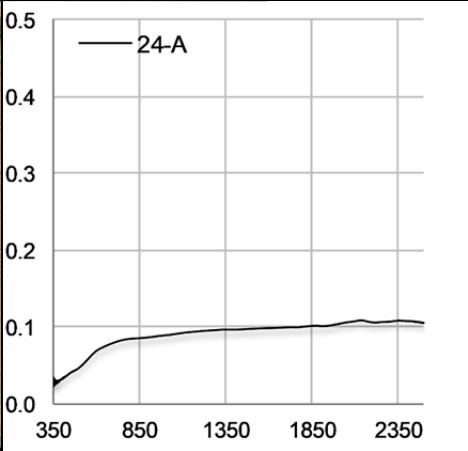
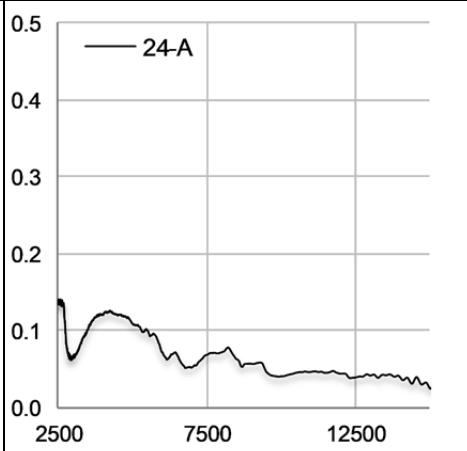

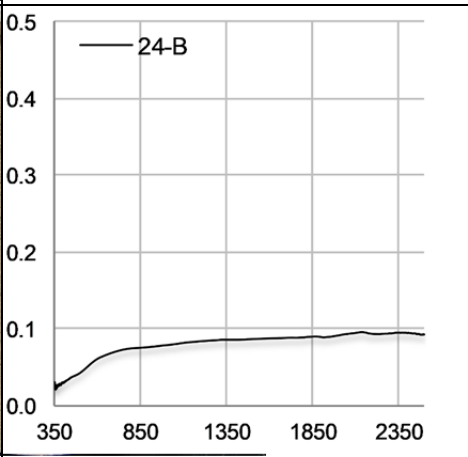
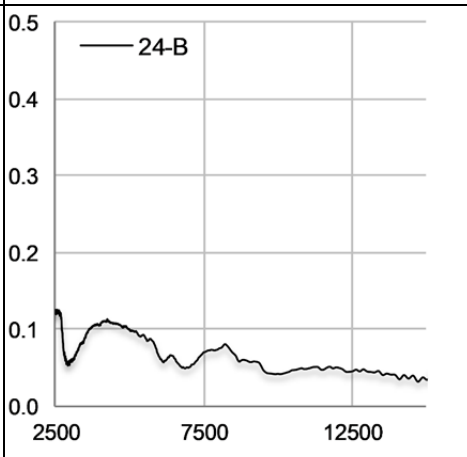
A5.6.10: VNIR/SWIR and MWIR/LWIR spectra of the “ladle furnace slag” sample.



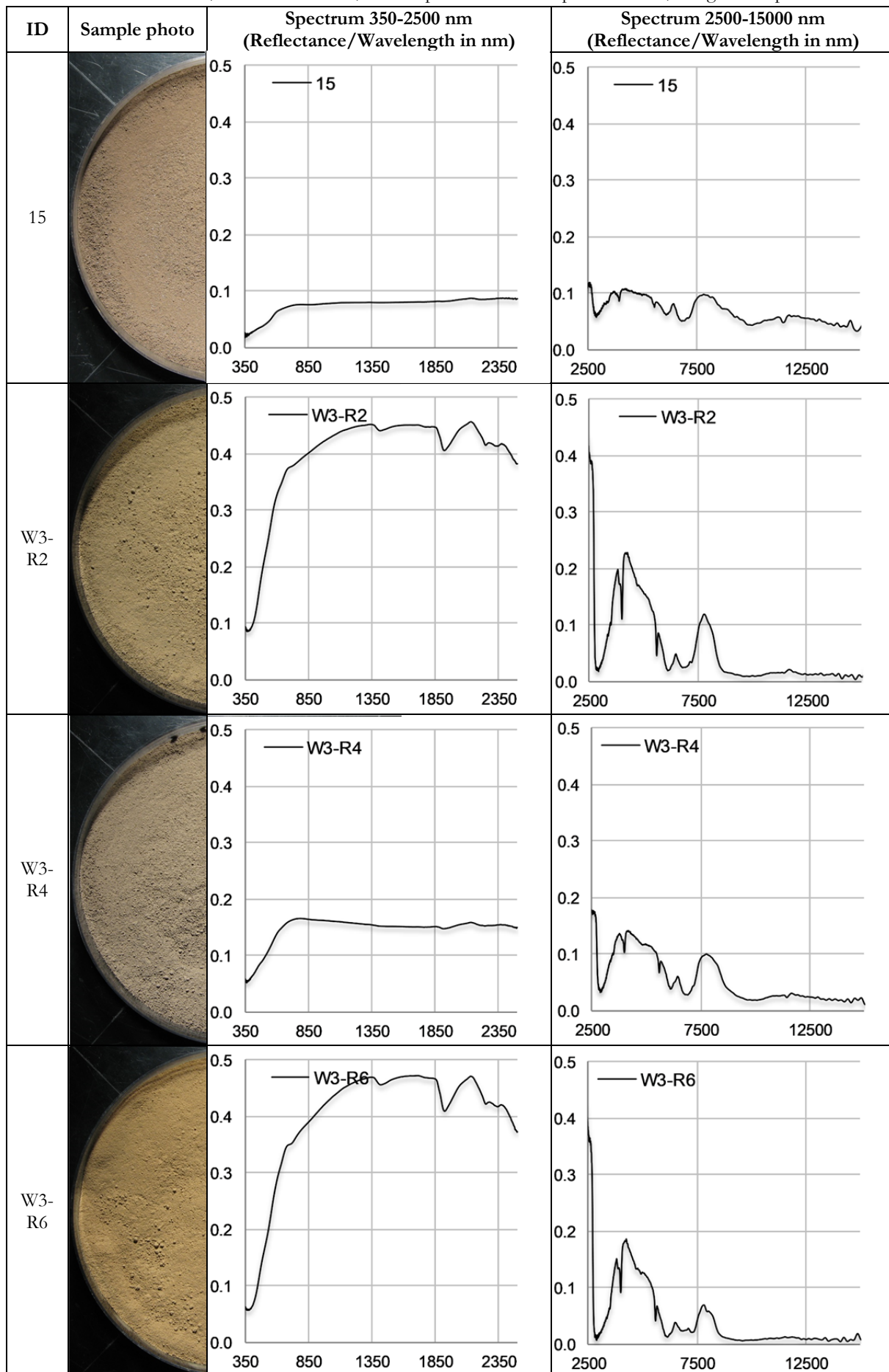
A5.6.11: VNIR/SWIR and MWIR/LWIR spectra of the “Unspecified steelworks slag” samples.


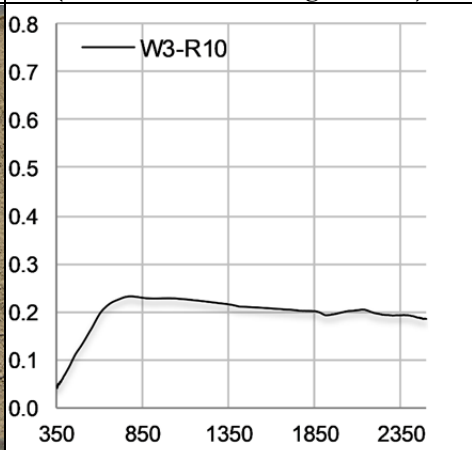
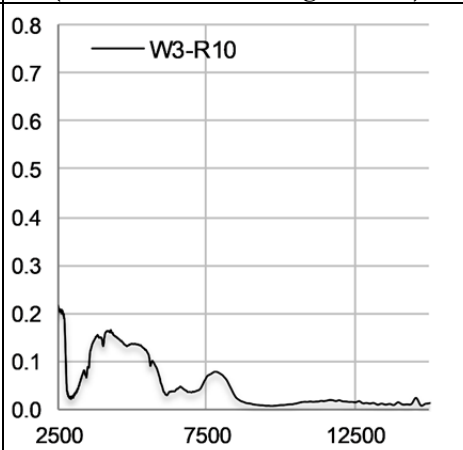

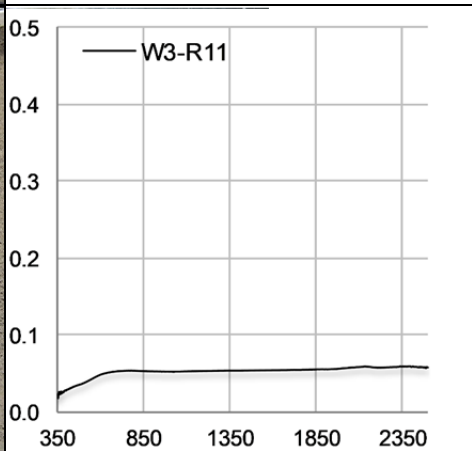
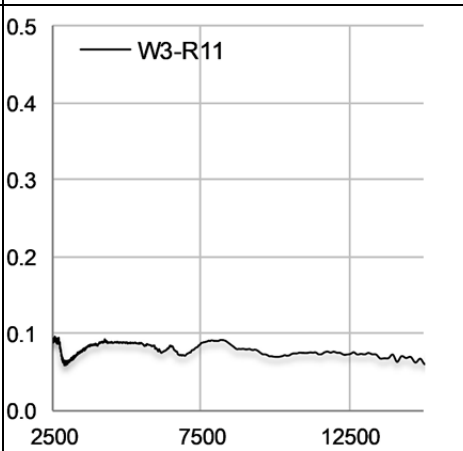

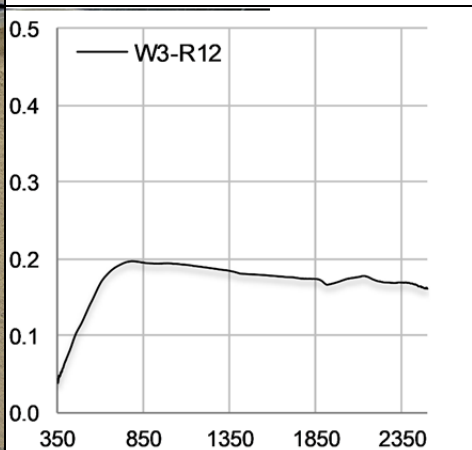

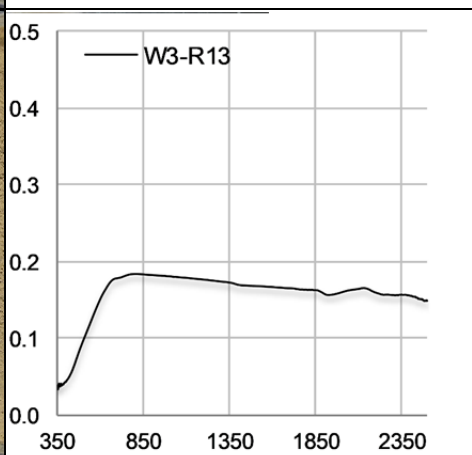
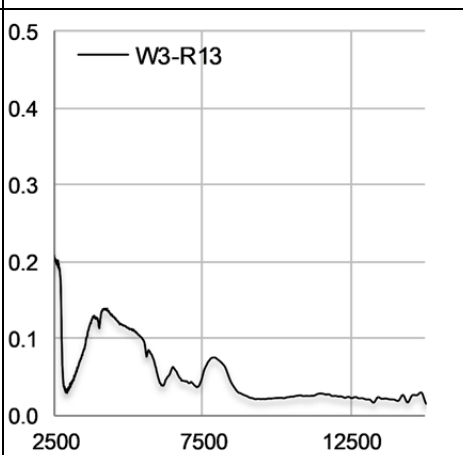
ID	Sample photo	Spectrum 350-2500 nm (Reflectance/Wavelength in nm)	Spectrum 2500-15000 nm (Reflectance/Wavelength in nm)
21-9			
GPS			

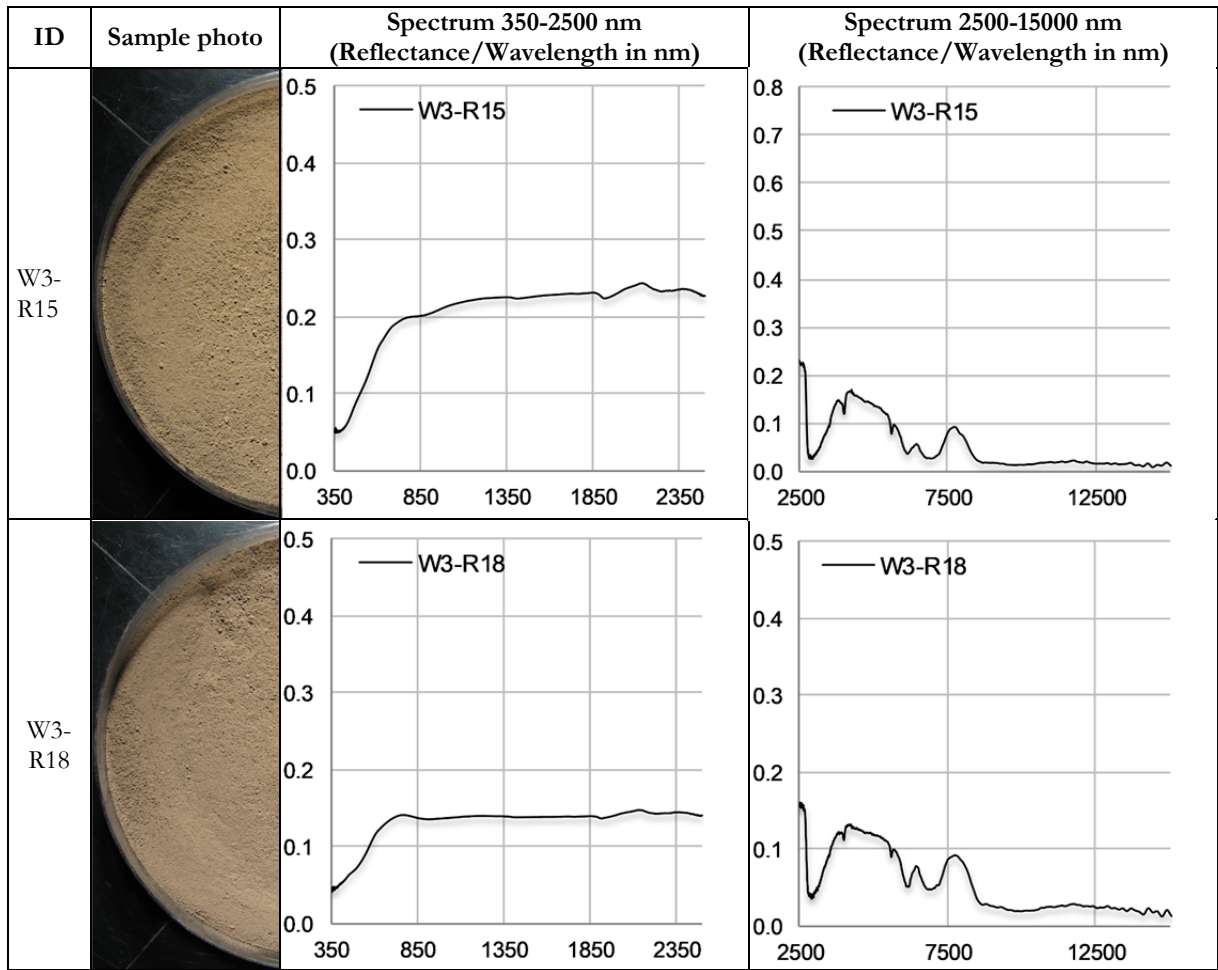
A5.6.12: VNIR/SWIR and MWIR/LWIR spectra of the “blast furnace flue dust” samples.

ID	Sample photo	Spectrum 350-2500 nm (Reflectance/Wavelength in nm)	Spectrum 2500-15000 nm (Reflectance/Wavelength in nm)
24-A			
24-B			

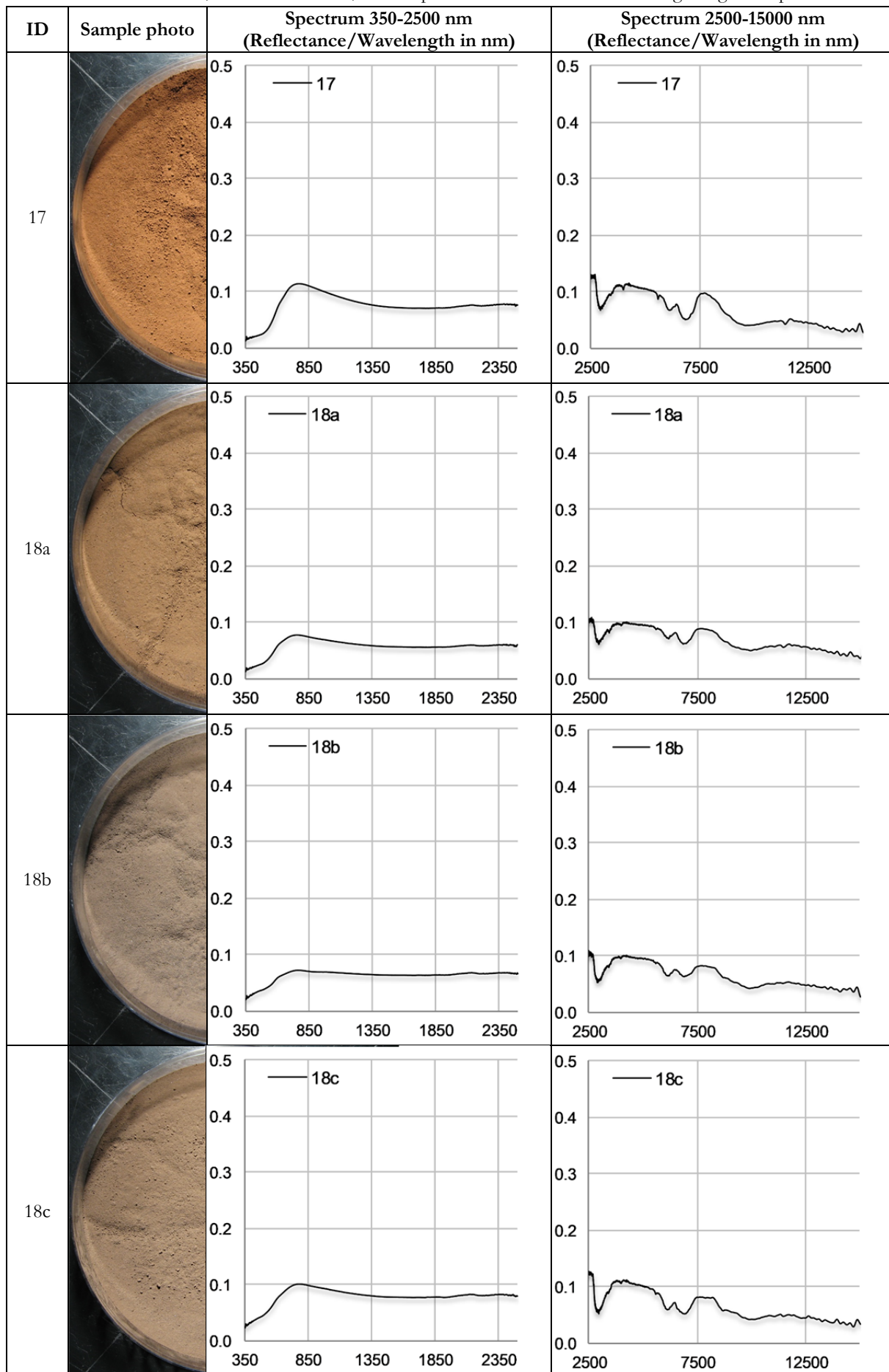
A5.6.13: VNIR/SWIR and MWIR/LWIR spectra of the “unspecified dusts/sludges” samples.


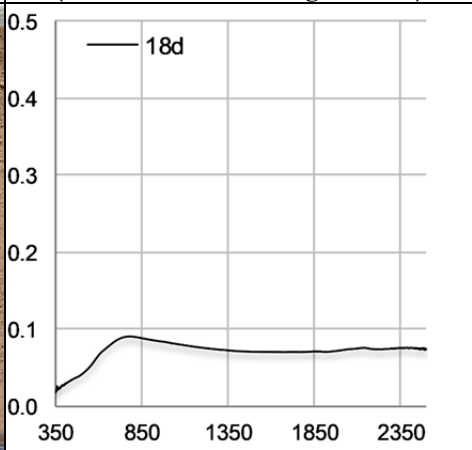
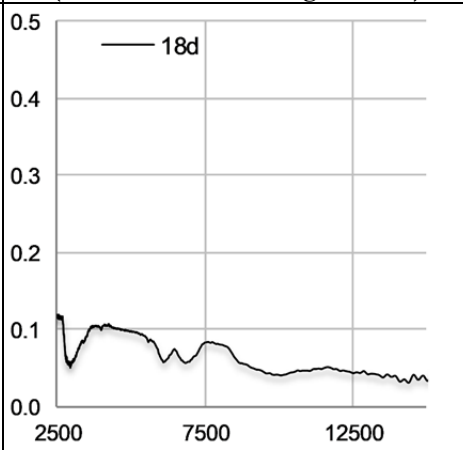

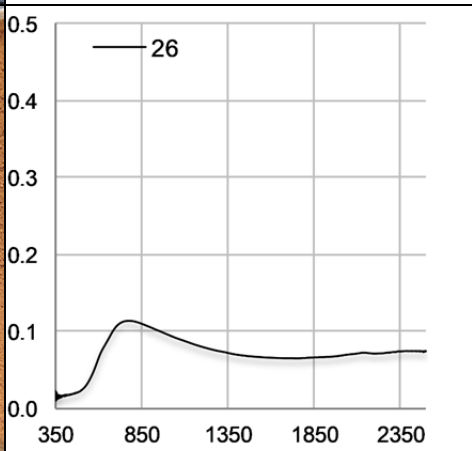
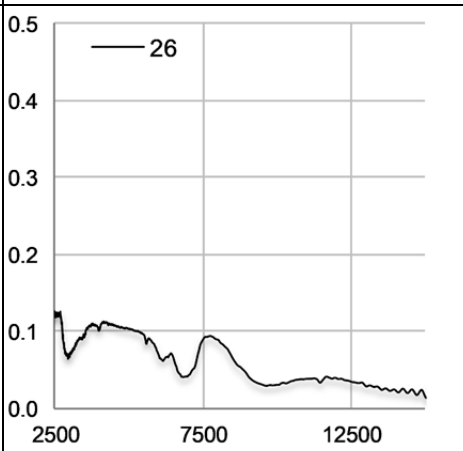

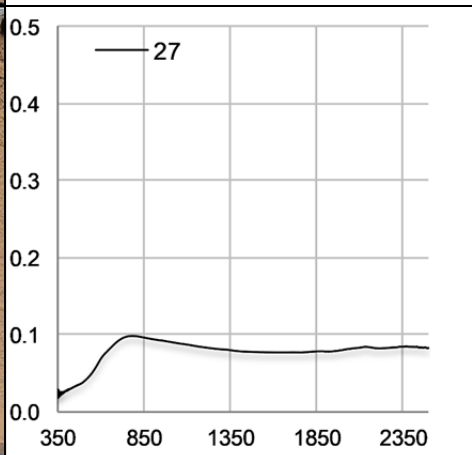
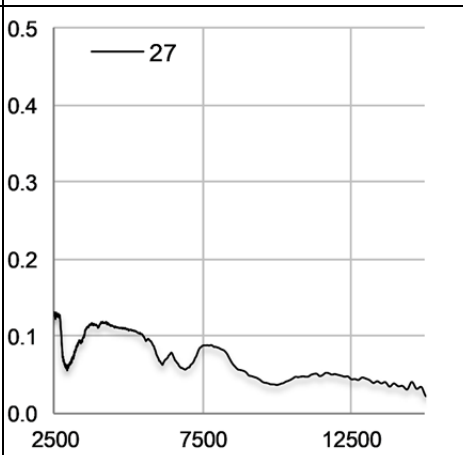


ID	Sample photo	Spectrum 350-2500 nm (Reflectance/Wavelength in nm)	Spectrum 2500-15000 nm (Reflectance/Wavelength in nm)
W3-R10			
W3-R11			
W3-R12			<p data-bbox="1050 1361 1283 1393">Missing measurement</p>
W3-R13			

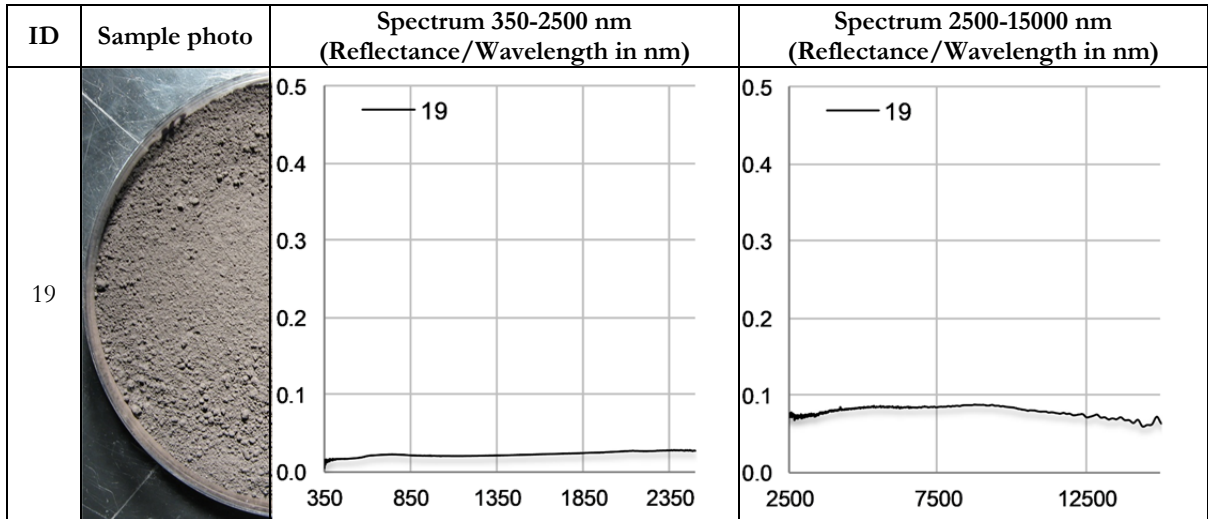


A5.6.14: VNIR/SWIR and MWIR/LWIR spectra of the “converter dedusting sludge” samples.

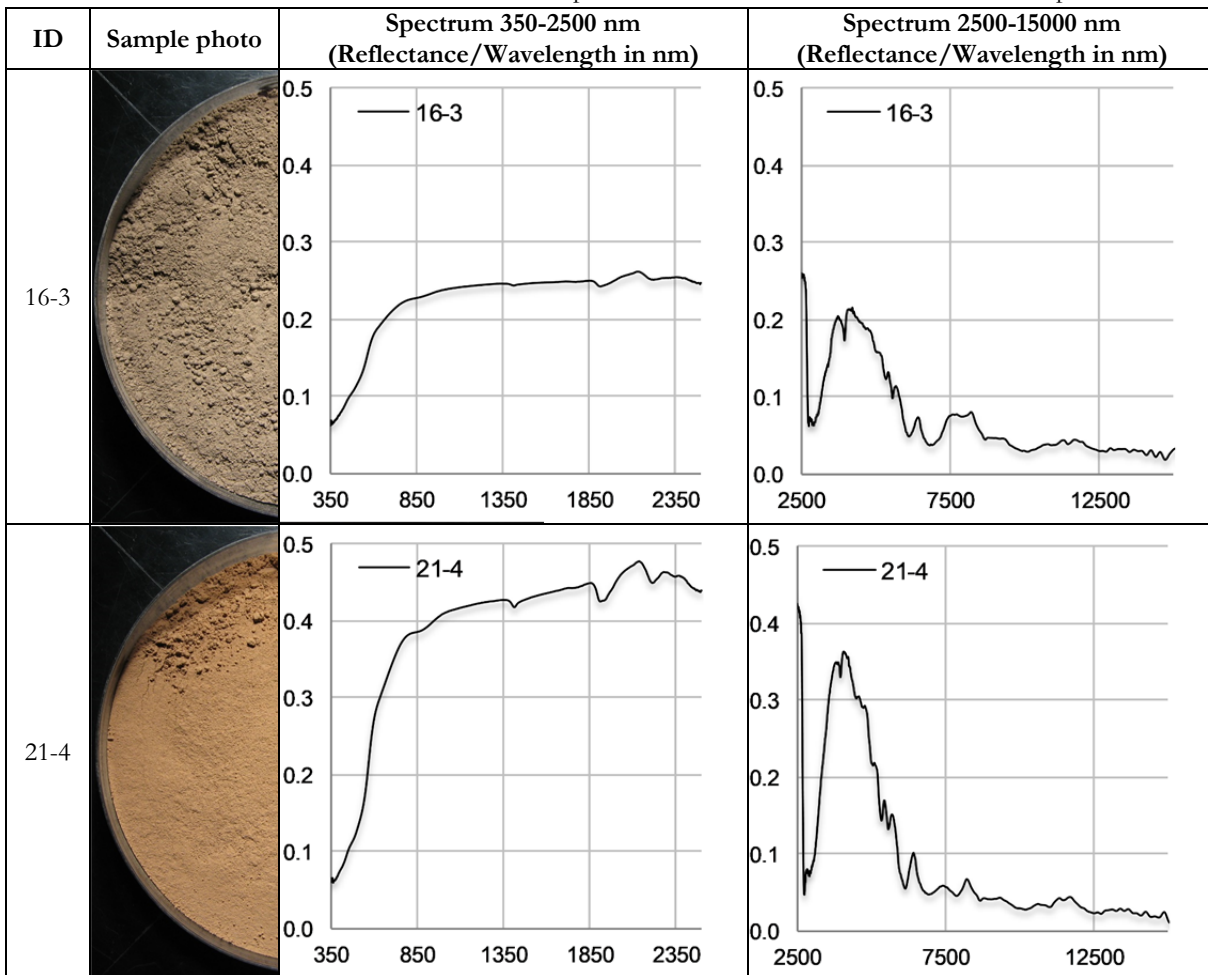



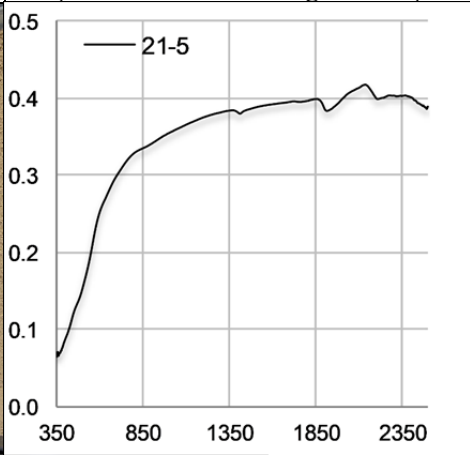
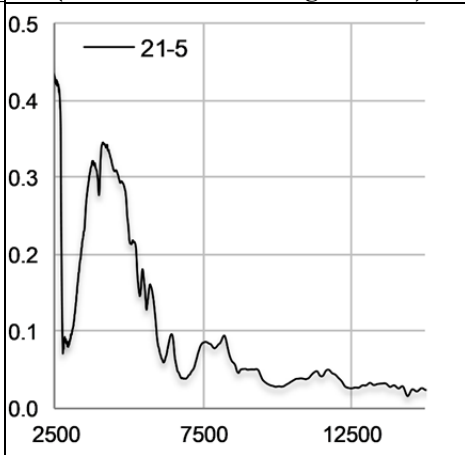

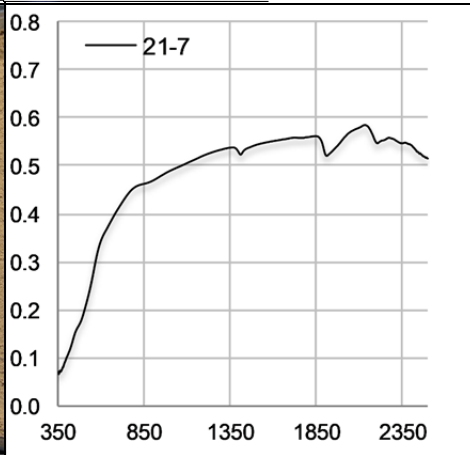
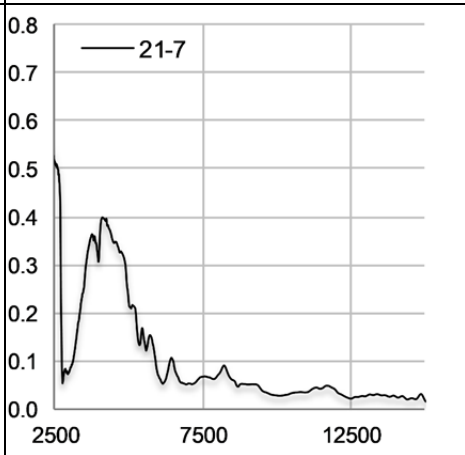

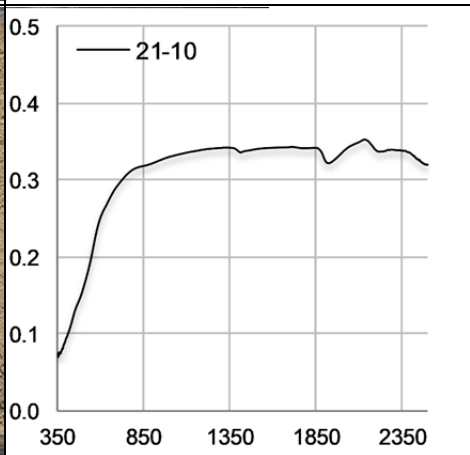
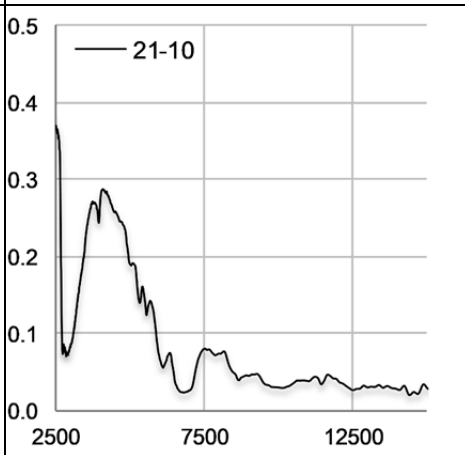

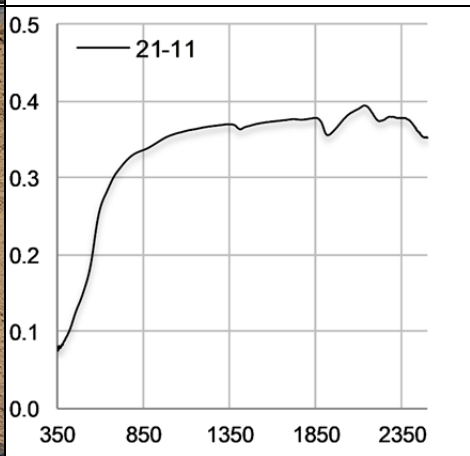
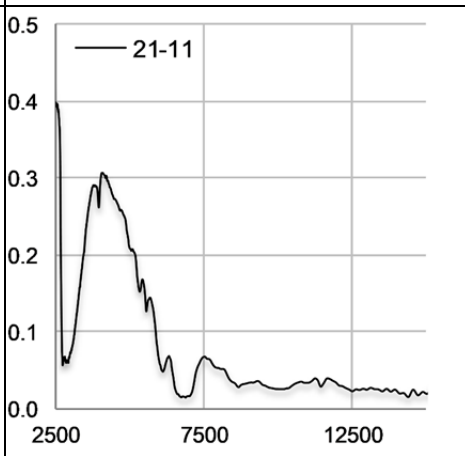
ID	Sample photo	Spectrum 350-2500 nm (Reflectance/Wavelength in nm)	Spectrum 2500-15000 nm (Reflectance/Wavelength in nm)
18d			
26			
27			

A5.6.15: VNIR/SWIR and MWIR/LWIR spectra of the “mill scale” sample.

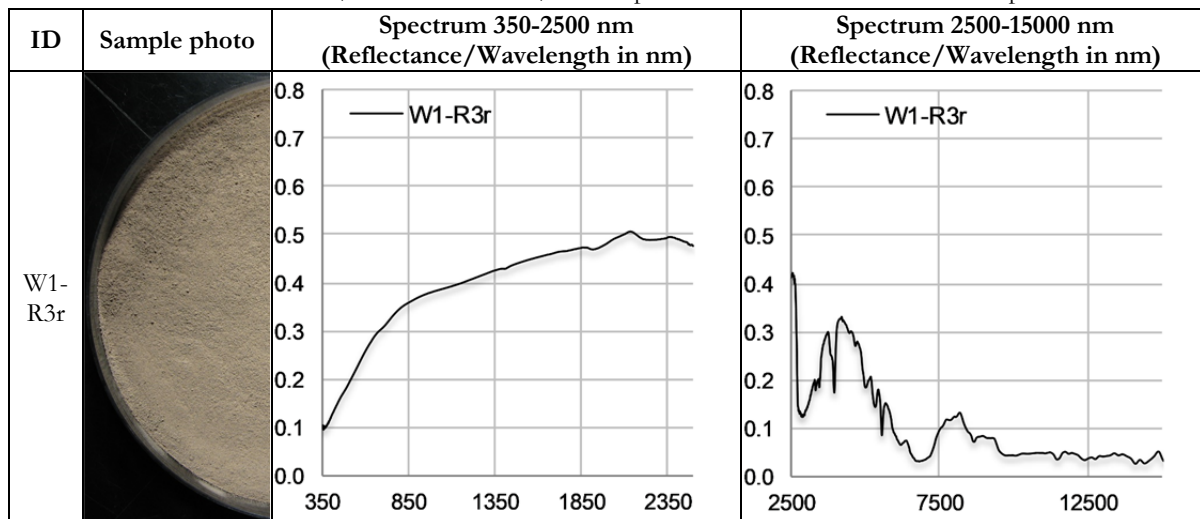


A5.6.16: VNIR/SWIR and MWIR/LWIR spectra of the “mixtures with natural sand” samples.

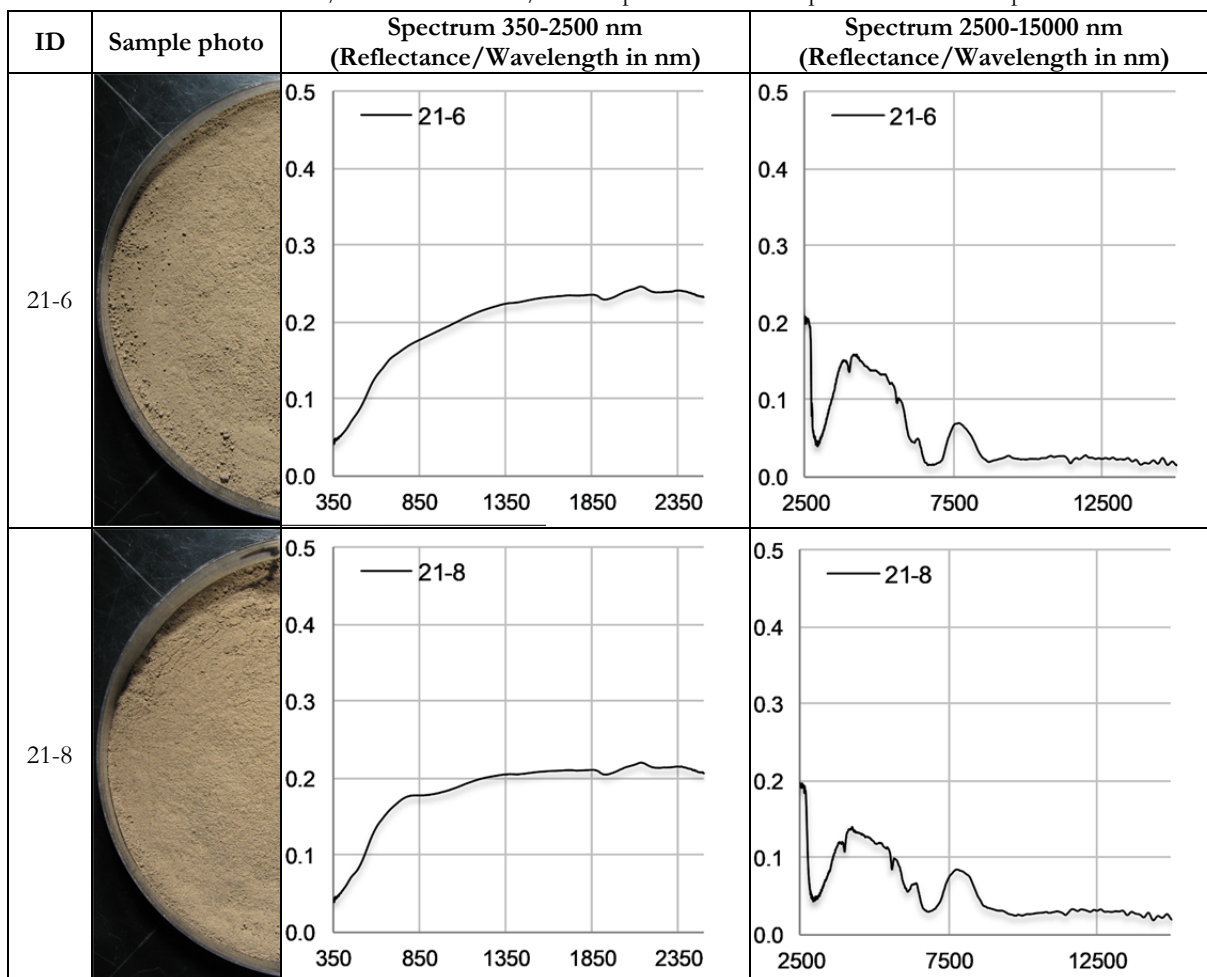



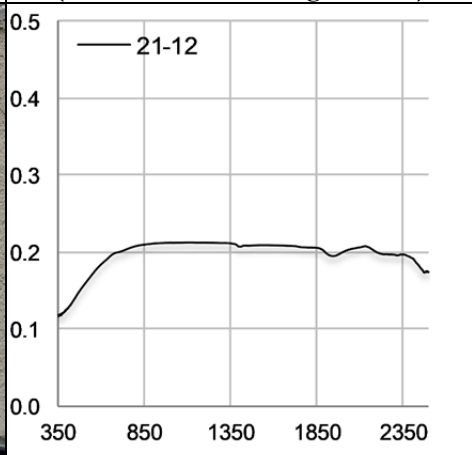
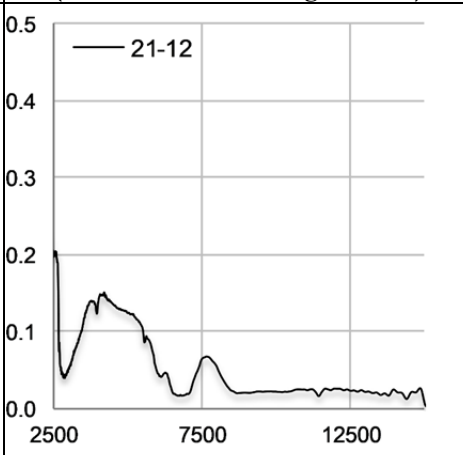

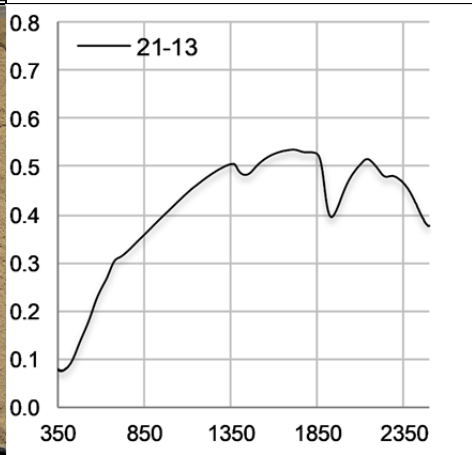
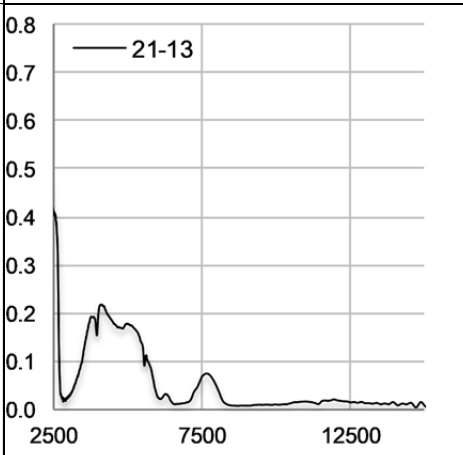

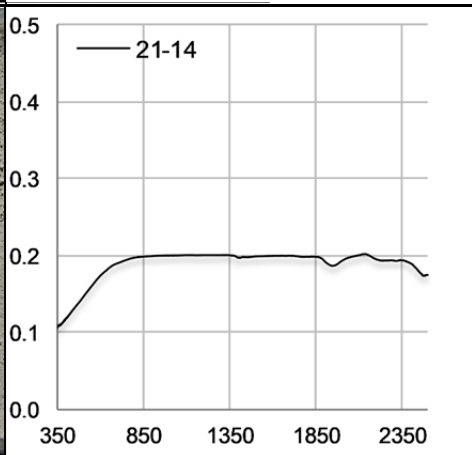
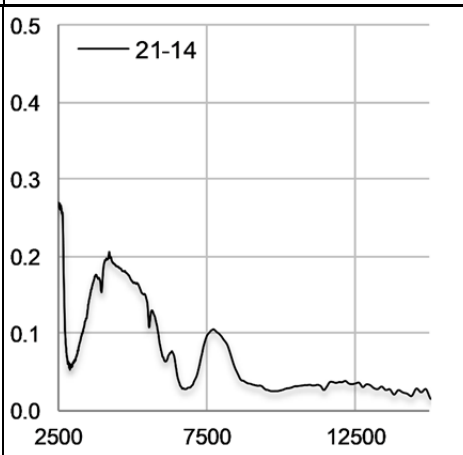

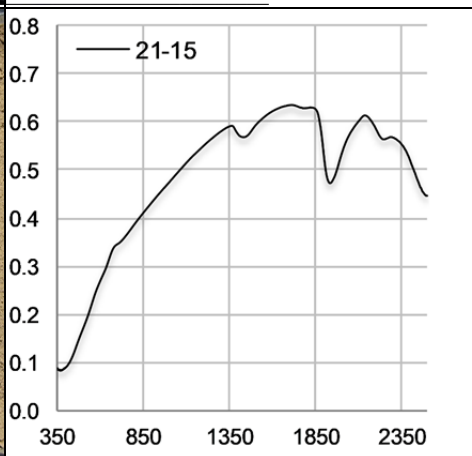
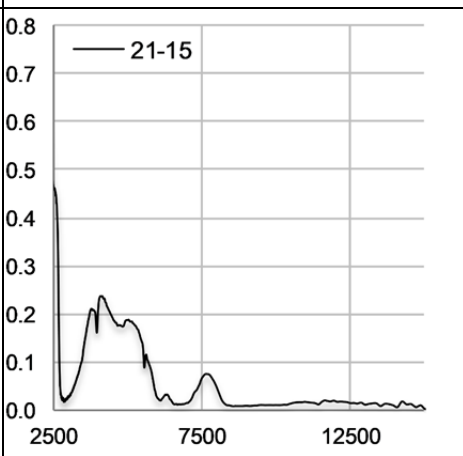
ID	Sample photo	Spectrum 350-2500 nm (Reflectance/Wavelength in nm)	Spectrum 2500-15000 nm (Reflectance/Wavelength in nm)
21-5			
21-7			
21-10			
21-11			


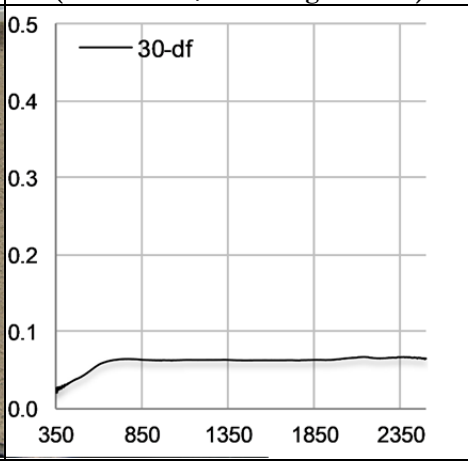
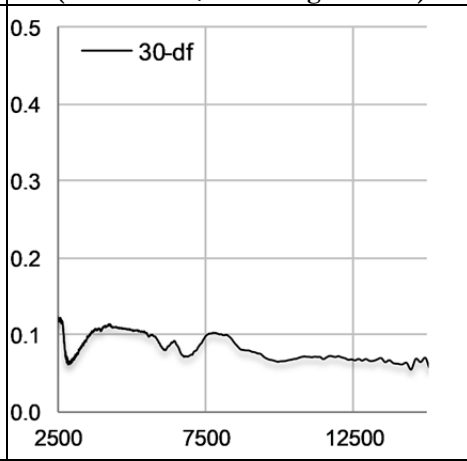

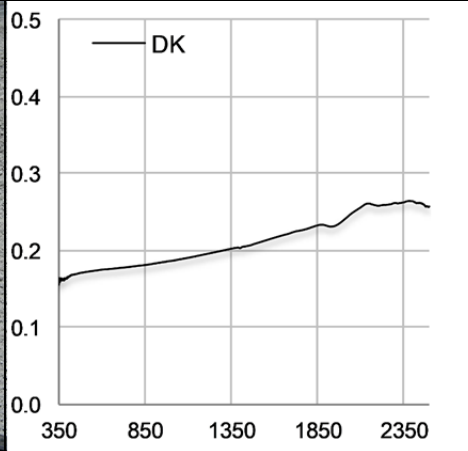
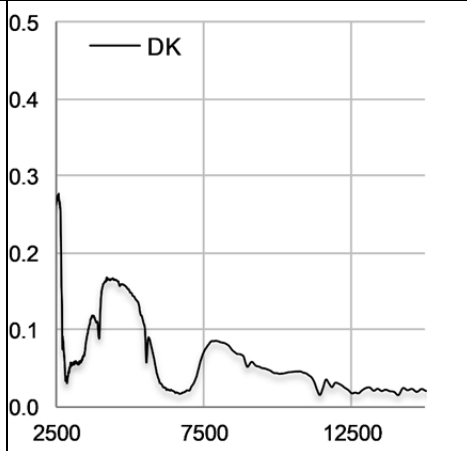

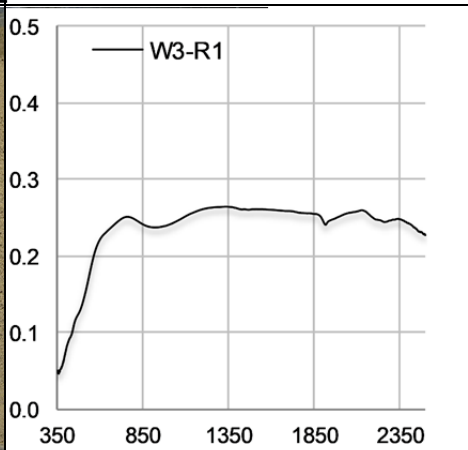
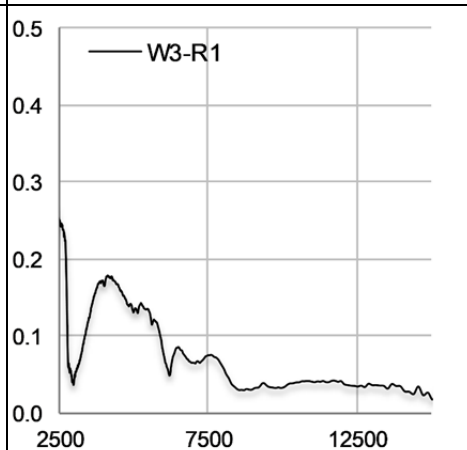

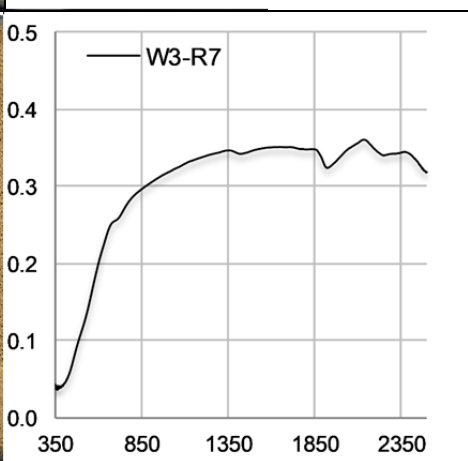
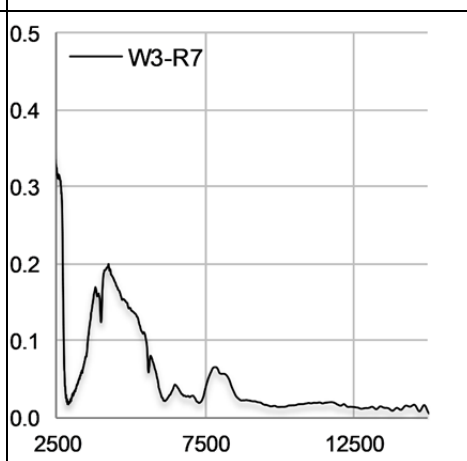
A5.6.17: VNIR/SWIR and MWIR/LWIR spectra of the “limestone+sand” sample.


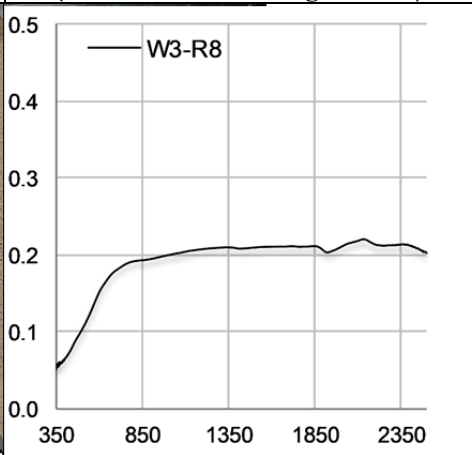
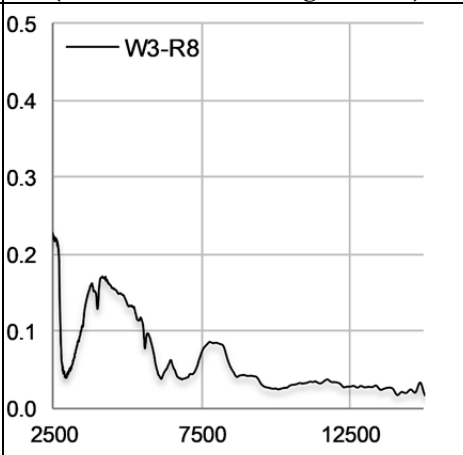

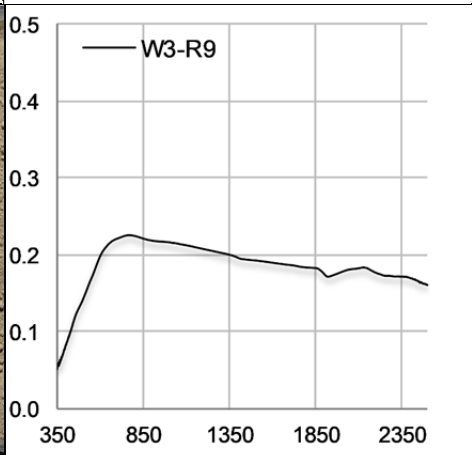
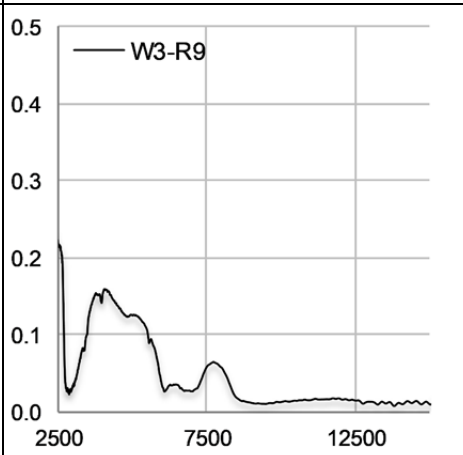

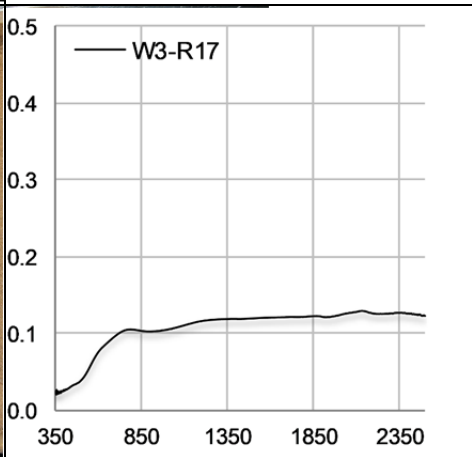
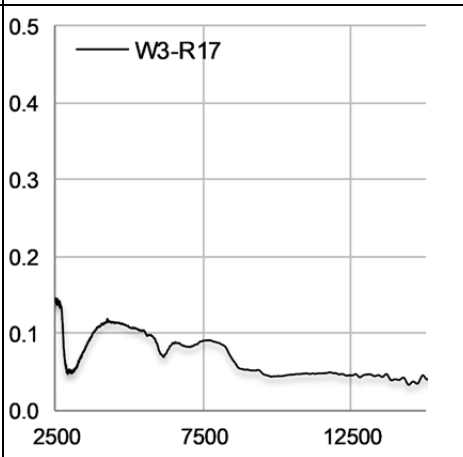


A5.6.18: VNIR/SWIR and MWIR/LWIR spectra of the “unspecified other” samples.



ID	Sample photo	Spectrum 350-2500 nm (Reflectance/Wavelength in nm)	Spectrum 2500-15000 nm (Reflectance/Wavelength in nm)
21-12			
21-13			
21-14			
21-15			

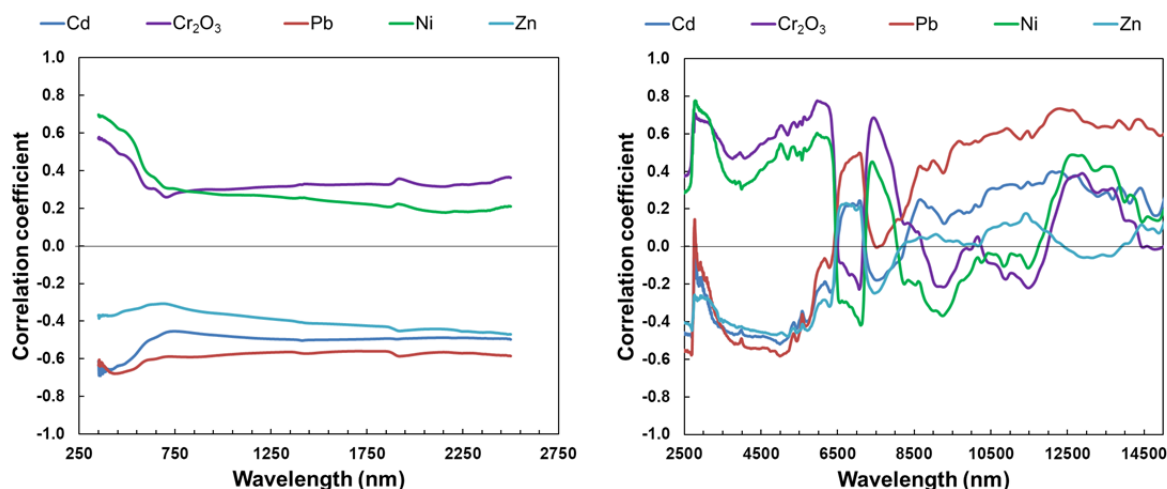
ID	Sample photo	Spectrum 350-2500 nm (Reflectance/Wavelength in nm)	Spectrum 2500-15000 nm (Reflectance/Wavelength in nm)
30-df			
DK			
W3-R1			
W3-R7			

ID	Sample photo	Spectrum 350-2500 nm (Reflectance/Wavelength in nm)	Spectrum 2500-15000 nm (Reflectance/Wavelength in nm)
W3-R8			
W3-R9			
W3-R17			

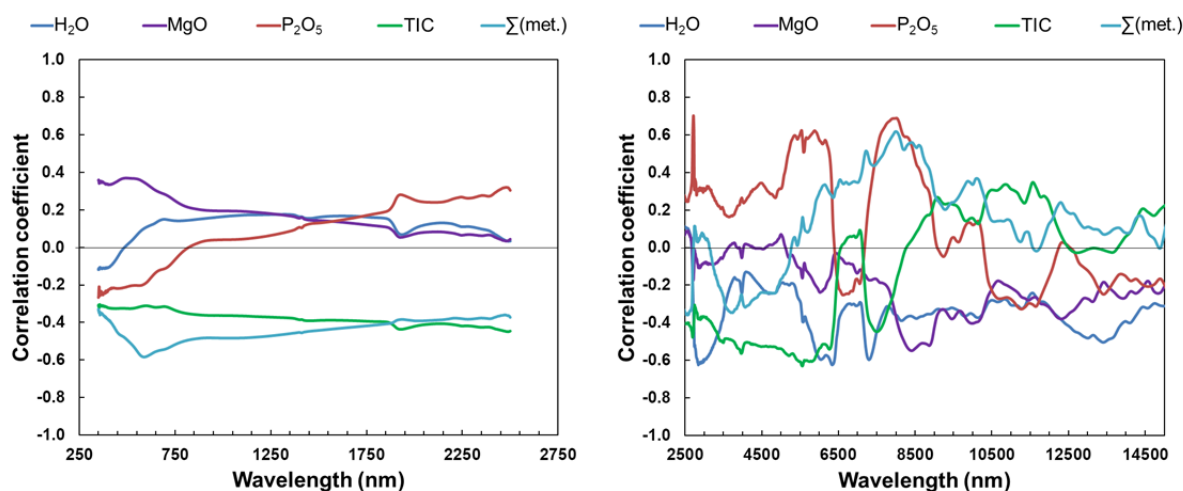
A5.7: List of the reflectance maxima observed in the LWIR spectra of the reference samples of the by-product classes considered relatively “pure” (positions in nm).

BFS	GBFS	TS	EAFScs	EAFSmas	EAFShas	EAFShlf	LFS	SSS	AODS	BFFD	CDS
7622	6388	6268	7452	7665	7371	7370	7579	7536	7536	8180	7754
11179	7709	7709	8130	9251	8825	9251	11564	10162	7891	9251	8884
11665	11665	8825	9125	10732	9721	9792	12567	10646	11086	11665	11273
		10162	9582	10995	10162	10162		11179	12085		11564
		11564	10906		10399	10646		12085	12537		12776
		12421	12776		11086	11871		12537	13829		
		14120			11665	12898		13282			
		14741			13282	13151					
		15072				13550					

BFS = Blast furnace slag, GBFS = granulated BFS, TS = Thomas slag, EAFScs = EAF slag from carbon steelmaking, EAFSmas = EAF slag from medium-alloy steelmaking, EAFShas = EAF slag from high-alloy steelmaking, EAFShlf = foamed EAF slag from high-alloy steelmaking, LFS = ladle furnace slag, SSS = stainless steel slag, AODS = AOD slag, BFFD = blast furnace flue dust, CDS = converter dedusting sludge



A5.8a: Correlations between the contents of Cd, Cr₂O₃, Ni, Pb and Zn and the reflectance values of the samples (left: VNIR/SWIR, right: MWIR/LWIR).



A5.8b: Correlations between the contents of H₂O, MgO, P₂O₅, TIC and Σ(Mo, Ni, V, Zn, Al, Cr, Fe, Mn) and the reflectance values of the samples (left: VNIR/SWIR, right: MWIR/LWIR).

A5.9.1: Variations of major absorption features in the VNIR/SWIR spectra of blast furnace slag samples (N = 6).

Feature		Position (nm)	Depth	Width (nm)	Area	Asymmetry
~ 400 nm	Mean	422	12.13	140.47	1710.39	0.33
	Min	400	7.39	120.95	894.11	-0.21
	Max	515	16.03	160.91	2075.27	0.49
~ 880 nm	Mean	880	0.55	122.85	74.15	0.32
	Min	873	0.26	93.49	23.86	0.14
	Max	884	1.16	170.89	198.36	0.45
~ 1290 nm	Mean	1292.8	0.11	55.52	7.90	-0.33
	Min	1287	0.07	31.32	2.15	-0.82
	Max	1296	0.20	140.55	28.70	-0.08
~ 1770 nm	Mean	1769.7	0.75	313.95	253.91	-0.72
	Min	1762	0.19	35.26	6.85	-0.97
	Max	1779	1.74	760.04	532.38	-0.50
~ 1930 nm	Mean	1926.5	5.34	377.40	1972.52	-0.46
	Min	1922	4.03	261.43	1732.00	-0.57
	Max	1930	6.72	468.40	2549.26	-0.31
~ 2220 nm	Mean	2224.7	2.42	125.79	304.96	0.22
	Min	2216	2.35	121.80	296.22	0.04
	Max	2235	2.51	129.07	316.65	0.34

A.5.9.2: Variations of major absorption features in the VNIR/SWIR spectra of “slag sand” samples (N = 6).

Feature		Position (nm)	Depth	Width (nm)	Area	Asymmetry
~ 400 nm	Mean	410	15.09	117.57	1816.36	0.30
	Min	396	9.69	73.14	991.11	0.13
	Max	418	21.59	138.74	2978.61	0.37
~ 1430 nm	Mean	1431	4.29	120.94	535.24	0.35
	Min	1426	1.96	97.60	191.42	0.21
	Max	1443	6.10	137.97	841.40	0.39
~ 1780 nm	Mean	1781.5	0.27	65.04	16.25	-0.41
	Min	1778	0.07	55.80	6.57	-0.92
	Max	1788	0.42	98.48	23.50	-0.12
~ 1930 nm	Mean	1928.5	17.26	141.09	2446.43	0.24
	Min	1925	12.05	124.76	1515.48	0.02
	Max	1934	20.47	171.05	3501.59	0.38
~ 2240 nm	Mean	2240	3.62	95.14	343.49	0.02
	Min	2234	2.48	79.29	196.66	-0.04
	Max	2243	4.70	108.97	453.14	0.07
~ 2475 nm	Mean	2474	0.98	50.72	50.91	-0.30
	Min	2467	0.58	42.47	24.67	-0.36
	Max	2480	1.43	58.01	82.96	-0.16

A.5.9.3: Variations of major absorption features in the VNIR/SWIR spectra of Thomas slag samples (N = 14).

Feature		Position (nm)	Depth	Width (nm)	Area	Asymmetry
~ 413 nm	Mean	413	16.04	173.02	3050.18	0.51
	Min	353	0.07	6.62	0.44	-0.16
	Max	505	32.44	257.22	6535.22	0.82
~ 714 nm	Mean	714	1.99	56.99	117.52	0.15
	Min	710	0.45	43.93	20.24	0.05
	Max	720	3.11	63.10	192.51	0.29
~ 1134 nm	Mean	1134	0.91	186.84	203.54	0.04
	Min	1075	0.05	41.55	1.91	-0.90
	Max	1162	2.11	240.94	507.96	0.83
~ 1413 nm	Mean	1413	2.44	114.37	535.94	0.13
	Min	1412	0.71	32.82	34.49	-0.22
	Max	1416	7.44	498.79	3713.21	0.44
~ 1940 nm	Mean	1940	2.91	184.68	451.11	0.24
	Min	1900	0.21	129.06	131.34	-0.06
	Max	1949	4.67	620.72	763.93	0.99
~ 2244 nm	Mean	2244	2.04	126.64	258.74	0.07
	Min	2225	1.75	122.99	218.64	-0.09
	Max	2261	2.45	138.08	338.72	0.28

A.5.9.4 Variations of major absorption features in the VNIR/SWIR spectra of stainless steel slag samples (N = 5) I.

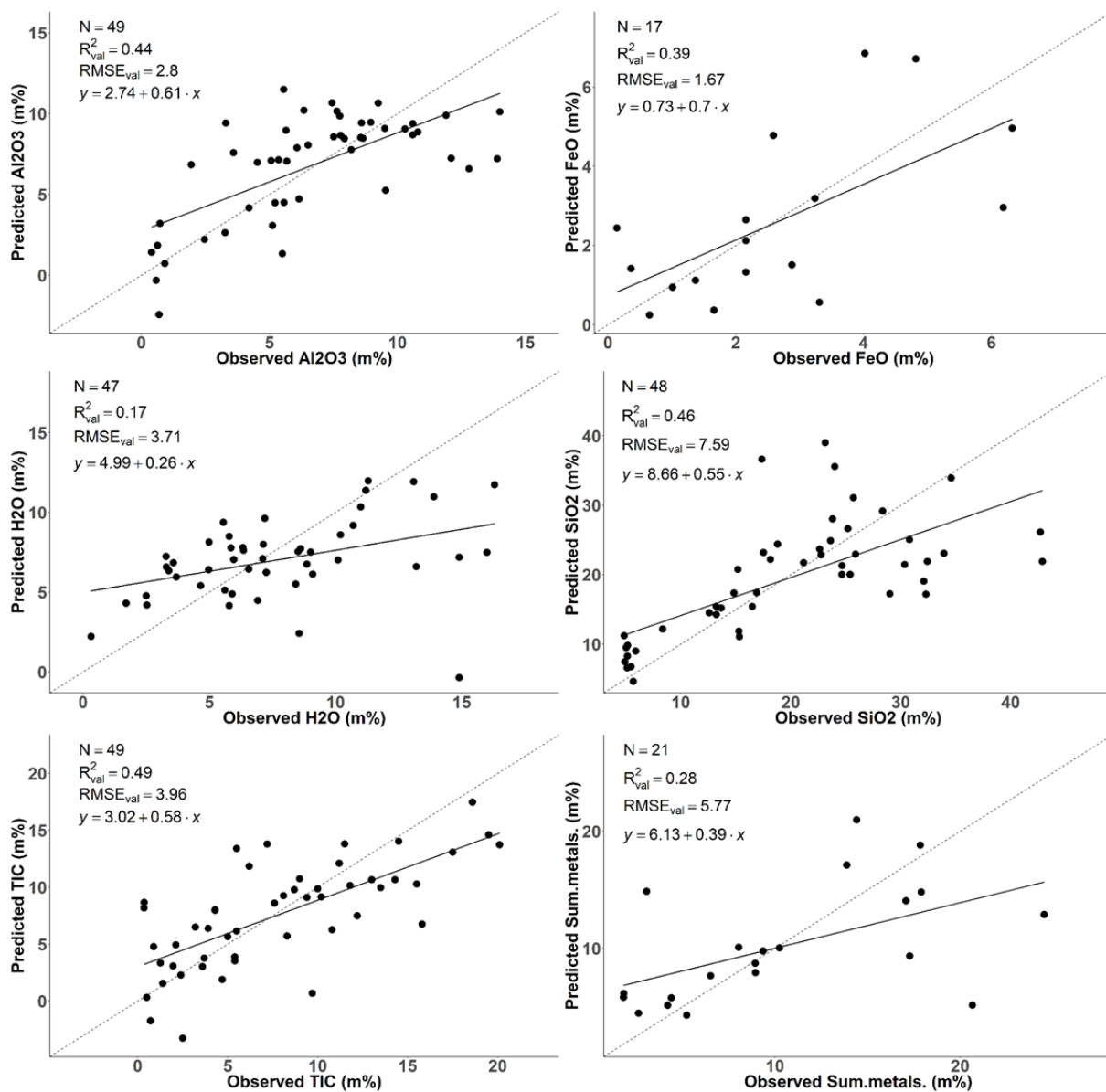
Feature		Position (nm)	Depth	Width (nm)	Area	Asymmetry
~ 378 nm	Mean	377.8	2.68	92.69	248.00	0.58
	Min	374	2.31	73.63	188.70	0.56
	Max	381	3.21	102.91	289.88	0.65
~ 424 nm	Mean	424.2	0.56	79.29	38.96	0.73
	Min	418	0.21	60.01	26.34	0.66
	Max	431	0.78	141.29	50.89	0.96
~ 592 nm	Mean	592.4	1.65	58.53	96.50	-0.01
	Min	590	1.53	57.20	90.91	-0.03
	Max	594	1.77	60.10	106.08	0.03
~ 697 nm	Mean	698	3.00	107.82	323.42	-0.37
	Min	693	2.33	101.95	246.38	-0.40
	Max	701	3.33	111.35	371.07	-0.35
~ 1207 nm	Mean	1208	0.00	8.78	0.01	0.04
	Min	1202	0.00	7.71	0.01	-0.15
	Max	1212	0.00	10.27	0.03	0.14
~ 1412 nm	Mean	1411.6	0.88	32.29	28.21	0.02
	Min	1411	0.30	24.93	7.58	-0.16
	Max	1413	1.39	40.25	42.29	0.13

A5.9.4: Variations of major absorption features in the VNIR/SWIR spectra of stainless steel slag samples (N = 5) II.

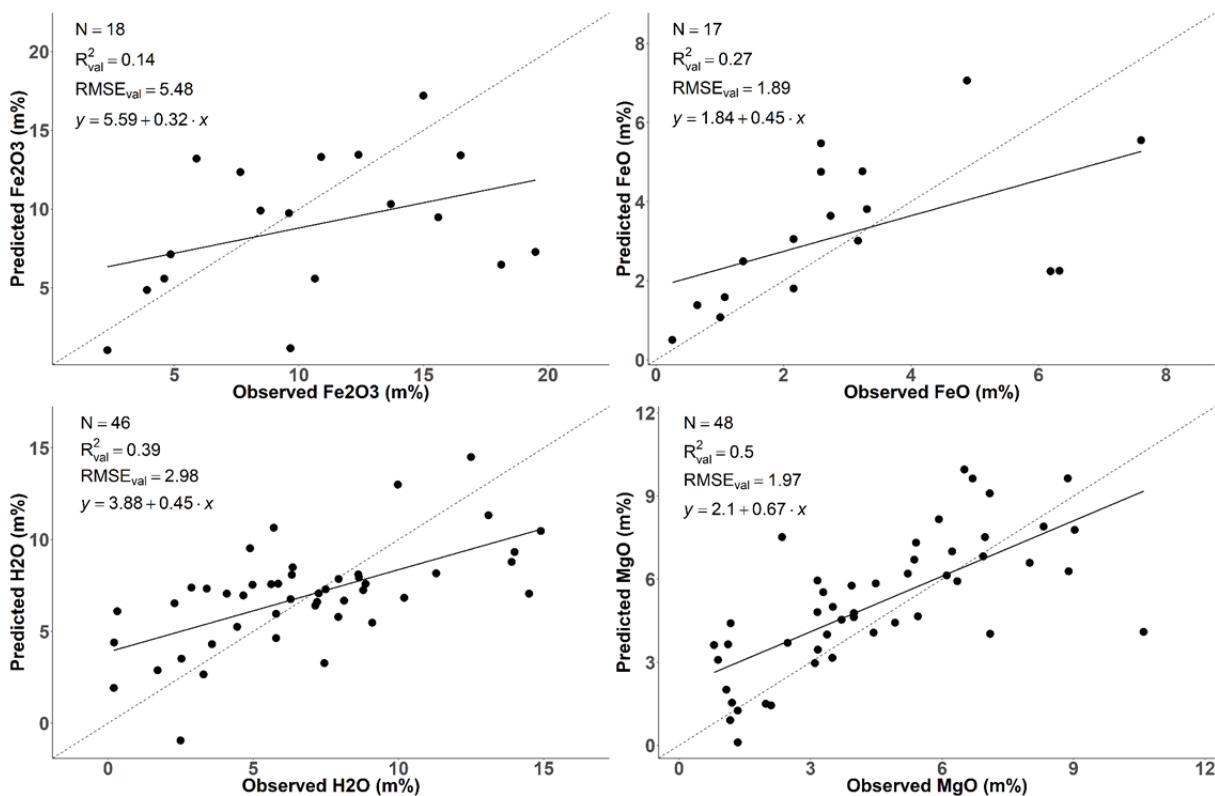
Feature		Position (nm)	Depth	Width (nm)	Area	Asymmetry
~ 1953 nm	Mean	1953.8	2.94	203.02	591.50	-0.06
	Min	1948	2.47	166.39	440.76	-0.35
	Max	1957	3.84	278.73	745.54	0.09
~ 2225 nm	Mean	2224.4	2.49	145.72	362.14	0.30
	Min	2224	2.39	134.50	339.68	0.23
	Max	2225	2.53	155.23	383.60	0.35
~ 2390 nm	Mean	2390	0.49	31.75	17.04	0.21
	Min	2388	0.08	17.94	1.47	0.01
	Max	2392	0.89	37.68	31.31	0.51

A5.9.5: Variations of major absorption features in the VNIR/SWIR spectra of converter sludge samples (N = 7).

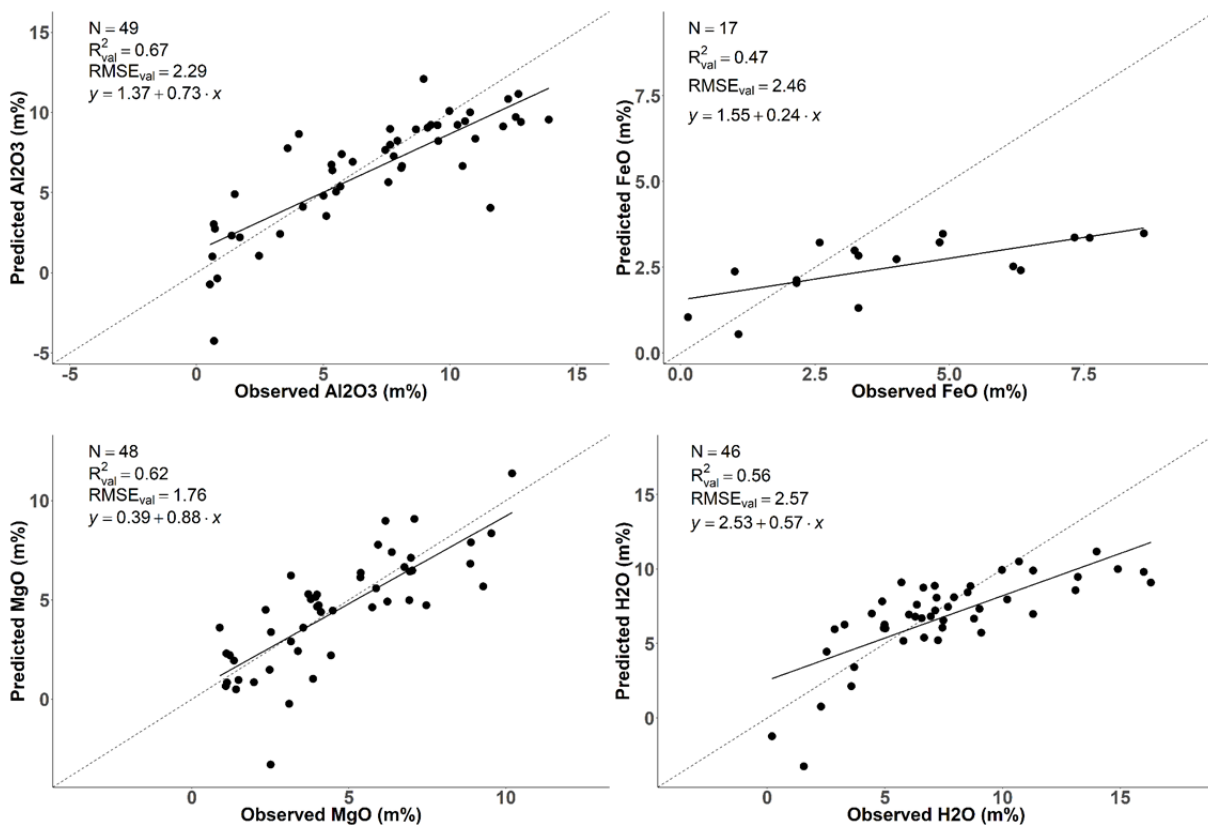
Feature		Position (nm)	Depth	Width (nm)	Area	Asymmetry
~ 494 nm	Mean	494	29.90	164.89	5317.80	-0.06
	Min	484	11.47	123.50	1416.84	-0.13
	Max	516	57.60	204.41	11774.09	-0.01
~ 1480 nm	Mean	1479.6	18.97	986.19	18830.29	0.15
	Min	1448	9.46	941.88	9322.47	0.11
	Max	1529	30.58	1029.62	31194.00	0.19
~ 2201 nm	Mean	2201.2	1.97	128.37	265.57	0.40
	Min	2183	0.88	48.97	43.00	-0.49
	Max	2212	2.45	195.70	347.96	0.82



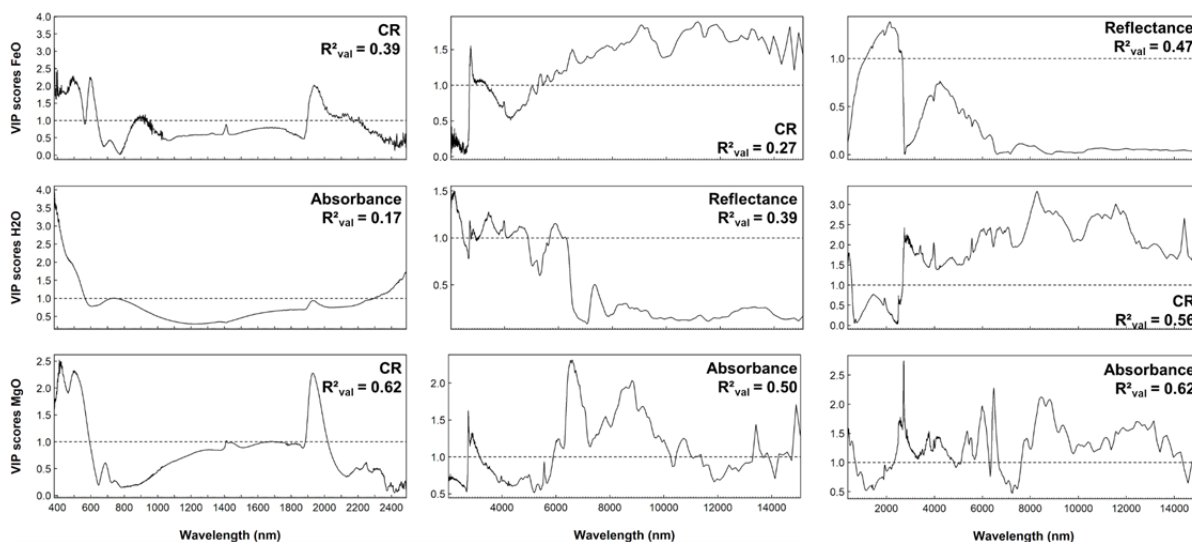
A5.10: PLSR results based on VNIR/SWIR spectra for selected iron- and steelworks by-product constituents.



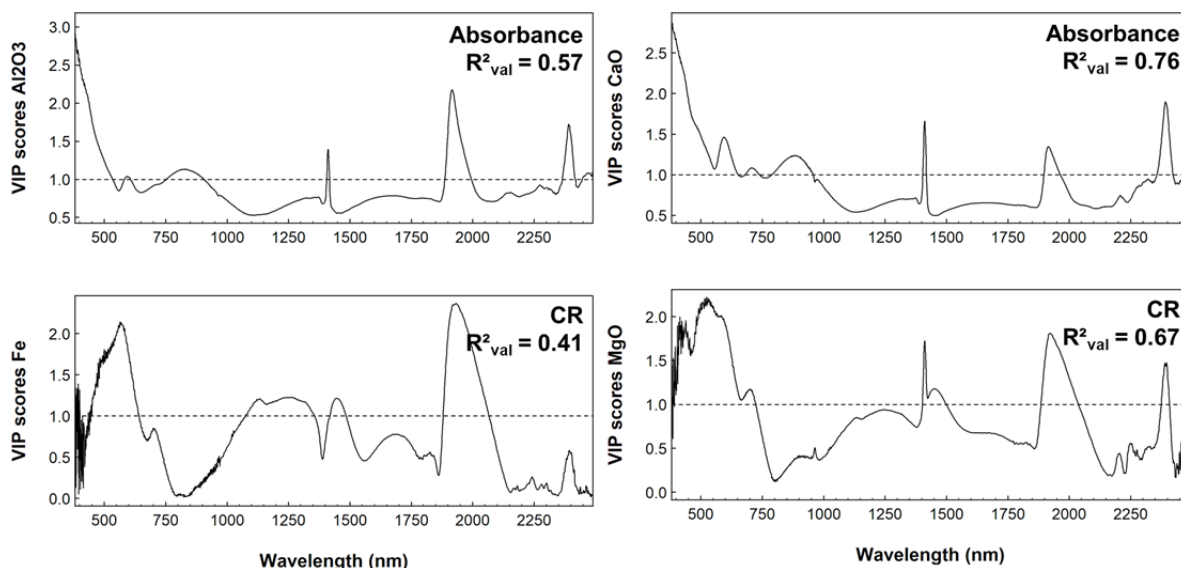
A5.11: PLSR results based on MWIR/LWIR spectra for selected iron- and steelworks by-product constituents.



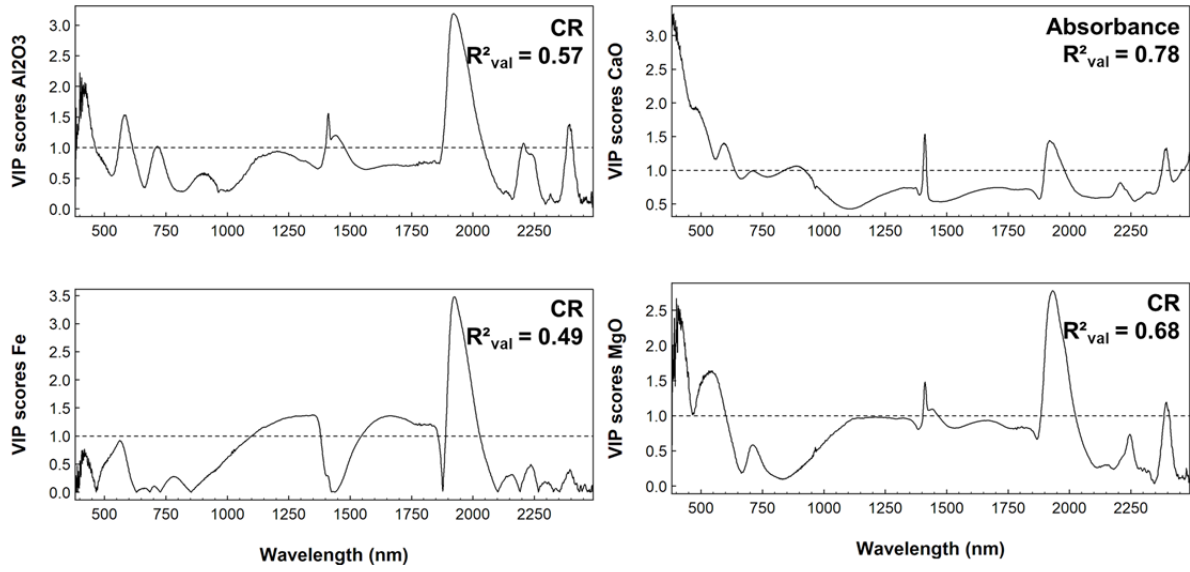
A5.12: PLSR results based on VNIR-LWIR spectra for selected iron- and steelworks by-product constituents.



A5.13: VIP scores for the best PLSR models obtained for Fe_{total}, H₂O and MgO using VNIR/SWIR, MWIR/LWIR as well as VNIR-LWIR spectra. R^2_{val} values and the preprocessing type (CR = continuum removal) utilised for building the specific models are additionally provided.



A5.14: VIP scores for the best PLSR models obtained for Al₂O₃, CaO, Fe_{total} and MgO using VNIR/SWIR spectra of air-dried but not further prepared sample material. R^2_{val} values and the preprocessing type (CR = continuum removal) utilised for building the specific models are additionally provided.



A5.15: VIP scores for the best PLSR models obtained for Al_2O_3 , CaO, Fe_{total} and MgO using VNIR/SWIR spectra of sample material with near *in situ* moisture. R^2_{val} values and the preprocessing type (CR = continuum removal) utilised for building the specific models are additionally provided.

Curriculum vitae Michael Denk

Name Michael Denk

Date and 14.08.1983

place of Birth Halle

Marital status Single

Languages German (mother tongue), English

Driv. lincence B

Work Experience

Since 2015 Scientific assistant in the Department of Remote Sensing and Cartography, Institute of Geosciences and Geography, Martin Luther University Halle-Wittenberg

2012 - 2015 Research associate in the project REStRateGIS (Conception and development of a resource land register for smeltery heaps applying geoinformation technologies and new strategies for recycling of resources) funded by the German Federal Ministry of Education and Research (BMBWF, funding code 033R103B)

2007-2011 Scientific Assistant in the departments Remote Sensing and Cartography and Physical Geography at the Institute of Geosciences and Geography

2006-2008 Student Assistant in the “Universitäts- und Landesbibliothek Sachsen-Anhalt“

Job-related Skills

- Processing and analysis of multispectral- and airborne and terrestrial hyperspectral imagery in geological and mineralogical mining related contexts
 - Laboratory and field reflectance measurements of minerals, rocks and soils as well as industrial by-products (e.g. slags, sludge and ashes) and vegetation
 - Qualitative and quantitative spectral analysis including chemometrical approaches
 - Spectral characterization of iron and steel work by-products for the detection of reusable raw materials in dump sites
 - Participation in interdisciplinary research activities related to geochemistry, geology and soil sciences in Azerbaijan, Burkina Faso and Uzbekistan
 - Trained in commercial (ArcGIS from ESRI, ENVI, ERDAS IMAGINE) and open source GIS and remote sensing software (QGIS, SAGA GIS)
-

Education and Training

2013/2014 Multiple research stays at the Virtual Outcrop Geology Group at the Centre for Integrated Petroleum Research (Uni Research CIPR), Bergen, Norway
Participant at the workshop “Hyperspectral Applications for Soil - A Demonstration and Practical Exercise for Modelling Soil Spectral Information” (DePeMossi) at the GFZ Potsdam

2011

2009 Summer school attendee of the Hyperspectral Imaging Network (Hyper-I-Net) in Pavia/Italy

2008 Internship at the Leibniz Centre for Agricultural Research
Internship at the Messel Pit research station

2003-2011	Martin Luther University Halle-Wittenberg (MLU), Institute of Geosciences and Geography, Diploma in Geography (Geography major subject, soil Science and Geology minor subjects), Intermediate diploma Diploma thesis “Reflexionsspektrometrische Inventarisierung mineralischer Oberflächen und sekundärer Mineralneubildungen in der Bergbaufolgelandschaft bei Teutschenthal”
2003	Abitur at the “Landesgymnasium Latina August Herrmann Francke”

Honours and awards

2011-2012:	PhD scholarship from the Graduate Scholarship Program of Saxony-Anhalt Winner of the “Karl-Kraus Junior Researcher Award” of the German Society for Photogrammetry, Remote Sensing and Geoinformation (DGPF), the Austrian Society for Surveying and Geo-information (OVG) and the Swiss Society for Photogrammetry and Remote Sensing (SGPF-SSPT)
2010	

Publications

Journal articles	<p>Riedel, F., <u>Denk, M.</u>, Müller, I., Barth, N., Gläßer, C. (2018): Prediction of soil parameters using the spectral range between 350 and 15,000 nm: A case study based on the Permanent Soil Monitoring Program in Saxony, Germany. <i>Geoderma</i> 315, 188-198, https://doi.org/10.1016/j.geoderma.2017.11.027.</p> <p>Götze, C., <u>Denk, M.</u>, Riedel, F., Gläßer, C. (2017): Interlaboratory Comparison of Spectrometric Laboratory Measurements of a Chlorite Rock Sample. <i>PFG</i> 85(5), 307-316, https://doi.org/10.1007/s41064-017-0031-2.</p> <p>Nühlen, J., <u>Denk, M.</u>, Gläßer, C., Teuwsen, S. & Algermissen, D. (2016): Sekundärrohstoffe in Hüttenhalden. Das Projekt REStrateGIS zeigt neue Strategien zur Haldendetektion und –analyse auf Basis von Geoinformationstechnologien auf. <i>ReSource – Abfall, Rohstoff, Energie. Fachzeitschrift für nachhaltiges Wirtschaften</i>, 29(3), 4-15.</p> <p><u>Denk, M.</u>, Gläßer, C., Kurz, T. H., Buckley, S. J. & Drissen, P. (2015): Mapping of iron and steelwork by-products using close range hyperspectral imaging: A case study in Thuringia, Germany. <i>European Journal of Remote Sensing, Vertical Geology Conference VGC-14 Special issue</i>, 48, 489-509, doi: 10.5721/EuJRS20154828.</p> <p>Witzke, T. & <u>Denk, M.</u> (2011): Eine temporäre Mirabilit-Mineralisation bei Teutschenthal, Sachsen-Anhalt. In: <i>Der Aufschluss. Zeitschrift für Mineralogie und Geologie</i>. 62 (2011), 353-360.</p>
Book contributions	<p>Nühlen, J., Mrotzek-Blöß, A., Jandewerth, M., <u>Denk, M.</u>, Gläßer, C., Algermissen, D., Mudersbach, D., Teuwsen, S., Müterthies, A. (2016): 21. REStrateGIS – Konzeption und Entwicklung eines Ressourcenkatasters für Hüttenhalden durch Einsatz von Geoinformationstechnologien und Strategieentwicklung zur Wiedergewinnung von Wertstoffen. In: Dürkoop, A., Brandstetter, C. P., Gräbe, G., Rentsch, L.: <i>Innovative Technologien für Ressourceneffizienz – Strategische Metall und Mineralien. Ergebnisse der r3-Fördermaßnahme</i>. Fraunhofer Verlag, 311-328, ISBN: 978-3-8396-1102-9.</p> <p>Nühlen, J., <u>Denk, M.</u>, Gläßer, C., Teuwsen, S. & Algermissen, D. (2016):</p>

Sekundärrohstoffe in Hüttenhalden – Strategien zur Haldendetektion und -analyse auf Basis von Geoinformationstechnologien. In: Thomé-Kozmiensky, K. J. (Hrsg.): Mineralische Nebenprodukte und Abfälle, Band 3. Neuruppin: TK Verlag Karl Thomé-Kozmiensky, 2016, 359-382, ISBN: 978-3-944310-28-2.

Jandewerth, M., Denk, M., Gläßer, C., Mrotzek, A. & Teuwsen, S. (2013): Reduktion von Rohstoffimporten durch Wertstoffgewinnung aus Hüttenhalden - Entwicklung eines multiskalaren Ressourcenkatasters für Hüttenhalden. In: Karl J. Thomé-Kozmiensky [Ed.]: Aschen - Schlacken - Stäube. Aus Abfallverbrennung und Metallurgie. TK Verlag, Neuruppin, 639-657, ISBN: 978-3-935317-99-3.

Denk, M.; Gläßer, C.; Jung, A. & Götze, C. (2010): Einsatz von Reflexionsspektrometrie und HyMap-Daten zur Erfassung geochemischer Parameter in der Bergbaufolgelandschaft bei Teutschenthal (westl. v. Halle/Saale). 30. Wissenschaftlich-Technische Jahrestagung der DGPF, 01.-03.07.2010, Conference proceedings, 440 – 446.

Selected oral presentations	<p>Denk, M., Riedel, F., Gläßer, C., Drissen, P., Algermissen, D., Mudersbach, D. (2017): Prediction of Chemical Properties of Various Iron and Steelwork By-products Based on VNIR/SWIR and MWIR/LWIR Reflectance Spectra. 10th EARSeL SIG Imaging Spectroscopy Workshop, 19.-21.04.2017, Zurich.</p> <p>Denk, M., Gläßer, C., Drissen, P., Mudersbach D., Algermissen, D. (2015): Analysis of iron and steelwork by-products using reflectance spectroscopy and hyperspectral imaging: A multi scale approach. GRSG AGM, 09.-11.12.2015, Frascati.</p> <p>Denk, M., Gläßer, C., Kurz, T. H., Buckley, S. J., Mudersbach D., Drissen, P. (2015): Hyperspectral analysis and mapping of iron and steelwork by-products. 9th EARSeL SIG Imaging Spectroscopy Workshop, 14.-16.04.2015, Luxemburg.</p> <p>Denk, M. & Gläßer, C. (2015): Hyper- und multispektrale Fernerkundungsmethoden zur Analyse von Industrie- und Bergbauhalden. BGR-Statusseminar „Forschungsaufträge im Bereich der Rohstoff- und Lagerstättenforschung“, 22.-23.07.2015, Hannover.</p> <p>Denk, M., Gläßer, C., Kurz, T. H., Buckley, S. J., Mudersbach, D., Drissen, P. (2013): Hyperspectral analysis of materials from iron and steel production using reflectance spectroscopy in a case study in Thuringia, Germany. GRSG AGM 2013 - Status and Developments in Geological Remote Sensing, 09.-11.12.2013, Berlin.</p> <p>Denk, M., Götze, C., Gläßer, C., Jung, A. (2013): SpecTour – Neue Ergebnisse aus dem Ringversuch zum Vergleich laborspektrometrischer Messungen. Dreiländertagung D - A - CH und 33. Wissenschaftlich-Technische Jahrestagung der DGPF, 27.02.-01.03.2013, Freiburg.</p> <p>Denk, M. & Gläßer, C. (2012): From Point to Pixel. Systematic Variation of Spectral Information in Lab and Field Measurements. 31. EAGE/GRSG</p>
-----------------------------	--

	Remote Sensing Workshop & Exhibition, 03.-05.09.2012, Paris.
	Denk, M. & Gläßer, C. (2011): Reflexionsspektrometrische Erfassung von Stoffausträgen aus Kalihalden am Beispiel der Bergbaufolgelandschaft bei Teutschenthal. 31. Wissenschaftlich-Technische Jahrestagung der DGPF, 13.-15.04.2011, Mainz.
	Denk, M. & Gläßer, C. (2011): Mapping of environmental impacts of salt mining dumps in Central Germany using spectroradiometric methods. 7th EARSeL SIG - Imaging Spectroscopy Workshop, 11.-13.04.2011, Edinburgh.
Selected poster presentations	Denk, M. & Gläßer, C. (2016): Mapping mining heaps using multi- and hyperspectral remote sensing: A case study in the Mansfelder Land region in Central Germany. 5. gemeinsame Jahrestagung der Arbeitskreise Fernerkundung der Deutschen Gesellschaft für Geographie (DGfG) e.V. und Auswertung von Fernerkundungsdaten der Deutschen Gesellschaft für Photogrammetrie, Fernerkundung und Geoinformation (DGPF) e.V., „Landschafts-prozessmonitoring mittels Multisensordaten“, 29.-30.09.2016, Halle.
	Denk, M., Gläßer, C., Kurz, T.H., Buckley, S.J., Mudersbach, D., Drissen, P. (2016): Exploration of Raw Materials in Dump Sites – A New Hyperspectral Approach. 36th EARSeL Symposium, 20.-24.06.2016, Bonn.
	Denk, M. & Gläßer, C. (2015): Mapping mining heaps using multi- and hyperspectral remote sensing: A case study in the Mansfelder Land region in Central Germany. GRSG AGM, 09.-11.12.2015, Frascati.
	Denk, M., Götze, C., Gläßer, C. (2015): SpecTour - Impacts of variability in spectral measurement setups on mineral absorption features. 9th EARSeL SIG Imaging Spectroscopy Workshop, 14.-16.04.2015, Luxemburg.
	Schulz, R., Denk, M., Gläßer, C., Kurz, T.H., Buckley, S.J., Drissen, P., Paasche, H. (2015): Geophysikalische und reflexionsspektrometrische Untersuchung eines Haldenkörpers aus der Eisen- und Stahlindustrie: Eine Multisensor-Fallstudie in Thüringen. 75. Jahrestagung der Deutschen Geophysikalischen Gesellschaft, 23.-26.03.2015, Hannover.
	Denk, M., Gläßer, C., Kurz, T. H., Buckley, S. J., Mudersbach, D., Drissen, P. (2014): Exploration of raw materials in dump sites - a new hyperspectral approach. Geological Remote Sensing Group (GRSG) Annual General Meeting (AGM) 2014 "25 Years of Geological Remote Sensing, 15.-17.12.2014, London.
	Denk, M., Gläßer, C, Kurz, T. H., Buckley, S., Mudersbach, D., Drissen, P. (2014): Detection of raw materials in waste sites from iron and steel production using multi-scale spectral and lidar measurement: Case study from Thuringia, Germany. Vertical geology conference 2014 (VGC-14) "From remote sensing to 3D geological modelling", 06.-07.02.2014, Lausanne.
	Denk, M., Gläßer, C., Kurz, T.H., Buckley, S.J., Mudersbach, D., Drissen, P. (2014): Detection of raw materials in waste sites from iron and steel

- production using multi-scale spectral and lidar measurement: Case study from Thuringia, Germany. r³-Statusseminar/5. Urban Mining Kongress, 11.-12.06.2014, Essen.
- Denk, M., Gläßer, C., Götze, C., Jung, A. (2013): SpecTour – New results from the international round robin test for the comparison of spectroscopic laboratory measurements. 8th EARSeL SIG Imaging Spectroscopy Workshop, 08.-10.04.2013, Nantes.
- Denk, M., Gläßer, C., Götze, C. (2013): SpecTour - Analysis of spectral variations of a chlorite rock sample within the international round robin test for the comparison of spectroscopic laboratory measurements. GRSG-Meeting "Status and Developments in Geological Remote Sensing", 09.-11.12.2013, Berlin.
- Denk, M. & Gläßer, C. (2011): Comparison of field spectra and Hymap spectra in terms of the detection of gypsum –a case study in a small scale heterogeneous environment. GRSG and OGEO AGM, 07.-09.12.2011, Frascati.
- Denk, M. (2011): Reflexionsspektrometrische Inventarisierung mineralischer Oberflächen und sekundärer Mineralneubildungen in der Bergbaufolgelandschaft bei Teutschenthal. 31. Wissenschaftlich-Technische Jahrestagung der DGPF, 13.-15.04.2011, Mainz.
- Denk, M., Schwefel, D., Jung, A., Gläßer, C. (2010): Spectroradiometric mineral mapping at the Teutschenthal potash salt mining site (Central Germany). 30. Wissenschaftlich-Technische Jahrestagung der DGPF, 01.-03.07.2010 Wien.
- Denk, M., Schwefel, D., Jung, A., Gläßer, C. (2010): Spectroradiometric mineral mapping at the Teutschenthal potash salt mining site (Central Germany). ESA Hyperspectral Workshop, 17.03.-19.03.2010, Frascati.
- Denk, M., Schwefel, D., Jung, A., Gläßer, C. (2009): Spectroradiometric mineral mapping at the Teutschenthal potash salt mining site (Central Germany). GRSG AGM 2009 "Exploration Remote Sensing", 15.12.-17.12.2009, London.
- Denk, M., Gläßer, C., Jung, A., Schwefel, D. (2009): Spektroradiometrische und geochemische Untersuchungen an der Kalirückstandshalde bei Teutschenthal (westlich von Halle). 87. Jahrestagung der Deutschen Mineralogischen Gesellschaft, 13.09.-16.09.2009, Halle (Saale).
-

Date / Datum

Signature of the applicant / Unterschrift des Antragstellers

Declaration Under Oath / Eidesstattliche Erklärung

I declare under penalty of perjury that this thesis is my own work entirely and has been written without any help from other people. I used only the sources mentioned and included all the citations correctly both in word or content.

Ich erkläre an Eides statt, dass ich die Arbeit selbstständig und ohne fremde Hilfe verfasst, keine anderen als die von mir angegebenen Quellen und Hilfsmittel benutzt und die den benutzten Werken wörtlich oder inhaltlich entnommenen Stellen als solche kenntlich gemacht habe.

Date / Datum

Signature of the applicant / Unterschrift des Antragstellers